The Radio Properties of Brightest Cluster Galaxies

HOGAN, MICHAEL,TIMOTHY

The Radio Properties of Brightest Cluster Galaxies

Michael Timothy Hogan

Abstract

Energetic feedback from the Active Galactic Nucleus (AGN) of the Brightest Cluster Galaxy (BCG) is required to prevent catastrophic cooling of the intra-cluster medium (ICM) in galaxy clusters. Evidence for this is seen through the inflation of cavities in the ICM by AGN-launched, radio-emitting jets, and understanding this process is an active area of research. Radio observations play an integral role in this, as they trace the active stages of the feedback cycle. Understanding the radio properties of BCGs is therefore paramount for understanding both galaxy clusters and AGN feedback processes globally.

Within this thesis, the BCGs in a large ($>$700) sample of X-ray selected clusters are studied. We observe these BCGs with a wide variety of facilities, building a census of their radio properties across a range of frequencies, timescales and angular resolutions. Radio spectral energy distributions (SEDs) are built for over 200 BCGs, and then decomposed into two components; a core, attributable to ongoing nuclear activity, and a non-core, attributable to historical accretion. Both components are not only more common, but also significantly more powerful in cool-core (CC) clusters than non-cool core (NCC) clusters. However, it is the presence of an *active* core that shows BCGs in CC clusters are constantly 'on' - explaining how they regulate their environments over gigayear timescales.

We observe 35 currently active BCGs at high (15 – 353 GHz) radio frequencies, and monitor their variability. Self-absorbed, active components are found to be common at high frequency. Little variability is seen on $<$year timescales, although longer term variation of $\approx$10% annually over few-decade timescales is observed. Evidence is presented for a hitherto unseen component in BCG spectra that may be attributable to a naked Advection Dominated Accretion Flow (ADAF). The milli-arcsecond scale radio properties of 59 sources are studied, with a large range of morphologies recovered although no evidence

is found for dual AGN being common in BCGs.

Finally, we present a study that has more than doubled the number of HI absorption systems known in BCGs. We show that both the detection rate and column densities observed are strongly affected by the multi-scale properties of the radio continuum. All our clear detections are redshifted or at the systemic velocity. Most HI appears to be located in a clumpy torus that is replenished by residual material cooling from the ICM, linking the environment to the central engine and completing the feedback cycle.

The Radio Properties of Brightest Cluster Galaxies

Michael Timothy Hogan

A thesis presented in accordance with the regulations for admittance to the degree of Doctor of Philosophy

Extragalactic Astronomy
Department of Physics
Durham University
United Kingdom

September 2014

To Ruth,

who once wanted to speak to somebody about Physics.

Declaration

The work described in this thesis was undertaken between October 2010 and September 2014 while the author was a research student under the supervision of Dr. Alastair C. Edge in the Department of Physics at Durham University. No part of this thesis has been submitted for any other degree at Durham University or any other university.

Sections of this thesis appear, or will appear, in the following papers:

- "A Comprehensive Study of the Radio Properties of Brightest Cluster Galaxies", M. T. Hogan, A. C. Edge, J. Hlavacek-Larrondo, K. J. B. Grainge, S. L. Hamer, E. K. Mahony, H. R. Russell, A. C. Fabian, B. R. McNamara and R. J. Wilman, 2014a, MNRAS, submitted

- "High Radio Frequency Properties and Variability Properties of Brightest Cluster Galaxies", M. T. Hogan, A. C. Edge, J, E Geach, K. J. B. Grainge, J. Hlavacek-Larrondo, T. Hovatta, A. Karim, B. R. McNamara, C. Rumsey, H. R. Russell, P. Salomé, H. D. Aller, M. F. Aller, D. J. Benford, A. C. Fabian, A. C. S. Readhead, E. M. Sadler and R. D. E. Saunders, 2014b, MNRAS, submitted

- "The Parsec-Scale Radio Properties of Brightest Cluster Galaxies - A VLBA Survey", M. T. Hogan *et al.* in prep.

- "A survey of HI Absorption against Compact Radio Cores in Brighest Cluster Galaxies", M. T. Hogan *et al.* in prep.

The work described in Chapters 3–6 was performed in collaboration with others (listed above). This work utilises data from a range of observing proposals. The proposal codes for these and the Principal Investigator (P.I.) for each are clearly stated in the relevant sections (in almost all cases, the relevant P.I. is Dr. Alastair Edge, Durham). All of the data presented for the first time in this thesis or within the above papers were reduced and analysed by the author, with the following exceptions:

- The SCUBA-2 data in Chapter 4 were reduced and supplied by Dr. James Geach (University of Hertfordshire)

- The OVRO data in Chapter 4 were supplied by Dr. Talvikki Hovatta and Prof. Anthony Readhead (Caltech)

- The WSRT data in Chapter 6 were reduced and supplied by Dr. Raymond Oonk (ASTRON)

So far as possible, all of the text has been written by the author. However, as stated, Chapters 3 and 4 were adapted from the papers listed above and hence some short sections may remain that were initially written by a collaborator and have been only edited by the author. Instances of this are believed to be limited to paragraph 2 of Section 3.3.4 (description of cavity power calculation), Section 4.3 (sample selection for Hogan *et al.* 2014b), paragraph 2 of Section 4.4.4 (description of OVRO), Section 4.4.5 (description of SCUBA-2 data reduction).

In addition to the work presented in this thesis, the author has also been involved in the following work during the period of their PhD:

- "A Non-Thermal Study of the Brightest Cluster Galaxy NGC 1275 - the Gamma-Ray Connection over Four Decades", Dutson K .L., Edge A. C., Hinton J. A., Hogan M. T., Gurwell M. A., Alston W. N., MNRAS 442 2048

- "The State of the Warm and Cold Gas in the Extreme Starburst at the Core of the Phoenix Galaxy Cluster (SPT-CLJ2344-4243)", McDonald M., Swinbank A. M., Edge A. C., Wilner D. J., Veilleux S., Benson B. A., Hogan M. T., Marrone D. P., McNamara B. R., Wei L. H., Bayliss M. B., Bautz M. W. 2014 ApJ 784 18

- "Radiative efficiency, variability and Bondi accretion on to massive black holes: the transition from radio AGN to quasars in brightest cluster galaxies", Russell H. R., McNamara B. R., Edge A. C., Hogan M. T., Main R. A., Vantyghem A. N., 2013 MNRAS 432 530

- "A stacked analysis of brightest cluster galaxies observed with the Fermi Large Area Telescope", Dutson K. L., White R. J, Edge A. C., Hinton J. A., Hogan M. T., 2013 MNRAS 429 2069

- "On the hunt for ultramassive black holes in brightest cluster galaxies", Hlavacek-Larrondo J., Fabian A. C., Edge A. C., Hogan M. T., 2012 MNRAS 424 224

- "Extreme AGN Feedback in the MAssive Cluster Survey: a detailed study of X-ray cavities at $z>0.3$", Hlavacek-Larrondo J., Fabian A. C., Edge A. C., Ebeling H., Sanders J. S., Hogan M. T., Taylor G. B., 2012 MNRAS 421 1360

Acknowledgements

As whoever is reading this will have noticed, a PhD is a rather chunky volume of work. This one would not have been possible without the help of a whole host of amazing people, and whilst there are far too many of you to name personally, you know who you are and I'll always be grateful to you for not only supporting me through the writing of this thesis but also for making life great along the way. That said, there are a few people who I'd like to give special thanks to, without whom this thesis wouldn't exist.

Firstly I would like to thank my supervisor, Alastair Edge, whose help, support and enthusiasm (not to mention endless patience in answering my many questions) have made this work possible. He has provided me with remarkable guidance as well as the freedom to pursue my own ideas, providing countless opportunities for me to grow as both a researcher and as a person. I look forward to many years of continued collaboration, and am proud to consider him not just a mentor, but a friend.

Throughout the four years I've worked on this PhD I've been lucky enough to collaborate with a lot of fantastic people. I'd like to thank them all for their much appreciated help and feedback, and want to give special thanks to Julie Hlavacek-Larrondo, Keith Grainge, Helen Russell and Brian McNamara for their support, advice and most of all for not being afraid to tell me when I'm just plain wrong. I'd also like to thank Alex Karim, not only for useful discussions and valuable career advice but also for giving me the opportunity to gain sub-mm experience observing with the JCMT, as well as my fourth year project supervisor Chris Done, who introduced me to the joy of research (and perhaps fashioned a lifelong fear of whiteboards). Many thanks also to my office mates both past and present, who have cheered me, put up with me and generally made Office 303 *the* place to be.

Whilst a PhD sometimes feels like it can take over your life, there is (unbelievably)

a world outside of it. I would like to thank all of my friends, both within the department and outside of it, for keeping me sane(ish) and generally being great and making life fun.

As the saying goes, you can't choose your family. However, if I ever did have the choice, I would choose mine. You've all been there for me throughout my life, and your love and support have made me who I am. For the advice, encouragement, visits, parties, DAUNOs, knowing that I like the big mug for my coffee, and everything else - I thank you all. Especially, I want to thank my Mum, Dad and Vicci. You've made me laugh, listened to me moan, kept me grounded and enabled me to fly. I love you all and I wouldn't be anywhere without you three.

Finally I would like to thank my wonderful wife Ruth, who has been there for me and whose love and support have been more important than anything. Marrying you was by far the proudest moment of my life, and every day I'm excited by the adventures that I get to share with you. On a final note - I still can't believe you convinced me to get a cat, although to be fair, she's all right (but you still have to teach her to bark).

Contents

List of Tables

List of Figures

CHAPTER 1

Introduction

1.1 Overview

Throughout the history of mankind people have gazed at the heavens with wonder, yet for most of this time the study of the cosmos was limited to the spectral range detectable by the human eye. It is less than a century since our window on the Universe was expanded beyond these boundaries with the first detection of radio waves from an extra-terrestrial source. Since then, new technologies and detection methods have opened up all sections of the electromagnetic spectrum (and beyond) to interrogation, and with it we have come to appreciate that the Universe contains objects and processes of more variety and peculiarity than had ever been imagined.

On the largest scales the Universe is comprised of galaxies distributed along a web-like structure according to the laws of gravity. At the nodes of this web, galaxies tend to group together and orbit their combined centre of mass. Once virialised, and massive enough, such a conglomeration is referred to as a galaxy cluster and, being bound, such structures constitute the largest single organised objects anywhere in the known Universe.

It is believed that every galaxy has, residing at its centre, a supermassive black hole (SMBH). As material accretes onto these SMBHs, its gravitational energy is released, leading to the phenomena now referred to as Active Galactic Nuclei (AGN). Once considered interesting peculiarities, over the past three decades both observational and theoretical work have shown that virtually all massive galaxies are at some point during their lifetimes expected to contain AGN. Furthermore, the energy generated by such events appears to play an integral role in the formation and evolution of all massive galaxies and their surroundings. Understanding the interplay between the energy generated by AGN

and the effect this has on its surroundings has thus grown to become a highly active area of astronomical research (see reviews by McNamara & Nulsen, 2007; Cattaneo et al., 2009; Alexander & Hickox, 2012; Fabian, 2012; McNamara & Nulsen, 2012; Heckman & Best, 2014). Radio observations play an important role within this, as they can be used to trace the energetic outflows and relativistic jets by which much of the AGN energy is imparted into its surroundings.

Some of the best laboratories for studying this so-called 'AGN-feedback' are found at the centres of galaxy clusters. Here, the AGN action of the largest galaxies anywhere in the known universe, Brightest Cluster Galaxies (BCGs), governs the properties of the cluster on scales many orders of magnitude larger than the AGN itself.

This thesis uses a wide variety of radio observations from a range of facilities in order to better understand the processes at play in the heart of these Universal behemoths. This first chapter gives a general overview of the topics to be covered. Initially, brief histories of radio astronomy and the discovery of galaxies and AGN are given. Following this is a summary of the properties of galaxies, clusters and AGN that will be referred to in the rest of the thesis. An overview of the current knowledge of the properties of Brightest Cluster Galaxies (BCGs) is then given before a brief overview of the techniques used within the thesis. An outline of the structure of the rest of the thesis is given beyond this.

1.2 The History of Radio Astronomy

1.2.1 Laying the Foundations

Ever since the mid-seventeenth century when Newton showed white light to be composed of multiple colours, scientists have been fascinated by the changing properties of radiation as a function of wavelength (λ). The first secure evidence that light also exists at frequencies outside of those visible to the human eye came around the end of the eighteenth century when William Herschel showed in a series of experiments that heat is radiated by wavelengths beyond the red end of the visible spectrum (i.e. in the 'infra-red'; Herschel, 1800). The spectral coverage was expanded essentially indefinitely by Maxwell in the late 1800s with his electromagnetic description of light, in which he showed that electromagnetic radiation could theoretically be produced (and hence detected) at any

wavelength. The first successful transmission of electromagnetic waves ('radio-waves, $\approx$5m) was achieved by Hertz in 1888, this wavelength being firmly in the radio regime ($\lambda \gtrsim$ mm) and hence ushering radio-waves into the scientists' arsenal.

As it was then believed that radiation from astronomical sources would be thermal, early attempts to detect extraterrestrial radio-waves focused on the Sun. Several attempts were made towards the end of the nineteenth century (e.g. by Edinson, Lodge, Nordmann, Wilsing and Scheiner). However all met with failure, largely due to inadequate detectors. This early lack of success, combined with contemporaneous theoretical advancements that suggested the blackbody profile of the Sun would emit very weakly at radio wavelengths and that the ionosphere would block most incoming radiation[1] meant that further detection experiments were largely abandoned. It would be another couple of decades before radio-astronomy truly began, somewhat serendipitously.

1.2.2 The Beginnings

In the 1920s Bell Telephone Laboratories assigned a young engineer, Karl J Jansky, the task of investigating sources of interference to their transatlantic radio links. To enable his investigation, Jansky built a steerable antenna with an operating frequency of 20.5 Megahertz (MHz). His initial results suggested three major sources of interference - local thunderstorms, distant thunderstorms and a more peculiar 'hiss', the amplitude of which appeared to vary with a one-day period. Initially the source of this cosmic hiss was assumed to be the long-sought detection of radio-waves from the Sun (First published Jansky 1932, re-published in Jansky, 2005). Continued observations throughout 1932/33 however showed the period to be not one solar day but instead one sidereal day, and the direction of the noise to be roughly from the constellation Sagittarius and thus it was realised that the source was outside of the Solar System (Jansky, 1933b,a). Although with hindsight this discovery is now considered one of the cornerstones of early radio astronomy (and even at the time it was front-page news in the New York Times, 5th May 1933),

[1] It is now known that radio-waves of most wavelengths can propagate quite freely through the atmosphere. However, stability of the ionosphere continues to be an issue that has to be corrected for, not least at long wavelengths. Furthermore, reflection from the ionosphere does place a lower limit to the achievable frequencies observable from Earth of around 10 MHz.

most contemporary astronomers were skeptical. Furthermore, Bell Laboratories found no practical use for the noise and after Jansky was re-assigned it was up to an amateur radio aficionado to take up the mantle.

Grote Reber was a radio enthusiast who openly admitted that after having contacted fellow enthusiasts on all six inhabited continents (a 'worked all continents' award) that he did not have any more "worlds to conquer". Instead, spurred on by an interest piqued by reading Jansky's papers he decided to devote his efforts to external worlds. At his own expense Reber built the world's first dedicated radio astronomy telescope in his own back garden - a $\approx$9.5m parabolic dish, which he completed circa 1937. The general belief that extraterrestrial sources would emit thermally and hence blackbody radiation would be highest at higher frequencies still persisted and meant that Reber's early efforts to use his instrument were at the highest frequencies technically feasible at the time (3.3 GHz, later 910 MHz). Although these attempts failed Reber persisted, eventually managing to map the sky at radio wavelengths for the first time, initially at 162 MHz and later at 410 MHz (Reber, 1940). In creating these maps Reber confirmed Jansky's detection of the galactic centre and also detected regions of high emission towards both Cygnus and Cassiopeia.

Installation of better instruments in 1943 allowed Reber to publish improved results (Reber, 1944). This paper was instrumental in two ways. Firstly a detection of the Sun was (finally![2]) made, which showed it to be sub-dominant in the radio sky. This led Reber to deduce that if the 'cosmic static' in Sagittarius was from solar-like stars then a large part of that constellation would be as bright in the optical sky as the surface of the Sun. With this realisation it became clear that radio waves trace predominantly non-thermal emission. Secondly, Reber's 1944 paper included the first treatment of terrestrially produced Radio Frequency Interference (RFI) as a source of noise for astronomical observations rather than cosmic sources being an annoyance to Earth based applications of radio technology. This could therefore be marked as the beginning of the long-running battle for the radio-spectrum!

During the world war there were huge leaps forward in radio technology (e.g. for

[2] In reality both Hey (1946) and Southworth (1945) had also detected the thermal radiation of the Sun at cm-wavelengths. However these detections were made using British and US Army equipment respectively during the Second World War and so their findings could not be disclosed until after the end of hostilities.

radar, trans-Atlantic communication, etc.). Once the war was over, a lot of the engineers and radio-scientists could turn their experience and attentions towards more peaceful ventures. Thousands of discrete celestial radio sources were discovered in the following years, of a variety of types and leading to many new breakthroughs. Radio Astronomy had well and truly begun.

1.2.3 Radio Interferometry

The angular resolution ‘θ’ achievable by a telescope is a function of its diameter ‘D’ and the observing wavelength ‘λ’ according to the relation, $\theta \approx 1.22\ \lambda$ / D. The long wavelengths of radio-waves therefore mean that for any given size the angular resolution of a radio-dish will be significantly less than for a comparatively large optical telescope. To achieve better resolution, radio-telescopes of increasing diameter were built. Practically though, a moveable dish becomes restrictively heavy and expensive beyond a diameter of $\approx$100m. Radio interferometry overcomes this limit by using aperture synthesis to combine the signals received by multiple telescopes to achieve an angular resolution equivalent to the furthest separation (baseline) of dishes (see also Section 2.2). This thesis relies heavily upon interferometric observations and so to place the importance of this technique in context we here provide a brief history of radio interferometry. For more thorough reviews, see Edge & Mulkay (1976), Sullivan (1991) and Ekers (2012).

Early radio interferometry used ‘sea interferometers’ (a.k.a. sea-cliff interferometry). This set-up uses a single receiver station positioned atop a cliff. A second receiver is essentially simulated by detecting incoming radio-waves both directly and also after reflection from a (preferably flat) surface below the cliff. The first radio interferometer therefore only used a single antenna! During October 1945, Joseph Pawsey and collaborators used a sea-cliff interferometer in Sydney, Australia to observe the Sun (e.g. Pawsey, 1946). The power of the technique was shown soon after in February 1946, when the same team managed to connect radio-outbursts from the Sun with the behaviour of a single sunspot[3] (McCready et al., 1947). Also in this paper it was pointed out that a single baseline interferometer meant only one Fourier component was sampled (see Section 2.2) and that

[3]It was convenient that the first sunspot detected in 1946 also turned out to be the radio-brightest such source of the century - science sometimes requires a touch of good fortune!

inversions of the Fourier plane to create practical images of the radio-sky required multiple samplings. McCready et al. noted that changing either frequency or baseline could achieve this but reckoned that changing frequencies for this purpose was impractical. This remained true for many years, but it should be noted that the recent clamour for wideband receivers on radio-telescope backends is essentially achieving just that!

Around the same time, across the globe the first practical Michelson Interferometer for radio-astronomy was conceptualised by Sir Martin Ryle in Cambridge, England. Early attempts to keep the phase of the incoming signal were thwarted by fluctuations in the receiver voltage. Ryle's set-up used a (now-called) Ryle-Vonberg receiver (Ryle & Vonberg, 1946) that basically compared the incoming signal to a known noise source. This meant that the noise itself then fluctuates with the signal and hence it is changes in the noise that matter, making the receiver much more robust against instrumental effects. Eventually these advancements led to the building of the 'Long Michelson' interferometer at Cambridge, with which the first Cambridge survey of the radio-sky (1C Survey Ryle et al., 1950) was compiled and catalogued roughly 50 'radio-stars'. The Australian teams had also been finding several discrete sources (e.g. Bolton & Stanley, 1948; Bolton et al., 1949; Pawsey, 1955). The improving resolution offered by interferometers allowed tentative optical counterparts to be identified for the discrete radio sources, although at the time these constituted a confusing array of sources such as supernova remnants and elliptical galaxies rather than the expected stellar counterparts. Further discrimination against noise came about with the addition of a phase-switch to the instrumentation (Ryle, 1952). This development culminated in the creation of the one-mile telescope (Ryle & Hewish, 1960), which laid the groundwork for all future interferometers.

Further developments in technology and techniques have resulted in major forward steps in radio astronomy since, and indeed there is a strong symbiosis between technological advancements and scientific discovery in the field. A major advance came with the realisation of Earth-rotation synthesis, where the rotation of the Earth itself is used to alter baselines and hence better fill the uv-plane (see Section 2.2). Coupled with the first use of a computer for enabling fast calculation of Fourier transforms, this allowed Ryle & Neville (1962) to publish an interferometric map of the Northern Polar Region[4]. The

[4]Christiansen & Warburton (1955) had published an earlier interferometric map of the Solar surface

quest for ever longer baselines led to the first successful interference fringes with trans-continental baselines using the technique of Very Long Baseline Interferometry (VLBI: Broten et al., 1967). More recently the radio-telescopes themselves have gone extra-terrestrial. Space-VLBI (sVLBI) was realised first with the Japanese HALCA satellite (Hirabayashi et al., 2000) and later the Russian-led RadioAstron satellite (e.g. Kardashev, 1997), meaning telescope arrays with the resolving power of a dish up to 400,000 km across have been achieved! One of the latest major advancements is electronic-VLBI (eVLBI) which uses the internet to interfere VLBI signals in real-time, meaning much faster responses to interesting sources can be made (e.g. Szomoru et al., 2004).

1.2.4 A Few Highlights of Radio Astronomy

As the radio-spectrum constituted new parameter space, it is perhaps unsurprising that a thorough treatment of all the breakthroughs is unfeasible. Here we highlight some of the most important milestones in radio astronomy over its first $\approx$80 years.

In 1945, the Dutch theorist Van de Hulst predicted that the spin-flip transition of neutral hydrogen (HI) would be weak, albeit detectable due to the expected high abundance of such gas (English translation in; Sullivan, 1982). Three teams near-simultaneously detected this 21 cm transition (Ewen & Purcell, 1951; Muller & Oort, 1951; Christiansen & Hindman, 1952)[5], which allowed the neutral dust of the Milky Way to be mapped and hence provided us with the first clear view of the spiral nature of our own galaxy[6].

Perhaps most prevalently for the current thesis is the role of radio astronomy in the discovery of AGN. Early radio-catalogues discovered numerous discrete sources (in particular the 3C catalogue, Edge et al., 1959; Bennett, 1962) one of which, 3C273, was found to be incredibly bright. Using lunar occultations Hazard et al. (1963) obtained a precise position, thus allowing a team from the Palomar Observatory to perform spectroscopic optical follow-up of the host. Schmidt (1963) interpreted the resultant spectrum as

although this relied on manual transforms.

[5]The results of Ewen & Purcell (1951) and Muller & Oort (1951) were published in the same journal, in which it was noted that the Australian group of Christiansen had also made a detection, although this was not published until later Christiansen & Hindman (1952)

[6]Note that Reber (1944) had actually suggested that the Milky Way had a similar structure to the other 'spiral nebulae', but had wrongly interpreted the Cassiopeia-A and Cygnus-A discrete radio-sources as extensions of the signal at the galactic centre to reach this conclusion.

being from the then assumed 'crazy' redshift of z≈0.16. This finding was reconciled with the realisation that this was one of a class of very high energy objects later to be known as quasars. See also Section 1.3.1.

In a fateful coincidence, two scientists working at Bell Laboratories were in the 1960s, much like their predecessor Jansky, assigned the task of discovering a source of radio-noise albeit this time for communications satellites. After removal of all possible sources, they found a pervasive ≈3.5 K excess signal permeating seemingly isotropically from all regions of the sky (Penzias & Wilson, 1965). Inspirationally, they suggested this may be due to the cosmic big bang background blackbody radiation as then recently suggested by Dicke et al. (1965). This signal is now known as the Cosmic Microwave Background (CMB) and is one of the best pieces of evidence for Big Bang cosmology[7].

A multitude of other findings could be mentioned, not least the famous discovery by Bell-Burnell and Hewish of pulsed emission from rapidly rotating neutron stars (i.e. pulsars Hewish et al., 1968). Whilst this discovery did not turn out to be attributable to 'LGM' (Little Green Men), radio astronomy did provide the first definite detection of an extrasolar planet (Wolszczan & Frail, 1992) and the Search for Extraterrestrial Intelligence (SETI, Tarter, 2001) continues! Other milestones have included the first detections of extra-terrestrial organic molecules, detection of planets and double pulsars (test-beds for extreme gravity). Furthermore, the discoveries show no signs of slowing down with the next generation of radio-arrays coming online.

1.3 Discovery of Galaxies

Since antiquity, extragalactic objects have unwittingly been recorded within the night sky (Abd al-Rahman al-Sufi 946, Book of Fixed Stars). With the invention of the telescope many more nebulous objects became known and catalogued (e.g. Messier, 1781; Herschel, 1786, 1864) leading to much debate over the ensuing centuries as to the nature of these peculiar objects. A few people suggested they may be outside of our own Milky Way (i.e. that they were 'extragalactic': although this term had not yet been coined). Starting the long association Durham has with extragalactic astronomy, Durham-born Thomas

[7]Note that the CMB is now more precisely determined to be 2.73K (Fixsen, 2009)

Wright in 1750 suggested the Milky Way might be a flattened disk, and that other nebulae may be ‘other Milky Ways’; a position supported by the famous philosopher Immanuel Kant, who in 1755 called them ‘island universes’. Rosse (1850) noted that some nebulae had a spiral structure, however it was not until the early 20th century that the true nature of galaxies became apparent.

Working from Lowell Observatory, Vesto M. Slipher used optical spectroscopy to show that a number of nebulae had velocities too high to be bound to the Milky Way (Slipher, 1913, 1915). Around the same time, Heber Curtis noticed that there were a number of nova in spiral nebulae (Curtis, 1917) that magnitude considerations suggested were too far away to be within the Milky Way. Curtis hence became a proponent of the ‘island universe’ theory[8]. In an attempt to solve the ‘nature of the nebulae’ riddle, a ‘great debate’ was organised between Curtis and Harlow Shapley on 26th April 1926, with Shapley arguing for a galactic origin of the nebulae and Curtis for an extragalactic origin. The issue was finally resolved by using the rotational velocity of the Andromeda galaxy (Opik, 1922) to show it was extragalactic and the use of Cepheids by Hubble to put distance limits (e.g. Hubble, 1925, 1929) on some nebulae showing them to be well beyond the edge of the Milky Way.

1.3.1 Discovery of Active Galactic Nuclei

The discovery of AGN is linked to the discovery of galaxies and the history of radio astronomy. Equally, it is a compelling story that could fill a section on its own. However, only a brief overview is given here (for a review see, Shields, 1999).

Over a century ago Edward Fath undertook spectral observations at Lick Observatory to determine the nature of the ‘spiral nebulae’ (see also preceding section), wishing to see if they exhibited mainly bright emission-line features as seen in the gaseous nebulae (such as the Orion nebulae) or whether they had more continuous spectra as would be expected for a mixed stellar population. Most of his objects displayed continuous spectra although one nebula, NGC1068, surprisingly showed both stellar but also strong line features (Fath, 1909). These lines were confirmed by Slipher (1917) at Lowell, who

[8]The events he observed were actually supernovae, but this phenomenon was unknown at the time.

noted the broad linewidths but rejected the idea they were attributable to a normal radial velocity spread as they were deemed too high. Over the following years a few others noted nuclear emission-lines in numerous nebulous spectra (e.g Hubble, 1926) although it was not until over a decade later that systematic spectral studies of the nebulae (by then known to be galaxies, see preceding section) were performed (Seyfert, 1943). Seyfert supposed that Doppler shifts were responsible for the wide linewidths and noted that two types of emission-line galaxy were seen. In some systems, lines from both the forbidden and permitted transitions had similar narrow linewidths whereas in other the forbidden lines were narrow but permitted lines had much broader widths. It is now known that these broad linewidths are due to dense clouds orbiting quickly a super-massive black hole in galactic centres, and the two types of galaxy came to bear Seyfert's name (i.e. Seyfert type-1 and Seyfert type-2s, see Section 1.6).

Even then, AGN were not taken overly seriously as they are rare. They finally became a major focus of research once our two history sections combined.

1.3.2 The Radio Connection

As discussed in Section 1.2, radio astronomy was maturing in the 1950/60s. Interferometers were being used to put better positional constraints on the many discrete sources being discovered and optical counterparts were being identified.

It was found that some radio sources had very high brightness temperatures that must be attributed to non-thermal emission. These sources were split into type-Is that appeared to be associated with the Milky Way and type-IIs that were distributed isotropically across the sky. Morris et al. (1957) limited the size of three type-II non-thermal sources to be $<$12". This suggested extremely high brightness temperatures, prompting them to suggest their sources could be very distant analogues to Cygnus-A (which had by then been shown to have very high, non-thermal radio-power, e.g. Baade & Minkowski 1954). The pace picked up with the 3C catalogues when true quasars were discovered (see Section 1.2.4).

In the following years, it became accepted that the radio-sky is synchrotron dominated. This showed the 'double-lobed' radio sources to be extremely powerful, requiring a huge energy source. The controversial suggestion was that this energy could originate from accretion of material onto a 'massive dark object', which eventually led to the realisation

that AGN are powered by accretion onto super-massive black holes (e.g Salpeter, 1964; Rees, 1984).

1.4 Galaxies and Clusters

1.4.1 Large Scale Structure

In the standard Λ-Cold Dark Matter (ΛCDM) cosmology, quantum fluctuations in the primordial Universe are amplified during inflation. During the subsequent growth of the Universe, the dark matter that dominates the gravitational potential of the Universe preferentially flows towards these overdensities. As the Universe evolves these structures grow hierarchically, with the baryonic matter that composes the visible Universe following the potential of the dark matter. Over time, regions of differing densities develop to create the regions such as voids, filaments, walls and clusters that today compose the so-called 'cosmic web' (for a review of cluster formation see Kravtsov & Borgani, 2012).

As the nodes of this cosmic web, fully virialised galaxy clusters constitute the largest single objects known. They occupy a critical cross-roads, being large enough to provide a reasonable sample of the constituency of the Universe whilst still small enough (in comparison to the non-virialised filaments and superclusters) to become bound in the hierarchical formation scenario. Therefore they are extreme laboratories and fully understanding their formation, distribution and continued evolution is paramount for many areas of physics. There are strong intrinsic links between galaxy clusters and the galaxies of which they are composed and hence understanding the galaxies themselves is also vital.

1.4.2 The Galaxy Zoo

There is a huge variety in the morphology, properties and hence types of galaxies seen within the Universe (e.g. Lintott et al., 2008). One of the earliest and most enduring classification schemes is the well-known Hubble scheme (Hubble, 1926) that splits galaxies by their optical morphologies; grouping galaxies into spirals (late-types), lenticulars and ellipticals (early-types) and irregular galaxies that show no clear structure. Whilst this

scheme has clear limitations, part of its endurance is perhaps due to the fact that the different morphologies do appear to relate to different physical properties. Late type galaxies typically have high angular momentum and specific star formation rate leading to blue overall spectra whereas the early-type galaxies are more commonly quiescent systems, with much lower star formation rates and a hotter stellar velocity dispersion (although see Emsellem et al., 2011). Large surveys such as the Sloan Digital Sky Survey (SDSS: York et al., 2000) have now allowed millions of galaxies to be imaged.

Theoretical models and simulations have had huge success in being able to reproduce the large scale structure seen in the Universe and many of the observed galaxy properties (e.g. Springel et al., 2005; Boylan-Kolchin et al., 2009). One critical observable that must be reproduced is the galaxy luminosity function and it has long been known that the high end curtailment of this luminosity function requires huge energy injection from AGN (Bower et al., 2006; Croton et al., 2006). This AGN action is most required in the most massive systems, at the centres of galaxy clusters where the largest galaxies are found.

Whilst a full overview of galaxy types and evolution is not possible here (see instead the recent review by Conselice, 2014), one important group of galaxies to introduce are those at the highest end of the mass distribution - the Brightest Cluster Galaxies (BCGs), which form the focus of this thesis (note that in general, luminosity is seen to scale with mass and hence the galaxy mass and luminosity functions trace essentially the same distribution of galaxies). These galaxies are typically found both spatially and dynamically at the centres of galaxy clusters (although it should be noted that in some instances they can be centrally offset, see e.g. Hamer et al. (2012)). They are the most massive galaxies observed and their growth and evolution are intrinsically linked to that of the host cluster (e.g Tremaine, 1990; Lin & Mohr, 2007). Their size, mass and location suggest that they have likely undergone different formation scenarios from many of the more ‘typical’ galaxies. Indeed the most massive BCGs, the cD galaxies, actually appear to have stellar masses that lie above predictions of the mass function; although it should be noted that in these systems there is contention as to what fraction of the stellar envelope is truly galactic as opposed to being attributable to the intra-cluster light (ICL).

It could be argued that BCG is a misnomer as not all BCGs are actually the brightest galaxy in their cluster at any given wavelength! However the majority are the brightest as

well as typically being the most massive galaxy within the cluster and importantly they dominate the central cluster regions. Therefore, BCG is typically used synonymously with central cluster galaxy or central dominant galaxy and within this thesis we use the term 'BCG' to refer to this class of galaxy. The properties of BCGs are more fully introduced in Section 1.5.

1.4.3 Density-Morphology Relation

A relationship exists between the distribution of galaxy morphological types and the environments they inhabit (Butcher & Oemler, 1978). Specifically, late-type (spiral) galaxies are preferentially found in less dense, field environments whereas the early-type galaxies (ellipticals and S0s) are preferentially found in the denser environments of groups and clusters (Dressler, 1980). This relation indicates that environmental density affects galaxy formation. In particular, the denser environments found within groups and clusters are believed to suppress star formation and so facilitate the conversion of star-forming late-type galaxies to more passively evolving late-types. Numerous mechanisms have been proposed to cause this such as ram-pressure stripping (e.g. Gunn & Gott, 1972; Quilis et al., 2000) and galaxy harassment (Moore et al., 1996), where baryonic gas is either removed ('stripped') from galaxies as they infall due to pressure exerted by the ICM, or is removed by enhanced rates of galaxy interactions in the higher density environments respectively. A further alternative is termed 'galaxy strangulation' - whereby neutral gas is stripped from the surrounding haloes of infalling gas-rich galaxies. Generally, it would be this gas envelope that replenishes gas used in star formation and hence removing it interrupts this process and more gently prevents further star formation (Larson et al., 1980).

Whichever method is invoked for the density-morphology relation, a major implication for this thesis is that it means that galaxies found towards the centres of galaxy clusters tend to be low-star formation rate, gas-poor systems. This has ramifications in that it means most mergers of systems into the BCG are expected to be dry (i.e. contain negligible gas) and hence not induce significant star formation. This is important for considering the formation scenarios of BCGs (see Section 1.5.1) and also when considering potential cold gas supplies for fueling AGN episodes.

As previously stated, the links between large-scale universal structure and the galaxies

contained within are perhaps most prevalent in galaxy clusters. As relating the AGN action of BCGs to their wider environments will be a central theme of this thesis we next provide a short overview of some of the more general properties of clusters.

1.4.4 Galaxy Clusters

Galaxy clusters and groups form a continuous mass sequence, with no clear distinction between the two (although some authors have suggested physically motivated distinctions, e.g. Stott et al., 2012). Typically clusters contain a few hundred to a few thousand individual galaxies, and have a mass of $\approx 10^{14}$-$10^{15} M_{\odot}$ and a physical extent of 2-3Mpc (Sarazin, 1986). In addition to the differences in galaxy populations contained within sparser and more dense environments (see preceding section), an interesting property of clusters is that a large component of their light is external to the galaxies (i.e. it is intracluster light, ICL). This effect appears to be most pronounced for the most massive systems ($\approx 10^{15} M_{\odot}$) where the ICL may account for up to 50% of emission in the near infra-red (K-band: Lin & Mohr, 2004). By enhancing the iron-yield this high amount of ICL may help to explain in part another observable feature of clusters, which is that they have very high central metallicities (e.g. Arnaud et al., 1992; Loewenstein & Mushotzky, 1996). This enhanced metallicity has also been invoked as evidence to suggest that there may be a 'non-standard' initial mass function (IMF) within clusters as supernovae feedback is insufficient to distribute enough heavy elements for a standard IMF (Portinari et al., 2004). Alternatively, it has been shown (e.g. Kirkpatrick et al., 2009, 2011) that metals can be uplifted by the jet-action of AGN which may help explain enhanced metallicities, particularly in the largest systems where central BCG-hosted AGN are most common.

One of the major properties of galaxy clusters, and one that is vital for the work contained within this thesis, is that they can be broadly split into two types. There are those with short central cooling times (t_{cool}) that exhibit strongly peaked X-ray profiles ('cool cores', CCs) and those that are more dynamically disturbed, which exhibit a flatter X-ray profile ('non cool-cores' NCCs; e.g. Million & Allen, 2009). The differing X-ray appearances relate to the X-ray emissivity increasing proportional to the square of the density, hence as gas cools and tends to pool towards the centre the X-ray cooling rate increases non-linearly. In the strongest cool cores, t_{cool} can be less than a gigayear

(Gyr) whereas in non cool-cores this can be greater than the Hubble time. The exact physical state of a cluster is therefore a combination of factors including its mass, time since formation and time since its last major merger. Of these, perhaps the most important is the merger factor, with the energy released during a major cluster merger sufficient to disrupt the cool-core. Cool-core clusters appear to have higher central metallicities than non cool-cores, which may be because mergers in NCCs (with accompanying lack of X-ray peak) can distribute metals more evenly across a cluster (Allen & Fabian, 1998; De Grandi & Molendi, 2001).

Identifying Cool Core Clusters

Directly measuring t_{cool}, or equivalently the central entropy, of a cluster is observationally expensive, requiring deep X-ray data (e.g. Donahue et al., 2006; Sanderson et al., 2009b; McDonald et al., 2013). Additionally, such entropy calculations can be strongly affected by resolution effects of the X-ray observations (e.g. see discussion by Panagoulia et al., 2014).

That many cluster cores contain extended, line-emitting (predominantly Hα+[NII]) filamentary nebulae around BCGs has been long known (e.g. Cowie et al., 1983; Heckman et al., 1989). In a study of 110 X-ray selected galaxy clusters for which Hα detections were available in the literature (mainly from Crawford et al. (1999)), Cavagnolo et al. (2008) found that detectable Hα emission (to a typical luminosity limit $\sim 1 \times 10^{40}$ erg s^{-1}, Crawford et al. (1999)) was predominantly found only in clusters with central entropies below 30keV cm^2, with a sharp dichotomy seen at this boundary (see Figure 1.1) (Cavagnolo et al., 2008). Converting this entropy to a central cooling time shows that these emission lines are typically only found in clusters with a $t_{cool} < 5\text{x}10^8$yr. Furthering this result, Rafferty et al. (2008) found that clusters with central cooling times below $t_{cool} < 5\text{x}10^8$yr show enhanced blue light indicative of star formation (see also; O'Dea et al., 2008), which is a phenomenon strongly associated with the presence of a cooling flow. Furthermore, this star-forming enhancement is only seen in clusters with low spatial offsets ($<$20kpc) between the BCG and the peak of the X-ray emission, indicative of a relaxed cluster core (see also; Sanderson et al., 2009a). Taken together, these results imply that the presence of optical emission lines can be used as a proxy measure for the pres-

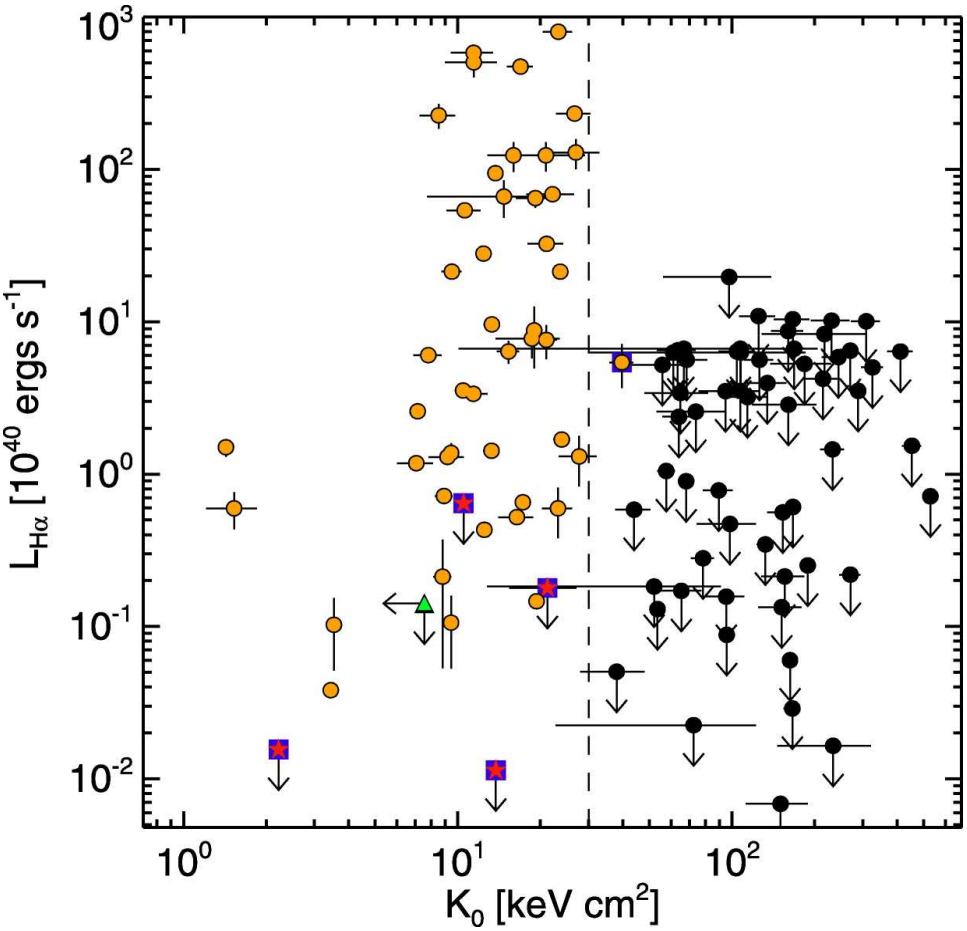

Figure 1.1: Central entropy versus Hα luminosity, Figure 1 from Cavagnolo et al. (2008). Orange circles show sources with detected Hα whereas black circles denote non-detection upper limits. A general trend for only BCGs in clusters with central entropies below 30 keV cm^{-2} (equivalent to t_{cool} <5x10^8yr) to show measurable Hα emission is seen, with very few (blue squares) sources bucking this trend. Within this thesis we use the presence of such optical emission lines as a proxy for the presence of a cool core in our large sample of clusters (see Chapter 2).

ence of a cool core (t_{cool} <5x10^8yr) where deep X-ray coverage is unavailable, with only a small fraction (<1%) of false negatives expected.

The specific ionisation origin of the observed Hα is still a matter of debate, with neither star formation nor the AGN believed to be wholly responsible. In particular the extended nature of the emission in many instances where it can be resolved has led authors to suggest more exotic origins such as ionisation induced by cosmic rays or hot X-ray plasma penetrating cold gas (Ferland et al., 2009), or perhaps even excitation by recombining magnetic field lines trailing in the wakes of rising cavitiess (Churazov et al., 2013). Regardless of its origin, the presence of Hα (and associated N[II]) shows un-

ambiguously the presence of cool ($\approx 10^4$K) gas in these systems and the presence of a multi-phase ICM, as associated with cool core clusters (Cavagnolo et al., 2008). It is for these reasons that we believe the presence of these optical emission lines to be a strong indicator of the presence of a strong cool-core cluster.

1.5 Brightest Cluster Galaxies

A large industry has built-up to fully understand the workings of BCGs and the relationship they have with their wider-scale environments. The main aim of this thesis is to provide a comprehensive study of the radio properties of BCGs. To help set the context for this, we here review some of the major properties of BCGs known through study at other wavelengths as well as an overview of the current knowledge of their radio properties.

1.5.1 Formation

Multiple mechanisms by which BCGs can grow to their massive size have been suggested. These include direct accretion from a cooling flow developed as the hot gas in cluster atmospheres cools (see Section 1.7.5) leading to growth (e.g. Silk, 1976), galactic cannibalism (i.e. dynamical friction and tidal stripping causes small galaxies to fall to centre of cluster and be enveloped by large galaxy, e.g.: Ostriker & Tremaine, 1975; White, 1976; Ostriker & Hausman, 1977) or by multiple (major) mergers that take place in a relatively short time during cluster collapse (e.g. Cowie & Binney, 1977).

The cooling flow scenario was long-ago ruled out - mainly due to the lack of a strong cooling flow in most galaxy clusters (see Section 1.7.5)! Some star formation is seen in the centres of the most massive cool-core clusters (e.g. McNamara & O'Connell, 1989), however it is much less than would be required to account for BCG growth (e.g. Crawford et al., 1999). Galactic cannibalism has been argued against since the dynamical timescales required for the least massive, stripped galaxies to accrete are too restrictively long to make this process viable (Merritt, 1985).

It is now generally accepted that the growth of BCGs is two-phase with the early (main) growth ($z>3$) occurring via the merger scenario. This process has been shown in N-body simulations to naturally occur when filamentary structures collapse to form

a cluster due to the preferential directions imparted to infalling galaxies (e.g. Dubinski, 1998). At later times this growth is supplemented by repeated minor mergers of existing (evolved) galaxies. Since these galaxies have already undergone their star-forming peaks and hence have depleted their cold gas reservoirs, these late-time mergers are not associated with any new (major) star formation and are dissipationless (e.g. De Lucia & Blaizot, 2007; Oser et al., 2010; Cooper et al., 2014).

An important consequence of these progenitor galaxies initially forming at a similar epoch to the BCG is that it means they contain similar, old stellar populations to the BCG. The post-merger combined stellar populations can therefore remain the same, explaining why BCGs can still appear to evolve passively despite repeated minor mergers (e.g. De Lucia & Blaizot, 2007; Ruszkowski & Springel, 2009). Additionally, it has been shown that this scenario can explain the 'puffing up' of BCGs that is required to explain their position lying above the main Kormendy (effective radii to surface brightness, i.e. they are bigger) relationship for other ellipticals (Naab et al., 2009; Ruszkowski & Springel, 2009; Laporte et al., 2013).

1.5.2 General Properties

One difficulty in studying BCGs arises due to the fact they are both the most massive galaxies anywhere as well as lying preferentially at the centre of galaxy clusters and hence are subjected to extreme external influences. This can therefore make determining whether any given property of a BCG is due to its mass or its environment quite complicated.

BCGs display a number of properties that set them apart from other ellipticals. They are ultraluminous (i.e. $\approx 10\times$ brighter than equivalent 'normal' galaxies in the luminosity function, e.g. Schombert, 1986) as well as being huge (e.g. Schombert, 1986; Gonzalez et al., 2000). Whilst the term 'BCG' is used to refer to all central dominant galaxies regardless of the specific morphological type, one striking class of BCGs to highlight are the cD galaxies. These galaxies constitute around 20% of all BCGs (Seigar et al., 2007) and are a sub-class of giant elliptical that are only found in group and cluster environments. They are notable for having a large-scale diffuse stellar envelope, believed to be accumulated over the history of the galaxy via mergers and tidal stripping of cluster mem-

ber galaxies. This envelope can extend many tens of kiloparsecs and has been highlighted as evidence of the symbiotic relationship between BCG formation and cluster properties (see e.g. Dressler, 1984; Oegerle & Hill, 2001).

Morphologically BCGs can come in a variety of types, with the lowest mass objects more favourably S0-like whereas higher mass ones are virtually always massive spheroidals regardless of the size of the host cluster or group (e.g. Guo et al., 2009). However, the majority of BCGs are typically ellipticals (≈92%, with ≈48% cDs Coziol et al., 2009) and show similar variety in type to other red-sequence galaxies (Hashimoto et al., 2014). Therefore they are expected as a population to behave similarly to other ellipticals but with added environmental effects.

An important property of elliptical galaxies is that they lie on a Fundamental Plane - a relationship between their effective radius, surface brightness and central velocity dispersion (Dressler et al., 1987; Djorgovski & Davis, 1987). This relationship builds from the Faber-Jackson relation (link between luminosity and velocity dispersion, Faber & Jackson, 1976) and is roughly equivalent to the Tully-Fisher relation for spirals in that it can be used as a distance indicator. BCGs are also claimed to lie on this Fundamental Plane, although they tend to lie off the Faber-Jackson relation (Oegerle & Hoessel, 1991). For a large sample of brightest group and cluster galaxies, von der Linden et al. (2007) found that compared to non-BCGs of similar stellar mass, BCGs are spatially larger (i.e. lie above the 'normal elliptical' Kormendy relation) and have higher velocity dispersion, implying that they contain a higher fraction of dark matter. They suggest therefore that although BCGs do appear to lie on the Fundamental Plane for ellipticals, they are actually on a 'different' Fundamental Plane (i.e. they align in 3-dimensions but have different relationships in 2-dimensions).

BCGs typically have low relative velocities (i.e. they are sat at or near the cluster dynamical centre, e.g. Beers & Tonry, 1986; Lin & Mohr, 2004, 2007). They are not however at rest, but do have much lower dispersions than the typical velocity dispersion (≈32% of the velocity dispersion of 'average' cluster galaxies, Coziol et al., 2009). Offsets between BCG position and the cluster X-ray peak tend to be higher for more dynamically disturbed clusters (Hashimoto et al., 2014) and less common for the cD-type BCGs. The stellar populations of BCGs are typically old and roughly consistent with other el-

lipticals (e.g. von der Linden et al., 2007; Loubser et al., 2009). They also have similar metallicities to other ellipticals but perhaps with α-enhancement (i.e. a high (α/Fe) suggesting stars may have formed over shorter time (von der Linden et al., 2007). There is however evidence for ongoing star formation particularly in the cool-core hosted objects (O'Dea et al., 2008; Rafferty et al., 2008). Overall stellar populations are consistent with an old population with a small $\sim$1% contribution from recent episodes of star formation although this is dependent on galaxy and cluster mass, with the more massive (and those that are cool-core hosted) having proportionally more young stars (Liu et al., 2012).

Additionally, BCGs contain the most massive black holes seen anywhere. Dynamical measures in local systems consistently return masses $>$few $10^9 M_\odot$ (McConnell et al., 2011, 2012) and there are suggestions from considering the position of BCGs on the fundamental plane of black hole behaviour (Ferrarese & Merritt, 2000; Merloni et al., 2003) that some BCG-hosted SMBHs may even be ultramassive ($>10^{10} M_\odot$, Hlavacek-Larrondo et al., 2012b).

Cluster Correlated Properties

In addition to being interesting galaxies in their own right, what really sets BCGs apart are their strong intrinsic links to the wider cluster environment. The most prevalent of these mutualisms for this thesis is their role in understanding the cooling flow problem (see Section 1.7.5). However, this is only one example.

It has been known for decades that for the cD class of BCGs, the extent and luminosity of the diffuse stellar envelope is a strong function of cluster richness and can extend up to 2Mpc in the richest clusters (Oemler, 1976). It has since been suggested that larger BCGs inhabit larger clusters but that the dominance of the BCG towards the total light fraction decreases with cluster mass (Lin & Mohr, 2004).

It has been claimed that there is a slight tendency for the BCG luminosity to increase with both cluster X-ray luminosity and velocity dispersion (Schombert, 1987). The optical and near infra-red (NIR) luminosity of BCGs is weakly correlated with X-ray luminosity (Edge, 1991) with central galaxies in high ($>2.3\times10^{44}$erg s^{-1}) X-ray luminosity clusters typically $\approx$0.5mag brighter at K-band (2.2μm) and also showing lower dispersion than in less X-ray luminous clusters (Burke et al., 2000). This luminosity trend may perhaps

be more prevalent at z>0.1 (Brough et al., 2002). Similarly, BCGs in more massive clusters tend to have bluer BCGs (Edge, 1991), which may be attributable to cooling-flow induced star-formation. Indeed, Stott et al. (2008) found that in clusters limited to X-ray luminosities $>10^{44}$erg s^{-1}, if the NIR BCG emission versus cluster X-ray luminosity is corrected for, then BCG stellar populations show passive evolution, as seen in lower X-ray luminous clusters by e.g. Burke et al. (2000) and predicted by De Lucia & Blaizot (2007). The J-K colour for the sample of Stott et al. (2008) is consistent with the bulk of the stellar population being formed prior to z≈2 but with additional blue colour for cooling-flow hosted BCGs, a scenario supported by the K-band Hubble diagram of Whiley et al. (2008). Recently, Rawle et al. (2012) used Herschel and Spitzer (24-500μm) data to show that infra-red luminosity is well-correlated directly with X-ray cluster cooling time, giving the strong inference that star formation is related directly to the presence and strength of a cool-core.

1.5.3 Radio Properties

As understanding the radio properties of BCGs is the main focus of this thesis, many aspects of this are covered at the relevant sections of the manuscript. In order to set the scene however, we additionally give here a brief overview of the broad radio properties.

It has been known for a long time that BCGs have increased likelihood of being radio-loud over non-BCGs (McHardy, 1978; Burns et al., 1981; Valentijn & Bijleveld, 1983; Burns, 1990). It was also suggested early on that there may also be a weak correlation for cDs to be more radio-loud in cooling flows than non-cooling flows (Zhao et al., 1989).

Some of this increased likelihood of radio-loudness is due to BCGs being massive galaxies, as it is known that there is a strong relationship between stellar mass of a galaxy and the likelihood for it to host a radio-source with $L_{1.4\ GHz} > 10^{23}$WHz^{-1} (Best et al., 2005). There is however also a clear environmental dependency, with BCGs much more likely to host radio-loud AGN (at 1.4 GHz with NVSS/FIRST) than non-BCGs regardless of stellar mass. This is most prevalent for less massive BCGs (>order of magnitude enhancement in probability for $M_{BCG} < 10^{11}$ M$_\odot$) but still relevant for the most massive systems (≈factor of 2 for $M_{BCG} \approx 5\times10^{11}$ M$_\odot$, Best et al., 2007). A similar relation shows that regardless of their central black hole mass, BCGs are more likely to be radio-

loud in FIRST if they are in a more massive cluster (Stott et al., 2012).

There is also evidence that the dynamical state of the host cluster is closely linked to the likelihood of a BCG being radio-loud. For example, Mittal et al. (2009) report detection fractions of 45%, 67% and 100% for non-cool cores, weak cool cores (1Gyr $<$ t_{cool} 7Gyr) and strong cool cores ($t_{cool} < 1$Gyr) respectively, for the HIFLUGCs sample of the 64 X-ray brightest galaxy clusters.

One of the major consequences of this enhanced radio-loudness is that BCG mechanical activity (as traced by radio) is now commonly postulated to provide the power required to regulate the atmospheres of galaxy clusters, as radio-lobes are seen to inflate cavities in the X-ray atmospheres of clusters that then couple this energy to the ICM (e.g. McNamara et al., 2000; Fabian et al., 2000). The dominance of the AGN activity appears to be linked to the wider cluster state. Whilst BCGs in the more massive clusters are most likely to be radio-loud, the dominance of AGN heating over gas cooling (as seen by a steeper L_X vs T_{Vir}, X-ray luminosity versus gas temperature) appears lessened in more massive clusters (Mittal et al., 2011). This is perhaps because radio-luminosity does not (strongly) correlate with cluster mass (Stott et al., 2012) and hence can have a higher proportional effect in smaller groups. These authors suggest a physical definition for the group/cluster boundary could be defined at an X-ray cut of 2 keV, as this is typically the division temperature beyond which cooling tends to dominate AGN action. This 'AGN feedback' action of BCGs is covered in more detail in Sections 1.7.4 and 1.7.5.

1.5.4 Extended Radio Structures

In addition to the increased likelihood for a BCG to host a radio-loud AGN over other galaxy types, a large variety of radio morphological types are seen in clusters. The central radio-AGN exhibit all classical radio-morphologies, with examples of Fanaroff-Riley FR type-Is (FRIs) and type-IIs (FRIIs Fanaroff & Riley, 1974), intermediate types, Compact Steep Spectrum (CSS) and Gigahertz Peaked Sources (GPS) all seen. Supplementing this, a variety of low surface brightness extended source-types can also be found within many clusters. We here provide a short note on this collection, introducing several of the terms that will be used within this thesis and highlighting which of the objects are believed to be BCG-related and which are related to more cluster-wide mechanisms. Within this thesis

we adhere as far as possible to the naming conventions described in Kempner et al. (2004) and outlined briefly below, to avoid confusion that can be introduced due to the jumbled nomenclature that is attributed to radio morphologies within the literature (for a more comprehensive review, see e.g. Kempner et al., 2004; Ferrari et al., 2008; Feretti et al., 2012).

Directly BCG Related

Amorphous Halo: Often surrounding a BCG, particularly those hosted by cool-core clusters, is seen a relatively small scale (less than a few tens of kiloparsecs) amorphous halo of emission (e.g. A2052 Venturi et al., 2004). Roughly spherical structures, these objects are consistent with being fading, albeit confused, homogenised and distorted AGN emission. Occasionally within the more amorphous emission, ageing radio-lobes from the central AGN can be distinguishable, such as is seen in the Perseus cluster. Shock fronts may be seen co-spatially with the outer extent of such sources, suggesting that the emission may be confined by a cooling flow, hence their alternative name, 'confined cluster cores'.

Core Relic: These are the detached dying lobes of BCG radio episodes seen long after the AGN activity has ceased, typically of a few tens of kiloparsecs in extent (e.g. A133 Slee et al., 2001). They have steep spectra and are necessarily found close to the BCG since they are powered merely by fading emission from a past injection period.

Indirectly BCG Related

Phoenix Relic: These are essentially core relics that have faded below observable limits but have continued to expand outwards. Their synchrotron-emitting populations are then re-accelerated so that they essentially re-ignite from their own ashes - hence the monicker (e.g. A85 Slee et al., 2001). They are typically filamentary in structure and may reach few hundred 100 kiloparsecs in extent.

Contentiously BCG Related

Mini-halo: These structures appear morphologically to look like larger analogues of the amorphous haloes in that they are roughly spherical, low-surface brightness sources that are centred on the BCG but a few hundreds of kiloparsecs in extent (e.g. Burns et al.,

1992; Owen et al., 2000; Giacintucci et al., 2014). However the electron diffusion time for sources of this extent is far beyond the emitting lifetime of electrons ejected into typical cluster core environments (unlike for amorphous halos), therefore the synchrotron emitting populations must be (re)accelerated in-situ and not by direct AGN action. The seed population may however originate from AGN ejecta and so these sources present a contentious middle-ground between BCG-related and cluster related processes. The (re)acceleration is postulated to be caused by either sloshing of the ICM (e.g Walker et al., 2014) or MHD turbulence in the cooling flow (e.g. Gitti et al., 2002). Alternatively, Pfrommer & Enßlin (2003) suggest a hadronic origin whereby cosmic rays interact with thermal protons and produce synchrotron emitting electrons locally. Radio mini-halos are (so far) exclusively found in cool-core clusters and hence a cooling flow origin for their re-acceleration is highly likely (see also Gitti et al., 2006, 2007).

Not BCG Related

Radio Gischt: Also commonly referred to as 'giant radio relics' or 'peripheral', these sources are huge elongated structures (up to $\approx$Mpc in extent) found on the periphery of some clusters (e.g. Rottgering et al., 1997; Kempner & Sarazin, 2001). Believed to be formed by shocks driven by cluster mergers they are completely independent of AGN action (e.g. Ensslin et al., 1998).

Radio Halo: These are truly giant (typically $>$1Mpc) sources, approximately spherical sources centred on the cluster dynamical centre (as opposed to the BCG for amorphous and mini haloes). There is a correlation between the X-ray luminosity of the host cluster and the radio luminosity (see short review by Feretti, 2000) and it seems that similar to gischt they are driven by cluster mergers as they are (almost) exclusively found in merging systems (see Bonafede et al., 2014, for a recent discovery of a giant halo in the settled cluster CL1821+643). Like gischt, this family of radio-sources are independent of the AGN action of the BCG and are included here only for completeness (see also e.g. Buote, 2001; Cassano et al., 2010).

1.6 The Standard Model of AGN

Although this thesis focuses on the radio properties specifically of BCGs and is not concerned with the multitude of other AGN types that exist, the radio emission is predominantly generated by the AGN and hence no treatment would be complete without describing the unified model of AGN (e.g. Antonucci, 1993; Urry & Padovani, 1995; Véron-Cetty & Véron, 2000). We first describe the fundamental accretion processes that power AGN, before discussing the unified model for 'typical AGN' and then relating this more specifically to BCGs.

1.6.1 Black Hole Accretion and the Eddington Ratio

At its most fundamental, an AGN consists of mass-energy being released as material accretes onto a super-massive black hole (SMBH). Such energy generation by the release of gravitational potential, is one of the most efficient processes known. The conversion efficiency (ε), that is the fraction of the total mass accreted per unit time (i.e. the mass accretion rate, '$\dot{m}$') converted to the bolometric luminosity of the AGN (L_{AGN}) can be parameterised as:

$$L_{AGN} = \varepsilon \dot{m} c^2 \tag{1.6.1}$$

Typically this efficiency factor is estimated to be $\approx$0.10, although values up to 0.42 are possible (Raimundo & Fabian, 2009) for a maximally spinning 'Kerr' black hole.

A theoretical limit to L_{AGN} (or indeed, any accreting body) is reached when the outwards radiation pressure balances the inwards attraction of gravity. This limit is termed the Eddington Luminosity. Typically, the system is simplified to that of a central point source emitting spherically symmetrically. For a black hole (BH), L_{Edd} can be written:

$$L_{Edd} = \frac{4\pi G M_{BH} c}{\kappa} \tag{1.6.2}$$

For AGN the accreting material can be modeled as being dominated by fully ionised hydrogen, where the opacity κ can be reasonably approximated as $\kappa \approx \sigma_T / m_p$ where σ_T is the Thompson cross-section and m_p the proton mass, allowing Equation 1.6.2 to be

written:

$$L_{Edd} = \frac{4\pi G M_{BH} m_p c}{\sigma_T} \tag{1.6.3}$$

$$\approx 1.26 \times 10^{31} \frac{\mathrm{M}}{\mathrm{M}_\odot} W \tag{1.6.4}$$

A useful parameter to then define is the Eddington ratio, λ_{Edd}:

$$\lambda_{Edd} = \frac{L_{AGN}}{L_{Edd}} \tag{1.6.5}$$

This 'limit' is of course a much simplified scenario. Indeed, it only accounts for the simplest geometry and non-radiative energy output from the black hole is ignored (although for a 'mechanical included definition', see Heckman & Best, 2014). Such omissions allow models (e.g. Abramowicz et al., 1988, see Section 1.6.2) to be developed that allow for so-called 'super-Eddington' accretion states (where $\lambda_{Edd} > 1$). However, λ_{Edd} is a highly useful parameter as it is directly scalable between black holes of substantially different masses. This is particularly useful as, due to the restrictively long dynamical times involved for systems accreting around SMBHs, much of the study of accretion flow structure and evolution has focused on stellar mass objects. The mechanisms involved however are believed to be largely scale-invariant, hence models and understanding developed for stellar mass black holes can be applied to the more massive SMBHs in AGN (e.g. Mirabel et al., 1992; Körding et al., 2006; Done et al., 2007). For a specific treatment of the jet connection see e.g. Meier (2003).

1.6.2 Accretion Modes and Jet Production

A thorough treatment of accretion processes could easily constitute a full thesis and so we do not attempt such an endeavour here, instead presenting only the very basic picture. For a more thorough review of accretion theory see e.g. Done et al. (2007); Abramowicz & Fragile (2013), for review of ADAFs see e.g. Narayan & McClintock (2008); Yuan & Narayan (2014) and for a specific treatment of the role and generation of jets, see e.g. Marscher (2006); Foschini (2011); Morabito & Meyer (2012).

Numerous stable and quasi-stable solutions to the accretion equations exist. Perhaps

the most widely known of these is the standard thin-disk model (Shakura & Sunyaev, 1973). Relevant at reasonably high accretion rates ($\lambda_{Edd} \approx 0.1$), in this idealised model the disk is geometrically thin (height/Radius, h/R $<<$ 1) and optically thick, allowing the accretion disk to thermalise and emit as a blackbody at all radii. Viscous stresses are described by the alpha-parameter, which although parametric is found to be a reasonable description regardless of the actual physical mechanism for angular momentum loss invoked (typically now believed to be magneto-hydrodynamic stresses) and often used in more complicated accretion solutions and models. The thin-disk collapses to a non-viscous flow at radii less than the innermost stable circular orbit (ISCO). Although a highly successful model, the thin-disk model is prone to temperature and density instabilities.

A physical model to overcome some of these instabilities is the slim-disk model described by Abramowicz et al. (1988). Density fluctuations within a thin-disk can result in the flow becoming locally optically thin and no longer able to radiate faster than the inflow speed. In this scenario energy is advected along with the flow since it can no longer be fully radiated locally. The slim disk has the advantage of having solutions down past the ISCO and is typically relevant for high accretion rates ($\lambda_{Edd} > 0.3$), giving a thicker disk (h/R $\approx$ 0.3). An alternative solution to the slim-disk is the (equally imaginatively named) thick-disk (e.g. Paczyński & Wiita, 1980). This solution solves the radiation pressure instability and can include solutions with different scale heights at different radii from the central accretor, having the advantage of solutions at very high accretion rates ($\lambda_{Edd} >$ L_{Edd}). Geometrically, at the highest accretion rates radiation pressure from the disk itself thickens the flow to the extent that the disk is embedded in a thick-flow of quasi-sphericity (h/R $\approx$ 1), which could lead to 'collimated beams' and may explain the high velocity outflows and/or jets seen in quasars. A further advantage of the thick-disk solutions (a.k.a. Polish Donuts) is that they are analytically simple, relying only on gravity and assuming a perfect fluid. They are therefore good for numerical codes as they have analytic solutions, meaning that many more complicated numerical models use this solution as a base.

Alternatively, at low mass accretion rates ($\dot{m}$) the gas density in an accretion flow may be so low that virtually all the energy is advected and deposited within the event horizon, leading to an Advection Dominated Accretion Flow (ADAF, alternatively Radia-

tively Inefficient Accretion Flow, RIAF). This type of accretion solution was described near-simultaneously by both Narayan and Abramowicz, (Narayan & Yi, 1994, 1995; Abramowicz et al., 1995) although it had also been earlier suggested by others (e.g Ichimaru, 1977; Rees et al., 1982). The flow has no disk-like structure, instead being geometrically near-spherical. Importantly, Rees et al. (1982) noted that the nuclei of radio galaxies emit little radiation, and suggested that they may be surrounded by a torus of hot ionised gas that anchors the magnetic field to the flow, dragging it around and ultimately enabling the launching of relativistic jets.

Much of the study of accretion processes has focused on stellar binaries since the dynamical times are low enough to be able to study entire outburst cycles. Two main types of accretion state are seen in stellar mass BHs. At low $\dot{m}$, a power-law like hard-state is observed, corresponding to ADAF-like accretion whereas at high $\dot{m}$, a dominant sum-of-blackbodies spectra is seen. Known as the soft-state, this corresponds to a more thermal disk-like structure. Combinations of these are also seen, with truncated disks believed to be ubiquitous at certain stages of the accretion cycle (Done et al., 2007).

It is geometrically thick, optically thin, inefficient flows of the ADAF type that are expected in the majority of BCGs and radio-galaxies. However, note that the high-power radio-luminous quasars are more likely powered by something more akin to a thick-disk.

The Radio Connection

There appears to be a strong link between the accretion phase of an accreting system and its ability to launch a radio jet. Specifically, it appears as if a large scale-height magnetic field may be required for efficient jet-launching. This can be created by a large scale-height flow such as an ADAF, naturally explaining the tendency for more massive systems to be more often radio-loud. Current belief is that production of a jet is powered either directly by extracting spin energy of the black hole by magnetic fields overlapping with the ergosphere of a rotating (Kerr) BH (see Blandford-Znajek (BZ) Mechanism, e.g. Blandford & Znajek, 1977) or due to dragging of the magnetic frame by the inner-accretion flow (see Blandford-Payne (BP) Mechanism, e.g. Blandford & Payne, 1982), the former of these mechanisms leading to highly relativistic jets whereas the latter typically produces jets with lower Lorentz numbers (Meier et al., 2001; Marscher, 2006).

An interesting idea proposed by Dexter et al. (2014) is that these two mechanisms could operate in the same object at different times in the accretion cycle as the magnetic structure of the flow changes, and correspond to the two major types of jets observed in compact binaries. In the hard-state the flow could be magnetically arrested (MAD Accretion) and steady, compact jets are seen which could be launched by the BP-mechanism (e.g. Mirabel et al., 1992; Fender, 2001). Alternatively, it has been observed that during transitions from the hard to soft state, binaries can launch high Lorentz factor, transient, ballistic jets. These could correspond to a collapse from MAD to Magneto-Rotational Instability supported (MRI) accretion, essentially leading to jet-death when the inner-edge of a thin-disk like accretion flow surges inwards launching a potentially BZ-powered fast jet (Remillard & McClintock, 2006; Mirabel & Rodríguez, 1994).

Whilst such wholesale restructuring of the accretion flow from hard to soft state (roughly equivalent to the onset of quasar activity) is not observable in AGN due to the timescales involved (much longer than a human lifetime!) there have been suggestions of similar links between accretion structure changes and jet response in AGN. Marscher et al. (2002) report X-ray flux drops preceding ejection of propagating VLBI-observed 'blobs' in the jet of 3C 120. Whilst not a direct analogue to the case in compact binaries, this does imply a connection between activity at the jet base and accretion structure. Furthermore, Livio et al. (2003) proposed that the inner-magnetic field changes from poloidal to turbulent, as the accretion flow switches from the low-hard state (steady jet) to high-soft state (ballistic/no jet). In an AGN setting, partial re-ordering of a turbulent magnetic field could occur on short timescales by random near-alignments, which could be responsible for short term jet launching.

Many open questions remain, perhaps most interestingly; how is the jet formed and collimated, what is its structure and what particles dominate the flow? This is an open area of research and the reader is encouraged to see the reviews of Marscher (2006); Foschini (2011); Morabito & Meyer (2012) as well as references therein. Ultimately, although it is the action of the jets that are most relevant and considered within this thesis, it is important to keep in mind the accretion structures that may be causing the observed properties and likewise how the environment may be dictating the accretion structure.

1.6.3 The Unified Model - 'Typical AGN'

AGN can be split into two families: the type-1 AGN that exhibit broad permitted and narrow forbidden lines, and the type-2 AGN that show narrow-lines only (although oftentimes a broadline region can be inferred through scattered emission). Likewise, they can be split into radio-loud and radio-quiet (although not radio-silent) objects and can additionally be split by their luminosities. Whilst a full description of the AGN family-tree is outside the scope of this thesis (the interested reader is directed towards the reviews by e.g. van den Bergh, 1998; Buta, 2011), the broadbrush properties can be described by the 'unified model' or 'standard model'. The assumed geometry is shown in Figure 1.2 (figure inspired by: Beckmann & Shrader, 2012a,b; Heckman & Best, 2014).

The standard model best relates best to radiatively efficient AGN (top panel, Figure 1.2) which we first describe here. In the model, a central SMBH is surrounded by an optically thick accretion disk. Surrounding the inner-accretion zone is a thick dusty torus. The exact nature of this is still unclear, although the general consensus is that it is clumpy with an inner-edge governed by dust-sublimation temperature (Nenkova et al., 2002; Dullemond & van Bemmel, 2005; Nenkova et al., 2008a,b).

Due to the high mass of the black hole, the accretion disk thermalises and emits profusely in the ultraviolet regime (e.g. 'the big blue bump' Sanders et al., 1989; Marchese et al., 2012). This provides a sea of ionising photons that is believed to irradiate the dense clouds that are orbiting close to the nucleus and thus under the gravitational influence of the black hole (e.g. Peterson et al., 2003). These fast moving clouds are too dense for forbidden lines but the permitted lines are ionised and the fast velocities close to the SMBH make this the broadline region (BLR, e.g. Marziani et al., 1996; Peterson et al., 2003; Kaspi et al., 2005). The thermal accretion disk is surrounded by a cloud of hot electrons, which are commonly invoked to Compton upscatter seed photons (from disk, jet-base, thermalised in torus) to X-ray energies (e.g. Zdziarski et al., 1995, 1996). Further from the accretion disk, less-dense clouds not directly gravitationally influenced by the SMBH can be ionised by remaining ionising photons. Here, densities are low enough to allow both permitted and forbidden lines and so it is this that constitutes the narrow-line region (NLR, e.g. Wampler et al., 1975; Stockton & MacKenty, 1987; Schmitt & Kinney, 1996; Greene et al., 2011). It is the obscuring torus that therefore creates the apparent di-

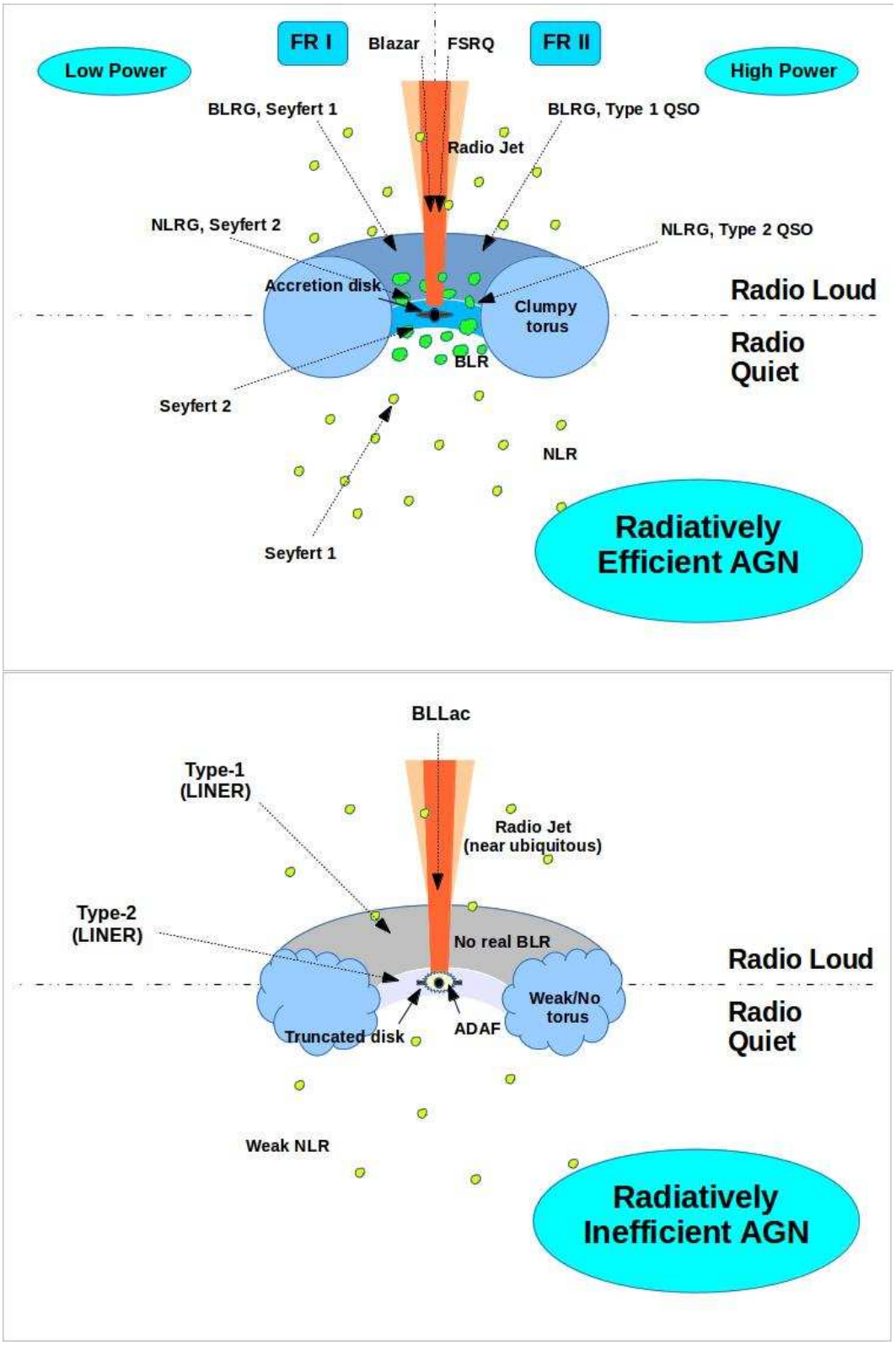

Figure 1.2: Cartoon depiction of the Standard Model of AGN, for a source accreting radiatively efficiently (top panel) and a source accreting radiatively inefficiently (bottom panel). These cartoons were inspired by Figure 3 in Heckman & Best (2014) and Figure 1 in Beckmann & Shrader (2012a).

chotomy between type-1 and type-2 AGN, as the BLR can only be seen from favourable alignments. Although plagued by selection effects, relative number counts of type-1 and type-2 AGN can therefore be used to put limits on the structure of the torus (e.g. Toba et al., 2014, and references therein.).

As indicated on Figure 1.2, AGN can be further classified into radio-loud and radio-quiet objects, with the viewing angle and radio-power dictating the type of galaxy seen. Viewing angles aligned within a few degrees of a jet will have their flux dominated by relativistically beamed emission and hence will present as blazars (Blandford & Rees (1978); see also the early and recent reviews by Stein et al. (1976) and Falomo et al. (2014) and references therein). Seen at a wider angle, AGN can be classified as radio-loud quasars or Seyferts and in the case of full-obscuration of the BLR by the torus a classical radio-galaxy can be seen, with higher and lower power objects typically corresponding to FR-II and FR-I sources respectively (Fanaroff & Riley, 1974; Owen & Ledlow, 1994). Radio-surveys of double-lobed systems are thus a powerful method by which to find obscured type-2 AGN. Similarly, the accretion luminosity (which may be related to the mass accretion rate, see Section 1.6.2) can be used to classify AGN, with the highest power objects referred to as quasars and the Seyfert galaxies being their lower power analogues. Only a small-fraction ($\approx$10%) of radiatively efficient AGN are radio-loud, although this fraction varies substantially with both the stellar mass of the host galaxy and the Eddington-normalised accretion rate of the AGN, perhaps reaching $\approx$25% for the most luminous systems (Jiang et al., 2007).

Focus on BCGs

As stated above, the majority of BCGs do not exhibit the canonical properties of radiatively efficient AGN, which are the primary focus of the unified model. Instead they typically accrete at much lower Eddington fractions (see Section 1.6.1) where an optically thick, geometrically thin disk, is replaced by a quasi-spherical geometrically thick but optically thin accretion flow (ADAF: See Section 1.6.2). Note however, that the disk may not be completely absent but merely truncated (e.g. Done et al., 2007). This requires slight modifications to the unified model, as are illustrated in the bottom panel of Figure 1.2. The removal of the thin-disk removes the major source of radiative emission and

hence the strong BLR and NLR regions are absent. However, the geometrically thicker accretion structure does lend itself to the efficient production of jets, and it is through bulk kinetic motion through these jets that the majority of these low-radiative efficiency AGN are seen to transmit their energy (see review by Heckman & Best, 2014).

Sitting alongside the BCGs on the radiatively inefficient branch of the AGN family tree are the Low Ionisation Nuclear Emission-line Region AGN (LINERs) (Heckman, 1980). These are often interpreted to be the lowest luminosity class of AGN although in some cases the ionisation may be provided by star-forming regions rather than an AGN (e.g. Ho, 2008). However, reflection studies have shown that at least in some LINERs, an obscured weak BLR is seen and hence low radiative efficiency AGN are believed to contain some form of obscuring torus (e.g. González-Martín et al., 2009).

The main consequence of this inefficient accretion mode in BCGs is that it means they have a very high mechanical energy output and a correspondingly high likelihood of being radio-loud (e.g. Best et al., 2007). There is a known link between the central cooling time of a cluster and the radio behaviour of its BCG. Chiefly, there appears to be a cooling time threshold of $<$5x10^{8}yr (equivalent to an entropy threshold of $\approx$30keV cm^2) below which bright radio emission ($\geq 7\times10^{23} WHz^{-1}$ at L-Band) is preferentially 'on' (Rafferty et al., 2008; Cavagnolo et al., 2008). As introduced more thoroughly in Section 1.7.5, without additional energy input this short cooling time can lead to runaway cooling in the core. This mechanical AGN action of the BCG is commonly invoked to counteract the expected cooling. Better understanding this process is central to this thesis, hence in the next section we provide a more thorough introduction to 'AGN Feedback', with particular focus on mechanical mode feedback.

1.7 AGN Feedback

In this section we initially introduce a few of the major results that have shown there to be irrefutable links between AGN and their environments and use them to further motivate the study of AGN feedback. We then consider the main processes by which AGN are believed to impact on their surroundings and finally we focus on the heating of hot atmospheres by mechanically dominated AGN, which is the main form of AGN action

provided by BCGs in cluster centres and hence the main topic of this thesis (also see the reviews by McNamara & Nulsen, 2007; Cattaneo et al., 2009; Alexander & Hickox, 2012; McNamara & Nulsen, 2012; Fabian, 2012; Heckman & Best, 2014).

1.7.1 Links Between AGN and their Hosts

Perhaps the clearest indication that AGN and their host galaxies share a strong intrinsic link has been the realisation that there is a tight relationship between the mass of a galaxy's stellar bulge and the SMBH at its centre (e.g. Kormendy, 1993; Kormendy & Richstone, 1995; Magorrian et al., 1998; Marconi & Hunt, 2003). This relationship, along with a similar correlation between the black hole mass and the stellar velocity dispersion of the bulge (Ferrarese & Merritt, 2000; Gebhardt et al., 2000), suggests that black holes and galaxy bulges must undergo linked evolution and formation. Models seeking to explain these relationships often require that energy generated by a central AGN during a particularly high period of growth (a 'quasar' period) is coupled to the gas in the galaxy either radiatively or via mechanical outflows (Silk & Rees, 1998; King, 2003). This AGN action removes gas and hence regulates star formation and subsequent growth of the stellar bulge, whilst also perhaps interrupting gas supply to the AGN itself so forming the basis for a self-regulating feedback cycle (see also Section 1.7.3 and the review by Kormendy & Ho, 2013, and references therein).

An interesting consequence of the King (2003) model of mechanical AGN outflows regulating growth is that it suggests most black hole growth occurs in periods of high λ_{Edd}, and hence it may be expected that the most luminous[9] AGN activity and the highest star formation rates trace each other temporally. Indeed it is observed that the cosmic star formation density and growth of SMBH are seen to follow a similar trend, peaking at a similar epoch ($z \approx 2$, Madau et al., 1996, 1998; Merloni et al., 2004) and subsequently growing at a seemingly steady combined rate to maintain the locally observed M_{BH}-M_{Bulge} relationship (e.g. Mullaney et al., 2012). Disentangling the signatures of star formation and AGN is observationally difficult and studies probing the links between

[9]Note that within this thesis, radiatively efficient AGN are referred to synonymously as luminous AGN, reflecting that they are much brighter in the 'traditional' optical bands than the radiatively inefficient AGN most often associated with radio sources and mechanical feedback.

these processes in samples of individual galaxies have sometimes conflicting results. For example, in some samples the AGN of galaxies with higher star formation rates typically have higher λ_{Edd} (Kauffmann & Heckman, 2009; Azadi et al., 2014) whereas others see only a weak correlation (Rosario et al., 2012). The latter of these studies also suggests there may be different fueling modes for high and low luminosity AGN, which is a topic we revisit within this thesis. Whatever the details of the processes involved, it appears that AGN and star formation are intrinsically linked and so their joint evolutionary histories provide further evidence for AGN acting on their host galaxies (Merloni & Heinz, 2013; Madau & Dickinson, 2014).

Further strong indication of the co-dependency of AGN and galaxy properties comes about due to the invocation of AGN processes for transferring galaxies from the star-forming main sequence (blue cloud) of the galaxy colour-magnitude diagram (Bell et al., 2004) to the red sequence. Using a large sample of visually identified galaxies, Schawinski et al. (2010) claim a trend where the highest SMBH mass-growth in blue galaxies is for the highest mass systems whereas for red-sequence early-type galaxies AGN growth is preferentially seen in the lowest mass systems. Essentially, this suggests that AGN are responsible for shutting down the star formation in blue galaxies and driving them quickly through the green valley to populate the red sequence (e.g. Martin et al., 2007). This evolutionary sequence is supported by red sequence galaxies typically inhabiting bigger, older haloes (e.g. Blanton et al., 2006). However, an interesting question to pose is that of what prevents red sequence galaxies from re-accreting cold gas and re-igniting their star formation? A key observation in answering this is that low-luminosity radio-loud AGN are most commonly hosted in red-sequence galaxies (e.g. Hickox et al., 2009; Janssen et al., 2012), with the inference being that mechanical AGN action can regulate the atmospheres around red sequence galaxies and so keep them quenched. This is a similar process to that which is believed to exist in the centres of cool-core clusters where the BCG regulates the environment and so shows that understanding the actions of BCGs has implications to understanding AGN feedback globally.

1.7.2 Two Types of AGN Feedback

It is now generally accepted that AGN come in two flavours, which have important properties for explaining the observations described previously and can be broadly understood using the topics introduced thus far. The distinction between the two AGN regimes is controlled by the accretion rate of the AGN and we discuss them in turn now.

1.7.3 'Quasar Mode' - Radiatively Efficient Feedback

AGN accreting at high λ_{Edd} ($\gtrsim$0.01 L_{Edd}) output the vast majority of their energy radiatively, as expected from the thin/slim disk models for accretion (see Section 1.6.2). Historically, the most luminous of these AGN have been identified as quasars (hence the common alternative name, 'quasar mode') with Seyferts believed to be the lower luminosity (but still radiatively efficient) versions. Radio-loud objects of this class are often called High Excitation Radio Galaxies (HERGs: e.g. Best & Heckman, 2012), with their radio-morphology most usually the FRII type associated with high radio-power. AGN of this sort are preferentially found in blue, main sequence galaxies and may be responsible for shutting down the star formation in these systems, however the process by which they do this is an ongoing research question (see review by Alexander & Hickox, 2012).

Large-scale galactic winds are near-ubiquitously seen in star-forming galaxies across both the local and distant universe (see reviews by Crenshaw et al., 2003; Veilleux et al., 2005). There is strong evidence that stellar processes themselves can (and do) drive winds via radiation pressure, supernovae and stellar mass loss (e.g. Heckman et al., 1990; Lehnert & Heckman, 1996; Chen et al., 2010; Steidel et al., 2010). However it is becoming more generally accepted that the energy input of a powerful AGN is required to drive the most powerful ionised outflows ('superwinds') that are required to fully shut down star formation (e.g. Benson et al., 2003; McCarthy et al., 2011). Evidence for such winds being traced over large distances ($>$10kpc in some cases) has been observed both using long-slit (e.g. Whittle & Wilson, 2004; Greene et al., 2011) and integral field unit (IFU) techniques (e.g Harrison et al., 2012; Liu et al., 2013; Förster Schreiber et al., 2014).

The actual driving mechanisms for these superwinds are a topic of debate (e.g. Rupke et al., 2005; Nesvadba et al., 2008; Faucher-Giguère & Quataert, 2012). At high accretion

rates, material can be lifted above the accretion disk by radiation pressure from the optically thick disk, and radiation pressure or magnetically-driven flows can then accelerate this material (e.g. Konigl & Kartje, 1994; Arav, 1996; Everett, 2005). Alternatively, it has been postulated that relativistic jets may provide the necessary momentum although the narrow collimation of the high powered jets found in radio-loud quasars can be difficult to reconcile with the large angular flows observed (e.g Whittle & Wilson, 2004). It should however be noted that the highest power quasars where this feedback is expected to be most prevalent are believed to be operating in the very high λ_{Edd} regime where jets from radiatively efficient flows are more commonly seen, although the correlations between jet launching and both the black hole and galaxy stellar masses must also be considered. Whatever the mechanism driving these outflows, it is capable of driving them to high speed over parsec-scale distances (e.g. Hewett & Foltz, 2003; Reeves et al., 2003; Zubovas & King, 2014). It is then believed that in order to provide effective feedback, this initially high speed flow must entrain gas over larger scales (few kiloparsecs), driving it out of the galaxy and so preventing further star formation and black hole growth as well as enriching the intergalactic medium (IGM).

1.7.4 'Mechanical Mode' - Radiatively Inefficient Feedback

When fueling onto an AGN is low and gas densities near to the SMBH drop the accretion flow becomes inefficient ($\lesssim$0.01 L_{Edd}). An example of such a scenario would be when a 'quasar mode' AGN has stripped its host environment of the large quantities of cold gas required for high star formation and its own continued radiatively efficient activity. In such scenarios, as discussed in Section 1.6.2, the AGN emits most of its energy mechanically in the form of jets. The work of these jets on their surroundings is observed to counteract cooling in a variety of hot-halo systems on multiple physical scales from single elliptical galaxies (i.e. the "keep 'em red and dead" requirement) through to groups and clusters. This mode of radiatively inefficient AGN feedback is variously referred to as 'mechanical mode', 'maintenance mode' and/or 'jet mode' feedback (see Heckman & Best, 2014). Virtually all of these galaxies contain radio-jets, meaning that the term Low Excitation Radio Galaxy (LERG: e.g. Best & Heckman, 2012) is also synonymously used.

Energetically, mechanical mode AGN can be fueled directly from the surrounding hot

gaseous halo, with Bondi accretion (Bondi, 1952) providing enough fuel *on average* (see McNamara & Nulsen, 2007). The rates are sufficient to power weak to regular power jets, with a correlation between jet power and Bondi power seen for low-power objects by Allen et al. (2006); although note that a much weaker correlation is seen by Russell et al. (2013). However, in real astronomical settings cooling gas will be imparted with angular momentum support, which makes infall times unreasonably long (>Gyr, e.g. Proga & Begelman, 2003; Pizzolato & Soker, 2010), meaning that Bondi accretion is insufficient to power the most powerful jets (e.g. Hardcastle et al., 2007; McNamara et al., 2011). These issues can be overcome via a two-phase accretion fuelling process whereby hot gas first cools within a few kiloparsecs of the AGN into cold clumps. These cold clouds can then provide enough fuel for short-term, powerful outbursts whilst still ensuring accretion relates to hot gas cooling over wider scales (e.g. Pizzolato & Soker, 2005; Soker, 2006). This type of fueling mechanism can also naturally account for the relatively large quantities of cold gas seen in BCGs and other ellipticals that are difficult to explain from a well-coupled purely hot-gas powered fueling flow (e.g. Edge, 2001; Salomé & Combes, 2003; Edge et al., 2010a).

Coupling of the mechanical energy to the surroundings occurs predominantly via the action of the relativistic jets, a process that is most readily observed in the dense cores of cool-core clusters where it is the AGN at the centre of the BCG that launches the jets. As the jets propagate outwards they perform work on the hot gas, heating it and inflating cavities in the X-ray emitting plasma (e.g. Boehringer et al., 1993; McNamara et al., 2000; Fabian et al., 2000; Hlavacek-Larrondo et al., 2012a). The radio emission attributed to these jets is seen to be co-spatial with the depressions in the X-ray surface brightness (the 'cavities'), showing phenomenologically that the mechanisms are linked. This relationship can be clearly visualised in Figure 1.3 (Gitti et al., 2012). These cavities subsequently rise buoyantly increasing cluster entropy and re-distributing energy. Detailed studies of local systems have shown that weak shocks and density sound-waves driven into the ICM from the cavities play an integral role in distributing the AGN energy (e.g. Fabian et al., 2005; Shabala & Alexander, 2007; Randall et al., 2011; Nulsen & McNamara, 2013). The hot gas is required to be prevented from cooling over all angles, which is at odds with the highly collimated jets themselves hence it is the action of the cavities and shock mixing

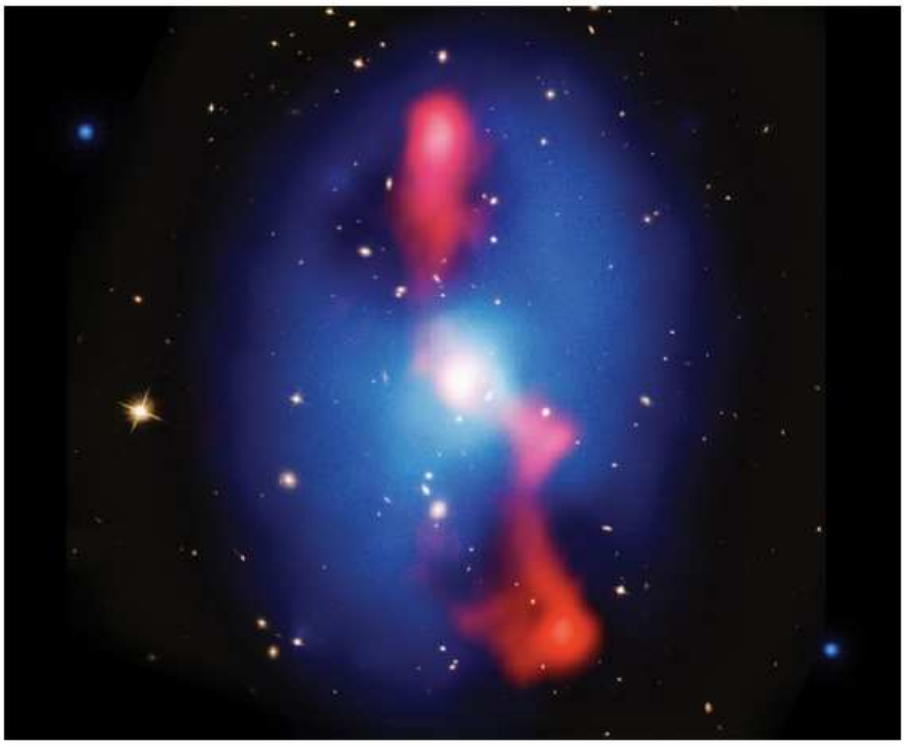

Figure 1.3: A composite image comprising the Chandra X-ray (blue) and VLA 330 MHz radio (red) emission overlaid onto an optical (Hubble) image of galaxy cluster MS 0735+7421, Figure 1 from McNamara et al. (2009). The radio jets are clearly seen to be co-spatial with regions of low X-ray surface brightness ('cavities'), demonstrating the cavity inflation scenario that is believed to counter-act cooling of the ICM in galaxy clusters. See also the text, Section 1.7.4.

that provide dissipation of AGN energy more isotropically (e.g. Nulsen et al., 2007).

Measuring the mechanical energy of a jet directly from its radio emission is difficult, not least because it requires assumptions to be made about uncertain magnetic field geometries, the particle constituents of the jet and synchrotron ageing models that are often under-constrained (see e.g. Bell, 1978a,b; Miley, 1980; Willott et al., 1999). A more direct measure of the mechanical energy output can be derived from deep X-ray observations by calculating the energy required to inflate cavities against the pressure of their surroundings (Bîrzan et al., 2004). However, even here there are large uncertainties due to numerous effects such as the difficulties of measuring cavity sizes, shapes and projection effects meaning that face-on cavities may often be missed. The necessary deep X-ray observations required to detect cavities and determine their energetics are unfeasible for very large samples. However it has now been shown that cavity powers are related to the

AGN radio luminosities, meaning that radio-power can be used as a proxy for feedback power albeit with large scatter (Bîrzan et al., 2008; Cavagnolo et al., 2010). This is a correlation that we revisit within this thesis, considering whether the scatter can be reduced by a more focused analysis of the radio-emission.

Studies using such correlations to constrain the energy available in cooling atmospheres have determined that the energy supplied is sufficient on average for the largest systems, although duty cycle considerations mean that the scatter for any individual cluster is large (Dunn & Fabian, 2008; McNamara & Nulsen, 2007, 2012). In smaller systems such as elliptical galaxies the imparted energy is actually found to be well above that required to counteract the cooling rate (Best et al., 2006; Mittal et al., 2011; Stott et al., 2012). In these systems a period of high activity can therefore overshoot the cooling and usher a period when cooling, hence star formation, is suppressed which fulfils the requirement for keeping red sequence galaxies 'dead' whilst reconciling that not all ellipticals host radio-sources at all times.

1.7.5 Classical Cooling Flow Problem

As stated in the preceding section, the best examples of direct mechanical feedback processes can be observed at the centres of galaxy clusters, which is also the most relevant environment for this thesis.

The radiative cooling time at the centres of cool core clusters is often much less than the Hubble time (e.g. Peres et al., 1998; Voigt & Fabian, 2004), giving expected cooling at a rate of 10^2-10^3 $M_\odot yr^{-1}$. This should lead to a sink of cold material on the order of a few 10^{11}-10^{12} $M_\odot$, however only ≈1-10% of this amount is observed - the classical 'cooling-flow problem' (for a review see Fabian, 1994). Star formation is seen in the strongest cooling clusters although typically only the few percent level of cooling (O'Dea et al., 2008; Rafferty et al., 2008) and whilst cold molecular gas and dust is observed, much less is present than if cooling dominated (e.g. Edge, 2001; Salomé & Combes, 2003; Edge et al., 2010a,b). Additionally, there is a deficit of gas seen at intermediate cooling temperatures (e.g David et al., 2001; Peterson et al., 2003; Sanders & Fabian, 2011) and the central gas temperature fails to cool below ≈30-40% of the ambient temperature at greater radii (Mittal et al., 2009). These therefore require revised X-ray cooling rates

from those predicted by the classical model, and these lower rates can be accounted for by the observed levels of star formation and cold gas accumulation. Combined these results highlight that some energy source must be counteracting the expected cooling, with the mechanical AGN action of the BCG usually invoked (for reviews see: McNamara & Nulsen, 2007, 2012; Fabian, 2012).

BCGs do not typically show quasar-like behaviour, instead they are believed to accrete inefficiently hence their mode of AGN feedback is more typical to that of the maintenance-mode previously described. Mechanical heating is therefore the favoured method by which energy is coupled from the AGN to the intra-cluster medium (ICM), via the inflation of cavities by the process outlined in Section 1.7.4.

As well as the mechanical action of cavities there are also suggestions from large-scale emission that other processes may also contribute to either the heating or decreasing the required energy budget. For example, low surface brightness structures such as radio mini-haloes found around BCGs suggest that cosmic rays may play an important role in counteracting cooling (Pfrommer & Enßlin, 2003) whereas there could be inefficient star formation in the cooling ICM itself that could account for some of the cooling problem (McDonald et al., 2014).

It is on these extreme cooling environments that this thesis focuses. This Introduction has motivated the need to understand AGN feedback processes globally and hopefully highlighted that radio observations can be used to trace this, and that by using a variety of radio observations we can better uncover the details of the processes. We now introduce some of the more technical radio terms that will be referenced within this thesis.

1.8 Radio Processes

The majority of radio emission from radio-loud AGN is synchrotron radiation produced in the radio jets (so inferred by spectral shape, uniformity and the high polarisation (can be $>$10%, e.g. Kempner et al., 2004) as ions and electrons are gravitationally accelerated by the release of accretion energy and then funneled through large scale polar magnetic fields. Here we provide a brief overview of the main processes that are involved.

1.8.1 Synchrotron Radiation

Synchrotron emission arises due to the acceleration of a charged particle traveling along curved paths through a uniform magnetic field. Note that it is observationally difficult to differentiate between a few particles in a strong field or many particles in a weak field, although the majority of astronomical synchrotron radiation appears to be explainable by electrons in weak fields.

The derivation of the spectral emission of a single electron are algebra intensive and not overly applicable to any astronomical setting. However, we can say that the energy distribution of a population of electrons is typically a power-law of the form N(E) dE $\approx KE^{-\delta}$ dE, where N(E) is the number distribution of electrons with energy E, K is a constant and δ is the spectral index of the electron energy distribution (Longair, 2011). To a reasonable approximation, the spectra of each individual electron can be modelled as if all its energy is radiated at a single frequency, which allows the emission coefficient 'ε', at frequency 'ν', to be written as $\varepsilon_\nu \propto B_{\delta+1}\ \nu^{(1-\delta)/2}$, where B is the magnetic field strength.

For a radio-source with a power-law spectrum we can say that $\varepsilon_\nu = f_\nu(\nu) \propto \nu^{-\alpha}$, where α is the measured index of the radio-spectrum. For this scenario we can therefore state that $\alpha \propto (\delta - 1)/2$. The locally measured value from cosmic rays is $\delta \approx 2.4$ (e.g. Müller, 2001), which is consistent with the $\alpha \approx 0.7$ measured for typical radio source spectra, lending further credibility to the synchrotron nature of most radio-emission (note however that the energy spectrum of cosmic rays may be species dependent and that the index of electrons only could be steeper, e.g. Aharonian et al. (2008)). For a full derivation and proper treatment of the synchrotron spectrum see (Longair, 2011).

Whilst this idealised scenario does give a reasonable first-order explanation to many radio-spectra over the commonly observed cm-wavelength ranges, there are of course additional processes that can alter the observed spectrum.

1.8.2 Synchrotron Self-Absorption

The brightness temperature (T_B) of a source is the temperature of a black-body that would provide the observed surface brightness of that source at a given frequency ν in

the Rayleigh-Jeans (classical) limit. For non-thermal sources, this temperature can, especially in extreme scenarios such as the inner-regions of powerful jetted sources, reach very high values. At the lowest frequencies this brightness temperature may approach the kinetic temperature of the emitting electrons (T_e). Thermodynamically a source is unable to emit at $T_B > T_e$ and hence the spectrum is truncated, which is termed synchrotron self-absorption.

Technically the energy spectrum is not in thermal equilibrium since the electrons are relativistic. However, the concept of temperature can be used if we assign the electrons each an energy E. This energy is then peaked at some critical frequency (ν_{crit}) and associating this energy with an electron temperature T_e such that $3k_BT_e = \gamma m_e c^2$ allows the T_e to effectively becomes a function of energy, i.e. it is an effective temperature (where $\gamma \propto \nu^{1/2}$). For a self-absorbed source then the effective and blackbody temperatures are equal. For a blackbody, the intensity $I_B \propto \nu^2$ and hence for a self-absorbed sources the intensity, $I \propto \nu^{5/2}$, below the critical frequency. We therefore see a spectral turnover at low frequencies. This type of self-absorption is important and often seen in very powerful, compact cores of AGN, in particular for recently ignited radio sources (i.e. the Gigahertz Peaked Sources and High Frequency Peakers, GPS and HFP respectively, e.g.: O'Dea, 1998; Dallacasa et al., 2000).

1.8.3 Free-Free Absorption

An alternative process by which low-frequency radio-spectra can be flattened or inverted is free-free absorption, or the absorption of energy by a free electron. Typically this effect is seen to flatten the low-frequency (less than a few hundred MHz) spectra of extended diffuse sources, such as the lobes of giant radio-galaxies (although note that this is only practical for smaller lobes and a curved underlying energy spectrum may be required for the largest systems; Duffy & Blundell, 2012). However, free-free absorption by warm clouds around nuclear regions has been postulated to provide steep spectral turnovers for spectra on sub-parsec scales (Gopal-Krishna et al., 2014)

1.8.4 Synchrotron Ageing

At the high frequency end of the synchrotron spectra, curvature is often seen. The distribution of energy losses in the underlying electron population, $\frac{dE}{dt} \propto \nu^2$ (Harwood et al., 2013), means that energy is preferentially lost at higher frequencies. An interesting application of this is that this leads to a characteristic break in the energy spectrum of a single-injection electron population. As the observed synchrotron spectrum reflects the underlying energy distribution, then by measuring the characteristic turnover of a spectrum an estimate of the age of the radio-source can be determined. Several models exist that use such arguments to produce curved fits to radio-spectra (e.g. Kardashev, 1962; Pacholczyk, 1970; Jaffe & Perola, 1973). This technique is not used within this thesis, as it is best applied to small numbers of densely sampled sources. However, we highlight the process as it shows that steep-spectrum sources, particularly those that show distinct spectral curvature to higher frequencies are most likely associated with more aged emission, which is an appreciation that is considered when distinguishing between emission attributable to ongoing and historical accretion (see Section 2).

1.9 Overview of Rest of Thesis

This thesis aims to provide a comprehensive study of the radio properties of Brightest Cluster Galaxies. To achieve this requires data from a wide variety of facilities, sampling the BCGs' radio emission on a variety of both spatial and temporal scales and over a broad frequency range. In particular we use a large data volume to initially consider the general properties of a large sample of BCGs. From this we select sub-samples for further study, focusing on the variability and very high resolution observations of their active cores, in addition to constraining the prevalence of cold HI gas in the cores of a subset of sources. A brief outline of the contents of each of the subsequent chapters is given below.

- **Chapter 2:** This chapter gives a basic overview of the facilities and data used within this thesis. An outline of the principles of dealing with radio data is given and we describe our parent sample of over 700 BCGs. We find that the radio emission can be largely split into two components - one attributable to ongoing accretion and one

attributable to historical accretion, and present our decompositions of the spectral energy distributions (SEDs) into these two components for over 200 BCGs drawn from our parent sample. The work in the second half of this chapter, in addition to that in Chapter 3, constitute work presented in Hogan *et al.* 2014a submitted.

- **Chapter 3:** In this chapter we explore the general radio behaviour of our large sample of BCGs. Initially we consider the monochromatic radio properties ($\approx$1.4 GHz) of the full parent sample before expanding upon this by considering the properties of the decomposed components, their inter-relationship and their relationship to the wider AGN and cluster properties. This work builds upon previous studies showing BCGs to have enhanced radio duty cycles. We go beyond the radio-loud to radio-quiet dichotomy to show that there are environmentally dictated differences not just in the frequency of radio-loud AGN activity in BCGs but in the nature of this activity.

- **Chapter 4:** This chapter looks at the high radio frequency (between 15 – 353 GHz) properties of a sub-sample of 35 BCGs that are chosen to contain significant ongoing core activity. Previously, very few constraints existed on the properties of BCGs within this frequency range. We show that these active components show typically slowly varying output, which shows that fueling of the central AGN appears relatively steady on decade timescales. We also find evidence for a potential additional component in the mm-range of low luminosity AGN that may be attributable to naked (i.e. not jet related) emission from an ADAF. The work in this chapter largely appears in Hogan *et al.* 2014b submitted.

- **Chapter 5:** In this chapter we consider the parsec-scale properties of a sub-sample of 59 BCGs using observations taken with the Very Long Baseline Array (VLBA). These observations trace the ongoing accretion activity, which we use to show that there is a significant variety in the core structure seen on such small scales. This sample alone constitutes the largest selection of BCGs observed with VLBI resolution. However, it forms only the first part of a large survey of BCGs on milliarcsecond scales. An additional 76 sources have been observed with the VLBA, which when combined with the data presented within this chapter are to be written

up as a comprehensive review of the parsec-scale properties of cool-core hosted BCGs (Hogan *et al.* in prep.).

- **Chapter 6:** In this chapter we present spectra searching for HI in absorption within cluster cores, using the VLA, ATCA and WSRT. We use the previous findings within this thesis to employ well-determined selection methods, which allows us to more than double the number of BCG HI-absorption systems known, showing that the detection success rate is a strong function of the morphology of the radio source. This greatly expanded sample allows us to consider for the first time the distributions of column densities and dynamics of this important cold phase of atomic gas for a sample of more than 10 BCGs. The work in this chapter is being done in collaboration with Dr Raymond Oonk of ASTRON. The author is leading the work with the VLA and ATCA, which when combined with observations with the WSRT led by Dr Oonk, are currently being written up as a paper (Hogan *et al.* in prep.).

- **Chapter 7:** This chapter summarises the findings within this thesis. We consider the current state of research and how the work contained herein contributes to the current understanding of the radio properties of BCGs and the wider context of AGN feedback. We consider outstanding questions to be addressed, and highlight the future work to be done.

- **Appendices:** Several appendices are presented beyond this. These contain notes on the individual sources studied within each of the chapters, tables of data products for the work presented within this thesis and SEDs for the sources studied in Chapter 4.

CHAPTER 2

Data and Reduction Techniques - The Sample

2.1 Abstract

Within this chapter we first provide a brief overview of the power of radio interferometry as a technique, its limitations and how interferometry data are handled. This section is intended to ensure that the reader is familiar with the main concepts and some of the terminology that will be used throughout this thesis. A more in depth description of data reduction for specific data-sets is provided in the relevant sections and a complete mathematical handling of interferometry theory can be found in Taylor et al. (1999a).

Following on from this, we introduce the parent sample of galaxy clusters and the spectral decompositions into active core (attributed to ongoing accretion activity) and inactive 'non-core' (attributed to historical activity) components that underpin much of the subsequent analysis.

2.2 Basics of Interferometry and Techniques

As introduced in Section 1.2.3, single dish radio-telescopes are limited in angular resolution due to the long wavelengths observed and infeasibility of dishes greater than about 100m across. Coupled to this, the pointing (and so tracking) accuracy of a single dish is limited by a multitude of effects such as gravitational sagging of the telescope as it tracks, torques due to wind and stresses due to differential heating of the reflector. Interferometers overcome many of these issues by combining signals from multiple dishes to achieve

an angular resolution equivalent to the longest distance between antennae (i.e. the longest 'baseline').

The received signals from every pair of antennae that form a baseline are correlated. That is they are multiplied and averaged together such that the output voltage from the correlator for a point-source interferes to produce a quasi-sinusoidal fringe. The phase of this is therefore not affected by uncorrelated noise and so effects such as fluctuations in receiver gain and atmospheric throughput that can adversely affect the response of a single-dish are largely mitigated. Furthermore, the fringe pattern is a highly sensitive measurement of the position of the point source on the sky. This means that the positional accuracy of an interferometer is more affected by the timing accuracy of the signal interference than by the pointing accuracies of individual antennae and since atomic clocks can provide extremely precise time measurements then very accurate positional measurements are possible.

Each baseline is responsive to only a single spatial frequency on the sky, or alternatively one component in Fourier space. To improve this point source response more samplings are required, which can be achieved by adding additional baselines, extending the frequency bandwidth covered and sampling at different hours of the day so that the rotation of the Earth changes the projected baselines (Earth rotation synthesis). This increasing coverage of spatial frequencies sampled is commonly referred to as 'filling the uv-plane', as it is often visualised as the combination of projected baseline distance in wavelengths sampled in both the east-west (u) and north-south (v) components. The point source response of an interferometer is the combination of all of the individual baseline responses. This is known as the synthesised beam (often shortened to just 'beam') of the interferometer and is essentially equivalent to the point-spread function (PSF) of an optical telescope. In the limit of many baselines the synthesised beam tends towards a Gaussian. It is important to note that for sources that are observed low on the sky, the projected sampling in one direction can often have much less dynamic range than the orthogonal component and so the synthesised beam can become highly elliptical. The shape of the beam is therefore an important consideration when interpreting the morphology of any interferometric map.

The overall response of the correlator is a product of the fringe patterns of the indi-

vidual baselines multiplied by the response pattern of each individual antenna on the sky. This 'primary beam' of each antenna therefore effectively limits the areal coverage that can be mapped per telescope pointing, since there will be insufficient sensitivity to sources too far from the pointing centre for directional antennas. The convolution of the primary beam with the combined point-source responses is only sensitive to the finite range of spatial frequencies governed by how well sampled the uv-plane is. Essentially, the more well-sampled the uv-plane then the more angular scales on the sky the interferometer can detect. Since it is the Fourier transform of these samplings that is used to produce the actual map then the length of the baseline is inversely related to the angular scale recovered. That is, long baselines correspond to small angles on the sky and shorter baselines to larger angles.

A mixture of baselines is required to fully recover a source. With inadequate short spacings, larger scale diffuse emission will not be sampled - a phenomenon referred to as this emission being 'resolved out'. Alternatively this can be used as an advantage. For example, if only long baselines are used then small-scale structure (such as within the core of an AGN) can be recovered without any diffuse obscuring 'fluff'. For a full treatment of interferometry theory and techniques see Taylor et al. (1999a).

2.3 Basics of Reduction

As with all telescopes, the data products from each individual radio interferometer have their own idiosyncrasies. Throughout this thesis a variety of software packages have been used for data reduction and handling, depending on what is optimised for each particular array. These are covered in more detail in the relevant sections. However the overall approach to reducing the data progresses along a similar path and so here we provide an overview of the typical actions that need to be performed on raw data to create science products.

The data products that are written by the correlator can be very large and so to produce more manageable files the first stage is often to average in both time and frequency. Following (and in some cases prior to) this, excising bad data is paramount for the final image quality. Bad data can be due to a huge host of causes, from individual antenna mal-

functions and shadowing (one antenna blocking another) to Radio Frequency Interference (RFI). Removing ('flagging') erroneous data is essential with the gambit that 'if in doubt - chop it out[1]' will typically solve more problems than it causes, particularly with the wide bandwidths and high data-rates of modern interferometers.

The actual calibration requires three main corrections to the data. Firstly, the differing response function of a typical receiver across its bandpass needs to be corrected for. This allows for robust flux measurements when multi-frequency synthesis imaging is employed to average together data in different frequency channels. This effect can be corrected by observing an unresolved source of known spectrum and comparing to the theoretical response. Secondly, the overall amplitude of the observations need to be set to a consistent flux scale. This is usually achieved by observing a well monitored, strong calibrator source to which the calibrator response can be scaled. Often, multiple visits to a strong flux calibrator may be scheduled during a single run or particularly when the array set-up is altered to track any changes in response.

Finally, the phases of the incoming signals need to be calibrated so that they are consistent between antennas. This is perhaps the most important step of the calibration, as if individual antennas are out of phase then the source may not be recovered. Furthermore, fast drifting of the phase will result in significant errors in the final images. Delays between antennas will naturally drift over time and, depending on observing frequency, can be greatly affected by the atmosphere. For bright science targets (the actual brightness required depends on the array, set-up and how well behaved everything is being), phases can often be calibrated from the observation of the source itself. This is due to the fact that most errors are assumed antennas based and so for N antennas with $N(N-1)/2$ baselines there will (for arrays with more than three components) always be redundant solutions. This 'self-calibration' however is dependent on having a bright enough science target and also requires a known source model. Often this is unknown. Practically, phase calibration tends to rely on regular observations of a known calibrator nearby to the science target (within the isoplanatic patch) and the time varying phase solutions of this calibrator are then applied to the science target. Often this is the only way to calibrate faint sources, and

[1] Thanks to Dr. Rob Beswick

even for bright targets this is typically used to produce an initial map and self-calibration then progresses cyclically using the recovered structure as the expected source model at each cycle.

In practice, the flux calibrator can also be used for bandpass correction and is often referred to as the primary calibrator. This is observed only a few times per observing block and the same source can be used to calibrate the amplitudes (gains) of all science sources in the block at the same frequency set-up. The major exception to this is at high frequencies ($>$20 GHz) where a planet is often required for flux calibration but is of course too resolved to act as bandpass calibrator. A phase calibrator is observed regularly (typically every few minutes but exact timing is dependent on set-up) for either each science target or each group of targets if these all fall within a small patch of sky. The phase calibrator is often also called the secondary calibrator.

Once the data are calibrated they can be mapped. Prior to this stage the data are often referred to as 'uv-data', and inferences about the science sources can be made from this but it is mapping that produces the images. The exact technique used for imaging depends on the software package used but typically involves three main stages. The data are initially inverted (Fourier transformed) to create a 'dirty map'. This is the sky-map convolved with the synthesised beam. Deconvolution then involves removing this beam pattern and can progress by any of a number of methods. The most widely used of these is via the CLEAN algorithm (Högbom, 1974), that works by assuming that the source can be composed of a finite number of point sources. The algorithm picks the peaks ('CLEAN components') and removes these iteratively with a set amount of dirty beam. The clean components are stored until some given threshold is reached, ideally once CLEAN has found all the true flux and has reached the noise. The final stage of mapping then involves restoring these CLEAN components with an idealised beam (typically a Gaussian) so that a final 'cleaned' image is recovered.

More information on the reduction techniques for radio interferometry data can be found by consulting the various 'cookbooks' that are available, e.g. for ATCA/CARMA data (the MIRIAD Cookbook: http://www.atnf.csiro.au/computing/software/miriad/) and for (J)VLA/VLBA data (the AIPS cookbook: http://www.aips.nrao.edu/cook.html). Consult also the e-MERLIN (http://www.e-merlin.ac.uk/data_red/tools/e-MERLIN_cookbook

_latest.pdf) and LOFAR (http://www.astron.nl/radio-observatory/lofar/lofar-imaging-cookbook) cookbooks.

2.4 Motivation - The Need for a Large Sample

An issue that often complicates the study of BCGs (and indeed all galaxies) using radio observations is that the observed emission can be separated significantly in both time and space from the event that created it (e.g. Harwood et al., 2013, for a discussion of spectral ageing). Single-band, often low spatial resolution observations are frequently the only radio information available for a BCG. This can result in an unresolved source with limited spectral information, hence whilst the galaxy can be said to be radio loud, there is large uncertainty both in the physical scale and age of this emission, thus making comparisons with AGN tracers at other wavelengths difficult. To overcome this issue, observations at a range of spectral frequencies and spatial resolutions for a large sample of BCGs are required.

In this thesis we aim to use a wide range of data from a variety of telescopes to more fully understand the nature of the radio emission in BCGs. To this end, we require a large parent sample of galaxy clusters. In selecting this parent sample it is highly important that it be fair, and free from being selected on the BCG activity, especially since radio emission is inherently affected by directional effects. In this thesis this is done by choosing an X-ray selected cluster sample, meaning that we select based on the isotropically emitting X-ray bright intra-cluster medium and not the BCG activity.

We describe our parent sample in the following section. From this parent sample we then create spectral energy distributions (SEDs) for nearly 300 BCGs, which we then decompose into an active component - attributable to current accretion, and an inactive component - attributable to historical accretion. These decompositions are described in the remainder of this chapter. Chapter 3 then considers these individual components in greater detail and uses them to link the central AGN activity to the relativistic outflows it generates and how the nature of this depends upon the larger cluster environment.

Note that the remainder of this chapter and Chapter 3 are largely composed of work that appears in Hogan *et al* 2014a. Overall, these chapters look at the general radio proper-

ties of the BCG population as a whole. They amalgamate and utilise a large data volume in order to decompose the radio emission to better understand what being a radio-loud BCG actually entails and how this activity relates to the wider environment.

2.5 The Sample

2.5.1 Parent Cluster Sample

Our parent sample is drawn from three ROSAT X-ray selected cluster catalogs - the BCS (Ebeling et al., 1998), eBCS (Ebeling et al., 2000) and REFLEX (Böhringer et al., 2004) samples, which contain 206, 107 and 447 sources respectively. Since publication, a minority of sources in these catalogues have been noted as initially mis-identified, most commonly due to AGN contamination in the X-rays or appear as duplicates. We therefore remove a minority of sources, leaving us with a sample of 199, 104 and 417 sources in the BCS, eBCS and REFLEX samples respectively. Our total X-ray selected parent sample therefore consists of 726 clusters.

The BCG for each of these clusters has been observed spectrally with either the Isaac Newton Telescope (INT) (Crawford et al., 1999) or the FORS instrument on the Very Large Telescope (VLT) (Edge et al.*in prep.*). These observations targeted the Hα and N[II] features, the presence of which provides a strong proxy indicator for a cool core cluster (see Section 1.4.4). The detection limits for the Crawford et al. (1999) observations range from an Hα luminosity of $\approx 4\times10^{39}$ erg s^{-1} at z$\approx$0.05 to $\approx 1.8\times10^{41}$ erg s^{-1} at z$\approx$0.3 with a typical L$\propto$z^2 relationship. Taken alone, this could lead us towards preferentially detecting only higher luminosity Hα emitters at higher redshifts. However, the $\approx$10x deeper detection limits of Edge et al., *in prep.* should mitigate this effect. Furthermore we note that the original work by Cavagnolo et al. (2008) used mainly Hα luminosities from Crawford et al. (1999) and that the use of these optical lines as an indicator of a cool core cluster requires only their *presence* and is not dependent upon their total luminosity, hence an accurate measurement of the Hα flux is not essential for our pruposes (see Section 1.4.4 and Figure 1.1).

We note that Crawford et al. (1999) found a higher detected fraction of line-emitters in X-ray selected clusters than optically selected targets, and that the detection fraction for

the X-ray selected clusters targeted by Edge et al.is comparable. This therefore suggests that the dichotomy seen by Cavagnolo et al. (2008) extends to the deeper Hα detection limit of Edge et al., and hence including these classifications is not believed to introduce any bias by way of non-cool cores exhibiting line emission at a weaker level than investigated by Cavagnolo et al. (2008) (see also Figure 1.1).

The use of a proxy measure for the cool-core to non cool-core dichotomy will almost certainly introduce a level of contamination, however we believe this to likely be below 1% (Cavagnolo et al., 2008). Furthermore, using this proxy allows us to classify a much larger sample than is currently possible from X-ray observations. Hereforth we split our parent sample of 726 clusters into those whose BCGs exhibit optical emission lines (line-emitters, henceforth LEs) and those which do not (non line-emitters, henceforth NLEs; see also Table 2.1) and refer to these (near-)synonymously with strong cool-core clusters and non cool-core clusters. It must be noted the absence of measured optical lines is not sufficient to rule out the presence of a weaker cooling core ($5x10^8 yr < t_{cool} < t_{Hubble}$), but their absence does point towards these clusters being less dynamically settled.

The BCS/eBCS sky coverage overlaps fully the NRAO VLA Sky Survey (NVSS) radio survey (Condon et al., 1998, DEC $>$ -40°, complete to $\approx$2.5mJy at 1.4 GHz). Of the 417 REFLEX clusters in our sample, 297 fall within the NVSS region and 156 within the complementary southern region covered by the Sydney University Molonglo Sky Survey (SUMSS: Mauch et al., 2003) (DEC $<$ -30°, complete to $\approx$6mJy for DEC$<$-50° and $\approx$10mJy for DEC$<$-30° at 0.843 GHz). These sub-samples are hereon referred to as the REFLEX-NVSS and REFLEX-SUMSS samples. There were 36 sources within the REFLEX sample that fall in the overlap between SUMSS and NVSS and hence there is some redundancy. We leave these sources in both the REFLEX-NVSS and REFLEX-SUMSS samples when these samples are treated independently. Additionally, these sources can be used to estimate the variation in spectral index across a sample of BCGs that were not selected from their radio-brightness and hence are free from priors associated with radio flux selected samples. Combining the BCS and eBCS catalogues provides a 303 source subsample that we henceforth refer to as the (e)BCS. The comparable number of clusters in (e)BCS and REFLEX-NVSS allows for self-consistency checks of any found results since the samples were independently compiled.

Table 2.1: BCGs within the (e)BCS and REFLEX galaxy cluster samples (after removal of 'contaminant sources'). The samples are broken down both by radio detection in NVSS and/or SUMSS and also the presence of extended optical emission lines around the BCG, which are indicative of the presence of a strong cool core.

	Lines	No Lines
BCS		
Detected	55	67
Non-detected	8	69
eBCS		
Detected	19	44
Non-detected	6	35
REFLEX - Total		
Detected	91	161
Non-detected	17	148
REFLEX - NVSS		
Detected	67	119
Non-detected	10	101
REFLEX - SUMSS		
Detected	36	58
Non-detected	7	55

2.5.2 Main Sample

We have targeted follow-up observations of 246 of these sources at either C- or X- ($\approx$5 or 8 GHz) band (or both) using the ATCA or VLA (see Appendices A and B). These sources constitute the 'Main Sample' of this chapter. They comprise 106 + 64 sources (detections + non-detections respectively) in the BCS, 13 + 2 in the eBCS, 39 + 7 in REFLEX and 9 + 6 additional sources that since publication of the catalogs have been found to fulfil the detection criteria but were not initially classified as clusters, typically due to expected AGN contamination. The extra sources are - Non-detections: A7, A2552, Zw15, Zw5029 and Z7833. Detections: A11, A291, A1664, A2228, and 4C-05.84). This constitutes follow-up completenesses of $\approx$85.4%, $\approx$14.4% and $\approx$11.0% for the BCS, eBCS and REFLEX catalogues respectively.

Whilst only a minority of eBCS clusters are included in the Main Sample, these were randomly selected from the eBCS prior to its publication and should constitute a fair addition to the Main Sample. The minority of clusters followed up from within the REFLEX sample were selected to be the radio-brightest (L-band) line-emitting BCGs. This introduces a selection effect into our Main Sample in that we include a greater proportion of

LE clusters than are present in the general cluster population. Indeed, this problem is exacerbated by our choice of X-ray catalogues for the parent sample since cool core clusters have a strongly peaked X-ray profile, which leads to a natural detection preference over non-cool core clusters. This is desirable since we are interested in comparing the radio properties of LE-hosted BCGs to those of the NLE-hosted BCGs. As $<$30% of the cluster population constitutes LEs, by skewing our selection to LEs we return a sample with a higher fraction of LEs than other cluster detection methods typically yield. This sample selection should be considered when investigating implications to the galaxy cluster population as a whole. The high completeness for BCS however provides us with a radio-observed, X-ray selected cluster sub-sample that is un-biased by any radio priors on the BCGs, which can be tested.

Main Sample+

To form a complete radio flux limited sample for considering the radio properties of BCGs in the full parent sample, we supplement the Main Sample by considering SEDs composed of literature values for all BCGs in the Parent Sample that are radio-matched to at least one of NVSS or SUMSS and have L-band fluxes $>$15mJy (we note that the 843 MHz observing frequency of SUMSS is technically below the traditional L-band range of 1-2 GHz, however we refer to both SUMSS and NVSS as 'L-band' for succinctness). Whilst without targeted follow-up, the decompositions of these sources (see Section 2.7 and Appendix F) contain a higher fraction of upper limits, the addition of these sources does ensure that we are drawing conclusions on the radio behaviour of BCGs from a complete flux-limited sample and immunises us against missing extreme (fainter *or* brighter) objects that may oppose any trends found from the targeted campaign. It should be noted that the decompositions obtained for these extension sources are less reliable than those in the Main Sample, often utilising only components of the SEDs close to the 1 & 10GHz frequencies of interest as opposed to full SED construction and subsequent decomposition. We refer to this flux-limited sample as the Main Sample+ (henceforth MS+).

Table 2.2: Breakdown of the ATCA and VLA observations used in this thesis that were published for the first time in Hogan et al.2014a (All: P.I. Edge). Note that we present a small amount of L-band data from project AE117. This data was used when compiling our SEDs and was presented for the first time in this paper.

Proposal ID	Year	Array	Frequency (GHz)	Sources Observed
C1958	2011	ATCA-6A	5.500	14
C1958	2011	ATCA-6A	9.000	14
C1958	2008	ATCA-6A	4.800	31
C1958	2008	ATCA-6A	8.640	31
AE125	1999	VLA-C	4.835	14
AE117	1998	VLA-A	1.385	12
AE117	1998	VLA-A	8.435	32
AE110	1997	VLA-C	4.835	23
AE107	1996	VLA-C	4.835	27
AE099	1994	VLA-C	4.835	59

2.6 Observations

This work has utilised data from a variety of observing campaigns, supplemented by measurements obtained from the literature.

Both pre and post-CABB (Compact Array Broadband Backend; Wilson et al., 2011) data from the ATCA were analysed. Additionally, VLA data from five observing campaigns were utilised (see Table 2.2). All of these observations followed a standard 'snapshot' schedule with multiple visits to each target source, separated by several hours to ensure good hour-angle (HA) coverage. Each visit was sandwiched between short observations of a nearby standard source for phase calibration. Absolute flux calibrators were observed at the beginning and end of each run with the phase calibrators also used for bandpass calibration where appropriate; otherwise the primary calibrator was used for this.

ATCA and VLA data were reduced and fluxes measured for the detected sources using the Multichannel Image Reconstruction Image Analysis and Display (MIRIAD: Sault et al., 1995) and the Astronomical Image Processing System (AIPS: Greisen, 2003) packages respectively, following the standard reduction procedures.

Literature searches were performed for all sources in the Main Sample (i.e. those observed in Table 2.2) and its extension. The SED of each of these BCGs was populated.

Data were taken from the major radio catalogues (e.g. Australia Telescope 20 GHz Survey (AT20G), Murphy et al. 2010; NVSS and Faint Images of the Radio Sky at Twenty-cm (FIRST) at 1.4 GHz, Condon et al. 1998; White et al. 1997; SUMSS at 843 MHz, Mauch et al. 2003; Texas Survey of Radio Sources (TEXAS) at 365 MHz, Douglas et al. 1996; Westerbork Northern Sky Survey (WENSS) and Westerbork In the Southern Hemisphere (WISH) at 325 MHz, Rengelink et al. 1997; De Breuck et al. 2002; TIFR GMRT Sky Survey (TGSS) at 150 MHz; VLA Low-Frequency Sky Survey (VLSS) at 74 MHz, Cohen et al. 2007). Additional fluxes found by searches around the radio-peak coordinates in the NASA/IPAC Extragalactic Database (NED), High Energy Astrophysics Science Archive Research Center (HEASARC) database and/or the National Radio Astronomy Archive (NRAO) were individually scrutinised to ensure matches.

The large variety of data used, originating from a variety of telescopes, naturally encompasses a range of angular resolutions. This means that the integrated derived fluxes may not be sampling the same spatial scales and hence are often not directly comparable. Careful consideration is given to this to ensure that 'missing flux' does not lead to imitated spectral breaks or variability. Whilst this effect is an extra consideration when interpreting fluxes measured with interferometric observations, it can also be advantagous since for many sources we are able to consider high and low resolution data seperately to study different scales within the same source. Further details on the consideration given to the varying angular resolution of the data used are given in Appendix A.

2.7 SED Decomposition

2.7.1 Core versus 'Non-core'

The total radio SED of each BCG can be decomposed into two major components - an active, typically flat-spectrum (spectral index[2] $\alpha<0.5$) component attributed to current activity within the AGN and a typically steeper spectrum component ($\alpha>0.5$) that comprises all other emission.

The steeper component is most likely to be due to lobe emission and so trace past

[2]Unless otherwise stated, we use: Flux $\propto \nu^{-\alpha}$

activity of the central engine. Alternatively it could be due to other acceleration processes towards the centre of the galaxy cluster in which the BCG resides, such as sloshing giving rise to a mini-halo or phoenix relics (e.g. van Weeren et al., 2011; ZuHone et al., 2013; Walker et al., 2014, and references therein). The specific morphological and energetic nature of this component is often difficult to determine and a large variety of nomenclature for the various source-types has arisen (see Kempner et al., 2004, for a detailed review). The steep spectrum means that this component becomes less prominent towards higher frequencies and is often faint at L-Band and above, rendering it difficult to detect if an active core component is present. Conversely, current AGN activity manifesting itself as a flat-spectrum core component can be swamped at lower frequencies. High resolution observations are required at low frequency to properly characterise these components. However, in this work we wish to address the difference in radio emission between ongoing core activity and older, steep-spectrum emission and henceforth use 'non-core' as an umbrella term to refer to the steeper spectrum component not associated with ongoing core activity, regardless of physical origin and spatial resolution.

The core component may show a synchrotron self-absorption turnover at $\approx$few GHz but tends to remain flat (or in rarer cases inverted) out to several tens of GHz. Similarly the 'non-core' component may show a turnover, albeit at much lower ($<$ a few hundred MHz) frequencies although this is more likely to be attributable to free-free absorption. Additionally, this component may exhibit a steepening index at higher frequencies due to synchrotron ageing of the underlying electron population. SEDs with a strong inverted core component and a steep low-frequency tail suggest recurrent activity whilst also requiring the re-ignition time-frame to be on timescales less than the lifetime of the steep component.

A Note on Non-AGN Related Cluster Radio Emission

Note that when present we exclude both cluster scale radio halos and peripheral relics (a.k.a. 'radio gischt'; e.g. Giacintucci et al., 2011b) from our non-core component, as these are both unrelated to the AGN activity of the BCG (e.g. Kempner et al., 2004; Ferrari et al., 2008). There are however a number of other radio structures seen in cluster cores such as mini-haloes and phoenix relics whose relationship to the BCG and the

cooling core is more uncertain (e.g. Gitti et al., 2002, 2006, 2007). There is debate in the literature as to the true nature of so-called 'mini-halos' and these present a somewhat contentious middle-ground between cluster related and AGN-related radio-emission. True mini-halos tend to be reasonably spherically symmetric, steep spectrum, low surface brightness sources ≈few 100s kpc in diameter centred on the BCG (e.g. Burns et al., 1992; Owen et al., 2000; Giacintucci et al., 2014). The electron diffusion lifetime is so long as to exclude acceleration by the central AGN. The emitting particles must therefore be accelerated in-situ and appear to be related to the cooling flow. It is however possible (and indeed likely) that the seed population originates in the AGN.

Confusingly, it appears that BCGs often contain a smaller ($<$ few 10s kpc) amorphous halo or *'confined cluster core'* (e.g. Venturi et al., 2004), that appears to be related directly to confined, ageing AGN ejecta, which is also occasionally referred to as a mini-halo. As the exact nature of the non-core emission is not paramount for our purposes, we may include in our non-core measures emission that could reasonably be called 'mini-halo' in the literature if it contributes a portion of the flux in low-resolution observations that provide such a measurement as the 'BCG flux'.

2.7.2 SED Fits

A graphical representation of the decision making process for determining the best method to differentiate the core and non-core emission in each source is shown in Figure 2.1. The remainder of this section explains this process, and the models used, in more detail.

The majority of sources were unresolved at the resolution limit of our observations (typically ≈4" at C-band, equivalent to ≈8 kpc at our median redshift of 0.126). Where clearly distinct core and non-core components were resolved, individual SEDs were produced and fitted directly for each component. This scenario was most likely for bright sources where the total flux is dominated by lobes with large angular size. Alternatively, in lobed systems with small angular size, the resolution was frequently adequate to distinguish lobes yet not be able to directly image a separate core.

Few-arcsecond resolution unresolved sources, without enlightening Very Long Baseline Interferometry (VLBI) observations, could consist of an active core only or small scale yet ageing non-core emission. For resolution limited sources, variability and spec-

tral shape were considered when attempting a breakdown of the SEDs on a case-by-case basis (see below). Where a strong case could not be made for unresolved sources being either core or non-core dominated, conservative assumptions were employed.

Main Sample

Four simple models were considered for each source SED - a single power law of the form:

$$S = A_0 \nu^{-\alpha} \tag{2.7.1}$$

a split power law of the form:

$$S = A_0 \nu^{-\alpha_1} + A_1 \nu^{-\alpha_2} \tag{2.7.2}$$

a 'dropline' model, which allows for a high frequency rollover to simulate synchrotron ageing:

$$S = A_0 \nu^{-\alpha} (1 - A_1 e^{-\frac{\nu_0}{\nu}}) \tag{2.7.3}$$

or a Gigahertz Peaked Source (GPS)-like model that allows for a spectral peak to simulate self-absorption (Orienti & Dallacasa, 2014)

$$Log(S) = A_0 + Log(\nu)(A_1 + A_2 Log(\nu)) \tag{2.7.4}$$

where S denotes measured flux and 'A's are constants to be determined.

These fits are not intended as physical models. Indeed it is clear that for the dropline model, extrapolation outside of the region being considered would lead to negative predicted flux. Instead they are merely phenomenological fits to the known data to provide a robust breakdown of the two broad emission types - core and non-core - to allow their properties to be separated.

The single power law provides the simplest possible fit. This often had to be employed particularly for poorly sampled SEDs. The index of this power law was considered, with a flat or inverted slope leading to the detection being attributed to a core component, or a steep slope meaning the detection was classed as a non-core. The nominal cut-off between these distinctions was taken as $\alpha = 0.5$. However, anything shallower than $\alpha =$

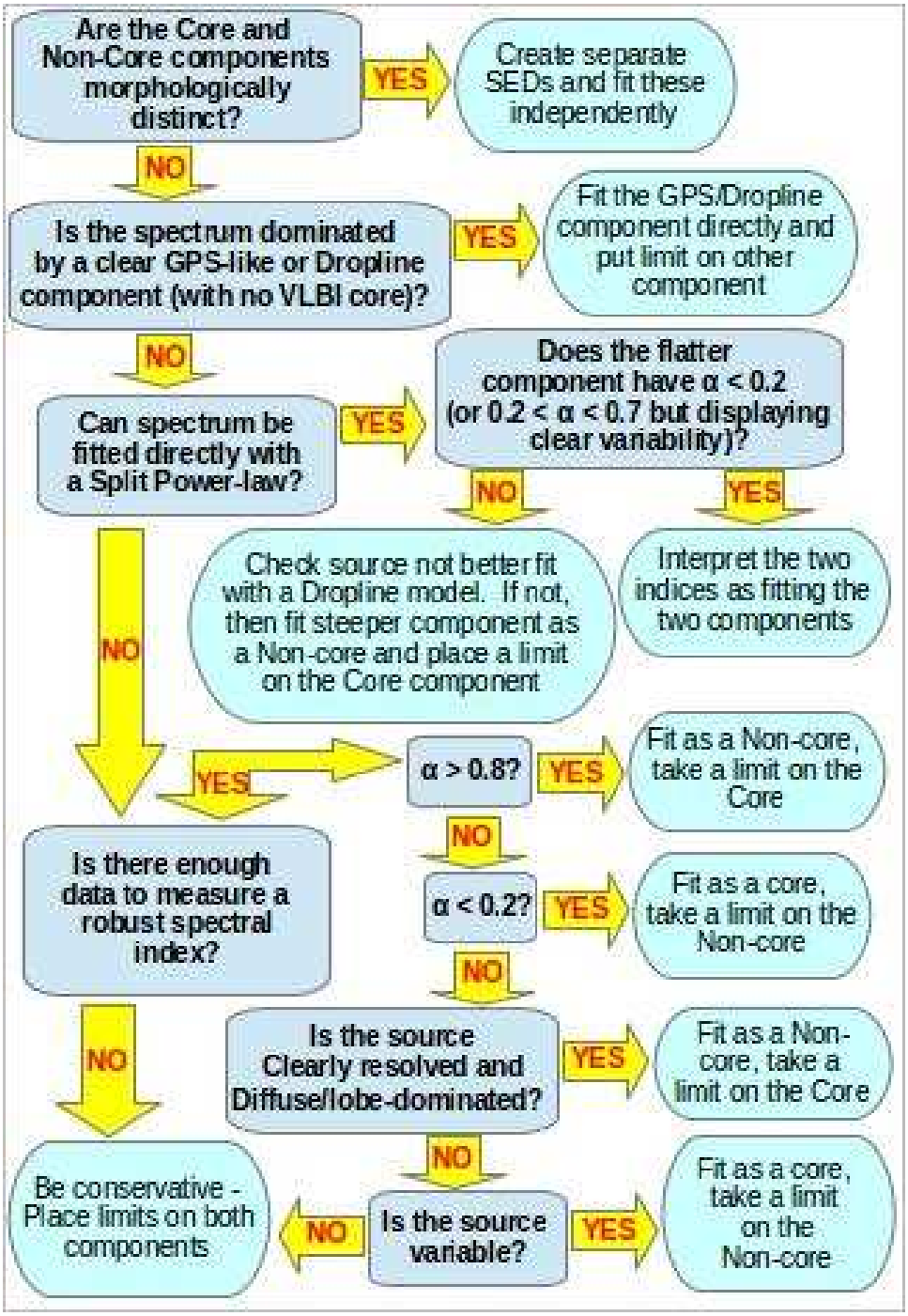

Figure 2.1: Graphical representation the decision making process when determining the best approach for each individual SED decomposition. Morphological, spectral and variability properties are all considered when determining the best classification of the core to non-core breakdowns.

0.8 or steeper than $\alpha = 0.2$ was further scrutinised. Hints of extension were searched for at each observed frequency and variability was considered, with the proviso that a core dominated system was more likely to vary on shorter timescales. In situations where there was strong evidence for one component dominating the observed flux and hence spectral shape, then the value of this component was taken as a measurement of that component. A limit was placed on the other component by extrapolating with a representative steep ($\alpha_{non-core} = 1.0$, see section 2.7.3) index from the lowest observed frequency or with representative shallow ($\alpha_{core} = 0.2$, see section 2.7.3) index from the highest observed frequency for non-core and core limits respectively.

Where a clear spectral break could be seen (e.g. see Panel b, Figure 2.2), a split power law was employed to fit the two components. Highly variable sources could display an apparently split spectrum if observations taken at different frequencies were substantially separated in time. We considered the timescales and any variations between observations at different frequencies to help distinguish between consistent and apparent spectral breaks.

SEDs that exhibited the high frequency rollover typical of an ageing electron population were fit with a dropline model. When only this component was apparent in an SED, the value derived was attributed to the non-core component and a limit placed on the core (e.g. Panel c, Figure 2.2).

Somewhat unexpectedly, a minority of sources exhibited a strongly inverted, peaked spectrum which was fit using the GPS-like model. This spectral shape is typical of a GPS source, commonly interpreted to be either a young or recently re-triggered AGN and as such is indicative of a strong, active core (O'Dea, 1998). However in a couple of cases a steep-spectrum, low frequency 'tail' of emission can also be seen in the SED, allowing the non-core component to also be measured (e.g. Panel a, Figure 2.2). Where only a GPS-like component was apparent a value is taken for the core and a limit derived for the non-core component (e.g. Panel d, Figure 2.2).

During the fitting, consideration was also given to the possibility of flux on spatial frequencies not sampled by observations and hence effectively resolved out. Again, caution was employed to ensure that such effects did not overly bias our breakdowns.

Full details of the breakdowns and the SEDs for each source in the Main Sample can

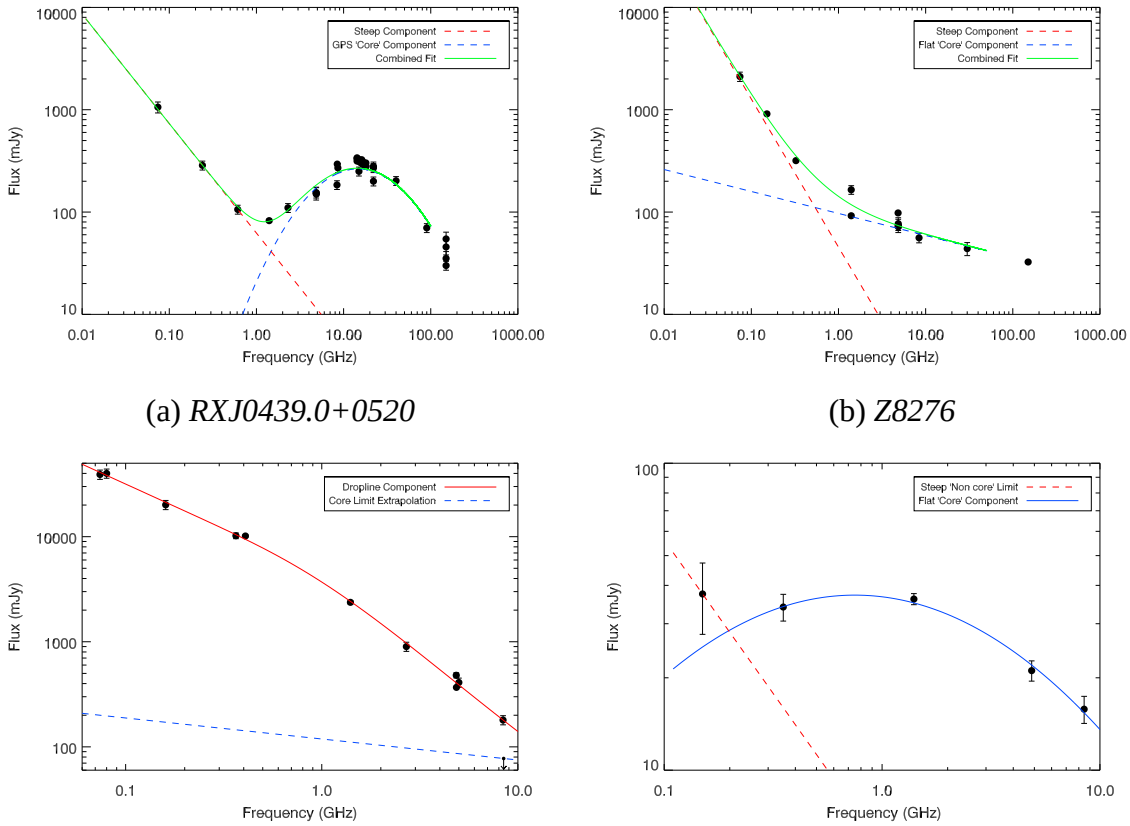

(a) *RXJ0439.0+0520* (b) *Z8276*

(c) *RXJ0747.5-1917* (d) *RXJ1315.4-1623 (NGC 5044)*

Figure 2.2: Example SEDs for four different source-types. In panel a, RXJ0439.0+0520 is dominated by a GPS-like core component at frequencies above ≈1 GHz although a clear steep spectrum component is seen at lower frequencies. Panel b shows Z8276 where such a dominant inverted core is not present yet there is still a distinct flattening of the spectral index to higher frequency suggestive of a significant active component in the system. This appears well represented by a split power-law. Not all sources can be fit with two distinct components. Panel c for example shows RXJ0747.5-1917, which appears to be well fit by a steep power law with a rollover to higher frequencies (i.e. a *'dropline'*, see text). This source is slightly resolved at X-band with the VLA-A, hence extrapolating from the peak of this observation allows an upper limit to be placed on a core contribution. Alternatively, panel d shows RXJ1315.4-1623 whose BCG is unresolved at all observed frequencies and exhibits a peaked SED, indicative of it being dominated by an active, self-absorbed core. There is a map detection at 150 MHz from TGSS that may indicate the presence of a weak non-core component although the uncertainty is too large to derive a strong measurement of this and hence a limit on the non-core is derived by extrapolating from this low frequency point.

be found in Appendices A - C.

Main Sample+

For many of the brighter members of the MS+ extension (e.g. Hydra-A and Hercules-A) clear morphological decompositions could be performed. Where this was not the case, partial spectral breakdowns were performed using the same criteria as for the Main Sample with the exception that, due to the typically much lower spectral coverage and less available data, GPS-like and dropline models were not used as they were poorly constrained. Often a single index fit around the normalisation frequency had to be taken.

For many of the sources in the MS+ extension, radio coverage was limited to only the L-band detection. In these instances the detection thresholds of higher frequency large-scale surveys, predominantly the Green Bank 6-cm at 4.85 GHz (GB6: Condon et al., 1994), the Parkes-MIT-NRAO surveys at 5 GHz (PMN: Griffith & Wright, 1993) and AT20G were considered to determine whether the source has a flatter spectrum component to high frequencies or whether the L-band flux is attributable to a dominant non-core. Where a limit on a higher frequency flux determined that the L-band detection must be due to a source with spectral index $\alpha>0.8$ then it was attributed to dominant non-core emission and an estimate of this made using a short extrapolation with $\alpha_{Steep}=1.0$. Core limits were then drawn using $\alpha_{Flat}=0.2$ from the higher frequency limits. These indices were chosen on the basis of being typical of the α values found for clearly identifiable components. In instances where the higher frequency limits did not rule out spectra flatter than $\alpha=0.8$ caution was employed and limits taken on both components, extrapolating from the L-band detection with indices $\alpha_{Steep}=1.0$ and $\alpha_{Flat}=0.2$ for the steep and flat components respectively (see also Section 3.3). Similarly, lower frequency survey limits were considered to ascertain whether a lower limit of $\alpha_{Flat}<0.5$ could be determined for any sources, so ruling out a source being steep spectrum dominated. However, the relatively shallow detection limits of most low frequency surveys (e.g. $\approx$700mJy for Molonglo Reference Catalog (MRC: Large et al., 1981), $\approx$400mJy for VLSS) coupled with the comparative depth of the L-band surveys meant that these limits were restrictive in only the brightest sources and these tended to have resolved morphology anyway.

Notes for the decomposition of each source in the MS+ can be found in Appendices

F and G.

2.7.3 Measured Indices

Figures 2.3 and 2.4 show the distributions of measured indices for our Main Sample and Main Sample+ respectively. Whilst (partly by nature of the differentiation criteria) there is a clear split between the shallow spectrum core component and the steep spectrum non-cores, some crossover of indices is seen. For the core components, not all will necessarily be flat and exhibit self-absorption. Indeed, for a 'naked core' where the base of a recently triggered jet can be seen then an injection index of $\approx$0.6 may be expected (Laing & Bridle, 2014). Alternatively, extended emission can have a relatively flat spectrum ($\alpha \leq 0.6$). A tail to inverted core spectra is seen, mirrored by a tail to ultra-steep components for non-cores.

Our choice of a representative indices of α_{core}=0.2 and $\alpha_{non-core}$=1.0 for extrapolations initially appear to be slightly too shallow and too steep respectively when considering Figures 2.3 and 2.4. These choices are however governed by conservatism. If we consider the median index for the core and non-core when all measured indices for each of these components are included, we arrive at α_{core}=0.33 and $\alpha_{non-core}$=0.96 (considering the Main Sample only, as this has most reliable index measurements). However, if we restrict our sample to the subset of sources where both a measure of the core and non-core were obtainable our median indices are α_{core}=0.28 and $\alpha_{non-core}$=1.08. Often when a source is detectable out to frequencies $>$10 GHz it either contains a clearly identifiable active core component or is a bright source, which in many cases have VLBI measurements. For these reasons in most cases where core extrapolation is required it is from below the 10 GHz normalisation. Therefore a shallower index provides a more conservative upper limit, hence our choice of α_{core}=0.2

On the other hand, the majority of extrapolations for the non-core component were from below the 1 GHz normalisation frequency and hence a flatter index is more conservative. We therefore choose $\alpha_{non-core}$=1.0 as our representative index. For cases where an extrapolation of a given component is required we employ uncertainties of $\alpha_{error}=\pm 0.2$.

The presence of a significant tail of ultra-steep non-cores suggests that such emission may be fairly common around BCGs. Amorphous and mini-halo emission is often found

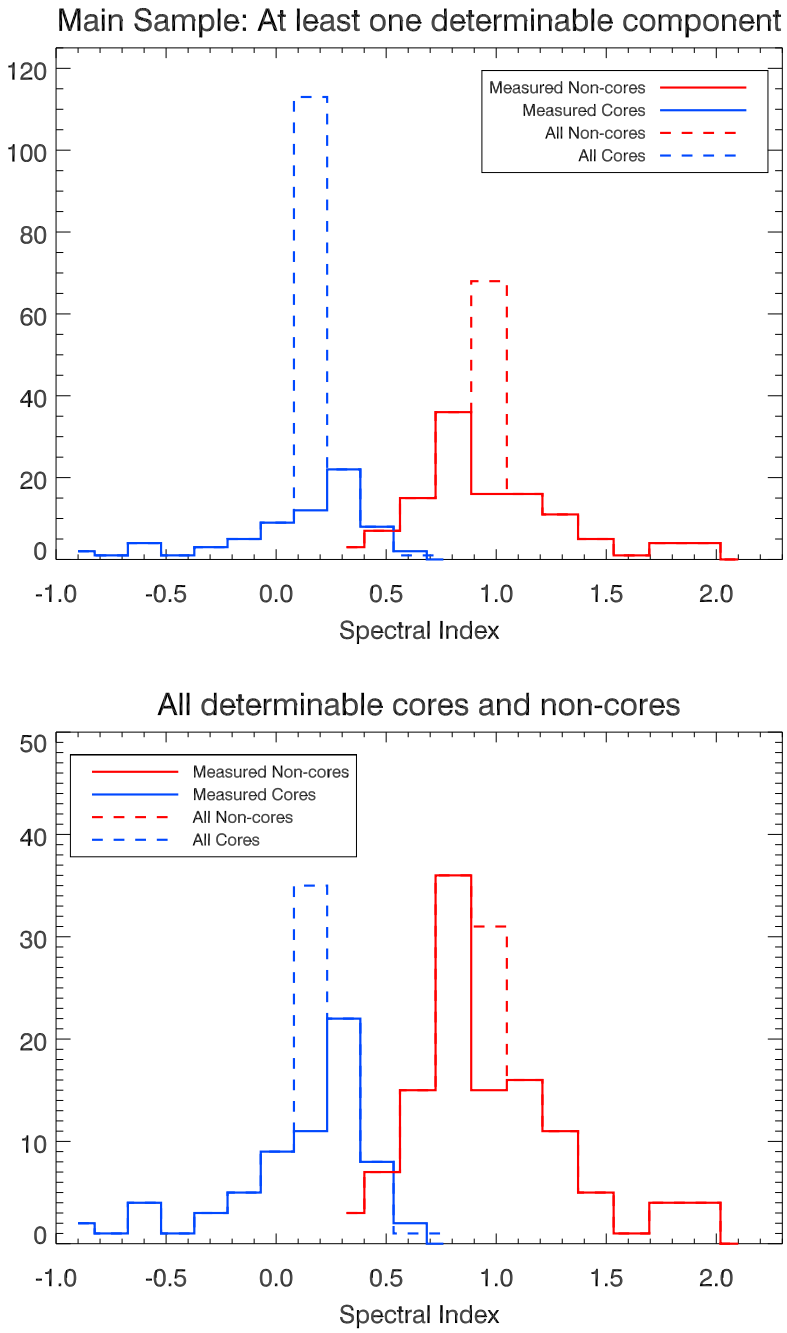

Figure 2.3: Incidence of fitted indices for the core and non-core fitted components to our Main Sample. In both panels, blue lines represent the fitted index of the core component and red that of the non-core. Solid lines are instances where the relevant component could directly be determined whereas the dotted lines include the components where a representative index had to be assumed (α_{Steep}=1.0 and α_{Flat}=0.2, see text for justification). For the top panel, all sources in the Main Sample are included for which at least one component could be measured, hence the high incidence of assumed indices as required for extrapolated limits. In the lower panel, the red lines trace all instances where a core value could be determined and the blue lines trace all instances where a non-core value could be determined. Note that limits remain in the lower panel for when a component could be resolved and had a measurement near to either normalisation (e.g. a VLBI core measurement) and only a small but secure extrapolation was required, nonetheless needing an index to be assumed. See also Appendix A.

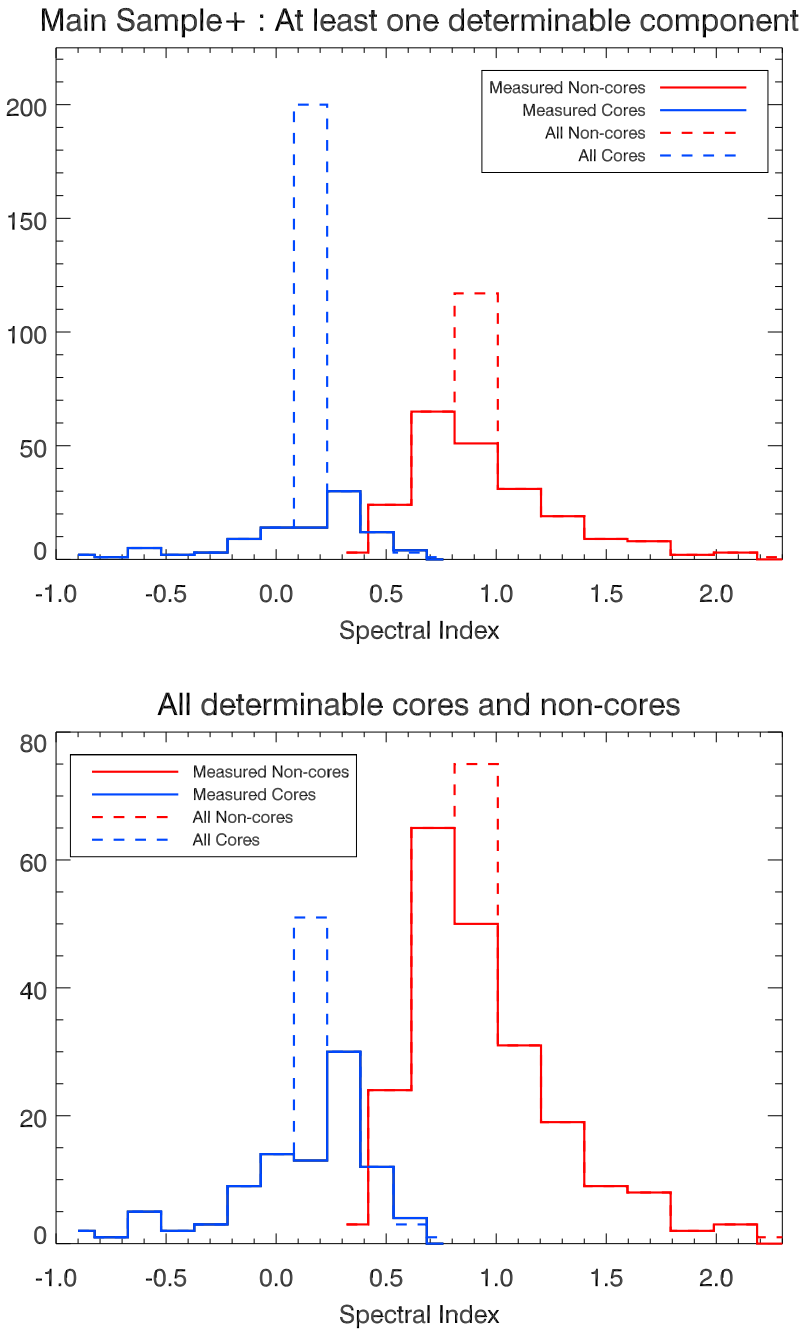

Figure 2.4: Same as for Figure 2.3 except now extended to include the full flux limited MS+. We again include sources with an assumed index as these highlight the ratio of instances where an index could be directly determined to when, even with our relatively good spectral coverage, an index had to be assumed for an individual component.

to be very steep ($\alpha > 1.5$), suggesting there may be a link between these structures and emission from a persistent AGN (see Section. 3.4.4).

For sources not detected in the pointed observations, literature searches were performed to determine whether there was any weak, steep spectrum emission present at lower frequencies. Limits on both the core and non-core limits were determined by extrapolating with representative indices from the relevant limits.

The relative importance of each of these radio components – core or non-core – are considered in the following chapter.

CHAPTER 3

The Broad Band Radio Properties of Cores and Non-cores

3.1 Abstract

In this chapter we use the sample of BCGs identified and whose radio SEDs were decomposed in the preceding chapter to study how the radio properties are related to the cluster environment. Line emitting BCGs are shown to generally host more powerful radio sources, exhibiting the presence of a strong, distinguishable core component in ≈60% of cases. This core component is found to more strongly correlate with the [OIII]5007Å line emission. We also find that for BCGs in line-emitting clusters, there is correlation of X-ray cavity power with both the extended and core radio emission, suggestive of steady fueling of the AGN over bubble-rise timescales in these clusters. The work presented within this chapter constitutes the second half of Hogan *et al.* 2014a.

3.2 Monochromatic L-Band Radio Properties

Initially we consider only the flux limited monochromatic radio properties of our Parent Sample around 1.4 GHz, to gain an overview of the general properties.

3.2.1 Radio Matching

The optical BCG positions of the entire parent sample were cross-referenced with the NVSS and SUMSS radio catalogues, initially searching within their respective positional uncertainties (1-7” for NVSS, 1-10” for SUMSS). Additional uncertainty for the radio

source position arises due to the relatively large beam sizes ($\approx$ 45"). Where a radio source was matched to within one beam size but greater than 2" from the optical position, the sources were inspected visually to ascertain whether a match could be claimed. Additionally, where multiple matches fell within the beam size they were visually inspected to ensure multiple components of individual sources were appropriately included.

A sizeable proportion of the (e)BCS clusters ($\approx$73%) fell within the FIRST (Becker et al., 1995) survey region (matched to SDSS, DEC limit $>$ -10), which has a smaller beam size ($\approx$ 5") and lower flux limit ($\approx$ 2mJy) than NVSS. A much smaller portion ($\approx$26%) of sources within the REFLEX-NVSS sample also fell within the FIRST region. Sources within this overlap region were additionally cross-matched with the FIRST survey and radio-optical overlays inspected. With the higher resolution data of FIRST, we find that $\approx$15% of sources tagged as matches in NVSS were likely not associated with the BCG. It should therefore be noted that the absence of a similarly high resolution southern survey is likely to introduce a bias in that mis-attributions of a radio-source to the BCG are less likely to be noticed in the southern hemisphere. However, we also find that $\approx$10% of sources in the FIRST footprint that were not detected by NVSS were either detected with the fainter threshold of FIRST or shown to be radio-loud independently of another nearby source and hence this bias is likely to be tempered by the lower detection threshold and higher resolution of the FIRST survey.

3.2.2 LE and NLE Match Rates

The number of BCGs matched to radio-sources can be seen in Table 2.1, along with a breakdown of whether these BCGs are optically line-emitting or not (LE or NLE). We find a detection percentage of $\approx$ 61.1$\pm$5.5%, 62.6$\pm$5.5% and 60.3$\pm$7.7% for (e)BCS, REFLEX-NVSS and REFLEX-SUMSS respectively, assuming simple binomial errors with a 95% confidence level.

These BCG radio-detection rates are slightly elevated compared to other X-ray selected samples. For example, Sun et al. (2009) found a 50.3% detection rate for a luminosity cut of $L_{1.4\ GHz} > 10^{23} WHz^{-1}$ for their sample of 43 nearby galaxy groups with Chandra archival data. A $\approx$50% detection rate was found for both the Brightest 55 (B55, Edge et al., 1990; Peres et al., 1998) and The HIghest X-ray FLUx Galaxy Cluster Sam-

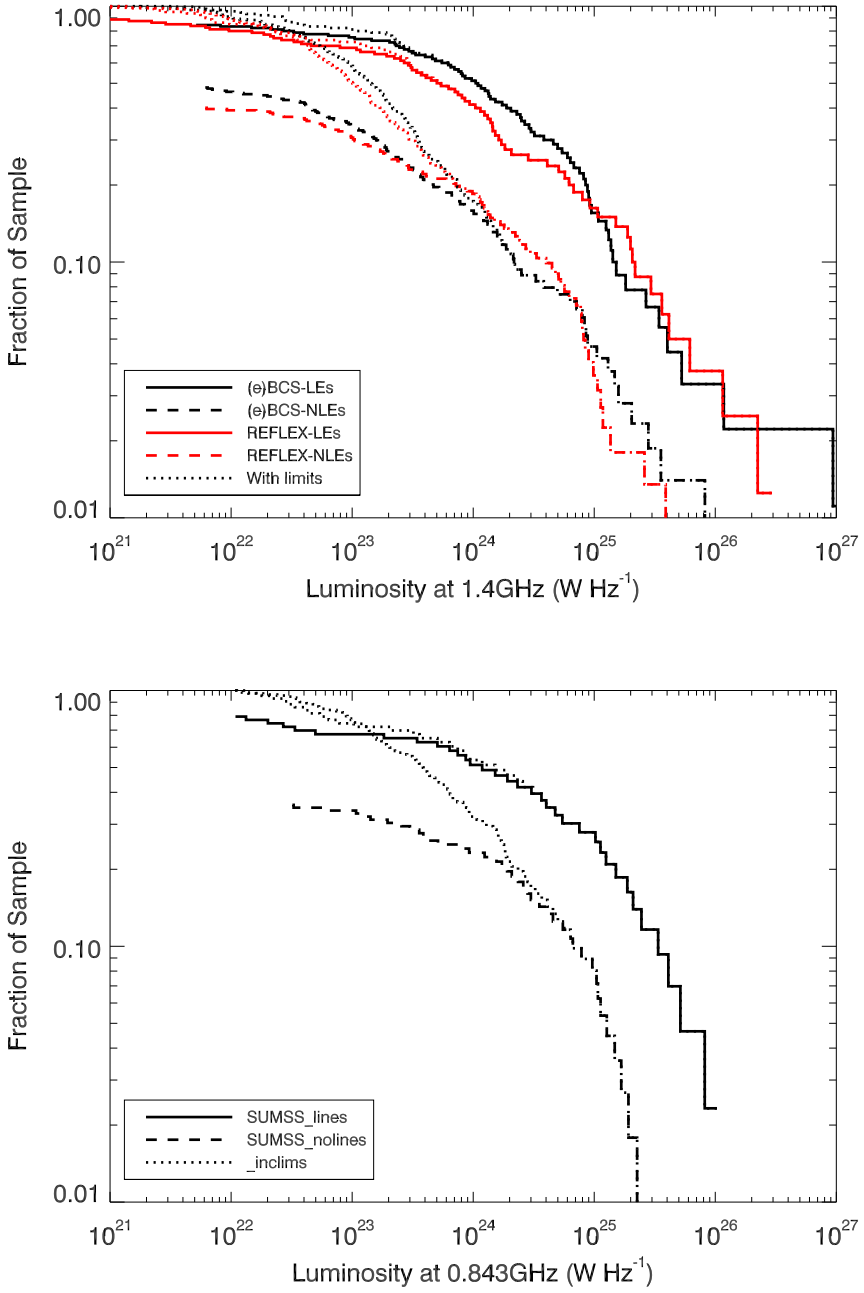

Figure 3.1: Radio luminosity distribution (RLD) for all BCGs within the (e)BCS and REFLEX-NVSS (top panel) and REFLEX-SUMSS (bottom panel) X-ray selected catalogues, separated by the presence of extended optical emission lines. In both figures, solid lines trace LEs, dashed lines trace NLEs and dotted lines trace upper limits for galaxies that are radio-faint to the detection limit of the relevant survey. A clear environmental dependence is seen for LEs to host more luminous sources. The top panel shows the 1.4 GHz RLD for all clusters that lie within the NVSS survey region for both the (e)BCS catalogue and REFLEX catalogue, with the relations for the two surveys showing good agreement and repeatability of the result. The bottom panel shows the 0.843 GHz RLD for clusters in the REFLEX catalogue which fall within the SUMSS survey region.

ple (HIFLUGCS) (Reiprich & Böhringer, 2002; Mittal et al., 2009) samples. Ma et al. (2013) studied a combined sample of 685 X-ray selected galaxy clusters. Matching to the NVSS, they found a matched detection rate between the cluster coordinates and radio-sources $>$3mJy (roughly equivalent to $\sim 1.7\times10^{24}$W Hz^{-1} at their upper redshift limit) of $\approx$52.1% (or $\approx$48.5% accounting for expected background contamination). However we note that where possible we have used the lower flux detection threshold of the FIRST survey and also matched the optical BCG positions rather than cluster X-ray positions, as these are not always equivalent and hence would result in some radio-loud BCGs being missed. Considering these factors, we have reasonable agreement with previous radio-BCG detection rates in X-ray selected clusters.

Our detection rate is significantly higher than for otherwise derived samples (e.g. $\approx$30% for optical selection, Best et al., 2007; Stott et al., 2012) with BCG mass dependency. This reflects the fact that X-ray selected samples are biased towards selecting the most massive, settled clusters which are more likely to host a radio-loud BCG (Burns, 1990; Mittal et al., 2009). However, a fraction of our non-detections are likely to be radio-loud but below our detection threshold and so our detection rate can only provide a lower limit on the overall duty cycle of radio-loudness of BCGs. The mis-identification of some clusters that contain central radio sources, due to X-ray emission being incorrectly attributed to the AGN rather than the ICM, may also contribute. We discuss possible cluster survey mis-identifications in Section 3.4.6.

More interesting is the difference in the detection rate between LE and NLE BCGs. We detect 84.1$\pm$7.6%, 87.0$\pm$7.5% and 83.7$\pm$11.0% of the LEs and 51.6$\pm$6.7%, 54.7$\pm$6.6 % and 51.3$\pm$9.2% of the NLEs in (e)BCS, REFLEX-NVSS and REFLEX-SUMSS respectively, again assuming a simple binomial errors with a 95% confidence level. We note that these detection fractions are affected by inconsistent flux limits and further that if we consider only our C-band pointed observations of the BCGs within our Main Sample then we recover detection fractions of 90.8$\pm$5.1% for LEs and 48.9$\pm$8.8% for NLEs down to our detection limit of $\approx$0.3mJy. These detection fractions compare favourably with those of Mittal et al. (2009), who report detection fractions of 45%, 67% and 100% for non-cool cores, weak cool cores (1Gyr $<$ t$_{cool}$ $<$ 7Gyr) and strong cool cores (t$_{cool}$ $<$ 1Gyr) respectively, for the HIFLUGCs sample of the 64 X-ray brightest galaxy clusters.

If the simplest case is taken whereby the detection rate is taken as a proxy for the duty cycle of AGN activity (e.g. Lin & Mohr, 2007) then this provides clear evidence that the duty cycle of BCGs in strong cooling flow environments is higher than for BCGs in less extreme cluster centres.

3.2.3 Luminosity Functions

A further clear distinction in the radio properties between LEs and NLEs becomes apparent by considering their luminosity distributions (see Figure 3.1). Radio sources in LE BCGs are on average more powerful than for NLEs. The distributions in Figure 3.1 are effectively complete to $\geq$few 10^{23}WHz^{-1}. Although the distributions in the directly comparable (e)BCS and REFLEX-NVSS samples (Figure 3.1 top panel) are not perfectly aligned (see below), the same general result is seen.

Redshift Considerations

Differences in the redshift distributions of clusters in the two samples may account for some of this scatter. Malmquist bias would suggest a preference for detecting higher luminosity sources in a sample with a higher redshift distribution. The redshift distributions of the clusters with radio-loud BCGs for the three sub-samples are shown in Figure 3.2, with 1σ uncertainties assuming Poissonian errors. We see no significant difference in the redshift distribution of our line emitting and non-line emitting BCGs, with neither LEs nor NLEs preferentially seen to higher redshifts. We do see that for the REFLEX sample, to low significance we have proportionally more LE BCGs in the lowest redshift bin ($z<0.1$). If anything however, this would suggest a higher redshift distribution for our NLEs than LEs and should therefore be expected to bias our NLE sample to be more luminous than LEs. Hence such a bias, if present, actually serves to strengthen our result.

To minimise any redshift related uncertainty, the distributions were re-plotted for only those clusters at $z < 0.1$ (see Figure 3.3). The distributions between the (e)BCS and REFLEX-NVSS samples now appear to agree with less scatter and the trend for LEs to host more powerful radio sources remains.

It should be considered that there is a decreasing fraction of strong cool cores observed to higher redshift, although this evolution is not believed significant over the redshift range

of our sample (Santos et al., 2010; Samuele et al., 2011; McDonald et al., 2013).

There were 36 matched BCGs within our sample which lie in the overlap of the NVSS and SUMSS regions. This relatively small sample was found to have a reasonably uniform range of $\nu_{0.843\ GHz}$ - $\nu_{1.4\ GHz}$ indices of α = -0.27 - 2.12. This range of indices highlights the wide diversity of radio activity found within the BCG population as a whole. It also highlights the large uncertainties that are invoked by assuming a single spectral index for a population of sources when extrapolating too far from a single frequency observation. As such we choose against extrapolating the whole REFLEX-SUMSS sample to 1.4 GHz for direct comparison to the others (Figures 3.1 and 3.3) and instead note only that the same luminosity distinction between LEs and NLEs is seen.

The tendency for the strongest cooling cores to host radio active AGN more frequently and of higher power than the weaker/non-cooling cores shows that the environment is having a direct effect on the BCG activity, with the strong inference being that there is increased energy output from the BCG in regions where more energy is required to suppress cooling, directly connecting the cooling/heating processes (see also Section 3.2.4)

3.2.4 Cluster X-Rays to L-band Radio Connection

To further investigate how the radio-behaviour of the BCG connects with the global properties of the host cluster we retrieve the integrated cluster X-ray emissions from the BCS, eBCS and REFLEX catalogues. Table 6a of the REFLEX catalogue contains the X-ray luminosities calculated using our cosmology. However, the BCS and its extension both give X-ray luminosities for an Einstein-de-Sitter universe with H_0=50 km s^{-1} $Mpc^{-}1$. We correct this to our cosmology, with typical conversion factors of 0.5-0.7 for our redshift range. We show in Figure 3.4 the monochromatic L-band radio powers for all sources in our Parent Sample as a function of the X-ray luminosity of their host clusters. A general trend for the highest radio luminosity sources to inhabit the most X-ray luminous clusters is seen, albeit with significant scatter. The extended nature of clusters means that the catalogue observations sample regions of much greater physical extent than just the cluster core. The integrated X-ray luminosity is therefore driven predominantly by the cluster mass, with more massive clusters corresponding to more X-ray luminous systems. The correlation observed in Figure 3.4 is therefore perhaps indicative of the most

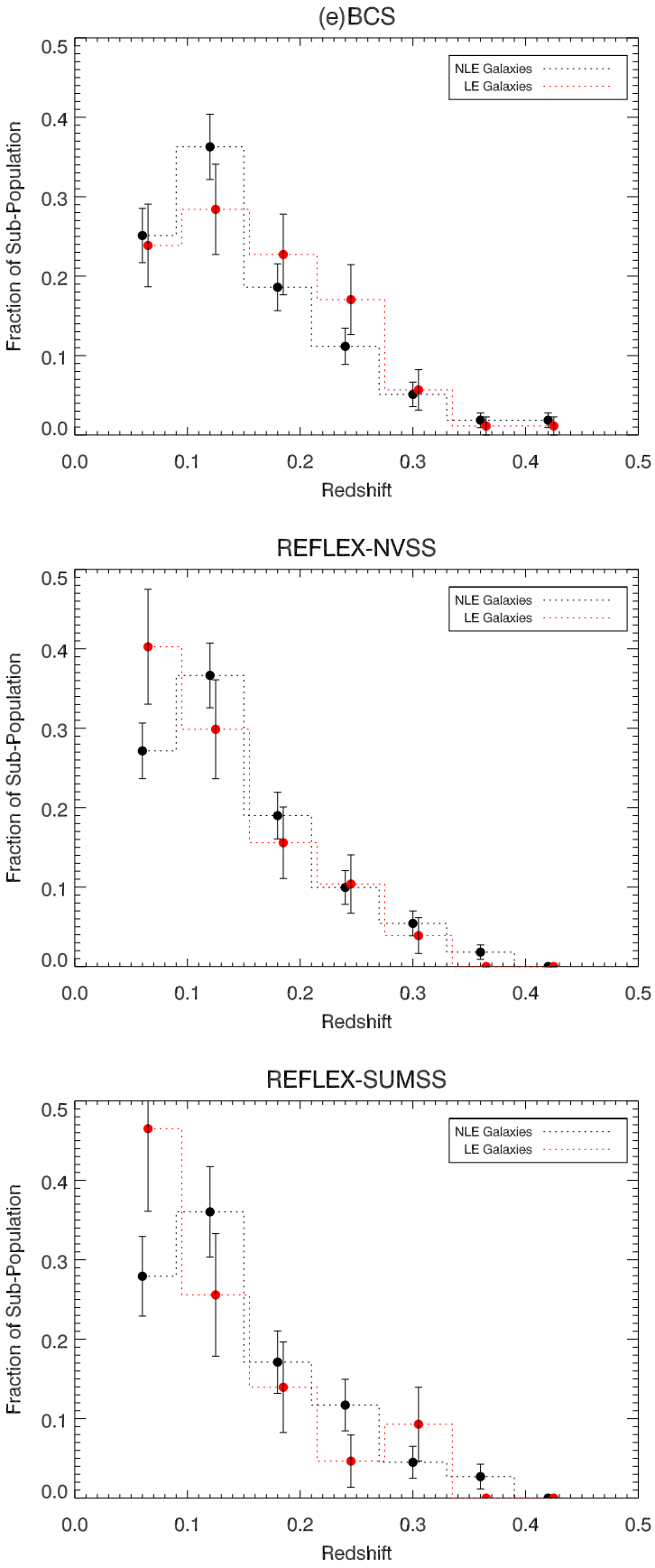

Figure 3.2: Binned redshift distributions for the radio-matched BCGs within the (e)BCS (top panel), REFLEX-NVSS (middle panel) and REFLEX-SUMSS (bottom panel) samples. Note that bin centroids have been shifted slightly for clarity.

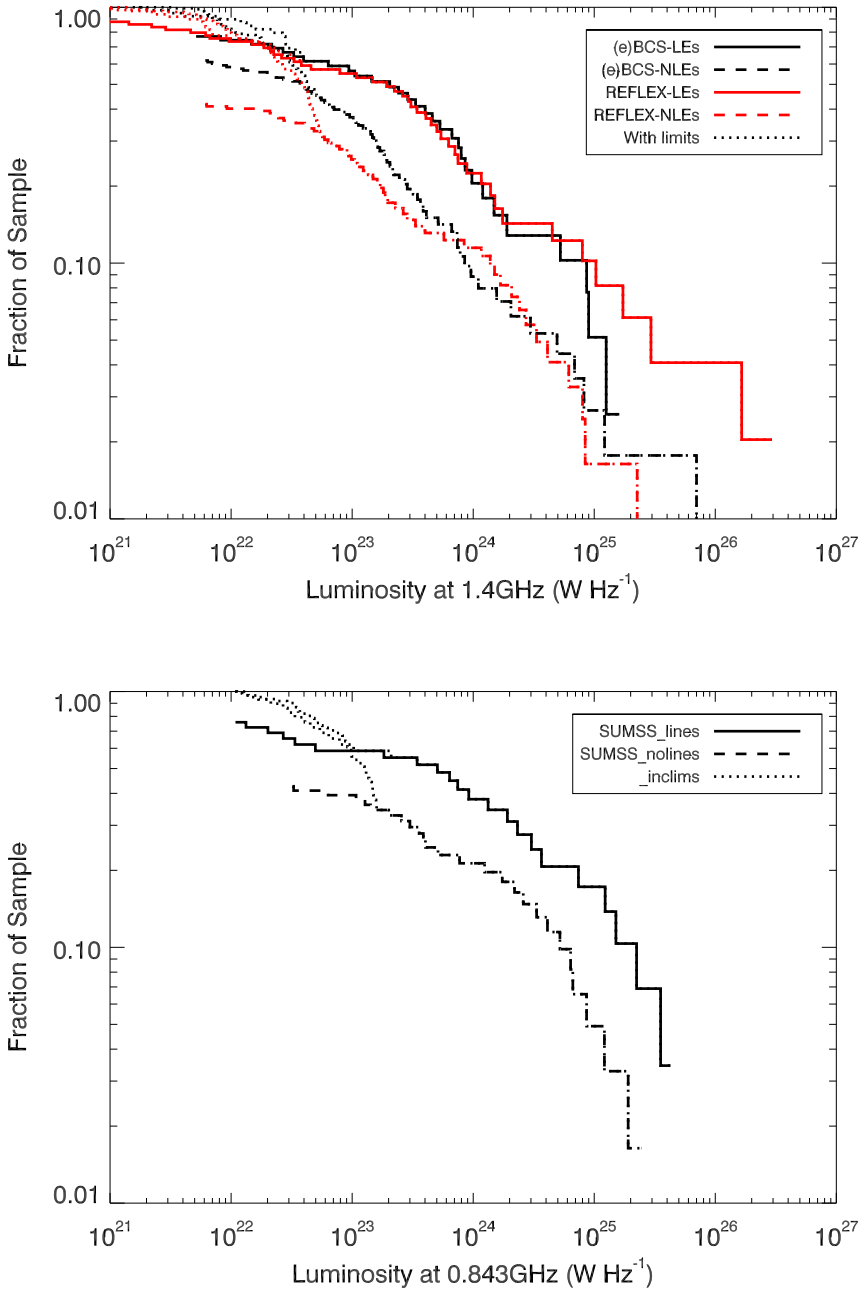

Figure 3.3: As for Figure 3.1 although restricted only to those clusters that lie within a redshift of 0.1. We see that the difference in the distribution between LE and NLEs remains, showing that it is a true physical result and not merely due to redshift bias. In particular note that the relations for (e)BCS and REFLEX-NVSS now appear to align better. Better identification of sources in REFLEX covered by NVSS but not FIRST at lower redshifts could account for this.

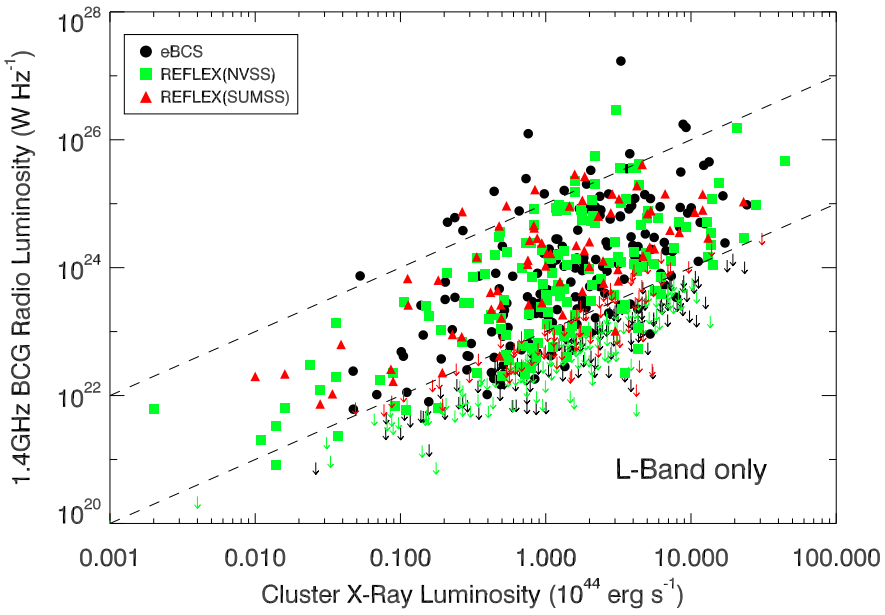

Figure 3.4: Monochromatic (1.4 GHz) radio luminosity of the BCG as a function of its cluster's luminosity. The empty corner to the bottom right reflects the detection limit of the radio surveys rather than a true correlation whereas the bound to the upper-left shows that more radio-luminous BCGs tend to inhabit more X-ray luminous clusters. Note that REFLEX-SUMSS radio fluxes were extrapolated using an index of -0.8 for inclusion/completeness. See Section 3.2.3 for why this extrapolation is uncertain. X-ray luminosities were corrected to a consistent cosmology. The dashed lines are illustrative only and represent one-to-one normalisation with a two order-of-magnitude separation.

massive clusters tending to host the most powerful radio-AGN, which may itself be due to more massive clusters hosting more massive BCGs and in turn more massive central black holes. A secondary effect, for cool-core clusters to have elevated X-ray luminosities due to the higher core densities could also be contributing. However this is likely to be a much more subtle effect than the mass dependency and is not the dominant driver of the correlation.

3.3 Core and Non-core Emission

As stated in Section 2.4, the true nature of any observed radio activity is difficult to understand when observing a sample at only one frequency. We now consider the properties of the decomposed core and non-core radio components, their relationship to each other and their separate and linked relationships to other cluster and AGN properties.

3.3.1 Linked Emission

For each of the sources within the Main Sample, we take monochromatic proxy measures of the core and non-core components at 10 and 1 GHz respectively. Ideally, the cores should be normalised at a higher frequency and non-cores at a lower frequency. However, often our radio SEDs are more sparsely sampled far away from the traditional cm-range wavelengths. Hence, our choice of 10 GHz and 1 GHz for the normalisations are a compromise between ensuring the relevant components can be separated whilst still being within the best-sampled section of the radio waveband. We plot a radio 'colour-colour diagram' of the 10 GHz core normalisation against the 1 GHz non-core normalisation in Figure 3.5.

We see that BCGs in strongly cooling clusters are much more likely to be core dominated yet both cluster types host powerful radio sources. To further elucidate this difference in distribution, in Figure 3.6 we plot a histogram of the ratio of the 10 GHz core measure to the 1 GHz non-core measure for the sources in the Main Sample for which we have well determined values for *both* components. As in Figure 3.5, we see a tendency for LEs to host much more core dominated radio-sources.

Strong core components only appear to be found in LEs. The presence of very powerful non-cores in NLEs, normally associated with classical Fanaroff-Riley type I (FR-I) and type II (FR-II) sources, belies that there must at some times be powerful core activity in these objects. It stands to reason that in a much larger sample we would find such events. However, that they are not present in the current sample suggests that such core outbursts must be short-lived. Indeed we find that for the 48.8% of sources that are identified as LEs in our Main Sample, 60.2% have a determinable core component of which 83.1% are $>10^{23}$WHz^{-1} (see also Section 3.4.1). However, of the remaining 51.2% of sources tagged as NLEs only 11.6% have an identifiable core component. Only 5% of these NLE core components are $>10^{23}$W Hz^{-1} and none has a core power $>5\times10^{23}$WHz^{-1} (see also Section 3.4). This suggests an upper limit to the *core* duty cycles of NLEs of $<1\%$ with core powers $>5\times10^{23}$WHz^{-1} whereas the prevalence of powerful core activity is much higher in LEs. It appears therefore as if the activity is more persistent in LEs. It is the presence (or lack) of an active *core* component that appears to be the most important distinction between the radio properties of LE and NLE BCGs, even more so than their

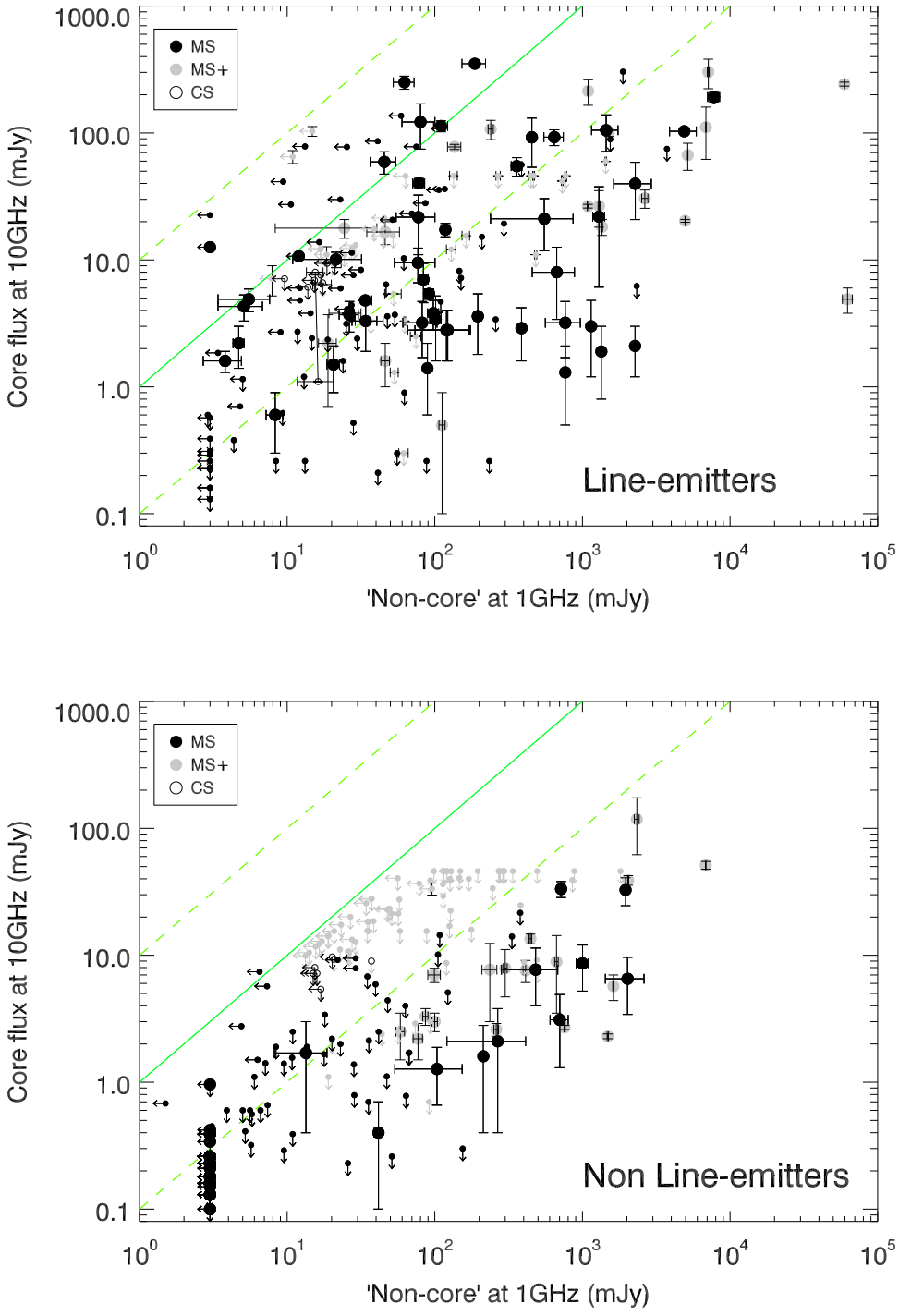

Figure 3.5: Comparison of the flux density of the radio core component (normalised at 10 GHz) to that of the more diffuse radio component (normalised at 1 GHz) for those objects that exhibit optical line emission (top) to those that do not (bottom). The solid line marks equal normalisation of both components, the dashed lines a factor of ten either side. It appears that LE clusters are significantly more likely to be core dominated radio sources whilst also undergoing the most powerful events. Solid grey points in both plots are sources in the MS+ (L-band $>$ 15mJy) which are not covered by the Main Sample (see text). Hollow points complete the radio coverage down to the flux limit of the SUMSS survey (15mJy $>$ S_{L-band} $>$10mJy) and hence occupy only a narrow range in flux density.

overall incidence of radio loudness (see Section 3.2.2).

The wide range of ratios of these two components has important implications for the variety of sources that will be contained within any flux selected radio sample, with samples selected at different frequencies containing vastly different source types. We discuss this in Section 3.4.6

Complete Sample

To ascertain whether our Main Sample is representative of the full parent sample, in Figure 3.5 we also show (in light grey) the decompositions for all sources in the Main Sample+ that do not fall within the Main Sample.

Considering the top panel of Figure 3.5 we see that for the LEs, the Main Sample well samples the parent sample. For the NLEs (bottom panel) it initially appears that many grey points lie above the black points. If we consider that the vast majority of these are upper limits on the core component for sources where there is no indication of a strong active core, and that the majority of sources in the Main Sample are similarly spread in non-core flux with deeper limits on the core components due to having deeper targeted observations at higher frequencies, then it appears reasonable to assume that the advent of deeper higher frequency surveys (e.g. AT20G deep, Franzen et al., 2014) will push these core limits down. We therefore believe that the Main Sample for NLEs is indicative of the true distribution of the parent sample.

Note that although the limits on NLEs in the Main Sample+ core components do tend to lie above the corresponding points in the Main Sample, they are still all below the brightest cores seen in LEs.

For further completeness, we also include in Figure 3.5 *approximate* positions for the remaining sources in the Parent Sample that have radio fluxes $10\text{mJy} < \text{S}_{L-band} < 15\text{mJy}$. This cutoff is chosen as the level to which *all* the L-band surveys used are complete. We refer to this as the Completeness Sample (CS) but note only that they do not appear to lie anywhere special on the diagram.

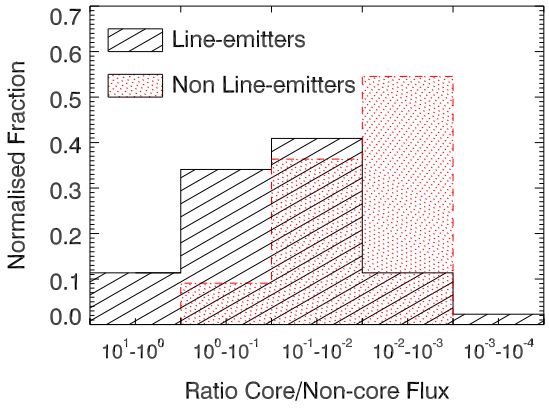

Figure 3.6: Distribution of the core to non-core ratio of normalisations for the sources in the Main Sample only that have determined values for both components. This sub-sample of data is incomplete yet represents the most well-sampled of the data displayed in Figure 3.5 and highlights that LE-BCGs are on average much more likely to host core dominated radio sources than NLEs.

3.3.2 Cluster X-Rays to Decomposed Radio Connection

For the Main Sample+ sources, we plot the luminosity of their core and non-core radio components against their cluster X-ray luminosities in Figure 3.7. Whilst there appears to be a general tendency that the most powerful cores only occur in the most X-ray luminous clusters, there is a population of powerful non-cores ($>10^{24}$ W Hz^{-1}) found in low X-ray luminosity ($<5\times10^{43}$ erg s^{-1}) clusters. In the simplest scenario it would be expected that bright cores should evolve into bright non-cores. The lack of bright cores alongside the presence of bright non-cores in low X-ray luminosity clusters is inconsistent with this simple picture, hence we must consider alternate explanations for the bright non-cores.

Activity Cycle Considerations

Whilst strong non-cores can be the result of either the superposition of multiple previous periods of activity or the fading of a single powerful outburst, a powerful core can only be observed as the result of strong, current activity. Powerful non-cores in low X-ray luminosity clusters could therefore be explained by a couple of different scenarios. Individual periods of core activity may be genuinely less powerful in less X-ray luminous clusters but happen relatively frequently, thus leading to a build-up of material. Alternatively, powerful core outbursts may occur in low X-ray luminosity clusters yet be relatively rare

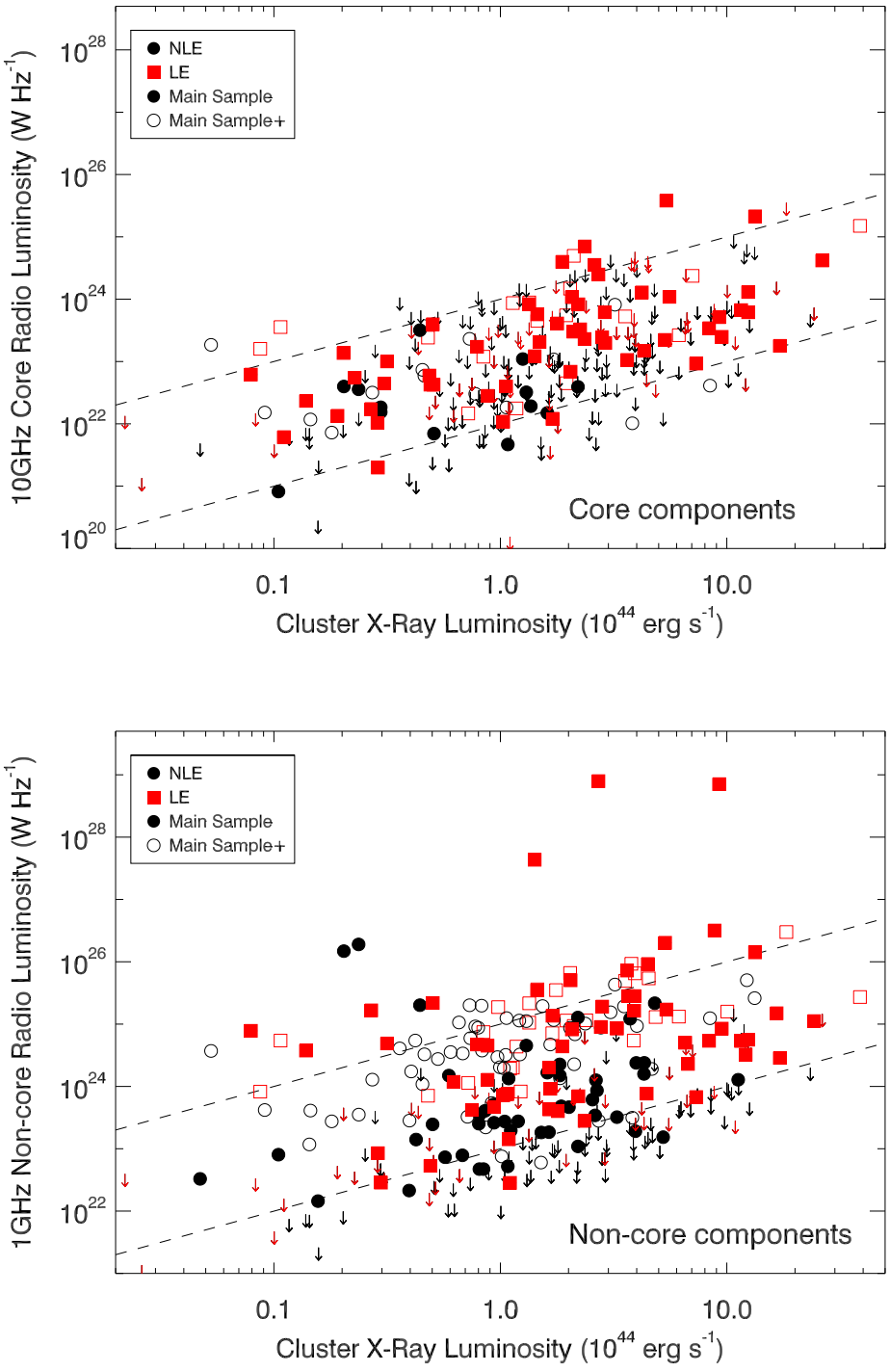

Figure 3.7: Relationship between the core (top) and non-core (bottom) radio components of the BCG to the overall X-ray luminosity of the host cluster. Note that the strongest cores appear only to occur in the most X-ray luminous and hence most massive clusters whereas strong non-cores, attributable to single outburst lobe-dominated systems may also be found in low X-ray luminosity clusters. Black points are non-line emitters (NLEs) whereas red points are line-emitters (LEs). The dashed lines are illustrative only and represent one-to-one normalisation with a two order-of-magnitude separation.

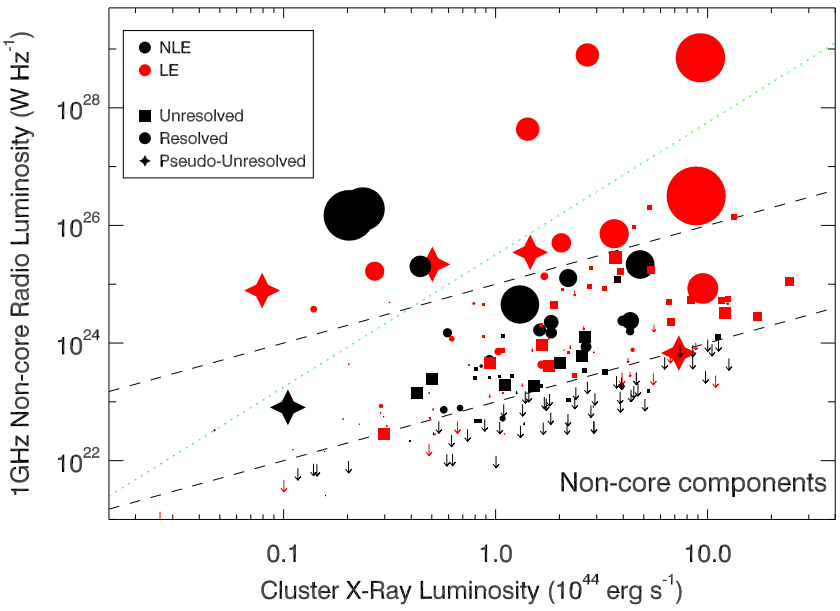

Figure 3.8: As for bottom panel of Figure 3.7 except only for the Main Sample and now symbols are sized by physical size of the non-core component, as seen at C-band with either the VLA C-Array or ATCA. Note that stars represent sources where extended emission is resolved out at this resolution but where lower resolution and/or lower frequency observations show distinctive lobed features - i.e. they are resolved-out with our sampling but there is known extended emission in the systems, so they are effectively 'pseudo-unresolved'. Colours again represent the state of the cluster (black NLEs, red LEs) although circles now show sources that are resolved (at this resolution) and squares those that are unresolved and hence represent upper limits. Sizes were measured as Largest Angular Size (LAS). For unresolved sources, the major axis of the beam was taken as the size limit. The dashed lines are illustrative only and represent one-to-one normalisation with a two order-of-magnitude separation. The dotted line represents a normalisation power-law of order three and is used only as a differentiator (see text).

and simply missed by our sample.

The former of these two possible explanations could potentially explain the observed 'amorphous haloes' observed around many BCGs (e.g. A2052, Blanton et al. 2001; Venturi et al. 2004), and of which our current sample contains several candidates (e.g. A2627, A407, AS753, AS861, RXJ1720.1+2638; also see Appendix A). This halo would contain multiple distinct populations of electrons from a number of previous outbursts, all at different stages of ageing but crucially none of which would be undergoing injection and hence manifest as an active, flatter spectrum core. In this scenario, the superposition of weak populations would build to give the overall bright non-core. High resolution spec-

tral index maps of amorphous haloes could support this, if the distribution of the spectral index across the haloes was found to be clumpy rather than smoothly varying, although resolution effects at the varying frequencies would make such an endeavour difficult.

To attempt to break the degeneracy between single outburst and accumulated non-cores, we considered the physical sizes of the sources in the Main Sample.

Size Considerations

We measured the largest angular size (LAS) at C-band (≈4.8 GHz) of each source in the Main Sample using VLA C-array band imaging for the northern sources and ATCA-6km for the southern sources. There is a small bias here in that the VLA-C is slightly more sensitive to resolving larger scale structures but this effect is expected to be negligible. Sizes were extracted using the AIPS task TVDIST for resolved sources or alternatively, the major-axis of the Gaussian beam as fit by the AIPS task JMFIT was taken as an upper-limit on the largest angular size (LAS) for unresolved sources. Angular sizes were converted to physical scales using the Interactive Data Language (IDL) routine, *'zang'*. In Figure 3.8 we re-plot the bottom panel of Figure 3.7 but now weight the symbol size by the physical size of the non-core that it represents (LAS in kpc scaled by constant but arbitrary factor). We do not include here the MS+ sources, in order to keep as much consistency as possible in the array configurations from which our LASs where measured. However, we note that archival images of the sources in the MS+ extension show similar size distributions to those observed in the MS.

The most powerful non-cores at any given X-ray luminosity - those sources found above the dotted line in Figure 3.8 - are typically large resolved sources. Specifically, in order of increasing cluster X-ray luminosity these sources are: A2634, RXJ2214.7+1350, A160, RXJ0058.9+2657, A407, A3581, Z1261, RXJ1320.1+3508, A2627a, A2055 and A1763. All of these except A3581 are large jetted systems, of which A2627(a) shows one sided jetted structure and all others show classical FRI/II type morphology. A3581 has only a hint of a resolved jet with ATCA-6km C-band observations. Canning et al. (2013) however use the hybrid VLA-AnB array at L-band to show this source has radio-lobes that fill the X-ray cavities in this system. The small extent and currently highly active core suggests the non-core emission here is recently injected and may perhaps be

expected to expand outwards in future, which could classify this source as a young FRI/II precursor. That the majority of the most powerful non-cores at any given X-ray luminosity are large FRI/II type sources supports the idea that powerful individual periods of activity may be responsible for the brightest non-cores and that in a larger sample we may expect to find bright cores in low X-ray luminosity clusters.

However, the general distribution shown by the bulk of the population below the dotted line in Figure 3.8, is comprised of a mixture of large extended resolved and smaller unresolved sources over the full range of X-ray luminosities. The extended sources here represent a mixture of FR-type and more amorphous sources. That there is a general trend for brighter non-cores to reside in more X-ray luminous clusters regardless of their size but that the brightest tend to all be large extended sources suggests there may be two different activity types occurring in BCGs.

Repeated core activity may lead to confused, fairly amorphous small scale structures ($<$20kpc) comprised of accumulated material from multiple periods of core activity. This emission may be visible for tens or even hundreds of Myrs after the AGN activity has shut down, dependent upon the specific environmental conditions. The tendency for more powerful cores to inhabit more X-ray luminous clusters would then naturally account for the tendency for brighter non-cores to inhabit these same clusters. However, any BCG (indeed, much like any other AGN) can experience a single strong outburst, powerful enough to eject material well-beyond the immediate BCG-vicinity and manifest as an FR-type source. This extended lobe emission would then dominate the steeper spectrum, non-core emission.

The overall brightness of the non-core will thus be a superposition of the accumulated material and the single powerful outburst, which could explain the extremely bright emission for the most-powerful non-cores in X-ray luminous clusters - if they are powerful FR-type non-cores superposed on top of a pedestal of accumulated emission.

In between large outbursts, the AGN remains persistently active albeit at a lower radio power, which is reflected in the high portion of (especially) LE BCGs that have an active core component. This suggests that when studying AGN it is important not only to look at the time a source is radio-loud for, but also the fraction of this time for which the AGN is actively launching jets.

3.3.3 [OIII]5007Å Correlations

To investigate the connection of radio-emission to other tracers of AGN activity we consider its relationship to the high ionisation [OIII]5007Å forbidden-line, which is a canonical tracer of current AGN activity (Maiolino & Rieke, 1995). Combining longslit observations taken with the New Technology Telescope (NTT) and Very Large Telescope (VLT) (Edge *et al.* in prep.) with those in Crawford et al. (1999), we have [OIII] fluxes for 97 of the sources within our Main Sample (of which 13 are in the MS+ extension).

These [OIII] fluxes are all from long slit observations of 1.2–1.5″ width so there will be some flux lost outside the slit. However, on the whole the nuclear [OIII] emission will dominate over the more extended, non-AGN emission so these fluxes should be representative of any underlying correlation. We consider the mid-infrared values of O'Dea et al. (2008), finding that four of these sources (A2146, A1068, RXJ0821.0+0752, Z3146) have their [OIII] measurements significantly affected by high MIR-dominated AGN activity. We highlight these in Figure 3.9 and remove them from the subsequent fits. To increase our coverage, we identify an additional 16 systems for which equivalent [OIII] measurements are available that do not fall within our parent sample yet have comparable properties and hence are included within this analysis. For each of these additional 16 sources, we populate their radio SEDs from the literature and perform decompositions (see Section 2.7 and Table H) allowing us to consider how the core and non-core components of the radio emission of our BCGs are directly related to the otherwise traced AGN activity for a subsample of 113 BCGs - the [OIII]-sample.

Using the *bhkmethod* tool within the Image Reduction and Analysis Facility (IRAF) we find that [OIII] flux is correlated with *both* the core and non-core radio flux. Both return a probability of no correlation <0.001 (the limit) with calculated Kendall's-τ coefficients of 0.7533 and 0.7272 respectively. We use the *buckleyjames* linear regression tool within IRAF to compute best-fits to the data. This algorithm can handle censors only in the dependent variable of a data-set. Neither of our variables is truly independent, however here we assign the [OIII] as our independent variable, since we have selected this sub-sample on the availability of [OIII] data and also it requires removal of the minimum number of data from our fits. We hence remove 9 sources with [OIII] limits and recalculate our Kendall's-τ coefficients to be 0.7661 and 0.7508 for the cores and non-cores

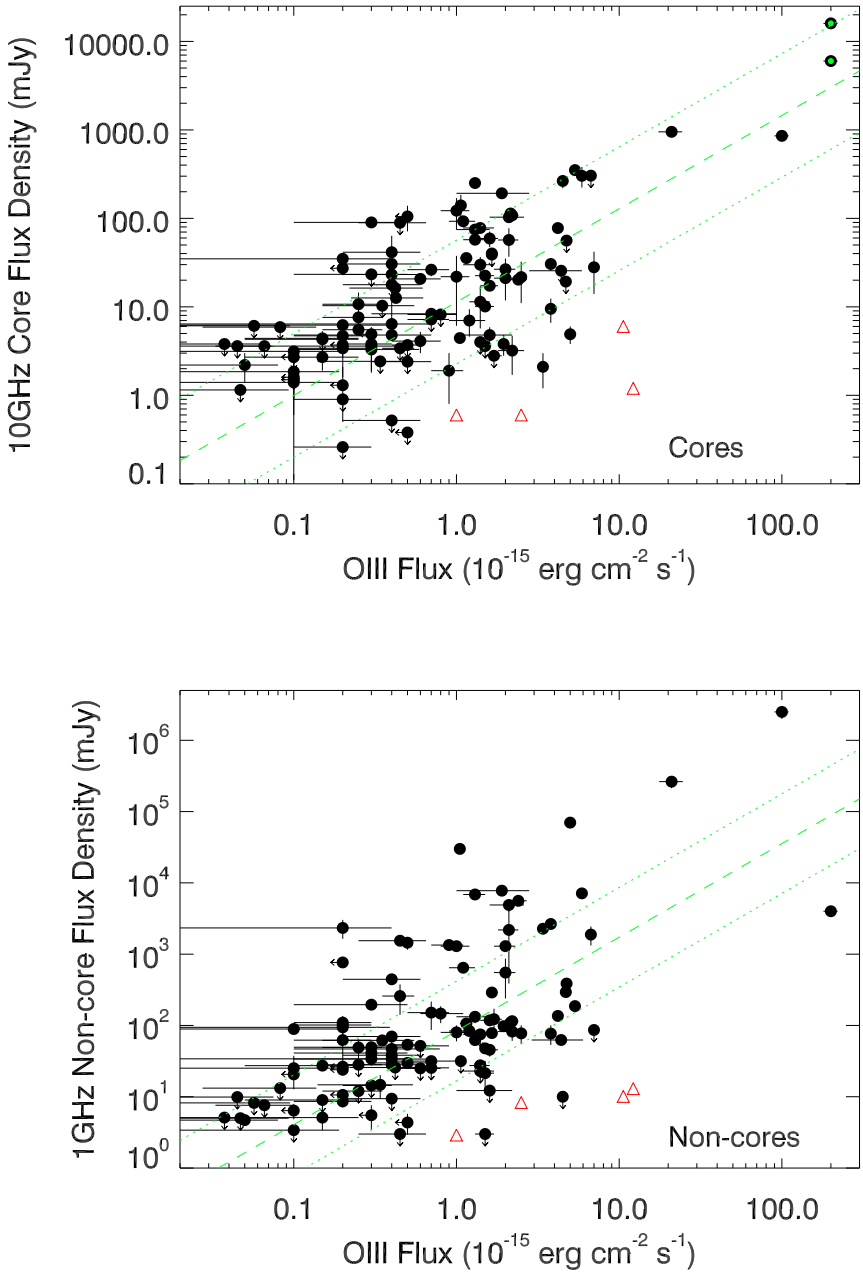

Figure 3.9: The 10 GHz and 1 GHz normalised respectively core and non-core radio flux components plotted against the [OIII]λ5007Å flux. The dashed line in the top panel marks a linear correlation between the [OIII]5007Å and core radio flux which spans four orders of magnitude in each parameter (see Section 3.3.3). The dotted lines mark a factor of twenty in scatter either side of the relation. A correlation is also found for the non-core (bottom panel), although with significantly increased scatter, as highlighted by the inclusion of the dotted lines again indicating a factor of 20 scatter in either direction. Red triangles are sources significantly contaminated by a mid infra-red (MIR)-dominated AGN and are not included in the fit (see text). NGC1275 is shown twice in the upper panel (inner green dot) to highlight the variability of its core over ≈decade timescales. Such variation in the sample as a whole is expected to account for a significant portion of the scatter (see Chapter 4.

respectively, showing that this removal has a minimal effect.

Between the [OIII] (in erg cm^{-2} s^{-1}) and core radio (mJy at 10 GHz) fluxes we find a best fit power-law:

$$log_{10}(S_{Core}) = (1.05 \pm 0.10)\, log_{10}(F_{OIII}) + (1.05 \pm 0.01) \tag{3.3.1}$$

which compares to an equivalent correlation with the non-core radio component (normalised at 1 GHz) of:

$$log_{10}(S_{NC}) = (1.31 \pm 0.16)\, log_{10}(F_{OIII}) + (1.92 \pm 0.06) \tag{3.3.2}$$

It should be noted that although it appears in Figure 3.9 as if the correlations are driven largely by the bright local sources NGC1275, M87 and Cygnus-A, if these sources are removed then IRAF returns consistent fits, still with a probability of no correlation $<$0.001. We therefore conclude that the presence of these correlations is robust.

[OIII] Discussion

The correlations between the radio component's flux and [OIII] flux (See Figure 3.9) support previously found correlations between radio and [OIII] luminosities (e.g. Rawlings et al. (1989) at 178 MHz, de Vries et al. (2007) at 1.4 GHz, Tadhunter et al. (1998) at 2.7-5 GHz). Of these, it is interesting to note that Rawlings *et al.* find their correlation between the [OIII] and total radio power finding only low-significance indication for a correlation between the resolved 'core' radio and the [OIII] in their sample. Here we see such a correlation, with reduced scatter over that of the more extended emission.

Our results show that whilst both radio components correlate with the [OIII], there is less scatter when considering only the radio core component (see Figure 3.9). Along with a loose intrinsic link between core and non-core power (see also Section 3.3), this suggests that the true correlation is with the core component, with the non-core correlation being secondary. We note that there is tentative evidence ($<2\sigma$) that the index we find for the correlation with the non-core component is steeper than for the core component. We interpret this as evidence for the core component driving the correlation, as the [OIII] forbidden line is collisionally de-excited and so traces recent AGN activity hence is more

contemporaneous with the core radio emission. Conversely, if the non-core emission is due to the cumulative effect of several previous activity cycles then it would be expected to show more radio emission for a given [OIII] flux.

Labiano (2009) found a correlation between the [OIII] and 5 GHz radio power that had increasing gradient when considering GPS, GPS+CSS (Compact Steep Spectrum), CSS and then GPS+CSS+FR-type radio sources respectively. Assuming the commonly quoted interpretation of these source types as a loose evolutionary sequence, GPS sources could be expected to be core-dominated whereas the large, extended FR-type sources are most likely to be dominated by their extended emission at 5 GHz. Indeed, the sources with the highest F_{NC}/[OIII] flux ratios in the bottom panel of Figure 3.9 correspond to the most physically extended sources (as seen in Figure 3.8). Under such assumptions this then supports our interpretation that the correlation is core driven. It follows that a significant portion of the scatter found in relations between radio-activity and AGN activity at other wavelengths is likely due to the varying timescales on which the emission was produced.

3.3.4 Cavity Correlations

Insight into the Activity Cycle

Obtaining deep X-ray observations is observationally expensive, but possible at low redshift. However, current X-ray telescopes do not have the required resolution and photon-collecting power to routinely observe cavities at higher redshift in all but the largest systems (Hlavacek-Larrondo et al., 2012a). It has been shown that for a statistically relevant sample, radio power of the BCG correlates well with the cavity power, albeit with large scatter (e.g. Bîrzan et al., 2004, 2008; Cavagnolo et al., 2010). These studies usually depend upon the total radio power at L-band. Here we attempt to expand upon this by considering how the cavity power correlates with both the core and non-core radio powers. A literature search for X-ray cavity systems amongst our Main Sample was performed, and supplemented by recently discovered cavity systems (Hlavacek-Larrondo, *private communication*). Twenty-six of our MS clusters were found to have known X-ray cavities, of which twenty-three are LEs, with the remaining three (A189, RXJ0419.6+0225 and RXJ1522.0+0741) being weak cavities in low redshift clusters.

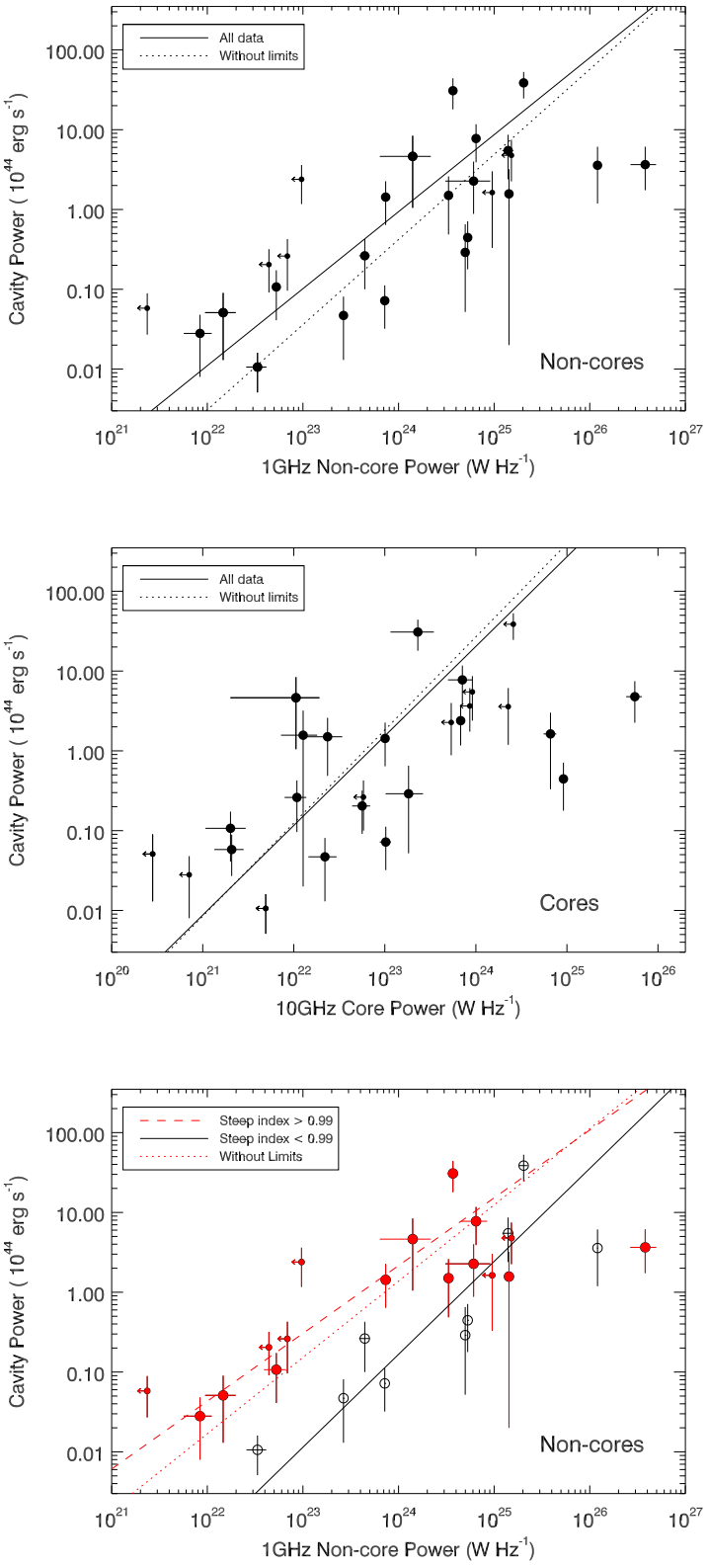

Figure 3.10: Correlations between both the cavity power and the non-core radio luminosity (top) and core radio luminosity (middle). Solid lines are the regression fits to the full data-sets and dotted lines are linear fits when the upper-limits on the radio-data are neglected. A correlation with the non-core emission is expected whereas the one with the core is less expected, suggesting that central AGN activity is persistent on bubble-inflation/rise timescales. Also shown is the non-core to cavity power relationship divided on the radio spectral index of the steep component (bottom). Filled circles have $\alpha_{steep}>0.99$ whereas open circles have $\alpha_{steep}<0.99$.

Cavity powers are estimated using the standard techniques (e.g Bîrzan et al., 2004). The total enthalpy is given by 4pV, where p is the thermal pressure at the radius of the bubble measured from X-ray observations and V is the volume of the cavity. We assume that the cavities are of prolate shape: $V = 4\pi R_w{}^2 R_l/3$, where R_l is the projected semi-major axis along the direction of the jet and R_w is the projected semi-major axis perpendicular to the direction of the jet. Errors on the radii are assumed to be $\pm$20%. Cavity powers are then calculated by dividing the enthalpy with the buoyancy rise time of the cavity (Churazov et al., 2001). The latter measures the time it takes a cavity to reach its terminal buoyancy velocity.

We plot the cavity power both as a function of the non-core radio component and the core component (Figure 3.10, top and middle panels). Using the *bhkmethod* tool for linear regression in IRAF we encouragingly find that the inferred feedback energies required to evacuate the cavities in these systems strongly correlate with the non-core radio emission from their BCGs (Kendall's $\tau = 0.9538$, with probability of no correlation 0.02%), thus reinforcing the feedback link. This correlation is expected, as the non-core emission is most commonly composed of dying radio emission in lobes that are co-spatial with cavities and hence more commonly traces the same outburst as that which evacuated them.

Interestingly, we also find a reasonably secure correlation (Kendall's $\tau = 0.5723$, with probability of no correlation $<$1%) between the cavity-power and the core radio component. This is more surprising, as the bubble-rise timescale should be long enough to decouple the cavity power from what is happening in the core unless the core activity is persistent over timescales $\sim$few Myrs. This is therefore indicative of reasonably steady AGN fueling in BCGs over bubble-rise timescales.

We perform regression fits to the data using the *buckleyjames* algorithm within IRAF. As in Section 3.3.3 neither of our variables is truly independent. We here assign the cavity power to be the independent variable for the fitting since this sub-sample was selected on the basis of having observed cavities. However, note that in Figure 3.10 we select to plot cavity power as the ordinate to ease of comparison with earlier studies. We find best fit

power-laws:

$$log_{10}(P_{NC}) = (1.022 \pm 0.18)\, log_{10}(P_{Cav}) + (24.03 \pm 0.16) \tag{3.3.3}$$

for the non-core component and:

$$log_{10}(P_{Core}) = (0.86 \pm 0.36)\, log_{10}(P_{Cav}) + (22.80 \pm 0.27) \tag{3.3.4}$$

for the core component respectively. Note that a fit to the integrated L-band power gives a consistent result with the fit to the non-core power, as should be expected since the non-core tends to dominate at this frequency.

We further consider the non-core to cavity power correlation, splitting the non-core radio component into those with the steepest spectral indices $\alpha > 0.99$ and those with flatter indices $\alpha < 0.99$ (see Figure 3.10 bottom panel). This value is chosen so as to include the limits as steeper spectrum objects, which is reasonable for these clusters as they tend to be well sampled in the GHz range and flatter components would be expected to be detected. We see a split in Figure 3.10 bottom panel where for a given cavity power, steeper spectrum non-core components tend to be lower power than shallower non-cores. Note that the apparent steep-spectrum outlier lies in a system (Abell 115) with prominent phoenix relics, which may be contaminating and inflating the non-core flux measurement. If limits are removed from this bottom panel then such a split is still observed. We propose that this apparent split is suggestive of evolution of the radio emission within individual cavities.

The regression fits return best fit power laws to our split data of:

$$log_{10}(P_{NC}) = (0.86 \pm 0.18)\, log_{10}(P_{Cav}) + (24.67 \pm 0.03) \tag{3.3.5}$$

for when the non-core component has index $\alpha < 0.99$ and:

$$log_{10}(P_{NC}) = (1.22 \pm 0.21)\, log_{10}(P_{Cav}) + (23.51 \pm 0.03) \tag{3.3.6}$$

for when the non-core component has index $\alpha > 0.99$ respectively.

When a radio jet ceases a period of cavity inflation and the inflated cavity detaches from the BCG and begins its buoyant rise through the ICM then the power of the cavity is virtually fixed. The increase in volume of the cavity as it propagates is counteracted by the lowering of the surrounding pressure. The detached cavity is removed from its AGN energy source and hence any change in total power is going to be relatively minor. However the synchrotron emitting electron population within the cavity will begin to age and hence the radio spectrum will steepen over time, contributing significantly to the scatter within the radio power to jet power ratio. Isolating the non-core radio emission and including the low-frequency radio spectral index of this as an additional parameter in such studies could therefore potentially eliminate much of the scatter.

3.4 Discussion

That BCGs exhibit increased likelihood of hosting radio-loud AGN is well established (e.g. Burns, 1990; Best et al., 2007). The trends presented above explore beyond this, showing that there is a great range of behaviour beyond generic 'radio-loudness' that appears to be driven largely by environment.

3.4.1 LE to NLE Differences

Striking differences are seen in both the frequency of radio-loudness and in the resulting radio luminosity of the AGN between those hosted by LEs and those hosted by NLEs. Considering Figure 3.1 we see that around 50% of LE-BCGs host AGN with radio powers above $10^{24} WHz^{-1}$ at L-band as opposed to only around 15% equivalent for NLEs. Our overall detection fractions for radio-loudness at L-band are equivalent to those of other X-ray selected cluster samples. However, they are above those for otherwise detected samples (see Section 3.2.2). When we remove LE-BCGs from the sample we recover a detection fraction similar to that of otherwise selected massive galaxies (e.g. Best et al., 2005). This suggests that the AGN activity of BCGs in these environments is largely governed by the same processes as isolated galaxies of similar mass, that is they affected mainly by their own circumgalactic envelopes. That the detection fraction for LE BCGs jumps significantly above this shows unequivocally that the cooling flow must be caus-

ing the increased duty cycle of radio loudness, therefore it seems natural that this same cooling is, directly or indirectly, fueling the AGN.

3.4.2 Decomposed Luminosity Functions

In the top and middle panels of Figure 3.11, we plot separate luminosity functions for the core and non-core components, considering only sources in the Main Sample. In the bottom panel of Figure 3.11 we show the equivalent plot to Figure 3.1 but incorporating only the sources in the Main Sample. We see that the total split at L-band is driven by the non-cores, as expected since this is the component that tends to be most dominant at $\approx$1 GHz, and most often brighter overall. However we see that the LE to NLE dichotomy is further enhanced if we consider only the cores, with those in LEs typically two orders of magnitude more powerful than those in NLEs.

This split between the LE-hosted and NLE-hosted core, non-core and integrated L-band radio components is equivalently shown in Figure 3.12. Here we show the ratio of the typical luminosity of the LE-hosted component to equivalent NLE-hosted component, taken at detected fractions of 5, 10 and 15% of the Main Sample. Note that this limited range of detection fractions is due to limitations imposed by the completenesses, particularly of NLE-hosted core components where in many cases a robust measurement is not available and only a limit can be imposed. Nonetheless we see that for a given detection fraction, the LE-hosted non-core components are typically a factor of ten more luminous than equivalent non-core components in NLEs, with a similar ratio seen for the total integrated L-band luminosity, as expected since this is most often dominated by the non-core. However, the core component of LE-hosted BCGs at a given detection fraction is typically a factor of around seventy times more luminous than an equivalent NLE-hosted core showing that it is the presence of an *active* component in the core that is perhaps the most prominent difference between LE- and NLE-BCGs. Note that the limits placed on non-precisely determined components are fairly conservative and that the 'errors' plotted in Figure 3.12 are the maximum and minimum separation of the distributions in Figure 3.11 if all cores lay infinitely or infinitesimally below the limits. The large lower uncertainties on the cores shown here are therefore expected to be hugely over-estimated by this method as it would require all sources with a core limit to have an active core so far

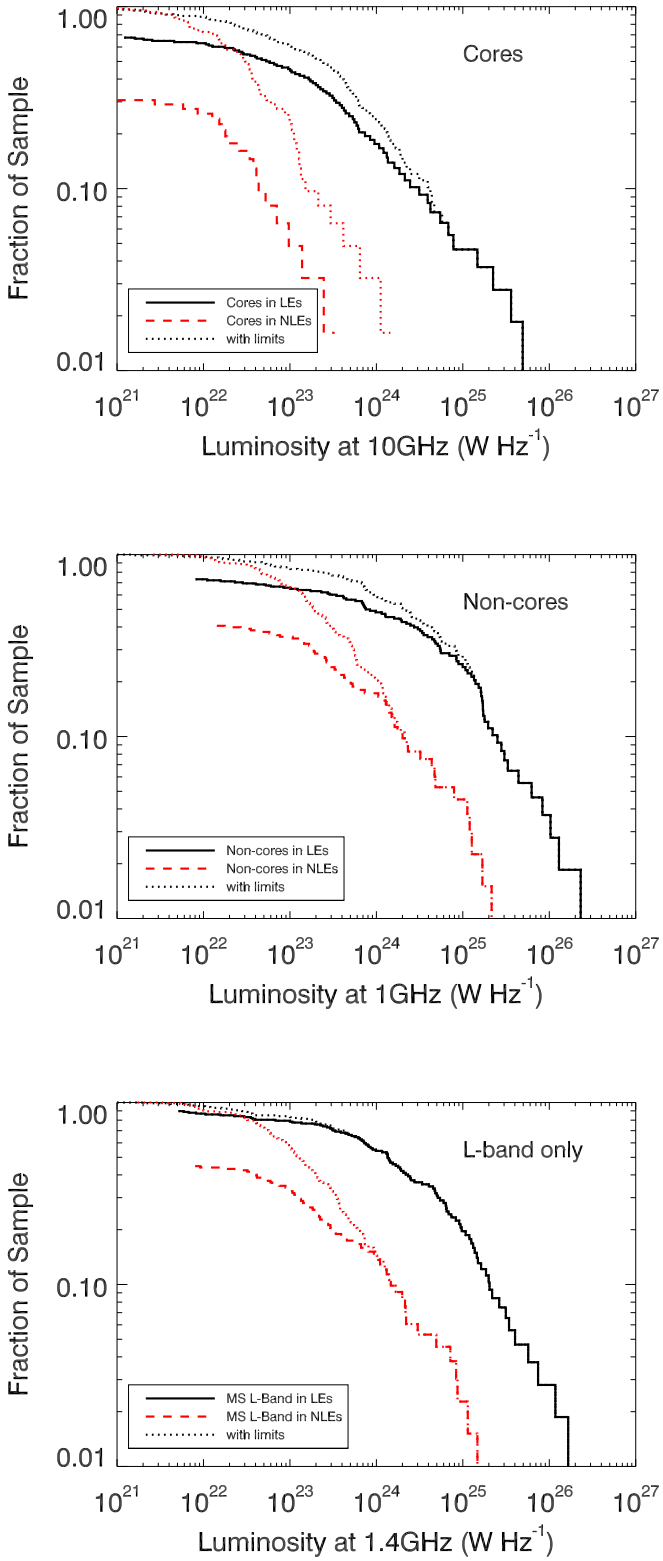

Figure 3.11: As for Figure 3.1 but now using only the core components at 10 GHz (top), the non-core components at 1 GHZ (middle) and the 1.4 GHz monochromatic flux for only those sources in the Main Sample. Note that the overall spectrum at 1.4 GHz is most often dominated by non-core emission, as is reflected in the similarity between the split at L-band and that of the non-core component. However, the core activity is apparently even more environmentally dependent, with core powers in NLEs typically being up to two orders of magnitude less than those in LEs.

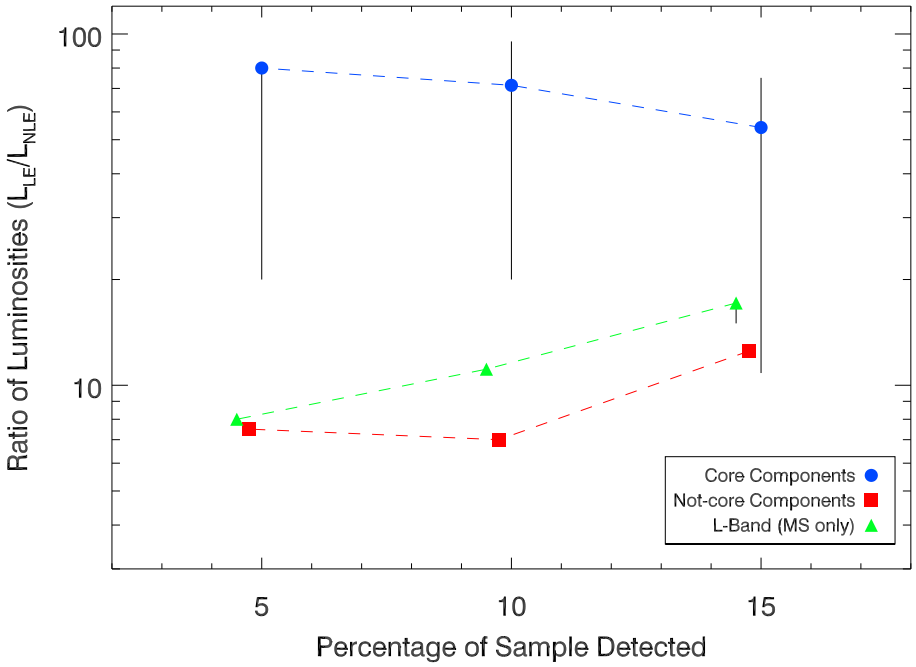

Figure 3.12: Ratio of luminosities of LE-hosted to NLE-hosted sources at the given detection fractions, for the core components, non-core components and the equivalent 1.4 GHz monochromatic LF for only those sources in the Main Sample, as shown in Figure 3.11. Effectively we are seeing the luminosity offset between LE and NLEs for the core, non-core and total. Whilst a split is seen in the non-core components, a much larger separation is observed amongst the core components, with cores in LE BCGs typically factors of several tens higher than in NLEs. Error bars are the maximum and minimum separation possible accounting for limits and hence are not truly 'errors'. The large lower uncertainties on the cores shown here are expected to be hugely over-estimated by this method as it would require all sources with a core limit to have an active core so far overlooked from observation, which we deem highly improbable. Considering this, a clear difference in core activity as a function of cluster environment is claimed. Note that X-positions have been shifted slightly for clarity.

overlooked from observation, which we deem highly improbable.

Radio Source Prevalence Effects

An alternative interpretation of the split seen in Figures 3.11 and 3.12, is that it may be driven only by the increased prevalence of radio sources in LE-BCGs. Essentially, this is the equivalent of a vertical shift in Figure 3.11, as opposed to a horizontal shift as is inferred due to LE-BCGs being more radio-luminous. In Figure 3.13 we create an equivalent plot to Figure 3.12, but now considering the ratio of detected fractions for LE to NLE-BCGs at fixed luminosities for the separate radio components. Essentially, this plot maps the vertical separation between the LE and NLE lines in Figure 3.11, rather than the horizontal separation seen in Figure 3.12. The gradients for the green and red lines within this plot are comparble to their analogues in Figure 3.12. From the current data a prevalence driven split for the non-cores cannot be fully ruled out, although this is deemed unlikely since if they were drawn from the same luminosity distribution then there is a high improbability of our X-ray selected cluster sample containing no NLE-hosted con-cores greater than 2×10^{25} W Hz^{-1} whereas $\approx$10% of non-cores in NLEs are this powerful. We also note that the range of fixed luminosities necessary in Figure 3.13 was driven by the detected luminosities rather than the sample completeness and hence does not provide a full picture of the function's shape, in particular at the brightest end. Indeed, the lack of cores greater than 1×10^{23} W Hz^{-1} means that our blue line in Figure 3.13 is largely unconstrained. However, if we consider the top panel of Figure 3.11 then we note a steeper profile for the NLE-hosted core components than for the LE-hosted cores. Even with a vertical shift for the NLE sample then these inconsistent profiles would create disagreement and hence we maintain that the split is most likely driven by an intrinsic luminosity difference in each of the radio components between the two populations. Upcoming deep, multi-wavelength surveys should allow this question to be answered unambiguously.

In Figure 3.14 we show the equivalent plot to Figure 3.11 but now include the full MS+ and again, a larger split is seen for the core components.

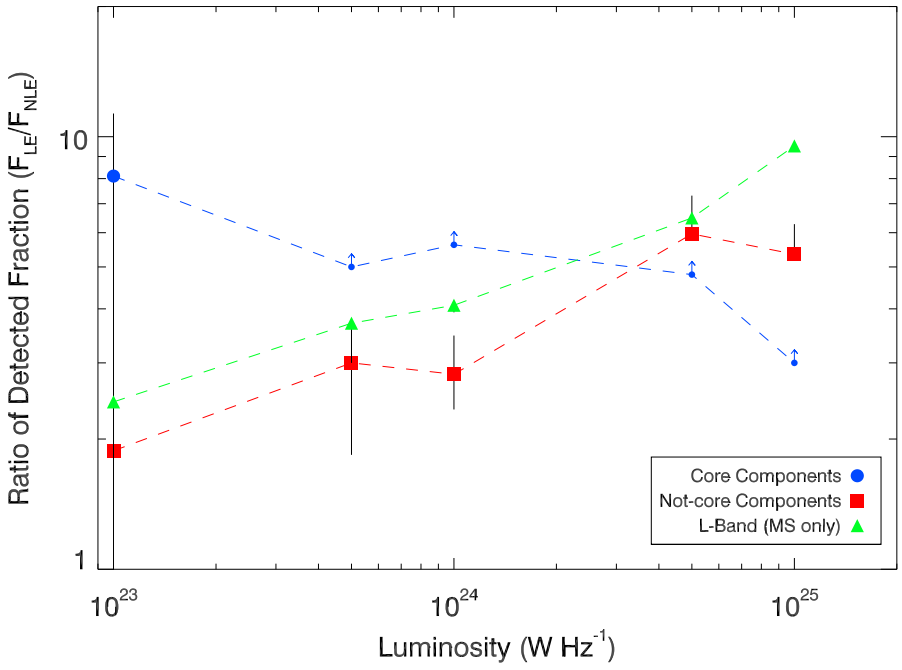

Figure 3.13: Ratio of detection fractions of LE-hosted to NLE-hosted sources at a range of fixed luminosities, for the core components, non-core components and the equivalent 1.4 GHz monochromatic LF for only those sources in the Main Sample, as shown in Figure 3.11.

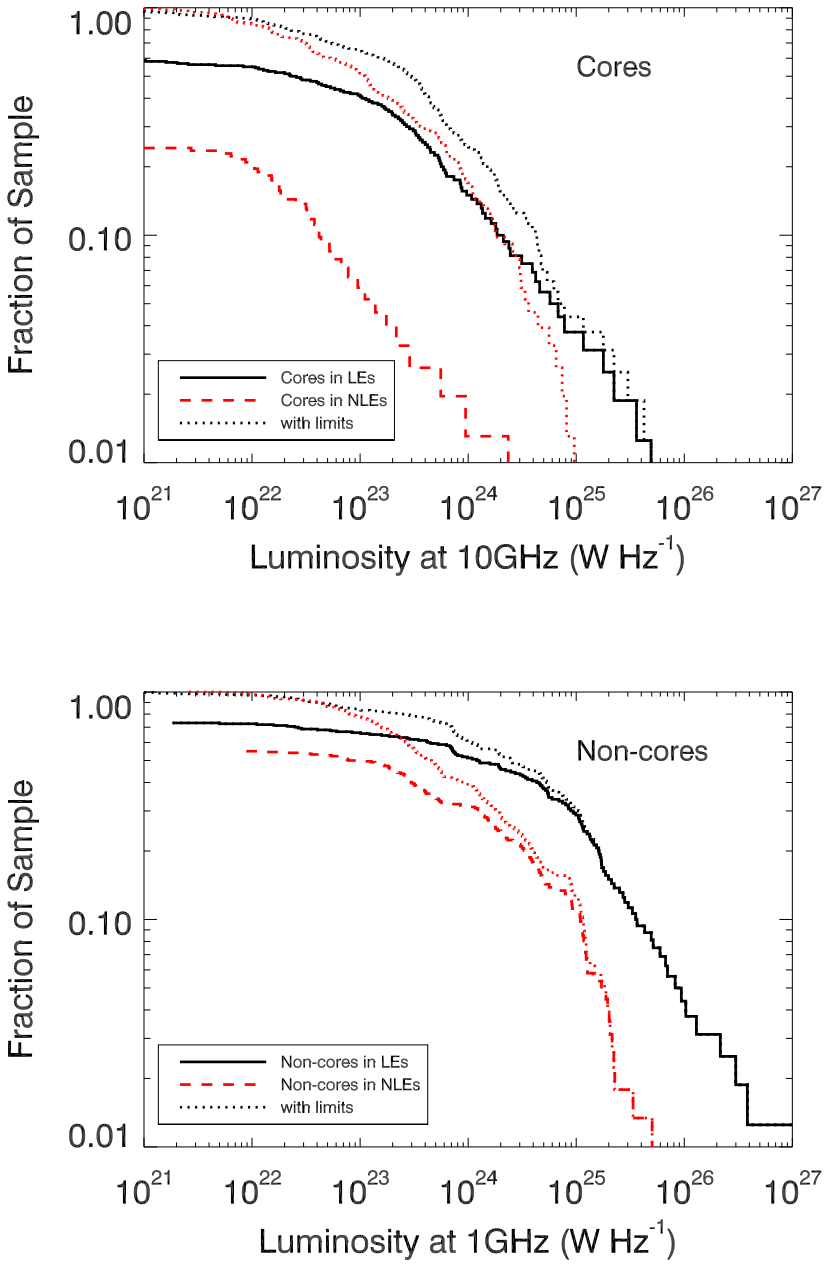

Figure 3.14: As for Figure 3.11 but using the full MS+. Note that unlike the MS, which was largely unbiased on radio priors (see Section 2.5.2), the MS+ extension is flux limited at L-Band radio and hence contains a smaller fraction of radio-quiet objects than is truly representative of the full parent sample. The LF extrema given when limits are included are hence essentially useless for inference purposes and stand only to highlight our ignorance of the full picture when limited data is available. Notwithstanding, we see here that the larger split is seen amongst the core values (it stands to reason that all cores should be detected within the radio loud rather than radio quiet sample!). The smaller split in non-cores (as compared to Figure 3.11) can be attributed to this bias, since with the plot being cumulative the relatively lower detection amongst NLEs in the parent sample would serve to separate the lines further. That the core split remains large amongst the entirety of the radio loud BCG sample (to given limit) further strengthens the case that this is a genuine example of the environment affects AGN behaviour in a systematic way throughout the Universe.

3.4.3 Dual-Mode Feedback - A Duty Cycle within a Duty Cycle

Whilst LE-BCGs have a higher duty cycle of radio-loudness than NLEs, what is really striking is that the fraction of radio-loud sources that contain an *active* core component is also much higher in LEs. In effect this is an *inner duty cycle* - the portion of radio-loud time for which an AGN is actively injecting radio-emitting populations - and it appears to be this factor that really characterises the difference between LEs and NLEs.

Several studies have shown that direct Bondi accretion of the hot gas on scales $<$1kpc from the nucleus can provide adequate fuel *on average* (see McNamara & Nulsen, 2007), although the rate is too low for the most extreme outbursts (e.g. McNamara et al., 2011). Additionally Allen et al. (2006) claim a strong correlation between the Bondi rate and their measured cavity powers in a small sample of well-observed, local systems. However, Russell et al. (2013) find a much weaker relationship.

In their recent review Heckman & Best (2014) argue that a plausible explanation for these disparate results may be that Bondi accreting gas goes through an intermediate stage where it cools prior to finally being accreted onto the black hole. Alternatively, the AGN may be fueled by cold phase accretion whereby blobs of cold gas condense non-linearly at scales $\approx$5-30kpc from the black hole and infall on less than the cooling timescale (e.g. Pizzolato & Soker, 2005). In a recent paper considering the origin of multi-phase gas in cool-cores, Voit & Donahue (2014) find that thermal conduction and cold-mode accretion are complementary processes in regulating cluster cores. At higher core entropies conduction prevents the core from cooling radiatively whereas at lower entropy, thermal instabilities cause the formation of cold clouds that subsequently precipitate onto the central black hole and power AGN feedback. These scenarios all require that in some systems there should be large amounts of cold gas near to the nucleus. Indeed there is evidence for rotating disks of cool gas in some BCGs (e.g. Simkin, 1979; Ekers & Simkin, 1983; Lim et al., 2000; Wilman et al., 2005; Hamer et al., 2014; Russell et al., 2014). The resultant cold clouds could then power the sporadic periods of high activity whilst the AGN activity could still relate to the wider Bondi rate *on average*.

Such a scenario appears likely within cluster cores, where the cooling flow deposits large amounts of molecular gas within the BCG. The steady build-up of such cold clouds ensures that the replenishment time is low and hence naturally explains the high duty

cycle of radio loudness in both NLEs and LEs. The high *inner duty cycle* of *active* core components in LEs is slightly trickier to comprehend purely by sporadic processes. We postulate that within the LE clusters both ready cooled material and direct hot phase gas fuel the AGN. Large, sporadic cold clouds would be responsible for the brighter periods of activity (Werner et al., 2014). In between these periods, a steady trickle of hot gas and continuous albeit lower level cold-cloud fueling would still be able to reach the nucleus ensuring the persistency of core emission.

A similar picture to this is found in the simulations of Li & Bryan (2014) who find that under idealised conditions, cool clumps condense from the ICM due partly to the actions of jetted outflows. It could be that the presence of a weak Bondi-powered jet catalyses the formation of cold clouds that can then fuel more powerful activity. Such a process may be partly responsible for the so called 'molecular fountains' seen in some BCGs (e.g. A1835, McNamara et al., 2014) where cool material appears to condense behind rising cavities before falling back towards the central engine.

Accretion Mode Considerations

We have not in this thesis explicitly classified our BCGs as low-excitation or high-excitation radio galaxies (LERGs or HERGs respectively), a distinction that appears strongly related to the accretion state (inefficient/efficient respectively for LERGs/HERGs: Best & Heckman, 2012). However, the vast majority of BCGs are LERGs, typified by accretion efficiences $L<0.01L_{Edd}$ (where L_{Edd} is the Eddington luminosity). At these low rates accretion is believed to be via an advection dominated accretion flow (ADAF). Whatever the coupling efficiency of the mechanical energy output by a BCG, this is not likely to substantially change over the range of luminosities we see in our sample as they almost always remain in the LERG, ADAF-stage. Changes in radio luminosity are therefore most likely to correspond to changes in mechanical feedback power (as corroborated by Figure 3.10), rather than large changes in the accretion structure such as the collapse of an ADAF into a classical Shakura-Sunyaev thin-disk (e.g. see review of accretion structures by Done et al., 2007).

Additionally, in analogy with the scenario seen in black hole binaries, the transition from an ADAF to a thin-disk mode may be expected to coincide with a switch from mag-

netically arrested to magneto-rotationally supported accretion and hence the launching of a short-term ballistic jet (Mirabel & Rodríguez, 1994; Remillard & McClintock, 2006; Dexter et al., 2014). Such an event would cause the collapse of the large scale-height magnetic fields present in the inner accretion zone that are required for the launching of a typical, steady jet (e.g. Mirabel et al., 1992; Fender, 2001). The apparently highly persistent activity we infer from our sample would argue against such a magnetic restructuring, certainly for our LEs. That the periods of higher activity correspond to a difference in accretion structure (namely, a transition to a thin disk) is therefore considered highly unlikely and instead more likely correspond to something more akin to a greatly scaled-up analogue of the flaring seen in Sgr A*.

3.4.4 The Mini-Halo Dilemma

Here we consider links between the persistency of BCG radio emission in LEs and the enigmatic 'mini-haloes' and other low surface brightness structures found in cool cluster cores that are being found with increasing frequency in low frequency searches.

Definitions

We first attempt to summarise the structures believed related, directly or indirectly to AGN action of the BCG. See the reviews by Kempner et al. (2004) and Ferrari et al. (2008). A more in-depth description of these structures is provided in Section 1.5.4.

Mini-halo: Approximately spherical structure ≈few 100s kpc in diameter centred on the BCG (e.g. RXJ1720.1+2638: Giacintucci et al., 2014). The emitting particles are (re)accelerated in-situ, potentially by sloshing (e.g Walker et al., 2014) or MHD turbulence in the cooling flow (e.g. Gitti et al., 2002) but the seed particles may be from the AGN. See also Section 2.7.1.

Amorphous Halo: Morphologically similar to a true mini-halo, these are roughly spherical and centred around the BCG (e.g. A2052 Venturi et al., 2004). The distinction is that they are of small enough physical extent (≈10s kpc) to be fully consistent with being fading, albeit confused, homogenised and distorted AGN emission. Also known as 'confined cluster cores'. Further evidence for direct AGN origin of these is that many contain disrupted radio-lobes.

Core Relic: The detached dying lobes of radio galaxies, typically ≈few 10s kpc in extent (e.g. A133 Slee et al., 2001). Steep spectrum and necessarily found close to the BCG as they are powered merely by fading emission from a past injection period.

Phoenix Relic: Analogously, these are perhaps to core relics what mini-haloes are to amorphous haloes. Essentially core relics that have faded below observable limits but have continued to expand outwards until re-accelerated so that they re-ignite from their own ashes, hence the monicker (e.g. A85 Slee et al., 2001). Typically filamentary in structure and ≈few 100kpcs in extent.

In addition to these structures the full range of 'normal' FR-type radio galaxies can be found in cluster cores.

The BCG Link

The seemingly persistent core radio activity we see within our sample coupled to the high prevalence of steep spectrum, unresolved and amorphous structures leads us to suggest that this supports an AGN-origin for the seed populations of radio mini-halos.

A simple picture to explain the above mini-zoo is that the (near) constant action of BCGs is responsible for injection of electrons to their immediate environments. Over time, this persistent injection coupled to its natural ageing leads a population of sub-relativistic electrons (+ protons) to build up, forming a 'sub-observable' pedestal. A combination of the atmospheric mixing, ageing and re-acceleration processes determine how the resultant population appears. Where the confinement is strong enough then this pedestal will tend towards being amorphous, whereas in instances of stronger AGN outbursts and into less dense cores then the ejecta will more commonly keep their structure until re-acceleration.

A Toy Model

A very simple toy model using diffusion time-frames can be constructed to test the outline feasibility of the above scenario. If we take the Alfvén speed of electrons in a typical cluster to be ≈100kms^{-1} (Ferrari et al., 2008) then this translates to a dispersal velocity of roughly 0.1 kpc Myr^{-1}. For a typical electron emitting lifetime of 100Myr then a structure ≈10kpc can be expected from simple diffusion alone. If we consider that even

in strongly confused cluster cores, the jets will provide some bulk transport away from the central black hole then it is clear that amorphous haloes are fully consistent with this toy model, assuming the dispersion is reasonably homogenous.

Extending this simple argument to longer timescales, we see that an electron population persistently injected at radius zero in a settled cluster could diffuse to become an amorphous seed mini-halo of radius 0.5Mpc in around 5Gyr. Established cool core clusters are found to be in place by redshifts >1 (e.g. Santos et al., 2010; McDonald et al., 2013, although they typically would only be classified as 'weak cool cores' locally). This would allow ample time for our persistently active BCGs to seed local mini-haloes and support an AGN derived seed population, if the BCG radio-activity that we see locally is representative of activity at higher redshift. It should be noted however that in order for this simple picture to explain the highest redshift mini-halo thus observed, in RXJ1347.5-1145 at z$\approx$0.451 (Gitti et al., 2007), then a settled structure by z$\approx$1.7 would be required.

In this simple picture it seems as if all cool core clusters could potentially host mini-halos. Their apparent rarity would then be due to the finely tuned conditions required for re-accelerating the plasma, most likely provided by sloshing action strong enough to churn the ICM but not strong enough to fully disrupt the cooling flow. A picture where the seed population is (near) continually centrally injected suggests there should be a density gradient across mini-haloes. Such a scenario could explain the index gradient seen in some sources whilst also, if constrained at greater radii by the cooling flow, providing a working surface for shocks associated with phoenix relics. Similarly, this simple scenario naturally explains the apparently continuous distribution of halo sizes from amorphous to mini-haloes.

Current low frequency observations of cluster cores such as those with the Low Frequency Array (LOFAR: van Haarlem et al., 2013) and the Murchison Widefield Array (MWA: Tingay et al., 2013) would be expected to find more amorphous haloes, of greater extent in this constantly fading injected emission scenario.

3.4.5 Considering Relativistic Beaming

For the size of our parent sample, geometry causes us to expect around 20 sources to have their jets aligned within 5° of the line-of-sight. Such a population may present

itself as a population of flat spectrum, apparently powerful cores but would have their intrinsic core powers overestimated by potentially large factors. However we note that we purposefully removed BLLac objects from our parent sample so as not to be overtly affected by a handful of strongly beamed sources. There is also no logical reason why LE-BCGs would more commonly have aligned cores than NLEs.

Relativistic beaming of the inner-jet in an existing radio source could account for some seemingly strong, flat spectrum components of otherwise steep spectrum sources if the jet-axis has precessed into favourable alignment since the steeper spectrum emission was ejected. Our sample does include a couple of sources that have previously been considered to be mildly beamed. For example, the BCG of A2055 appears to be a head-tail source on few-arcsecond scales, but the bright core may be beamed (Pimbblet et al., 2006). Similarly, A2627(a) only appears to have marginally resolved jet structure on arcsecond scales but its AGN is X-ray dominated, hence the flux may be boosted by the presence of a beamed BLLac-like nucleus (Rector et al., 1999). However, for this to account for all our split spectrum sources would require a very high precession speed in a significant number of sources. Additionally, the long timescales between some of the archival data we use in compiling our SEDs shows that the flat and GPS-like behaviour is persistent over $>$decade timescales and hence unlikely to be purely the result of beaming as this would give significant, short-term variation (see Chapter 4). Furthermore, VLBA imaging of the central regions shows symmetrical two-sided structures on few parsec scales in many of our active BCGs hence showing that the source is not favourably aligned for strong beaming. For consideration of the milli-arcsecond scale radio properties of BCGs as recovered with the VLBA, see Chapter 5.

Overall, we concede that some blurring of results due to relativistic effects are essentially unavoidable for any large sample of radio-AGN, however due to the arguments stated here we do not believe beaming to overtly affect our results.

3.4.6 Implications for Surveys

Clusters - X-ray and SZ Surveys

X-ray cluster surveys are sensitive to contamination by strong AGN. Indeed the most X-ray luminous cluster known, 'The Phoenix' (McDonald et al., 2012) was initially overlooked in X-ray cluster surveys due to it containing a powerful ($L_{2-10keV} \approx 3 \times 10^{45}$erg s^{-1}) obscured AGN. The true nature of the source was not realised until detection with the South Pole Telescope (SPT: Carlstrom et al., 2011) using the Sunyaev-Zel'dovich (SZ) effect (Williamson et al., 2011). Similarly, mis-aligned but flat-spectrum radio BCGs can be erroneously interpreted as AGN, broad-line radio galaxies (BLRGs) or BLLacs. This can result in massive clusters being overlooked as their X-rays will be attributed to the AGN, potentially leading to un-representative samples. Conversely, X-rays from strong radio sources within clusters may be erroneously attributed to the extended ICM leading to over-estimated cluster masses (Rector et al., 1999).

BCGs whose radio spectra flatten towards higher frequencies are likely a considerable contaminant in Sunyaev-Zel'dovich (SZ) cluster surveys. To map the large spatial scales required for SZ detections at the characteristic ≈15-200 GHz range, single dish telescopes and short-baseline arrays are employed. However, the observed flux decrements can be affected by radio point sources and hence often flux measurements from higher resolution observations taken at lower frequencies are extrapolated up to the frequency of interest (e.g. Knox et al., 2004; Coble et al., 2007; Lin et al., 2009). Even with a measured rather than assumed spectral index, this method has obvious shortcomings for the cases of spectral flattening or inversion.

As an example, extrapolating from the low frequency flux measurements in NGC1275 without accounting for its highly variable and energetically dominant self-absorbed core component would lead to underestimating the 100 GHz *Planck* flux density by around two orders of magnitude (see also Dutson et al., 2014). Even in instances where the host cluster is still detected such contamination could nevertheless severely affect resulting mass measurements. If found to be common this would have potentially wide-reaching consequences cosmologically in terms of not only future survey planning but also current and past SZ-survey interpretation. The contamination is further exacerbated by the fact

that in many cases these active core components are found to be variable on month-to-year timescales (see Chapter 4).

It is therefore apparent that having multi-scale, contemporaneous (as much as possible) radio observations over a comparable frequency range to the SZ observations are required to properly address this issue within SZ surveys. Further consideration of the level of this contamination is given in the following chapter that considers the high radio frequency properties and variability of a sample of BCGs with prominent flatter spectrum emission (Chapter 4).

Blind Radio Surveys and Mimicked Evolution

The presence of two very different spectral radio components means that the source population sampled in a flux-limited radio survey of AGN is highly dependent upon the observed frequency; unlike the case for a population of single spectral index sources. Higher frequency samples (roughly comparable to a horizontal split on Figure 3.5) will contain a higher proportion of core-dominated systems whereas low frequency selected samples (more equivalent to a vertical split on Figure 3.5: e.g. van Haarlem et al., 2013; Tingay et al., 2013) will favour those dominated by steeper spectrum emission (see also Sadler et al., 2014). Whilst it is already well established that high frequency surveys will preferentially detect young sources, for BCGs the effect is slightly more subtle in that high frequency samples will preferentially detect those sources with the highest *inner duty cycle* of core activity (i.e. BCGs that are more persistent).

As the youngest and most recent AGN activity will peak spectrally at higher frequencies due to their GPS-like nature (e.g. O'Dea, 1998; Sadler et al., 2014), samples taken at frequencies below the characteristic turnover will preferentially detect older outbursts. Samples at progressively higher frequencies will therefore contain a greater proportion of younger sources. Conversely, for a single observing frequency, matching samples at increasing redshift will show the same effect such that the population of radio sources to higher redshift, particularly for redshifts of $\geq$2 (where a restframe $\approx$15 GHz characteristic GPS peak would be redshifted below 5 GHz), will appear younger and more active - effectively mimicking evolution in the source population.

Much increased spectral coverage is required before improvements to the radio k-

correction above a simple power-law extrapolation can be confirmed possible/necessary or not. However, the effect should be considered when studying the redshift evolution of the radio population.

3.4.7 Beyond BCGs - Implications to AGN Feedback Globally

Whilst trying to explain the entire AGN population by studying only the BCGs would be clearly unwise given their extreme nature, BCGs are nonetheless the extreme end of the galaxy mass function and hence understanding them does have implications for AGN globally.

Fundamentally, the black hole at the centre of a BCG is governed only by mass and spin, the same as for any other. The unique behaviour of BCG-hosted AGN is then due only to their size and location. One implication of this environment is that BCGs have such a high duty cycle because they essentially remain eternally young. They undergo repeated periods of activity with a halo replenishment time much shorter than for normal galaxies due to the cooling flow. Due to this we can see the effects of AGN feedback as it is still ongoing. One important implication we see here is that it is the core components that appear to be the main differentiator between LE and NLEs. Timescale considerations are therefore paramount to ensure that the radio emission being considered was powered by the same activity causing the other AGN tracers. This may be less prevalent in field AGN where they are expected to have much longer recurrence times than BCGs, however it is clear that to fully link the radio-behaviour to the AGN then information beyond the radio-quiet/radio-loud dichotomy is required.

3.5 Conclusions

We have studied the radio properties in BCGs drawn from a large sample of X-ray selected galaxy clusters. The sample is split by the presence of optical emission lines (Hα+[NII]), using the proxy that when these lines are present the cluster most likely corresponds to being a strong cool core and when absent the dynamical state of the cluster is markedly less relaxed. We present and collate a large radio data volume for this sample and consider the overall radio properties of the sample as a function of environment. Furthermore, we

decompose the BCG radio emission into two components - a core, attributable to ongoing injection AGN activity and a non-core comprising everything else. We then consider these components in order to better understand the activity. Chiefly we find that:

- The duty cycle of radio-loudness is significantly higher for BCGs in strong cool-core clusters ($>$85%) than for those in non strong cool-core clusters ($>$52.5%).
- LE BCGs are typically much more radio-powerful AGN at than those in NLEs - $\approx$50% of LE BCGs hosting a radio source $>10^{24}$WHz^{-1} at 1.4 GHz whereas only $\approx$15% are similarly radio-powerful in NLEs.
- The prevalence, and typical power, of an *active* radio core is highly dependent on cluster state. 60.2% of LE BCGs in our sample contain a distinguishable core of which $\approx$83.1% are $>10^{23}$WHz^{-1}. Conversely, only 11.6% of our NLE BCGs contain a distinguishable core, with only $\approx$5.0% of our NLE BCGs containing an active core of $>10^{23}$WHz^{-1}.
- This core component shows better correlation with the canonical AGN tracer, [OIII] 5007Å, than the ageing non-core component. It is thus likely that significant scatter often found in studies between radio emission (particularly from low resolution surveys) and other AGN tracers is due to the timelapses between emission periods being long enough that the different relative lifespans of different populations (e.g. deionisation time of atoms versus synchrotron lifetime of electrons) will dominate the relative emission ratios.
- The brightest cores are only hosted by the most X-ray luminous clusters, although bright non-cores can be hosted by both high and low X-ray luminosity clusters.
- Both non-core and core radio emission correlates with cavity power in LEs. It appears that BCGs are persistently radio-active over bubble-rise timescales in these environments.
- The radio-power versus cavity-power correlation appears to evolve with the spectral index of the radio source.

- An increasing fraction of flat and inverted spectrum sources in samples selected at increasing radio frequency may mimic luminosity evolution in the total radio population if not fully accounted for. Additionally, such sources likely present an important contaminant to SZ observations.

Overall, we find that BCGs are a varied population with a wide variety of radio behaviour. Future studies in the so-called ‘new golden age’ of radio astronomy that we are now entering with existing and upcoming facilities should uncover many more facets to these intriguing behemoths.

CHAPTER 4

High Radio Frequency Properties and Variability of Brightest Cluster Galaxies

4.1 Abstract

In this chapter we consider the high radio frequency (15 – 353 GHz) properties and variability of 35 Brightest Cluster Galaxies (BCGs). These are the most core-dominated sources drawn from the parent sample of more than 700 X-ray selected clusters, thus allowing us to relate our results to the general population. We find that $\geq$3.4% of the BCGs in our parent sample contain a peaked component (Gigahertz Peaked Spectrum, GPS) in their spectra peaking above 2 GHz, increasing to $\geq$8.5% if only cool-core clusters are considered. We see little evidence for strong variability at 15 GHz on short (week-month) timescales although we see variations greater than 20% at 150 GHz over 6-month timeframes for 4 of the 23 sources with multi-epoch observations. Much more prevalent is long-term (year-decade timescale) variability, with amplitude variations greater than 1% annually at 15 GHz being commonplace. There is a weak trend towards higher variability as the peak of the GPS-like component occurs at higher frequency. We demonstrate the complexity that is seen in the radio spectra of BCGs and discuss the potentially significant implications of these high-peaking components for Sunyaev-Zel'dovich cluster searches. Tentative evidence is seen for an additional component in the mm/sub-mm spectra of BCGs that may be attributable to direct emission from the central accretion flow rather than originating in a jet. Such a component may be present in the spectra of all low-accretion rate AGN but usually saturated by jet-emission, only becoming visible at high radio frequencies and for sources with weak jets.

The majority of the work presented within this chapter constitutes the submitted paper, Hogan *et al.* 2014b.

4.2 Introduction - High Radio Frequency Properties and Variability of BCGs

There has apparently been a fine balance between heating and cooling within clusters in place for at least half the Hubble time (e.g. Vikhlinin, 2006; Pratt et al., 2010; McDonald et al., 2014). Furthermore, the energy imparted by AGN activity does appear to be sufficient to offset cooling *on average* (e.g. McNamara & Nulsen, 2007; Dunn & Fabian, 2008). However this is not the case at all times, suggesting that periods of cooling must be interspersed by periods of AGN energy injection. Added to this is the growing realisation that in the most settled cool-core (CC) clusters where there is a central peak in the cluster X-ray surface profile indicative of substantial cooling, the BCGs have a radio-loud duty cycle approaching unity (e.g. Burns, 1990; Mittal et al., 2009, , also see Chapter 3). This suggests that in these systems there must be cyclic activity whereby the BCG is more active in some periods than others.

Most previous studies using radio observations to trace this AGN feedback have been carried out at $\leq$1.4 GHz (e.g. Best et al., 2007; Stott et al., 2012) and so the radio properties of BCGs in the $\approx$10-300 GHz range are somewhat poorly constrained. Single-dish surveys of the sky at the higher end of this range are typically shallow and have relatively low resolution (e.g. Planck Collaboration et al., 2013b) whereas even at the lower end, small beam sizes make interferometric surveys of any sizeable area both difficult and expensive. However it must be noted that several recent surveys have allowed for huge advances in the understanding of the radio-sky at greater than 10 GHz (e.g. 10C at 15.7 GHz, AMI Consortium et al. 2011; AT20G at 20 GHz, Murphy et al. 2010 and the AT20-deep (pilot) also at 20 GHz, Massardi et al. 2011; Franzen et al. 2014). Consequently, only a few of the brightest BCGs have well characterised radio-spectra in this crucial spectral range.

In Chapter 3 we considered the radio properties of BCGs in a parent sample of over 700 X-ray selected clusters (Ebeling et al., 1998, 2000; Böhringer et al., 2004). These

were split into CCs and non cool-cores (NCCs) using the presence of optical emission lines around the BCG. Such lines are only found in systems with central cooling times less than 5×10^8 years, equivalent to a central entropy less than 30 keV cm^2 and hence can be used as a proxy for the cluster state (Cavagnolo et al., 2008; Rafferty et al., 2008; Sanderson et al., 2009a). The radio spectral energy distributions (SEDs) of the BCG in 246 of these were populated, typically between 74 MHz and 20 GHz, and decomposed into active and inactive components attributable to ongoing and historical accretion respectively (see Chapter 3). Not only was the radio duty cycle of BCGs in CCs seen to be substantially higher than in NCCs, it was found that the majority of CC-hosted BCGs showed evidence for ongoing core activity that manifests itself primarily as a spectral flattening above a few GHz. Often this emission is missed in low frequency surveys. Further confounding the lack of information, increased variability is postulated to higher radio frequencies as the emission is expected to originate from increasingly smaller physical scales.

In this chapter we select a sub-sample of the BCGs studied in Chapter 3, believed to contain the most dominant active cores. These sources all reside in CC clusters where active feedback is prevalent. Furthermore, the dominance of the radio core component in these sources indicates that the SMBH is actively accreting at a significant rate. We observe them with a variety of facilities to extend their radio coverage up to 353 GHz as well as observing a number of them at different epochs which, alongside historical observations, allows us to study their variability. This permits us to explore the origin of the point-like central radio emission as well as to constrain the amplitude of variation in the accretion rate during active periods of ongoing feedback. Whilst the feedback powers derived from X-ray cavities trace the AGN energy output averaged over tens of megayears, this shorter term variability provides insights into the more instantaneous processes within the core.

One system that has been well-monitored at radio frequencies greater than a few GHz, and indeed constitutes one of the most well-studied examples of active AGN feedback in a cluster core is NGC1275/3C84 in the Perseus Cluster (e.g. Boehringer et al., 1993; Conselice et al., 2001; Abdo et al., 2009). Large amplitude variations in the radio spectrum of this source have been known for many years (Pauliny-Toth & Kellermann, 1966).

Recently Dutson et al. (2014) undertook a comprehensive study of the radio and gamma-ray properties of NGC1275, considering its radio variability over five decades in both time and frequency. The radio spectrum consists of a steep spectrum power-law at frequencies below approximately 1 GHz and an inversion above this leading to a peaked profile. It should be noted that the source is not strongly beamed (Krichbaum et al., 1992; Nagai et al., 2010). The power-law component, attributed largely to the presence of extended lobes and a 300kpc mini-halo (Burns et al., 1992), is constant in its flux. However the peaked component is found to vary significantly in both flux (more than an order of magnitude) and turnover frequency on few year/decade timescales. Such variations have been previously linked to individual components in the jet on milli-arcsecond scales, as recoverable using Very Long Baseline Interferometry (VLBI, e.g. Suzuki et al., 2012). Interestingly, Dutson et al. (2014) find compelling correspondence between this few-year variation of the high radio-frequency peaked component and the high energy gamma-ray emission but no strong connection between the short-term 'flaring' seen in the gamma-rays and the 1.3mm flux. In a study of the core X-ray properties of 57 BCGs, Russell et al. (2013) found that roughly half contained an X-ray point source at Chandra resolution. It is worth noting that three of these (A2052, Hydra-A and M84) were seen to vary over similar 6-month to decade timescales, which is similar to the timescale of variation seen in the radio emission of NGC1275.

One of the aims of the current chapter is to investigate whether the high radio frequency properties of NGC1275 mark it out as a peculiar object or whether such periods of high activity in the spectral range above 10 GHz are common amongst the BCG population.

Recently the Sunyaev-Zel'dovich (SZ) effect (Sunyaev & Zeldovich, 1972) has been used to compile large catalogues of galaxy clusters (e.g. Vanderlinde et al., 2010; Reichardt et al., 2013; Marriage et al., 2011b; Hasselfield et al., 2013; Planck Collaboration et al., 2011a, 2013c,a). Unresolved radio sources present a significant systematic for these searches and may lead to underestimated or completely removed SZ decrement in the 15-200 GHz range (see e.g. Knox et al., 2004; Coble et al., 2007; Lin et al., 2009). Furthermore, the single-dish nature of many SZ-observatories means that often the removal of contaminating point sources relies on uncertain extrapolation of higher resolution but

lower frequency data. Our results therefore have potentially significant implications for SZ studies of clusters.

4.3 Sample

The sample of sources chosen for this study were selected primarily from Chapter 3 as having the brightest ($>$ 10mJy), flat-spectrum cores ($\alpha < 0.5$), so that a detection above 100 GHz was possible. The parent sample described in Chapter 2 covers an all-sky, X-ray flux-limited sample of over 700 clusters as outlined above but the number of sufficiently bright sources is relatively small ($<$ 30 or $<$ 4%).

To increase the target list we added seven bright ($>$50mJy at 5 GHz) sources either in fainter clusters and/or clusters that have been mis-identified until now. Four of these sources are in fainter clusters (A11, Perlman et al. 1999; 4C+55.16, Iwasawa et al. 1999; A2270, Healey et al. 2007; and RXJ2341+00) and three in clusters above the eBCS/REFLEX flux limit (RXJ1350+09; RXJ1832+68, Böhringer et al. 2000; Gioia et al. 2003; and E1821+64, Russell et al. 2010). All seven of these sources have been identified as AGN, given the association of radio and X-ray emission. However, only E1821+64 is actually strongly (more than 50%) contaminated in the X-ray by an AGN, in this case a QSO. In the other six cases the cluster has *previously* been mis-identified as a BLLac as a result of them having seemingly flat radio spectra and so the X-rays had been attributed to the AGN. However, all six of these clusters have central galaxies with strong, narrow optical line emission, characteristic of cooling flow BCGs (Crawford et al., 1999) and in all other aspects are similar to the sources selected in Chapter 2. Therefore, we propose a re-identification of each source such that the X-rays are predominantly from the cluster and not a central AGN.

The source selection is by no means complete but is representative of the brightest, core-dominated radio sources in cluster cores. Therefore we believe that the spectral and variability properties we determine for this radio-bright sample can be used to constrain the properties of the complete, X-ray selected sample as a whole.

4.4 Data and Reduction

4.4.1 GISMO

GISMO is a 150 GHz (2mm) bolometer camera built by the Goddard Space Flight Centre (Staguhn et al., 2008) for use on the IRAM-30m telescope[1], which is located at an altitude of 2850m on Pico Veleta, Spain. GISMO operates as a visitor instrument being operable for around a two week period every six months. During its time on the telescope GISMO is operated in a shared risk pool observing mode, during which telescope focus and pointing observations are regularly performed on IRAM calibrator sources.

We obtained data from 3 epochs, using GISMO to observe 29, 24 and 17 sources in the April 2012, November 2012 and April 2013 observing runs respectively, with as many source overlaps between runs as possible (see Table I.1). Sources were typically observed for 5-10mins using a standard lissajous scanning script. The telescope has a typical FWHM of 16.7" and the absolute flux calibration of GISMO is found to have a typical 16% uncertainty[2].

Data were reduced using the GISMO specific section of the CRUSH software package (Kovács, 2008). Pointing and flux models specific to each run are updated during each GISMO run and the package itself is being continually updated. We therefore reduced our data using a version of CRUSH (2.15-2) that post-dates all of our data collection and hence contains optimised parameters for each of our data-sets.

Most of our sources have signal-to-noise ratios (SNRs) less than 10 for each scan. We therefore found the -faint option within CRUSH to deliver the best results in most cases. For non-detections we re-mapped the data using the -deep filtering. Only one source (A1885) was recovered using -deep but not -faint. Since the -deep option is known to over-filter sources with SNR greater than 5 and will create negative flux haloes, we took our flux measurements from the maps created using the -faint option. A1885 was recovered with a SNR of $\approx$4 and hence measuring the flux from the -deep map for this source is not believed to introduce any additional error. The specific filtering mode used for each source is shown in Table I.1. Atmospheric extinction is automatically corrected

[1] IRAM is supported by INSU/CNRS (France), MPG (Germany) and IGN (Spain)

[2] Performance reports available for each run at http://www.iram.es/IRAMES/mainWiki/Continuum/GISMO/Main

for within CRUSH, using an estimate of the most recent tau (225 GHz) value as measured by the on-site tau-meter. However, some of our data (particularly during the Nov. 2012 run) suffered from a faulty tau-meter not inserting the correct measurement into the FITS file. Time-dependent records of the on-site tau values were recorded manually during each run, which were compared to the values recorded automatically in the log files. To ensure consistency, we manually inputted the best estimate zenith tau-value using the *-tau.225 GHz* option within CRUSH for each of our source reductions.

Maps were produced and fluxes extracted using the CRUSH tool 'show'. Gaussian fits were performed for each source with the resultant flux and FWHM reported along with source peak and map RMS in Table I.1. Only Hydra-A showed significant extent and hence its flux was extracted from a user-defined region. Fluxes were additionally verified using the kvis data-display tool (Gooch, 1996).

4.4.2 CARMA

Twenty three sources were observed at 90 GHz using the CARMA interferometer (e.g. Woody et al., 2004) in D-array between 21st May - 15th June 2012, of which twenty overlap with our GISMO sources. These observations were performed in queue mode by initiating pre-determined blocks, which could be started and abandoned part way through, depending on observing conditions and at the discretion of the telescope operator. Each block contained an observation of a planet for primary flux calibration. This observation is run through CARMA pipelines to provide a primary flux scale for the observations. Additionally, a strong bandpass calibrator was observed for each block (the bandpass calibrator used was either 3C279, 3C345, 3C454.3 or 3C446, depending on observability). Science targets were visited several times at various hour angles to maximise uv-coverage and sandwiched between 1 minute observations of a nearby phase calibrator.

Data were reduced by the standard methods using the CARMA optimised version of the MIRIAD data-reduction software package (developed and maintained by University of Maryland). Some automatic flagging of bad data is performed, but the visibilities were also inspected and flagged interactively. Files with basic calibration, taken at the time of observation were provided and used as a calibration starting point. Corrections for antenna positions were performed using the most co-temporal *antpos* models provided by

the observatory. Further bandpass, phase and flux corrections were applied using standard MIRIAD tasks as determined from the observed calibration sources.

Deconvolution and cleaning of the subsequent maps were also performed using MIRIAD and the kvis data-display tool used to extract fluxes, verified by additionally extracting fluxes using the AIPS task JMFIT.

4.4.3 AMI

The Arcminute Microkelvin Imager (AMI, Zwart et al., 2008) is a versatile instrument located at the Mullard Radio Astronomy Observatory (MRAO). Optimised for study of the SZ effect, AMI consists of two interferometer arrays: the Small Array (SA), with ten 3.7 m antennas with baselines of 5-20 m; and the Large Array (LA) with eight 12.8 m antennas with baselines of 18-110 m. These arrays are thus optimised for large (3 – 10 arcmin) and small (30 arcsec – 3 arcmin) scale observations respectively. This set-up allows study of the large-scale SZ effect with accurate characterisation of the contaminating radio source environment. Both arrays measure the I+Q polarisation at the central frequency 16 GHz. Data are taken in six channels, each of width 0.72 GHz, over the range 13.9- 18.2 GHz, allowing a local spectral index to be determined for strong sources.

We used the AMI-LA to observe seventeen of our sources, with each target visited either two or three times in 2012 (see Table I.2). Observations consisted of 8 minute integrations sandwiched between 1 minute phase calibrator scans. In the April-June scans the sources were themselves used for self-calibration. For the September follow-ups we additionally observed nearby phase calibrator sources. 3C 48 and 3C 286 were observed for use as amplitude calibrators.

Data reduction was performed using the local (to MRAO) in-house software REDUCE. Reduction pipelines were used to apply amplitude and phase calibration, flag for telescope errors and Fourier transform to produce frequency channels. Additional flagging for bad data was carried out interactively through visual inspection of the channel data.

Data are written out of REDUCE as uv-FITS files which were read into AIPS for deconvolution and cleaning using IMAGR. Maps were produced for each channel in addition to a single image for the full bandwidth. None of our sources were found to be resolved and so fluxes were extracted using the AIPS task JMFIT and verified using kvis.

We investigated the flux calibration and find a typical 5% uncertainty, which we propagate into in our uncertainties.

4.4.4 OVRO and UMRAO

Since 2007 the Owens Valley Radio Observatory (OVRO) has been using its 40m telescope to undertake a 15 GHz monitoring campaign of over 1500 radio sources (mainly blazar Fermi-LAT gamma-ray candidates, see Richards et al., 2011). Five of the sources in our sample have been monitored as part of this OVRO monitoring campaign. Additionally, since January 2013 eleven extra BCGs with strong high radio-frequency emission selected from this work have been included within the dynamic queue, allowing regular (typically every 10 days) observations for these sources (see Table 4.1).

The OVRO 40 m uses off-axis dual-beam optics and a cryogenic high electron mobility transistor (HEMT) low-noise amplifier with a 15.0 GHz centre frequency and 3 GHz bandwidth. The two sky beams are Dicke switched using the off-source beam as a reference, and the source is alternated between the two beams in an ON-ON fashion to remove atmospheric and ground contamination. A noise level of approximately 3-4 mJy in quadrature with about 2% additional uncertainty, mostly due to pointing errors, is achieved in a 70 s integration period. Calibration is achieved using a temperature-stable diode noise source to remove receiver gain drifts and the flux density scale is derived from observations of 3C 286 assuming the Baars et al. (1977) value of 3.44 Jy at 15.0 GHz. The systematic uncertainty of about 5% in the flux density scale is not included in the error bars. Complete details of the reduction and calibration procedure are found in Richards et al. (2011). We check the pipeline data for, and remove, individual scans whose amplitude is obviously discrepant (of which we find less than 1%). Additionally we remove a small minority of points where uncertainties reach more than 40%.

One of our sources (4C+55.16) that is included within the OVRO monitoring campaign was also monitored at 15 GHz by the 26m telescope of the University of Michigan Radio Astronomy Observatory (UMRAO; Aller et al., 1985, 2014). The UMRAO monitoring of this source is not ongoing, however the addition of the UMRAO data to the OVRO and AMI data means that for this source we have well-sampled lightcurves at 15 GHz extending forwards from 1985 to the present.

4.4.5 SCUBA-2

The SCUBA-2 (Holland et al., 2013) observations were made as part of a poor weather programme (JCMT weather Bands 4 and 5, $\tau_{225\mathrm{GHz}} = 0.15$–$0.3$) as part of Canadian and UK projects (M12AC15, M12BC18, M12BU38, M13AC16 and M13AU38) between February 2012 and July 2013. The observations were made in small map ("CV Daisy") mode with integrations of 30 minutes each.

The observations were reduced using the standard SMURF package (Jenness et al., 2011; Chapin et al., 2013). We used the standard flux calibration of $\mathrm{FCF}_{850} = 527 \pm 26$ Jy beam^{-1} pW^{-1}. The resulting maps reached noise levels of typically 4–8 mJy beam^{-1} (depending on conditions) which was sufficient to detect over half of the sources observed.

Note that the SCUBA-2 data reduction was done by Dr James Geach of the University of Hertfordshire.

4.5 Results

4.5.1 Spectral Energy Distributions

In Chapter 3 we performed spectral decompositions for a large number of BCG SEDs finding that in many cases the spectrum flattens above a few GHz, indicative of these sources containing an underlying strong core component. In the current chapter we expand the spectral coverage for our subsample of 35 of these sources into the mm/sub-mm regime. We indeed see that in many instances these active components extend to high frequency and typically rollover at the highest radio-frequencies, consistent with recently accelerated synchrotron populations.

We performed fits to each of our extended SEDs, using the CURVEFIT program of IDL. Generally our sources could be well fit by either a power-law, Gigahertz Peaked Source (GPS)-like

, equations 10.0.2 and 10.0.1. Also see][]Orienti14 component or a combination of these. Individual SEDs, fitting notes and parameters are presented in Appendix J. Our SCUBA-2 data were included in the SEDs although excluded from the spectral fits as in several cases it appears to be indicative of an additional albeit poorly constrained compo-

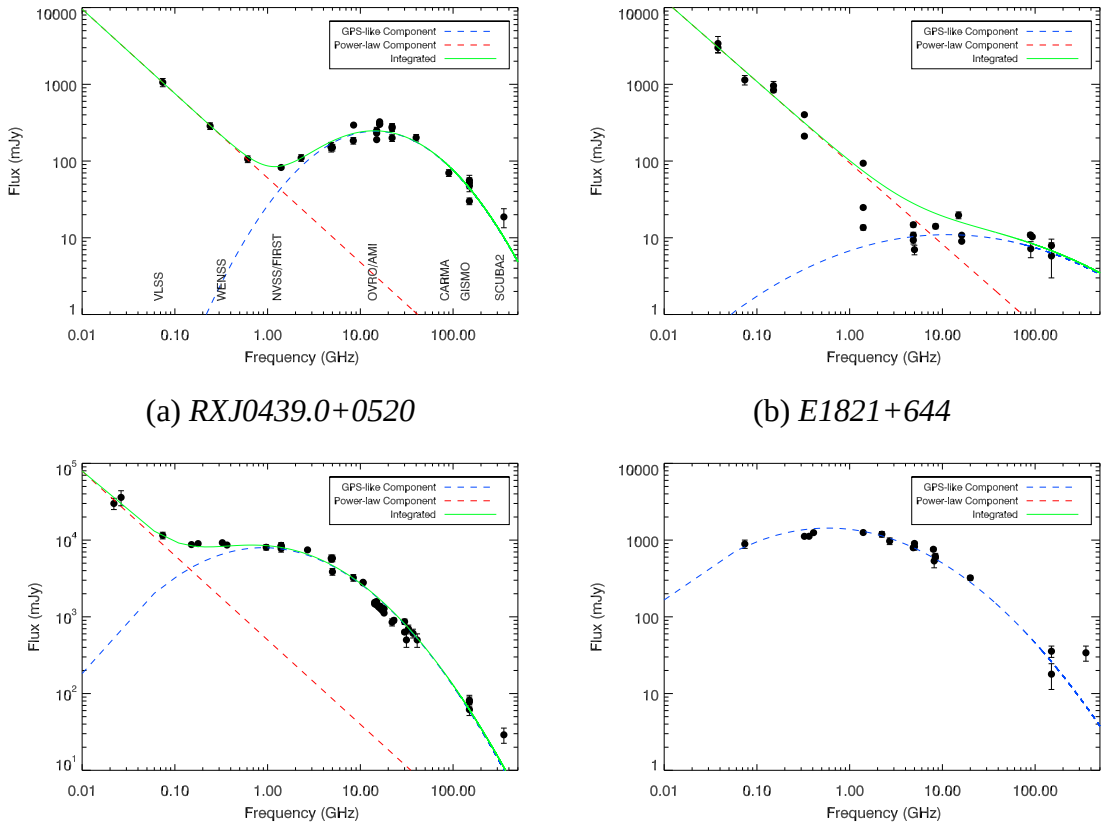

(a) *RXJ0439.0+0520* (b) *E1821+644*

(c) *4C+55.16* (d) *MACS0242.6-2132*

Figure 4.1: Example SEDs for four objects. In panel (a) we highlight the frequencies of the observations presented within this chapter, in addition to the widely used radio-surveys NVSS/FIRST, WENSS and VLSS to help contextualise our frequency coverage. We see a variety of spectral shapes, sometimes well-fit by a single component as in MACS0242-21 whereas in other cases requiring both a power-law and a GPS-like component (see text). Note that the SCUBA-2 data-points at 353 GHz are included in the SEDs but excluded from the plots as they often appear to be suggesting the presence of an additional, poorly constrained component at the highest frequencies (see Section 4.6.6).

nent becoming prominent in the mm/sub-mm regime (see Section 4.6.6). Four example SEDs are shown in Figure 4.1.

In some instances, as in RXJ0439+05 (panel a of Figure 4.1) the GPS-like component is distinct and inverts the spectrum above a break frequency below which we see a steep spectrum power-law tail to lower frequency. These sources are likely to be undergoing powerful recent activity in their cores. At frequencies below the self-absorption turnover of the core component the spectrum becomes dominated by an underlying steep spectrum power-law component, that may be suggestive of either unresolved radio lobes or the presence of an amorphous halo of confused emission (Kempner et al., 2004). In other instances, as shown in E1821+644 and 4C+55.16 (panels b and c of Figure 4.1) the integrated spectrum shows only a flattening in the GHz range which may stay flat to high frequencies as in E1821+644 or tail off as in the case of 4C+55.16. We are likely seeing sources at different stages of their AGN life-cycles, with the power and timing of the latest outburst dictating the ratio of powerful high radio-frequency core emission to steeper low-frequency emission from more physically extended regions. The multiple components hint towards relatively short (less than 10Myr) time-frames between major periods of activity in BCGs. Yet other sources, such as MACS0242-21 (panel d, Figure 4.1) appear well fit by a GPS model with a turnover frequency below 1 GHz. These may be instances dominated by a single period of older activity where the ejected emission has propagated outwards and expanded, permitting the peak to move towards lower frequency. When the peak falls much below 1 GHz, such sources may be classified as compact steep spectrum (CSS, O'Dea, 1998).

Notes on the General BCG Population

Twenty-six of the thirty-five sources are found to contain a GPS-like peaked component. Physically, GPS sources are believed to be young radio sources whose spectra are peaked due to synchrotron self-absorption (O'Dea, 1998). That we find strongly peaked components within our BCG spectra is indicative of powerful emission on small-scales. This could be either due to restarted radio-sources in these objects or a recent period of heightened activity amongst a continuously active source. Either of these scenarios are consistent with the high duty cycle expected for these cool-core hosted AGN. We plot in Figure

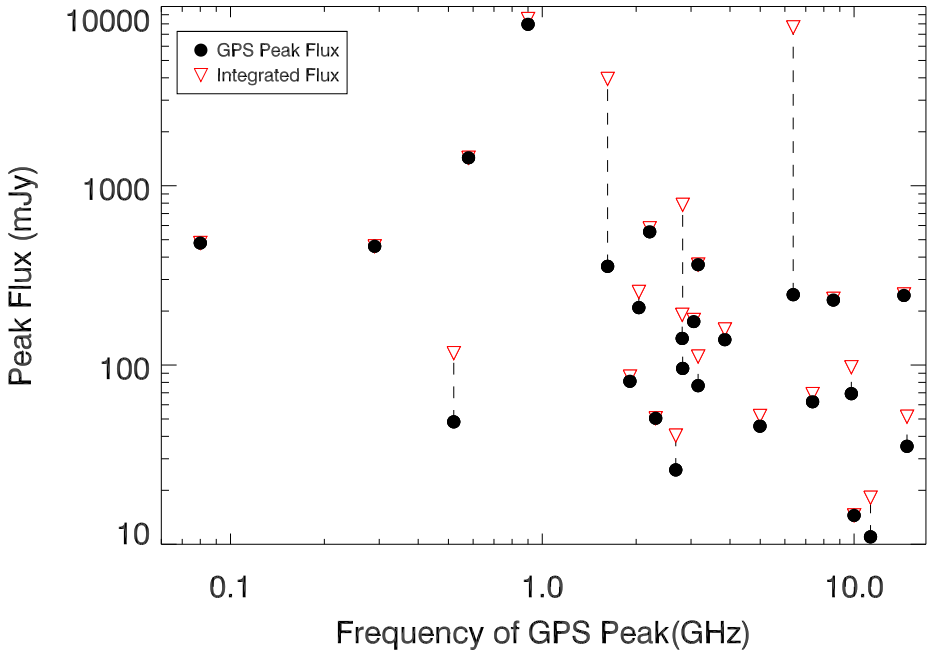

Figure 4.2: Flux of the GPS-like component as a function of the frequency at the peak. Note that in the classification scheme of O'Dea et al.(1998), the lowest peaking of these components, if an isolated source, would likely be identified as CSS rather than GPS. However, we note that in the evolution scenario for this family of sources, CSS sources are just slightly older GPS sources and hence we refer to all of these peaked components as 'GPS-like' for brevity. Each source is represented twice (connected by dashed lines). Circles show the peak flux of the GPS component whereas downfacing triangles show the combined flux of both the GPS and any power-law component measured at the GPS turnover frequency. In the majority of instances we see that at the turnover frequency the GPS component is dominating the flux. It should be noted that *virtually all* radio-loud BCGs *may* contain a peaked active component, although in most systems these would be expected to peak far below the integrated flux and hence be undetectable in all but the brightest systems.

4.2 both the peak flux of the fitted GPS-component and the combined power-law + GPS-component flux of each of our GPS-containing sources as a function of the GPS turnover frequency. These are mainly found to be GPS dominated, with only a minority of sources found where the combined flux is significantly greater than the GPS component alone.

We find that the spectral turnover of the GPS component in nineteen of these twenty-six sources lies above 2 GHz, of which only Hydra-A has a sub-dominant core that does not overtly affect the integrated spectral shape at frequencies greater than a few GHz. In the simplest case we can use this to put a limit on the number of BCGs containing powerful peaked cores that greatly affect the spectrum above the observing frequency of most wide-sky surveys (e.g. NVSS/FIRST at 1.4 GHz, WENSS/WISH at 325 MHz, VLSS at 74 MHz, see Appendix J, Condon et al., 1998; White et al., 1997; Rengelink et al., 1997; De Breuck et al., 2002; Cohen et al., 2007). Our sample was drawn from the 726-source Parent Sample described in Chapter 2. If we subtract from this the 196 sources that fall below Declination -30° and so were not considered by our initial GISMO selection criteria (see Section 4.3) then we find that $\geq$3.4% of BCGs contain a brighter than 10mJy synchrotron self-absorbed active core component peaking above 2 GHz. This fraction increases to $\geq$8.5% if we consider only the cool-core clusters. Our incomplete spectral coverage of the full sample means that this number is only a lower limit and that the true fraction of BCGs with GPS-cores may be much higher. Indeed this simple analysis neglects systems whose spectra appear to be persistently flat out to high radio frequencies where multiple superposed flux components may be present.

That strong spectral deviations at frequencies higher than a few GHz are not uncommon in BCGs has important implications, including but not limited to the activity of the population as a whole and also the expected contamination rate and extent of peaked AGN components in BCGs on SZ signals. We consider this further in Section 4.6.

4.5.2 Nature of Variability

Understanding the radio variability of AGN is important as it informs us on several physical processes. Short-term variation allows to place size constraints on the region from where any observed radio-flux propagates (i.e. a source cannot vary on less than the crossing-time) whereas longer term (few year) variation can inform us as to the likely

fueling mechanisms of AGN. At radio frequencies, the variation itself can be due to differing energy densities within the jet, which may be due to a change in the accretion structure and fueling rate at the jet-base. Alternatively, changes in flux may be due to individual components within a jet becoming brighter as they interact with other material. However, fully characterising the radio variability of AGN is inherently difficult as the measured variability can be attributed to different mechanisms and will be most prevalent on different timescales depending on the observing frequency.

As an example, consider a synchrotron self-absorbed source sampled at a frequency just below the turnover which shows a flux increase. Without contemporary observations at and above the peak it would be difficult to say whether the additional received flux is due to an increase in total power-input to the jet by the AGN (and hence the normalisation of the entire SED should increase) or whether overall the power-output is falling but that the lower intensity and expanded physical scales of the emitting regions lead to the turnover moving to lower frequency and so giving a flux increase below the peak while the overall normalisation remains constant. Ideally the entire SED would be sampled simultaneously and fitted, accounting for self-absorption at a variety of epochs in order to recover the true variability in the underlying power output. Unfortunately, such a campaign is prohibitively expensive. Nevertheless, limits can be placed on the variability of BCGs at different frequencies and timescales.

4.5.3 Monochromatic Variability

Variability Index

We use the debiased variability equation (e.g. Akritas & Bershady, 1996; Barvainis et al., 2005; Sadler et al., 2006) to attempt to place quantitative limits on the monochromatic flux variability of our sources. This index accounts for the uncertainties in flux measurements and hence should be robust against artificial positives. The Variability Index (V.I.) is defined as

$$V_{RMS} = \frac{100}{< S >} \sqrt{\frac{\sum (S_i - < S >)^2 - \sum \sigma_i^2}{N}} \tag{4.5.1}$$

where S_i is an individual flux measurement, σ_i the associated uncertainty, $< S >$ the mean flux and N the number of observations of a given source. For lightcurves with a

large number of points this statistic gives a measure of the typical variability of a source about its mean flux. This analysis begins to falter for lightcurves with a small number of points where the mean is not necessarily representative of all measured fluxes however it is useful even in the limit of N=2 as a positive returned V.I. is indicative of significant variation whereas an imaginary returned V.I. suggests any observed flux difference is most likely attributable to measurement uncertainty. A limitation of this method is that over-estimation of the error on flux measurements can mask real variability. However, this variability would be below any limits found for variation below the given errors. Given limits on variability would therefore be correct, albeit less restrictive than if less conservative flux uncertainties were used. Although it should be noted that such a limit does not of course restrict the potential for the source to vary below this level. Similarly, under-estimation of errors can falsely indicate variability where there is none.

Variability at 15 GHz: OVRO

For the eleven sources added to the OVRO monitoring campaign circa MJD 56320 (January 2013; see bottom panel, Table 4.1) we find that no sources have a positive Variability Index. This suggests that for all eleven sources the difference in measured flux is within the 1-σ uncertainties of the individual measurements such that this leads to an imaginary value for the square root. This is somewhat surprising, since for a non-varying population we might expect around half to have slightly positive V.I.s and half slightly negative V.I.s. The lack of any positive V.I.s may therefore indicate that our flux uncertainties are over-estimated. A positive V.I. requires that the numerator within the root of Equation 4.5.3 be positive, which at the most basic level just requires that the average fractional flux deviation from the mean flux be larger than the mean fractional error.

In Figure 4.3 we plot the typical percentage deviation from the mean flux for each source, as well as the mean fractional error on the flux (displayed as a percentage). Additional data are provided in Table 4.1. We see that in all instances of the eleven sources monitored since January 2013 the typical flux deviation is less than the typical error, hence showing why no real V.I.s were returned. For a non intrinsically-varying population of sources we might expect $\sim$68% of flux measurements to lie within one standard error of the mean. That our typical percentage uncertainties are around twice our typical

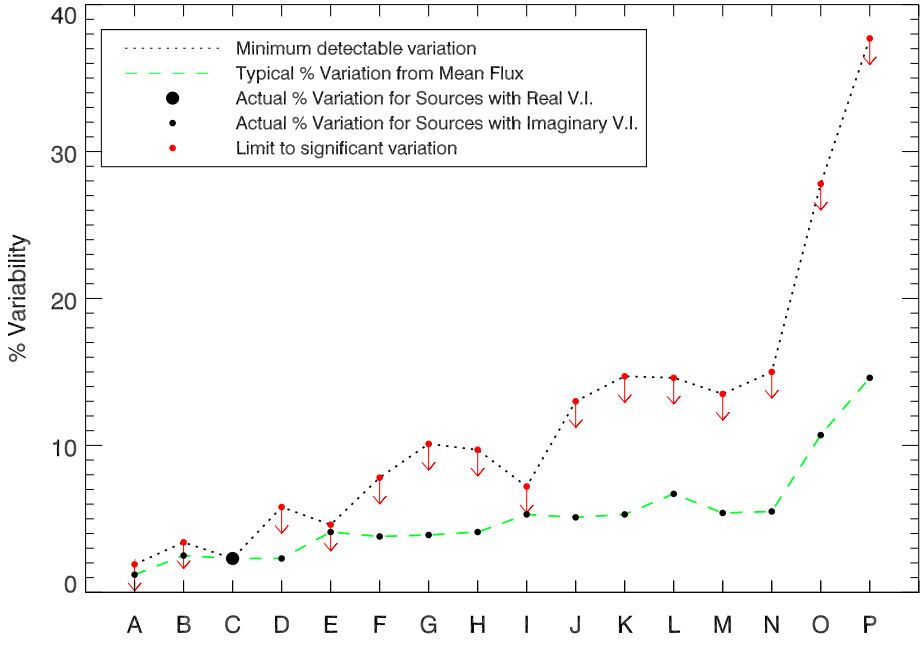

Figure 4.3: Dotted line shows the minimum percentage variabilities that would have corresponded to a positive Variability Index (typical deviation from mean flux greater than mean fractional error) for the OVRO sources, sampled at 15 GHz on typically one-week timescales. The green dashed line shows the actual typical deviation from the mean flux for each source respectively. Note that only A2270 shows significant variation (dashed line above dotted line). Sources are arranged left-to-right by their maximal measured flux at 15 GHz. The detectable percentage variation is typically much lower for brighter sources, with some deviation from a one-to-one correlation due to uncertainties on flux measurements varying by source. Sources are: A) 4C+55.16, B) RXJ0439*, C) A2270*, D) A2052, E) RXJ1558*, F) RXJ2341, G) RXJ0132, H) AS780*, I) RXJ1350*, J) A2055, K) A2415, L) Z8276, M) A2627, N) A2390, O) A646 and P) A1348. Note that five of these (indicated with *) were in the initial OVRO monitoring list and hence longer time-baseline data are available, where plotted values are those calculated when the time-frame was matched to the other eleven. See also Table 4.1.

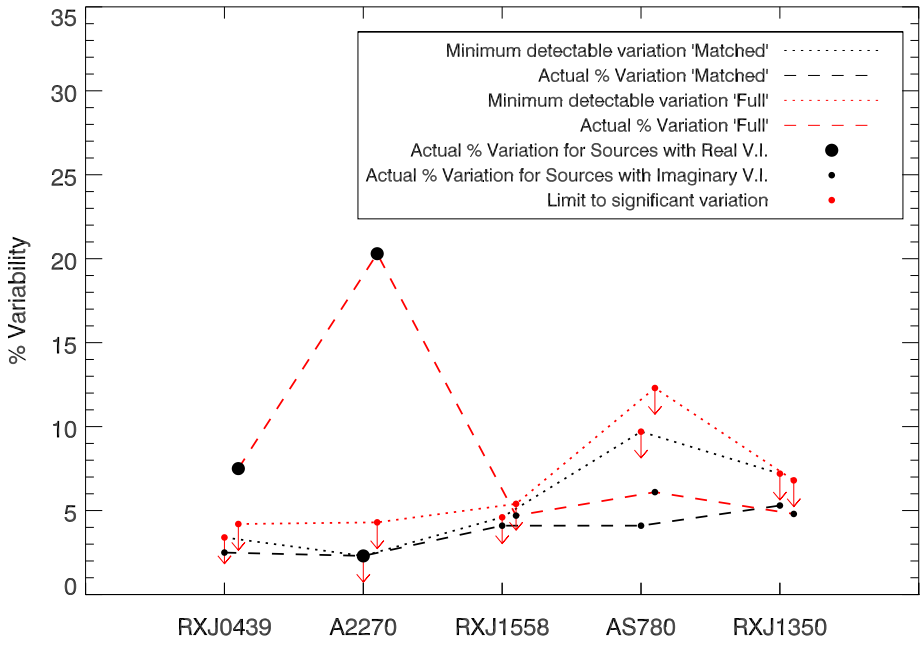

Figure 4.4: OVRO variabilities for only the five sources in the original lists, measured for the full (from January 2008 onwards, red lines and offset for clarity) and restricted (January 2013 onwards, black lines) time-frames. Dotted lines show the minimum percentage variabilities that would have corresponded to a positive Variability Index (typical deviation from mean flux greater than mean fractional error), whereas dashed lines show the actual typical deviation from the mean flux for each source respectively. Note that only A2270 shows low-level significant variation (dashed line above dotted line) when only data during the matched time period whereas when using the full data, both A2270 and RXJ0439 show significant variability, as would be expected by considering the lightcurves in Figure 4.5. Although not a perfect measure, this does show evidence that variability at 15 GHz is most prominent over longer time-frames, hence considering variation of BCGs on longer than single year timescales is important. As in Figure 4.3 we order the sources left to right by their maximal measured flux at 15 GHz. See also Table 4.1.

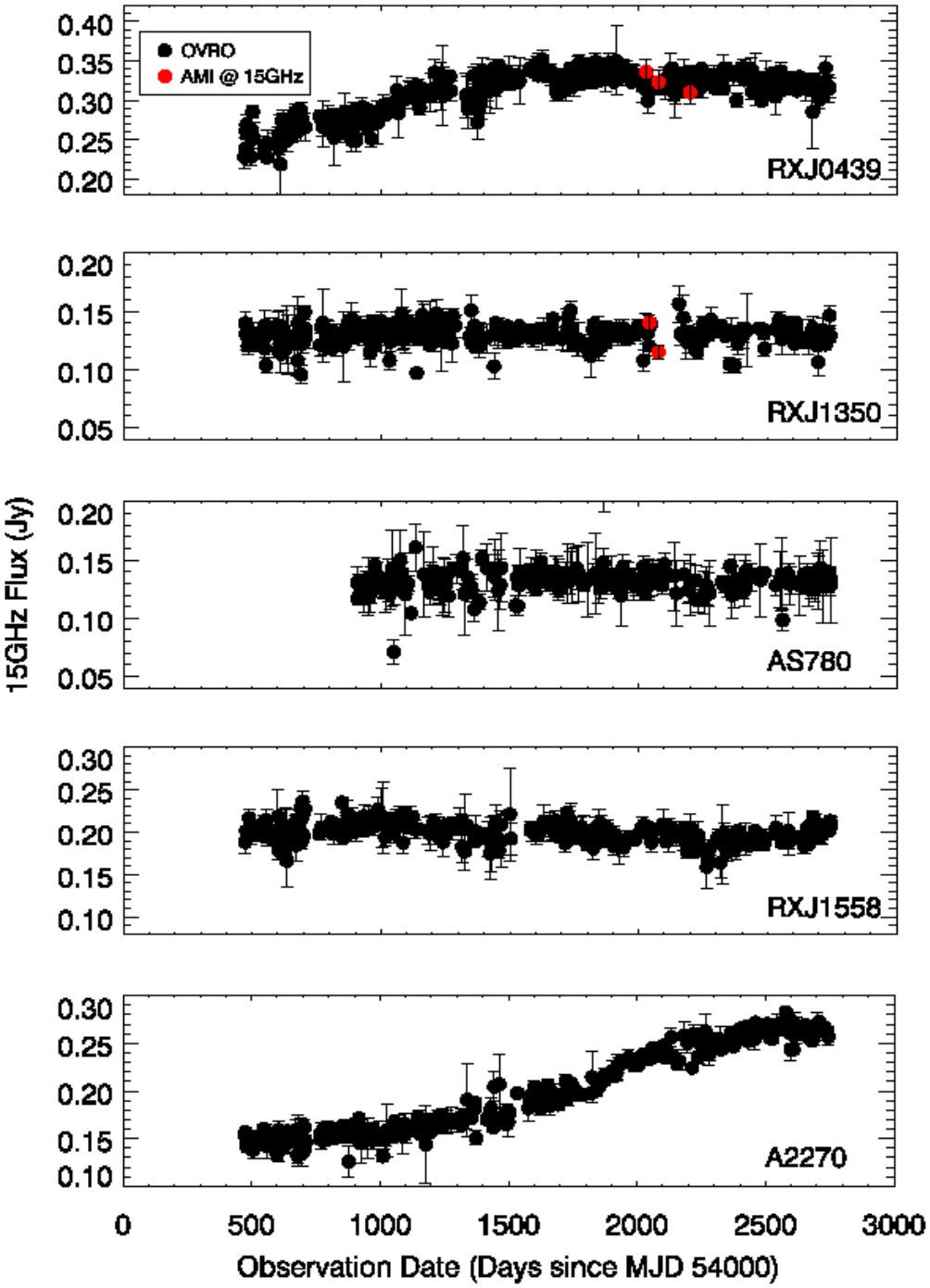

Figure 4.5: Longer term lightcurves for the five sources that were in the original list of OVRO targets. Where AMI observations were available, the flux is corrected to 15 GHz using an index fitted to the AMI data split over the six channels for that observation specifically. We see strong variation over typically year timescales in both RXJ0439 and A2270 at 15 GHz. Note that MJD 54000 corresponds to September 22nd 2006.

flux deviation from the mean suggests that our errors are over-estimated by a factor of 2-3. However, we cannot steadfastly claim that our sources are intrinsically non-varying and that they should therefore adhere to Gaussian statistics and hence we merely claim that they typically are restricted to varying by $\leq$10% on roughly one-week timescales, although note that this limit may in fact be a factor of 2-3 lower.

Two of the five sources that were in the OVRO monitoring campaign over the full period (top and middle panels, Table 4.1) return real Variability Indices when the V.I. is calculated over the full timerange (A2270 and RXJ0439) but only one (A2270) is recovered when the V.I. is calculated over a timerange restricted to match that of the other eleven sources (see Figure 4.4). In Figure 4.5 we show the 15 GHz lightcurves for these five sources. Clearly both A2270 and RXJ0439 display large flux increases over the full timescales considered although it is interesting to note that the variability of RXJ0439 as shown by the increase from MJD 54500 - 55500 would be missed if considering only the restricted timescale. It is interesting to note that when only the matched timeframe data is used, A2270 returns a barely significant variability but when the longer-term monitoring is included then a very high level of variability is seen. This suggests that at 15 GHz, variability of sources is most likely to be seen over greater than year time-frames.

The measureable percentage variation that would have returned a real V.I. (and therefore a significant measure of variability above the noise) varies from source to source, typically being lower for brighter objects. However, by inspection of Figure 4.3, we can claim that the 15 GHz variability of these BCGs is typically restricted to $\leq$10% on roughly one-week timescales (see Table 4.1). Additionally, we see evidence that much larger magnitude variation may be common in BCGs on few-year timescales. This mirrors the finding of Hovatta et al. (2007) who found variability on few-year timescales in a sample of blazars from a greater than 25 year monitoring campaign with the UMRAO and Metsähovi telescopes. The OVRO monitoring campaign is ongoing hence the statistics on this longer-term variability will naturally improve with time.

Variability at 150 GHz: GISMO

Of the thirty-five individual sources observed with GISMO, twenty-three had at least one repeat observation hence allowing variability to be measured. Of these, and considering

Table 4.1: Variability Indices for the OVRO data. The mean and median timescales between observations are given in days, with N being the total number of times OVRO observed each source during the considered monitoring period (MJD 54470 to MJD 56750, 5^{th} Jan 2008 – 3^{rd} Apr 2014). Note that a real V.I. is recovered for RXJ0439 when the full monitoring period is considered but not when only using the restricted timescale (see also Figure 4.5. A much better understanding of the longer-term variability of BCGs is expected to become apparent with continued monitoring.

Source	V.I.	Typical % variation from mean flux	Mean fractional error (as %)	Mean Timescale	Median Timescale	Mean Flux (mJy)	N
		Extended Time Baseline (from MJD 54470)					
RXJ1558	NaN	4.7	5.4	7.5	4.0	195.8	303
RXJ0439	8.0	7.5	4.2	5.8	4.0	131.9	393
AS780	NaN	6.1	12.3	9.0	6.0	130.0	205
A2270	22.0	20.3	4.3	7.0	4.0	308.4	326
RXJ1350	NaN	4.8	6.8	7.1	4.0	201.2	321
		Matched Time Baseline (from MJD 56320)					
RXJ1558	NaN	4.1	4.6	8.3	5.0	261.1	52
RXJ0439	NaN	2.5	3.4	6.3	5.0	131.5	67
AS780	NaN	4.1	9.7	9.6	5.9	128.9	45
A2270	1.7	2.3	2.3	7.1	5.0	321.9	60
RXJ1350	NaN	5.3	7.2	8.4	5.0	195.5	50
		Added to Monitoring List MJD 56320					
4C+55.16	NaN	1.2	1.9	6.8	5.0	1539.2	63
A1348	NaN	14.6	37.7	11.4	7.0	55.2	37
A2052	NaN	2.3	5.8	6.1	4.2	272.5	71
A2055	NaN	5.1	13.0	6.2	4.9	120.1	70
A2390	NaN	5.5	15.0	5.6	4.8	88.5	76
A2415	NaN	5.3	14.7	7.3	5.0	123.1	59
A2627	NaN	5.4	13.5	5.5	4.2	99.4	77
A646	NaN	10.7	27.8	9.1	5.0	58.2	47
RXJ0132	NaN	3.9	10.1	7.2	5.0	155.5	60
RXJ2341	NaN	3.8	7.8	6.6	4.1	156.9	65
Z8276	NaN	6.7	14.6	6.8	4.3	95.3	62

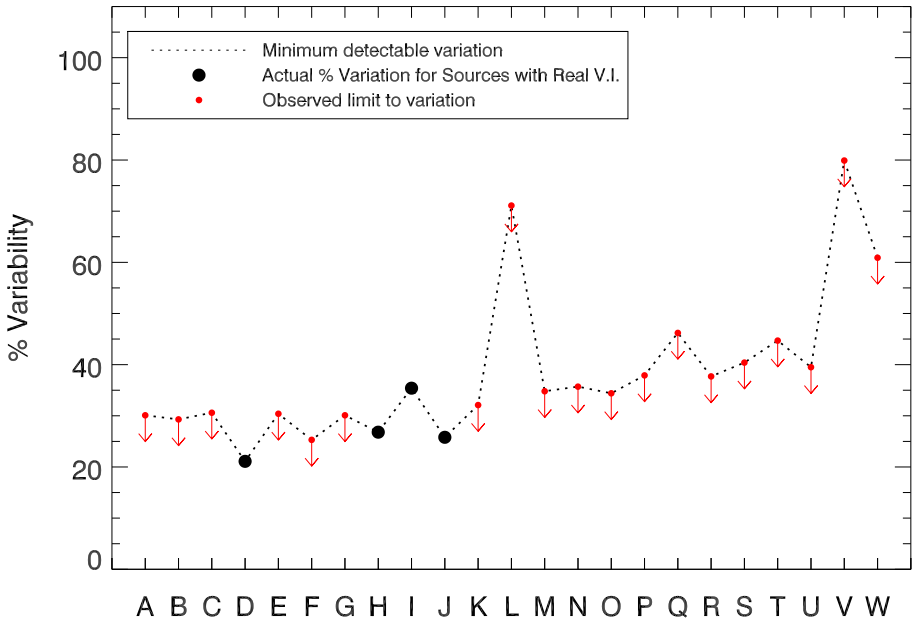

Figure 4.6: Detectable variabilities that would have corresponded to a positive Variability Index for the GISMO sources, sampled at 150 GHz on approximately 6 month timescales. Sources are arranged left-to-right by their maximal measured flux at 150 GHz. The detectable percentage variation is typically much lower for brighter sources, with some deviation from a one-to-one correlation due to uncertainties on flux measurements varying by source. Sources are: A) Hydra-A, B) 4C+55.16, C) A3581, D) A2270, E) RXJ0439, F) RXJ2341, G) A2052, H) RXJ1558, I) MACS0242, J) Z8276, K) A2415, L) RXJ0132, M) AS780, N) A2627, O) RXJ1350, P) A2055, Q) Z8193, R) A646, S) RXJ1832, T) A2390, U) A496, V) E1821, W) PKS0745.

only detections, seven sources were observed at all three epochs with the remaining sixteen observed twice. Only four sources returned real V.I. values, namely Z8276 (V.I.=43.5 : 2 observations), A2270 (8.2 : 3), MACS0242 (23.2 : 2) and RXJ1558 (10.2 : 3).

However it should be noted that working out the V.I. for our GISMO observed sources is less informative than for those observed with OVRO since the V.I. works primarily by determining the difference from the mean flux. Clearly, when only two (or three) observations of a source are available then such an average is less meaningful due to the large uncertainties on the flux. Nonetheless, a real V.I. still indicates which sources are really variable at the investigated cadence. Therefore instead of calculating the minimum detectable typical percentage variation about the mean (as was done for the OVRO data, see Figure 4.3), for GISMO we instead calculate:

i) For sources with two observations - the *actual* minimum required percentage change between the first and second fluxes to return a real V.I. (assuming the reported uncertainties)

ii) For sources with three observations - the *total* minimum required percentage change across three epochs, from the first measured flux assuming a simple model where the observations are symmetrically distributed around the flux of the central observation (i.e. $S_1 - S_2 = S_2 - S_3$). This is a simplistic approach and would require a source that does not vary between epochs 1 and 2 to vary by twice the expected mean between epochs 2 and 3 to be detected, however it does allow an *estimate* of the minimum average variation per six-month window that would be detectable.

The results of this are plotted in Figure 4.6, where we see that we are sensitive only to variation of above typically 30%. The *actual* percentage variations of the four sources with real V.I. values are also shown.

In Figure 4.7 we plot the fractional flux changes between each pair of GISMO observations for a source. As in Figure 4.6 we see that the majority of observed variability is within the error envelope. The large variations of some sources as seen in Figure 4.6 are again apparent. One point that becomes obvious in this particular representation is that the majority of our observed variation is of sources fading over the 1-2 years covered. This may hint towards systematic flux offsets between GISMO runs, however these are carefully checked for[3] and should not dominate. A natural alternative explanation arises simply because we selected the sources to be (likely) the brightest amongst our parent sample at 150 GHz as a result of their lower frequency spectral shapes. Most physically motivated models for variability have the higher frequency emission preceding lower frequency flux rises. This is due to a jet (or ejecta) on small-scales being self-absorbed when first launched. As this emission propagates to larger scales then the self-absorption turnover will move to progressively lower frequencies such that the lower frequency flux rises lag behind those at higher frequencies. It therefore stands to reason that a source which is brightest in the few GHz range is likely to be at a later stage in its outburst and therefore more likely to be faintening at higher frequencies.

[3]Performance reports available for each run at http://www.iram.es/IRAMES/mainWiki/Continuum/GISMO/Main

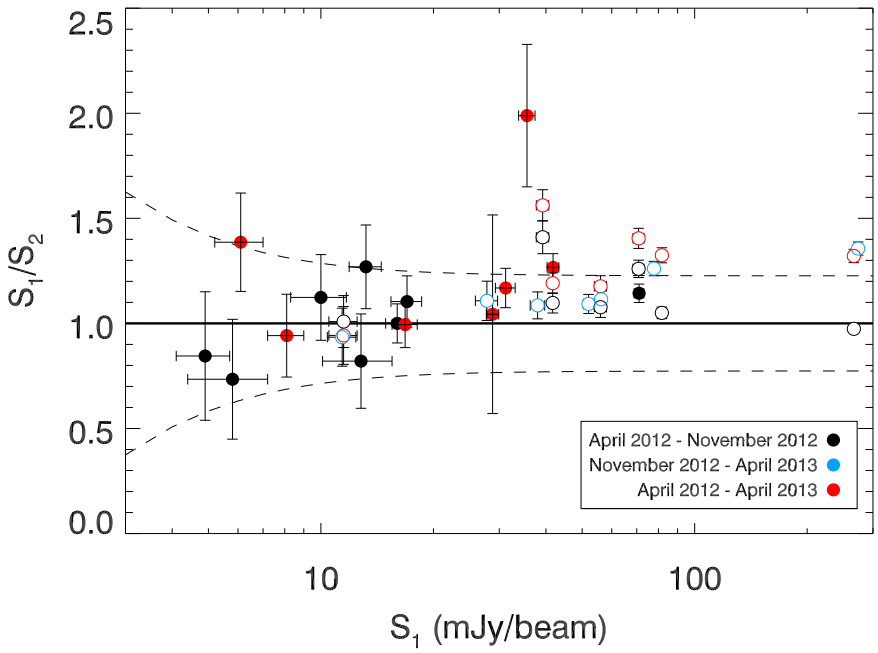

Figure 4.7: Ratio of the measured GISMO fluxes at 150 GHz between each of the two epochs. The dashed lines indicate the error envelope due to the 16% typical flux uncertainty. Open symbols are for sources that appear more than once due to being observed during all three epochs; consult also Table I.1. Sources typically appear to be fading, as expected for a sample chosen as the brightest at the selection epoch. The source that appears to show very strong variation is Z8276, which is seen to fade drastically at 150 GHz between April 2012 and April 2013.

The April 2013 observation of M0242-21 was observed with a high optical extinction (tau = 0.70), which may contribute to the GISMO flux drop of about 50%. However, we note that this source is a Submillimeter Array (SMA) calibrator and shows a similar percentage flux decrease over this period (at 1.3mm[4]) suggesting that the variability is real.

Given the high error envelopes, that we detect variability amongst our sample of repeat observations at 150 GHz suggests that significant variation of such sources at high radio frequencies may be relatively commonplace over 6-month to year timescales. Such variability has important implications particularly for Sunyaev-Zel'dovich observations (see Section 4.6).

4.5.4 Measuring Percentage Variation

In addition to a V.I., we also determined a measure of the typical annual absolute percentage variability of our sources at 15 GHz. Measuring the maximal percentage variation of a source over any given time period is highly susceptible to measurement uncertainty since one bad outlying flux can greatly skew the result if not correctly identified as erroneous. Instead we effectively determine a robust measure of the maximal gradient of the lightcurve during the monitored period.

For the sources with OVRO monitoring at 15 GHz we calculate the percentage variation between the maximum and minimum measured fluxes over this period. This is found to be highly skewed by erroneous outliers hence instead we take a mean of the six percentage differences measured between the 95&5th, 94&6th, 93&7th, 92&8th, 91&9th and 90&10th percentiles (n.b. for sources only in the monitoring list since Jan 2013 with less than 100 observations, we used the 95&5th percentile range and the 5 unique ranges below this to a minimum of 85&15th percentiles beyond which we automatically classified any resulting measured variability as an upper-limit). This range is more robust against measurement uncertainty yet still gives a good measure of the maximal variation over a given period.

A mean over six ranges was chosen, by trial and error, to be a reasonable compromise

[4] http://sma1.sma.hawaii.edu/callist/callist.html

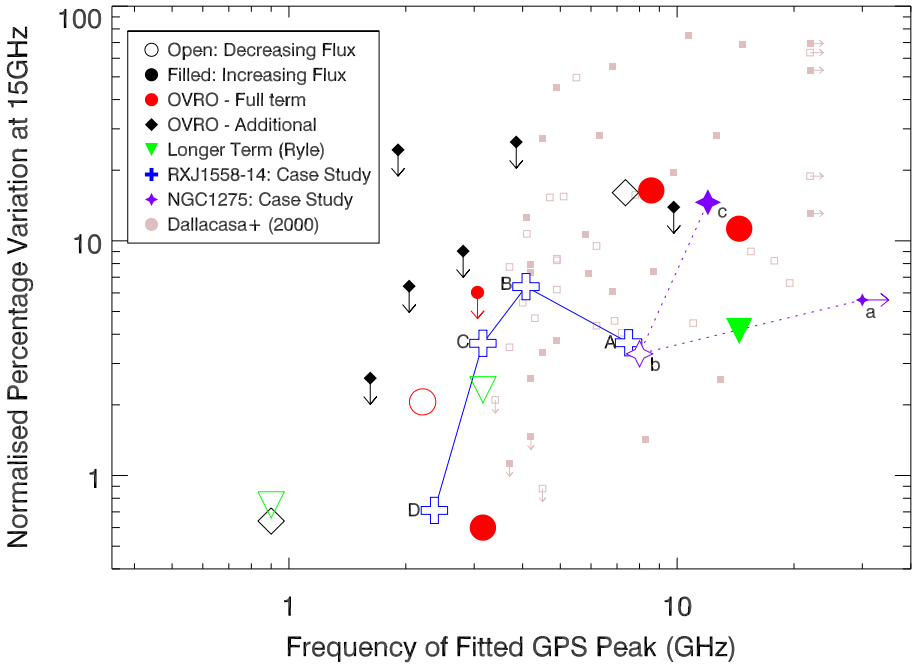

Figure 4.8: Percentage variation at 15 GHz as a function of the position of the fitted GPS peak. OVRO sources correspond to those calculated in Section 4.5.4. Three sources have historical observations from the 1970/80s at 15 GHz with the Ryle telescope (see text Section 4.5.4) and we include the percentage variations over these longer time-frames, calculated in a similar way for comparison. Open symbols denote flux decreases over the monitored period whereas filled symbols denote flux increases. We see a general tendency for higher peaking sources to be more variable although this is not a strong trend and the ratio is highly dynamic, as highlighted by the case studies of RXJ1558-14 (shown as large crosses) and NGC1275 (shown as large stars) also see Section 4.6). For comparison we plot as faded points the normalised percentage variations in the OVRO monitoring for the HFP sample of Dallacasa et al.(2000). These inhabit a similar distribution to the peaked components within our BCGs showing that these are not dissimilar to young radio sources elsewhere.

between too few measurements being susceptible to random fluctuations but too many moving to percentiles over which less variation was measured, as well as being even and so more easily allowing non-varying sources to have variations averaging to effectively zero (note that in practice the probabability of it *actually* averaging to precisely zero is minimal, however the probability of it approaching zero is increased with an even number).

To determine whether these measured percentage variations most reliably constitute genuine variability or an upper-limit on variability, we took a measure of the two-point Variability Index (Equation 4.5.3 with N=2) for each of these six percentile ranges. We required that a minimum of four of these return real V.I. values for the percentage variation to be classified as a value, otherwise it was taken as an upper-limit. We normalise our mean measured percentage variation values by the mean difference in years between the measurements used, thus recovering a measure of typical annual variation. Where only a limit on variation is recovered, we normalise by the total monitored period in years (roughly 1 year for 11 sources added to OVRO list).

Three sources (4C+55.16, RXJ0439+05 and Z8193) have historical 15 GHz data preceding OVRO monitoring from either the UMRAO campaign or pointed observations with the Ryle Telescope. We combine these with the OVRO data and find the percentage variations over longer timescales.

In Figure 4.8 we show our calculated absolute percentage variations at 15 GHz as a function of the peak position of the fitted GPS. A mixture of sources increasing and decreasing in brightness is seen. A weak general trend for the highest peaking sources to show most variability is seen. Such a trend is expected, as a higher turnover frequency suggests self-absorption closer to the jet-base and hence emission from smaller scales, which can more easily translate to faster emitted variability. However, it must be noted that the GPS-peak frequency is expected to move and also the variability is non-constant, hence both parameters are expected to undergo linked evolution. We illustrate this dynamic relationship by including on Figure 4.8 evolutionary tracks for two sources with long-term monitoring; RXJ1558-14 and NGC1275. Both are seen to move extensively across Figure 4.8 but always remain within the region occupied by the other points. We consider these sources as case studies in sections 4.6.2 and 4.6.3.

For comparision with the more general galaxy population we additionally include on Figure 4.8 the normalised percentage variations at 15 GHz for the fifty sources (of fifty six) in the High Frequency Peaker (HFP) sample of Dallacasa et al. (2000) that are in the OVRO monitoring list. These show a similar weak trend to the peaked components of our BCG spectra, suggesting that our peaked components can be explained as being recently (re-)activated emission on small scales. Such emission may either be attributable to an effectively 'new' source that has not been previously radio-emitting or, perhaps more likely in BCGs, a large recent enhancement in the radio-output of the AGN.

A GPS link to variability?

The behaviour of NGC1275 and RXJ1558-14 suggest that a direct link between GPS-peak frequency and variability is not present. Instead a dynamic ratio is seen between these parameters whereby the position (and indeed presence) of a self-absorption peak in relation to the observed frequency of a source can have a large effect on the amount of variability seen.

The position of the peak appears to weakly correspond to how quickly a source can vary at a given frequency although not necessarily how quickly it does vary over any given epoch. Indeed, whilst the presence of a flat or peaked component in a BCG's SED can be indicative of it being more likely to vary at high radio frequencies there does not appear to be a single observable proxy for the level of variation and hence the only way to robustly remove high frequency contaminants remains contemporaneous observation.

It should be noted that GPS sources actually constitute a range of types and that many sources classified in the literature as GPS and HFPs are actually flaring flat spectrum quasars or blazars (see Discussion by Torniainen et al., 2007). The variability of these sources is naturally expected to be different to genuine, long-term GPS objects. Amongst genuine GPS sources the peaked spectral shape is maintained over decade timescales and long-term variation of the absolute flux level of this is seen (Aller et al., 2002). This longer term variation (years to decades) is similar to what we see in the peaked components of NGC1275 and RXJ1558-14 and hence further supports that the variability herein is likely due to similar physical processes to that in more typical GPS objects, which may be related to opacities within the jet flow.

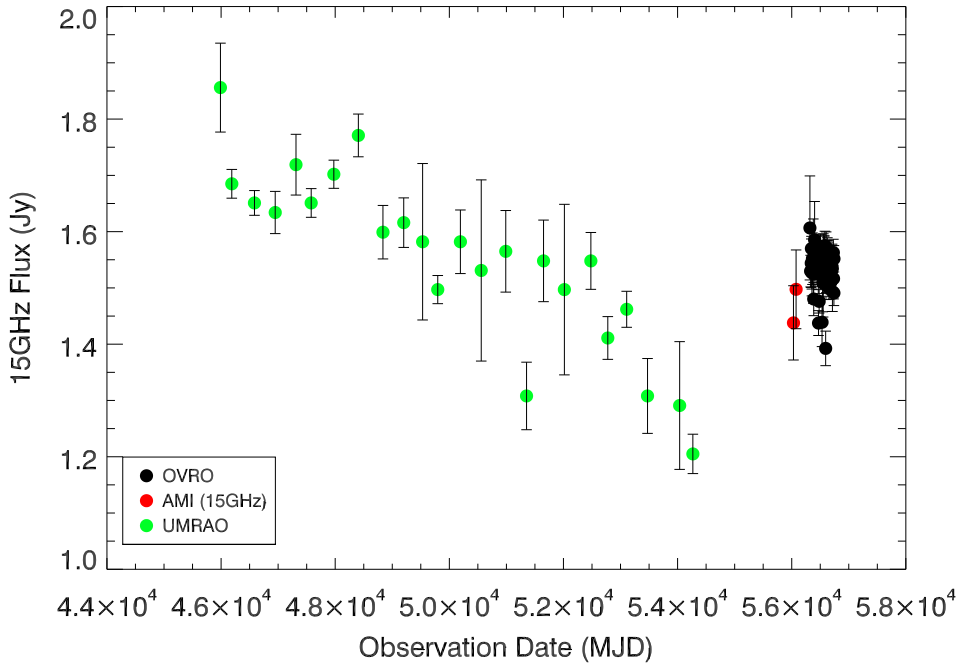

Figure 4.9: Lightcurve for 4C+55.16. UMRAO points are the yearly average. Note that AMI observations have a central useable frequency of 16.05 GHz, which was corrected to the value shown here using the in-band spectral index.

4.6 Discussion

4.6.1 Case Study: 4C+55.16

As mentioned in Section 4.4.4 one of our sources, 4C+55.16, has near-continuous 15 GHz lightcurves available for almost two decades, allowing us to consider its longer term activity. In Figure 4.9 we show the combined lightcurve consisting of UMRAO, AMI and OVRO observations. Note that our AMI observations have a central frequency of 16 GHz. We fit a single spectral index to the SED of 4C+55.16 above 10 GHz, recovering an index of 1.29[5] and use this to correct our AMI fluxes to 15 GHz.

A steady decline in total flux density is seen towards the end of the UMRAO lightcurve for this source (2007, MJD $\approx$ 54000). Our AMI fluxes are consistent with those recovered with OVRO, within the errors. However, if we remove the absolute flux calibration of the AMI observations then they are perhaps self-consistent with having caught the source as

[5] $S = A\nu^{-\alpha}$

it brightens, before it is then reasonably steady throughout the OVRO monitoring. Variability of this at 15 GHz is slow, varying by approximately 20% on decade timescales. This compares to significantly less variability on typically one-week timescales. However, from the GISMO observations of this source we do get faster variation at higher frequencies showing that although the overall SED may only vary slowly over several years, short-term 'flickering' of the flux at frequencies above 100 GHz is still evident over much shorter periods.

4.6.2 Case Study: RXJ1558-14

RXJ1558-14 shows remarkably similar behaviour to NGC1275, albeit displaying around an order of magnitude less flux. NGC1275 is a well-studied source which constitutes the prototypical example of a variable BCG with a GPS-like component showing steady mm-variability over few year timescales (see Dutson et al., 2014, for a thorough discussion of the variability properties of NGC1275).

RXJ1558-14 has been monitored by OVRO since 2008 and shows little variation at 15 GHz over this time-frame. However, the source has historically been used as both a VLA and VLBA phase calibrator and has a wealth of observations available in the NRAO archive meaning we can study its behaviour over long timelines.

In the top panel of Figure 4.10 we show long-term lightcurves at both X-band (8.4 GHz) and C-band (4.8 GHz) for RXJ1558-14. Data were compiled from the literature and by downloading FITS images for all available observations in the NRAO-archive and extracting flux measurements using IMFIT. We split the lightcurves into four time-windows, indicated on Figure 4.10 as 'A', 'B', 'C' and 'D'. In panel A (see Wright & Otrupcek, 1990) we see that the 5-to-8 GHz spectrum was inverted[6], although this is not the case at later times.

In the middle panel we plot the SED for RXJ1558-14 with data-points coded to correspond to these four time-windows. In the bottom panel we focus only on the GPS-like part of the spectrum, again coding the data-points although here we additionally show illustrative GPS-models to the data in each of the time windows. As we move through

[6]We use 'inverted' within this paper to refer to radio spectra with increasing flux to higher frequency, which is the opposite to the usual scenario for a typical, unobscured synchrotron spectrum.

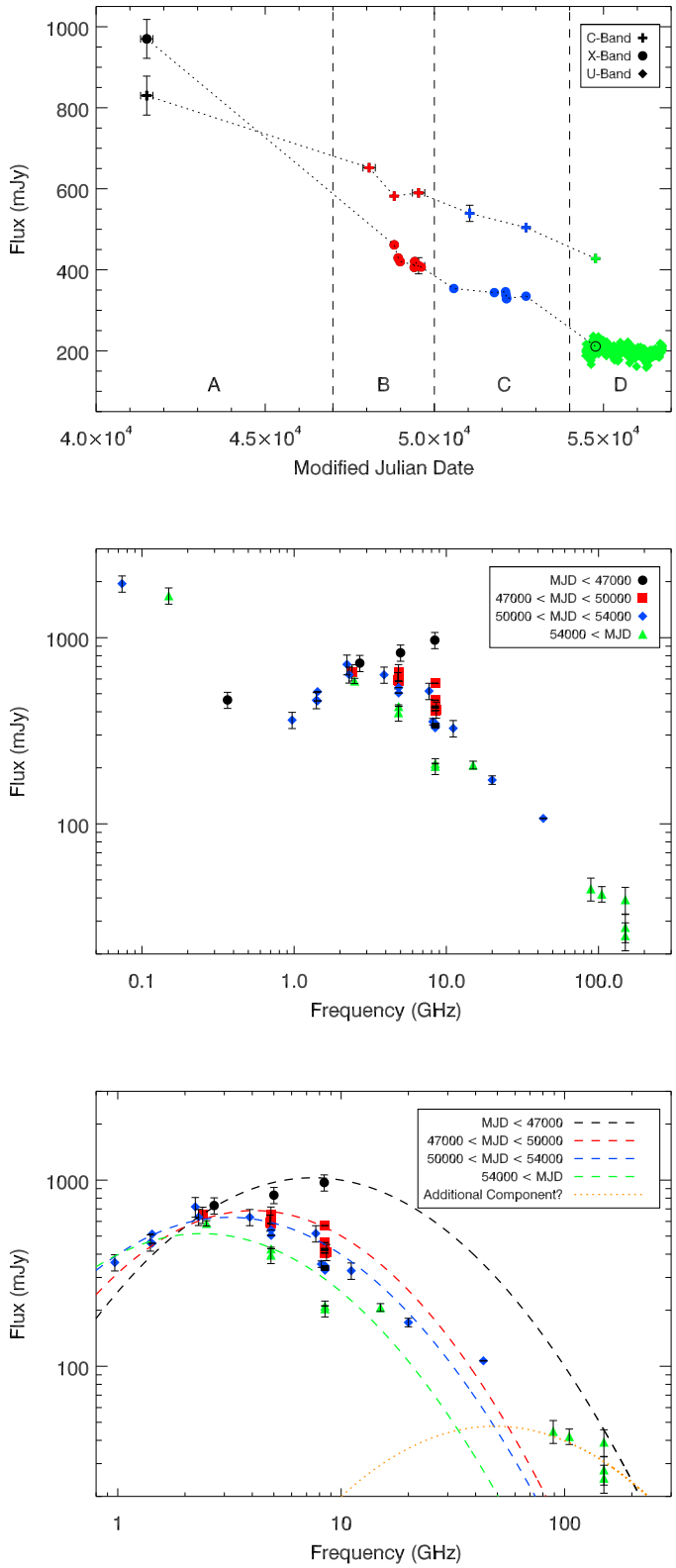

Figure 4.10: Top panel: C- and X-Band light-curves for RXJ1558-14, showing steady decline since 1972. Middle panel: SED where points coloured corresponding to the time-windows indicated in top-panel. Bottom panel: Illustrative fits to the GPS component of the SED for each of the time windows. As time goes on the GPS-peak appears to move downwards in both flux and lower frequency. Note that the highest frequency points in time-window D (and to a lesser degree window C) appear discrepantly high - this is discussed in the text. Note that MJD 40000 corresponds to 24^{th} May 1968.

time windows A to D we see the GPS-peak appear to move both downwards in flux and also in turnover frequency.

RXJ1558-14 displays double-lobed structure on parsec scales with an unresolved central core, as seen at 2.224 and 8.154 GHz in 1997 by Fey & Charlot (2000) and more recently at 4.86 GHz in 2012 (see Chapter 5). Although these observations are at different frequencies and thus cannot be used to get any secure measure on the expansion, it is worth noting that no new features are seen to arise between these observations. The lobes seen in the 4.86 GHz map presented in Chapter 5 lie approximately equidistantly 7 milli-arcseconds either side of the central component. If we associate the high core fluxes observed in 1972 with the launching of these knots then in the intervening 40 years the knots travel with an apparent transverse velocity of approximately 1.02 c, permitting viewing angles between 45° and 90° that are entirely consistent with the symmetry seen in the source. It is therefore consistent, and indeed highly likely, that the very high core fluxes observed in the 1970s were attributable to the emission of the features which are now observed as expanding lobes on milli-arcsecond scales and the subsequent fall in flux is attributable to these lobes propagating away from the core. Such a scenario would suggest that variability of RXJ1558-14 (and indeed other sources) above a few GHz may be associated with the launching of individual jet components and may precede the time at which these are observable given current angular resolutions. VLBI monitoring of self-absorbed sources that are varying above a few GHz may therefore allow such flux changes to be directly linked to individual parsec-scale jet components, as has so far only been observed for a few bright sources (e.g. NGC1275: Suzuki et al., 2012).

The highest frequency data in window D (and a lesser degree, window C) appear discrepantly high and may be indicative of a new period of activity that will become apparent at lower frequencies only as the emitting knots move down-jet and the self-absorption turnover peaks to lower frequency. VLBI monitoring of the source may therefore detect new knots forming and propagating outwards in the coming decade.

In further analogy to NGC1275 we note that RXJ1558-14 has a steep spectrum power-law tail to low frequency. In NGC1275 this tail is associated with a 300kpc radio mini-halo. A similar structure may be present around RXJ1558-14, however we note that in the TIFR GMRT Sky Survey (TGSS) imaging of this source there appears to be reasonably

symmetric structure extending almost 200 kpc from the core (PA $\approx$ 91.8) and hence the steep spectrum emission may be indicative of large scale lobes. Such lobes may be the result of either a previous large outburst, or evidence that the source has been continuously active for a long period albeit with varying levels of activity during this time. Interestingly, X-ray cavities are detected by Chandra in this source (Hlavacek-Larrondo et al., 2013; Russell et al., 2013) with total physical extent of 17.1$\pm$2.3kpc.

Due to its relatively good long-term SED monitoring we consider RXJ1558-14 as a case study in Figure 4.8. We calculate the GPS-peak frequency and measured variability in RXJ1558-14 for each of the four epochs highlighted in Figure 4.10. We can directly measure the 15 GHz percentage variability in epoch D only, during which OVRO monitoring data are available. For each of the other three epochs, we measure the C band (4.86 GHz) and X band (8.44 GHz) values at the epoch boundaries, using these to extrapolate an estimate of the 15 GHz flux. We plot the position of RXJ1558-14 on Figure 4.8 during each of these four epochs. Initially, in epoch A we find typically 4% variation annually at 15 GHz. During this epoch the peak is just below 15 GHz and hence the spectrum is still relatively self-absorbed at this frequency. In epoch B we are further in time from the event that caused the peaked component of RXJ1558-14's spectrum. The peak has moved to lower frequency meaning that a steeper part of the spectrum crosses 15 GHz and hence contrary to the general trend we see higher variability during this epoch. In epochs C and D the variability continues to lessen as the turnover frequency drops. It may be possible that a second, sub-dominant component peaked at much higher frequency (see Figure 4.10, bottom panel) is also present in the spectrum. If this component varied differently to a lower peaked component then it could show increasing flux as the other was decreasing at 15 GHz and hence could lessen observed monochromatic variability.

4.6.3 Case Study: NGC1275

As presented and discussed in Dutson et al. (2014), NGC1275 has been regularly monitored for over four decades and shows long term variability both in terms of its GPS-peak frequency and spectral normalisation.

In order to place NGC1275 on our Figure 4.8 we take estimates of the GPS-peak fre-

quency and 15 GHz variability in three epochs: 1979-83 (epoch a, Figure 4.8), 1983-2005 (epoch b) and 2005-2013 (epoch c) (see also Figure 5, Abdo et al., 2009). Initially, during epoch a, the peak is well above the 15 GHz monitoring frequency and we see a sharp increase of around 5.5% annually. During epoch b, the self-absorption peak 'rolls up' the spectrum to lower frequency and is accompanied by a relatively steady decline of about 3% annually over an extended period that may be coinciding with expanding features on parsec scales. Finally in epoch c there is another period of sharply increasing flux (almost 12% per year) which coincides with the peak moving to higher frequencies. Overall the trend is for long-term climbs followed by troughs, with the variability at 15 GHz dependent on both the position of the peak relative to this as well as the underlying variability in the total normalisation of the spectrum.

4.6.4 Comparisons to the general GPS population

An important consideration to make is whether the variability and wide variety of spectral shapes that we are seeing in BCGs is exclusive only to this special class of objects or whether they are applicable to the wider population of radio sources.

There are many examples of high peaking sources in the literature (e.g. Rodríguez et al., 2014) but large samples are required to fully determine how common these are amongst the overall radio-source population. Classifying peaked radio sources is difficult. Often only non-contemporaneous observations are available meaning that variability of inherently flat spectrum sources can lead them to be mis-classified (e.g. see Tornikoski et al., 2009, and references therein). Alternatively, even when a spectrum is sampled at multiple frequencies and a peak observed, without follow-up over several years it is very difficult to determine whether this is a true, slowly varying GPS source or a usually flat-spectrum source undergoing a rapid flare. Further complicating the issue, it appears as if the contamination of GPS catalogues by variable sources and BL-Lacs is dependent upon the GPS host galaxy, with quasar-type GPS sources much more commonly mis-identified than those in more typical galaxies (Torniainen et al., 2005, 2007).

In the AT20G survey of the southern sky at 20 GHz (Murphy et al., 2010), there are 3763 sources (detection limit of 40mJy at 20 GHz) that have simultaneous observations at 5, 8 and 20 GHz. Of these, 21% are found to have peaked spectra, 14% show a spectral

upturn over this range and 8% are inverted, suggesting a peak above 20 GHz. This fraction of inverted and peaked sources is significantly higher than the $\geq$3.4% of our parent sample peaking above 2 GHz. There is however a clear selection bias towards a higher fraction of inverted and peaked sources in the 20 GHz selected sample than in our sample of BCGs detected at high radio frequencies but selected from a parent sample unbiased by radio priors. Indeed, in the 5 deg^2 sampled down to 2.5mJy for the AT20-deep pilot survey (Franzen et al., 2014) 83 sources are detected and have near-simultaneous spectra from 1.4-20 GHz. Of these only 2.4% show a spectral upturn, 15.7% are peaked and 6.0% are peaked above 20 GHz. These reduced fractions of 'exotic' spectral types in comparison to the full AT20G suggest that the area-limited nature of the survey coupled with the deeper detection limit means that more of the 'typical' single-spectrum sources that constitute the bulk of extragalactic radio sources are detected. Franzen et al. (2014) find that about 12% of their sources vary by more than 15% over 3 years at 20 GHz, which is comparable to the levels of variability we detect for our sources at 15 GHz (see Figure 4.8).

Dallacasa et al. (2000) matched 1740 sources with $S_{4.9\ GHz} > 300$mJy in the GB6 catalogue (Condon et al., 1994) to the NVSS catalogue (Condon et al., 1998), finding 102 candidate inverted spectra. Simultaneous follow-up of these candidates at 1.35 - 22.5 GHz with the VLA revealed 55 to be genuinely inverted sources whereas the remaining 47 were flat spectrum sources whose variability meant that non-contemporaneous observations had caused their spectra to appear peaked. These 55 sources (their HFP 'bright sample') thus mean that 3.2% of their initial matched sample have spectral peaks $\geq$3.4 GHz. Taking the same frequency cut we find more than 1.9% of our parent sample peak at similarly high frequencies. Whilst still lower than the detected fraction of Dallacasa et al. (2000), if we consider that our sample contains BCGs detected irrespective of their radio-loudness and hence contains a portion of radio-quiet objects then our detection samples appear to be in reasonable agreement. We note that in a follow-up paper, Stanghellini et al. (2009) define an HFP 'faint sample' of sources with $S_{4.9\ GHz}$ between 50 and 300 mJy in the GB6 sample. Sixty-one HFPs with peaks at frequencies above 1.3 GHz are identified in this sample however they do not state the size of the parent sample, meaning a comparison to their detection fraction cannot be made.

Overall it appears as if the peaked components of our BCG spectra are reasonably sim-

ilar in their properties to the general GPS/HFP populations. However, a worthwhile point to note is that of the 26 sources in which we fit a GPS-like component, 20 of these (representing 76.9%) also contain a steep spectrum power-law to low frequencies. If the usual interpretation of peaked sources being young radio sources (O'Dea, 1998) is assumed then this suggests that BCGs are typically either continuously active but go through repeated periods of higher activity that may be associated with the launching of jet knots, or they are regularly restarted sources. Hancock et al. (2010) followed up 21 sources found to be inverted in the AT20G between 8 and 20 GHz with the Australia Telescope Compact Array (ATCA) at 40 and 95 GHz. Of these 21 targets, 12 were found to be genuine peaked sources, of which 3 (25%) showed evidence of being restarted rather than truly young radio-sources. Although caution must be employed for the small numbers that we are considering, this tentatively supports the idea that peaked components in BCGs are much more commonly attributable to continuously restarted activity than in the GPS population as a whole.

We point out that continuous radio core activity over a long time is known in galaxies not selected as BCGs; for example, FRII radio sources, which have measured ages of up to 10^8 years (see e.g. Machalski et al., 2007; Mathews & Guo, 2012) – and are *still* being powered – can have cores with radio luminosities similar to those in this chapter, with many having flat or rising spectra. However, if the AGN activity of BCGs has been regulating cluster cores for around half the Hubble time (e.g. Vikhlinin, 2006; Pratt et al., 2010; McDonald et al., 2014) then this implies activity timescales over an order of magnitude longer than even these long-lived sources.

4.6.5 Implications as an SZ contaminant

Considering the SED shapes of our sampled sources (see Appendix K), it is clear that extrapolation of the spectra from below 10 GHz towards the interesting range for SZ decrements (between roughly 15 and 200 GHz) will in many cases underestimate or completely overlook the contribution of an active self-absorbed component. Added to this is the further complication that variability brings, requiring contemporaneous high-resolution observations to ideally account for contaminants (as is of course possible with interferometric SZ instruments such as AMI and CARMA).

For a sample of 45 galaxy clusters observed at 140 GHz with BOLOCAM, Sayers et al. (2013) used the 1-30 GHz spectral index in addition to limits from their 140 GHz maps to constrain the contamination by point sources. Although they concluded that typically only about 25% of the clusters showed a greater than 1% fractional change of the SZ signal, they noted that this level of contamination was much more prevalent in cool-core clusters (11/17, roughly 65%). We note that *all* of the BCGs in our current sample are believed to lie in cool-core clusters. Sayers et al. (2013) detect no clear point sources at 140 GHz from their sample of 17 cool cores with typical map centre RMS values of 0.7-1.5mJy, whereas from our significantly larger parent sample (40% of our 530 cluster parent sample are tagged as cool core, see Chapter 3) we detect 32 at 150 GHz. This suggests $\geq$6.0% of BCGs in all clusters exhibit bright BCG emission in the mm-range rising to $\geq$15.1% if only cool-core clusters are considered. These values are lower-limits since our 150 GHz follow-up is flux limited and also incomplete in that some clusters are not observed at 150 GHz. The true level of contamination in cool-core clusters could therefore be even higher. We note that the prevalence of flattened or inverted spectral components in non cool-core clusters at frequencies below 20 GHz is much reduced (see Chapter 3), hence the level of contamination at 150 GHz is expected to be significantly lower in these systems.

Interestingly, of the $\geq$15.1% of the CC-hosted BCGs in our sample, more than half ($\geq$8.5% of the total CCs) have a peaked component with a turnover above 2 GHz. Underestimating the point-source contamination will be particularly severe for extrapolation of the steep component that dominates the lower frequency spectra in these types of object, if higher frequency observations are not available by which to identify the spectral flattening (or inversion). SZ catalogues are therefore potentially biased against the inclusion of cool-core clusters and may regularly underestimate the true Y_{SZ} in these systems, due to BCG radio emission canceling the SZ decrement. Interestingly this could suggest that the mass bias between X-ray and SZ derived cluster masses is more prevalent than previously assumed.

During their observations, the Planck Consortium compiled extensive catalogues of high radio frequency sources (e.g. Planck Collaboration et al., 2013b, 2011b). In Planck Collaboration et al. (2011b) the extragalactic source counts agree with those of the South

Pole Telescope (SPT, Mocanu et al., 2013), Atacama Cosmology Telescope (ACT, Marriage et al., 2011a) and the Wilkinson Microwave Anisotropy Probe (WMAP, Komatsu et al., 2011), at the lower frequency range of Planck. However, Planck Collaboration et al. (2011b) show that there may be a steepening of the typical spectral index above 70 GHz which could mean that contamination of the Cosmic Microwave Background (CMB) power spectrum by radio sources below the Planck detection limit could be less than currently thought. However, this may only apply to the bright end of the luminosity function. A population of GPS/HFP sources (in addition to a potentially ubiquitous mm/sub-mm component, see Section 4.6.6) in low-luminosity AGN (LLAGN) and BCGs could present a low level contaminant to the CMB power spectrum. Deep, high radio frequency radio surveys are required to shed light on the luminosity function of faint sources in this range.

4.6.6 Potential Additional sub-mm Component

Examination of our SEDs (see Section K) shows that a number of sources have inverted spectra between our GISMO observations at 150 GHz and SCUBA-2 observations at 353 GHz. That is, the spectral slope switches from being falling at frequencies below 150 GHz to rising just afterwards. This is most notable in A646, MACS1931-26 and RXJ1504-02. The observed indices are too shallow to be solely attributable to dust-emission (Edge et al., 1999) although extrapolation of the flat spectrum core component in conjunction with Herschel-SPIRE observations at 250, 350 and 500μm for the Herschel Lensing Survey (HLS, Egami et al., 2010; Rawle et al., 2012) shows that these components combined can explain the spectral upturn in MACS1931-26. However, there is still unaccounted for flux of $\sim$20 and 10mJy at 353 GHz in A646 and R1504-02 respectively after accounting for both these contributions, roughly equivalent to $P_{353\ \mathrm{GHz}}$ of 1×10^{24} W Hz^{-1} for both sources.

An intriguing explanation to account for this 'missing flux' is that we may be seeing an additional component in the radio/sub-mm spectrum caused by an Advection Dominated Accretion flow (ADAF: e.g. Mahadevan, 1997; Narayan et al., 1998; Ulvestad & Ho, 2001; Narayan & McClintock, 2008). These are believed to exist, commonly in conjunction with jets, in low radiative efficiency accretion sources and multiple models

exist that attempt to explain the bolometric spectra of low luminosity AGN often invoke ADAF+jet models (e.g. Falcke, 1996; Wu et al., 2007; Nemmen et al., 2014). A common feature of ADAF models is the existence of a synchrotron self-absorbed component that typically peaks at mm-wavelengths. To investigate whether such a component could explain our anomalous SCUBA-2 fluxes we take the base model of Mahadevan (1997) for a black hole mass of 5 $\times 10^9 M_\odot$, with a viscosity parameter of 0.3 and a ratio of gas to total pressure of 0.5. For a typical BCG accretion rate in the ADAF range (e.g. see Russell et al., 2013) of 3 $\times 10^{-4}$-3 $\times 10^{-5}$ M_{Edd} this predicts an ADAF-power of $\sim 1 \times 10^{22-23}$ W Hz^{-1} at 353 GHZ, which we note is an order of magnitude lower than would be inferred if all of the missing flux at 353 GHz in A646 and R1504-02 were from an ADAF component. The modeled ADAF-powers scale with black hole mass and accretion rate, however to align these with our missing flux would require unfeasibly high black hole masses or accretion rates that would no longer be compatible with an ADAF-like accretion structure. Furthermore, the simplest models predict that the upturned spectral index be close to $\alpha \propto 0.4$ for a single synchrotron self-absorbed spectrum. Whilst our fitted core components in A646 and RXJ1504-02 do unpredict the measured 150 GHz fluxes in both instances (by 1.0 and 0.3mJy respectively), a simple interpolation between these 'missing fluxes' would give indices far too steep to be attributable to simplest case self-absorption. Alternatively, extrapolation with an index $\propto 0.4$ from the missing flux at 353 GHz would overpredict our measured fluxes at 150 GHz.

For the reasons given above we rule out the presence of a strong ADAF component to explain our missing flux, although we note that our findings do not rule out the presence of an ADAF component hidden well below our observed (or missing!) flux. The most likely explanation for the 'missing flux' then becomes a combination of low level dust emission and variability in the jetted core component.

4.7 Relationship to X-ray Point Source

We have shown both in this, and the preceding chapters that our 150 GHz GISMO observations are typically well above the self-absorption turnover frequency for the radio core component. Therefore these measurements should in most cases provide a measurement

of the core that is unaffected by self-absorption.

In a study considering the nuclear emission properties of 50 BCGs, Russell et al. (2013) found no apparent correlation between the nuclear X-ray 2–10keV flux and the 5 GHz core radio flux in a sub-sample of 22 central cluster galaxies (see their Figure 9). The core radio fluxes used in their study were from SED decompositions (see Chapter 2) and the authors noted that these may in some cases overestimate the true core radio flux if contaminated by remaining non-core emission. Perhaps more prevalently, given Figure 5.1, the 5 GHz sampling frequency is also likely to be below the self-absorption turnover in many of these cores and hence the true core radio power may be being underestimated. The lack of a correlation suggested that the nuclear X-rays are less likely to originate from the jet base.

Nuclear X-ray 2–10keV fluxes derived from Chandra observations are available for 24 of our GISMO observed BCGs (Russell (*private communication*), Russell et al., 2013; Hlavacek-Larrondo & Fabian, 2011; Hlavacek-Larrondo et al., 2013). X-ray fluxes for a further 6 BCGs that have good radio-coverage at higher radio frequencies and for which a reasonable 150 GHz flux can be inferred were also used (these additional sources are: 3C 186, Cygnus-A, I0910+41, IC1459, NGC 1275 and Phoenix-A). In Figure 4.11 we plot these X-ray fluxes against our 150 GHz radio fluxes. Whilst there is significant scatter, a general trend does begin to become apparent in that there appear to be two different relationships. The majority of BCGs accrete radiatively inefficiently, and considering only these objects a weak correlation between the nuclear X-ray and 150 GHz radio fluxes is seen. However, as highlighted by the cases of A2052, Hydra-A, MACS0242 and Z8276 these parameters are *both* found to vary over few year timescales which may suggest that there is an underlying relationship and that the nuclear X-rays (at least partly) originate from the jet base. Differing variability timescales of both components will serve to lower the observability of this relation, particularly for radio frequencies below any self-absorption turnovers.

Apparent on Figure 4.11 is that there are a population of BCGs that appear to have highly elevated X-ray fluxes in comparison with their radio emission. The highest X-ray excess is found in E1821+644, a well known but rare radiatively efficient BCG. Also showing X-ray excess are sources that appear to have more BL-Lac like beamed central

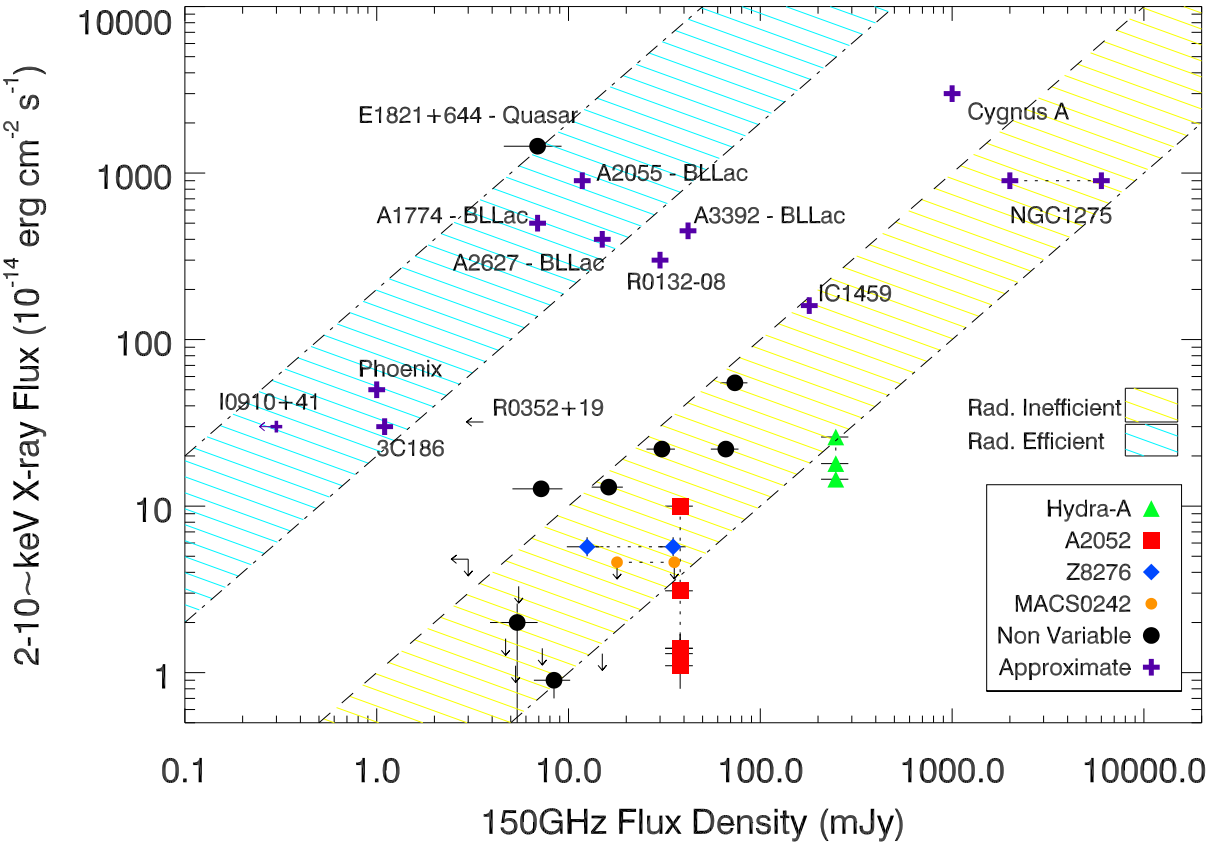

Figure 4.11: Plot showing the X-ray ($F_{2-10keV}$) vs Radio (150 GHz) fluxes. Most sources align and are consistent with being low accretion rate, hard-state equivalent objects whereas there are a small number of sources with an X-ray excess above this. These constitute quasar-like objects that are more likely to be accreting with greater radiative efficiency as well as the most BL-Lac like objects, which suggests a jet-origin for at least a component of the nuclear X-ray flux that is more favourably boosted than the radio emission.

engines. This relationship points at two modes of accretion in BCGs. In the majority of cases the BCGs accrete radiatively inefficiently and a weak trend between central X-ray and radio fluxes is seen, but in rare instances BCGs can accrete more efficiently and will lie above this relationship. That the apparently more highly beamed objects also have an X-ray excess suggests that there is at least a component of the central X-rays that originate in the jet, and that these are more boosted than the radio emission. Uncovering the full picture requires clean radio core measures that are unaffected by self-absorption.

4.8 Conclusions

We have expanded the radio SEDs of a sub-sample of 35 BCGs selected from the sample of over 700 clusters presented in Chapter 2 and studied in Chapter 3. These sources are all hosted by cool-core clusters where active feedback is believed to occur, and show the brightest flat or inverted components in their spectra at high radio frequencies. These bright cores suggest that the central SMBH is currently accreting at an appreciable rate and so determining the spectra of these cores to higher frequency allows us to investigate possible physical origins for the radio emission. We considered the variability of these sources at both 15 & 150 GHz, enabling us to better understand the amplitudes of variation in SMBHs during their more active phases. We find a wide variety of spectral shapes and in many cases see that these core components exhibit a spectral peak above 2 GHz, similar to the GPS/HFP population of young radio sources. Our results can be summarised as follows:

- Cool-core hosted brightest cluster galaxies contain distinguishable active radio core components in over 60% of cases (Chapter 3). This core can become dominant at frequencies higher than a few GHz. We see from our current sub-sample that $\geq$15.1% of cool-core hosted BCGs contain a radio source greater than 3mJy at 150 GHz (equivalent to a radio power of $\approx 1.2\times10^{23}$W Hz^{-1} at our median redshift of 0.126) and that more than half of these ($\geq$8.5% of all CCs) contain a distinguishable peaked component to their spectra with a turnover frequency above 2 GHz that would be missed by lower frequency observations. This shows that the majority of CC-hosted BCGs show recent activity, of which a significant fraction show strong active accretion at any given time.

- These core components appear to be similar to the GPS/HFP populations that are usually interpreted as young radio sources. That these peaked components are usually accompanied by steeper spectrum power-law emission at lower frequencies suggests that BCGs show regularly restarted, ongoing activity - these sources essentially enjoy a repeated youth.

- Sources do not commonly show strong variability at 15 GHz on short (week to month) timescales, with a typical limit of $<$10% indicating steady accretion over

these timescales. We note however that there could be variability that we are missing due to it being hidden within error. There is an increased incidence of variation on 6 month timescales at 150 GHz although accounting for measurement uncertainty we find that in most cases this variability can only be restricted to an upper limit of $<$35%. That we do see variability on less than 6 months at 150 GHz suggests this emission originates within the inner 0.01 pc of the and hence is tracing the inner regions of the jet or accretion flow.

- We find that sources can show steady variation at 15 GHz over 1-5 year timescales, although typically with less than 10% per annum. Variability of up to 20% pa is observed in a small number of sources during the most active periods of their lightcurves (although we note that our selection of the currently brightest systems may more favourably select highly varying objects).

- This year-scale variability is found to be weakly related to the position of the peak in the GPS component of the spectrum. Whilst for any individual source the position of the peak at any given time *does not* serve as a proxy for the definite amount that source will vary, a higher peak *does* indicate an increased likelihood of large scale fluctuations.

- We find that $\geq$3.4% of BCGs in our parent sample of 530 sources at Declinations greater than 30° contain peaked components peaking above 2 GHz.

- The fraction of BCGs with a peaked components peaking above 2 GHz increases to $\geq$8.5% if only cool-core clusters are considered. Overall, we find $\geq$15.1% of cool-core clusters contain a 150 GHz point source greater than 3mJy. This suggests that much more than half of all cool-core clusters with bright 150 GHz central point sources have spectra whereby even well-determined spectral indices below a few GHz would give very large underestimates of the flux at 150 GHz if extrapolated and hence constitute a potential contaminant for SZ surveys as these sources can wipe out any SZ decrements if not fully accounted for.

- We find evidence of a potentially ADAF-related component in the mm/sub-mm spectra of some of our sources, similar to those seen in several local LLAGN. If

such a component was confirmed then this would be very interesting as it would allow much improved understanding of the accretion processes in these systems, especially understanding the state of the black hole in between major activity periods. Whilst further study is required to confirm whether ADAF components that dominate the mm-range radio spectrum are present in a sizeable fraction of BCGs (and indeed the general radio galaxy population) such a component, even if typically not isolatable, could be an important contributor to the overall radio-power of radio-sources and potentially a low-scale contaminant to both SZ-observations and the CMB power-spectrum.

CHAPTER 5

High Resolution Core Properties A VLBA Survey

5.1 Abstract

In this chapter we consider the parsec-scale radio properties of a sub-sample of 59 brightest cluster galaxies, using new observations taken with the VLBA over the period 2009 - 2013. These galaxies were selected as having a high probability of containing active parsec-scale core components as a result of their lower resolution and spectral radio properties, as described in the preceding chapters. We find a range of small-scale morphologies in cluster cores, suggestive of diverse variety in both the initial launching conditions as well as the inner-environment within these clusters. Additionally we find a large number of unresolved sources, further supporting the idea that low level accretion with a high duty cycle is common amongst cool-core-hosted BCGs.

5.2 Introduction - The Parsec-scale Radio Cores of BCGs

Perhaps surprisingly given that they are well known as a class of interesting radio sources, Brightest Cluster Galaxies have been relatively little studied on parsec-scales; as is achievable with VLBI observations. Nevertheless, several studies have looked at these small-scale properties, although often restricted to only the most famous and bright BCGs. Even amongst this small sample of studied objects, variety is seen in the recovered properties.

Taylor (1996) used multi-frequency VLBA observations to study Hydra-A, finding it to have highly symmetric inner jet structure where both the core and inner-jets showed

evidence of being either free-free or synchrotron self absorbed. Similar symmetric and absorbed structure was found in the centre of A2597 (Taylor et al., 1999b), again using the VLBA. In both of these systems atomic hydrogen (HI) is seen in absorption against the core, which the authors suggest may be situated within a $\sim$30 pc torus with the symmetric jets propagating away from the plane of the disk. More recently, Augusto et al. (2006) undertook a comprehensive study of the BCG in A2390 using arrays at a variety of resolutions. They found a two-sided but non-symmetric source on VLBA-scales. However, on slightly larger scales with eMERLIN they found a medium-sized compact symmetric core that they suggest may be a source at an early stage (10^3-10^4 yrs) of X-ray cavity inflation. This source also shows significant HI absorption against the core (see Chapter 6). Bucking this apparent trend is 3C 338 (BCG in A2199) which has symmetric jets (Gentile et al., 2007) but with no HI seen in the system (Dwarakanath et al., 1994). Interestingly, Gentile et al. (2007) consider the X-ray cavity and larger scale radio properties in A2199 and find that there is discord between the core power and the energy required to inflate the cavities leading them to conclude that the accretion power onto the central engine is not constant.

Not all BCGs exhibit symmetric parsec-scale jets. Lara et al. (1999) find one-sided structure in 3C 264 within A1367 using the European VLBI Network (EVN). On VLBI scales NGC 1275 is asymmetric, with the counter-jet consistent with being free-free absorbed within a mildly beamed source (Biretta et al., 1991; Walker et al., 1994; Vermeulen et al., 1994). In other cases, one-sided jets are seen in the inner-regions of BCGs (e.g. 3C 465 in A2634 and B0936+29 in A690, Venturi et al., 1995). These two examples are taken from a larger, flux-limited, complete sample of radio-galaxies and show that the inner-properties of BCGs can be similar to typical FR I sources (Giovannini et al., 2001). Giovannini et al. (2001) also show that for a flux limited sample of VLBI cores, the parsec-scale properties of both high and low power radio sources are qualitatively morphologically similar. They suggest therefore that the launching mechanisms for radio jets may be consistent across source types and that subsequent variation of morphology (e.g. FR I or FR II) may be a result partly of the launching power but dominantly affected by the external environment.

A common theme throughout these targeted studies is that the Lorentz Factor (γ) of

the jets is uncertain. For A2634 and A690, Venturi et al. (1995) find the jets to be beamed and highly relativistic (greater than 0.6c). This potentially puts them on a par with typical highly relativistic jets in FRIs where γs greater than 3 (equivalent to a velocity above about 0.94c) are not unusual (Giovannini et al., 2001). However, it has been noted that symmetric parsec-scale sources are rare in flux limited VLBI samples but relatively common in cooling-flow hosted BCGs. This has been used to suggest that the dense inner-environments of clusters can greatly retard initially highly relativistic jets over the order of only a few parsecs (e.g. Liuzzo et al., 2009). Further confounding this issue is that often, the interpretation of a given source is degenerate, in that it could be explained by either highly relativistic jets at a wide angle to the line-of-sight or mildly relativistic jets more closely aligned (e.g. Taylor, 1996; Gentile et al., 2007). Additional variety in the inner-jet morphologies could arise due to precession of the black hole or gas motion bending initially straight jets, perhaps explaining the Z-shaped inner-morphology of A1795 (Liuzzo et al., 2009).

One aspect that is unclear is what, if any, effect the wider cluster properties have on the radio properties of BCGs in their innermost regions? Liuzzo et al. (2010) studied the BCGs in a nearby, optical richness selected sample of 34 clusters using the VLBA and recovered a 52% detection rate. They also found evidence for a systematic difference whereby BCGs in cool cores commonly exhibit two-sided jet structure and those in NCCs most commonly showing one-sided jets. They interpret this as possible differences in the jet speed; with highly relativistic jets in NCCs preferentially one-sided due to Doppler boosting whereas mildly relativistic jets interact more quickly with the denser environment in CCs and hence appear two-sided closer to the nucleus. Their study was unbiased by cluster type, however, which meant that they were restricted to only four CCs within their main sample. This was increased to ten by the addition of literature CC systems although it is possible that subtle biases may affect this (see also Section 5.5.3).

In this chapter we aim to test whether most (if not all) BCGs in cool-core clusters have symmetric structure on parsec-scales. Of our sample of 59 clusters, only RXJ0341+15 is not classified as line-emitting (Crawford et al., 1999) and even this has potentially weak lines. Proxy therefore suggests that we are investigating a heavily cool-core dominated sample. Additionally, Liuzzo et al. (2010) found that for their mainly NCC sample they

typically recovered more than 80% of the unresolved arcsecond scale flux. We can here test whether similarly high fractions are recovered in CC-hosted BCGs, as well as reinforcing our core decompositions from previous chapters. For the high radio-active duty cycle scenario it may be expected that significant structure at spatial frequencies intermediate between the milli-arcsecond scales sampled by VLBA and the few arcsecond scales of one-site interferometers is present. This suggests we may expect to recover a smaller fraction of the unresolved arcsecond-scale core flux for more constantly restarted and persistent central engines than single outburst systems where, if they are caught during a period of high core emission, they are more likely to be short-lived and hence have the bulk of this emission on smaller scales.

5.3 Sample Selection

We select our VLBA targets from the parent sample of ≈750 X-ray detected galaxy clusters from the combined BCS, eBCS and REFLEX (Ebeling et al., 1998, 2000; Böhringer et al., 2004, respectively), as described in Chapter 2, supplemented by the addition of the MAssive Cluster Survey (MACS, Ebeling et al., 2001). This brings our total parent sample to be considered for VLBA follow-up to ≈875 clusters. As in Chapter 4 we restrict this sample by here using a northern telescope that can observe (at a push!) down to DEC$\geq$-30° and so we draw from a sample of 530 clusters.

In the present chapter we are interested in the small-scale properties of BCGs within strongly cooling core clusters. To maximise our likely detection fraction we therefore targeted all BCGs in line-emitting clusters for which the radio spectrum decompositions performed in Chapter 3 predict there to be an active core component above a threshold of 10mJy at 10 GHz (11.5mJy at 5 GHz for representative core index of α=0.2) that are in regions of the sky observable with the VLBA (DEC>-30°)[1]. These systems are believed to be undergoing current accretion episodes and thus are expected to display flux on milli-arcsecond scales, enabling us to observe this inner environment at a crucial point of the

[1]Note that this sample will be greatly extended with the inclusion of all likely active cores in the full observable parent sample, observed to a lower flux level. These data constitute an additional 76 sources and were observed in summer 2014. See Chapter 7.

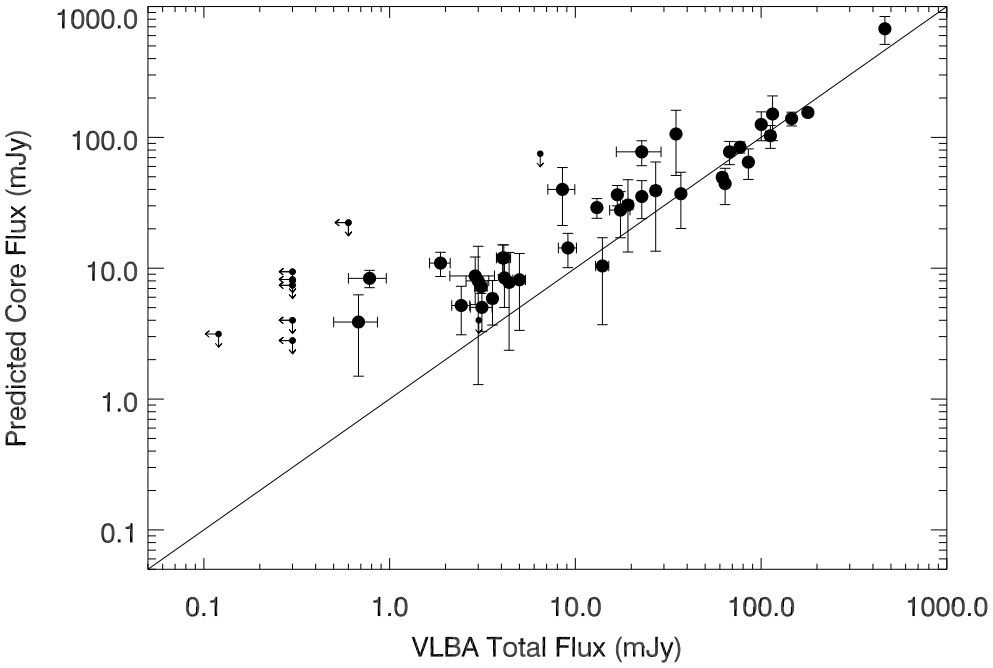

Figure 5.1: Total flux recovered on parsec-scales with the VLBA versus the predicted core component fluxes at 5 GHz predicted by the spectral decompositions in Chapter 3.

AGN feedback cycle.

Additionally we observed six sources (A795, A1668, RXJ0331-21, Z2701, Z3179 and Z8197) of varying brightness at C-band on arcsecond scales yet for which the spectral decompositions of Chapter 3 predict negligible contributions from an active component. These six sources can be used as a control when applying our findings in the present chapter to the cool-core hosted BCG population as a whole, in addition to providing a test of the predictive power of the techniques employed in Chapter 3. Thirteen sources from within the parent sample but not decomposed in Chapter 3 were added to our VLBA sample as they were predicted to contain parsec-scale structure as a consequence of their high radio frequency behaviour (see Chapter 4).

The VLBA data utilised within this chapter was taken at C-band ($\approx$5 GHz) and spans two observing programs: BE056, which consisted of 37 observations that included 21 unique clusters and BE063, which comprised a further 38 unique sources (one split over two nights). There was no overlap of targets between these proposal IDs and so our sample is comprised of 59 unique clusters of which 9 were observed at two epochs and 4

were observed at three epochs. See Table L.3 for the full sample list.

Our predictions of core activity in Chapter 3 were vindicated by the present data and hence we believe that our sample is representative of BCGs in strongly cooling core clusters (see Figure 5.1).

5.4 VLBA Data

5.4.1 Observations

All of our data were taken in full polarisation, phase-referencing mode. Sources were observed for between 24 and 96 minutes to achieve comparable signal to noise for our predicted fluxes, split over several visits to increase uv-coverage. The VLBA underwent a back-end upgrade with a new correlator fitted towards the end of 2010 (see Deller et al., 2007). BE056 data were taken before this update and hence have 32 MHz bandwidth with a central frequency of 4.971 GHz whereas BE063 data benefit from the updated receiver and so have 128 MHz bandwidth at central frequency 4.852 GHz. On-source integration times were adjusted accordingly.

BE056 data were taken over three runs: Run 1 on the 23rd/24th December 2009, Run 2 on the 5th February 2010 and Run 3 on 31st May/1st June 2010. BE063 data were observed as a 'filler project' and as such the observations were split into short 2 to 3 hours blocks, each containing between 3 and 5 science targets. There were 11 of these blocks taken between 5th March and 6th July 2013. Each of the three runs for BE056 observed a global fringe-finding calibrator at the beginning, middle and end of the run, whereas for the shorter observing blocks in BE063 a fringe-finding calibrator was observed only at the beginning and end. Each science observation was sandwiched between 1-minute phase calibrator scans. Additionally, two further nearby calibrators were observed for each science target to improve fringe and amplitude calibration.

5.4.2 Reduction

All data were correlated using the co-temporal VLBA correlator at Socorro. Specifically this was the VLBA-Hardware/Cray for BE056 (Benson, 1995) and the VLBA-DiFX for

BE063 (Deller et al., 2007). Reduction and imaging were performed using the AIPS software package.

We used the VLBA-specific package of reduction tasks within AIPS to first load and check the data consistency. We then corrected for the ionosphere and earth orientation parameters (EOPs) using VLBATECR and VLBAEOPS respectively before running VLBACALA to correct the sample voltage offsets and amplitude calibrate the data. We further checked the data to ensure reliable results and flag discrepant data (using AIPS tasks UVFLG and WIPER). Most of our data were quite clean with little RFI. We did note unavoidable increases in noise when looking towards low declinations, particularly in the northernmost antenna (Hancock and Brewster). To attempt to maintain a reasonable synthesised-beam shape we usually chose to remove only the worst data and accept a slight noise increase by keeping these antennae to improve north-south coverage. We only completely removed antennae where absolutely necessary or if it substantially affected overall final calibration of an individual source. In these instances, data were re-reduced without the worst affected baselines. Additionally, the Owens Valley antenna was found to be blocked by the mountains for a small number of scans at low elevation and was subsequently removed for these scans.

Antenna parallactic angles were corrected using VLBAPANG and instrumental delay residuals were removed globally using VLBAPCOR. Fringe fitting to remove global frequency and time-dependent phase errors was performed using VLBAFRING. Calibrators were globally fringe fitted. Science sources found to be strong ($>$50mJy) were self-fringed. Below this cut-off, it was found that self-fringing occasionally introduced significant errors. We attempted to fringe-fit all sources using both methods (self and not-self), finding results to be more reliable if self-fringing was restricted only to the very brightest sources. The final method used for each individual source is recorded in Appendix L.

Further inspection was performed to ensure reliable calibration tables, with a small amount of post-calibration flagging required. Relevant calibration tables were applied to science sources, which were subsequently split into individual uv-files using the AIPS task SPLIT. Imaging was performed using IMAGR, with several iterations then performed to ensure dependable recovery of any extended emission.

5.5 VLBA Results

5.5.1 Detection Rates

We detect with the VLBA all 53 of the sources predicted to contain active core components (see Section 5.3) including two VLBA detections with recovered fluxes that are consistent with core limits imposed in Chapter 3 where a core was suspected present but not confidently predictable. Of the six sources observed for which the decompositions predicted no active core component, none were recovered with the VLBA (to a typical 3 σ limit of $\leq$0.4mJy). We therefore claim that our predictions of core activity were vindicated by the present data and hence believe that our sample is representative of BCGs in strongly cooling core clusters.

Our VLBA sample is purposefully biased towards sources with active components and hence our high (90%, 53/59) detection rate cannot be claimed to truly reflect the duty cycle of CC-hosted BCGs (although note that it is comparable to the 8/10 detection rate for CC-hosted BCGs found by Liuzzo et al. (2010)). However, if we consider Chapter 3 where upwards of 60% of cool-core clusters were found to have a spectrally distinguishable core coupled with our 100% recovery of predicted cores and the two cases where parsec-scale cores were recovered consistent with predicted limits, then we can expect over 60% of cool-core hosted BCGs to contain recoverable flux on milli-arcsecond scales down to $\approx$0.4mJy. This further supports a very high duty cycle of activity in these systems. For more discussion of the duty cycle of BCGs see Section 5.6.2.

5.5.2 Recovered Fluxes

We find good agreement between the integrated recovered flux and core component predicted in Chapter 3 as shown in Figure 5.1. There does however appear to be a tendency to over-predict the core contribution for fainter sources.

It is worth reiterating here what is meant by ‘core’ component. Core predictions were for the total emission that can be attributed to ongoing activity, hence are best compared to the integrated VLBA emission. In instances of sources that are resolved on milli-arcsecond scales, the unresolved central VLBA components (see Section 5.5.3) are of course lower than the integrated emission for resolved sources. By separating the core

component and finding that it agrees with the emission on milli-arcsecond scales (which can only be attributable to recent, few-decade long activity) we implicitly see that remaining emission is attributable to previous activity episodes or an extended outburst. As such it is further evidence that BCGs are frequently restarted.

Core predictions in Chapter 3 were often significantly lower than the unresolved C-band flux recovered at arcsecond scales, where typical resolutions with the VLA and ATCA were a couple to a few arcseconds. In Figure 5.2 we show the fraction of the unresolved arcsecond scale flux that is recovered at milli-arcsecond scales for the sources in the current sample that were also observed at C-band with either the VLA or the ATCA. We show this recovered fraction both in the total integrated emission recovered with the VLBA and also that contained only in the unresolved milli-arcsecond VLBA core. In a minority of cases we see that more flux is recovered with the VLBA than was detected in the previously observed unresolved arcsecond observations. This is attributable to low-level variability over year-decade timescales (the time between VLA and VLBA observations being up to two decades, see also Chapter 4).

A clear difference is seen in Figure 5.2 between sources observed in campaigns BE063 and BE056. This is attributable to the observing strategy and discussed more in Section 5.6.1. What is apparent in Figure 5.2 is that there is a wide range of recovered fractions. Coupled to the correlation in Figure 5.1 this indicates that BCGs as a population experience widely varying activity cycles. In some situations, almost all of the radio emission at C-band appears to have been accelerated in a single activity cycle whereas in others there appears to be a much lower fraction of the total emission being attributable to ongoing accretion even when the core is in an active state, which points towards short re-ignition time-frames ($<$10Myr) or persistent core activity.

5.5.3 Morphology

Classification

Within our sample we find a variety of morphologies. We parameterise this variety by classifying sources as two-sided, one-sided or unresolved. Features that appear above 4 times the local noise are considered. To increase robustness, for sources visited more than

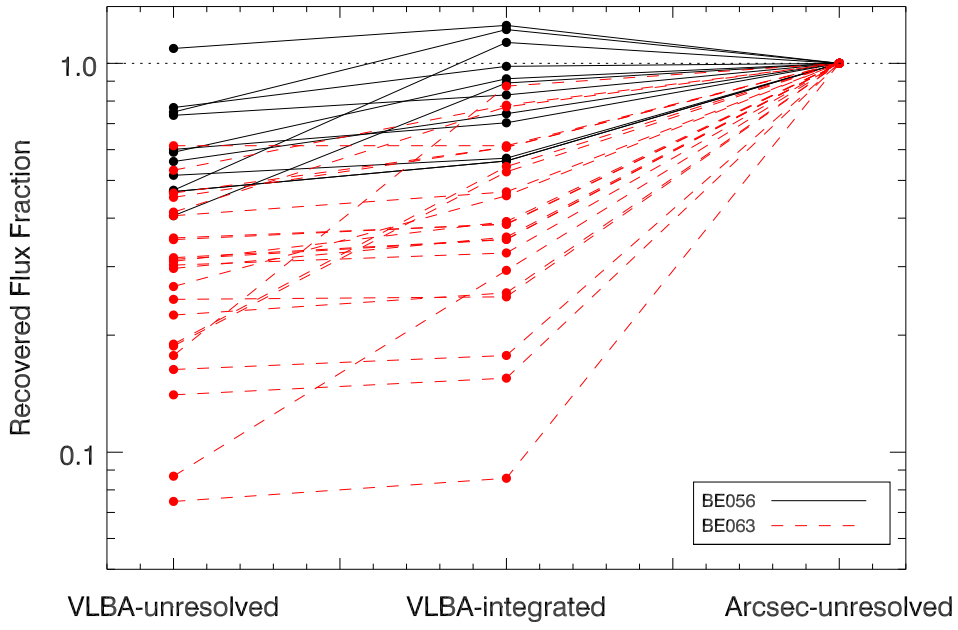

Figure 5.2: Flux fraction of arcsecond scale C-band measurement recovered by VLBA. A clear difference is seen between sources in proposal ID BE063 and BE056. See Section 5.6.1 for a discussion of why this may be the case.

once (specific to BE056) we produce maps for each individual scan in addition to a concatenated image with the proviso that repeatedly recovered structure is highly likely to be real rather than a mapping artefact. Additionally, we inspected overlays of the sky-maps with the synthesised beam maps to help minimise instances of poorly CLEANed and phase-error induced artefacts being erroneously interpreted. Notes on individual sources alongside image and source parameters can be found in Appendix L.

In Figure 5.3 we show six example sources to highlight these morphologies. In the top-left panel we show RXJ1558-14, which is classified as being two-sided where the source exhibits a miniature symmetric double structure with inner hot-spots that are clearly distinct from the central core. Alternatively, two-sided sources may have jets that are blended with the core as in Z8193. In the middle panel of Figure 5.3 are a couple of one-sided sources, with bright central cores and then a relatively bright and faint single jet in NGC 6338 and RXJ1350+09 in the left and right panels respectively. When the source shows no robust structure that is inconsistent with the beam shape then we classify it as unresolved, as for Z2844 and A646 (bottom panels of Figure 5.3).

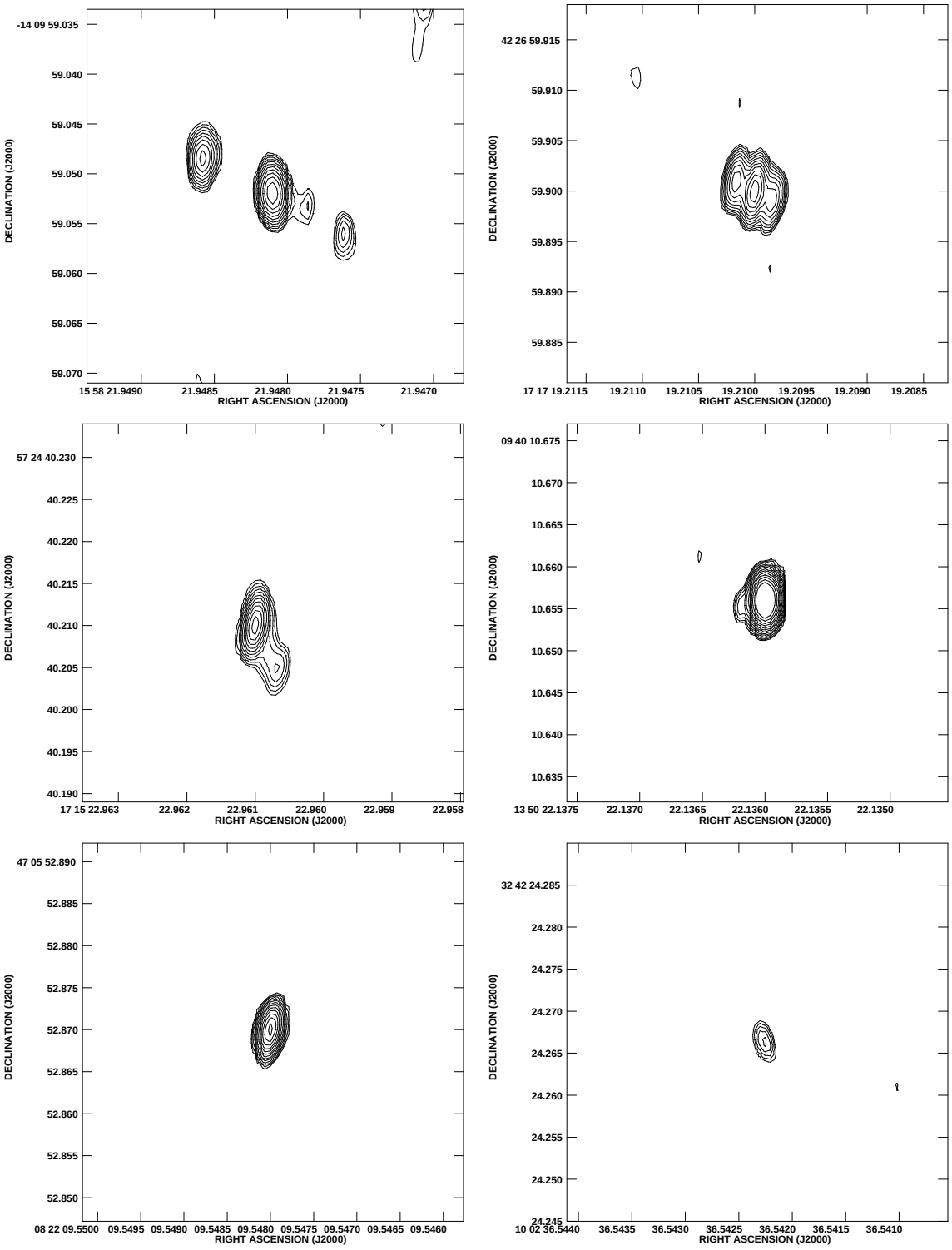

Figure 5.3: Example parsec-scale morphologies for RXJ1558-14, Z8193, RXJ1350+09, Z2844, A646 and NGC 6338, clockwise from top-left respectively. Contours are $\sqrt{16}$, $\sqrt{32}$, $\sqrt{64}$, etc $\times$ the noise in each panel. Note that two-sided, one-sided and unresolved sources are all present. See text for more details.

One source, the low declination RXJ2014-24, could not be reliably mapped. Multiple components appear present in the source but it could not be robustly recovered and hence is not considered in the following.

Distribution of Morphologies

Of the 52 detected sources that could be reliably mapped, we find that 21 (40.4%) are unresolved, 23 (44.2%) are one-sided and 15.4% (8/53) are two sided. This breakdown of morphologies differs from the results of Liuzzo et al.(2010) who for their sample of 10 CC-hosted BCGs found 7 to be two-sided and 1 unresolved, with the remaining 2 not detected. We do however find an increased fraction of two-sided sources above that of their NCC-hosted sample where they found no two-sided sources, 14 one-sided and 1 unresolved in a sample of 24, with the remaining 9 not detected. Two sources, A2052 and A2390 are present in both our current sample and the sample of Liuzzo et al. (2010). These sources are classified as two-sided by both studies although we note that the two-sided nature of A2390 only becomes apparent in our concatenated image. It may be therefore that our snapshot campaign is less able to recover extended emission. Deeper maps with increased uv-coverage may be expected to recover a higher fraction of two-sided sources within our sample and hence we suggest that our 15.4% of detected sources in CC-hosted BCGs being two-sided is best interpreted as a lower limit. There is however a large mis-match with the almost 90% previously claimed and so our results oppose the hypothesis of two-sided sources being near-ubiquitous in CCs due to their jets being mildly relativistic and quickly retarded (e.g. Rossi et al., 2008).

Alternatively, we note that the two-sided sources within our sample appear to be in the most core dominated systems (see Figure 5.4). These are typically bright systems that are experiencing strong, ongoing accretion. Many of the strongest most studied radio sources are in such a state hence the BCGs studied so far in the literature with VLBI resolution may be biased towards these types of object, perhaps therefore explaining the seemingly very high incidence of two sidedness in BCGs. Alternatively, we may be limited by the signal to noise ratio and the true two-sided fraction may be much higher, although we note that the flux ratios between the central component and the ‘lobes’ would need to be higher in many cases than the ratios seen in the brightest most well-studied objects in order for

the two-sided fraction to approach unity.

It appears as if all common parsec-scale morphological types are present in CC-hosted BCGs. We therefore find that both one- and two-sided milli-arcsecond scale structures appear in strong cooling clusters. We note that our sample does not include NCCs and so we cannot comment on the related claim that two-sided structures are not found in NCCs (the only NLE within our sample appears one-sided). Whilst there does appear to be a dependence on cluster property of overall prevalence of core activity, the observed morphology of this short-term activity will be dependent mainly upon where in the activity cycle the AGN is when observed. This structure is therefore expected to vary on few-decade timescales.

It is possible that our one-sided sources do fit the mildly-relativistic jet scenario of Liuzzo et al. (2010) if they are assumed to be recently launched and hence the receding jet has not yet reached the distance at which it becomes visible. This is however deemed unlikely due to the high fraction of one-sided structures and the fact that they inhabit clusters with a range of core dominance and so do not appear to be merely restricted to recently activated cores.

Beaming is likely to affect a portion of our objects and perhaps contribute to the one-sided fraction although we do not expect this to be a dominant factor. The parent sample compiled in Chapter 3 was X-ray selected and objects classified as BL Lacs were excluded. This should mean that our sources are less likely to be biased by beaming than a radio-selected sample, although it cannot be ruled out that precession could mean that whilst the larger-scale radio emission appears to be misaligned the inner-jets may be closer to the line of sight.

5.5.4 Core Dominance

There is a general trend between the prevalence of the core component to the overall emission of a source (i.e. the ratio of the core-component (10 GHz)/non core-component (1 GH z), see also Chapter 3) and the recovered flux fraction (top panel, Figure 5.4). In a handful of cases, more flux is recovered in the current VLBA observations than was seen at lower resolutions. This shows that highly core dominated sources exhibiting powerful ongoing activity can vary by upwards of 20% at 5 GHz over timescales of a few years to decades

(dependent on exact observation date with ATCA/VLA - see Appendix A, also Chapter 4). There is significant scatter in this relationship, which may be due to a number of factors. One is the scale of the non-core emission. As the 'recovered fraction' refers to the fraction of the central unresolved arcsecond scale component, then this is dependent upon the overall scale of non-core emission. For large extended sources, the recovered fraction is often higher as the arcsecond core better reflects current emission. For more frustrated sources where emission is contained closer to the AGN a higher fraction if any, of the non-core emission remains unresolved at arcsecond resolution and hence the fraction of this emission attributable to ongoing activity decreases.

We see tentative evidence that two-sided structures may be more common in the most core dominated systems (top panel, Figure 5.4) and that in these sources a higher fraction of overall emission is contained on milli-arcsecond scales (lower panel, Figure 5.4). Negligible difference is seen in the recovered fraction of sources which are classified as unresolved and one-sided. It is unlikely that we are losing enough flux beneath the noise to consolidate these figures. More likely is that for the less core dominated sources, more of the total emission is on spatial scales too large to be sampled with the VLBA.

5.5.5 Variability

For the subset of sources we have multi-epoch VLBA observations for, we see little evidence for variability of the innermost core component on few-month timescales. The only source for which we see a significant change is Z8276, which brightens by $\approx$15% between Run 1 and Run 2 of BE056. This is consistent with what we see at higher frequencies for this source, which appears to be experiencing a particularly active period (see Chapter 4).

5.6 VLBA Discussion

5.6.1 Sample Variance

In Section 5.5.2 we saw a marked difference in the fraction of the unresolved arcsecond scale central component recovered on milli-arcsecond scales between campaigns BE056 and BE063. This can be explained by considering the observing strategy of these respec-

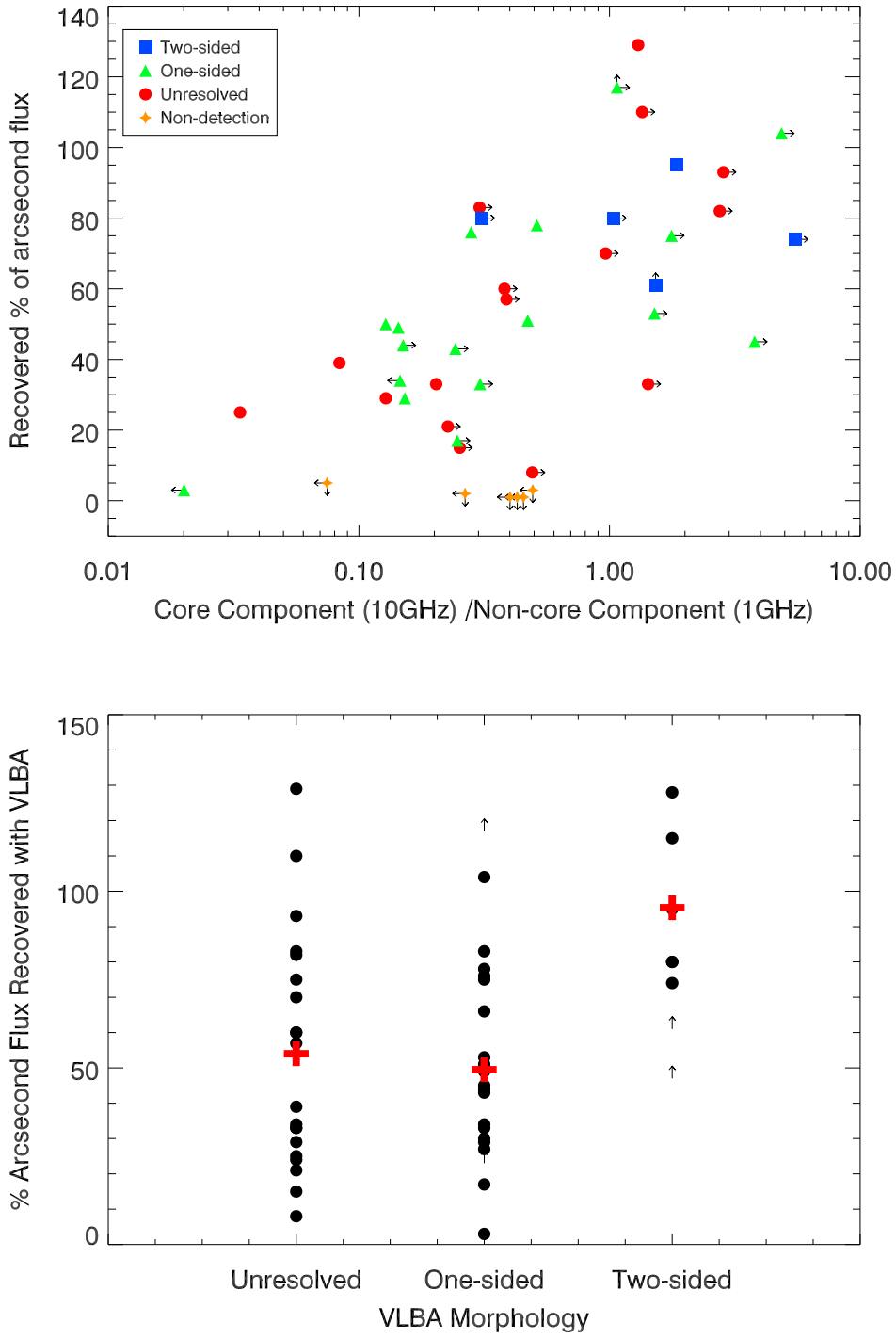

Figure 5.4: Top panel: Fraction of the flux of the unresolved arcsecond-scale central component that is recovered on milli-arcsec scales as a function of the core dominance of the system (shown as the core to non-core ratio, normalised at 10 GHz and 1 GHz respectively, see Chapter 3). As expected, the general trend is for sources that appear more core dominated on macro-scales with flatter specra to have more of their total flux concentrated in the current outburst. Non-detections with the VLBA are generally steep spectrum but not necessarily resolved on arcsecond scales, having low core to non-core ratios. Lower panel: Range of recovered arcsecond-scale flux fraction on milli-arcsec scales as a function of the milli-arcsecond scale morphology. We see a higher average recovered fraction with much smaller range for two-sided sources. Red crosses mark the average for the recovered fraction of each morphology.

tive programmes.

BE056 specifically targeted highly core dominated systems where is was believed that an active core contributed most of the integrated flux for the source over all scales. Conversely BE063 targeted mainly sources where an active component was predicted to be present but not dominant at C-band (see Chapter 3), even for (and indeed commonly for) sources that are unresolved at C-band with baselines of the order a few kilometres (mainly VLA-C / ATCA-6km). It stands to reason therefore that less of the unresolved arcsecond flux is expected to be recovered on milli-arcsecond scales, with significant flux expected on intermediate scales. e-MERLIN is the best facility to attempt to recover this emission and will be vital for fully understanding these sources. This observing strategy can therefore explain the apparent dichotomy seen in Figure 5.2.

5.6.2 Duty Cycle

It is reassuring to note that all of the VLBA non-detections are in systems classified as being non-core dominated (see Figure 5.4). In Chapter 3 we found that although $\geq$80% of BCGs in CCs are classified as radio-loud ($>10^{23}$W Hz^{-1}) at L-band, only around 60% are classified as having a distinguishable currently active core component. Whilst this is a lower limit, our current non-detections confirm that this fraction of currently active systems does not reach unity. Although these systems would commonly be classified as radio-loud AGN on the basis of their lower-resolution L-band powers, they are not currently radio-active AGN to the detections limits of our data. The recurrent nature of the AGN activity within BCGs leads us therefore to conclude that when considering the duty cycle of AGN that there are two, likely dependent, duty cycles to consider - the near-unity duty cycle during which the BCG undergoes active feedback whereby there is large scale interaction with the environment (i.e. the radio loud phase) and the duty cycle within this active phase during which the AGN is actively launching jets on milli-arcsecond scales. This inner-duty cycle of radio activeness is not unity although is high ($>$60%).

5.6.3 Two-sided Sources

Eight sources within our sample are classified as showing (near) symmetric, two-sided structure. Liuzzo et al. (2010) suggested that similar structure found in 3C84 and 3C338 could be due to rapidly decelerated mildly-relativistic jets. Such a scenario could explain the observation that significant ongoing activity at the cores of cool-core hosted BCGs does not necessarily always translate into large scale persistent classical jet structures. Dense material towards the centres of cooling flow BCGs may rapidly decelerate the jets so that they are ultimately able to progress less far (Rossi et al., 2008). These frustrated jets could then give rise to both the steep-spectrum sub-arcsecond emission and eventually the small scale, steep-spectrum amorphous structures commonly observed around BCGs.

In this scenario Liuzzo et al. (2010) suggest an intrinsic difference in the jets of CC and NCC-hosted BCGs. The jets in both are launched highly relativistically and hence are likely to be light jets with initially lower mechanical power. However, in CCs the high density ratio between the jet and dense inner-ICM creates Kelvin-Helmholtz instabilities that perturb the jet causing it to slow down, entrain material and become 'heavy' close to the nucleus (sub-kpc scale). Such jets are more mechanically powerful, and the work required directly links the jet to the ICM on sub-kpc scales where cavity inflation occurs. It is therefore cooling material within the BCG which essentially dampens mechanical feedback. Small scale frustrated jets may also help to increase the local turbulence of the cold gas phase, increasing the interaction between this and hot-phase gas which must exist at some level to link large scale cooling of the hot phase to heating from the radio-AGN and effective removal of excess cold molecular material (e.g. Russell et al., 2014; McNamara et al., 2014).

It is worth noting that Liuzzo et al. (2010) found that their two-sided sources were all in cool-core clusters with cooling rates greater than 90 $M_{\odot}yr^{-1}$. We do not have cooling rates for our clusters and hence cannot perform a direct comparison. It could be that our lower fraction of two-sided sources is in part due to the inclusion of weaker cool cores in our sample. Our use of the presence of optical emission lines should ensure our cool core clusters are all reasonably strong cool cores ($t_{cool} < 5 \times 10^8$ years) however a strong cool core does not necessarily equate to a high central mass deposition rate as measured spectrally (Hudson et al., 2010). Determining the sensitivity of inner radio structure to

the precise ICM density is a topic for future work.

5.6.4 Dual AGN

Systems hosting dual SMBHs are expected to be important for understanding galaxy evolution, however it is not yet certain what the best observational signatures for finding these systems is likely to be (Comerford et al., 2013). Nevertheless, a small number of dual-AGN have been confirmed such as in NGC 6240, NGC 3393 and Mrk 739, with separations of 900pc, 150pc and 3.4kpc respectively (Komossa et al., 2003; Fabbiano et al., 2011; Koss et al., 2011). Only one object, 0402+379, has hitherto unambiguously been shown to host dual black holes with $<$10pc separation (Rodriguez et al., 2006). As BCGs are believed to undergo semi-regular mergers (see Section 1.5.1), they may prove to be abundant hosts of dual black holes as SMBHs from mergers fall to the dynamical centre. One issue with detecting dual SMBHs beyond the local neighbourhood is that in order to detect them, both must be active at the same time. The high duty cycles of AGN within regularly fueled CC-hosted BCGs may provide optimal conditions for such a scenario and therefore VLBI studies of the central regions of CC-hosted BCGs could prove bountiful in searches for $<$kpc separated SMBHs.

Recently, Gitti et al. (2013) reported a candidate black hole binary system in the BCG of the CC cluster RBS 797. This BCG has an almost orthogonally aligned dual jet system on kpc scales (Gitti et al., 2006) and so is an intriguing candidate to host a potential dual AGN. The authors undertook EVN-VLBI imaging and find two compact components at $\approx$77pc separation, which they interpret as either dual nuclei in a close binary or as a core-knot system where the connecting jet emission is below their detection limit. Coupled to the large scale mis-aligned emission then the former of these scenarios could betray the presence of a second SMBH in the system. Multi-frequency VLBA observations are required to break the degeneracy.

We find several examples in our current sample of systems with multiple distinct components. Of our two sided sources, RXJ1558-14 has clearly distinct knots (see Figure 5.3) although here the interpretation is clear in that we are just not recovering the connecting emission in our snapshot campaign rather than the multiple components being evidence for the source containing multiple nuclei. Abell 2390 is similarly classified here as two-

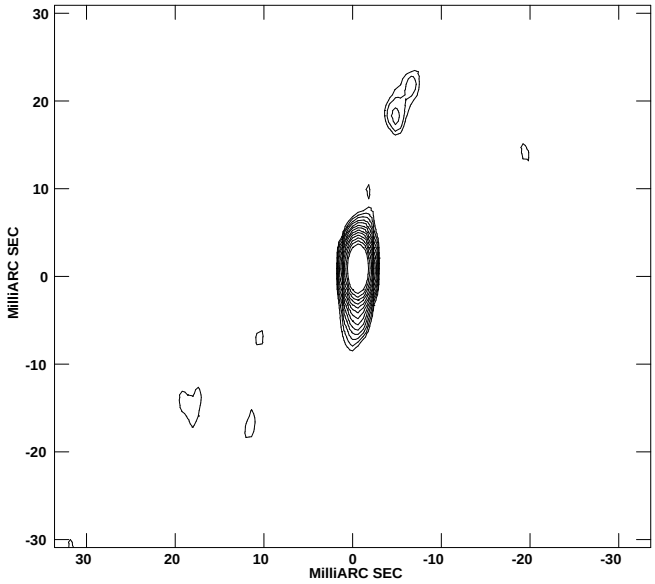

Figure 5.5: Central regions of A2390. Contour levels are the same as in Figure 5.3 although now the positions are shown relative to the central component. There is a jetted extension to the south of the nucleus with distinct knot-like feature seen 20mas to the north. This structure is also recovered in the VLBA maps of Augusto et al. (2006). We do not believe the northern structure to be indicative of a second nucleus in this source, instead preferring the interpretation of this as a knot in the northern jet that aligns with the larger-scale structure and therefore we classify this source as two-sided. See the text for more details.

sided, however it is different in that it has southern ≈10mas extent (equivalent to a physical extent of ≈33pc) attached to the nucleus and the distinct second component is ≈76pc to the North, consistent with the positions of structure found by Augusto et al. (2006) and also seen in Figure 5.5. We could be seeing a one-sided source with the detached component being a second nucleus. The relative orientation of this distinct component to the Southern extent and the lack of any other potential dual-AGN signatures in this source however suggest this to be unlikely and that we are seeing a single-nucleus system with a knot.

Similarly several of our sources (A11, A2627, MACS 0242-21, NGC 5044, RXJ0132-08, RXJ0352+19, RXJ2341+00) that are classified as one-sided have what appear to be a distinct nucleus with the one-sided nature manifesting itself as a distinct knot. However, in most cases the nuclear component shows extent in the direction of the second component and that the projected separation is small (≈few pc) and so it is expected that deeper observations would detect bridging emission. MACS 0242-21 is the exception, where

both detected components are fully unresolved, however archival VLBA maps at S- and X-band serve to show that this too is a core-knot system (Beasley et al., 2002). Additionally none of the sources that are flagged as having multiple distinct components at VLBA resolution are flagged as 'double-double' radio sources on kpc scales similar to RBS 797. Interestingly the majority of the sources that in Figure 4.11 were found to be X-ray bright and for which we have VLBA observations, are found to be one-sided on milli-arcsecond scales. This may point towards mild beaming in these cores and perhaps suggests that the X-ray emitting and radio emitting regions of the jet are not entirely aligned, which may have implications for jet precession and helical jet models.

We note that we are limited only to the inner few tens of parsecs in most cases and that our observations are relatively shallow. It appears that multiple milli-arcsecond scale components are fairly common within BCGs. However, we find little evidence to suggest any of our BCGs host dual AGN or that short separation dual SMBHs are common in CC-hosted BCGs. Our detections of CC-hosted BCGs with multiple distinct components would suggest that the core + knot scenario is the most likely explanation for the double component seen in RBS 797 (Gitti et al., 2013).

5.7 A Note on the Fundamental Plane of Black Hole Activity

As mentioned in Sections 1.5.2 and 4.6.6, a Fundamental Plane of Black Hole Activity exists that relates the 2–10keV nuclear X-ray luminosity, the 5 GHz nuclear radio luminosity and the black hole mass across many orders of magnitude from stellar mass to super-massive black holes (Ferrarese & Merritt, 2000; Merloni et al., 2003).

$$log\ L_{5\ GHz} = 0.60\ Log\ L_{X_{2-10keV}} + 0.78\ Log\ M_{BH} + 7.33 \tag{5.7.1}$$

In a study of 19 clusters, Hlavacek-Larrondo et al. (2012b) found that their BCGs all lay systematically on or *above* this Fundamental Plane. This implies that either the usual scaling relations do not hold for this class of object or that black holes in BCGs may be ultramassive ($>10^{10}M_{\odot}$).

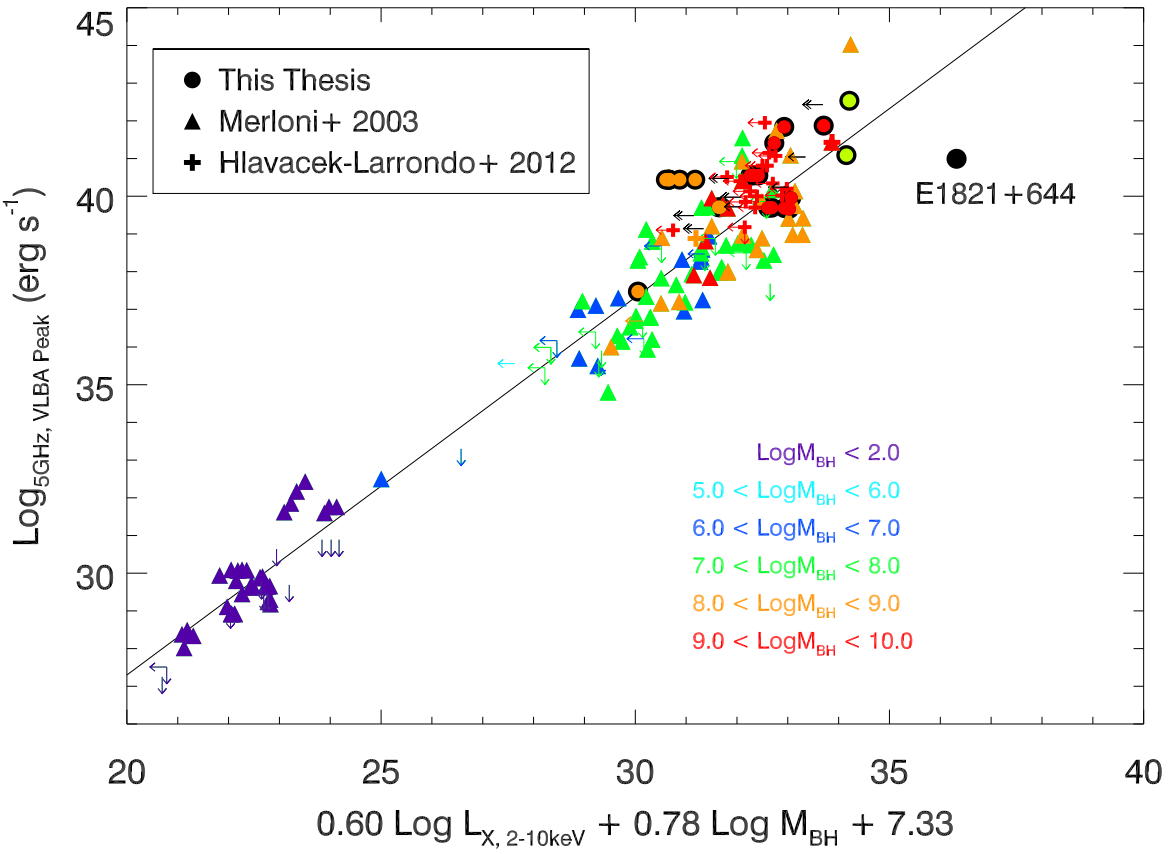

Figure 5.6: Reproduction of Figure 5 in Merloni et al. 2003 with sources observed with the VLBA during this project overlaid, alongside those of Hlavacek-Larrondo et al. 2012b for comparison. The sources observed within this project align favourably with the BCG sample of Hlavacek-Larrondo et al. 2012b. E1821+644 is a radiatively efficient source and hence is not theorised to lie on the plane, an interpretation supported by its outlying position.

Chandra measurements of the X-ray 2–10keV fluxes of the central point sources are available for 23 of our VLBA observed BCGs (Russell (*private communication*), Russell et al., 2013; Hlavacek-Larrondo & Fabian, 2011; Hlavacek-Larrondo et al., 2013) and our VLBA observations of these objects allow direct measures of the 5 GHz central flux. To allow us to place our objects onto the Fundamental Plane we retrieved the K-band magnitudes for each of our objects from the 2MASS catalogue (Skrutskie et al., 2006) and used these to estimate the black hole masses using the M_{BH}-K relation (Graham, 2007). We removed RXCJ1347.5-1145 as it does not have a 2MASS measurement, leaving us with a sample of 22 BCGs of which 14 have measured central X-ray fluxes and 8 have X-ray limits. These sources are plotted onto the Fundamental Plane in Figure 5.6. We find that the majority of our sources lie in a similar position to those of Hlavacek-Larrondo et al. (2012b) (of which we have two common sources; A2390 and PKS0745-191). This supports the interpretations of Hlavacek-Larrondo et al. (2012b) although we caution that our mass estimates are highly uncertain. One of our sources, E1821+644, is found to lie well below the plane. The Fundamental Plane is however only derived for inefficiently accreting black holes whose accretion progresses in an ADAF-like flow (Merloni et al., 2003). This supports the interpretation of E1821+644 as a rare, radiatively efficient BCG and also shows that the majority of BCGs are inefficient accretors.

5.8 Summary

In this chapter we have presented VLBA data from a sample of 59 cool-core hosted BCGs. Taking the population as a whole it would appear as if there is not a ‘holy grail’ activity timescale or outburst energy for BCGs - they may all on average counteract cooling (e.g. McNamara & Nulsen, 2012) but each BCG at any given moment can be in a wide variety of states. In particular we find that BCGs in cool core clusters can exhibit a wide range of parsec scale morphologies encompassing both one-sided and two-sided alongside unresolved structures. We also find no evidence that short-separation dual SMBH are common in CC-hosted BCGs.

CHAPTER 6

HI Absorption
Probing the Gas at the Centres of BCGs

6.1 Abstract

In this chapter we present a search for HI absorption against the radio continuum of 17 BCGs that uses data taken using the VLA, ATCA and WSRT. We describe our evolving selection criteria that use the continuum and small-scale properties described previously within this thesis to recover a high (up to 70%) detection rate and present the resultant spectra. Overall we clearly detect HI absorption within 5 sources, tentative detections in 3 and recover upper-limits on the HI content in the remaining 9. A range of column densities are recovered. We additionally consider 5 clear detections from the literature to give us a combined sample of 13 HI absorption systems within BCGs, which more than doubles the number of such systems known. We show that in all clear cases, the material appears either at the systemic velocity or mildly redshifted. The work within this chapter was performed in collaboration with Dr Raymond Oonk of ASTRON, and forms the basis of a paper to be written up.

6.2 HI Introduction

6.2.1 Motivation

An important constituent of understanding the AGN activity and feedback cycles in the centres of clusters is determining the distribution and quantity of gas within the systems after it cools from the hot phase. Not only is the cold and cooling gas one of the major

reservoirs for material depositing from the cooling flow, it is also this cooled material that is believed to power the central AGN and give rise to the radio emission that constitutes the focus of this thesis. Several studies over the past few years have revealed there to be substantial quantities ($\sim 10^{10} M_{\odot}$) of cold ($\leq$100 K) material at the centres of the most massive cooling clusters. Such studies have targeted a variety of lines tracing a range of species; including optical lines to trace atomic and ionised gas (e.g. Balmer and Nitrogen lines, Crawford et al., 1999), molecular lines to quantify the H_2 in the mid- and far-IR (e.g. Edge et al., 2002; Egami et al., 2006; Donahue et al., 2011), CO lines (McNamara & Jaffe, 1994; O'Dea et al., 1994b; Edge, 2001) and atomic cooling lines (e.g. C[II], O[I] and N[I], Edge et al. 2010a,b).

One species that is under-sampled is atomic hydrogen (HI). The 21cm transition has not thus far unambiguously been detected in emission within a BCG. However, detecting HI in *absorption* against the radio-continuum is a powerful technique, although it has only so far been detected in a small number of clusters (e.g. Jaffe et al., 1988; McNamara et al., 1990; O'Dea et al., 1994a; Taylor, 1996, see Section 6.2.4). Not only does this provide a probe of the cool gas ($\approx$100 K) that ultimately powers the AGN and star formation, detecting absorption in a pencil-beam observation against a very small central source provides us with the best method, given current limitations, for measuring the gas within the central regions of the BCG ($<$100pc). Essentially we are able to trace the material that is in the final stages before going on to power the AGN. Furthermore, the depth of the absorption signal depends only upon the intervening HI column density and the brightness of the background source. This means that unlike HI emission that is extremely difficult to detect beyond the low redshift universe, HI absorption can in theory be detected at all redshifts (although in practice it would be limited by receiver technology, strength of the continuum source, RFI and the ionosphere below about 30 MHz, equivalent to redshift $\approx$ 50, e.g. Curran et al., 2013b). There is of course the added complication that before a very high redshift (e.g. z$>$10) source can have absorption observed against it, such a source with high continuum flux at z$>$10 needs to be found!

6.2.2 General Early-Type Galaxies - HI Emission Studies

Several large surveys have been performed, aimed at understanding the distribution of atomic hydrogen in the general early-type galaxy (ETG) population (e.g. WSRT-SAURON, Morganti et al. 2006; Oosterloo et al. 2010; ATLAS^{3D}, Cappellari et al. 2011; Serra et al. 2012; ALFALFA, e.g. Fabello et al. 2011). The resultant HI emission maps have revealed there to be a broad range of HI masses and column densities seen in ETGs. There appears to be environmental dependence, with around 40% of field ETGs typically found to contain detectable HI gas whereas this fraction drops to around 10% for ETGs within the Virgo cluster (Oosterloo et al., 2010; Serra et al., 2012). A range of gas morphologies is seen. In about half of the nearby ETGs with detected HI, this gas is distributed in either a disk-like morphology or a massive ring-shaped reservoir (up to 190kpc; Emonts et al., 2010). These structures are similar to the distribution of ionised gas (e.g. Morganti et al., 2006) and suggest that the different gas phases are related dynamically. In the remaining sources however there is evidence for both inflowing and outflowing gas, tidal streams and disturbed morphologies (Morganti et al., 2006) and it appears as if these disturbed morphologies may be more common in group member galaxies (Serra et al., 2012).

6.2.3 HI Absorption Studies

HI absorption against radio cores has been used to trace gas motions, with typically around a 30% detection rate in compact radio galaxies to an optical depth (τ) greater than 0.01 (e.g. van Gorkom et al., 1989). The detection fraction is however heavily dependent upon not only the intrinsic column density but also the covering fraction (c_f) of the intervening gas, that itself is dependent upon the gas morphology. Measured column densities are found to vary broadly, which may be intrinsic or perhaps at least in part due to observational effects. Indeed the measured column density is found to anti-correlate with the linear extent of the background source (Curran et al., 2013a), perhaps suggesting that uncertainties in c_f are limiting in many cases. Additionally, these same authors note that a common spin temperature (T_{spin}) is often assumed although not really justified.

From a sample of 23 sources selected from the 2Jy sample (Wall & Peacock, 1985; Tadhunter et al., 1993, 1998) and observed with the Very Large Array (VLA), Australia

Telescope Compact Array (ATCA) and Westerbork Synthesis Radio Telescope (WSRT), Morganti et al. (2001) found a detection fraction for FRIs (1 detection out of 10) consistent with the HI in these galaxies being distributed in a thin disk (see also Curran & Whiting, 2010) whereas for other radio sources the presence of a thick torus coupled with more disturbed blueshifted outflows was inferred. This mirrors the findings of Emonts et al. (2010) who find large extended FRIs to occur largely in galaxies without large ($\geq 10^8 M_\odot$) neutral gas reservoirs but also not to be associated with wet mergers. Alternatively, compact radio sources are found to preferentially occur in HI-rich (up to $2\times10^{10} M_\odot$) systems where the gas is distributed in giant tori. These authors suggest that the radio jets in these systems are confined by the large amount of gas present or alternatively that they may be fueled by different processes to the giant radio galaxies. According to AGN unification schemes (see Section 1.6), the zeroth order view is that HI absorption should be more likely in type-II AGN as our line of sight traverses the torus. Geometry is therefore often used to explain the detection fractions of HI absorption within AGN. However, that HI is detected in several types of radio-morphology systems is used as evidence against the requirement for a torus in radio AGN (e.g. Morganti et al., 2001). Alternatively it has been suggested that some of the HI non-detections could be due to the UV-continuum ionising the gas, as it appears that HI is never seen in galaxies with $L_{UV} > 10^{23}$W Hz^{-1} (Curran et al., 2008; Curran & Whiting, 2010).

Recently Gereb et al. (2014) observed a sample of 93 radio-AGN with the WSRT. Their almost 30% detection rate was comparable to previous studies, although interestingly they used a stacking technique to show that this is not purely a threshold dependent characteristic. Amongst their detected sample they found a typical τ of 0.02 whereas amongst the non-detections the limit was pushed to $\tau<0.0002$, showing there to be an intrinsic dichotomy. The diverse range of profiles seen is suggestive of multiple clouds within these systems rather than an isotropic toroidal distribution. Furthermore, the authors find that their detection fraction increases to $\approx$42% for sources that are compact in FIRST (5 arcsecond resolution White et al., 1997), and increases further to $\approx$55% if only sources that are confirmed compact on milli-arcsecond scales by the Compact Radio sources at Low-redshift (CORALZ de Vries et al., 2009) survey are considered. Additionally, a deeper τ is found for more compact sources. The authors suggest that this may

be an evolutionary effect whereby compact sources are preferentially young and that the presence of HI in these systems may trigger activity although the trend could be related to c_f.

6.2.4 Focus on BCGs

Using HI in absorption to search for the cooling gas in cluster cores has been done for many years. McNamara et al. (1990) used Arecibo and (prior to its collapse!) the Green-Bank 300-ft telescope to survey 14 CC and 2 NCCs, detecting HI against two of the CC-hosted BCG, namely MKW3s/NGC 5920 and 2A0335+096. Coupled with the detection of HI in NGC1275 (De Young et al., 1973; Crane et al., 1982; Jaffe et al., 1988), this was given as the first evidence for HI forming directly by cooling out of the cooling flow. Only a handful of other BCGs have had HI observed against them. O'Dea et al. (1994a) found a narrow ($\approx$200 km^{-1}) component that appeared redshifted with respect to the systemic velocity as well as a broader component ($\approx$400 km^{-1}) consistent with no dynamical offset in A2597. As mentioned in Chapter 5, both Hydra-A and A2597 have HI absorption against their milli-arcsecond cores as sampled by the VLBA that is consistent with being distributed in a 30pc scale-height torus (Taylor, 1996; Taylor et al., 1999b). HI is also seen in another powerful radio-BCG, Cygnus-A (Conway & Blanco, 1995), again against the central component. Other than these very powerful BCGs, few detections have been made (although there have been many limits). In a sample of flat spectrum radio sources Curran et al. (2006) observed the BCG PKS1555-140/RXJ1558-14, finding strong HI absorption against it. Véron-Cetty et al. (2000) detect a broad absorption in PKS 1353-341/RXJ1356-342 that is a large elliptical situated within an overdensity of galaxies and thus qualifies as a BCG. Note that this cluster had previously been overlooked because the bulk of the X-ray flux was incorrectly attributed to the central flat-radio spectrum AGN, rather than the extended ICM (see also Section 4.3). Once again, the HI within this BCG appears to be distributed in a disk several kiloparsecs across.

This somewhat heterogeneous sampling of BCGs is mirrored in the recovered gas properties, as they show a wide range of widths ($\approx$100-1000km s^{-1}), optical depths ($\approx$0.001-0.07) and column densities ($\approx$few$\times 10^{21-23}$ cm^{-2}). The presence of HI appears to be linked to the presence of a strong cooling flow, however there does not appear to

be a consensus on the gas dynamics, with studies claiming that the gas can be redshifted, blueshifted or at the systemic velocity. The gas in the inner-regions is expected to be clumpy and so a wide range in profile shape is expected. Within this chapter we describe our campaign to increase the number of BCGs with detected HI in absorption in order to build the statistics to be able to conclusively determine whether the material is situated in a torus or outflows/inflows.

6.3 Sample

We have thus far made 21 observations for HI absorption in BCGs. Of these, four sources observed with the VLA were re-observed with the WSRT; in two instances confirming detections and in two instances returning deeper limits. These observations have been spread over more than a decade and hence the selection criteria have evolved. We first describe the data themselves and then after this describe the sample evolution and the implications this has on the detection rate (Section 6.5.1).

6.4 Data and Reduction

6.4.1 VLA Observations

Seven sources were observed with the VLA over the period 9-12th June 1999 under project code AE130 (P.I. Edge) with the array in a hybrid A/D configuration (for sources, see Table 6.1). The data were taken with the (pre-WIDAR) VLA-correlator in right-hand circular polarisation spectral mode, with a bandwidth of 6250 kHz split across 64 channels giving a spectral resolution of $\approx$98 kHz. This narrow bandwidth meant that each observation was tuned to the expected systemic velocity and so band-centres varied slightly between $\approx$1.15-1.35 GHz.

Data were reduced using AIPS. Loading, inspection and flagging were all performed using the standard methods (see e.g. Chapter 2). Overall flux scaling was done using the primary calibrator 1331+305, with a separate calibrator observed nearby to each science target for phase calibration. However, the primary was not observed at each of the individual frequencies. The flux scale for each source was therefore set (with SETJY)

using spectral models for each of the phase calibrators fit using the contemporaneous observations in the NRAO calibrator list, with the bias accounted for by comparison to the primary. Otherwise the pseudo-continuum data were calibrated according to the standard procedures[1] and then applied to the spectral line data using TACOP. Calibrated science targets were then SPLIT off and image cubes produced with IMAGR. Spectra were extracted with ISPEC and read into IDL for further analysis.

6.4.2 ATCA Observations

Four sources were observed with the ATCA over the period 11-14th January 2011 under the project code C2152 (and observed concurrently with C1958, see Chapter 2; P.I. Edge) with the array in the ATCA-6A configuration. Data were taken with the CABB correlator (Compact Array Broadband Backend; Wilson et al., 2011), which allows for dual-mode observations in full polarisation. A 64 MHz bandwidth split over 2049 channels gives a spectral resolution of 31.2 kHz. This is supplemented by sixteen 'zoom-bands', each with 1 MHz bandwidth and a fine resolution of 0.5 kHz. These zoom bands can be placed apart within the 64 MHz bandwidth or successively, to provide up to 16 MHz worth of finely sampled spectrum. For each source we placed eight of the zoom-bands successively about the expected systemic velocity for associated HI within the system and eight were successively positioned to search for OH, although we made no detections of this and do not mention it further.

The primary ATCA calibrator (1934-638) was observed at the observing frequency of each science target and used for absolute flux calibration. Additionally, 0823-500 was observed tuned to the frequencies of RXJ1558-14 and A1348 for further verification of the flux scaling. Each of the four science targets was visited several times across a wide hour-angle range to maximise uv-coverage, with each visit sandwiched between short scans of a nearby phase calibrator. On source integration was about nine hours for each of A3112 and S555, eight hours on RXJ1558-14 and four hours on A1348. However, very bad RFI meant that significant fractions of this time were lost, most notably for RXJ1558-14 where only about three hours of integration was useable.

[1] As described in the AIPS cookbook, http://www.aips.nrao.edu/cook.html

Reduction was done using the ATNF MIRIAD package. Data were loaded and known RFI ('birdies') flagged automatically using *atlod*. The HI rest frequency was also set at this stage. Data were inspected in the usual ways and discrepant points and RFI flagged using *blflag* and *uvflag*. Significant flagging of RFI was performed manually using *blflag*. The data were then flux and phase calibrated in the usual way (see Section 2.3), using the standard MIRIAD tools (*mfcal*, *gpcal*, *gpboot* and *gpcopy*). The bandpass was calibrated by running *mfboot* on the primary calibrator (unresolved at these frequencies), with the solutions applied to the science targets. Data cubes were created, CLEANed and restored in MIRIAD. The spectra recovered from these cubes were found to still be affected by strong RFI. In each case, it was found that using the images to define the source region and then extracting spectra from the calibrated uv-files using *uvspec* produced the best results. The spectra were then read into IDL for further analysis (see also Section 6.5).

6.4.3 WSRT Observations

Ten sources were observed with the WSRT. These were split over three proposal codes: R11A/005 and R11B/024 (both P.I. Edge) that were observed between December 2010 and August 2011, and proposal code S11B/008 (P.I. Oonk) that was observed between April and December 2012. The data were taken in dual polarisation spectral mode, and had 1024 channels spread across a 20 MHz bandwidth giving a spectral resolution $\approx$19.5 kHz. As always, band centres were tuned to the expected redshifted positions of HI associated with the systemic velocities.

Data were reduced and subsequent fit parameters provided by Dr Raymond Oonk of ASTRON. Reduction was performed using the Common Astronomy Software Applications (CASA) package, utilising a script (casa_wsrt.py) developed by Dr Raymond Oonk and Dr Reinout van Weeren (previously of ASTRON, now an Einstein Fellow at Harvard CfA). Full details of this part of the data reduction will be provided in an upcoming paper, of which this chapter forms the basis.

6.5 Spectra and Results

As mentioned in the previous section, spectra from the VLA and ATCA campaigns were loaded into IDL for plotting and further analysis. For each spectrum we fit the line free channels with a second order polynomial using the IDL routine *'POLY_FIT'*, in order to remove the continuum. In most instances the continuum was well fit by a power-law, but the addition of the quadratic term allowed better removal of any remaining bandpass errors. We present the resultant spectra for the VLA data in Figures 6.1 and 6.2. The ATCA spectra are presented in Figure 6.3. On each of these spectra we show the position of the redshifted systemic position for HI as well as the continuum flux level at the position of the line minimum (or the systemic HI position for non-detections). Note that spectra for the WSRT data were created by Dr Raymond Oonk and are not presented here although will be included in the subsequent paper.

The HI absorption troughs in A2390 and Z8276 were each fitted with a single gaussian component using the IDL routine *'GAUSSFIT'*. The absorption profile seen in RXJ1558-14 was better fitted using a two component model, which was performed using the IDL routine *'CURVEFIT'* (see Figure 6.4). The RMS for each spectrum was measured and a 3σ detection limit imposed for sources with no detected absorption. In Table 6.1 we present the recovered optical depths and linewidths. Note that parameters reported for the sources observed with the WSRT were determined by Dr Raymond Oonk.

Column densities (in cm^{-2}) were calculated according to:

$$N_{HI} = 1.823 \times 10^{18} \frac{T_{spin}}{c_f} \int \tau(v)\, dv \tag{6.5.1}$$

where c_f is the covering fraction, T_{spin} the spin temperature and the integrated optical depth is in km/s (Wolfe & Burbidge, 1975; Gereb et al., 2014). We used a consistent spin temperature of 100K for our calculations of N_{HI}. This is believed to be representative for gas outside the immediate nuclear vicinity (e.g. Taylor et al., 1999b) as may be sampled by our arcsecond scale resolution observations. However, if the gas is indeed situated very close to the central SMBH then a value of 8000K may be better (e.g Conway & Blanco, 1995), in which case the true column densities would be significantly higher than calculated herein. We assume a covering fraction of unity although we note that this is

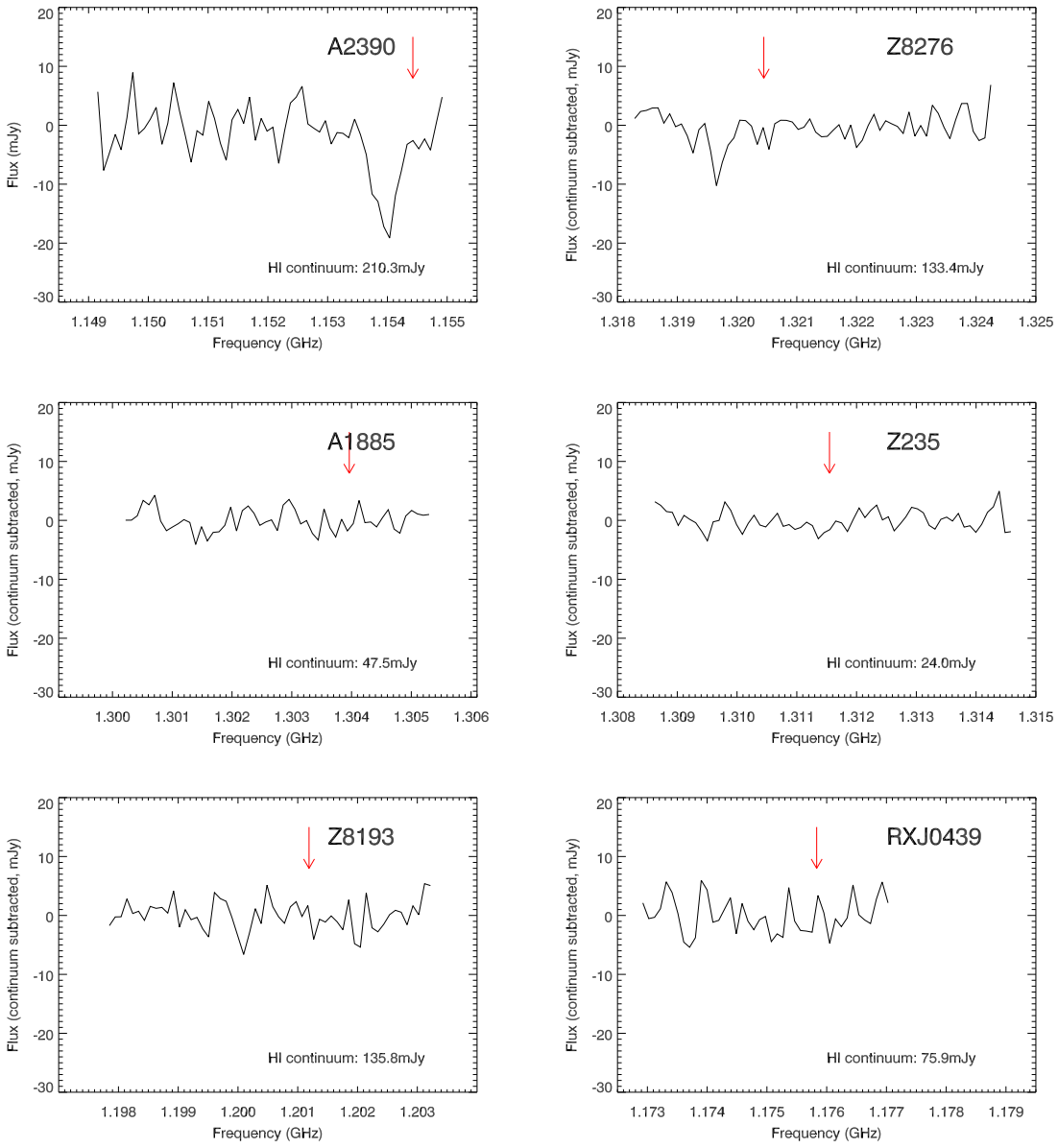

Figure 6.1: VLA spectra at the redshifted positions for HI absorption in 6 of our 7 sources observed with the VLA (see also Figure 6.2). Red arrows indicate the systemic poition for redshifted HI. Clear detections are made for A2390 and Z8276 that were corroborated by follow-up detections with the WSRT. There is potentially a low significance detection in Z8193 although this is consistent with noise and hence requires deeper follow-up.

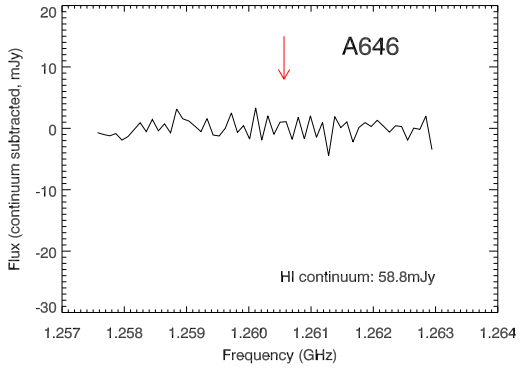

Figure 6.2: VLA spectrum of A646, where the red arrow indicates the expected systemic redshifted position for HI absorption. See also Figure 6.1.

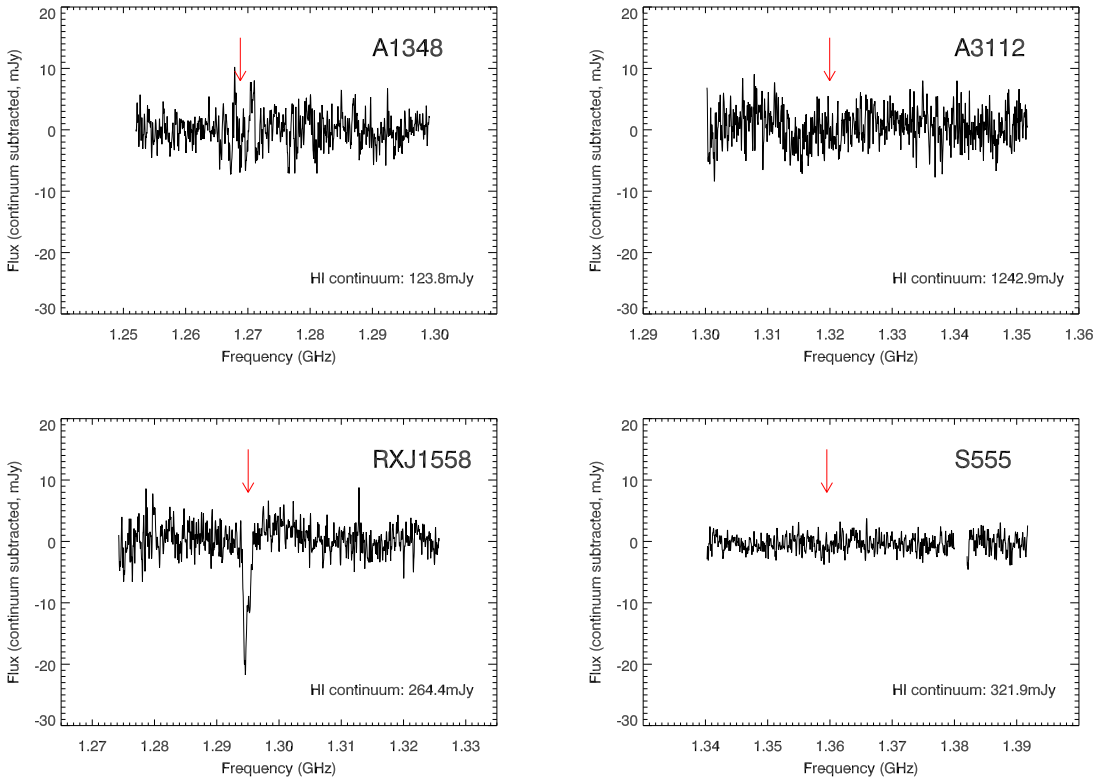

Figure 6.3: ATCA spectra at the redshifted HI for the four sources observed in project C2152. Red arrows indicate the expected systemic position of HI absorption. The wider 64 MHz CABB spectral bands are displayed here although note that these are entirely consistent with the higher resolution zoom band recovered spectra.

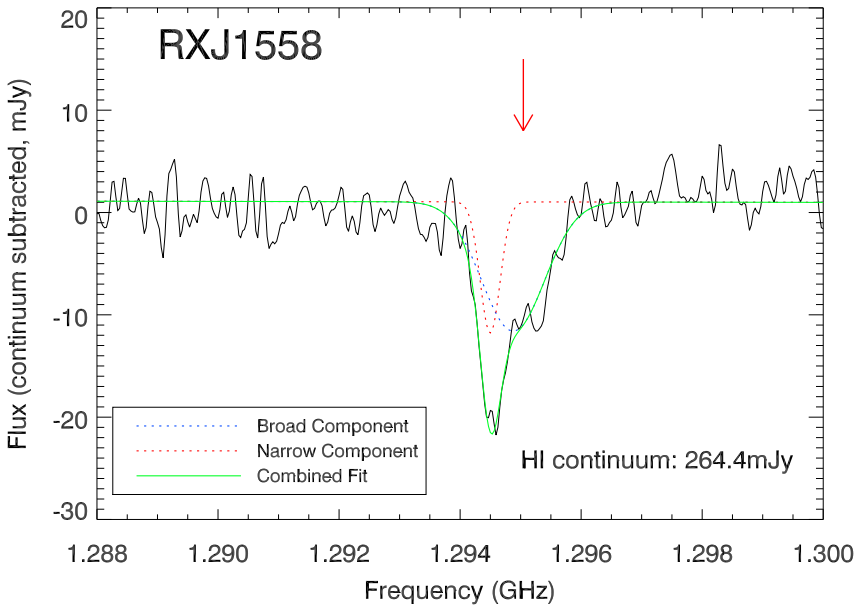

Figure 6.4: Two Gaussian fit to HI absorption line profile in RXJ1558-14, showing there to be a broad component centred near to the systemic velocity and a narrow component that is redshifted with respect to this.

likely to be highly uncertain and almost certainly an overestimate (see also Section 6.7). Calculated column densities are reported in Table 6.1. In systems without detected HI absorption we take a 3σ limit on tau and assume a linewidth $<$200 km/s.

6.5.1 Detection Rates - Using Radio Priors to Increase Detection Likelihood

The earlier data taken with the VLA targeted flat spectrum radio BCGs, returning a detection rate of 2/7. Although these predated the SED decompositions (Chapter 2), their flat spectrum nature means that these were typically core dominated systems. However, the detection rate is still relatively low although this is perhaps partly due to the much higher detection limits and narrow sampled bandwidths when compared to our later observations, coupled to the fairly low continuum fluxes in some cases.

The ATCA targets were selected as a result of their bright, unresolved on arcsecond scale, continuum fluxes. One source was detected, RXJ1558-14, although the presence of HI in this system was previously known (Curran et al., 2006) and hence our success

Table 6.1: The sources targeted for HI absorption with recovered parameters. Sources observed with the VLA were under project code AE130 and were performed June 1999, those with ATCA were code C2152 and performed January 2011. Sources observed with the WSRT were observed under proposal codes R11A/005 and R11B/024 (both P.I. Edge) between December 2010 and August 2011, and proposal code S11B/008 (P.I. Oonk) between April and December 2012. Note that all of the WSRT observations were reduced by Dr. Raymond Oonk of ASTRON - they are not the author's own work. BCG redshifts are from: [1] VIMOS, Hamer *et al* 2014 submitted; [2] CO, Edge *et al* 2015 in prep.; [3] SDSS (e.g. Ahn et al., 2014); [4] Wilman et al. (2006); [5] Crawford et al. (1999). *These values are for tentative detections and were measured from plots.

Array	Source	Redshift	RMS (mJy/bm/bin)	τ (peak)	FWHM (km/s)	N(HI) 1×10^{20} cm^{-2}
VLA	A2390	0.2304[1]	3.75	0.084 ± 0.011	154.0 ± 24.9	25.1 ± 7.3
VLA	Z8276	0.0757[2]	2.15	0.072 ± 0.015	58.2 ± 14.0	8.1 ± 3.7
VLA	A1885	0.0893[3]	1.89	<0.131	<200	<50.8
VLA	Z8193	0.1825[4]	2.58	<0.063	<200	<24.5
VLA	RXJ0439+05	0.2076[1]	3.07	<0.133	<200	<51.6
VLA	A646	0.1271[3]	1.55	<0.087	<200	<33.8
VLA	Z235	0.083[5]	1.64	<0.226	<200	<87.7
ATCA	RXJ1558-14					
ATCA	1-Gaussian	0.0968[1]	2.23	0.067 ± 0.002	118.0 ± 4.1	15.3 ± 1.0
ATCA	Broad	0.0968[1]	2.23	0.048 ± 0.002	132.6 ± 6.0	12.4 ± 1.1
ATCA	Narrow	0.0968[1]	2.23	0.048 ± 0.003	41.8 ± 3.5	3.9 ± 0.6
ATCA	Combined	0.0968[1]	2.23	0.082 ± 0.019	Combination	16.3 ± 1.3
ATCA	A3112	0.0760[1]	2.80	<0.007	<200	<2.7
ATCA	A1348	0.1199[1]	2.54	<0.068	<200	<26.4
ATCA	S555	0.0448[1]	1.23	<0.013	<200	<5.0
WSRT	A1795	0.062[5]	0.75	0.0051	600	5.9
WSRT	RXJ1350+09	0.1325[3]	0.25	0.0054	280	2.9
WSRT	A2390	0.2304[1]	0.84	0.0787	190	29.0
WSRT	Z8193	0.1825[4]	0.36	0.015*	217*	6.3*
WSRT	NGC6338	0.0273[3]	1.20	0.052*	257*	25.9*
WSRT	RXJ1832+68	0.2049[2]	0.31	0.011*	200*	4.3*
WSRT	Z8276	0.0757[2]	2.17	0.082*	62.5*	9.9*
WSRT	NGC4104	0.0282[3]	0.25	<0.206	<200	<80.0
WSRT	RXJ0000+08	0.0387[2]	0.27	<0.012	<200	<4.6
WSRT	Z235	0.083[5]	0.68	<0.059	<200	<22.9

rate for blind targets was 0/3. Although the three other sources were all unresolved on arcsecond scales, we can now see with the hindsight of the SED decompositions performed in Chapter 2 that they are dominated by their non-core emission. It is therefore unsurprising that we make non-detections in these sources as the HI gas is believed to most likely be distributed on small scales close to the nucleus. Ideally to observe this we would like a pencil-beam observation through the intervening absorbers as is essentially provided in highly core dominated systems where the majority of the unresolved emission on arcsecond scales is actually distributed on *milli-arcsecond* scales (see Chapter 5), at the frequency of HI. That these sources are non-core dominated suggests that we should expect most of the emission to be extended on intermediate scales and therefore the absorption signal of any intervening gas clouds is highly likely to be diluted by the more extended continuum.

With WSRT we made three clear detections, four tentatives (of which one, Z8276, was also detected with the VLA and hence we now claim to be a secure detection) and in three sources HI remains undetected. Including the tentatives we therefore have a high detection rate of 7/10. These sources were selected for observation *during* the work on spectral decompositions presented in previous chapters. This selection was therefore dynamic and sought to select targets with high core dominance. The much elevated detection rates show not only that the gas is indeed most likely to be centrally located but also that pre-selection of targets based on core dominance determined using the methods laid out within this thesis promises the best rate of success for finding cold absorbers. Such target selection can therefore aid in building a larger sample of HI absorption systems to better understand the distribution and dynamics of this gas that will ultimately fuel the AGN.

6.5.2 Literature Detections

We add to our sample the five BCGs that have unambiguously had HI detected in absorption against them (see Table 6.2). Note that we do not include the less pronounced detections in MKW3s and 2A0335+096 (McNamara et al., 1990) that were taken with single dish observations.

Both A2597 and NGC1275 had HI detected with the VLA (O'Dea et al., 1994a; Jaffe, 1990, respectively), and in both instances there is a broad component seen centred on the

systemic velocity and a narrower component that appears to be redshifted relative to the BCG, which is similar to the profile seen in our observation of RXJ1558-14 (see Figure 6.4).

PKS 1353-341 and Cygnus-A are both reported in Table 6.2 as being fitted only by a single Gaussian, which in both cases appears to be centred near to the systemic velocity. However, in both instances the detected lines can also be fitted with two Gaussians. For Cygnus-A (Conway & Blanco, 1995) these appear to be of roughly similar width and distributed slightly to either side of the systemic velocity. Using the VLBA to observe the core regions of Cygnus-A on milli-arcsecond scales, Struve & Conway (2010) recover a broad (231km/s) component and a narrow ($<$30km/s) component slightly redshifted ($\approx$+50km/s) relative to this. For PKS 1353-341, Véron-Cetty et al. (2000) state that it can be fit with a deeper, broader component at -125 km/s and a shallower, narrow component at +75 km/s. Considering their Figure 4, an alternative interpretation would be the presence of a shallower broad component centred on the optical velocity (and so similar to in A2597, NGC1275 and RXJ1558-14) with a deeper, narrow component that is slightly *blueshifted* relative to the systemic velocity. It should be noted however that the systemic redshift for this BCG is not certain, and these shifts are actually consistent with the systemic velocity within error.

The final BCG where HI absorption is known, Hydra-A, was observed in a detection experiment with the VLA D-array and then in much higher resolution follow-up with the VLBA by Taylor (1996). A low N_{HI} was detected in the low resolution VLA detection experiment (see Table 6.2), although it was noted that the observation was being diluted by the strong extended emission within the system. In the higher resolution follow-up with the VLBA, absorption was detected against the nucleus and the inner-jets on milli-arcsecond scales. The much higher column densities recovered with the VLBA are indicative of the covering fraction being higher, as is expected for centrally located gas if observed against only the central continuum (as is the case with VLBI observations). Intermediate between these observations in terms of resolution, Dwarakanath et al. (1995) observed Hydra-A with the VLA-A array. Absorption was found only against the central component, and appeared to be composed of multiple components with a combined linewidth of $\approx$100km/s and a $\tau\approx$0.1-0.5. This gives an approximate column density of

Table 6.2: HI absorption parameters for five additional secure detections from the literature. Note that we have taken τ and FWHM measurements from the respective papers and recalculated N(HI) values assuming a consistent T_{spin}=100K with c_f=1 and therefore in some cases our column densities differ from those reported initially. References are - 1, O'Dea et al. (1994a); 2, Jaffe (1990); 3, Véron-Cetty et al. (2000); 4, Conway & Blanco (1995); 5, Taylor (1996); 6, Dwarakanath et al. (1995).

Array	Source	Redshift	τ (peak)	FWHM (km/s)	N(HI) 1×10^{20} cm^{-2}	Ref
VLA	A2597					1
VLA	Broad	0.0823	0.0056	412	4.5	
VLA	Narrow	0.0823	0.0187	221	8.0	
VLA	NGC1275					2
VLA	Broad	0.0176	0.0021	477	1.9	
VLA	Narrow	0.0176	0.0009	66	0.1	
ATCA	PKS 1353-341	0.2227	0.125	155.4	37.8	3
VLA	Cygnus-A	0.0565	0.12	270	62.9	4
VLBA	Hydra-A					5
VLBA	North Inner Jet	0.0549	0.46	38	33.9	
VLBA	VLBA Nucleus	0.0549	0.99	78	149.8	
VLBA	South Inner Jet	0.0549	0.55	57	60.8	
VLA D-array	Core region	0.0549	0.0015	150	0.4	
VLA A-array	Core region	0.0549	0.1 - 0.5	100	5.8	6

5.8×10^{20} cm^{-2} that is intermediate between the VLA-D array and VLBA recovered values (see Table 6.2).

It is worth noting that the sources within our sample for which we recover the highest N_{HI} values are typically found to be those that have the most core dominated continua. The commonly used assumption of unity covering fraction is expected to be erroneous, and so the actual column densities within these sources are expected to be higher than commonly reported. Ultimately, both T_{spin} and c_f are highly uncertain parameters and so any calculated column densities are likely to be similarly uncertain.

We take the reported systemic redshifts, optical depths and linewidths as reported in the papers referenced in Table 6.2. From these we recalculate the column densities assuming a constant 100K and hence our values in some cases differ from those in the respective papers.

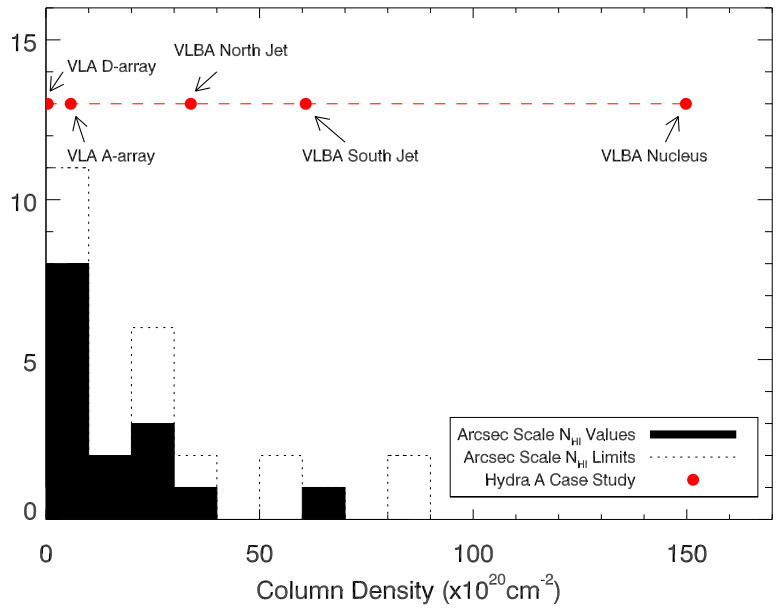

Figure 6.5: Distribution of the peak HI column densities for our full sample of sources (including the 5 literature detections). The values derived from the arcsecond scale observations are represented as a histogram. Note that for sources with both a broad and a narrow component, the *combined* column density at the position of the peak is used. Additionally, Hydra A is shown as a case study with the recovered column densities from observations of the central regions with the VLA-D (resolution≈45 arcsec), VLA-A (≈1 arcsec) and VLBA (≈5 milli-arcsec) shown. The large range in column densities seen at these different resolutions highlight the importance of the covering fraction and shows that even within the inner-core, the distribution of HI gas is inhomogeneous.

6.6 Discussion

6.6.1 Column Densities

We show in Figure 6.5 the distribution of calculated N_{HI} values for the combined sample of our targeted sources and the literature detections. We also show as a case study the range of recovered column densities reported towards Hydra-A, as seen with arrays of varying spatial resolution. For the sources observed on arcsecond scales we see a reasonably low distribution, with only two sources (PKS 1353-341 and Cygnus-A) having $N_{HI} > 3.0 \times 10^{21} cm^{-2}$. This low range of column densities means that for any given sample we expect only to be seeing the tail of systems where the gas content is either high or favourably aligned and hence pre-selection of the most likely targets is important.

We note that all but one of the sources where we have made pointed detections of HI

absorption are in core dominated systems (see Chaper 3) and in all instances have the majority of their arcsecond scale flux distributed on milli-arcsecond scales (with greater than 80% recovered fluxes in all cases except A2390 where a limit of $>$61% was recovered, see Chapter 5). The exception to this is A1795, where the integrated SED is dominated by the non-core. However, importantly this source is resolved on arcsecond scales and hence the central component can be isolated. Previous VLBA observations of this source (Liuzzo et al., 2009) have shown it to contain considerable extent on milli-arcsecond scales, with a Z-shaped inner-morphology. The scenario of A1795 is repeated in the literature detections of Hydra-A, NGC1275, Cygnus-A and A2597, which although all having integrated fluxes at $\leq$1.4 GHz being dominated by their extended emission, this extended emission is resolved and hence clear sightlines to the core regions are available. PKS 1353-341 appears in the Second VLBA Calibrator Survey (VCS2 Fomalont et al., 2003). On milli-arcsecond scales the source is observed to have multiple one-sided components at L-band and has $\approx$60% of its arcsecond scale continuum flux (at both 1.4 and 8.4 GHz Condon et al., 1998; Murphy et al., 2010, respectively) recovered, therefore confirming the core dominated nature of this source.

Considering the above, it shows that the covering fraction is very important for the detection of HI absorption. Using the example of Hydra-A, as discussed in Section 6.5.2 the measured N_{HI} increases as progressively smaller angular scales are looked at, hence as the dilution by continuum not intersected by HI clouds goes down. That we detect HI in core dominated systems on its own does not unambiguously determine that the c_f is paramount. Indeed, Gereb et al. (2014) suggest that a relationship for higher HI gas masses in more compact radio sources may suggest that the HI is triggering the behaviour and hence the small extent is dependent only on age. However we have previously shown that the activity in BCGs is persistent over long timescales and coupled with the case study of Hydra-A we therefore claim that it is the covering fraction that is the dominant effect. It is worth noting also that the range of column densities recovered in Hydra-A is wider than the full distribution of column densities seen with arcsecond scale resolutions. Any inferred gas masses are therefore likely to be highly uncertain, with the majority of reported estimates perhaps best interpreted as lower limits.

6.6.2 Velocity Offsets and Gas Distribution

In addition to the covering fraction, the distribution of the HI gas is important for the likelihood of detection. In Figure 6.6 we plot the offsets from the systemic velocity of the recovered HI absorption profiles, where the width of each line corresponds to its FWHM (see Table 6.3). The typical uncertainties on our systemic velocities are $\pm$100km/s. In all cases where the HI detection is secure and the systemic velocity is well determined, we see that the absorption is either at the systemic position or else slightly redshifted. Furthermore, for the three sources (NGC1275, A2597 and RXJ1558-14) where both a broad and a narrower component could be determined we see that the broader component is consistent with the systemic velocity whereas the narrower component is redshifted relative to this. Additionally, whilst we see only a relatively narrow (154km/s) redshifted (+145km/s) component in A2390, a broad (465km/s) component consistent with the systemic velocity was found in a thus-far unpublished Arecibo detection by Salter *et al.* in 2004 (see http://www.naic.edu/ csalter/a2390/poster.ps) and is included in Figure 6.3.

These observations begin to point towards a consistent picture. The distribution of the broad HI absorption on the milli-arcsecond scales in A2597 (Taylor et al., 1999b; Araya et al., 2010) and Cygnus-A (Struve & Conway, 2010), with the highest column densities seen against the counter-jet and nucleus as opposed to the forward jet, have been argued to be most naturally explained by the presence of a large scale torus. Whilst we do not have HI observations at VLBI resolutions for our sample, all thirteen BCGs with HI detected against them have had their milli-arcsecond scale continuum morphologies observed with the VLBA (e.g. Chapter 5; Taylor, 1996; Taylor et al., 1999b; Fomalont et al., 2003; Taylor et al., 2006a; Liuzzo et al., 2009, 2010; Araya et al., 2010; Struve & Conway, 2010; Suzuki et al., 2012). All of these sources, except Z8276 where only a narrow ($\approx$60km/s) absorption profile is seen, show resolved structure on milli-arcsecond scales. Furthermore, all but PKS1353-341, RXJ1350+09 and NGC6338 show *two-sided* structure on milli-arcsecond scales, which naturally includes all of the sources where a broad and narrow component is seen. This suggests a proportionality between the extent of the core structure on milli-arcsecond scales and the resultant width of any lines recovered. This is naturally explained since the more sightlines to extended sources (on milli-arcsecond scales) will tend to intersect multiple clouds with a range of velocities, which therefore

Table 6.3: Velocity offsets for our detected HI absorption systems in addition to the literature detections. In instances where the HI is consistent with no offset from the otherwise determined systemic velocity then we report zero offset. Where a source is detected with both the VLA and WSRT observations, we report only the velocity offsets as calculated using the VLA data - in both cases these are consistent with the WSRT measurements. Redshift references are as for Table 6.1. [1] There was a broad component detected in an Arecibo observation by Salter *et al* in 2004 observation (see Section 6.6.2) that is not detected in our observations. Note that we have shifted this velocity offset to be consistent with our slightly different redshift for A2390. [2]Offsets for peak of single component fits within given references.

Source	Systemic Redshift	Velocity Offset (km/s)	Ref
A2390 - Broad	0.2304	-110	Salter (Arecibo 2004)[1]
A2390	0.2304	+145	VLA - this work
Z8276	0.0757	+219	VLA - this work
A1795	0.062	Systemic	WSRT - this work
RXJ1350+09	0.1325	Systemic	WSRT - this work
Z8193	0.1825	Systemic	WSRT - this work
NGC6338	0.0273	-200	WSRT - this work
RXJ1832+68	0.2049	-773	WSRT - this work
RXJ1558-14			
Broad Component	0.0968	+43.0 (systemic)	ATCA - this work
Narrow Component	0.0968	+159.7	ATCA - this work
	Literature Detections		
A2597			O'Dea et al. (1994a)
Broad Component	0.0823	Systemic	
Narrow Component	0.0823	+250	
NGC1275			Jaffe (1990)
Broad Component	0.0176	Systemic	
Narrow Component	0.0176	+50	
PKS 1353-341	0.2225	-52.8[2]	Véron-Cetty et al. (2000)
Cygnus-A	0.0565	Systemic[2]	Conway & Blanco (1995)
Hydra-A Core	0.0549	Systemic	Taylor (1996)

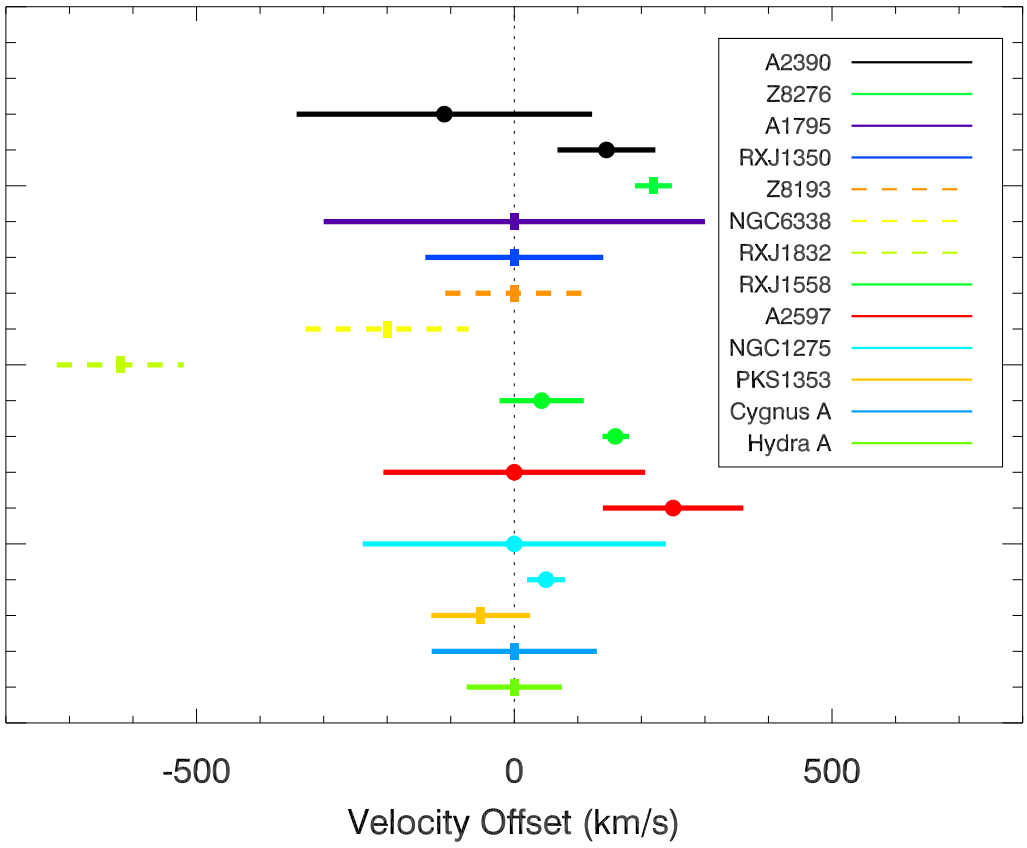

Figure 6.6: Velocity offsets for the detected HI absorption, ordered by the positions they appear in Table 6.3. The widths of the lines correspond to the FWHMs shown in Tables 6.1 and 6.2. The width for Hydra-A corresponds to the integrated width detected with the VLA-D by Taylor (1996). Tentative detections with uncertain systemic velocities are shown as dashed lines. Centroids are given as standing bars for sources with only one clear component and filled circles for sources with both a broad and narrow component. Note that in all four instances where both a narrow and a broad component were detected in absorption (A2390, RXJ1558, A2597 and NGC1275) the broader component is consistent with the systemic velocity and the narrower component is redshifted relative to this. Note that the typical uncertainties on our systemic velocities are $\pm$100km/s.

leads to the naturally broader absorption profile. Conversely, sources with unresolved extent on milli-arcsecond scales are more likely to intersect only a single (or very few) cloud(s) and hence give a narrower profile, such as in Z8276. This is therefore broadly consistent with the majority of absorption being attributable to a central toroidal structure and the narrower components in each instance perhaps attributable to infalling clouds going on to feed the AGN or replenish this torus. Indeed, Struve & Conway (2010) calculate that the gas mass inferred to be in the central torus is not adequate to power the currently high activity seen in Cygnus-A indefinitely but that the narrower components are consistent with this structure being replenished by infalling material from further out.

This model, whilst speculative, is entirely consistent with the behaviour of BCGs as previously shown throughout this thesis. Persistent core activity can be fueled by a central torus of cold material, which is regularly replenished by additional cold material forming out of the residual cooling flow. This does not then preclude denser clouds raining down onto the BCG that can power higher periods of core activity - indeed it is intriguing that the four BCGs (A2390, NGC1275, A2597 and RXJ1558) seen to have both a broad *and* a narrow component are currently seen to be experiencing strong central activity (see Chapter 4). Observing this central gas reservoir is however dependent on having a direct sightline to the central regions without too much diluting emission on larger scales. Likewise, that not all core dominated systems are observed to have HI absorption shows that the gas is not isotropic within the central regions and hence a clumpy torus model with additional dense, infalling clouds is favoured.

6.7 Conclusions

Within this chapter we have presented spectra and parameters for observations searching for redshifted HI in absorption against the radio continua of seventeen BCGs. We make five clear detections, three tentative detections and place upper limits on the column density of HI towards the remaining nine. We add to this sample the five clear HI absorption detections against BCGs in the literature to enable us to consider the HI absorption properties in a sample of more than ten BCGs for the first time. We find:

- The detection rate of HI absorption is highly dependent upon the radio continuum

distribution and origin - core dominated systems where the majority of the emission is on milli-arcsecond scales are the most suitable targets for pencil-beam observations through intervening clouds. Observing emission that is unresolved at the resolution is not adequate, the emission must be genuinely on physically small scales.

- Only a narrow range of column densities are found towards BCGs, with the majority of systems having $N_{HI} < 3.0 \times 10^{21} cm^{-2}$.

- The column density is a strong function of the scale of the central radio source, in conjunction with the amount of diluting continuum within the beam.

- In all clear cases where HI absorption has been observed with a secure systemic redshift known, the absorption is either systemic or redshifted. Typically, broader components are systemic whereas redshifted components tend to be narrower. This is consistent with cooled material from the cooling flow feeding the AGN, perhaps via an intermediary torus in some cases.

- HI absorption is not ubiquitous in core dominated BCGs. The material therefore is likely to be in clouds with high density but low covering fractions rather than distributed isotropically throughout the core.

We have shown that careful pre-selection of targets can greatly enhance the detection rate of HI absorption in radio sources and have used this to more than double the number of HI absorption systems known in BCGs. Future large scale HI surveys can benefit from this pre-selection, in addition to considering the core to non-core breakdown when interpreting observed HI absorption.

CHAPTER 7

Conclusions and Future Work

7.1 Overview

Within this thesis we have studied the radio properties of a large sample of BCGs, comprehensively looking at this population of sources at a variety of radio frequencies, time and spatial scales. We have considered the nature of their radio emission over a broad range of radio powers; connecting the rich variety of behaviours seen to the wider topic of 'AGN Feedback'. In this final chapter we re-iterate some of the major conclusions and new findings that have been discovered during this study and attempt to link these to provide a full picture of the radio properties of BCGs. Beyond this we then consider what is still unknown and outline future work that is planned to address these remaining questions.

7.2 General Radio Properties of BCGs

Having described our sample selection of galaxy clusters in Chapter 2 and decomposing the radio emission from this selection of BCGs into active and inactive components, in Chapter 3 we considered the radio properties of the general BCG population. We found that the radio loudness of central cluster galaxies is a strong function of the cluster type, with over 85% of LE-BCGs being radio detected compared to only about half of NLE-BCGs. It was shown that not only is the prevalence of radio activity higher in cool-core clusters, the actual radio power is significantly higher with around half of LE-BCGs hosting a radio source more powerful than 10^{24}WHz^{-1} at 1.4 GHz whereas only around 15% are similarly radio-powerful in NLEs.

Importantly we showed for the first time in a large sample of clusters unbiased by radio priors, that not only the prevalence and power of radio AGN in BCGs depends on the wider cluster environment but that the *nature* of the observed radio emission differs between strong cool-core and non strong cool-core clusters. CC-hosted BCGs are typified by the presence of *ongoing* activity within their centres that manifests as a flattened or inverted component in the radio SEDs that is often not apparent at frequencies below a few GHz. We find that 60.2% of LE BCGs in our sample contain a distinguishable core of which ≈83.1% are more powerful than 10^{23}WHz^{-1}. Conversely, only 11.6% of our NLE BCGs contain a distinguishable core, with only around 43.1% of these (i.e. only 5.0% of our NLE BCGs) containing an active core of greater than 10^{23}WHz^{-1}. It is the presence of this *active* component that shows unambiguously that BCGs in CC-clusters are constantly active, explaining how they can regulate their environments on gigayear timescales.

We showed that *both* the ageing non-core radio component and the currently active core components correlate with the long-term power of the AGN as derived by measuring X-ray cavity powers. This is evidence for the consistency of this activity over at least the last few hundred megayears and most likely longer. By considering beyond the monochromatic radio luminosities of BCGs we showed that radio emission as a tracer of AGN activity benefits from full consideration of the timescales on which it was accelerated and subsequently aged.

7.3 High Frequency Properties and Variability

Having identified that it is the presence of an active core component that constitutes the main difference between LE and NLE BCGs, in Chapter 4 we selected a sub-sample of 35 BCGs to study at higher radio frequencies (15 – 353 GHz) where this core component dominates. These were all hosted by cool-core clusters and allowed us to study the short-term variability of cluster centre AGN that are known to be undertaking current AGN feedback.

We determined that ≥15.1% of cool-core hosted BCGs contain a radio source greater than 3mJy at 150 GHz (equivalent to a radio power of $\approx 1.2\times10^{23}$W Hz^{-1} at our median

redshift of 0.126) and that more than half of these contain a distinguishable peaked component to their spectra with a turnover frequency above 2 GHz. This constitutes 3.4% of our observable parent sample containing peaked radio components, increasing to $\geq$8.5% if only cool-core clusters are considered. Coupled to the high incidence of distinguishable core components in LE-BCGs found in Chapter 3 this suggests that more than half of all cool-core clusters with bright 150 GHz central point sources have spectra whereby even well-determined spectral indices below a few GHz would give very large underestimates of the flux at 150 GHz if extrapolated. These therefore constitute a potential contaminant for SZ surveys, as these sources can wipe out any SZ decrements if not fully accounted for.

The peaked core components behave similarly to the GPS/HFP populations that are usually interpreted as young radio sources. That these peaked components are usually accompanied by steeper spectrum power-law emission at lower frequencies suggests that BCGs show regularly restarted, ongoing activity.

BCGs are not found to show strong short-term (week to month) variability at 15 GHz, with a typical limit of $<$10% indicating steady accretion over these timescales. We also limit the typical variability of BCGs to less than 35% on 6 month timescales at 150 GHz, though it is shown that sources *can* vary over this time-frame and at this frequency which shows the emission to originate from within the inner 0.01 pc of the AGN. However, we show that sources can show steady variation at 15 GHz over 1-5 year timescales, typically with less than 10% per annum, but ranging up to 20% pa. Such variability within cluster cores on relatively short time-frames (compared to the tens to hundreds of megayears X-ray cavity inflation times) highlights the importance of considering emission timescales when studying the effects of AGN activity.

Tentative evidence is presented that the radio spectra of BCGs may contain a hitherto unseen component that becomes prevalent at roughly mm wavelengths. This component may be attributable to a naked ADAF. Such a component would constitute the first time that such activity has been identified beyond the local extragalactic neighbourhood (where similar spectral components have been seen in LLAGN). This component is difficult to observe and requires finely tuned conditions to be observable. Wide, deep mm observations of non-dusty galaxies that are low power radio sources in the more typical GHz

range are essentially unexplored. If the potential ADAF component that we find in our BCGs is found to be ubiquitous in low accretion efficiency AGN then this would have wide-reaching consequences as a contaminant in SZ and CMB power-spectrum observations, star formation studies, the radio power of non-jetted AGN and beyond.

7.4 Core Properties on Milli-arcsecond Scales

In Chapter 5 we examined the milli-arcsecond scale properties of a sample of 59 cool-core hosted BCGs that have been observed with the VLBA. This constitutes the first half of a larger survey that is providing a census of the small scale nature of these sources. Initially we use these direct measurements of the central regions to verify our core component decompositions from Chapter 2.

From the initial sample of 59 sources we have already shown there to be a wide variety of parsec scale morphologies within CC-cluster cores; including unresolved, one-sided, two-sided and more amorphous structures. This range shows that there is likely to be a diverse variety in the initial launching conditions and inner-environment within these clusters. We recover flux on parsec-scales in $\approx$90% (53/59) of our targeted BCGs, including 100% of the sources where a core component was predicted, with the non-detections consistent with the expected limits. Whilst this is not the full sample, that we identify $>$60% of BCGs to have distinguishable core components in Chapter 3 leads us to suggest that a similarly high ($>$60%, although less than unity) fraction of CC-hosted BCGs are expected to have recoverable ($>$0.4mJy) flux on milli-arcsecond scales. In particular, even for systems whose large-scale integrated radio emission is dominated by non-core emission, the large number of unresolved sources that we find supports the conclusions that persistent low level core activity is near ubiquitous in cool-core clusters.

No evidence is found for small-separation dual SMBH being common in BCGs. We additionally place a sub-sample of our VLBA observed clusters, which also have high-resolution Chandra X-ray observations, onto the Fundamental Plane of Black Hole Activity. This suggests that BCGs are in most cases inefficiently accreting systems, whilst also confirming the outlying radiatively efficient accretion nature of E1821+644. The position of the BCGs on this plane also supports previously found conclusions (Hlavacek-

Larrondo et al., 2012b) that these galaxies may in fact host ultra-massive ($>10^{10}M_{\odot}$) black holes.

7.5 HI Absorption within BCGs

Understanding not only the nature of the AGN-originated radio emission within BCGs, but also what ultimately fuels this AGN activity, is paramount for fully deciphering the processes that shape galaxy clusters as well as AGN activity globally. As part of a large ongoing campaign to provide a full census of the gas and dust properties within BCGs (see Section 6.2.1), we in Chapter 6 present a search for HI absorption against BCGs. This provides the best method for sampling the cold gas in the vicinity of the central black hole that is ultimately believed to power the AGN.

Using sample selection techniques that utilise the previous findings of this thesis, we successfully use the VLA, ATCA and WSRT to more than double the number of known HI absorption systems in BCGs. Combining our new detections with those previously known from the literature, we demonstrate that a narrow range of column densities is found and that the recovered values are critically dependent on the physical extent of the central radio source within the BCG and the amount of extended, diluting continuum emission.

We show that detection of HI absorption in BCGs is dependent on their core dominance but that it is not ubiquitous in core dominated BCGs. Furthermore, where clear detections are found, we typically find that broad components are consistent with the systemic velocity of the systems whereas narrower components are typically mildly redshifted. This is consistent with cooled material from the cooling flow fueling the AGN, but that this material is not isotropic within the core. Instead it is most likely distributed in dense clouds with a low covering fraction that may in some cases be distributed in a clumpy torus.

7.6 Future work

The work contained within this thesis has greatly expanded our understanding of the radio properties of BCGs. However, the findings raise further questions and much work remains to fully elucidate the feedback processes at play within cluster cores. The most immediate undertakings are the conversion of the findings of Chapter 6 into a paper to be published, and the addition of the 76 further BCGs that have been observed with the VLBA to those presented in Chapter 5. This VLBA sample will then also be presented in the form of a paper and represent, by far, the largest consensus of the parsec-scale radio properties of BCGs.

The timing of this thesis coincides with a new 'golden-age' for radio astronomy. Several Square Kilometre Array (SKA, e.g. Dewdney et al., 2009) pathfinder and precursor facilities are either currently, or soon to be, operating. These include, but are not limited to - the Australian SKA Pathfinder (ASKAP, e.g. Johnston et al., 2008), the MeerKAT Karoo Array Telescope (MeerKAT, e.g. Booth et al., 2009), Murchison Widefield Array (MWA, e.g. Lonsdale et al., 2009; Tingay et al., 2013) and the Low-Frequency Array (LOFAR, e.g. van Haarlem et al., 2013). Each of these facilities represents huge advancements in technology and capability. Combined they will, ultimately along with the SKA, perform many wide, deep surveys of the radio sky at multiple scales and frequencies. The findings of this thesis will not only aid in the interpretation of this huge upcoming data-set, but also provide a foundation by which radio AGN - not only in BCGs but everywhere - can be better understood. Of particular relevance to furthering the work in this thesis, the Multifrequency Snapshot Sky Survey (MSSS; Heald & LOFAR Collaboration, 2013, 2014) currently being undertaken with LOFAR will provide a comprehensive low-frequency (30 – 180 MHz) survey of the northern radio sky at ≈arcminute resolution. Subsequent LOFAR survys should then reach higher resolutions (1 – 2 arcsecond). Cross-matching these surveys with our sample will allow proper characterisation of the non-core components in this large sample of BCGs, which will fully uncover the amorphous/mini-halo problem. In the Southern Hemisphere, the First Large Absorption Survey in HI (FLASH[1]) survey will sample thousands of sightlines, using ASKAP's wide bandwidth to detect HI

[1] http://www.caastro.org/research/evolving/flash

in absorption to redshift 1. In conjunction with a deep ATCA survey of the BCGs in the SPT cluster sample (accepted proposal, P.I. Edge), this will allow us to expand the study of the radio properties and fueling of BCGs to cover their evolution over half the age of the Universe.

All being well, I will be undertaking a joint postdoctoral position between the University of Waterloo and the Perimeter Institute for Theoretical Physics, where I hope to continue learning just how little we actually know about anything.

Appendix A

Main Sample - Comments on Individual SED Decompositions

VLA - AE125

A1991 Unresolved at both C and X bands. Fit to get a measurement of the non-core flux then extrapolate for a core upper limit. Likely to be a Compact Steep Spectrum (CSS) source.

A2146 Flat spectrum, two observations at C-band show that it is variable which suggests we are seeing a dominant core. Fit this using the most contemporal C-band observation to get a core measurement. Get an upper-limit for the non-core by taking the lowest frequency data-point (WENSS) and extrapolating to 1 GHz. Do this as expect the lowest frequency point to be non-core dominated but not directly observed near 1 GHz so a limit.

RXJ1657.8+2751 Best fit using a dropline model. Use this to get a measurement of the non-core. Clear that there is no dominant core. Large difference between the peak and integrated fluxes at C-band. Use the peak of this with a core index of α=-0.2 to get an upper-limit for the core flux.

RXJ1720.1+2638 Core and non-core can be clearly spectrally separated in the radio SED. There is a clear core component at C-band and L-band (using VLA-A) in addition to being consistent with the peak of the FIRST flux and with a BIMA flux for the core. These points show a flat core component which can be fitted to get a clear core at 10 GHz. Shows that this source is non-core dominated at low frequencies. VLSS, NVSS and integrated

flux at C-band (AE125) can be used to get a measure of this component at 1 GHz. Central core appears surrounded by amorphous diffuse emission. Extrapolation would suggest a contributing non-core flux component at 10 GHz, resolved out at high resolution.

Z7160 Shows a flat core component, consistent with the unresolved X-band observation, unresolved C-band and BIMA observation. Fit this using the unresolved VLA-A flux measurement as the 1.4 GHz flux. At L-band, it is clear that lower resolution observations are picking up more diffuse emission from the non-core component. Hence, we know that NVSS is picking up the non-core so connect this to lower frequency GMRT obtained flux to get a measurement of the non-core component.

Z8193 Seeing a clear flat core component at higher frequencies that transitions to being dominated by a clear steep, non-core component at lower frequencies. Extrapolating this steeper component back, it is consistent with being the difference between the interferometric flux measured at C-band and the single-dish measures which would pick up this extended emission. Fit the flat component to get a core measurement then fit only the lower frequency points and extrapolate to 1 GHz to get a limit for the non-core flux.

Z8276 See a clear split power law, that is well sampled enough to be fit directly. There is a flat component for the core, which appears slightly variable at C-band (see also Chapter 4). Appears potentially slightly resolved at C-band but well-fit with unresolved gaussian. See a clear, steep non-core component.

A407 Large, resolved source. Fit the extended non-core with a power law and then use the VLBA point (Liuzzo et al., 2010) to extrapolate for a measure of the core (negligible at 1 GHz). Potentially could include a third component, non-core exhibits spectral turn-up at lower frequencies. For the purposes of this current statistical study, we can ignore the lowest frequency data as this component, if present, would only be important at frequencies much below 1 GHz. This does however suggest that there have been multiple, powerful periods of activity in this source. Some of the steepest emission may potentially be attributable to inner-relics. Note that the position given is that of the high peak and hence most likely to be a hot-spot; it does not appear as if the core is resolved at the resolution of our imaging.

A621 Appears to be a classic steep spectrum source, not showing any spectral curvature. Elongated but not clearly resolved into components at C-band. There is a clear split be-

tween peak and integrated fluxes at both C and X-bands but morphologically this appears to be due to partially resolved double-lobe structure and hence the peak is likely just the brighter hotspot. Fit for non-core value but then extrapolate from the peak at X-band to derive a limit on the core.

A757 Only sampled at L and C bands although the sources is clearly flat and unresolved, which is suggestive of core dominance. Fit for a core value and then extrapolate for a non-core limit.

RXJ1053.7+5450 Weak source. Sampled at L and C bands only. Appears slightly resolved but not enough to clearly see a core. Fit the steep spectrum integrated component then extrapolate from the peak at C-band for the core limit.

A1423 There is a head-tail source nearby but this is centred on a non-BCG galaxy. The BCG itself is undetected in our C-band imaging.

A1366 Consistent steep spectrum between 38 MHz and 43.3 GHz. Appears to be a head-tail in C-band map but clearly not resolving the core, just a hot spot. Fit with a single power and then extrapolate back from the 43.3 GHz observation to get a limit on the core.

A1190 Appears to be slightly diffuse although not truly 'resolved'. There is a clear peak-to-integrated deficit seen from the fit but morphologically the source appears unresolved. The source has published limits at 23.5 and 43.3 GHz (Lin et al., 2009) showing that there is no strong, flat component. Fit with a steep spectrum for the non-core and extrapolate back from 43.3 GHz limit to get a limit on the core. There is a large, bright (250mJy) Wide-Angled Tail (WAT) source only $\approx$80" to the north-west.

A1773 CSS sampled only at L and C bands. Source is unresolved. Fit an index to retrieve a measure of the non-core and extrapolate for a core limit.

A1775(SE) Large, messy source. Hint of spectral flattening towards higher frequencies, however it is only sampled up to C-band and so a true split-power model is not able to be robustly performed. Clearly losing some flux at higher resolution but not adequately resolving the source for a direct decomposition. Additionally, it could be argued that instead, there is actually spectral steepening towards lower frequencies. This appears more believeable from the morphology and so best to neglect lowest frequency points, fit the extended emission with a power law and then extrapolate from the peak (most likely to be a hot spot rather than the active core) to get a limit on the core.

A1775(NW) Diffuse source, there is resolution but no clearly defined core. Appears to be reasonably steep ($\alpha \approx 0.7$). Fit the diffuse component. There are limits at 22.5 and 43.3 GHz (Lin et al., 2009) that show that there cannot be a flat core component attributable to the peak at C-band. Extrapolate back from the limit at 43.3 GHz to get a limit on any core.

RXJ1442.2+2218 Sampled at just L and C bands. NVSS picks up excess flux over FIRST peak. Unresolved at C band. Extrapolate the flat component to get a measure of the core, then extrapolate from NVSS to get a limit on the non-core.

A2009 Resolved core at L band, unresolved core/resolved-out extended emission at C and X bands. Fit the flat component. Integrated flux at L-band consistent with unresolved NVSS flux, which along with VLSS suggests the presence of an ultra-steep spectrum (USS: $\alpha_{Steep} > 1.5$) component. Interpolate for the USS component, accounting for the expected core contribution at 1 GHz when inferring non-core component.

A2033 Resolved double-lobed system. Low resolution literature values sample only the integrated flux which is steep spectrum. Fit this with a power law. Able to get a core measurement at C-band, extrapolate from this with generous uncertainty to retrieve a core value.

A2055 Resolved head-tail. Core is very bright, flat spectrally ($\alpha \approx 0.2$) from L to C bands whereas extended/integrated emission is relatively steep spectrum ($\alpha \approx 0.63$; see also Chapter 4). Split-power won't adequately decompose due to small coverage of core, however can fit a power law to each component and derive non-core component contribution.

RXJ1522.0+0741 Commonly known as MKW3s. Literature values at low frequencies show that this is a past-outburst source with ageing emission (e.g. Kellermann et al., 1969; Giacintucci et al., 2007). Fit a dropline to this. Unresolved core seen at C-band, extrapolate with appropriate uncertainties from this to get a measure for the core flux at 10 GHz.

A2063 Unresolved at X band and a limit at 22.5 GHz (Lin et al., 2009). Peaks at L and C band consistent with there being an active, flat core component. Extended emission at C-band and L-band shows there is a steeper, non-core component. Fit the components separately, accounting for core when deriving non-core contribution.

A2064 Extended source, possible head-tail or perhaps uneven lobes. No clearly resolved core, integrated spectrum consistent with classic steep spectrum lobe emission, peak most likely a lobe rather than the core so can only realistically get a limit on the core. Note that this position is from fit of small double, hence position may better reflect a hot-spot rather than the true nucleus. There is a reasonably bright (≈25mJy), partially resolved source only ≈80" to the west.

A2175 CSS source. Fit for non-core, extrapolate for core limit.

Z1953 Busy field. Cluster is at high redshift (z≈0.374) and appears to have blended double BCGs. Several literature observations match radio-sources to the BCGs but higher resolution imaging shows that the BCG(s) is(/are) radio undetected.

A1132 Another busy field, some literature fluxes flagged as likely being confused. Appears as a steep, double lobed source. No clearly resolved core, extrapolate from the peak (likely lobe) to get core limit. Note that the given position is from a fit of the double and hence may better reflect a lobe position rather than the true nucleus. Fit for non-core.

A761 Resolved source. Measured core flux consistent with VLA-A (Jetha et al., 2006) observation of the core. Fit the integrated emission for the non-core component and then extrapolate from the core measurement with appropriate uncertainty for the core.

A1023 Only sampled at L and C bands, unresolved CSS. Fit for non-core and obtain a limit on the core.

RXJ1206.5+2810 CSS. Only sampled at L and C bands. Fit for non-core and then extrapolate for a core limit.

Z4673 CSS. Only sampled at L and C bands. Fit for non-core, extrapolate for the core limit.

Z4803 Weak detection at C-band, no additional detections in the literature, including NVSS limit. Extrapolate for limits on both components.

A1668 Remove single dish GB6, which appears to be confused with other nearby sources, and then consistent with a steep power law for the non-core. Source is unresolved at C-band but becomes resolved into two lobes (≈0.94", PA 54.6) at VLA-A array X-band. VLBA observation (see Chapter 5) shows that there is no active core component.

A1763 Large, head-tail source. Not resolving out the core here but there is a high resolution observation (Hardcastle & Sakelliou, 2004) of the core. Extrapolate from the resolved

core component of this to get a value for the core and then fit the extended emission for the non-core component. Note that position quoted herein is the peak of emission, which here constitutes a hot-spot as opposed to the SMBH core.

A1677 See a deficit from peak-to-integrated measured flux at C band (and FIRST) but does not appear to be a separated core, the source appears unresolved. Integrated spectrum consistent with being non-core dominated steep spectrum. Fit this and extrapolate for a limit on the core.

A2241 Appears to be unresolved CSS although a slight peak-to-integrated flux deficit. Fit for non-core, extrapolate for core limit. Companion source only ≈25" to south-west and also a brighter ≈30mJy head-tail only ≈2' to the north.

A2390 Very powerful core, well covered by Augusto et al. (2006). Spectrum steepens at low frequencies indicative of there being a non-core component. Fit with a split power model.

RXJ2214.7+1350 Powerful (3C442) radio source. Much extended emission, steep spectrum to be fit for the non-core. High resolution C-band data resolves out the extended emission revealing the core. Extrapolate from this for the core component, negligible compared to integrated emission but consistent when applied to split power model.

A2572A Slightly resolved source although there is no clearly distinguishable core component. Integrated emission suggests a dominant steep spectrum non-core and so the flux deficit is more suggestive of the peak being due to one of two lobes rather than a strong core. Fit for the non-core, extrapolate from the peak to get a core limit.

RXJ0000.1+0816 Only sampled at L and C bands but well-sampled at these. Variability shows that it is core dominated. Choose most co-temporal observations, fit for the core (allowing for variability in the uncertainty) and extrapolate to get a limit on the non-core component.

RXJ0021.6+2803 Weak CSS, only sampled at L and C bands. Undetected in AE110 but weak detection in AE125. Fit the non-core and extrapolate for the core.

Z235 Flat-spectrum, core dominated source. Potentially curves above 100 GHz but large uncertainty on the highest radio-frequency data means this cannot be confirmed hence best to fit only with a power-law (Chapter 4). Fit for the core and extrapolate for the non-core component.

RXJ0058.9+2657 Beautiful looking double lobed source. Core peak in reasonable agreement with VLBA measurement of the core (Liuzzo et al., 2009). Fit the extended emission for the non-core component and then extrapolate from the core flux measurement with appropriate uncertainties to infer a value for the core component.

A160 Large, clearly resolved source. Spectrally see a difference between the steep (potentially sometimes contaminated in low resolution observations) extended emission and the flat, apparently active core. Fit these separately for the respective components.

A2634 Another large resolved source, commonly known as 3C 465. Literature observations splits between higher resolution core observations and low resolution 'total' observations. Can fit these separately, accounting for the very bright core when determining the non-core contribution. C-band observation (AE125) does hint at recovering some emission from hot-spots although this would not account for all 'missing flux'. Only core component is reported.

RXJ0107.4+3227 NGC383. Associated with the strong FRI source 3C 31. Majority of literature fluxes appear to be integrated, showing the total emission to be dominated by the steep spectrum non-core component. Fit this, removing fluxes that resolve out significant sections of the total flux. Resolved core flux from AE125 agrees well with the core flux reported by the Combined Radio All-Sky Targeted Eight GHz Survey (CRATES, Healey et al., 2007). Extrapolate from these to get a measure for the core value.

RXJ0123.6+3315 NGC507. Another powerful extended source. Extended emission is resolved out at C-band observations leaving just the unresolved core. Fit the lower frequency emission for the non-core component and then extrapolate with reasonable uncertainties for a measure of the core component.

A262 Slightly resolved source. Extended emission dominating integrated spectrum, clear steep component down to $\approx$10 GHz. VLBA observation (Liuzzo et al., 2010) of the core at 5 GHz shows that there is an unresolved core component. Spectral flattening to higher frequencies suggests this component is flat spectrum and the source is fit with a split-power model.

RXJ0740.9+5526 Double source, resolved lobes but no clearly resolved core hence only a limit can be determined for this at C band. No VLBI observations so can only extrapolate from the limit for a limit on the core component and fit the steep spectrum lobe

emission for the non-core component. Position given is estimated nuclear position.

A115 Large, fuzzy double lobed source (3C 28). No clear core so only a limit on this, which can be used in conjunction with limits at 22.5 and 43.3 GHz (Lin et al., 2009) to get a limit on the core with the integrated emission being fit to retrieve the non-core component. Position given is estimated nuclear position.

VLA - AE110

A75 Weak unresolved detection at C-band but no additional literature fluxes. Extrapolate from this point to get limit on the core, no match in NVSS so extrapolate from this limit for a limit on the non-core.

A76 Only two fluxes. Unresolved at C-band. Steep spectrum, fit to get non-core flux and extrapolate from C-band flux with α=-0.2 to get upper limit on the core.

A77 Source unresolved at C-band. Appears to become diffuse at X-band with VLA-A array. Moderately flat spectrum although diffuse nature and rollover suggests best fit with a dropline model to get the non-core flux and then extrapolate from the X-band flux with α=-0.2 to get upper limit for the core. Integrated X-band measurement consistent with Lin et al. (2009), suggests rollover is real. A limit at 22.5 GHz from this paper adds further weight that this is relatively compact yet ageing emission rather than a flat spectrum core.

A147 Unresolved faint detection at C-band. No literature fluxes. Taking the NVSS snapshot image of the region there is a faint source at the position that is not in the NVSS catalogue. The peak of this source is taken as the flux at 1.4 GHz. These flux measurements suggest a steep power-law. Fit to get a measure of the non-core flux and extrapolate C-band point with α=-0.2 to get upper limit on the core.

A168 Only got data at L- and C-band. However, see that NVSS picks up a lot of extra flux in comparison with the peak of the FIRST detection so extrapolate this NVSS flux with α=-1.0 to get a non-core flux limit. Taking the peak of the FIRST detection with the effectively unresolved (peak $>$70% integrated) C-band flux then we see a flat core component so use this to estimate the core contribution at 10 GHz.

A193 USS source. Could potentially be resolving out flux at C-band. There is slight extent seen at C-band (peak >70% integrated). Use α=-0.2 from the peak of the C-band observation to get upper-limit for the core and interpolate the integrated fluxes for a reasonable estimate of the non-core.

A189 Appears slightly elongated at C-band and is a known cavity system (Dong et al., 2010). No clear structure although is a ≈35% flux deficit also suggesting that this source is marginally resolved. Hint of spectral steepening for the extended emission although only got three points so fit these just with a single power and then extrapolate the C-band peak to 10 GHz with α=-0.2 to get an estimate of the core flux.

RXJ0419.6+0225 Faint unresolved at C-band. Steep spectrum, fit a single power law for a non-core measurement and then extrapolate for a core limit.

Z6718 Fairly steady steep spectrum from which the non-core can be determined. Potentially slightly extended at C-band. Extrapolate from the peak of the Cband observation for a limit on the core.

A1902 Observed only at L and C-bands, this source is nevertheless unresolved with a steep index. From this, estimate the non-core and then extrapolate from C-band for a core limit.

A1927 Appear to be seeing unresolved, steep component. Use this to get a measurement of the non-core flux and then extrapolate with α=-0.2 from the unresolved C-band flux to get an upper-limit for the core. There is a brighter (12mJy) source ≈2' to the north-east as well as diffuse emission ≈5.3' to the north-west that may be a phoenix-relic. These independent sources may be confused with the BCG in low resolution observations.

A1930 There is a flat component between the unresolved FIRST and C-band observations that can be fitted for a core estimate. NVSS shows additional flux to FIRST, perhaps indicative of there being a weak non-core component being better sampled at this lower-resolution. The low frequency observation from WENSS confirms that a steeper component is present. Extrapolate from this point using α=-1.0 to get an estimate for the non-core. **RXJ1440.6+0327** Observed at only L and C -bands. Unresolved at C-band, steeper than would be an unambiguous core (α=0.62) but appears consistent with being attributable to an active core component between the FIRST peak and unresolved C-band observation. Measure core from this, allowing for large uncertainty. Seeing the more

diffuse emission from NVSS so extrapolate this point with α=-1.0 to get a measure of the non-core flux.

A1978 The unresolved C-band flux is consistent with a steep component if linked to the NVSS observation. Take a measurement of the non-core from this and then extrapolate the C-band peak to 10 GHz with α=-0.2 to get a limit on the core component.

MACS1532.9+3021 CSS, unresolved at both C- and X-band. Fit with a single power to take a measurement of the non-core. Extrapolate back from the BIMA measurement at 28 GHz (Coble et al., 2007) using α=-0.2 to get an upper-limit for the core.

A2110 Composed of an USS component (α=-1.9) and then a flatter (α=-0.25) core component that can be directly fit with a split power model. Consistent with it being unresolved at C-band.

A2108 (a) & (b) No additional literature fluxes for sources at either of these positions. Brighter source nearby could have swamped catalogue detections. No SED fit possible, urge caution using given fluxes, potentially spurious.

RXJ1604.9+2356 Resolved source. Appears disturbed, shows potential FRI-like lobes or maybe head-tail morphology. Have a steady source that hints at synchrotron ageing although steep component adequately fit with a single power law to get the non-core flux. Very resolved at C-band and clear that the FIRST point is resolving out much of the lower spatial frequency flux compared to NVSS. Use the C-band peak to get a measure of the core flux from this flat component. Note that given position is estimate of nuclear position, falling between dominant lobes.

A2204 Source well-fit with a split power model, showing spectral flattening to higher frequency. Appears unresolved at C-band although a gaussian fit suggests a flux decrement from the peak, maybe hinting that it is beginning to be resolved at VLA-C resolution.

A2228 Weak unresolved detection at C-band but no additional literature fluxes. Extrapolate from this point to get a limit on the core. Non-detection in NVSS, use this for a non-core limit.

A2244 Faint CSS. Fit for non-core and extrapolate for a limit on the core. There are two brighter sources within 2' seen at C-band - one an unresolved $\approx$4.1mJy source to the north, the other a $\approx$30mJy double to the east. These may be confused with the BCG at lower resolution.

RXJ1715.3+5725 NGC 6338. Flat, core dominated source, hint of mild variability. Consistent with WENSS flux still being core dominated. Fit with a single power to get core flux then extrapolate with α=-1.0 from the WENSS flux to get a non-core upper-limit. See also Chapter 4

Z8197 CSS. Unresolved at C- and X-bands. Consistent with a steep, single power. Get the non-core from this and then extrapolate from the X-band flux with α=-1.0 to get an upper limit on the core.

RXJ1733.0+4345 There appear to be inner-relics nearby judging by low resolution, low frequency observations. The BCG itself is unresolved at C-band. Fit a flat component to this and the FIRST peak to get a measurement of the core. NVSS is picking up non-core flux above that recovered in FIRST so extrapolate (using α=-1.0) from this to estimate the non-core flux.

A2443 A reasonably well-sampled field although there is a large relic in the cluster (Cohen & Clarke, 2011) that causes confusion in some images. Spectral decomposition has used only observations with the necessary resolution to isolate BCG. The BCG looks largely resolved at C-band, although may be jetted to north-east. Fit steep component from NVSS to integrated C-band flux to get non-core then extrapolate using α=-0.2 from the C-band peak to get an upper limit on the core. This is a very dynamic field. In addition to the relic there is a diffuse, $\approx$5mJy source $\approx$2' to the south as well as a WAT ($\approx$23mJy) and a head-tail source ($\approx$10mJy) both 2-3' to north-west. There is therefore strong potential for confused observations of this BCG.

A2457 Weak unresolved detection at C-band but no additional literature fluxes. Extrapolate from this to get limits on both the non-core and the core.

A2495 Only two observations. Slightly resolved at C-band. Fit steep component from NVSS to integrated C-band flux to get non-core then extrapolate using α=-0.2 from the C-band peak to get an upper limit for the core.

A2626 Sources contains and extremely steep (α=-2.2) component at low frequencies and is well sampled over wide frequency range. Unresolved at C- and X-band. Fit the two components separately. Good example of a young, flat core but with extreme USS component.

A2627 a Got an active core component as seen by GISMO/CARMA (see Chapter 4). Re-

solved into fairly amorphous jetted structure at C-band, no extent at X-band. Can fit the flatter, high frequency component to the unresolved X-band flux for a measure of the core component. There is a hint of extended emission at lower frequencies. Still relatively flat but now what is classified as non-core so fit these seperately and subtract the expected core component to infer a non-core contribution.

A2627 b This source is not particularly faint, however there appear to be no additional fluxes for it in the literature. This may be due to confusion with A2627 (a). This could also contribute to over-estimating non-core flux for A2627(a). This source could not be robustly independently fit with current data. Consider the two components when studying this source.

A2665 Spectrum shows a higher frequency turnover that is consistent with an ageing synchrotron population. Resolved at C-band and unresolved at X-band suggests seeing the edge of the non-core and then the underlying core component. Fit a dropline model to get the non-core component and then extrapolate from the unresolved X-band flux to get an estimate of the core component.

A2675 VLSS to NVSS interpolation gives a very steep spectrum (α=1.55). Unresolved C-band observation suggests there is a core component contributing at higher frequencies although extrapolation to 10 GHz would be uncertain. Cautiously just fit lowest two fluxes to get a reasonable estimate for the non-core then extrapolate from the C-band flux to get an upper limit on the core. There are no other sources apparent in field at C-band to suggest that the VLSS is confused.

A2622 SED has a turnover to high frequency and can be well fit with a dropline model. No active core is apparent in this system. Only a diffuse envelope is detected at C-band and there is only an upper-limit from the X-band observation. Fxtrapolate from this upper limit to get a very stringent upper limit on the core flux. Note that this interpretation is in agreement with Giacintucci et al. (2007) who considered this galaxy to be a dying radio source that is not currently being fed by nuclear activity.

A566 There is no detection in the C-band VLA imaging at the position of BCG. There are two nearby radio galaxies. The BCG position is coincident with what appears to be inner core-relic emission, resolved so as to be able to isolate it in NVSS. Clearly not active but does appear to be directly related to activity of the BCG within emitting lifetime hence

include as a non-core component.

RXJ0751.3+5021 Only got detections at L and C bands, unresolved at both and the non-detection in WENSS shows this source to have a flat index. Fit for the core and extrapolate from 1.4 GHz with index $\alpha = 1.0$ to get a limit for the non-core.

Z2089 Only got detections at L and C bands, unresolved at both with a steep index. Fit for the non-core and extrapolate from 4.86 GHz with index $\alpha = 0.2$ to get a limit for the core.

A763 BCG is a large, tailed source. Resolve out the components and there is a published high-resolution VLA core flux (Jetha et al., 2006) which agrees with the recovered core flux from our map. Fit the core as a single power law from these, the FIRST resolved peak and higher frequency observations of the core. Appears that the interferometric observations may be resolving out some of the more extended flux. Fit a dropline model to the non-core.

Z1665 Only got observations at L and C bands, unresolved at both with flat index showing it to be core dominated. Fit for the core and extrapolate from 1.4 GHz with index $\alpha = 1.0$ to get a limit for the non-core.

Z2844 Flat core dominated source with a hint of extra emission at low frequency from WENSS. Fit the core with a power law and then extrapolate from WENSS to get a limit on the non-core.

A1035 Only has fluxes at three frequencies. Unresolved at L and C bands with a flat index suggesting core dominance. Fit these to get a measure for the core and then extrapolate back from the WENSS point to get a limit on the non-core.

A1204 Only got observations at L and C bands, unresolved at both, flat index, core dominated. There is a slight hint that there may be extra emission being picked up by NVSS over FIRST but equally this could be attributed to variability within an active core. Hence can only reasonably fit for the core and extrapolate from 1.4 GHz with index $\alpha = 1.0$ to get a limit for the non-core.

A1235 This source is in the FIRST region but is not in the FIRST catalogue. It is however detected at C-band (weakly) and there is a clear source in the FIRST cutout. This gives a flat index suggestive of a core so take an estimate of this and then extrapolate for a limit on the non-core.

A1553 Appears to be a CSS. Slightly elongated at C-band and got a clear peak deficit. A lot more flux picked up by NVSS than by FIRST but restricted to just two frequencies. See a diffuse, core-relic like structure ≈10arcsec to north-west in FIRST, not detected at C-band and confused at lower resolution. Fit (with suitably large errors) for the non-core and then extrapolate to get a limit on the core.

RXJ1326.3+0013 Slightly resolved image suggests a one sided source. Fit the extended emission to get the non-core, extrapolate from the peak at X-band to get a limit on the core.

VLA - AE107

RXJ0341.3+1524 Unresolved at C-band and has a flat index consistent with it being core dominated. Fit this and then extrapolate from NVSS using the usual α=-1.0 to get upper limit for the non-core.

RXJ0503.1+0608 Unresolved at C-band although no additional fluxes in the literature. Not particularly faint (≈5mJy) suggesting either that previous observations were confused by other sources (there are several radio-bright sources in the vicinity) or that this is core-dominated and variable. Indeed, considering the NVSS map suggests that both of these scenarios may contribute. There is a bright nearby confusing source that would be confused at any lower resolution. Additionally, the BCG can be isolated in NVSS (below the catalogue limit) and shows that the spectrum is inverted and therefore core dominated. Fit for an estimate of the core and then extrapolate for a non-core limit.

A611 Faint and unresolved at C-band. No additional detections in the literature with only an upper-limit in NVSS. Use these to get limits on both components using the representative indices.

RXJ0819.6+6336 Spectrum is well-fit by a fairly steep (α=-0.8) single power law. C-band image hints at lobes which is confirmed by high resolution image at X-band with VLA-A array. In X-band a core component can be clearly distinguished. Other observations do not have the necessary resolution to confidently separate this so fit their integrated fluxes as a single power to get a measure of the non-core (which here is shown to be extended

lobes). Extrapolate the core measurement at X-band to 10 GHz, with representative index and conservative uncertainty to get a relatively robust measure of the core flux.

A667 Steep source that appears marginally resolved at C-band although only two fluxes are available. Extrapolate from the C-band peak for a core upper limit. There is a ≈7mJy double source only ≈30" to the south-east that is likely confused at lower frequencies. Source appears confused in NVSS imaging.

A971 Source appears in the 7C catalogue (Waldram et al., 1996) but this appears to be confused, otherwise would suggest incredibly steep ($\alpha>3.25$) index that is hard to explain physically. Excluding this point then the spectrum can be fit with a reasonably steep power law ($\alpha\approx0.82$) to get a realistic non-core flux. Extrapolate from the unresolved C-band flux to get an upper limit on the core.

A980 Steep spectrum source ($\alpha\approx1.42$) with excess flux picked up by NVSS over FIRST. A single power law gives a reasonable measurement of the non-core flux. Appears to be a small double in FIRST and marginally resolved at C-band. Extrapolate from the peak of the C-band measurement to get an upper limit for the core. Note that the given position is the C-band peak and may best represent a lobe rather than the true nucleus.

A1045 Unresolved at C-band with a hint of a slight peak-to-integrated flux deficit at L-band although no clear extent. Spectrum continues to be steep down to WENSS. Appear to be seeing a non-core component dominating at lower frequencies. The core cannot be unambiguously separated with available data hence fit for the non-core only and take a limit on core.

RXJ1715.1+0309 Spectrum is a steep power law and source is resolved at C-band showing that the fit gives a good measure of the non-core. Extrapolate from the peak at C-band to get an upper limit for the core. Note that source appears to be resolved into lobes with no clear core. Perhaps a small-scale double. Position given is that of the peakflux and most likely represents a hot-spot rather than nucleus.

A2261 Steep spectrum ($\alpha\approx1.4$) source that appears unresolved at C-band. Fit to get a measure of the non-core flux and then extrapolate from C-band to get upper limit for the core. Potential confusing source for low resolution observations ≈2.5' to north-west.

RXJ1750.2+3504 Flat spectrum, appears to be core dominated. Fit with a single power-law to obtain a measurement of the core then extrapolate back from the lowest frequency

point (7C; Waldram et al., 1996) to get an upper limit on the non-core.

RXJ2129.6+0005 Unresolved at C-band, X-band and has a BIMA point (Coble et al., 2007). Fitting these returns a flat spectrum from which a core component can be inferred. There is a clear flux difference between the peak of the VLA-A observation at L-band and NVSS that suggests that NVSS is picking up excess flux which can be associated with the non-core. Extrapolate from NVSS using α=-1.0 to get an estimate of the non-core flux, accounting for the inferred core.

VLA - AE099

A291 Only got observations at L-band and C-band. Unresolved at both but interpolation is flat and there is a hint of variation between repeat observations at L-band suggesting that source is core dominated. Take an estimate of this and then extrapolate from NVSS to get a limit on the non-core.

Z1121 Head-tail source where the tail is bent, wide and diffuse. There is only a marginal variation in the power law index of the SED. The peak-to-integrated flux and the resolved morphology, both at C-band enable the core to be isolated, however a direct split power fit to the integrated SED gives an unreasonable core estimate. Instead, fit the integrated fluxes with a single steep power law to get the non-core flux and then extrapolate from the resolved core component at C-band with α=-0.2 and conservative uncertainty to obtain an estimate of the core flux.

RXJ0821.0+0752 Appears to be a CSS although only observed at L- and C-bands. Unresolved at both although the index is steep (α=-0.8). Extrapolate to get an upper limit on the core. Note that there is a strong ($\approx$30mJy at C-band) head-tail only $\approx$30" to the south-west. The BCG is confused with this source in NVSS although FIRST does separate them, hence only FIRST and AE099 can be used.

Z2701 Source is an USS ($\alpha\approx$2.0). There appears to be a slight kink in the higher frequency tail. Source is unresolved at C-band (highest frequency observed at) although this source is also observed with the VLBA (see Chapter 5) that shows there is no active core component on milli-arcsec scales. Therefore fit for the non-core and then extrapolate for

an upper-limit on the core.

Z3146 Unresolved at C-band. L-band fluxes suggest that NVSS is picking up extra flux from the non-core compared to FIRST whilst the peak of the FIRST detection is consistent with being attributable to an active core, giving a flat ($\alpha \approx 0.4$) index when combined with the C-band and BIMA fluxes (Coble et al., 2007). Fit this flat core component and then extrapolate from NVSS flux to get a measure of the non-core.

Z3916 Taking the integrated fluxes then the SED is well fit by a dropline model with a steep power-law component (α=-1.5). From the L-band and C-band imaging there are hints that the peaks are partially separating the core but this is not unambiguosly well-resolved as to be able to make a confident core measurement hence extrapolate from the C-band peak for an upper limit on the core. In the radio imaging alone the source appears to be an FRII at C-band (AE099) and FIRST. However, overlaying these maps onto optical images of the region shows that there are actually three, roughly aligned radio-galaxies in the vicinity. The BCG is the brightest (30mJy at L-band) and then two other unresolved sources, (3mJy and 10mJy at L-band) lie $\approx$14" and $\approx$28" to the north-west respectively. These sources are confused in NVSS and therefore note that this source likely suffers from confusion and hence the non-core figure may be an overestimate. It should be noted though that using only the fluxes from AE099 and FIRST would still classify this source as steep spectrum.

A1651 Consistent with being a CSS although only observed at L- and C-band. Fit to get estimate of the non-core flux and then extrapolate with a flat index to get an upper limit on the core flux.

A1664 Source is unresolved at both C- and X-band, showing a strong core with a reasonably flat (α=0.5) index from which a measurement of the core can be derived (note that this is confirmed by a VLBA observation (Chapter 5). The spectrum steepens below 1 GHz (α=1.4). A direct split-power fit fails and combing the two power-law fits to the individual components over-estimates the flux in the $\approx$1 GHz range. This suggests that the core component likely turns over (self-absorbs) in GHz range. However, fitting the lower frequency points separately but accounting for the inferred core component gives a reasonable value for the non-core.

A1084 Unresolved at L- and C-bands with the interpolation between these suggesting a

flat core component ($\alpha \approx 0.1$). The source falls within the TGSS region, with the recovered flux suggesting the presence of a steeper spectrum component at lower frequencies. Extrapolate with α=1.0 from this 150 MHz observations to get an upper limit for the non-core at 1 GHz. Appears to suggest a very core dominated source at $\approx$ GHz range frequencies, perhaps with a very steep spectrum amorphous halo of material to low frequency.

A1885 Multi-epoch coverage shows this source to be variable at C-band suggesting core dominance. WISH (De Breuck et al., 2002) observation confirms this core dominance. There is no significant non-core component, the source appears to be either a flat spectrum sources or a GPS. Fit to get the core flux and extrapolate from the WISH detection to get an upper limit on the non-core.

A1682 Cluster has twin BCGs. A1682(b) is a non-detection in our C-band imaging. A1682(a) is initially matched as a powerful double-lobed source however further investigation with the optical overlays shows this to be a projected background source and that the BCG itself is radio undetected.

VLA - AE117 L-Band

Z808 Source contains inner-relics that are clearly visible in the C-band imaging. These appear to be associated with the BCG and hence dominate the integrated spectrum, which can be well-fit with a dropline model to give a measure of the non-core. A distinguishable, flat spectrum core is apparent in the L-, C- and X-band imaging. Fitting this seperately enables a measurement of the central, active core to be obtained.

A478 This source was not covered by our VLA-C observations, however it was observed at both L- and X-bands as art of project AE117, showing one-sided morphology at L-band with the structure resolved out at X-band leaving only an isolated core. Interpolating between the high resolution L-band peak and the unresolved X-band flux returns a flat spectrum. There is also a BIMA observation (Coble et al., 2007) that suggests this source may contain a variable component, thus reinforcing that it is core dominated at higher frequencies. The measured core index is marginally steeper than usual when skewed by

the BIMA measurement but the resolved nature suggests this is still attributable as a separate core component. NVSS appears to recover the non-core component above the flux expected from the active core so extrapolate from this using α=-1.0 to get an estimate of the non-core component.

Z1261 The BCG is associated with the radio source 4C+53.16, which is a clearly resolved FRI/II. There are distinguishable inner jets at C-band but also clear hot-spots with spherical cap-like lobes. The integrated SED can be well-fit with a dropline model, highlighting that there is likely synchrotron ageing in the lobes. Use this fit to retrieve a measure of the non-core. Observations at L-, C- and X-band show a clearly resolved core, the isolated SED for this component only displaying an inverted index from which a measure of the core can be obtained. There is also a Very Small Array (VSA; Cleary et al., 2005) observation at 33 GHz. This array only has 0.5degree resolution so unlike other high frequency observations does not provide a good measurement of the core flux. However, the flux measured is consistent with the dropline component so restrains the magnitude of the synchrotron ageing.

RXJ1320.1+3308 Clearly resolved diffuse emission at both L- and C-band (using VLA-A and VLA-C array respectively) with only an unresolved core recovered at X-band (using VLA-A array). The integrated high-resolution L-band flux is consistent with the flux given by NVSS suggesting we are not losing emission at intermediate scales. Fit the SED for the resolved core seperately to get a measurement of the active component. The SED for the diffuse emission alone has a relatively shallow spectrum ($\alpha\approx$0.56) suggesting this component is resolved out rather than below the detection limit at X-band. Fit the lower frequency components to get a measure of this diffuse emission, accounting for the core as this is non-negligible at 1 GHz.

A1835 Source is a fairly classic CSS. Unresolved at all observed frequencies and has a BIMA point at 28.5 GHz (Coble et al., 2007) that shows the steep spectrum is consistent to higher frequencies. Fit this to get a measurement of the non-core and then extrapolate from the BIMA flux with index α=0.2 to get an upper limit on the core.

VLA - AE117 X-Band

MACS0159.8-0850 Source is undetected at low frequency (e.g. in VLSS, Cohen et al., 2007) and displays an inverted spectrum in the GHz-range, showing it to be core dominated. Spectrum is steady to 20 GHz (AT20g, Murphy et al., 2010) so a GPS-fit is not-limiting although a turnover is expected above 20 GHz. Fit a single power-law to get a measurement of the core contribution at 10 GHz and then extrapolate from the VLSS non-detection to get an upper limit on non-core flux.

RXJ0352.9+1941 Unresolved at C- and X-band and has a mildly inverted component that can be fitted to get a measure of the core. Appears to be flat spectrum to low-frequency, extrapolate from NVSS with α=-1.0 to get a limit on the non-core. See also Chapter 4.

RXJ0439.0+0520 This source contains a very strong, self-absorbed core component that dominates above $\approx$1 GHz and a steep spectrum tail below this. Fit the steep spectrum component to lower frequencies for a measure of the non-core and fit the peaked component with the GPS-like model to get a measure of the core.

A646 Source is core dominated with an inverted/peaked component that can be fit to measure the core flux. Extrapolate from the WENSS flux to get an upper limit for the non-core. See also Chapter 4.

A795 Unresolved at C-band but shows a steep single power law spectrum. Fit with a single power to get non-core flux. There is slight resolution at X-band. Extrapolate from the X-band peak to get an upper limit on the core.

Z3179 SED can be well fit using a dropline model to get the non-core. Extrapolate from the X-band flux to get an upper limit on the core.

A1068 Appears marginally resolved at C-band and part of a double, however the second component appears un-associated and is not present at X-band. Fitting to L-band suggests continuation of steep index, indicative of a CSS. Fit to get a measure of the non-core and then extrapolate from X-band to get an upper limit on the core.

A1361 BCG associated with the extended radio-source 4C+46.23 that has two-sided morphology at C-band. The integrated spectrum can be fit with a dropline model to get the non-core component. The extended emission is resolved out with the VLA-A at X-band to leave an isolated core. Extrapolate from this to get a reasonable estimate of the core component at 10 GHz.

RXJ1504.1-0248 Flat spectrum source to high frequency (see Chapter 4), and unresolved on milli-arcsecond scales at C-band as seen by Bourda et al. (2010) and within this thesis (Chapter 5) with the VLBA. Fit this for a measure of the core. Source contains a known mini-halo (Giacintucci et al., 2011a). This emission can be isolated from the BCG and the radio-power of this is not believed to be provided directly by the AGN hence fit the flat-component to get a core flux and then extrapolate from the NVSS point to get an upper limit for the non-core.

4C -05.84 Large, extended source with a spectrum that can be fit with a dropline model. VLA-A array X-band observation appears to resolve out all the large scale emission leaving just the unresolved core which is two orders of magnitude below what a straightforward extrapolation of the dropline shape would predict. Fit the integrated SED with a dropline model to get the non-core then extrapolate from the unresolved X-band core flux to get the measurement at 10 GHz for the core.

Z9077 The centre of this cluster contains two radio-sources that are close enough in projection ($<$45") to be confused in NVSS and at lower frequencies. Extrapolate from the peak of the isolated BCG to get an upper limit on the core flux. Give two values for the non-core: one for if only higher resolution data are used where the source is clearly separated and a significantly higher non-core estimate taken by just fitting the low resolution literature fluxes. The BCG is indistinct at C-band, appearing as a slightly elongated but faint source whereas the other source appears to have a short northern jet.

ATCA - C1958 - 2011

A2734 Unresolved at C- and X-band with the ATCA, in conjunction with the NVSS measurement this source has a reasonably steep ($\alpha\approx0.8$) power law spectrum. It has a marginally matched VLSS detection however inspection of this overlaid onto optical imaging of the BCG suggest this is not associated. Fit the steep component to measure the non-core and then extrapolate with α=0.2 to get upper limit on the core.

A2746 Unresolved at C- and X-bands. These fluxes give a flat (α=0.4) index consistent with core emission. SUMSS (Mauch et al., 2003) detection suggests there may be

a steeper component at lower frequencies although this is only constrained enough to be able to get an upper-limit for the non-core by extrapolating with α=1.0.

A3112 This source has multi-epoch observations suggesting evidence of variability at C-band and higher frequencies. Additionally, the source appears potentially slightly resolved with a small jet to the south and there is a larger peak-to-integrated flux discrepancy at X- than C-band. However, whilst there is evidence of core activity in this source the integrated spectrum is steep and appears to be dominated by the non-core. There is no clearly resolved core at the current resolutions, hence interpolate between the peak of X-band observation and the 20 GHz observation (Murphy et al., 2010) to get an upper limit on the core. Fit the steep component to get a flux at 1 GHz. Note that there is a 95 GHz observation of this source (Sadler et al., 2008) that is consistent with the integrated spectrum continuing to high frequency and highlights that the core limit derived herein is not expected to be stringent. The source appears to be similar to an FRI/II in behaviour and may perhaps an inadequately resolved FR-type source.

RXJ0528.9-3927 Faint, unresolved detection at C-band and only an upper limit at X-band. Extrapolate from the X-band limit to get an upper limit on the core and then fit the C-band observation with lower frequency detections that return an USS ($\alpha\approx$1.7) to get a measure of the non-core.

MACSJ0547.0-3904 One of the 34 most luminous MACS clusters (Ebeling et al., 2010). Unresolved at C- and X-band (potential hint of extent at C-band to the north-west but remapping suggests this is most likely an artefact), the inferred flat ($\alpha\approx$0.1) index is consistent with the SUMSS flux. However, the source appears as an NVSS object with almost twice the flux expected flux from the spectral fit. Overlaying the NVSS and SUMSS maps shows a consistent unresolved source. Possible that this is a highly variable source or that perhaps the NVSS flux is inflated. The position (Dec$\approx$-39) is just above the NVSS horizon. We exclude the NVSS flux from our fit, recovering a core measurement and then extrapolate from the SUMSS detection for a limit on the non-core.

AS701 Unresolved at both C- and X-bands and see a spectral inversion between these frequencies showing the presence of a core component. At lower frequencies the spectrum steepens as shown by a TGSS detection, fit therefore for a measure of the non-core.

A3605 Unresolved at C- and X-bands with a flat ($\alpha\approx$0.1) spectral component from which

a core component can be inferred. Extrapolating from the 150 MHz TGSS detection (with α=1.0) gives a flux at L-band that is consistent with the flux difference at 1.4 GHz between that expected from the core fit and that recovered in NVSS hence it appears reasonable to claim a non-core flux from TGSS only. This approach constrains the position of the self-absorption turnover of the core component to $<$1.4 GHz.

RXJ1539.5-8335 Source is flat spetrum and appears to be core dominated. Unresolved at C- and X-bands, the SUMSS detection is more suggestive of there being a self-absorption turnover between L and C bands rather than any additional non-core flux component at lower frequencies. Fit with a single power law to get a measurement for the core and extraolate from the SUMSS detection to get a limit on the non-core.

AS805 Source has a consistently steep power-law index between 843 MHz and 9.0 GHz and is unresolved at all observed frequencies, classifying the object as a likely CSS. Fit the spectrum to obtain a non-core flux and extrapolate from the X-band peak to get an upper-limit on the core component.

RXJ1931.6-3354 BCG associated with the radio source PKS 1928-34. Unresolved at C- and X-band with ATCA-6km but considering the SED it appears as if there is likely a steep spectrum component that is being resolved out. Fit this steep component seperately, then fit the unresolved core.

RXJ1947.2-7623 Steep spectrum source, fit with single power-law to get a measure of the non-core and then extrapolate from the X-band peak to get an upper-limit on the core.

A3992 Weak detection at C-band, undetected at X-band and no literature detections. Detection limits do not limit the spectrum to be sufficiently flat or steep and hence from the available information it cannot be claimed to be dominated by either core or non-core dominated. Extrapolate therefore from the C-band detection with flat index to get core limit and then extrapolate from the SUMSS detection limit for an upper-limit on the non-core component.

ATCA - C1958 - 2008

A11 Multi-epoch C-band observations suggest this source may be slightly variable. There

is a distinct steep component in the SED from which to get a measure of the non-core. The spectrum flattens to high frequency, interpolating between the X-band peak and 20 GHz flux (Murphy et al., 2010) gives a reasonable estimate of the core component.

A3017 Unresolved at C- and X-bands. 20 GHz detection along with the X-band flux shows that the spectrum flattens to higher frequency and hence is expected to be core dominated at 10 GHz. The spectrum steepens below this and there appears to be an ultra steep component (α>1.5) to SUMSS. These components can be fit separately for reasonable estimates of the core and non-core respectively.

RXJ0331.1-2100 The integrated spectrum can be well fit with a dropline model, indicative of it being non core dominated. Therefore fit to get a measure of the non-core and then extrapolate from the 20 GHz detection (Murphy et al., 2010) to get an upper limit on the core. Source is perhaps best classified as a CSS with a spectral rollover to lower frequencies (see e.g. O'Dea, 1998), perhaps indicative of extended diffuse emission at $<$100 MHz.

A496 VLSS (Cohen et al., 2007) and CULGOORA (Slee, 1995) detections show there to be an USS component to this source, whereas higher frequency observations show a strong, variable core component that flattens the spectrum and is dominant above a few GHz. Fit to fluxes at frequencies above 1.4 GHz to get a measure of the core and then separately fit to the lowest frequency observations to get the non-core. NVSS (1.4 GHz) is in the 'crossover zone' where the core and non-core are believed to contribute roughly equally and hence is used to check that the relative proportions of the components are consistent.

RXJ0543.4-4430 Unresolved at both C- and X-bands. SED shows both a flat and a steep component that canbe fit with a split power-law model to obtain measures of the core and non-core components respectively.

AS555 Source is extended in the C- observations although the core cannot be reliably isolated. Fit SED with a single power law to get the non-core flux. There is a peak-to-integrated flux decrement at X-band although again, the core cannot be isolated and hence extrapolate from the peak at X-band to get an upper limit on the core component at 10 GHz.

A3378 The SED has a well sampled steep component from which the non-core flux can

be measured. The peak of the X-band detection in conjunction with the two 20 GHz (Murphy et al., 2010, and Mahony, *private communication*) fluxes suggest that there is an active core in this system that becomes more important to higher frequencies although this is not clearly being isolated. An unambiguous measure of the core contribution cannot therefore be claimed, hence extrapolate from the lower 20 GHz flux to get an upper limit for the core.

RXJ0747.5-1917 This source is perhaps best classified as a CSS with a low frequency turnover. Unresolved at C- and X-bands although the imaging suffers from an elliptical beam shape. Fit a dropline model to the SED to get a measure of the non-core component and then extrapolate from the X-band peak to get an upper limit on the core.

A1348 Source contains a variable core component that can be well-fit with a GPS-like model. This core dominance is confirmed by VLBA imaging (Chapter 5). There is a steeper component in the SED at lower frequencies as seen in VLSS (Cohen et al., 2007) and WISH (De Breuck et al., 2002), with the shape consistent with the steep component just catching the turnover of the GPS-like core component. Fit a GPS model to the core and then fit a power law to the steep component to obtain a measure of the non-core, ensuring that the core contribution is accounted for.

RXJ1304.3-3031 Source is unresolved at C- and X-bands, consistent with the GPS-like shape of the SED showing that this source is core dominated. Source does not currently match to the TGSS catalogue but does appear in the thumbnail image, below the catalogue limit. Nonetheless, the positions match and hence extrapolate from this TGSS detection to get an upper limit on the non-core.

RXJ1315.4-1623 This source is unresolved and has an apparently self-absorbed spectrum, consistent with it being core dominated. There is a WISH detection at 352 MHz (De Breuck et al., 2002) that shows it to be peaked and a tentative TGSS map detection at 150 MHz. This map detection may be indicative of a low-level non-core component although it should be stressed that this flux is recovered just above the noise. Hence, extrapolate from this to get only an upper limit on the non-core.

A3581 Source is flat spectrum ($\alpha \approx 0.5$) down to low frequency (e.g. 74 MHz with the VLSS Cohen et al., 2007) and shows signs of variability in repeat observations at both C- and X-bands. The source is resolved with the VLBA (Chapter 5), with the integrated flux

of this roughly consistent with the unresolved C-band flux thus showing this source to be highly core dominated. Fit the resolved core component then remove this from the recovered flux of the lower resolution observation for an estimate of the non-core component. Also see Chapter 4.

AS780 Source is variable (Chapter 4) and has a flat spectrum showing it to be core dominated. Fit the flat spectrum to get a core flux and then extrapolate back from WISH (De Breuck et al., 2002) to get an upper limit on the non-core. Non-detection in VLSS (Cohen et al., 2007) suggests that this source must turnover to low frequency.

RXJ1524.2-3154 The detected fluxes imply a flat spectrum although this source is undetected by TGSS at 150 MHz and the upper limit implies that this source must be a GPS . Fit the core component and then extrapolate from the TGSS limit to get an upper-limit on the non-core.

RXJ1558.4-1410 This source contains a very dominant, self-absorbed core component along with a steep spectrum power-law component to low ($<$1 GHz) frequencies. Fit the core with a GPS-like model and then fit the steep component seperately with a power-law to obtain a value for the non-core. See Chapter 4 for a more in-depth look at this source.

A3638 This source is unresolved and has a steep spectrum ($\alpha \approx 0.93$) between C-band, X-band and 20 GHz (Murphy et al., 2010) but no other literature fluxes are available. However, there is a nearby bright source that is confused with the BCG at low resolutions and hence could explain why this source is apparently missing in some low frequency catalogues. From the high resolution data the source can be classified as a CSS. Fit the steep spectrum to obtain a measurement of the non-core and then extrapolate from the 20 GHz detection to get an upper-limit on the active core component.

A3639 Steep spectrum source although there is a detection at 20 GHz in AT20g (Murphy et al., 2010) that suggests the spectrum may flatten to higher frequencies, which is indicative of this system containing an active core. There are insufficient data points to adequately fit using a direct split power model although the steep component can be fit with a single power-law for a non-core component and then interpolating between the 20 GHz and X-band data with conservative uncertainty allows for the core component to be estimated.

AS851 Source has a flat spectrum and multi-epoch observations at C-band suggest that

it varies, indicating that this is core dominated. Fit to get a measure of the core flux and then extrapolate from the SUMSS detection for an upper limit on the non-core.

RXJ2014.9-2430 A steep spectrum source that is potentially slightly extended to the West as seen with the ATCA-6km array at C-band although this is not apparent at X-band. Fit the SED to get a non-core flux and then extrapolate from the X-band detection to get an upper limit on the core.

RXJ2213.1-2754 The SED for this source suggests significant variability at GHz frequencies. Additionally, it appears as if some low resolution observations may suffer from confusion. Fitting a power-law to the SED returns a flat index ($\alpha\approx0.5$). Use this to obtain an estimate of the core component and then extrapolate from the NVSS detection (lower frequency observations appear to be confused and hence are excluded) to get an upper limit on the non-core.

A3880 The BCG is associated with the radio-source PKS 2225-308, and shows extended single-sided structure at both C- and X-band. From lower resolution data at C-band (e.g. with Parkes, Wright & Otrupcek, 1990) it appears as if the interferometric observations are still missing extended emission. Fitting a single power-law to the SED comprising the integrated fluxes returns a steep index ($\alpha\approx0.99$). Use this to obtain a measure of the non-core flux and then extrapolate from the resolved core's peak flux at X-band to obtain an estimate of the active core component.

AS1101 Extended FRI-like structure seen at C-band although this is split into a more one-sided FRII-like morphology comprising a core and a hot spot at X-band. The integrated fluxes are consistent with a steep ($\alpha\approx1.4$) index for the integrated emission that can be fit this to get a measure of the non-core. Extrapolate from the resolved X-band core with $\alpha=0.2$ to get an estimate of the core flux at 10 GHz.

A2580 Source can be fit with a dropline model suggesting that it is non-core dominated. Extrapolate from the X-band flux to obtain a core limit. The WENSS flux (Rengelink et al., 1997) suggests that this source may turnover and flatten to lower frequency which could be suggestive of it being wrongly interpreted and actually being a core-dominated source. Multi-epoch of milli-arcsecond scale observations are required to unambiguously characterise this source.

A2667 The SED is too undersampled to be reasonably directly fit using a split power.

However, both C and X-band images show it to be unresolved, which combined with the 20 GHz flux (AT20g, Murphy et al., 2010) suggest that this source is core dominated and perhaps variable. The NVSS (1.4 GHz) flux is above the flatter index fitted at higher frequencies, which suggests there could be additional diffuse emission in the system although there are no lower frequency detections to reliably constrain this. Therefore, fit the flat spectrum component with a power-law to get a measurement of the core component and then extrapolate from the NVSS flux to get an upper limit on the non-core.

A4059 Source is resolved into two-sided structure at C-band, with a clearly distinguishable core component. The SED of the integrated fluxes is well fit with a dropline model and confirms that this system is dominated by ageing emission in the lobes. The core component can be estimated by extrapolating from the peak of the X-band emission.

ALL THE NON-DETECTIONS

All the non-detections were cross-matched with NVSS and/or SUMSS, depending on their position in the sky. The relative detection thresholds of these surveys and our C-band observations are such that where there was a match (confirmed by inspection of visual overlays to optical data) then this was taken as evidence of the system being dominated by a steep component. The catalogue flux was in these instances extrapolated to obtain an estimate of the non-core component and a core limit derived by extrapolating from the higher frequency limit. In most instances there was no detection in either catalogue. In these situations, an extrapolation was made from the NVSS/SUMSS limit for the non-core and again, the higher frequency limit was extrapolated from to obtain a a core limit, using the usual indices as described in the main text.

Appendix B

Main Sample - Data Tables

Table B.1: Recovered C-band fluxes. Note that the value given in the core column is the peak of the emission if unresolved or the peak of the core component for resolved sources. Redshifts are from Crawford et al.(1999) unless otherwise stated.

		Position(J2000)		Fluxes (mJy)				
Cluster	BCG	RA	DEC	Core	Total	RMS	Redshift	Lines?
VLA-C Array								
AE125 : 1999 : 50 MHz								
RXJ0000.1+0816	UGC12890	00:00:07.09	08:16:45.2	41.90	46.62	0.06	0.040	√
RXJ0021.6+2803	IV Zw 015 NOTES01	00:21:36.82	28:03:02.6	0.39	0.37	0.05	0.094	x
Z235	2MASX J00435213+2424213	00:43:52.17	24:24:21.1	27.32	30.28	0.27	0.083	√
RXJ0058.9+2657	NGC326/4C+26.03	00:58:22.63	26:51:58.7	11.21	558.63	0.26	0.048	x
RXJ0107.4+3227	NGC 383	01:07:24.93	32:24:45.6	83.63	1037.00	1.51	0.0175	√
A160	VV 382 / MCG 02-04-010	01:12:59.57	15:29:28.8	7.74	257.26	0.27	0.044	x
RXJ0123.6+3315	NGC 507	01:23:39.90	33:15:21.8	1.47	1.46	0.06	0.0169	x
A262	NGC 708	01:52:46.40	36:09:06.1	7.49	17.96	0.06	0.0166	√
A407	UGC 02489	03:01:51.39	35:50:22.5	21.69	202.69	0.09	0.0484	√
RXJ0341.3+1524	III Zw054	03:41:17.53	15:23:47.5	11.52	12.98	0.05	0.029	x

Continued on Next Page...

Table B.1 – Continued

A621	2MASX J08111245+7002284	08:11:12.48	70:02:29.9	11.26	24.83	0.06	0.223	x
A646	2MASX J08220955+4705529	08:22:09.60	47:05:52.7	79.38	85.47	0.07	0.1268	√
A761	2MASX J09103593-1034568	09:10:35.47	-10:35:00.7	11.04	90.41	0.15	0.091	x
A757	2MASX J09130775+4742307	09:13:07.74	47:42:30.3	10.27	11.10	0.06	0.0520	N
Z2661	SDSS J094952.48+170737.4	09:49:52.47	17:07:37.3	0.63	0.61	0.04	0.3825	x
Z2701	2MASX J09524915+5153053	09:52:49.17	51:53:05.1	3.63	3.85	0.06	0.215	√
Z2844	NGC 3099	10:02:36.54	32:42:24.3	8.50	8.87	0.06	0.0502	N
Z3179	2MASX J10255796+1241086	10:25:57.97	12:41:08.2	21.81	24.75	0.05	0.1432	√
A1023	LCRS B102528.0-063237	10:27:58.68	-06:47:55.8	2.71	2.90	0.05	0.1165	N
RXJ1053.7+5450	2MASX J10533658+5452047	10:53:36.49	54:52:04.9	0.65	1.34	0.08	0.070	x
A1132	2MASX J10582366+5647417	10:58:23.79	56:47:40.7	2.89	6.60	0.07	0.1365	x
A1190	MCG +07-23-031	11:11:43.66	40:49:15.8	4.42	6.33	0.08	0.0772	x
A1361	4C +46.23	11:43:39.59	46:21:20.4	71.01	208.44	0.12	0.1167	√
A1366	2MASX J11443683+6724211	11:44:36.70	67:24:21.4	39.44	70.82	0.10	0.1155	x
Z4673	2MASX J11565578+2415362	11:56:55.81	24:15:35.6	0.79	0.76	0.05	0.1419	x
Z4803	NGC 4073	12:04:27.10	01:53:45.7	0.28	0.27	0.05	0.0194	x
RXJ1206.5+2810	NGC 4104	12:06:38.89	28:10:26.8	0.53	0.44	0.05	0.0281	√
A1668	IC 4130	13:03:46.60	19:16:17.5	18.34	21.00	0.05	0.0640	√

Continued on Next Page…

Table B.1 – Continued

A1677	MCG +05-31-128	13:05:50.71	30:54:15.8	16.65	23.10	0.05	0.1845	x
RXJ1320.1+3308	NGC5098	13:20:14.76	33:08:37.7	10.77	35.39	0.11	0.0377	√
A1763	4C +41.26	13:35:20.43	40:59:59.3	72.83	217.31	0.07	0.2280	N
A1775(SE)	UGC 08669	13:41:50.58	26:22:17.9	24.95	88.14	0.08	0.0700	x
A1775(NW)	UGC 08669 NED01	13:41:49.22	26:22:26.5	3.15	7.04	0.08	0.0758	x
A1773	2MASX J13420967+0213381	13:42:09.67	02:13:35.6	0.52	0.74	0.05	0.0763	x
A1885	2MASX J14134379+4339450	14:13:43.72	43:39:45.0	35.03	36.72	0.06	0.090	√
RXJ1442.2+2218	UGC9480	14:42:19.37	22:18:11.9	10.60	11.03	0.05	0.0970	√
A1991	NGC 5778	14:54:31.39	18:38:32.4	10.7	11.4	0.1	0.0595	√
Z7160	SDSS J145715.10+222034.4	14:57:15.10	22:20:34.3	2.09	2.41	0.09	0.2578	√
A2009	2MASX J15001950+2122108	15:00:19.52	21:22:09.9	4.65	4.74	0.05	0.1532	√
A2033	UGC9756	15:11:26.48	06:20:57.2	9.24	187.00	0.10	0.078	N
A2055	2MASX J15184574+0613554	15:18:45.79	06:13:56.2	106.99	213.36	0.16	0.1019	N
A2064	MCG +08-28-020	15:20:52.36	48:39:37.8	11.17	28.66	0.06	0.0741	x
RXJ1522.0+0741	NGC5920	15:21:51.86	07:42:31.8	2.41	2.50	0.05	0.0451	x
A2063	CGCG 077-097	15:23:05.27	08:36:33.0	1.70	4.46	0.09	0.0342	x
A2146	2MASX J15561395+6620530	15:56:14.00	66:20:53.8	6.7	6.6	0.1	0.2343	√
A2175	2MASX J16203111+2953276	16:20:31.15	29:53:27.7	1.03	1.31	0.05	0.0961	x

Continued on Next Page. . .

Table B.1 – Continued

RXJ1657.8+2751	NGC 6269	16:57:58.11	27:51:16.5	4.87	9.90	0.07	0.035	x
A2241	4C +32.52C	16:59:43.95	32:36:55.0	5.09	6.60	0.07	0.0984	x
Z8193	B3 1715+425	17:17:19.21	42:27:00.2	83.3	86.7	0.2	0.1754	√
RXJ1720.1+2638	2MASX J17201001+2637317	17:20:10.01	26:37:32.0	2.71	13.26	0.08	0.1611	√
Z8276	2MASX J17441450+3259292	17:44:14.50	32:59:28.8	63.8	72.7	0.2	0.075	√
A2390	ABELL 2390:[YEA96] 101084	21:53:36.83	17:41:44.2	202.19	213.63	0.10	0.2328	√
RXJ2214.7+1350	3C442/NGC7237	22:14:46.89	13:50:27.2	46.02	48.17	0.13	0.026	√
A2572A	NGC 7578B	23:17:13.78	18:42:27.6	7.87	13.42	0.05	0.0400	x
A2634	NGC 7720	23:38:29.37	27:01:53.2	250.90	253.19	2.33	0.0298	√
Core limit								
A115	3C 028	00:55:50.11	26:24:34.7	<7.18	140.79	0.11	0.1970	√
RXJ0740.9+5526	UGC 03957	07:40:58.16	55:25:40.0	<1.98	18.14	0.11	0.0340	x
Upper limits								
RXJ0123.2+3327	NGC 499	01:23:11.6	33:27:36	<0.18	<0.18	0.06	0.0141	N
A665	2MASX J08305736+6550299	08:30:57.3	65:50:32	<0.18	<0.18	0.06	0.1824	x
Z1953	2MASX J08500730+3604203	08:50:07.4	36:04:15	<0.3	<0.3	0.10	0.374	x
A781	SDSS J092025.17+303131.6	09:20:25.1	30:31:33	<0.3	<0.3	0.10	0.304	x
A1173	2MASX J11091531+4133412	11:09:15.2	41:33:43	<0.15	<0.15	0.05	0.0767	x

Continued on Next Page...

Table B.1 – Continued

A1185	NGC3550	11:10:38.3	28:46:03	<0.15	<0.15	0.05	0.0348	x
A1302	2MASX J11331462+6622454	11:33:14.6	66:22:46	<0.18	<0.18	0.06	0.1148	x
A1423	2MASX J11571737+3336399	11:57:17.4	33:36:40	<0.15	<0.15	0.05	0.213	x
RXJ1205.1+3920	2MASX J12051040+3920476	12:05:10.2	39:20:49	<0.15	<0.15	0.05	0.037	x
RXJ1223.0+1037	NGC 4325	12:23:06.7	10:37:17	<0.15	<0.15	0.05	0.0259	√
Z5247	2MASX J12341746+0945577	12:34:17.5	09:46:00	<0.15	<0.15	0.05	0.229	x
A1589	MCG +03-32-083	12:41:17.4	18:34:30	<0.18	<0.18	0.06	0.0709	x
A1831	CGCG 162-041	13:59:15.0	27:58:34	<0.18	<0.18	0.06	0.0760	x
A1914	2MASX J14255668+3748589	14:25:56.7	37:49:00	<0.18	<0.18	0.06	0.170	√
A2061	2MASX J15211133+3035023	15:21:11.1	30:35:03	<0.15	<0.15	0.05	0.0753	x
A2111 (a)	2MASX J15394049+3425276	15:39:40.5	34:25:27	<0.21	<0.21	0.07	0.2317	x
(b)	2MASX J15394179+3424426	15:39:41.8	34:24:43	<0.21	<0.21	0.07	0.2300	x
A2124	UGC 10012	15:44:59.1	36:06:35	<0.15	<0.15	0.05	0.0663	x
A2201	2MASX J16265900+5528298	16:26:59.0	55:28:30	<0.18	<0.18	0.06	0.130	x
A2208	2MASX J16293891+5831526	16:29:38.9	58:31:53	<0.3	<0.3	0.1	0.1329	x
A2249	2MASX J17094864+3427320	17:09:48.6	34:27:32	<0.24	<0.24	0.08	0.0873	x
Z8852	NGC 7499	23:10:22.3	07:34:52	<0.90	<0.90	0.30	0.0399	x
A2572B	NGC 7571	23:18:30.3	18:41:21	<0.21	<0.21	0.07	0.0370	x

Continued on Next Page...

Table B.1 – Continued

AE110 : 1997 : 50 MHz								
A75	2MASX J00392858+2113480	00:39:28.55	21:13:48.4	0.67	0.66	0.12	0.062	N
A76	IC 1568	00:39:55.97	06:50:55.4	0.47	0.34	0.11	0.0407	x
A77	UGC 00428	00:40:28.26	29:33:21.3	4.81	5.04	0.09	0.071	x
A147	UGC 00701 NED02	01:08:12.07	02:11:38.6	0.50	0.38	0.11	0.042	x
A168	UGC 00797	01:14:57.61	00:25:51.3	1.30	1.88	0.1	0.0443	x
A193	IC 1695	01:25:07.62	08:41:58.0	1.97	2.60	0.09	0.0484	x
A189	NGC 0533	01:25:31.41	01:45:33.2	6.79	10.45	0.12	0.019	x
RXJ0419.6+0225	NGC 1550	04:19:37.91	02:24:35.0	0.82	0.83	0.15	0.0133	x
Z1261	4C +53.16	07:16:41.22	53:23:09.5	33.6	615.4	0.2	0.064	x
RXJ0751.3+5012	UGC 04052	07:51:21.01	50:14:10.0	5.83	5.98	0.06	0.0236	√
A646	2MASX J08220955+4705529	08:22:09.54	47:05:52.8	81.5	84.4	0.3	0.1268	√
Z1665	IC505	08:23:21.66	04:22:20.8	8.21	8.29	0.07	0.0311	N
Z2089	2MASX J09003684+2053402	09:00:36.88	20:53:40.5	3.14	3.47	0.09	0.235	√
A763	MG1 J091235+1600	09:12:35.09	16:00:00.1	1.13	24.03	0.13	0.0892	x
A795	2MASX J09240529+1410217	09:24:05.31	14:10:21.6	24.18	24.77	0.16	0.1355	√
Z2844	NGC 3099	10:02:36.54	32:42:24.4	8.59	9.14	0.11	0.0502	N

Continued on Next Page. . .

Table B.1 – Continued

A1035	2MASX J10321392+4016164	10:32:13.95	40:16:16.4	3.55	3.52	0.11	0.078	N
A1204	2MASX J11132052+1735409	11:13:20.49	17:35:41.0	1.79	1.76	0.10	0.1706	√
A1235	SDSS J112315.72+193547.1	11:23:15.72	19:35:47.1	0.81	0.65	0.09	0.104	x
A1553	MCG 02-32-109	12:30:43.27	10:34:43.3	1.92	2.58	0.10	0.1634	x
RXJ1326.3+0013	2MASX J13261760+0013177	13:26:17.39	00:13:23.4	4.50	7.15	0.09	0.0821	x
Z6718	MCG +08-26-021	14:21:35.84	49:33:04.3	1.3	1.5	0.1	0.071	x
A1902	2MASX J14214046+3717304	14:21:40.55	37:17:30.9	0.7	0.7	0.1	0.160	x
A1927	2MASX J14310681+2538013	14:31:06.80	25:38:00.6	2.9	3.3	0.1	0.0967	x
A1930	MCG +05-34-067	14:32:37.97	31:38:48.7	5.7	5.7	0.1	0.1316	√
RXJ1440.6+0327	NGC 5718	14:40:42.86	03:27:55.3	1.1	0.9	0.1	0.0274	N
A1978	2MASX J14510936+1436432	14:51:09.35	14:36:43.3	0.72	0.53	0.09	0.1468	x
MACS1532.9+3021	SDSS J153253.78+302059.3	15:32:53.78	30:20:59.3	8.78	8.82	0.08	0.3615	√
A2110	2MASX J15395079+3043037	15:39:50.79	30:43:04.1	1.75	1.90	0.08	0.0976	N
A2108 (a)	2MASX J15401594+1752292	15:40:15.87	17:52:28.4	0.8	0.9	0.1	0.092	x
(b)	2MASX J15401902+1751232	15:40:19.17	17:51:25.2	1.0	1.6	0.1	0.092	x
(c)	2MASX J15401797+1753042	15:40:18.0	17:53:04	<0.3	<0.3	0.1	0.092	x
RXJ1604.9+2356	NGC 6051	16:04:56.65	23:55:57.5	38.5	190.3	0.2	0.0324	x
A2204	VLSS J1632.7+0534	16:32:46.95	05:34:32.7	21.3	27.2	0.1	0.1514	√

Continued on Next Page...

Table B.1 – Continued

A2228	2MASX J16480084+2956575	16:48:00.82	29:56:56.7	0.39	0.39	0.07	0.1013	x
A2244	2MASX J17024247+3403363	17:02:42.48	34:03:37.3	0.73	0.82	0.07	0.0980	x
RXJ1715.3+5725	NGC 6338	17:15:22.98	57:24:40.4	29.2	30.5	0.1	0.0282	√
Z8193	B3 1715+425	17:17:19.21	42:26:59.7	86.5	88.7	0.15	0.1754	√
Z8197	2MASX J17181198+5639563	17:18:11.93	56:39:55.9	7.4	8.9	0.06	0.1140	√
RXJ1733.0+4345	IC 1262	17:33:02.01	43:45:34.7	5.2	5.5	0.1	0.0331	√
Z8276	2MASX J17441450+3259292	17:44:14.46	32:59:29.3	68.2	71.7	0.13	0.075	√
A2443	2MASX J22260792+1721228	22:26:07.94	17:21:22.2	4.57	9.04	0.06	0.1105	x
A2457	2MASX J22354078+0129053	22:35:40.77	01:29:05.9	0.37	0.32	0.06	0.0592	x
A2495	MCG +02-58-021	22:50:19.72	10:54:12.6	1.82	2.85	0.09	0.0808	√
A2626	IC 5338	23:36:30.49	21:08:47.5	6.66	7.27	0.04	0.0552	√
A2627 (a)	B2 2334+23	23:36:42.12	23:55:29.0	88.4	138.7	0.1	0.127	N
(b)	2MASX J23364245+2354442	23:36:42.47	23:54:44.6	19.1	20.2	0.1	0.122	N
Z9077	2MASX J23503544+2929386	23:50:35.15	29:29:44.4	1.92	3.95	0.06	0.015	√
A2665	MCG +01-60-039	23:50:50.56	06:08:58.6	4.77	7.93	0.09	0.0567	√
A2675	2MASX J23554260+1120355	23:55:42.61	11:20:35.5	3.9	3.9	0.1	0.0746	x
Diffuse envelope only								
A2622	4C +27.53A	23:35:01.5	27:22:21	<0.24	5.91	0.08	0.061	x

Continued on Next Page...

Table B.1 – Continued

Upper limits								
A7	2MASX J00114523+3224562	00:11:45.2	32:24:56	<0.18	<0.18	0.06	0.1017	x
A21 (a)	2MASXi J0020373+283928	00:20:37.4	28:39:28	<0.3	<0.3	0.1	0.0967	x
(b)	2MASX J00203715+2839334	00:20:37.1	28:39:34	<0.3	<0.3	0.1	0.0967	x
RXJ0021.6+2803	IV Zw 015 NOTES01	00:21:36.8	28:03:02	<0.3	<0.3	0.1	0.094	x
A84	2MASX J00415507+2122379	00:41:55.0	21:22:38	<0.78	<0.78	0.26	0.103	x
A104	2MASX J00494980+2427021	00:49:49.8	24:27:02	<0.45	<0.45	0.15	0.082	x
A272	V Zw 139 NED05	01:55:10.6	33.53:48	<0.15	<0.15	0.05	0.0898	x
RXJ0228.2+2811	IC 0227	02:28:03.6	28:10:31	<0.3	<0.3	0.1	0.0351	x
A566	KUG 0659+633	07:04:28.6	63:18:41	<0.3	<0.3	0.1	0.0945	x
A602	2MASX J07531662+2924051	07:53:16.5	29:24:06	<0.48	<0.48	0.16	0.0601	x
A750	2MASX J09091273+1058286	09:09:12.6	10:58:29	<0.33	<0.33	0.11	0.177	N
A961	2MASX J10162281+3338170	10:16:23.0	33:38:19	<0.27	<0.27	0.09	0.124	x
A1177	NGC 3551	11:09:44.4	21:45:34	<0.3	<0.3	0.1	0.0323	x
A1201	2MASX J11125450+1326093	11:12:54.5	13:26:10	<0.27	<0.27	0.09	0.1679	x
A1437	2MASX J12002533+0320490	12:00:25.3	03:20:50	<0.21	<0.21	0.07	0.1336	x
Z4905	2MASX J12101679+0523097	12:10:16.8	05:23:11	<0.36	<0.36	0.12	0.0766	N
A1800	UGC 08738	13:49:23.6	28:06:26	<0.27	<0.27	0.09	0.0750	x

Continued on Next Page...

Table B.1 – Continued

A1809	2MASX J13530637+0508586	13:53:06.4	05:08:59	<0.3	<0.3	0.1	0.0796	x
A1918	2MASX J14252238+6311524	14:25:22.5	63:11:53	<0.27	<0.27	0.09	0.139	x
A1983 (a)	2MASX J14525528+1642106	14:52:55.3	16:42:11	<0.45	<0.45	0.15	0.0442	x
(b)	CGCG 105-055	14:52:56.9	16:43:41	<0.45	<0.45	0.15	0.0459	x
A2034	2MASX J15101172+3329112	15:10:11.7	33:29:11	<0.3	<0.3	0.1	0.111	x
A2050	2MASX J15161794+0005203	15:16:17.9	00:05:21	<0.27	<0.27	0.09	0.118	x
A2069	2MASX J15240841+2952553	15:24:08.4	29:52:55	<0.3	<0.3	0.1	0.1138	x
A2072	2MASX J15254866+1814093	15:25:48.7	18:14:09	<0.3	<0.3	0.1	0.127	√
A2107	UGC 09958	15:39:39.0	21:46:58	<0.36	<0.36	0.12	0.042	x
A2219	2MASX J16401981+4642409	16:40:19.8	46:42:41	<0.3	<0.3	0.1	0.2248	x
A2294	2MASX J17241223+8553116	17:24:12.1	85:53:12	<0.27	<0.27	0.09	0.178	√
RXJ1740.5+3539 (a)	CGCG 199-007 NED02	17:40:34.3	35:39:13	<0.3	<0.3	0.1	0.0416	x
(b)	CGCG 199-007 NED01	17:40:32.1	35:38:46	<0.3	<0.3	0.1	0.0448	x
Z8338	NGC 6582 NED02	18:11:05.1	49:54:33	<0.27	<0.27	0.09	0.047	x
A2318	2MASX J19051142+7805369	19:05:11.4	78:05:37	<0.33	<0.33	0.11	0.1405	x
A2537	2MASX J22082334-0209489	22:08:23.3	-02:09:49	<0.24	<0.24	0.08	0.295	x
A2589	NGC 7647	23:23:57.4	16:46:38	<0.3	<0.3	0.1	0.0407	x
A2593	NGC 7649	23:24:20.1	14:38:50	<0.45	<0.45	0.15	0.0423	x

Continued on Next Page...

Table B.1 – Continued

AE107 : 1996 : 50 MHz								
RXJ0341.3+1524	III Zw 054	03:41:17.49	15:23:40.6	10.49	11.31	0.08	0.029	x
RXJ0503.1+0608	2MASX J05030697+0607564	05:03:06.97	06:07:56.9	5.4	5.5	0.2	0.088	x
A611	2MASX J08005684+3603234	08:00:56.85	36:03:23.0	0.45	0.40	0.05	0.288	N
RXJ0819.6+6336	2MASX J08192591+6337256	08:19:25.86	63:37:26.1	5.5	10.0	0.1	0.1186	x
A667	2MASX J08280587+4446005	08:28:05.84	44:46:01.1	2.16	3.46	0.06	0.145	x
A971	2MASX J10195207+4059179	10:19:52.08	40:59:18.6	1.8	2.1	0.1	0.093	x
A980	2MASX J10222849+5006200	10:22:28.43	50:06:20.1	1.6	2.6	0.1	0.158	x
A1045	2MASX J10350012+3041380	10:35:00.14	30:41:38.2	2.24	2.46	0.09	0.1381	x
RXJ1715.1+0309	2MASX J17151218+0309380	17:15:12.14	03:09:42.6	17.6	45.7	0.1	0.1647	√
A2261	2MASX J17222717+3207571	17:22:27.06	32:07:58.1	0.64	0.59	0.05	0.224	x
RXJ1750.2+3504	2MASX J17501683+3504587	17:50:16.90	35:04:58.5	31.0	31.9	0.1	0.1712	√
RXJ2129.6+0005	2MASX J21293995+0005207	21:29:39.96	00:05:21.6	8.01	9.05	0.07	0.2346	√
Upper limits								
A68 (a)	2MASX J00370686+0909236	00:37:06.8	09:09:24	<0.18	<0.18	0.06	0.250	x
(b)	ABELL 0068:[CAE99] b	00:37:04.9	09:09:47	<0.18	<0.18	0.06	0.259	x
A267	2MASX J01524199+0100257	01:52:42.0	01:00:26	<0.21	<0.21	0.07	0.230	x

Continued on Next Page. . .

Table B.1 – Continued

RXJ0439.0+0716	2MASX J04390053+0716038	04:39:00.5	07:16:04	<0.15	<0.15	0.05	0.2452	x
RXJ0448.2+0953	2MASXJ04481277+0953010	04:48:12.8	09:53:01	<0.15	<0.15	0.05	0.154	x
A523	2MASX J04591293+0849411	04:59:12.9	08:49:41	<0.1	<0.1	0.03	0.1036	x
Z1478	SDSS J075944.36+535856.0	07:59:44.4	53:58:56	<0.12	<0.12	0.04	0.104	x
A655	2MASX J08252902+4707598	08:25:29.0	47:08:01	<0.18	<0.18	0.06	0.129	x
A671	IC 2378	08:28:31.6	30:25:53	<0.27	<0.27	0.09	0.051	N
A990	2MFGC 08048	10:23:39.9	49:08:39	<0.12	<0.12	0.04	0.142	x
A1033	2MASX J10314436+3502291	10:31:44.3	35:02:29	<0.27	<0.27	0.09	0.1259	x
A2254	2MASX J17174586+1940482	17:17:45.8	19:40:48	<0.3	<0.3	0.1	0.178	x
A2259	2MASX J17200968+2740077	17:20:09.7	27:40:08	<0.21	<0.21	0.07	0.164	x
A2409	2MASX J22005255+2058087	22:00:52.5	20:58:09	<0.21	<0.21	0.07	0.1470	x
A2552	2MASX J23113330+0338056	23:11:33.3	03:38:05	<0.24	<0.24	0.08	0.3025	x
A2631	SDSS J233741.06+001705.7	23:37:41.0	00:17:06	<0.3	<0.3	0.1	0.278	x
AE099 : 1994 : 50 MHz								
A291	2MASX J02014311-0211474	02:01:43.14	-02:11:48.1	5.43	5.49	0.08	0.196	√
Z808	4C +01.06	03:01:38.21	01:55:14.8	6.89	23.8	0.07	0.169	√
RXJ0352.1+1941	2MASX J03525901+1940595	03:52:58.98	19:40:59.7	7.23	7.68	0.05	0.109	√

Continued on Next Page. . .

Table B.1 – Continued

RXJ0439.0+0520	2MASX J04390223+0520443	04:39:02.25	05:20:43.2	146.2	149.6	0.1	0.208	√
Z1121	3C 162	06:31:22.73	25:01:06.9	121.4	330.9	0.2	0.083	√
RXJ0821.0+0752	2MASX J08210226+0751479	08:21:02.20	07:51:48.3	0.70	0.85	0.07	0.110	√
Z2701	2MASX J09524915+5153053	09:52:49.21	51:53:05.3	3.82	4.20	0.03	0.215	√
Z3146	2MASX J10233960+0411116	10:23:39.62	04:11:10.7	0.81	0.78	0.07	0.2906	√
Z3179	2MASX J10255796+1241086	10:25:57.99	12:41:08.5	23.4	24.6	0.1	0.1432	√
A1068	2MASX J10404446+3957117	10:40:44.50	39:57:11.2	2.16	2.62	0.06	0.1386	√
A1084	2MASX J10443287-0704074	10:44:32.85	-07:04:07.5	28.6	29.0	0.1	0.1326	N
Z3916	2MASX J11142180+5823195	11:14:21.66	58:23:19.8	5.40	6.76	0.05	0.204	√
A1651	2MASX J12592251-0411460	12:59:22.47	-04:11:46.5	1.58	1.73	0.06	0.0860	x
A1664	2MASX J13034252-2414428	13:03:42.58	-24:14:42.4	14.45	14.38	0.07	0.1276	√
A1835	2MASX J14010204+0252423	14:01:02.09	02:52:42.6	12.52	13.35	0.05	0.2523	√
A1885	2MASX J14134379+4339450	14:13:43.72	43:39:45.0	35.9	35.3	0.1	0.090	√
A2146	2MASX J15561395+6620530	15:56:13.89	66:20:53.2	9.10	9.68	0.05	0.2343	√
Upper limits								
A409	2MASX J03032123+0155344	03:03:21.2	01:55:32	<0.18	<0.18	0.06	0.153	x
A644	2MASX J08172559-0730455	08:17:25.6	-07:30:46	<0.15	<0.15	0.05	0.0705	x
A697	2MASX J08425763+3622000	08:42:57.5	36:21:59	<0.21	<0.21	0.07	0.282	x

Continued on Next Page...

Table B.1 – Continued

A773 (a)	2MASX J09175344+5143379	09:17:53.4	51:43:37	<0.21	<0.21	0.07	0.216	x
(b)	2MASX J09175344+5144009	09:17:53.5	51:44:01	<0.21	<0.21	0.07	0.224	x
A1682 (a)	2MASX J13064570+4633305	13:06:46.13	46:33:29.8	<0.3	<0.3	0.1	0.2190	x
(b)	2MASX J13064997+4633335	13:06:50.0	46:33:33	<0.3	<0.3	0.1	0.2330	x
ATCA-6A Array								
C1958 : 2011 : 2048 MHz								
A2734	ESO 409- G 025	00:11:21.65	-28:51:15.1	3.8	3.6	0.1	0.0619	√
A2746	2MASX J00141626-6604211	00:14:16.21	-66:04:21.3	3.4	3.4	0.1	0.1592	√
A3112	ESO 248- G 006	03:17:57.66	-44:14:17.6	464.0	596.7	1.7	0.0761	√
RXJ0528.9-3927	RBS0653	05:28:53.02	-39:28:18.0	0.7	0.7	0.2	0.2839	√
MACSJ0547.0-3904	NVSS J054701-390426	05:47:01.50	-39:04:26.4	15.4	15.9	0.1	0.210	√
AS701	2MASX J12364841-3531511	12:36:48.42	-35:31:51.7	1.4	1.3	0.1	0.0736	√
A1664	2MASX J13034252-2414428	13:03:42.54	-24:14:41.8	13.6	14.9	0.1	0.1276	√
A3605	2MASX J14350691-2820306	14:35:06.93	-28:20:30.5	4.6	4.5	0.1	0.0638	√
RXJ1539.5-8335	2MASX J15393387-8335215	15:39:34.25	-83:35:22.3	31.3	31.1	0.2	0.0758	√
AS805	IC 4765	18:47:18.15	-63:19:52.2	6.7	6.9	0.1	0.0150	√

Continued on Next Page...

Table B.1 – Continued

RXJ1931.6-3354	PKS 1928-34	19:31:38.23	-33:54:42.0	33.4	33.2	0.2	0.098	√
RXJ1947.2-7623	2MASX J19471489-7623442	19:47:14.71	-76:23:43.6	18.5	20.2	0.1	0.2175	√
A3992	2MASX J23194046-7313366	23:19:40.62	-73:13:36.7	1.4	1.3	0.1	0.0985	√
Upper limits								
AS384	MCG -07-08-006	03:45:46.3	-41:12:16	<0.6	<0.6	0.2	0.0600	√
C1958 : 2008 : 128 MHz								
A11	2MASX J00123392-1628086	00:12:33.88	-16:28:07.3	31.2	33.4	0.2	0.1510	√
A3017	LCRS B022355.8-420821	02:25:53.05	-41:54:52.4	8.97	10.11	0.06	0.2195	√
A3112	ESO 248- G 006	03:17:57.67	-44:14:17.0	527.5	616.7	1.0	0.0761	√
RXJ0331.1-2100	2MASX J03310587-2100326	03:31:06.04	-21:00:32.9	28.9	32.9	0.1	0.1890	√
A496	MCG -02-12-039	04:33:37.84	-13:15:43.2	67.7	68.6	0.3	0.0328	√
RXJ0543.4-4430	2MASX J05432445-4430290	05:43:24.45	-44:30:29.0	13.42	16.39	0.09	0.1637	√
AS555	ESO 364- G 018	05:57:12.51	-37:28:36.5	84.5	156.9	0.2	0.0448	√
A3378	PKS 0604-352	06:05:54.05	-35:18:07.8	346.6	474.4	0.1	0.1412	√
RXJ0747.5-1917	PKS 0745-19	07:47:31.32	-19:17:39.9	247.1	368.1	0.4	0.1028	√

Continued on Next Page...

Table B.1 – Continued

A1348	LCRS B113851.7-115959	11:41:24.19	-12:16:38.4	135.0	149.2	0.4	0.1195	√
RXJ1304.3-3031	NGC 4936	13:04:17.12	-30:31:34.5	19.9	21.6	0.1	0.0104	√
RXJ1315.4-1623	NGC 5044	13:15:23.97	-16:23:08.0	17.6	21.1	0.2	0.0093	√
A3581	IC 4374	14:07:29.76	-27:01:04.1	290.3	342.2	0.6	0.0218	√
AS780	2MASX J14592875-1810453	14:59:28.77	-18:10:45.4	148.6	158.1	0.3	0.2344	√
RXJ1524.2-3154	2MASX J15241295-3154224	15:24:12.92	-31:54:22.7	36.0	36.9	0.2	0.1022	√
RXJ1558.4-1410	PKS 1555-140	15:58:21.95	-14:09:58.3	409.8	427.7	0.2	0.0970	√
A3638	2MASX J19252969-4257106	19:25:29.72	-42:57:11.1	7.0	6.8	0.2	0.0771	√
A3639	2MASX J19281277-5056244	19:28:12.82	-50:56:24.4	27.0	28.7	0.1	0.1507	√
AS851	NGC 6868	20:09:54.07	-48:22:46.5	104.6	114.3	0.3	0.0095	√
RXJ2014.9-2430	2MASX J20145171-2430229	20:14:51.73	-24:30:22.7	38.7	49.8	0.2	0.1576	√
RXJ2213.1-2754	2MASX J22130601-2754205	22:13:05.97	-27:54:20.9	45.4	49.9	0.2	0.0608	√
A3880	PKS 2225-308	22:27:54.46	-30:34:32.0	42.2	58.8	0.3	0.0581	√
AS1101	ESO 291- G 009	23:13:58.64	-42:43:39.7	13.5	48.9	0.1	0.0564	√
A2580	2MASX J23212630-2312281	23:21:26.31	-23:12:28.5	6.8	7.6	0.1	0.0863	√
A2667	2MASX J23513947-2605032	23:51:39.43	-26:05:02.8	8.9	9.0	0.1	0.2346	√
A4059	ESO 349- G 010	23:57:00.76	-34:45:33.1	8.6	61.1	0.2	0.0491	√

Upper limits

Continued on Next Page...

Table B.1 – Continued

A133	ESO 541- G 013	01:02:41.7	-21:52:55	<0.3	<0.3	0.1	0.0569	√
A3088	2MASX J03070207-2839574	03:07:02.1	-28:39:57	<0.3	<0.3	0.1	0.2529	√
A3444	2MASX J10235019-2715232	10:23:50.2	-27:15:24	<0.3	<0.3	0.1	0.2537	√
A1060	NGC 3311	10:36:42.8	-27:31:42	<0.3	<0.3	0.1	0.0120	√
A3998	ESO 347- G 009	23:21:37.8	-41:53:50	<0.24	<0.24	0.08	0.0903	√

Table B.2: Main Sample L Band fluxes.

		Position(J2000)		Fluxes (mJy)				
Cluster	BCG	RA	DEC	Core	Total	RMS	Redshift	Lines?
VLA-C Array								
AE125 : 1997 : 50 MHz								
RXJ0341.3+1524	III Zw054	03:41:17.50	15:23:47.0	17.51	18.14	0.35	0.029	x
A646	2MASX J08220955+4705529	08:22:09.50	47:05:52.7	48.68	49.86	1.10	0.1268	√
Z2844	NGC 3099	10:02:36.54	32:42:24.3	9.84	10.03	0.16	0.0502	x
VLA-A Array								
AE117 : 1998 : 50 MHz								
Z808	4C +01.06	03:01:38.21	01:55:14.8	17.7	358.1	0.1	0.169	√
A478	2MASX J04132526+1027551	04:13:25.27	10:27:54.7	15.3	24.5	0.2	0.086	√
Z1261	4C +53.16	07:16:41.22	53:23:09.5	19.3	1580.6	0.4	0.064	x
RXJ1320.1+3308	NGC5098	13:20:14.72	33:08:36.2	11.3	83.3	0.1	0.0360	√

Continued on Next Page...

Table B.2 – Continued

A1835	2MASX J14010204+0252423	14:01:02.10	02:52:42.7	25.95	30.25	0.06	0.2523	√
Z7160	SDSS J145715.10+222034.4	14:57:15.10	22:20:34.3	4.12	4.19	0.07	0.2578	√
A2009	2MASX J15001950+2122108	15:00:19.52	21:22:10.0	6.65	20.09	0.05	0.1532	√
RXJ1720.1+2638	2MASX J17201001+2637317	17:20:10.04	26:37:32.0	4.5	5.7	0.1	0.1611	√
A2261	2MASX J17222717+3207571	17:22:27.06	32:07:58.1	3.2	4.1	0.1	0.224	x
RXJ2129.6+0005	2MASX J21293995+0005207	21:29:39.97	00:05:21.0	16.4	22.6	0.3	0.2346	√
Z9077	2MASX J23503544+2929386	23:50:35.25	29:29:44.8	5.31	31.64	0.08	0.015	√
Resolved lobes with no distinct core								
RXJ0819.6+6336	2MASX J08192591+6337256	08:19:25.86	63:37:26.1	<0.6	31.8	0.1	0.1186	x

Table B.3: Main Sample X Band fluxes.

		Position(J2000)		Fluxes (mJy)				
Cluster	BCG	RA	DEC	Core	Total	RMS	Redshift	Lines?
VLA-C Array								
AE125 : 1997 : 50 MHz								
RXJ0341.3+1524	III Zw054	03:41:17.54	15:23:47.6	10.82	11.09	0.09	0.029	x
A646	2MASX J08220955+4705529	08:22:09.54	47:05:52.7	72.09	74.57	0.06	0.1268	√
A621	2MASX J08111245+7002284	08:11:12.38	70:02:30.4	5.26	14.73	0.09	0.223	x
Z2844	NGC 3099	10:02:36.55	32:42:24.2	6.95	7.14	0.09	0.0502	x
VLA-A Array								
AE117 : 1998 : 50 MHz								
RXJ0000.1+0816	UGC 12890	00:00:07.033	08:16:45.04	26.8	27.8	0.3	0.0387	√
A77	UGC 00428	00:40:28.261	29:33:21.32	0.22	2.31	0.05	0.071	x
MACS0159.8-0850	SDSS J015949.34-084958.7	01:59:49.353	-08:49:59.01	59.1	59.2	1.0	0.4051	√

Continued on Next Page...

Table B.3 – Continued

Z808	4C +01.06	03:01:38.208	01:55:14.76	1.37	2.92	0.05	0.169	√
RXJ0352.9+1941	2MASX J03525901+1940595	03:52:59.004	19:40:59.67	10.4	9.9	0.2	0.109	√
A478	2MASX J04132526+1027551	04:13:25.277	10:27:54.78	5.9	5.8	0.1	0.086	√
RXJ0439.0+0520	2MASX J04390223+0520443	04:39:02.263	05:20:43.70	291.9	294.2	0.15	0.208	√
Z1261	4C +53.16	07:16:41.221	53:23:09.54	28.4	28.9	0.1	0.064	x
RXJ0819.6+6336	2MASX J08192591+6337256	08:19:25.863	63:37:26.06	0.4	8.68	0.1	0.1186	x
A646	2MASX J08220955+4705529	08:22:09.547	47:05:52.90	93.3	94.4	0.4	0.1268	√
A795	2MASX J09240529+1410217	09:24:05.304	14:10:21.52	7.4	11.1	0.1	0.1355	√
Z3179	2MASX J10255796+1241086	10:25:57.992	12:41:08.44	7.1	8.5	0.1	0.1432	√
A1068	2MASX J10404446+3957117	10:40:44.499	39:57:11.20	1.0	1.2	0.1	0.1386	√
A1361	4C +46.23	11:43:39.594	46:21:20.36	2.2	2.0	0.2	0.1167	√
A1668	IC 4130	13:03:46.597	19:16:17.46	2.9	8.1	0.1	0.0640	√
RXJ1320.1+3308	NGC5096 NED02	13:20:14.728	33:08:36.13	5.8	6.2	0.1	0.0360	√
RXJ1326.3+0013	2MASX J13261760+0013177	13:26:17.6	00:13:17	0.8	3.0	0.08	0.0821	x
A1835	2MASX J14010204+0252423	14:01:02.100	02:52:42.74	6.6	6.9	0.1	0.2523	√
A1991	NGC5778	14:54:31.389	18:38:32.42	6.7	6.6	0.1	0.0595	√
Z7160	SDSS J145715.10+222034.4	14:57:15.099	22:20:34.34	1.6	1.5	0.1	0.2578	√
A2009	2MASX J15001950+2122108	15:00:19.519	21:22:09.92	3.2	3.3	0.1	0.1532	√

Continued on Next Page. . .

Table B.3 – Continued

RXJ1504.1-0248	LCRS B150131.5-023636	15:04:07.518	-02:48:16.64	29.9	30.0	0.2	0.2171	√
MACS1532.9+3021	SDSS J153253.78+302059.3	15:32:53.777	30:20:59.42	6.6	6.3	0.1	0.3615	√
A2204	VLSS J1632.7+0534	16:32:46.946	05:34:32.74	14.1	14.3	0.1	0.1514	√
Z8197	2MASX J17181198+5639563	17:18:11.944	56:39:56.23	7.7	8.6	0.1	0.1140	√
4C -05.84	2MASX J20243532-0516413	20:24:35.352	-05:16:41.42	3.1	3.2	0.2	0.0822	√
RXJ2129.6+0005	2MASX J21293995+0005207	21:29:39.960	00:05:21.21	4.0	4.2	0.1	0.2346	√
A2626	IC 5338	23:36:30.491	21:08:47.46	5.7	5.9	0.1	0.0552	√
A2627	B2 2334+23	23:36:42.094	23:55:29.20	50.6	59.8	0.2	0.127	N
Z9077	2MASX J23503544+2929386	23:50:35.189	29:29:44.78	0.27	0.21	0.06	0.015	√
A2665	MCG +01-60-039	23:50:50.558	06:08:58.56	1.48	1.46	0.06	0.0567	√
Upper limits								
A2622	4C +27.53A	23:35:01.5	27:22:21	<0.3	<0.3	0.1	0.061	x
ATCA-6A Array								
C1958 : 2011 : 2048 MHz								
A2734	ESO 409- G 025	00:11:21.65	-28:51:15.7	2.5	2.6	0.2	0.0619	√
A2746	2MASX J00141626-6604211	00:14:16.21	-66:04:21.6	2.8	2.8	0.1	0.1592	√

Continued on Next Page. . .

Table B.3 – Continued

A3112	ESO 248- G 006	03:17:57.66	-44:14:17.6	311.1	456.7	2.0	0.0761	√
MACSJ0547.0-3904	NVSS J054701-390426	05:47:01.50	-39:04:26.5	14.1	15.3	0.2	0.210	√
AS701	2MASX J12364841-3531511	12:36:48.41	-35:31:52.2	2.0	2.0	0.1	0.0736	√
A1664	2MASX J13034252-2414428	13:03:42.54	-24:14:41.8	9.3	10.6	0.1	0.1276	√
A3605	2MASX J14350691-2820306	14:35:06.93	-28:20:30.5	4.3	4.3	0.1	0.0638	√
RXJ1539.5-8335	2MASX J15393387-8335215	15:39:34.25	-83:35:22.3	18.8	19.6	0.2	0.0758	√
AS805	IC 4765	18:47:18.14	-63:19:52.2	4.5	4.6	0.1	0.0150	√
RXJ1931.6-3354	PKS 1928-34	19:31:38.23	-33:54:42.1	22.4	23.5	0.2	0.098	√
RXJ1947.2-7623	2MASX J19471489-7623442	19:47:14.71	-76:23:43.6	10.5	13.3	0.2	0.2175	√
Upper limits								
AS384	MCG -07-08-006	03:45:46.3	-41:12:16	$<$0.42	$<$0.42	0.14	0.0600	√
RXJ0528.9-3927	RBS0653	05:28:53.0	-39:28:18	$<$0.6	$<$0.6	0.2	0.2839	√
A3992	2MASX J23194046-7313366	23:19:40.9	-73:13:38	$<$0.51	$<$0.51	0.17	0.0985	√
C1958 : 2008 128 MHz								
A11	2MASX J00123392-1628086	00:12:33.88	-16:28:07.5	21.8	24.2	0.1	0.1510	√
A3017	LCRS B022355.8-420821	02:25:53.03	-41:54:52.6	3.8	4.2	0.1	0.2195	√
A3112	ESO 248- G 006	03:17:57.67	-44:14:17.0	317.0	421.7	1.0	0.0761	√

Continued on Next Page...

Table B.3 – Continued

RXJ0331.1-2100	2MASX J03310587-2100326	03:31:06.04	-21:00:32.7	8.2	12.2	0.1	0.1890	√
A496	MCG -02-12-039	04:33:37.84	-13:15:43.2	50.1	52.3	0.2	0.0328	√
RXJ0543.4-4430	2MASX J05432445-4430290	05:43:24.45	-44:33:28.8	3.09	3.26	0.09	0.1637	√
AS555	ESO 364- G 018	05:57:12.53	-37:28:36.5	58.0	101.8	0.3	0.0448	√
A3378	PKS 0604-352	06:05:54.06	-35:18:07.6	122.5	260.9	0.6	0.1412	√
RXJ0747.5-1917	PKS 0745-19	07:47:31.32	-19:17:39.9	77.5	117.9	0.2	0.1028	√
A1348	LCRS B113851.7-115959	11:41:24.19	-12:16:38.4	88.3	110.5	0.4	0.1195	√
RXJ1304.3-3031	NGC 4936	13:04:17.12	-30:31:34.5	12.9	14.0	0.1	0.0104	√
RXJ1315.4-1623	NGC 5044	13:15:23.97	-16:23:07.6	13.6	15.6	0.1	0.0093	√
A3581	IC 4374	14:07:29.76	-27:01:04.3	198.3	223.4	0.6	0.0218	√
AS780	2MASX J14592875-1810453	14:59:28.77	-18:10:45.4	109.9	119.8	0.4	0.2344	√
RXJ1524.2-3154	2MASX J15241295-3154224	15:24:12.92	-31:54:22.7	17.3	18.9	0.2	0.1022	√
RXJ1558.4-1410	PKS 1555-140	15:58:21.95	-14:09:58.3	191.1	210.9	0.9	0.0970	√
A3638	2MASX J19252969-4257106	19:25:29.72	-42:57:10.9	4.1	4.1	0.2	0.0771	√
A3639	2MASX J19281277-5056244	19:28:12.82	-50:56:24.4	15.45	17.61	0.09	0.1507	√
AS851	NGC 6868	20:09:54.07	-48:22:46.5	77.7	98.8	0.3	0.0095	√
RXJ2014.9-2430	2MASX J20145171-2430229	20:14:51.74	-24:30:22.5	13.6	20.0	0.1	0.1576	√
RXJ2213.1-2754	2MASX J22130601-2754205	22:13:05.97	-27:54:20.9	21.2	25.3	0.1	0.0608	√

Continued on Next Page. . .

Table B.3 – Continued

A3880	PKS 2225-308	22:27:54.48	-30:34:31.8	21.8	34.9	0.2	0.0581	√
AS1101	ESO 291- G 009	23:13:58.64	-42:43:39.5	3.0	15.4	0.1	0.0564	√
A2580	2MASX J23212630-2312281	23:21:26.33	-23:12:27.5	1.5	1.5	0.1	0.0863	√
A2667	2MASX J23513947-2605032	23:51:39.43	-26:05:03.0	6.8	7.2	0.1	0.2346	√
A4059	ESO 349- G 010	23:57:00.74	-34:45:33.5	2.14	13.50	0.15	0.0491	√
Upper limits								
A133	ESO 541- G 013	01:02:41.7	-21:52:55	<0.3	<0.3	0.1	0.0569	√
A3088	2MASX J03070207-2839574	03:07:02.1	-28:39:57	<0.3	<0.3	0.1	0.2529	√
A3444	2MASX J10235019-2715232	10:23:50.2	-27:15:24	<0.3	<0.3	0.1	0.2537	√
A1060	NGC 3311	10:36:42.8	-27:31:42	<0.3	<0.3	0.1	0.0120	√
A3998	ESO 347- G 009	23:21:37.8	-41:53:50	<0.27	<0.27	0.09	0.0903	√

Appendix C

Main Sample - SED Decomposition Values

Table C.1: Flux contribution of the core component at 10 GHz and the non-core component at 1 GHz as inferred from model fitting when fit best using two power law model. Note that radio SEDs are almost invariably too under sampled to perform a complete, unequivocal spectral breakdown. These fits were conservatively performed using a simple yet consistent, physically motivated model. See Chapter 2 for a description of the fitting and models. Also see Appendix A for comments and justification for individual sources. Fit labels 1: Resolved core component seen in images fit separately. 2: Core component fit separately, inferred non-core flux for lower resolution literature fluxes from SED shape. 3: Two components fit direct from SED using a split power model. 4: Only a single component reliably extractable SED, extrapolate to get limits. 5: Single observed flux or two fluxes with indeterminate index, extrapolate for both limits. (i) When core component considered negligible at 1 GHz hence total flux at 1 GHz taken as non-core flux. (ii) Core expected to contribute significant fraction of measured flux at 1 GHz, non-core contribution taken as the difference between total fitted flux at 1 GHz and core contribution at this frequency. (*See notes)

Cluster	Non-core (1 GHz)	Core (10 GHz)	Steep Index	Flat Index	Flat normalisation	Fit Label	Lines?
Core and Non-core Values							
A11	77.4 ± 22.7	21.7 ± 10.7	0.85 ± 0.12	0.35 ± 0.22	48.8 ± 7.4	2(ii)	0
RXJ0058.9+2657	2022.1 ± 592.1	6.5 ± 3.1	0.79 ± 0.16	0.2 ± 0.2	10.35 ± 3.39	1(i)	0
RXJ0107.4+3227	4895.7 ± 1006.0	103.1 ± 5.4	0.74 ± 0.09	-0.29 ± 0.03	52.88 ± 2.78	1(i)	1

Continued on Next Page...

Table C.1 – Continued

A160	1002.4 ± 96.2	8.6 ± 3.4	0.89 ± 0.09	0.33 ± 0.18	18.49 ± 7.32	1(i)	0
RXJ0123.6+3315	103.4 ± 49.8	1.27 ± 0.61	1.30 ± 0.35	0.2 ± 0.2	2.02 ± 0.65	1(i)	0
A262	82.1 ± 21.3	3.2 ± 1.5	1.07 ± 0.16	0.0 ± 0.2	3.2 ± 1.1	1/3	1
A3017	97.7 ± 8.3	3.8 ± 1.0	1.52 ± 0.15	0.05 ± 0.10	4.2 ± 1.1	2(i)	1
A407	702.2 ± 98.7	3.1 ± 1.8	0.80 ± 0.18	0.2 ± 0.2	4.83 ± 1.58	1(i)	1
A478	33.8 ± 3.6	4.8 ± 0.3	1.0 ± 0.2	0.59 ± 0.07	18.8 ± 1.2	1(ii)	1
A496	78.1 ± 7.2	40.1 ± 3.7	1.80 ± 0.04	0.30 ± 0.09	80.3 ± 14.5	3	1
RXJ0543.4-4430	195.6 ± 11.6	3.6 ± 1.8	1.85 ± 0.55	-0.55 ± 0.19	1.0 ± 0.5	2(i)	1
Z1121	1447.5 ± 293.8	105.1 ± 33.8	0.93 ± 0.21	0.2 ± 0.2	166.6 ± 53.5	1	1
RXJ0819.6+6336	41.5 ± 2.8	0.4 ± 0.3	0.82 ± 0.05	0.2 ± 0.2	0.6 ± 0.3	1	0
A761	481.7 ± 198.9	7.7 ± 3.7	0.96 ± 0.26	0.2 ± 0.2	12.21 ± 3.93	1(i)	0
Z3146	8.3 ± 1.1	0.6 ± 0.3	1.0 ± 0.2	0.41 ± 0.34	1.6 ± 0.9	2(ii)	1
AS701	4.7 ± 0.4	2.2 ± 0.8	1.41 ± 0.05	-0.72 ± 0.19	0.4 ± 0.2	2(i)	1
A1664	21.4 ± 10.5	10.1 ± 1.4	1.12 ± 0.17	0.50 ± 0.22	31.7 ± 13.9	2(ii)	1
RXJ1320.1+3308	83.7 ± 6.6	7.0 ± 2.4	0.56 ± 0.04	0.27 ± 0.09	12.96 ± 4.42	1(ii)	1
A1763	764.8 ± 203.8	3.2 ± 1.5	1.15 ± 0.13	0.2 ± 0.2	5.06 ± 2.23	1(i)	1
A3581	131.6 ± 14.2	92.7 ± 13.2	1.15 ± 0.08	0.48 ± 0.02	776.3 ± 96.6	1(ii)	1
A1930	5.5 ± 2.1	4.9 ± 1.0	0.86 ± 0.11	0.20 ± 0.18	7.8 ± 1.5	2(ii)	1

Continued on Next Page. . .

Table C.1 – Continued

A3605	5.1 ± 1.7	4.3 ± 1.0	1.0 ± 0.2	0.09 ± 0.12	5.3 ± 1.3	2(ii)	1
Z7160	20.6 ± 2.0	1.5 ± 0.6	1.09 ± 0.10	0.49 ± 0.34	4.8 ± 2.0	2(ii)	1
A2009	34.0 ± 6.5	3.3 ± 1.4	1.81 ± 0.05	0.38 ± 0.29	7.80 ± 3.45	1(ii)	1
A2033	669.7 ± 212.7	8.0 ± 4.6	0.78 ± 0.19	0.2 ± 0.2	12.68 ± 4.08	1(i)	1
A2055	454.3 ± 15.4	92.4 ± 38.7	0.63 ± 0.01	0.20 ± 0.14	147.53 ± 12.61	1(ii)	1
A2063	13.4 ± 5.2	1.7 ± 1.3	0.82 ± 0.30	0.42 ± 0.39	3.95 ± 3.66	1(ii)	0
A2110	3.8 ± 1.1	1.6 ± 0.3	1.89 ± 0.06	0.18 ± 0.10	2.4 ± 0.3	3	1
RXJ1604.9+2356	717.0 ± 9.0	33.3 ± 4.8	0.82 ± 0.01	0.2 ± 0.2	53 ± 17	1	0
A2204	76.8 ± 23.5	9.5 ± 2.9	1.16 ± 0.10	0.32 ± 0.10	20.0 ± 4.0	3	1
RXJ1720.1+2638	101.3 ± 8.8	3.4 ± 1.8	1.08 ± 0.03	0.19 ± 0.12	5.3 ± 1.2	1(ii)	1
Z8276	45.5 ± 9.0	59.2 ± 11.8	1.45 ± 0.07	0.21 ± 0.06	96.9 ± 12.7	3	1
A3639	117.9 ± 6.5	17.3 ± 2.1	0.89 ± 0.08	0.09 ± 0.05	21.4 ± 2.6	2(i)	1
RXJ1931.6-3354	1293.8 ± 120.1	21.9 ± 15.8	1.10 ± 0.07	0.76 ± 0.28	120.8 ± 88.3	2(i)	1
RXJ2129.6+0005	26.4 ± 3.9	3.7 ± 1.0	1.2 ± 0.2	0.44 ± 0.11	10.3 ± 2.9	2(ii)	1
A2390	80.0 ± 20.1	122.1 ± 47.5	1.43 ± 0.10	0.38 ± 0.13	293.0 ± 75.4	3	1
A3880	551.3 ± 312.8	21.1 ± 9.3	0.99 ± 0.42	0.2 ± 0.2	33.4 ± 14.7	1	1
AS1101	386.7 ± 13.2	2.9 ± 1.3	1.32 ± 0.09	0.2 ± 0.2	4.6 ± 2.1	1	1
RXJ2214.7+1350	2278.7 ± 650.4	39.8 ± 19.0	1.03 ± 0.15	0.2 ± 0.2	69.84 ± 19.00	1(i)/3	1

Continued on Next Page. . .

Table C.1 – Continued

A2626	91.5 ± 6.8	5.4 ± 0.5	2.09 ± 0.06	0.28 ± 0.03	10.4 ± 0.6	2	1
A2627(a)	359.2 ± 29.8	54.8 ± 9.2	0.62 ± 0.01	0.50 ± 0.07	174.0 ± 29.4	1(ii)	1
A2634	7773.3 ± 720.2	192.1 ± 16.2	0.88 ± 0.01	0.41 ± 0.04	494.35 ± 41.78	1(ii)	1
Core Values with Non-core Upper Limits							
RXJ0000.1+0816	<116.9	28.3 ± 11.3	1.0	0.50 ± 0.10	89.92 ± 7.05	4	1
A2746	<9.0	2.7 ± 0.8	1.0	0.39 ± 0.15	6.7 ± 1.9	2	1
Z235	<69.9	23.2 ± 17.1	1.0	0.39 ± 0.54	56.91 ± 42.06	4	1
A168	<6.3	1.5 ± 0.5	1.0	0.20 ± 0.15	2.3 ± 0.8	2	0
MACS0159.8-0850	<13.2	78.3 ± 15.4	1.0	-0.41 ± 0.08	30.2 ± 3.7	4	1
A291	<14.4	3.8 ± 0.7	1.0	0.51 ± 0.18	12.2 ± 2.2	4	1
RXJ0341.3+1524	<39.1	9.47 ± 1.58	1.0	0.34 ± 0.13	20.69 ± 3.44	4	0
RXJ0352.9+1941	<27.4	11.4 ± 5.7	1.0	-0.55 ± 0.27	3.2 ± 1.6	4	1
RXJ0503.1+0608	<7.3	5.7 ± 1.2	1.0	-0.05 ± 0.19	5.1 ± 2.3	4	0
MACSJ0547.0-3904	<16.5	13.8 ± 2.2	1.0	0.31 ± 0.27	27.9 ± 17.0	2	1
RXJ0751.3+5012	<12.2	4.80 ± 1.08	1.0	0.29 ± 0.21	9.28 ± 2.09	4	1
A646	<41.0	90.02 ± 7.47	1.0	-0.24 ± 0.05	51.79 ± 4.30	4	1
Z1665	<23.0	5.97 ± 2.88	1.0	0.45 ± 0.15	16.79 ± 2.06	4	1

Continued on Next Page. . .

Table C.1 – Continued

A757	<22.0	9.19 ± 3.56	1.0	0.21 ± 0.12	14.88 ± 1.67	4	1
Z2844	<6.5	7.41 ± 3.98	1.0	0.11 ± 0.40	9.42 ± 5.07	4	1
A1035	<4.9	2.76 ± 2.53	1.0	0.34 ± 0.37	6.08 ± 1.78	4	1
A1084	<10.6	27.3 ± 4.5	1.0	0.09 ± 0.01	33.2 ± 5.5	4	1
A1204	<3.4	1.85 ± 1.74	1.0	-0.05 ± 0.85	1.63 ± 1.55	4	1
A1235	<1.5	0.68 ± 0.34	1.0	0.25 ± 0.44	1.19 ± 0.60	4	0
A1885	<9.4	41.4 ± 22.1	1.0	-0.08 ± 0.17	34.40 ± 18.38	4	1
RXJ1440.6+0327	<4.8	0.7 ± 0.3	1.0	0.62 ± 0.41	2.9 ± 1.1	2	1
RXJ1442.2+2218	<31.6	8.35 ± 1.10	1.0	0.39 ± 0.13	20.32 ± 2.67	4	1
AS780	<59.1	136.7 ± 15.1	1.0	0.03 ± 0.02	146.0 ± 6.8	4	1
RXJ1504.1-0248	<86.4	28.0 ± 14.0	1.0	0.40 ± 0.33	70.6 ± 35.4	4	1
RXJ1524.2-3154	<3.0	22.5 ± 2.3	1.0	0.34 ± 0.07	49.5 ± 5.0	4	1
RXJ1539.5-8335	<51.7	20.7 ± 2.4	1.0	0.45 ± 0.07	58.1 ± 6.6	4	1
A2146	<10.1	6.0 ± 0.7	1.0	0.48 ± 0.05	20.4 ± 2.5	2	1
RXJ1715.3+5725	<22.9	29.9 ± 6.7	1.0	0.41 ± 0.14	53.1 ± 3.8	2	1
Z8193	<74.9	77.9 ± 4.1	1.07 ± 0.04	0.30 ± 0.04	154.2 ± 8.2	2	1
RXJ1733.0+4345	<25.5	4.1 ± 1.1	1.0	0.34 ± 0.19	8.9 ± 1.7	2	1
RXJ1750.2+3504	<25.4	26.3 ± 4.1	1.0	0.47 ± 0.03	77.6 ± 3.8	4	1

Continued on Next Page. . .

Table C.1 – Continued

AS851	<114.7	108.3 ± 7.6	1.0	0.10 ± 0.03	135.6 ± 9.5	4	1
RXJ2213.1-2754	<106.5	35.6 ± 4.3	1.0	0.42 ± 0.07	92.8 ± 11.2	4	1
A2667	<28.1	7.6 ± 2.1	1.0	0.20 ± 0.17	13.1 ± 10.1	4	1
Non-core Values with Core Upper Limits							
A2734	14.7 ± 5.4	<2.42	0.77 ± 0.31	0.2	3.83	4	1
RXJ0021.6+2803	5.70 ± 3.66	<0.32	1.71 ± 0.67	0.2	0.51	4	0
A76	5.20 ± 1.9	<0.41	1.52 ± 0.72	0.2	0.645	4	0
A84	47.6 ± 3.2	<1.11	1.00 ± 0.20	0.2	1.07	5	0
A104	10.9 ± 0.8	<0.39	1.00 ± 0.20	0.2	0.62	5	0
A115	2331.7 ± 695.3	<6.22	1.13 ± 0.13	0.2	9.85	4/1	1
A133	233.9 ± 15.8	<0.26	1.00 ± 0.20	0.2	0.41	5	1
A193	66.6 ± 7.8	<1.7	2.05 ± 0.22	0.2	2.7	4	0
A189	39.7 ± 9.3	<5.9	0.83 ± 0.26	0.2	9.3	4	0
A3112	1881.8 ± 556.7	<304.0	0.71 ± 0.18	0.24 ± 0.23	525.0 ± 303.1	4(2)	1
AS384	28.1 ± 1.0	<0.52	1.00 ± 0.20	0.2	0.44	5	1
RXJ0419.6+0225	35.5 ± 12.5	<0.7	2.10 ± 0.55	0.2	1.1	4	0
RXJ0439.0+0716	44.4 ± 3.0	<0.13	1.00 ± 0.20	0.2	0.21	5	0

Continued on Next Page. . .

Table C.1 – Continued

RXJ0528.9-3927	9.3 ± 3.7	<0.62	1.54 ± 0.67 0.2	0.98	4	1
AS555	387.1 ± 13.7	<56.1	0.57 ± 0.03 0.2	88.9	4	1
A3378	1542.7 ± 13.4	<89.2	0.86 ± 0.01 0.2	141.4	4	1
A566	51.2 ± 3.5	<0.26	1.00 ± 0.20 0.2	0.41	5	0
RXJ0740.9+5526	67.19 ± 27.91	<1.71	0.74 ± 0.31 0.2	2.72	4/1	0
A621	122.56 ± 4.19	<5.09	0.92 ± 0.01 0.2	8.06	4	0
RXJ0821.0+0752	2.9 ± 1.2	<0.6	0.79 ± 0.46 0.2	1.0	4	1
A667	13.6 ± 2.6	<1.9	0.85 ± 0.23 0.2	3.0	4	0
Z2089	11.75 ± 3.74	<2.72	0.80 ± 0.37 0.2	4.31	4	1
A795	151.3 ± 64.8	<7.2	1.17 ± 0.26 0.2	11.3	4	1
Z2701	25.14 ± 12.41	<3.14	2.00 ± 0.35 0.2	4.98	4/2	1
A971	10.8 ± 1.8	<1.56	0.82 ± 0.16 0.2	2.47	4	0
A980	28.3 ± 2.5	<1.38	1.46 ± 0.08 0.2	2.20	4	0
A3444	13.2 ± 0.0	<0.26	1.00 ± 0.20 0.2	0.41	5	1
A1023	18.81 ± 3.69	<2.35	1.20 ± 0.22 0.2	3.72	4	1
A1045	8.4 ± 1.3	<1.9	0.65 ± 0.15 0.2	3.1	4/5	0
A1060	87.9 ± 5.9	<0.26	1.00 ± 0.20 0.2	0.41	5	1
A1068	13.0 ± 7.8	<1.2	1.09 ± 0.13 0.2	1.84	4	1

Continued on Next Page. . .

Table C.1 – Continued

RXJ1053.7+5450	5.77 ± 2.86	<0.56	0.92 ± 0.75 0.2	0.89	4	0
A1132	41.66 ± 6.21	<2.50	1.13 ± 0.50 0.2	3.97	4/1	0
A1190	22.96 ± 3.72	<2.00	0.74 ± 0.14 0.2	3.17	4	0
A1366	333.07 ± 100.21	<14.05	0.94 ± 0.14 0.2	22.27	4	0
Z4673	7.37 ± 2.59	<0.66	1.42 ± 0.80 0.2	1.04	4	0
RXJ1206.5+2810	4.35 ± 1.41	<0.38	1.33 ± 0.36 0.2	0.60	4	1
A1553	17.8 ± 10.5	<1.66	1.28 ± 0.59 0.2	2.63	4	0
A1651	9.5 ± 2.3	<1.4	1.08 ± 0.31 0.2	2.2	4	0
A1668	122.3 ± 49.0	<2.8	1.20 ± 0.24 0.2	4.4	4	1
A1677	107.95 ± 37.87	<14.41	0.96 ± 0.24 0.2	22.84	4	0
RXJ1326.3+0013	28.5 ± 4.0	<0.79	1.03 ± 0.11 0.2	1.26	4	0
A1775(NW)	35.73 ± 16.46	<2.13	0.92 ± 0.22 0.2	3.38	4	0
A1775(SE)	378.86 ± 106.66	<21.60	0.92 ± 0.22 0.2	34.23	4	0
A1773	3.09 ± 1.26	<0.45	0.90 ± 0.49 0.2	0.71	4	0
A1835	47.7 ± 6.2	<3.6	0.84 ± 0.21 0.2	5.6	4	1
Z6718	6.0 ± 1.4	<1.1	0.92 ± 0.23 0.2	1.8	4	0
A1902	3.9 ± 2.5	<0.6	1.09 ± 0.09 0.2	1.0	4	0
A1927	10.9 ± 3.7	<2.5	0.76 ± 0.48 0.2	4.0	4	0

Continued on Next Page. . .

Table C.1 – Continued

A1978	5.0 ± 1.8	<0.6	1.22 ± 0.48 0.2	1.0	4	0
A1991	46.8 ± 5.9	<6.4	0.91 ± 0.13 0.2	10.1	4	1
A2064	105.05 ± 61.97	<10.13	0.81 ± 0.51 0.2	16.05	4	0
A2072	8.6 ± 0.6	<0.26	1.00 ± 0.20 0.2	0.41	5	1
MACS1532.9+3021	27.4 ± 2.8	<4.0	0.66 ± 0.08 0.2	6.34	4	1
A2175	7.12 ± 3.22	<1.41	1.16 ± 0.74 0.2	1.41	4	0
A2241	47.93 ± 21.10	<4.41	1.40 ± 0.30 0.2	6.98	4	0
A2244	5.6 ± 1.8	<0.6	1.29 ± 0.30 0.2	1.0	4	0
RXJ1715.1+0309	208.5 ± 7.5	<15.2	0.88 ± 0.03 0.2	24.1	4(1)	1
Z8197	53.6 ± 4.0	<3.7	1.01 ± 0.05 0.2	10.2	4	1
A2261	6.6 ± 0.3	<0.6	1.33 ± 0.06 0.2	0.9	4	0
Z8338	25.8 ± 1.7	<0.23	1.00 ± 0.20 0.2	0.37	5	0
AS805	27.3 ± 4.2	<4.4	0.81 ± 0.16 0.2	6.98	4	1
A2318	9.5 ± 0.6	<0.29	1.00 ± 0.20 0.2	0.45	5	0
A3638	29.8 ± 0.8	<2.40	0.93 ± 0.14 0.2	3.30	5	1
RXJ1947.2-7623	61.7 ± 1.9	<10.3	0.76 ± 0.03 0.2	16.3	4	1
RXJ2014.9-2430	294.1 ± 8.2	<19.3	1.03 ± 0.03 0.2	30.7	4	1
A2443	63.2 ± 6.3	<4.0	1.23 ± 0.14 0.2	6.3	4	0

Continued on Next Page. . .

Table C.1 – Continued

A2495	23.9 ± 4.0	<1.6	1.35 ± 0.24	0.2	2.5	4	1
Z8852	63.8 ± 4.3	<0.78	1.00 ± 0.20	0.2	1.23	5	0
A2572A	34.92 ± 3.31	<6.81	0.61 ± 0.05	0.2	10.8	4	0
A3998	41.2 ± 2.8	<0.21	1.00 ± 0.20	0.2	0.33	5	1
Z9077	55.5 ± 6.6	<0.3	0.82 ± 0.30	0.2	0.4	4	1
Z9077*	100.5 ± 6.1	<0.3	0.91 ± 0.03	0.2	0.4	4	1
A2675	18.0 ± 4.1	<3.4	1.55 ± 0.20	0.2	5.4	4	0
Upper Limits on both Core and Non-core							
A7	<3	<0.16	1.0	0.2	0.25	5	0
A21 (a)	<3	<0.26	1.0	0.2	0.41	5	0
(b)	<3	<0.26	1.0	0.2	0.41	5	0
A68 (a)	<3	<0.16	1.0	0.2	0.25	5	0
(b)	<3	<0.16	1.0	0.2	0.25	5	0
A75	<3	<0.57	1.0	0.2	0.91	5	1
RXJ0123.2+3327	<3	<0.16	1.0	0.2	0.25	5	1
A267	<3	<0.18	1.0	0.2	0.29	5	0
A272	<3	<0.13	1.0	0.2	0.21	5	0

Continued on Next Page. . .

Table C.1 – Continued

RXJ0228.2+2811	<3	<0.26	1.0	0.2	0.41	5	0
A409	<3	<0.16	1.0	0.2	0.25	5	0
A3088	<3	<0.26	1.0	0.2	0.41	5	1
RXJ0448.2+0953	<3	<0.13	1.0	0.2	0.21	5	0
A523	<3	<0.13	1.0	0.2	0.21	5	0
A602	<3	<0.42	1.0	0.2	0.66	5	0
Z1478	<3	<0.10	1.0	0.2	0.09	5	0
A611	<3	<0.39	1.0	0.2	0.62	5	1
A644	<3	<0.13	1.0	0.2	0.21	5	0
A655	<3	<0.16	1.0	0.2	0.25	5	0
A665	<3	<0.16	1.0	0.2	0.25	5	0
A671	<3	<0.23	1.0	0.2	0.37	5	1
A697	<3	<0.18	1.0	0.2	0.29	5	0
A750	<3	<0.29	1.0	0.2	0.45	5	1
Z1953	<3	<0.26	1.0	0.2	0.41	5	0
A773 (a)	<3	<0.18	1.0	0.2	0.29	5	0
(b)	<3	<0.18	1.0	0.2	0.29	5	0
A781	<3	<0.26	1.0	0.2	0.41	5	0

Continued on Next Page. . .

Table C.1 – Continued

A961	<3	<0.23	1.0	0.2	0.37	5	0
A990	<3	<0.10	1.0	0.2	0.09	5	0
A1033	<3	<0.23	1.0	0.2	0.37	5	0
A1173	<3	<0.13	1.0	0.2	0.21	5	0
A1177	<3	<0.26	1.0	0.2	0.41	5	0
A1185	<3	<0.13	1.0	0.2	0.21	5	0
A1201	<3	<0.23	1.0	0.2	0.37	5	0
A1302	<3	<0.16	1.0	0.2	0.25	5	0
A1423	<3	<0.15	1.0	0.2	0.24	5	0
A1437	<3	<0.18	1.0	0.2	0.29	5	0
Z4803	<3	<0.23	1.0	0.2	0.37	5	0
RXJ1205.1+3920	<3	<0.13	1.0	0.2	0.21	5	0
Z4905	<3	<0.31	1.0	0.2	0.49	5	1
RXJ1223.0+1037	<3	<0.13	1.0	0.2	0.21	5	1
Z5247	<3	<0.13	1.0	0.2	0.21	5	0
A1589	<3	<0.16	1.0	0.2	0.25	5	0
A1682	<3	<0.26	1.0	0.2	0.41	5	0
A1800	<3	<0.23	1.0	0.2	0.37	5	0

Continued on Next Page. . .

Table C.1 – Continued

A1809	<3	<0.26	1.0	0.2	0.41	5	0
A1831	<3	<0.16	1.0	0.2	0.25	5	0
A1914	<3	<0.16	1.0	0.2	0.25	5	1
A1918	<3	<0.23	1.0	0.2	0.37	5	0
A1983 (a)	<3	<0.39	1.0	0.2	0.62	5	0
(b)	<3	<0.39	1.0	0.2	0.62	5	0
A2034	<3	<0.26	1.0	0.2	0.41	5	0
A2050	<3	<0.23	1.0	0.2	0.37	5	0
A2061	<3	<0.13	1.0	0.2	0.21	5	0
A2069	<3	<0.26	1.0	0.2	0.41	5	0
A2107	<3	<0.23	1.0	0.2	0.37	5	0
A2111 (a)	<3	<0.18	1.0	0.2	0.29	5	0
(b)	<3	<0.18	1.0	0.2	0.29	5	0
A2124	<3	<0.13	1.0	0.2	0.21	5	0
A2201	<3	<0.16	1.0	0.2	0.25	5	0
A2208	<3	<0.26	1.0	0.2	0.41	5	0
A2219	<3	<0.26	1.0	0.2	0.41	5	0
A2228	<3	<0.34	1.0	0.2	0.53	5	0

Continued on Next Page. . .

Table C.1 – Continued

A2249	<3	<0.21	1.0	0.2	0.33	5	0
A2254	<3	<0.26	1.0	0.2	0.41	5	0
A2259	<3	<0.18	1.0	0.2	0.29	5	0
A2294	<3	<0.23	1.0	0.2	0.37	5	1
RXJ1740.5+3539 (a)	<3	<0.26	1.0	0.2	0.41	5	0
(b)	<3	<0.26	1.0	0.2	0.41	5	0
A2409	<3	<0.18	1.0	0.2	0.29	5	0
A2552	<3	<0.21	1.0	0.2	0.33	5	0
A2572B	<3	<0.18	1.0	0.2	0.29	5	0
A3992	<5	<1.15	1.0	0.2	1.83	5	1
A2537	<3	<0.26	1.0	0.2	0.41	5	0
A2589	<3	<0.26	1.0	0.2	0.41	5	0
A2593	<3	<0.39	1.0	0.2	0.62	5	0
A2631	<3	<0.26	1.0	0.2	0.41	5	0

Table C.2: Flux contribution of the core component at 10 GHz and the non-core component at 1 GHz as inferred from model fitting when fit best using a dropline model. Fit label 1: Clearly separated core and non-core components in map. 2: Inferred non-core flux contribution for lower resolution fluxes by considering SED.

Cluster	Non-core (1 GHz)	Core (10 GHz)	Dropline Parameters	Flat Index	Flat Norm.	Fit Label	Lines?
Core and Non-core Values							
Z808	765.2 ± 11.8	1.3 ± 0.8	1235.2 1.13 1.10 1.06	0.2 ± 0.2	2.10 ± 1.12	1	1
Z1261	1959.8 ± 29.7	32.7 ± 8.1	1962.1 0.61 0.63 6.28	-0.23 ± 0.15	19.1 ± 4.7	1(i)	0
A763	213.1 ± 9.8	1.6 ± 1.2	213.1 0.77 0.99 4.35	0.10 ± 0.34	2.0 ± 1.5	1(ii)	0
A1361	1342.3 ± 29.0	1.9 ± 1.1	1857.9 0.57 0.85 0.75	0.2 ± 0.2	3.1 ± 1.4	1(i)	1
RXJ1522.0+0741	266.7 ± 145.8	2.1 ± 1.7	2500.9 1.24 1.02 0.17	0.2 ± 0.2	3.3 ± 1.1	1(ii)	0
4C-05.84	1146.0 ± 25.2	3.0 ± 1.8	1146.3 0.87 0.33 6.97	0.2 ± 0.2	4.75 ± 2.53	1	1
A2665	89.1 ± 3.0	1.4 ± 0.8	109.8 0.86 1.13 1.80	0.2 ± 0.2	2.27 ± 1.21	2	1
A4059	2271.8 ± 60.3	2.1 ± 0.9	3409.5 1.08 1.02 1.17	0.2 ± 0.2	3.29 ± 1.47	1	1
Non-core Values with Core Upper Limits							
A77	20.1 ± 4.0	<2.2	20.1 0.83 1.79 14.4	0.2	3.54	1	0
RXJ0331.1-2100	258.4 ± 117.2	<3.4	929.2 0.41 1.01 0.34	0.2	5.45	2	1

RXJ0747.5-1917	3738.0 ± 57.3	<75.0	4475.5 0.85 0.78 0.97	0.2	118.8	2	1
Z3179	146.6 ± 38.9	<8.2	147.44 0.82 1.32 5.45	0.2	13.0	2	1
Z3916	109.6 ± 26.2	<4.7	119.7 1.18 1.07 2.54	0.2	7.4	2	1
RXJ1657.8+2751	61.9 ± 30.1	<4.2	62.0 0.85 1.54 6.63	0.2	6.68	2	0
A2580	62.2 ± 32.0	<1.4	72.8 0.33 1.21 2.17	0.2	2.10	2	1
A2622	154.5 ± 6.8	<0.3	162.8 1.33 1.43 3.33	0.2	0.46	1	0

Table C.3: Flux contribution of the core component at 10 GHz and the non-core component at 1 GHz when using the GPS model. Fit label 1: Clearly separated core and non-core components in map. 2: Inferred non-core flux contribution for lower resolution fluxes by considering SED.

Cluster	Non-core (1 GHz)	Core (10 GHz)	GPS Parameters	Steep Index	Fit Label	Lines?
Core and Non-core Values						
RXJ0439.0+0520	62.3 ± 10.0	250.8 ± 29.5	1.32 1.89 -0.81	1.07 ± 0.10	2	1
A1348	110.2 ± 12.0	113.5 ± 11.3	1.96 0.62 -0.52	0.92 ± 0.08	2	1
RXJ1558.4-1410	186.7 ± 34.0	351.2 ± 6.6	2.59 0.86 -0.90	0.90 ± 0.09	2	1
Core Values with Non-core Upper Limits						
RXJ1304.3-3031	<3.0	12.6 ± 0.9	1.58 -0.03 -0.45	1.0	2	1
RXJ1315.4-1623	<5.6	12.8 ± 3.8	1.56 -0.09 -0.35	1.0	2	1

Appendix D

Main Sample - SEDs

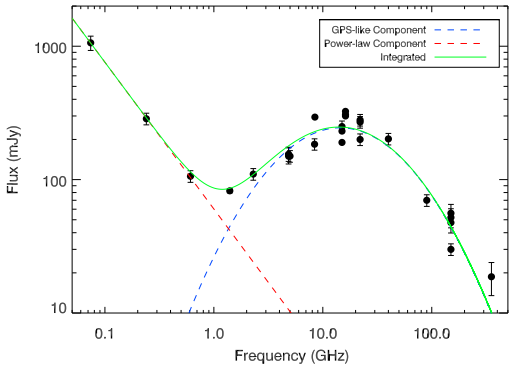

RXJ0439.0+0520

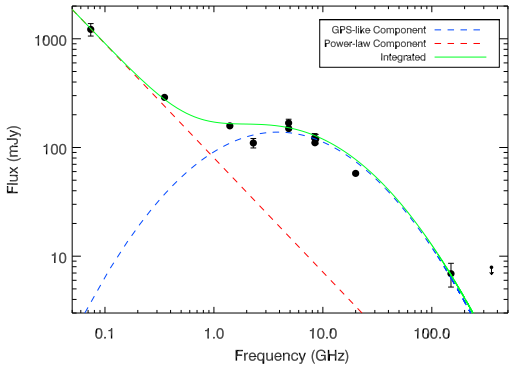

A1348

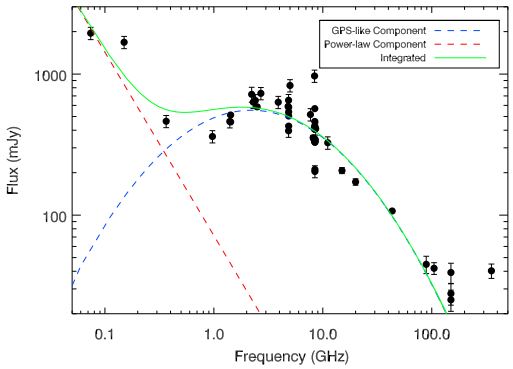

RXJ1558.4-1410

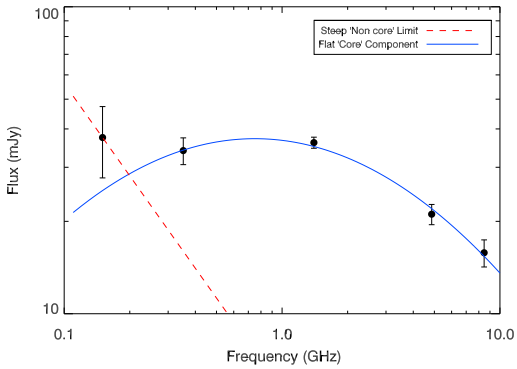

RXJ1315.4-1623

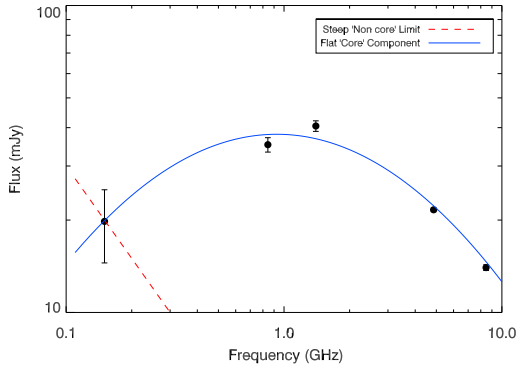

RXJ1304.3-3031

Figure D.1: SEDs for Main Sample sources with a core component best fitted using a GPS model. Solid lines denote a fit in instances where a value has been placed on the corresponding component whereas dashed lines indicate a fitted or extrapolated component where only a limit has been placed. See preceding section for more information on the spectral fits.

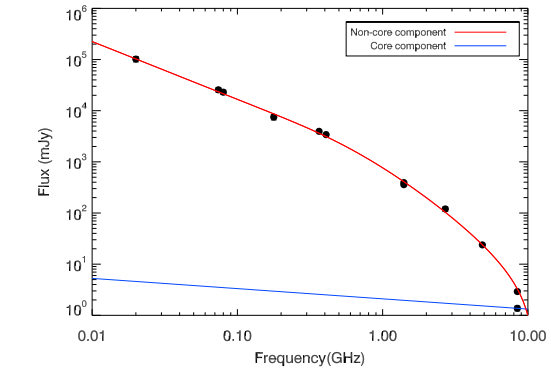

Z808

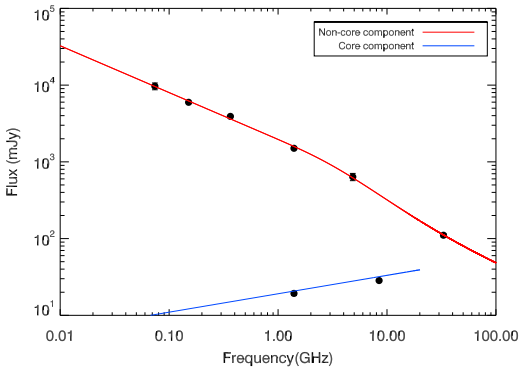

Z1261

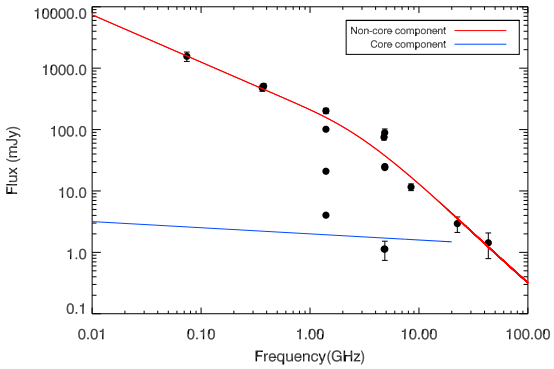

A763

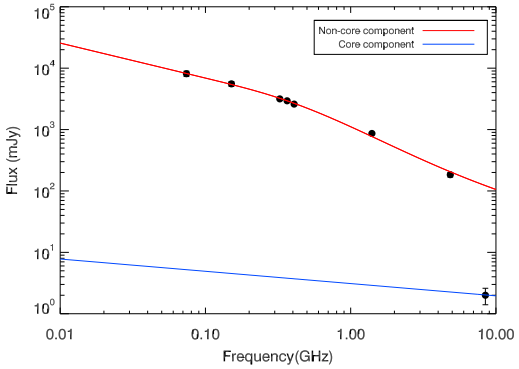

A1361

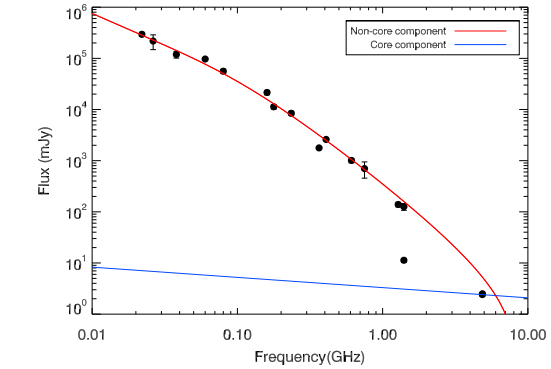

RXJ1522.0+0741/MKW3s

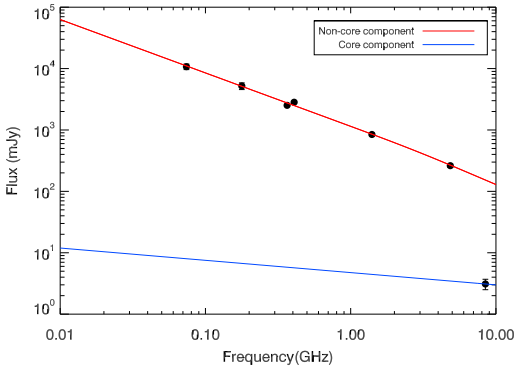

4C-05.84

Figure D.2: SEDs for Main Sample sources with a non-core component best fitted using a dropline model. Solid lines denote a fit in instances where a value has been placed on the corresponding component whereas dashed lines indicate a fitted or extrapolated component where only a limit has been placed. See preceding section for more information on the spectral fits.

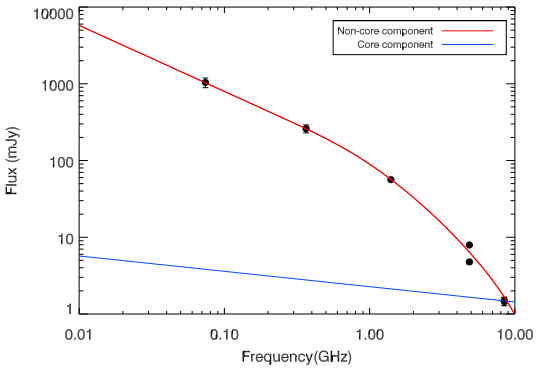

A2665

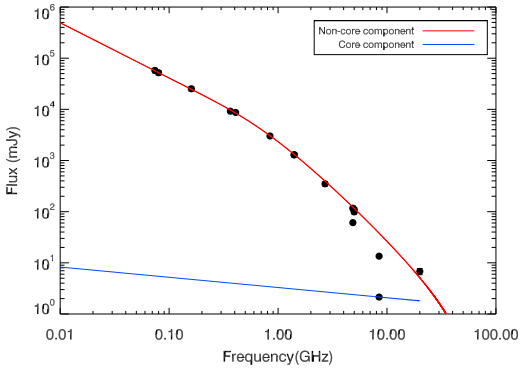

A4059

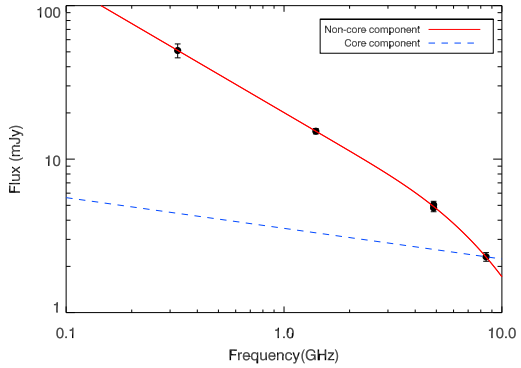

A77

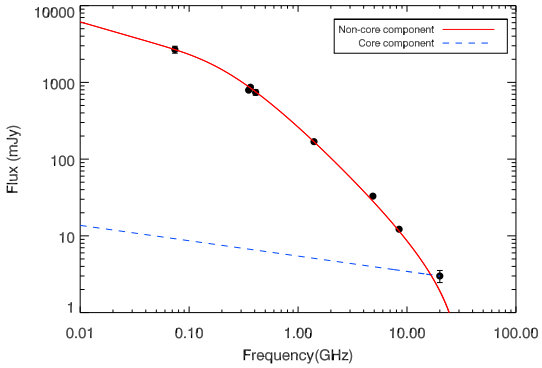

RXJ0331.1-2100

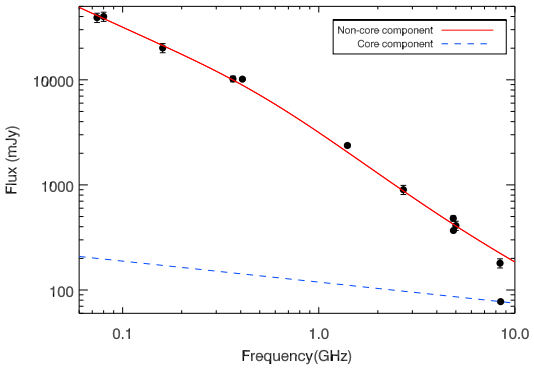

RXJ0747.5-1917

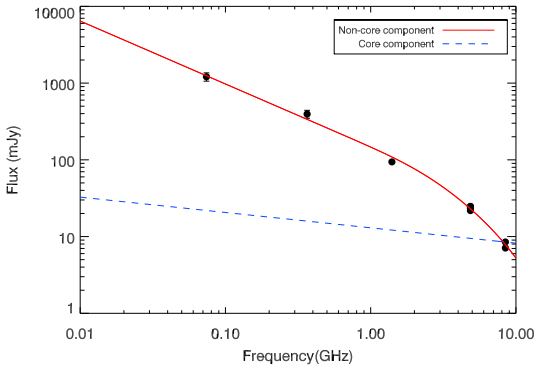

Z3179

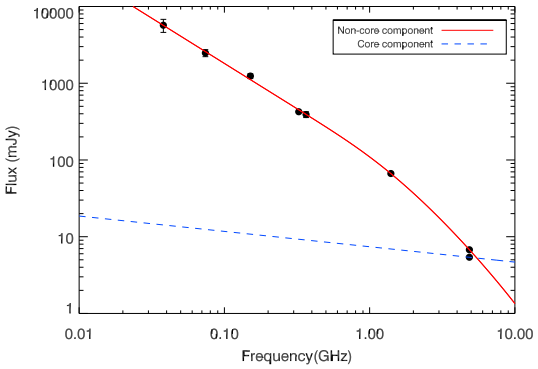

Z3196

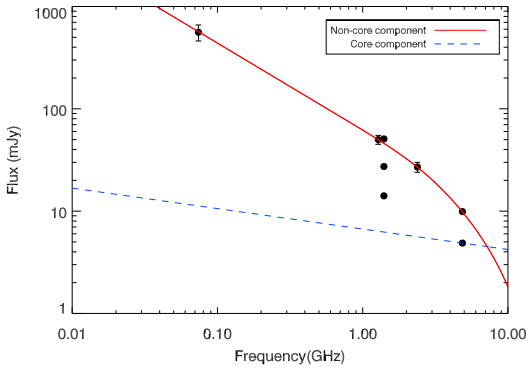

RXJ1657.8+2751

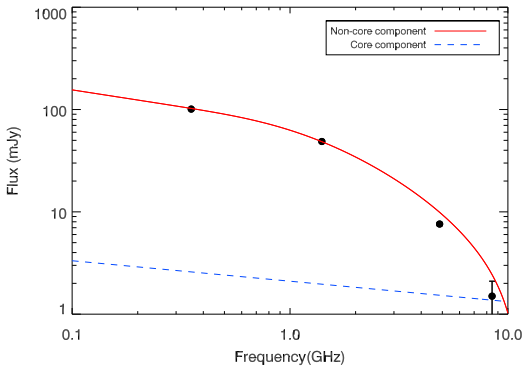

A2580

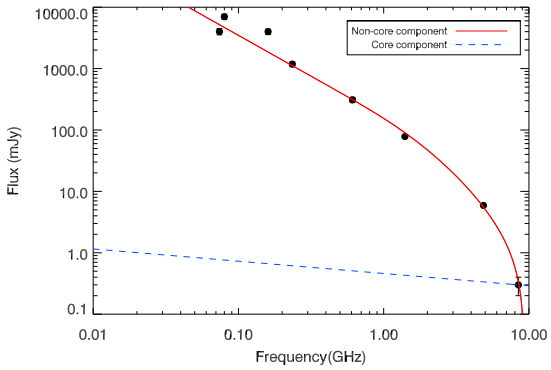

A2622

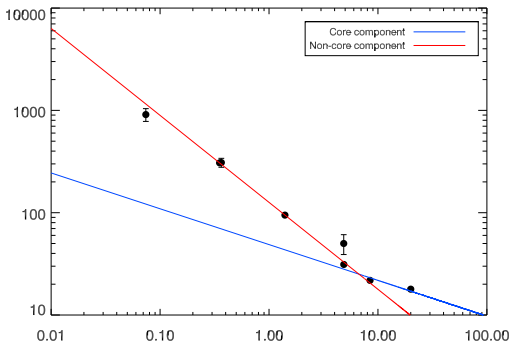

A11

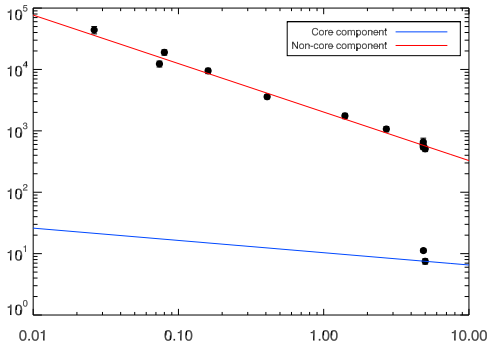

RXJ0058.9+2657

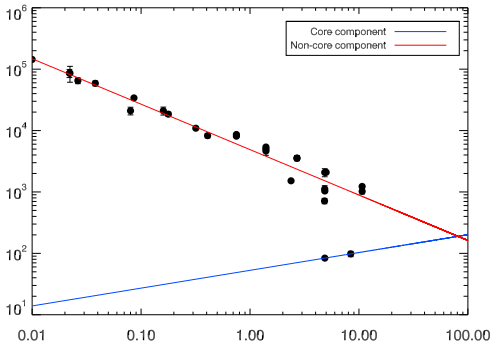

RXJ0107.4+3227

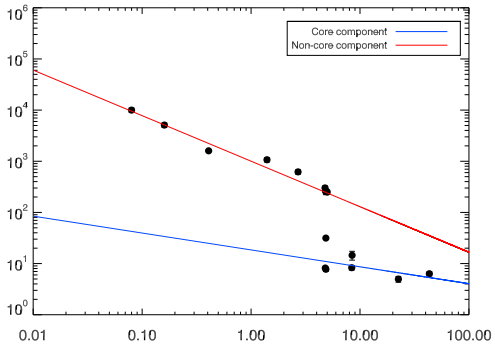

A160

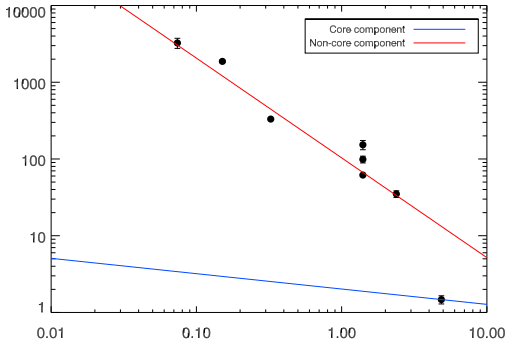

RXJ0123.6+3315

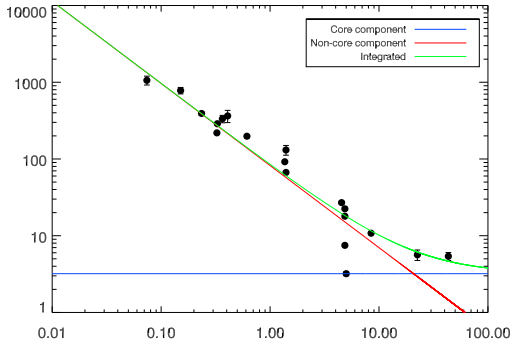

A262

Figure D.3: SEDs for Main Sample sources where both components are best fitted using power-law models. Solid lines denote a fit in instances where a value has been placed on the corresponding component whereas dashed lines indicate a fitted or extrapolated component where only a limit has been placed. See preceding section for more information on the spectral fits.

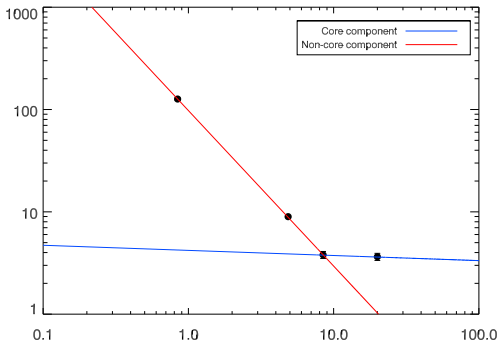

A3017

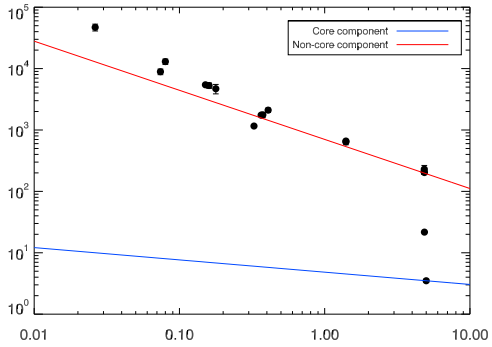

A407

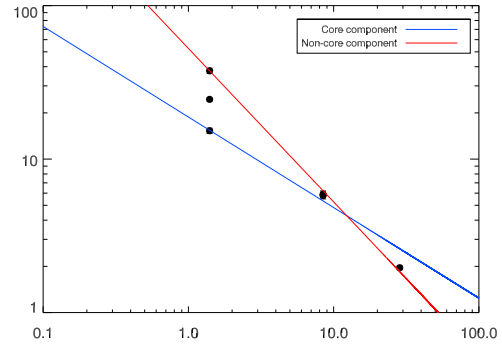

A478

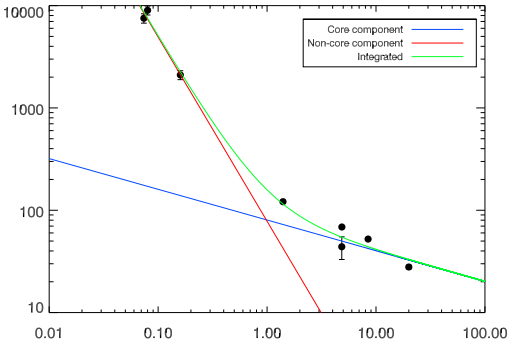

A496

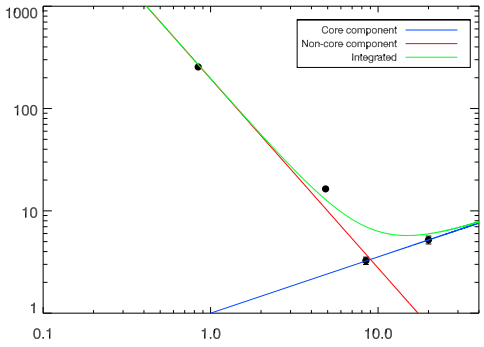

RXJ0543.4-4430

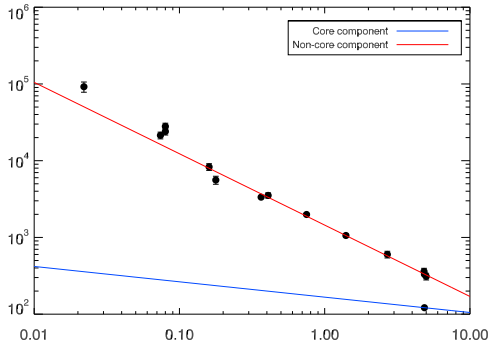

Z1121

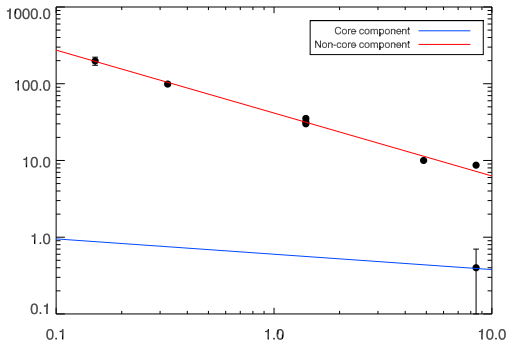

RXJ0819.6+6336

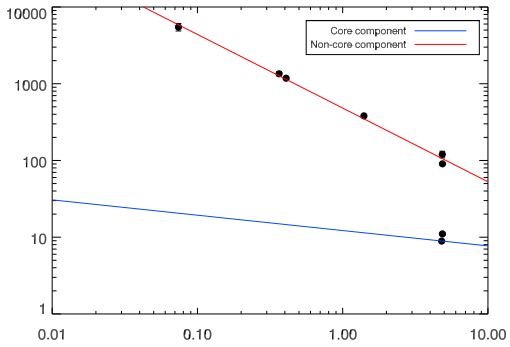

A761

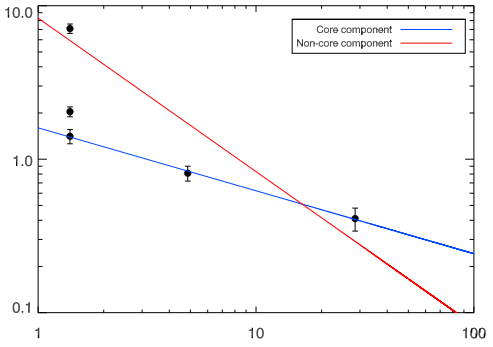

Z3146

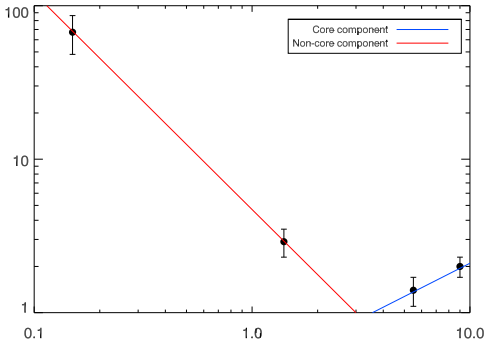

AS701

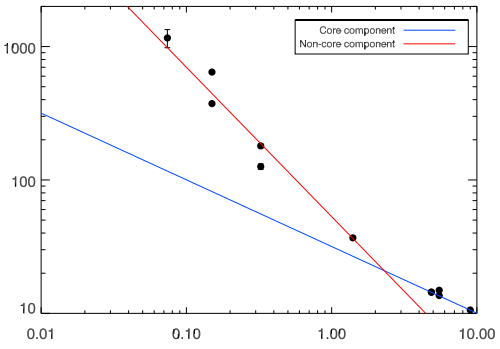

A1664

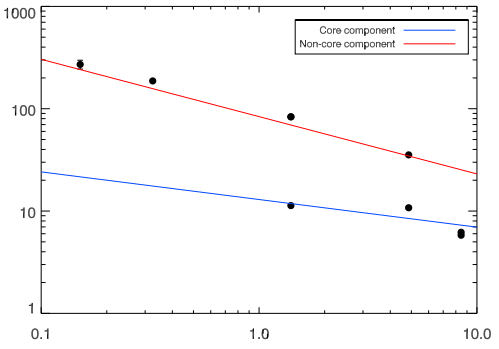

RXJ1320.1+3308

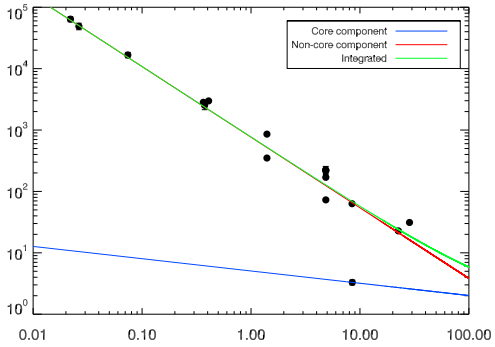

A1763

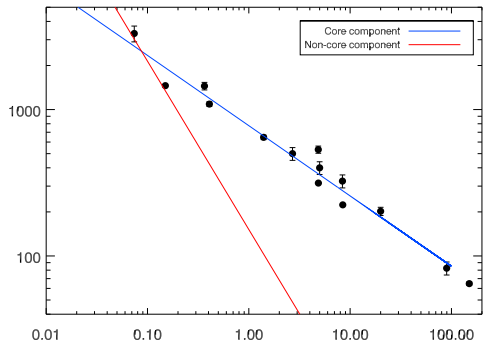

A3581

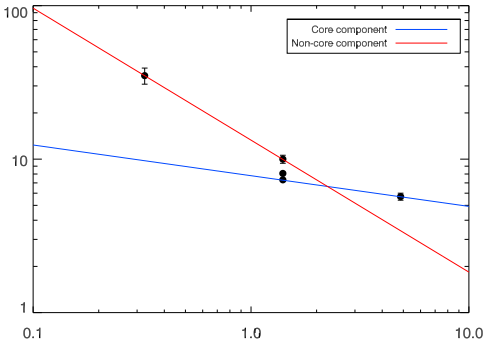

A1930

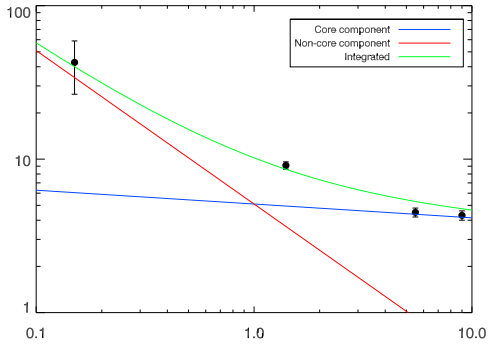

A3605

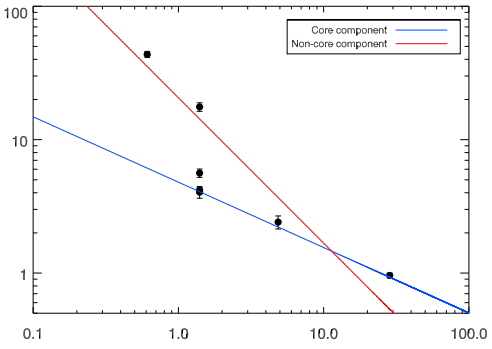

Z7160

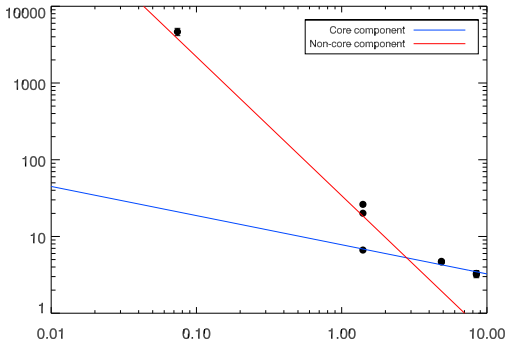

A2009

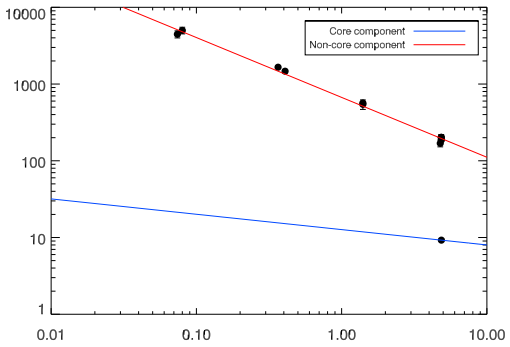

A2033

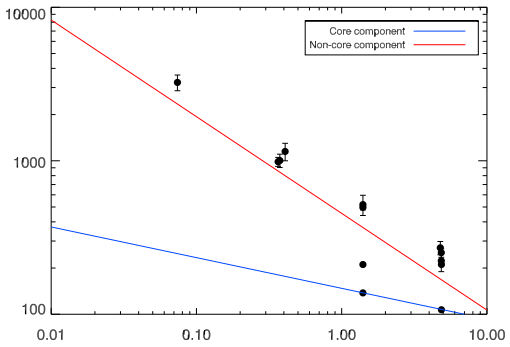

A2055

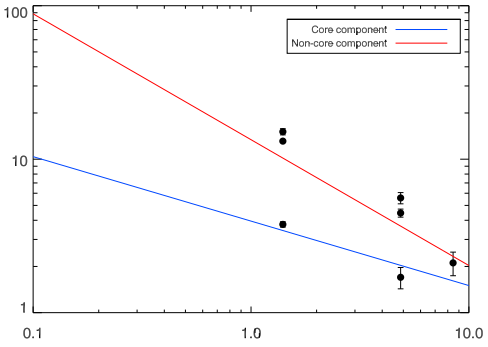

A2063

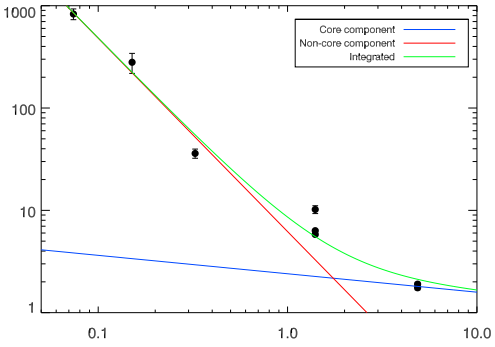

A2110

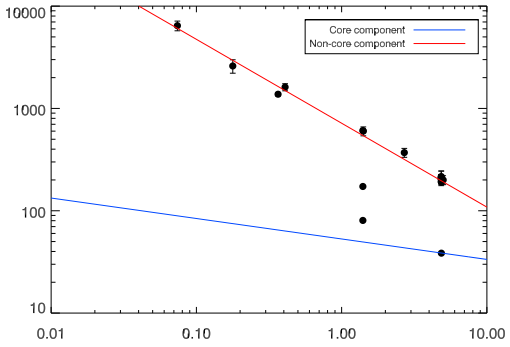

RXJ1604.9+2356

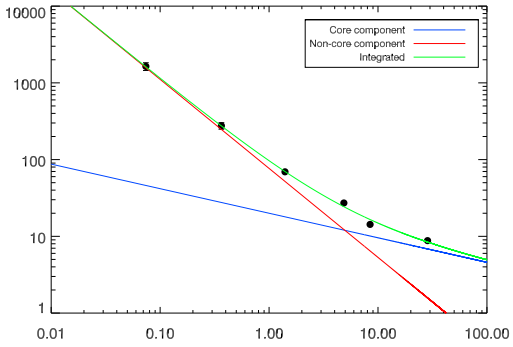

A2204

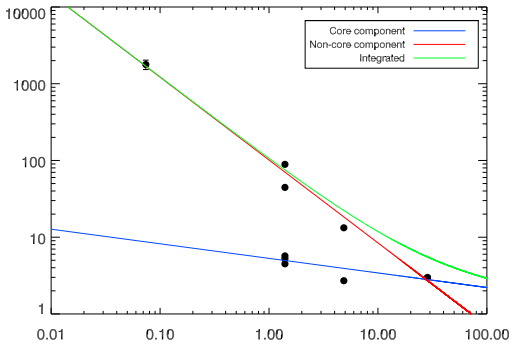

RXJ1720.1+2638

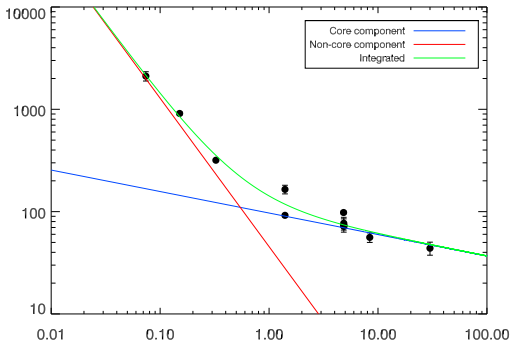

Z8276

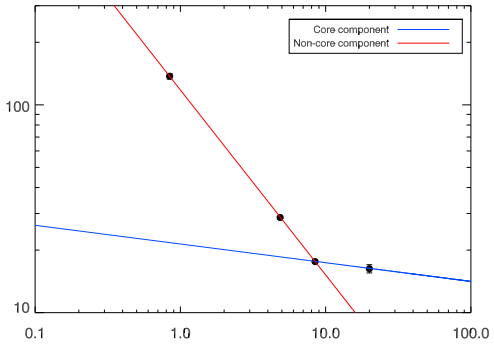

A3639

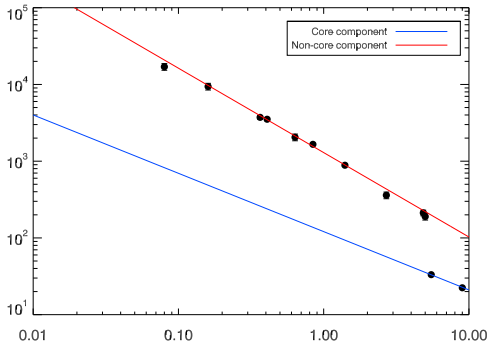

RXJ1931.6-3354

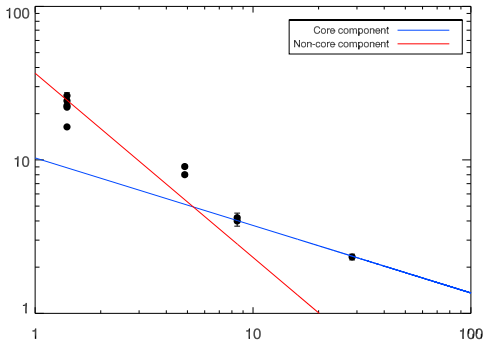

RXJ2129.6+0005

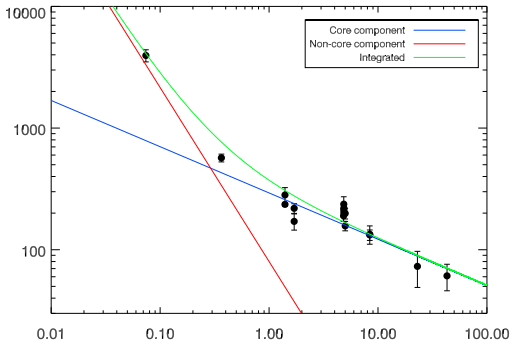

A2390

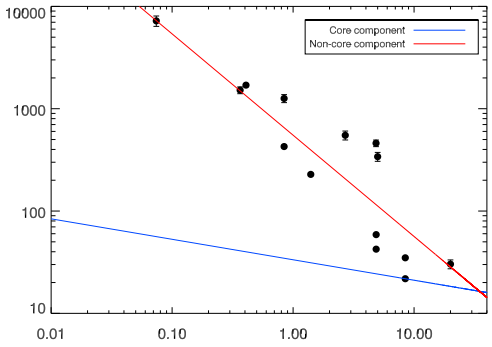

A3880

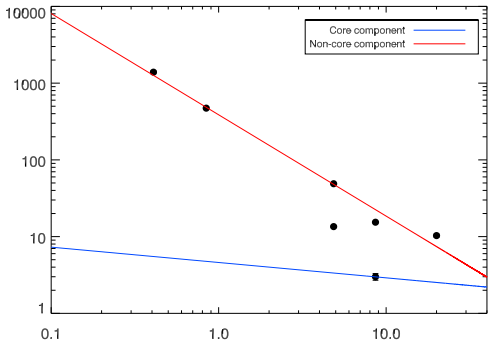

AS1101

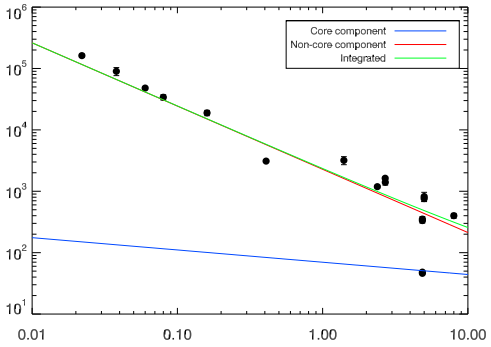

RXJ2214.7+1350

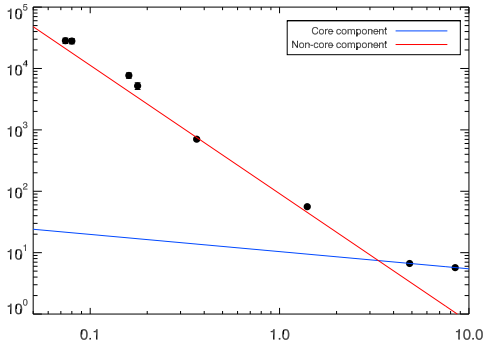

A2626

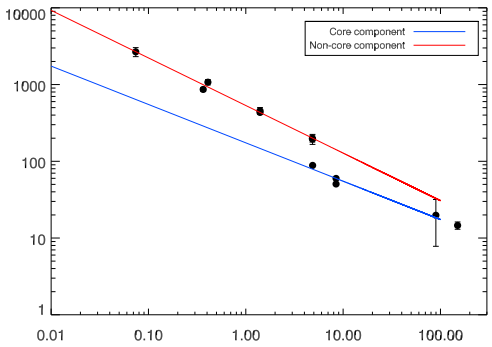

A2627(a)

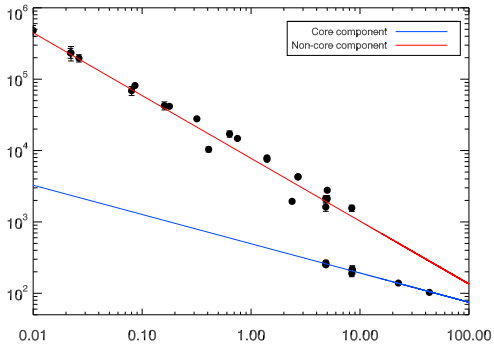

A2634

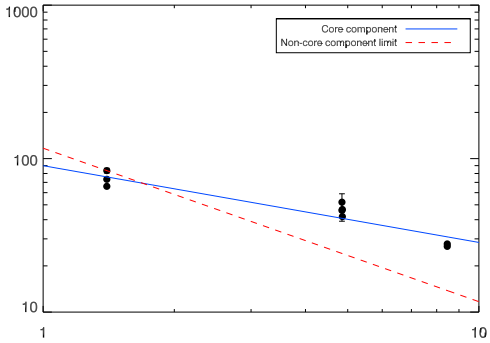

RXJ0000.1+0816

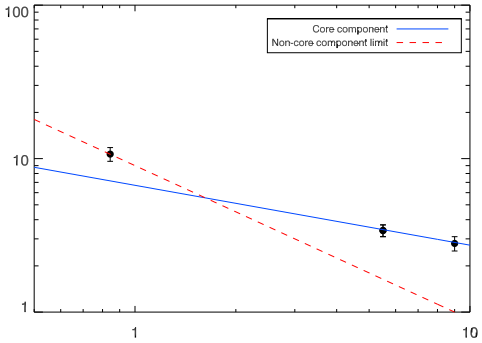

A2746

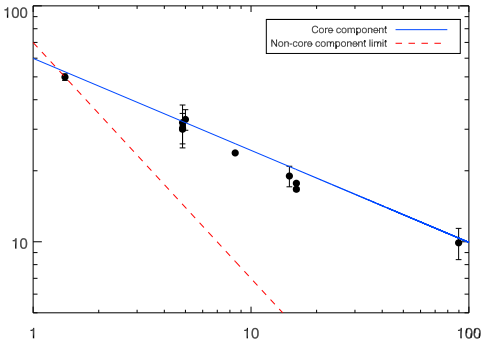

Z235

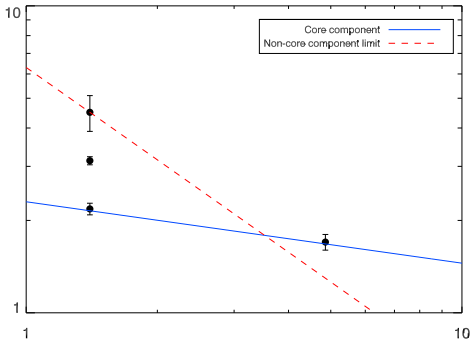

A168

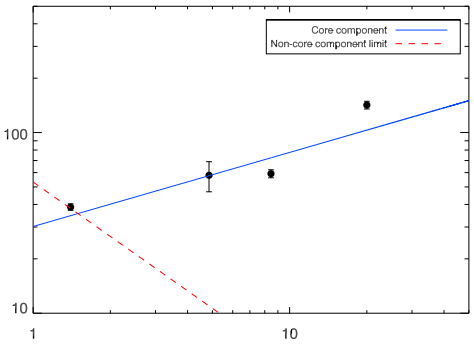

MACS0159.8-0850

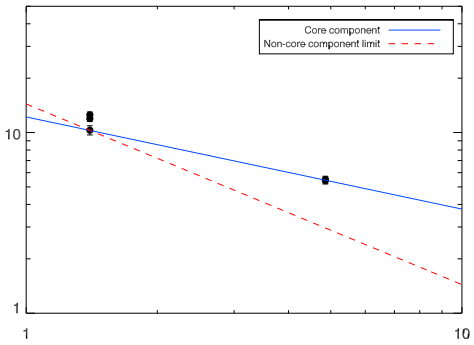

A291

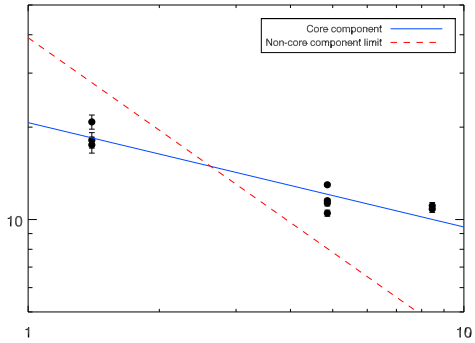

RXJ0341.3+1524

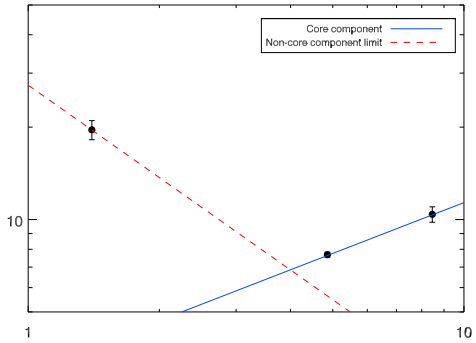

RXJ0352.9+1941

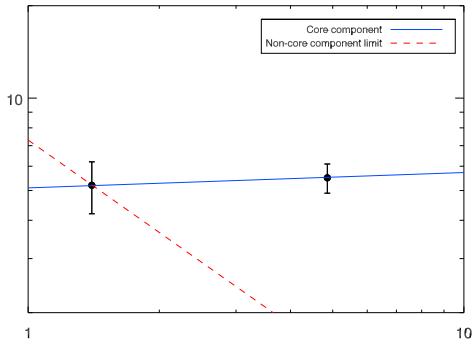

RXJ0503.1+0608

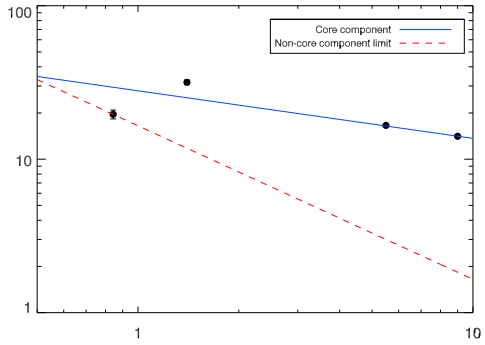

MACSJ0547.0-3904

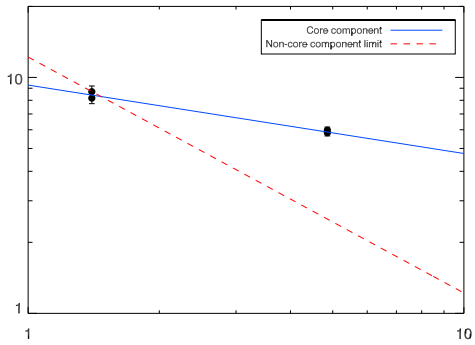

RXJ0751.3+5012

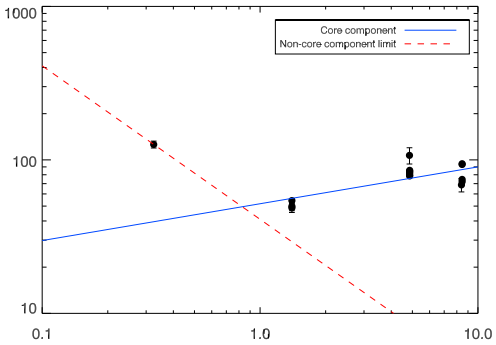

A646

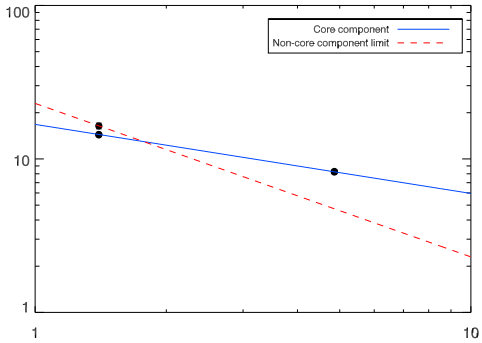

Z1665

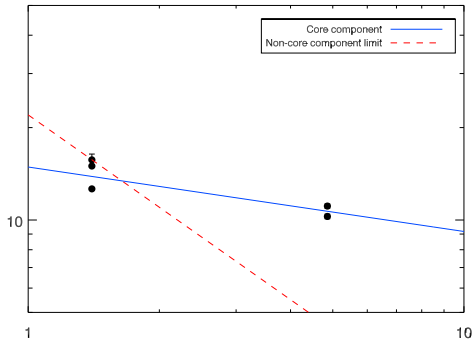

A757

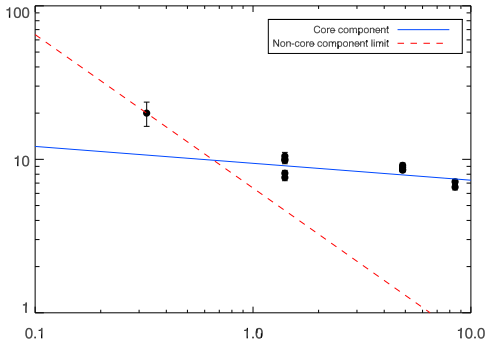

Z2844

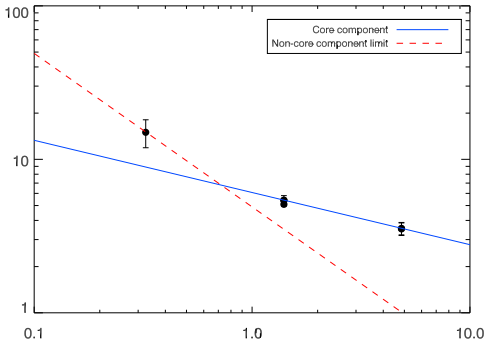

A1035

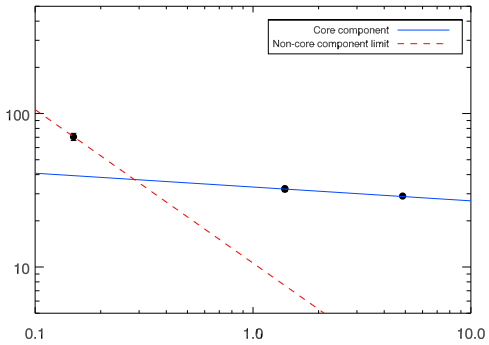

A1084

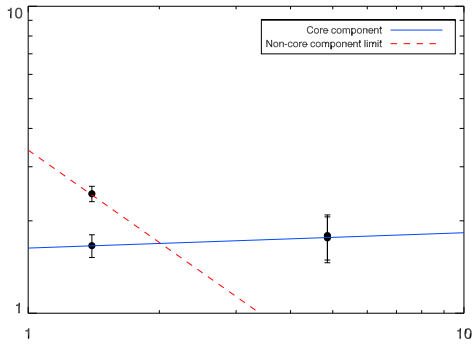

A1204

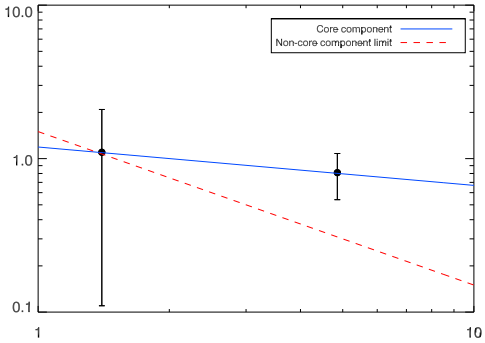

A1235

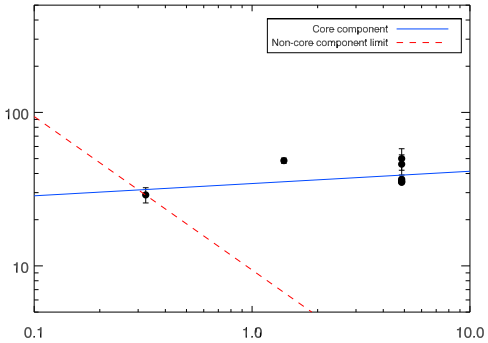

A1885

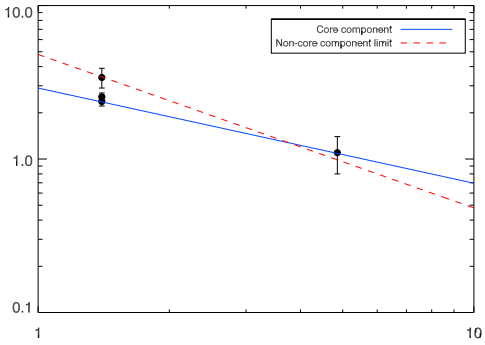

RXJ1440.6+0327

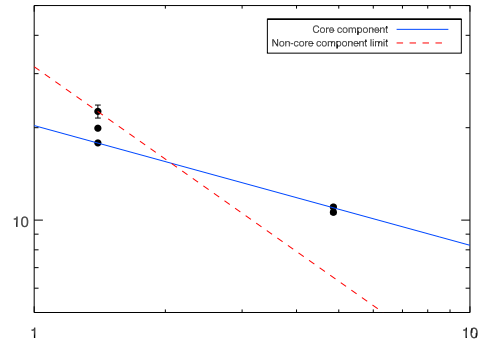

RXJ1442.2+2218

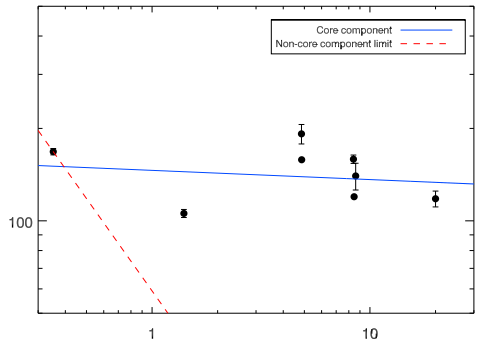

AS780

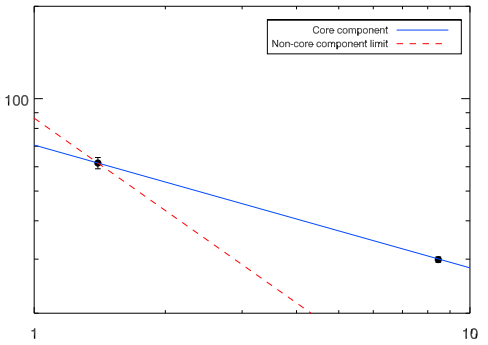

RXJ1504.1-0248

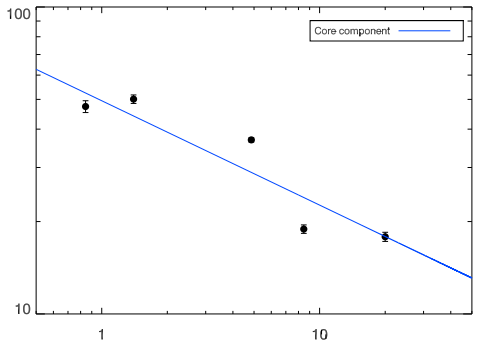

RXJ1524.2-3154

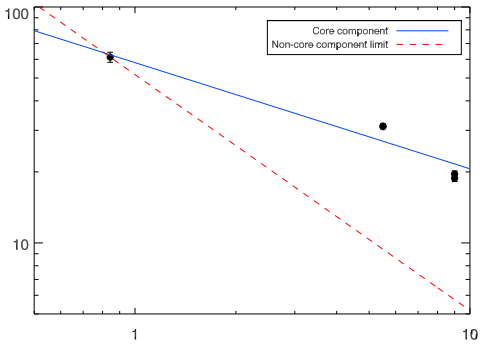

RXJ1539.5-8335

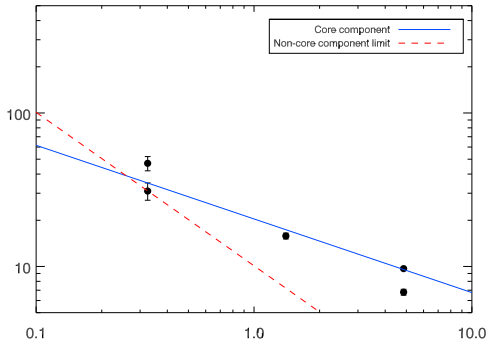

A2146

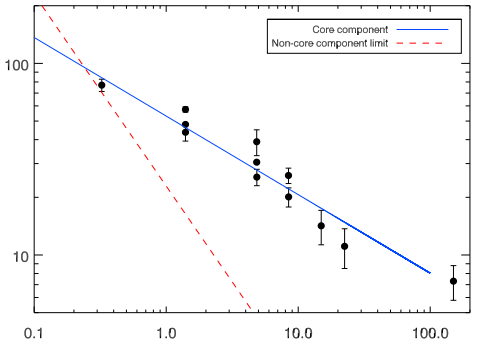

RXJ1715.3+5725/NGC6338

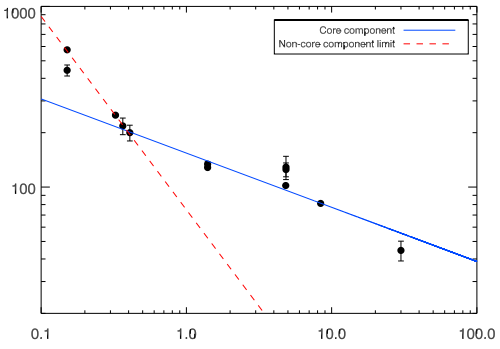

Z8193

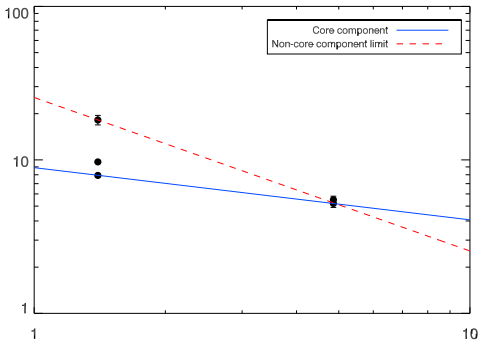

RXJ1733.0+4345

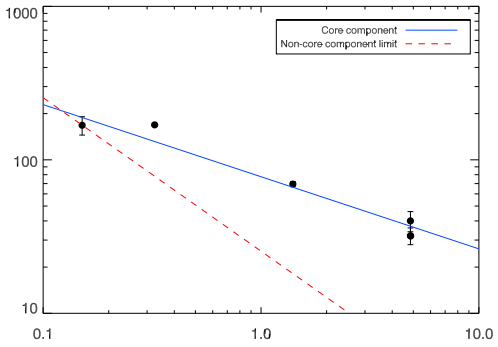

RXJ1750.2+3504

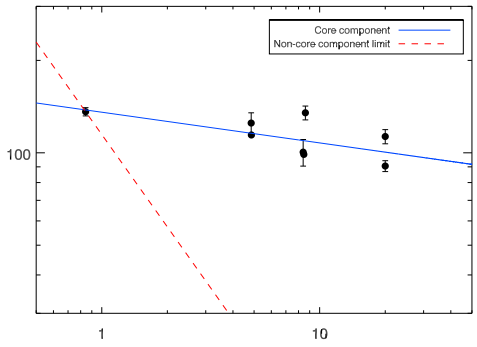

AS851

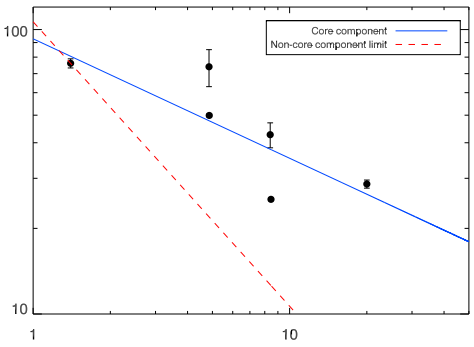

RXJ2213.1-2754

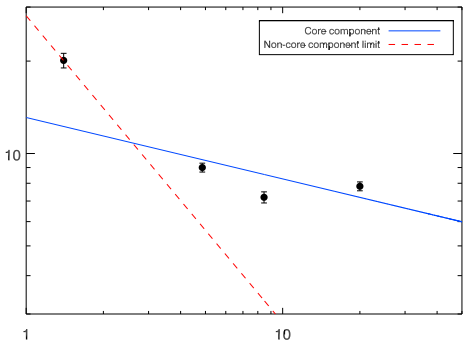

A2667

Appendix E

Main Sample - SEDs continued

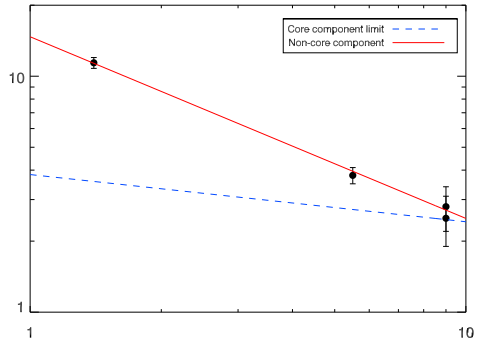

A2734

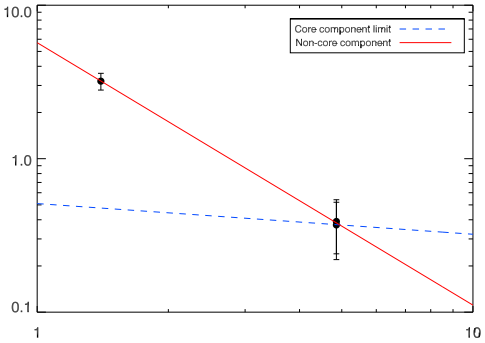

RXJ0021.6+2803

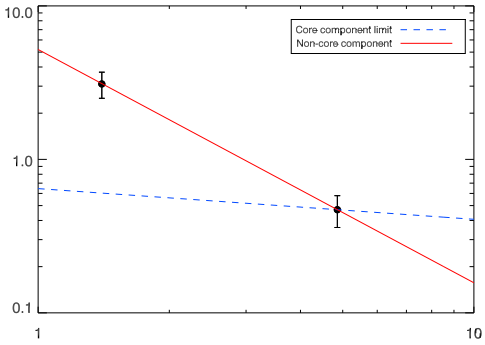

A76

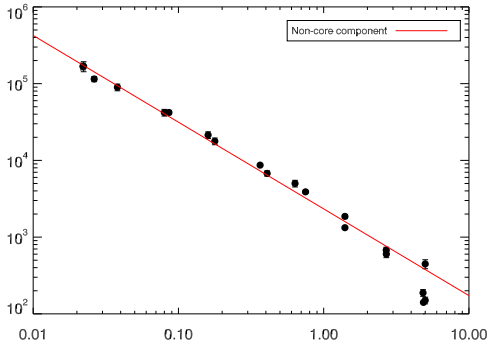

A115

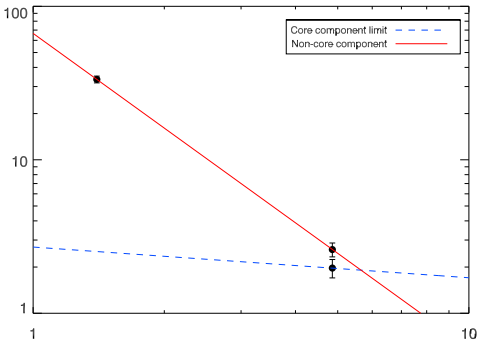

A193

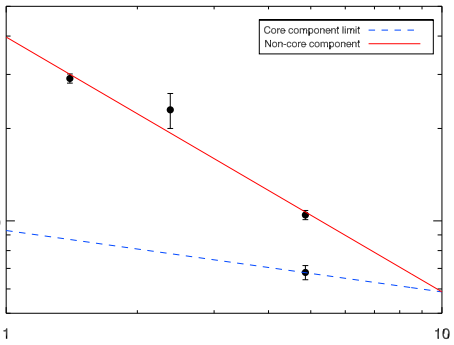

A189

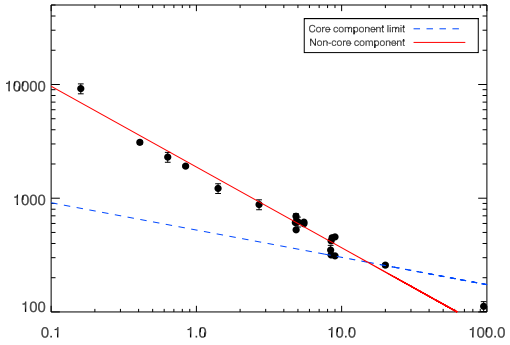

A3112

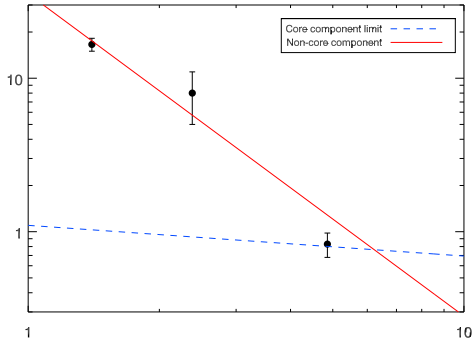

RXJ0419.6+0225

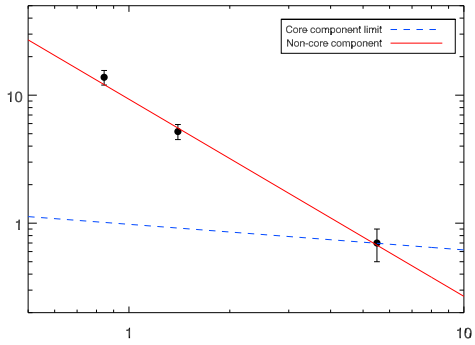

RXJ0528.9-3927

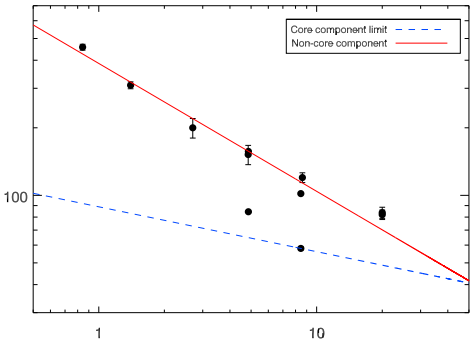

AS555

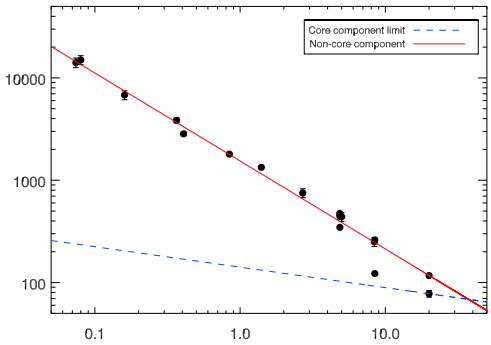

A3378

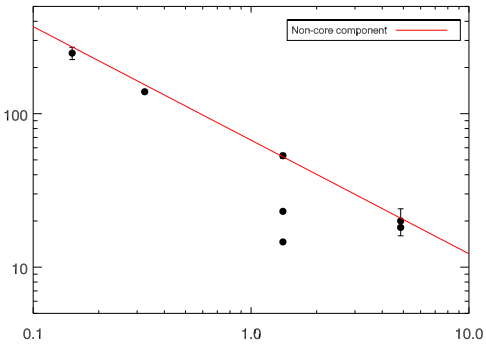

RXJ0740.9+5526

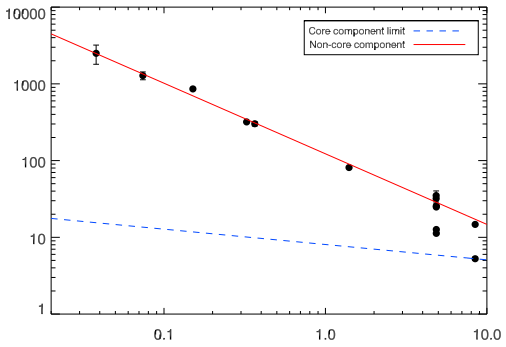

A621

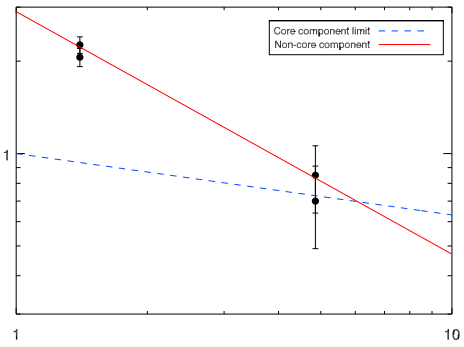

RXJ0821.0+0752

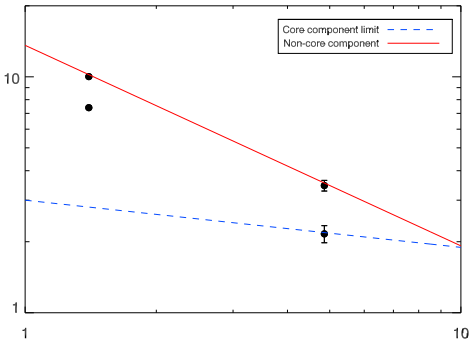

A667

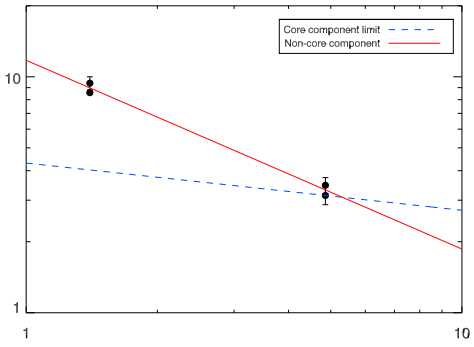

Z2089

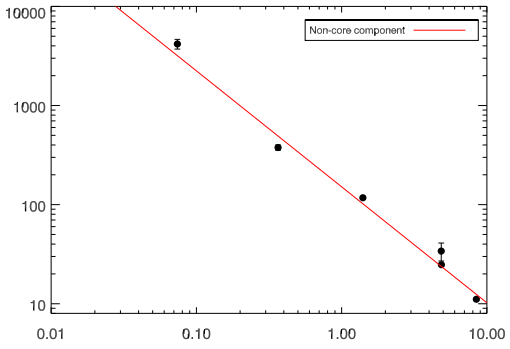

A795

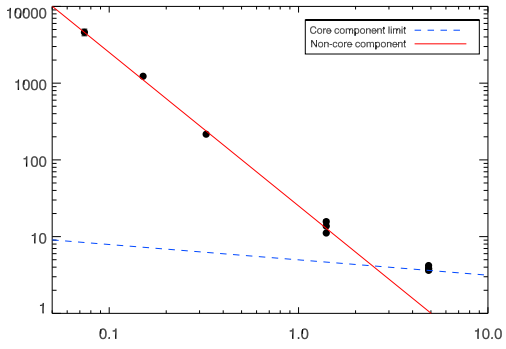

Z2701

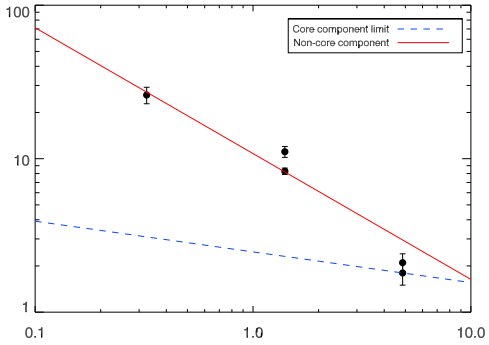

A971

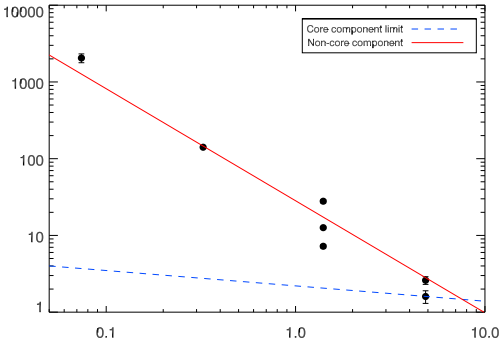

A980

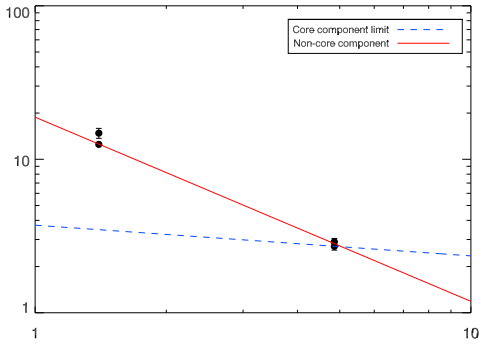

A1023

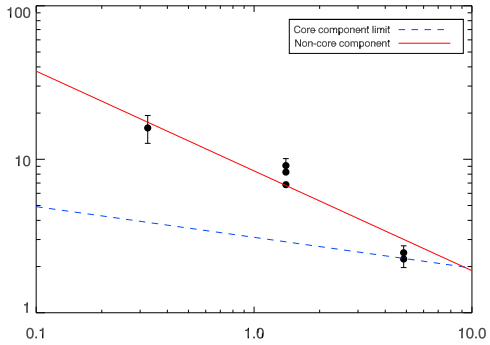

A1045

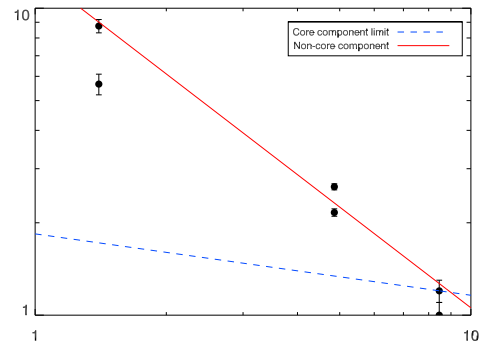

A1068

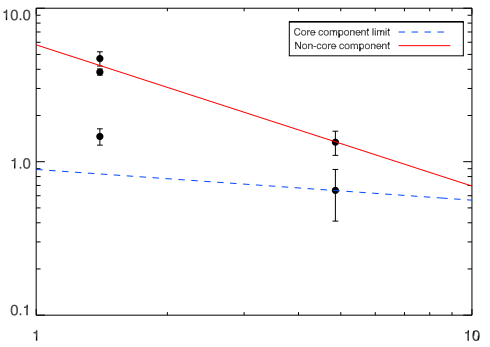

RXJ1053.7+5450

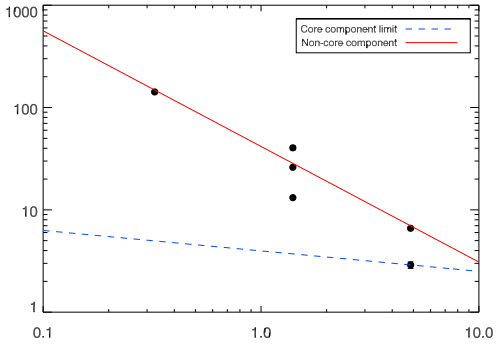

A1132

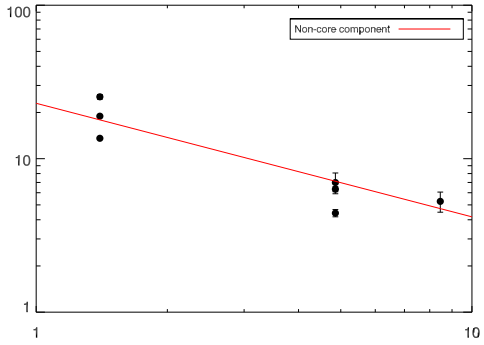

A1190

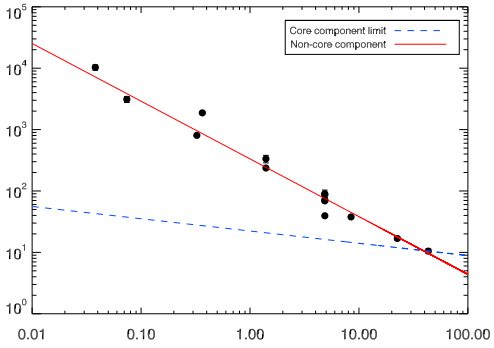

A1366

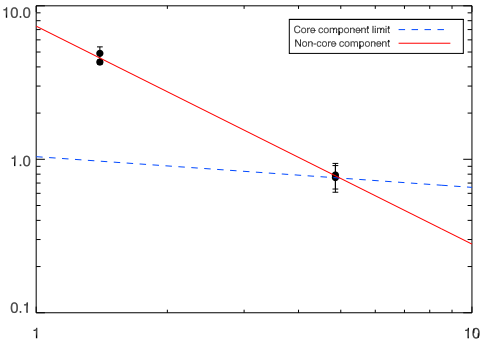

Z4673

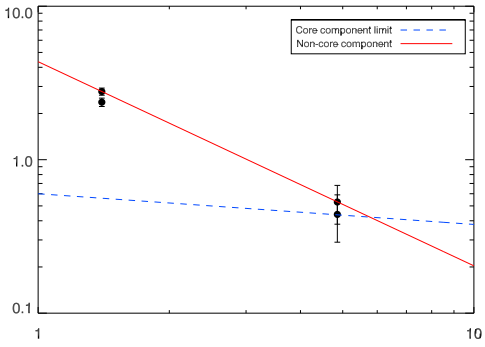

RXJ1206.5+2810

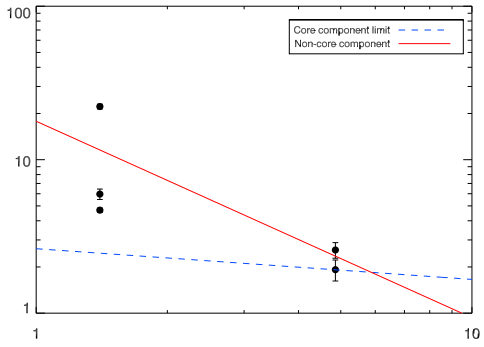

A1553

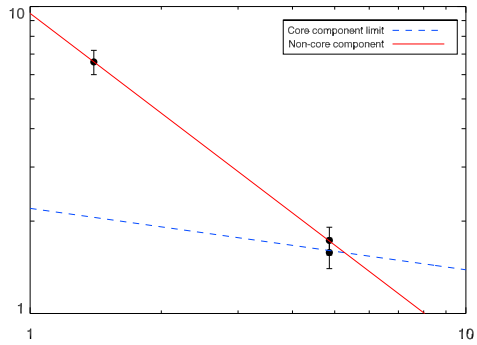

A1651

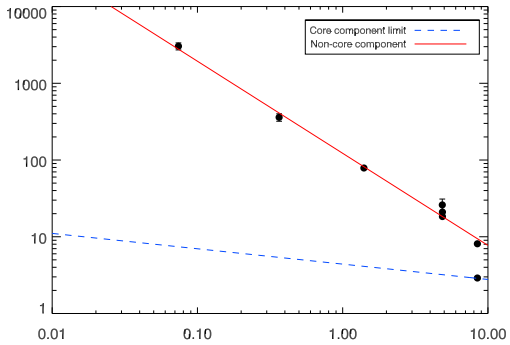

A1668

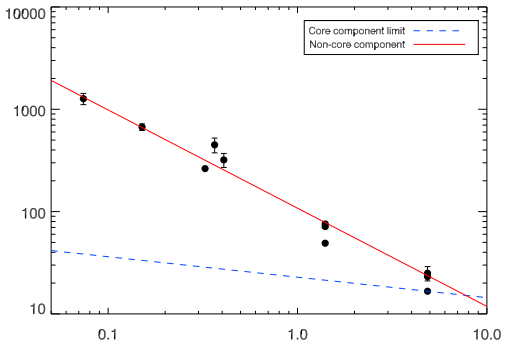

A1677

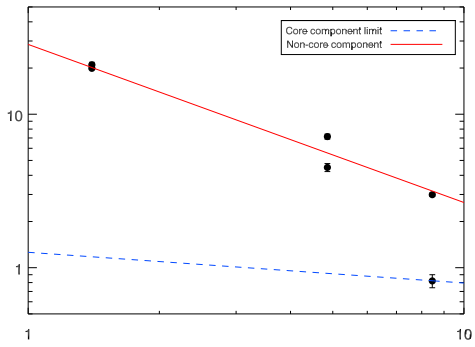

RXJ1326.3+0013

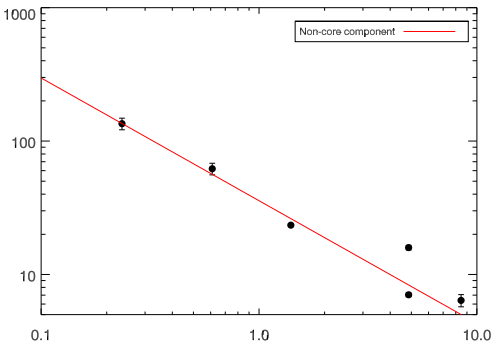

A1775(NW)

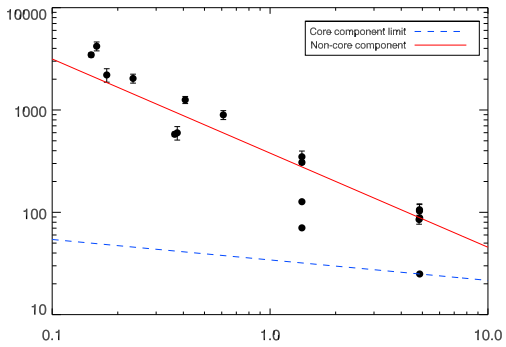

A1775(SE)

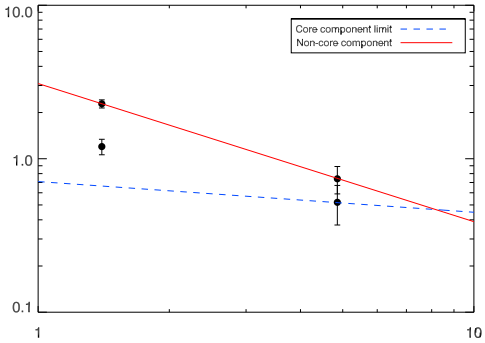

A1773

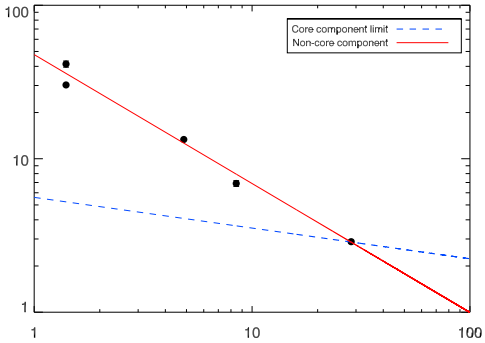

A1835

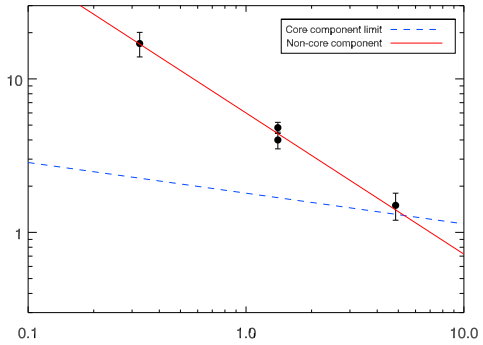

Z6718

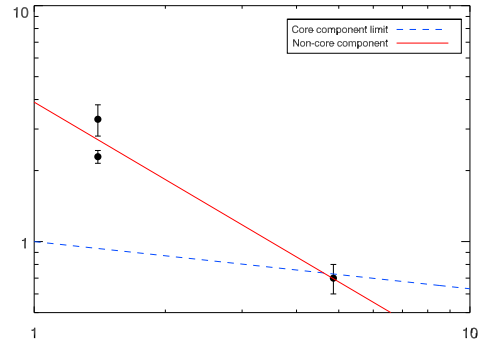

A1902

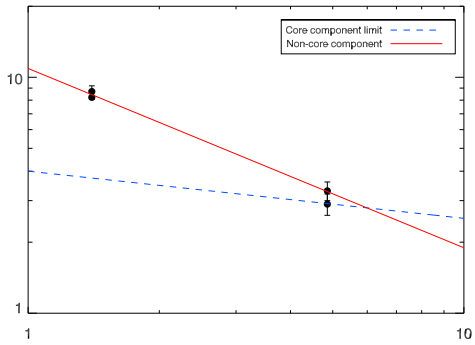

A1927

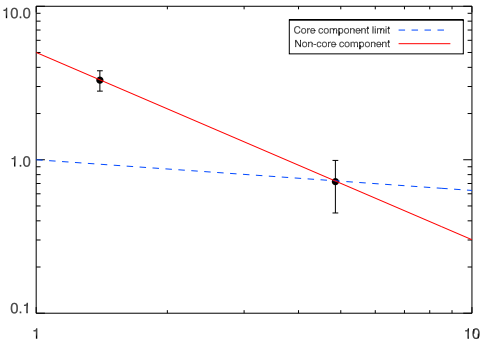

A1978

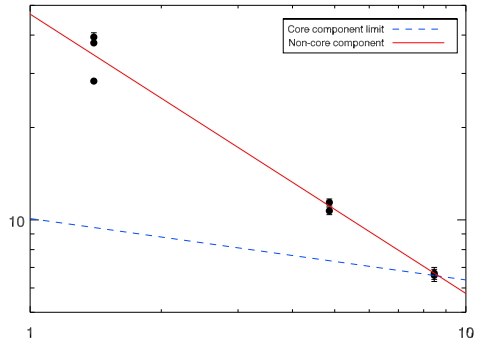

A1991

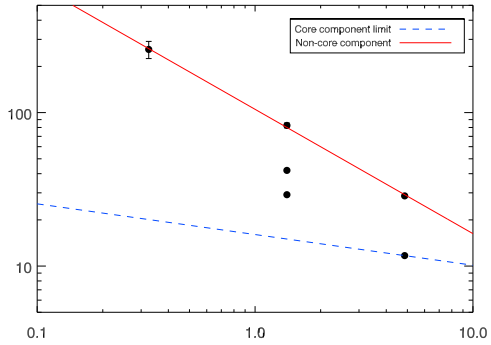

A2064

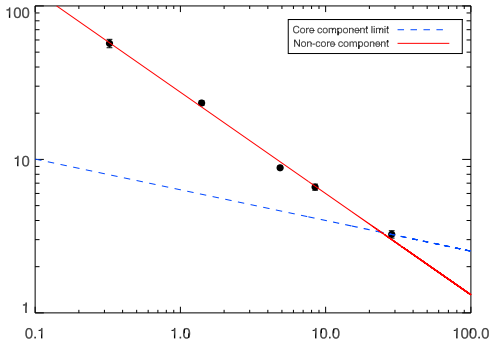

MACS1532.9+3021

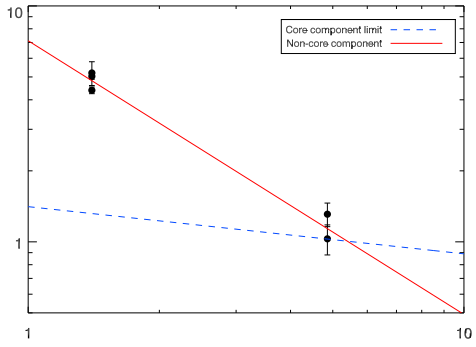

A2175

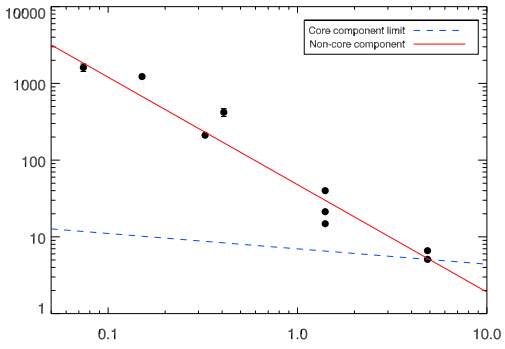

A2241

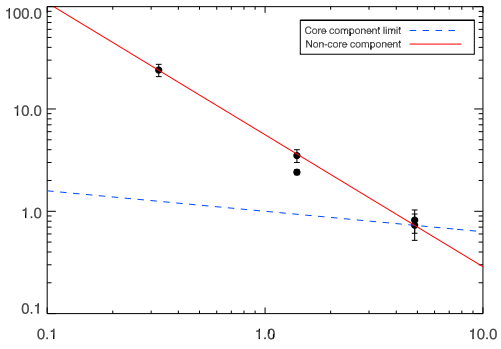

A2244

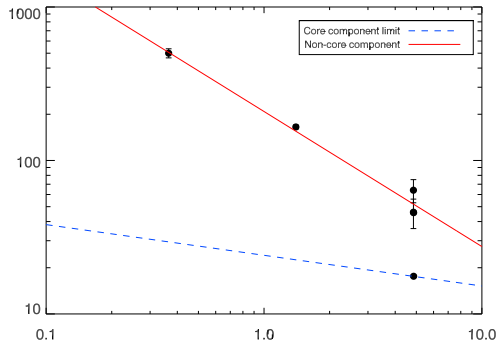

RXJ1715.1+0309

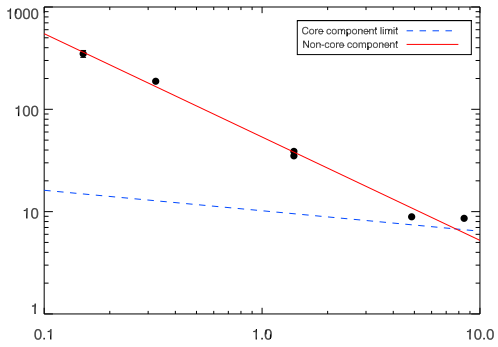

Z8197

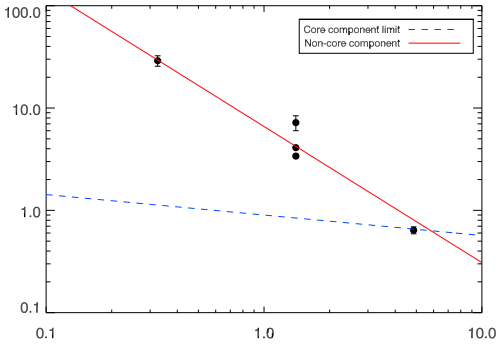

A2261

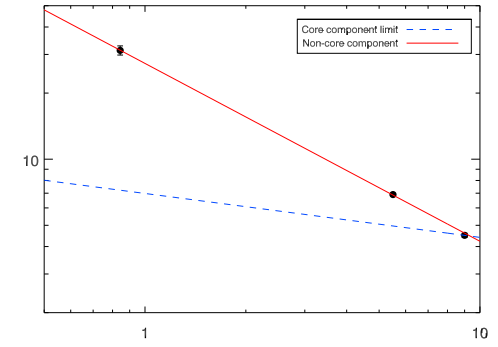

AS805

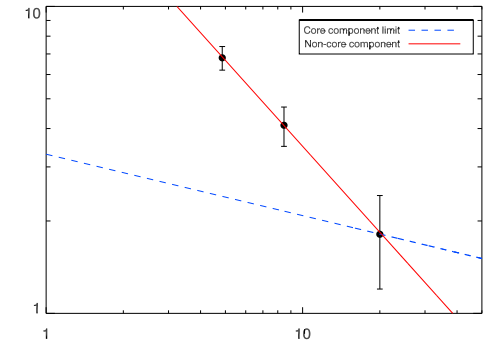

A3638

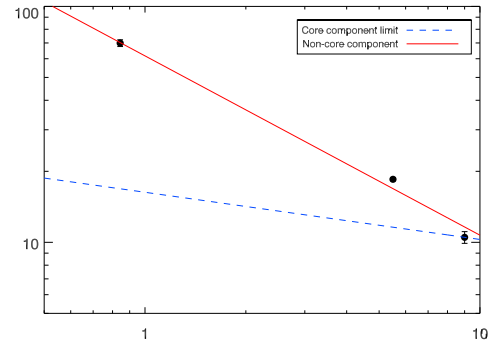

RXJ1947.2-7623

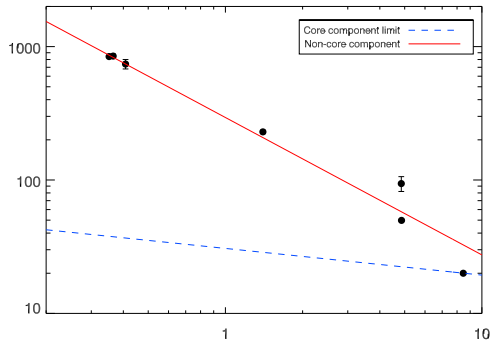

RXJ2014.9-2430

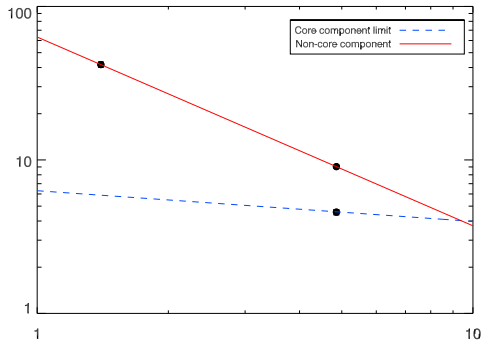

A2443

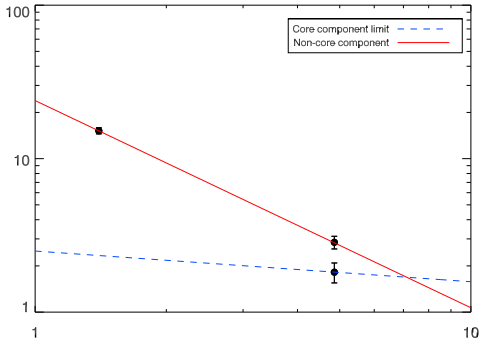

A2495

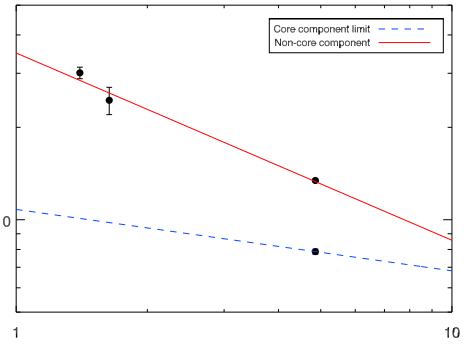

A2572(a)

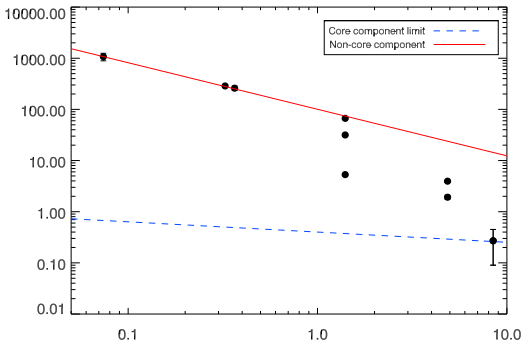

Z9077

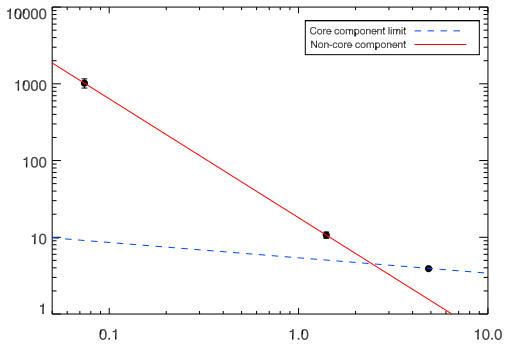

A2675

Appendix F

Main Sample+ - Comments on Individual SED Decompositions

These clusters do not have targeted observations presented within this study and so do not appear in the flux lists. We therefore give in the notes below the name of the BCG for each cluster. Fluxes were taken from the NED and HEASARC databases as well as being retrieved from FITS image downloaded from the NRAO's Image Archive (https://archive.nrao.edu/archive/archiveimage.html).

BCS - LEs

Hercules A A well studied classic FRII, bright object with esily distinguishable core and lobes. There are a large number of literature data points of integrated emission available in NED from which to get a measure of the non-core. Extrapolate from a 14.9 GHz VLA observation (Dicken et al., 2008) of the core region for an estimate of the core component. This cluster is also known as RXJ1651.1+0459, and the radio source associated with the BCG is often called 3C 348.

A2052 UGC 09799, associated with the radio source 3C 317. Extended source with clearly distinguishable core. The source is reasonably well studied (see e.g. Chapter 4). Fit to the SED of integrated fluxes for a non-core measurement. Source has multi-frequency VLBA observations (Venturi et al., 2004) that isolate the core. Fit to these separately to retrieve a measure of the active core component.

A2199 NGC6166, with associated radio source 3C 338. Extended, FR-II like source. VLBI measurements at several frequencies (Ly et al., 2004; Gentile et al., 2007) show a sub-dominant but inverted core component. Fit this VLBI SED separately for a measurement of the core component and then fit the integrated flux SED for a measurement of the non-core.

A1795 CGCG 162-010. Extended source, some high resolution observations in NRAO archive from which the core can be isolated. Create and fit individual SEDs for the core and extended components to enable measurements of both the core and non-core respectively. See also Chapter 4.

RXJ0338.7+0958 2MASX J03384056+0958119. Appears to be a compact steep spectrum object, hence fit the integrated spectrum to retrieve an estimate of the non-core component. An NRAO archival observation at X-band shows it as unresolved. Extrapolate from this to obtain an upper limit on the core component.

A1367 NGC3862. Powerful extended radio source with a well sampled SED that can be fit directly to obtain an estimate of the non-core component. There have been a number of high resolution VLBI observations of the core of this system (Lara et al., 2004; Kharb et al., 2009) from which a core-only SED can be created. Fit this for a measure of the core component.

BCS - NLEs

A2029 IC 1101. A wide-angle tailed (WAT) source with a morphologically distinct but energetically sub-dominant core. Fit the archival SED for a measure of the non-core component and then extrapolate from a high resolution VLA archival image at X-band of the isolated core (Jetha et al., 2006) to get a core estimate with appropriate uncertainty.

A1656 NGC4874. Source appears to be a small-scale WAT. Integrated emission is lobe-dominated, hence fit the archival SED for a measure of the non-core. There is no clearly discernible core in the majority of observations however there is a VLBA observation at C-band (Liuzzo et al., 2010) and higher frequency observations that seem to isolate the core (Lin et al., 2009) that can be fitted separately to get a reasonable measure of the core.

A2312 2MASX J18540626+6822565. Steep spectrum source that appears to be an FRI at 38 MHz (Roettgering et al., 1994). There is no archival data above C-band and only the subtlest hint of potential spectral flattening at C-band but not enough to claim unambiguosly the presence of a strong core component. Fit the lobe dominated integrated SED for a measurement of the non-core and then extrapolate from C-band (Gregory & Condon, 1991) for an upper-limit on the core.

A1314 IC 0712. Source seems to be a CSS with consistent index to high frequency (43.3 GHz, Lin et al., 2009). Fit the SED for non-core and then extrapolate from the 43.3 GHz point for a core limit.

A2147 UGC 10143. Source appears unresolved in available archival images. The index fitted to the SED is relatively shallow ($\alpha \approx 0.67$), however the source is undetected at 22.5 GHz (Lin et al., 2009) and hence cannot be dominated by a flat core and is perhaps best classified a CSS. Take an estimate of the non-core from the fitted SED and then extrapolate from the limit at 22.5 GHZ for an upper limit on the core.

A2065 2MASS J15222917+2742275. Source only appears to have been detected at L-band. Marginally resolved by FIRST and there is a relatively large flux decrement between the FIRST and NVSS resolutions hence it seems reasonably to believe this source is dominated by its non-core emission. Extrapolate with appropriate indices and uncertainties for a non-core measurement and an upper limit on the core component.

eBCS - LEs

A2396 4C +12.76. This is a strong, lobed source that has good archival coverage at lower resolution but no clear measurements of a distinct core. Fit the total SED for a measurement of the non-core. The highest frequency detection is at C-band (Gregory & Condon, 1991) although the single-dish resolution is too low to isolate the core. The highest resolution map is from FIRST, hence take the average of the central pixels in this and extrapolate from these to obtain the best limit on the core contribution.

A2036 2MASX J15110875+1801529. This source is a WAT although there is no obviously distinct core component. Single dish C-band observations would suggest flattening,

however this is most likely due to confusion as interferometric observations at C-band are consistent with a steady steep index to X-band detection and a non-detection at 22.5 GHz (all Lin et al., 2009). This non-detection shows the spectrum does not substantially flatten. Use only the higher resolution maps to create an SED and fit this for a measure of the steep non-core component and then extrapolate back from limit at 22.5 GHz for core limit.

A923 B2 1003+26. The available archival observations show the source to be an unresolved CSS up to C-band. Higher resolution VLA-A image in VLA archive (see also Fanti et al., 1986) shows the presence of an active core component at $\approx$0.5mJy. There is also an X-band image in the NRAO database taken in VLA-D/A array. Although the automatic pipeline image suffers from phase issues, blindly taking the peak pixel of the recovered source does suggest a $\approx$0.5mJy source is present. Fit the integrated lower resolution SED for a measure of the non-core component and then extrapolate from the VLA-A detection at C-band with index α=0.0 to recover an estimate for the core.

A580 2MASX J07255712+4123069. Higher resolution maps at C and X-band (Parma et al., 2007) show the radio-source to be associated with the BCG. Additionally associating the archival radio source B3 0722+414 with the BCG would suggest that the source could be best fit by a dropline model for the ageing non-core (with parameters: 54.69, 1.26, 0.91, 3.85). Below 2 GHz the SED displays a reasonably steady power-law and so for the MAIN SAMPLE+ estimate the non-core component by fitting only to these lowr frequency fluxes. The source is potentially slightly resolved in the X-band imaging although the core is not distinct. Extrapolate from the peak of this observation for a limit on the core component.

Z1883 2MASX J08425596+2927272. Archival detections are available only at L and C band, which show the source to be steep spectrum. Fit for a measure of the non-core and extrapolate for an upper limit on the core.

Z1370 4C +74.13. The BCG is associated with an unresolved, ultra-steep spectrum radio source. There are X and U-band observations available in the VLA Image database although neither recovers the source and both limits are consistent with the extrapolated index. Fit the observations of the USS $>$0.074 GHz to retrieve an estimate of teh non-core and then extrapolate from the limit imposed by the non-detection at U-band to put

an upper-limit on the core component. Note that there are very low frequency (38 and 22 MHz) observations that suggest the USS index may flatten to lower frequencies.

Z3959 SDSS J111551.90+012955. Distant cluster ($z \approx 0.35$), at FIRST resolution the BCG is consistent with being associated with a steep spectrum radio source. See that there is a large flux deficit between FIRST and NVSS suggesting that this source is resolved between the respective resolutions of these catalogues. Combined these imply that the source is dominated by its non-core emission. Therefore fit the spectrum for an estimate of this component and then and extrapolate from the peak of the FIRST detection to get an upper limit on the core.

A853 2MASX J09421480+1522509. The radio source is only apparently detected by the FIRST and NVSS surveys, although the FIRST resolution shows that this is associated with the BCG. The source is unresolved in NVSS but is resolved into a small WAT in FIRST showing that it is non-core dominated. This interpretation is consistent with the limits of other surveys (such as GB6, Condon et al., 1994) showing that the index must be steep, and that the spectrum does not flatten to show a shallow core component. Extrapolate from the NVSS integrated emission for an estimate of the non-core and then extrapolate from the peak of the FIRST detection with index α_{core}=0.2 for an upper limit on the core.

RXJ0004.9+1142 UGC 00032. SED can be fit with a split power law showing the presence of an active core in addition to a steeper component. Fit the SED therefore to obtain measures of the core and non-core components from the flat and steep spectrum components respectively.

eBCS - NLEs

RXJ1844.1+4533 3C 388. A bright FRII with a morphologically distinct but energetically sub-dominant core component. Fit the integrated SED to recover a measure of the non-core. Retrieve images from the NRAO image archive at L-, C-, X- and U-bands to measure distinct core fluxes. Use these to create a core only SED from which to determine the active core component.

A1446 4C +58.23. A bright WAT source. Fit the integrated fluxes for a measurement of the non-core component and then fit a separate SED of the isolated core fluxes (e.g. Laurent-Muehleisen et al., 1997) separately for a core measurement.

RXJ2250.0+1137 NGC 7385. The integrated SED returns a fairly flat index ($\alpha \approx 0.53$). However, morphologically the source is clearly dominated by its extended emission. Fit the integrated spectrum therefore to obtain a measure of the non-core component. Additionally there does appear to be an active core component. From images retrieved from the NRAO Image Archive, a distinguised core is detected at ≈118mJy at both X and U band. The is a VLBA observation by Fomalont et al. (2000). No map is presented as the source is too structured to recover reasonably. The authors present the uv data and from the amplitudes it is clear that ≈50mJy is recovered on even the longest baselines. It appears as if there may be a currently active component or perhaps that this source was very recently shut down. For a core estimate, fit the unresolved core components at X and U band with suitably large uncertainties.

A278 B2 0154+32. BCG is associated with a head-tail source. Fit the integrated flux SED for a measure of the non-core. Archival VLA-B observations at L and C band recover structure but do not fully isolate core component. For an estimate of the core contribution at 10 GHz, extrapolate from the 'head' component on the optical BCG position in the highest resolution map in the VLA Image Archive (at L-band). The recovered estimate is consistent with the limits imposed by low resolution observations at wavelengths higher than L-band. Note than an alternative interpretation of this source could be that it is an under-resolved FRII and hence could be a background contaminant rather than associated with the BCG.

A2625 2MASX J23360272+2032455. Steep spectrum source that is unresolved in NVSS. There are few archival observations, the highest radio-frequency of which is at C-band where the spectrum is still steep. Source appears to be a CSS. Fit the spectrum to get an estimate of the non-core component and then extrapolate from the C-band detection (Gregory & Condon, 1991) with α_{core}=0.2 for a core limit.

A2445 2MASX J22265584+2550094. There are three NVSS (Condon et al., 1998) sources coincident with the cluster, the brightest of which appears to be associated with the BCG. There are no higher resolution observations in the VLA archive and the source is not

within region covered by FIRST. The source does not appear within the VLSS catalogue but a steep extrapolation from the NVSS detection suggests it should be just below the catalogure limit. Indeed, an overlay of the VLSS (Cohen et al., 2007) shows that there is a weak detection below the catalogue limit at the position of the BCG. This VLSS source is partially blended with the distinct NVSS source to the West. Take the VLSS peak at the position of the BCG, which along with NVSS and GB6 (Condon et al., 1994) detections gives a steep index. Classify this source therefore as a CSS and fit for an estimate of the non-core. There are no higher resolution or higher frequency observations avaliable, so extrapolate from the C-band flux to get a limit on the core.

A2149 SBS 1600+540A. This cluster contain three potential BCGs. The most dominant elliptical (16:01:28.14, 53:56:49.7) appears to be associated with a radio source. This is a steep spectrum source, which can be fitted for measure of non-core. The source is morphologically identified as head-tail object in FIRST imaging although the head still appears confused and thus does not represent a truly naked core. The source was observed by Laurent-Muehleisen et al. (1997) and found to have a core component at 5 GHz. Extrapolate from this with reasonable uncertainties for an estimate of the non-core. Other candidate BCGs at ≈16:01:28.43, 53:54:15.0 and ≈16:01:23.14, 53:51:59.8 are both radio undetected at the FIRST detection limit.

RXJ0027.6+2616 2MASX J00274579+2616264. Source is steep spectrum and has no clear core component. It is undetected in the GB6 catalog (Condon et al., 1994) hence see no flat component. Therefore fit for a non-core estimate and extrapolate from the GB6 limit to put an upper limit on the core component.

RXJ1652.6+4011 2MASX J16525325+4009130. BCG is associated with a radio source as matched in both FIRST and NVSS. It does not appear in the VLSS catalog (Cohen et al., 2007) but inspecting an overlay of the region reveals a weak detection at the BCG position. The derived index suggests that the source could be core-dominated but it is undetected in the GB6 catalogue (Condon et al., 1994) and similarly undetected with the VLBA ($<$3mJy, Bourda et al., 2010), which shows this source to be non-core dominated. The index derived using the map detection in the VLSS imaging may therefore be an underestimate. Fit this spectrum nonetheless for an estimate of the non-core componant and then extrapolate from the VLBA detection limit for a fairly stringent upper limit on the

core component.

A1291 MCG +09-19-110. The BCG is revealed to be associated with a small WAT in FIRST (White et al., 1997). Lin et al. (2009) observed this source at multiple frequencies and showed it to be steep spectrum. Fit the SED for a non-core measurement then extrapolate from the X-band detection for a core limit. This is consistent with less stringent limits imposed by extrapolating from non-detections at 22.5 & 44.3 GHz.

RXJ1852.1+5711 2MASX J18520859+5711430. Source is resolved but displays amorphous structure. The SED could be fitted with a dropline model and indicates that the source is dominated by ageing emission, perhaps a core relic. Fit the SED for a measurement of the non-core component. Highest resolution available in the NRAO Image Archive is at C-band. There is no distinguishable core so take the peak of the emission and extrapolate for an upper-limit on the core.

A2512a UGC 10187. Head-tail source. Integrated fluxes to lower frequency give a steep spectrum, which appears to flatten to higher frequency suggestive of increasing core dominance. Taking the peak fluxes of the nuclear region it appears as if an active core component is present but appears to be confused with the more extended emission in most of the available observations. Extrapolate back from the seemingly clean core observation at 22.5 GHz Lin et al. (2009) for the best estimate of the core component.

A1986 2MASX J14530832+2153396. This cluster appears to contain several large ellipticals. The largest of these (and hence the most likely candidate for BCG) is associated with a steep spectrum radio source. The source is undetected in all of the major C-band catalogues, which confirms this steep spectrum. Fit the SED for a non-core measurement and then extrapolate from the C-band limits for an upper limit on the non-core component.

A2315 2MASX J19001653+6956599. BCG appears to be associated with a steep spectrum radio source. Fit the SED for an estimate of the non-core and then extrapolate from the detection limits at C-band (e.g. Condon et al., 1994) for a limit on core component.

REFLEX(NVSS) - LEs

Hydra A Little introduction required. A powerful, extended source that is very well-studied in the literature (e.g. McNamara et al., 2000; Hamer et al., 2014, and references therein). The source is dominated by its extended emission so fit the SED for a measure of the non-core component. Use VLBI observations (e.g. Taylor, 1996; Araya et al., 2010) of the central core regions only to independently fit for the core component. CLuster is also known as A780 and RXJ0918.1-1205.

A2597 The BCG is associated with the powerful extended radio source PKS 2322-12. The archival SED is dominated by the extended emission hence fit this for a measure of the non-core. NRAO archival images at X-band with the VLA-A array allow the core to be isolated. The flux of this component agrees reasonably well with the flux recovered on milli-arcsecond scales with the VLBA (Taylor et al., 1999b). Use a representative index of α_{core}=0.2 to extrapolate from the VLBA detection for an estimate of thr core component at 10 GHz.

A3532 PKS1254-30. This is a large extended source, with the lobes looking disturbed. Clear that the archival SED is dominated by the extended emission hence fit to this to get a measure of the non-core component. There are no available observations at high resolution or frequencies greater than 4.85 GHz. Extrapolate from the peak of an archival VLA C-band image to obtain an upper limit on the core.

RXJ0132.6-0804 PKS 0130-083. The SED of this source has a flat spectrum and appears to be highly core dominated. VLBI observations (Bourda et al., 2010, 2011; Petrov, 2011) show it to be slightly extended on ≈few parsec scales. A separate SED for the core can be produced from the VLBI imaging, from which the core component can be estimated. Extrapolating from the WENSS (Rengelink et al., 1997) detection (using α_{steep}=1.00) agrees well with the missing flux at 1 GHz between the VLBI obtained core contribution and the flux recovered in lower resolution maps. Hence, use this extrapolation to infer an estimate for the non-core component.

A2415 2MASX J22053865-0535330. This source has a steep spectrum source at low frequencies ($<$1 GHz). At higher frequencies than this it appears to be dominated by a self-absorbed core component (Chapter 4). VLBA imaging shows extent on ≈few pc scales (see Chapter 5) the integrated emission of which is consistent with lower resolution

fluxes, confirming the source to be core dominated at higher frequencies. For the purposes of the MS+, fit two separate power laws to the steep and flat components in the SED to obtain estimates of the non-core and core component respectively. Note that the given indices are measured locally to the normalisation frequencies for each component.

RXJ1206.2-0848 Also known as MACS J1206.2-0847, this is a high redshift cluster ($z\approx0.44$), whose BCG is identified in NED only as as 'MACS J1206.2-0847 BCG'. This is associated with a steep spectrum radio source. It is undetected in the PMN (Griffith & Wright, 1993) and AT20g (Murphy et al., 2010) surveys showing that there is no significant inverted/flat component. Fit the SED for a measure of the core component and then extrapolate from the higher frequency non-detections to get a limit on the core contribution.

RXJ0501.6+0110 2MASX J05012816+0110357. The relatively sparsely sampled SED appears to have a relatively flat index ($\alpha\approx0.7$) but is undetected at GB6 (Condon et al., 1994) and above which suggests the spectrum steepends to higher frequency. The SED can therefore be attributed to dominant non-core emission. Extrapolate from the non-detections for an upper-limit on the core component.

A1644 2MASX J12571157-1724344. Flat spectrum source that appears to be variable considering multi-epoch C-band observations. Not a clear GPS-like spectrum with the available archival coverage but can fit the spectrum with a shallow index power law to obtain a measurement of the core component. There is a faint detection at the BCG position in WENSS that is just below the catalogue limit (Rengelink et al., 1997), suggesting that the spectrum turns over in the GHz range. Extrapolate from this to get a limit on the non-core component.

RXJ0445.1-1551 NGC1650. Appears to be a core dominated flat spectrum radio source. Fit the SED for a measurement of the core component and then extrapolate from the WENSS detection (Rengelink et al., 1997) for an upper limit on the non-core.

A85 MCG -02-02-086. The BCG is associated with a CSS source. VLA images from the NRAO Image Archive at X, U and K bands show that the source remains unresolved and steep out to above 20 GHz. Fit the SED for a measure of the non-core and then extrapolate from the 22.5 GHz flux to place an upper limit on the core component.

RXJ1347.5-1144 GALEX J134730.7-114509. High redshift ($z\approx0.45$) cluster with a pow-

erful radio source associated with the BCG. Gitti et al. (2007) report the presence of a radio mini-halo within this cluster. Archival, higher resolution (VLA-A) observations at C- and X-band show that there is a morphologically distinguishable core component associated directly with the BCG. Interpolating between these core-only fluxes returns a flat spectrum, that can be extrapolated for an estimate of the core component at 10 GHz. The SED steepens to lower frequencies although this is likely contaminated by the mini-halo emission. Fit the fluxes at frequencies below 1 GHz for an estimate of the non-core component, accounting for the expected core contribution at 1 GHz. Note that this is potentially affected by mini-halo emission.

A383 2MASX J02480342-0331447. The BCG is associated with a radio source that maintains a steady steep spectral index at least as high as 22.5 GHz (BIMA, Coble et al., 2007). Fit for a measure of the non-core and then extrapolate from a non-detection at 31 GHz (OVRO, Mason et al., 2009) for a core limit.

A1663 2MASX J13025254-0230590. The BCG appears associated with an NVSS source that is also matched to a source detected at 1.28 GHz with the GMRT (Giacintucci et al., 2007). We are unable to determine structure from these observations. The source is undetected at both PMN (Griffith & Wright, 1993) and AT20g (Murphy et al., 2010), however the limits do not rule out the presence of a flat component. Equally the limit from the MRC (Large et al., 1981) does not rule out a steep spectrum. The emission cannot therefore strongly be claimed to be attributable to either core or non-core dominated emission and so extrapolate with appropriate α_{core}=0.2 and $\alpha_{non-core}$=1.0 indices for limits on both components.

A3698 NGC6936. BCG optical position coincident with NVSS, however no other radio detections are available. Cannot attribute to steep or shallow source by limits at other frequencies hence extrapolate for limits on both components.

RXJ1050.4-1250 USGCS152/NGC3402. The BCG of this small group appears to be associated with a reasonably active radio source. The source is well sampled at L-band in the archives, although it is not clearly resolved. There is a large flux decrement between NVSS and the higher resolution observations indicative potential extended emission on intermediate scales. O'Sullivan et al. (2007) observed this source at L-, C- and X-bands with the VLA and showed that it contains a flat spectrum core component. Fit for this

then extrapolate from the NVSS flux for an estimate non-core emission, accounting for the expected core contribution at 1 GHz.

A2402 2MASX J21582888-0947489. The BCG is optically matched to an NVSS radio source, however there are no additional radio detections. Limits at other frequencies do not limit the spectrum to be unambiguously associated with a flat core or a steep non-core and hence the best approach is to extrapolate from the NVSS detection with relevant indices for limits on both the core and non-core components.

A2566 2MASX J23160519-2027528. The BCG is matched to a radio source in NVSS. There are no other radio detections and survey limits do not clearly distinguish this source to be either core or non-core dominated hence use relevant indices to extrapolate from the NVSS detection to place a limit on both the core and non-core components.

RXJ1506.4+0136 NGC5846. This is the brightest member of a relatively local group ($z \approx 0.006$) and is a well studied LINER. The radio SED has a flat index, appears to be variable and is detected on milli-arcsecond scales with the VLBA (Nagar et al., 2005), confirming it to be core dominated. Use the most contemporaneous observations and fit for an estimate of the core component. Extrapolate from the lower frequency detection at 750 MHz (Heeschen & Wade, 1964), accounting for the expected 1 GHz core contribution, for a limit on any potential non-core component in the system.

RXJ2147.0-1019 2MASX J21470043-1019118. BCG is associated with a radio source in NVSS (at 1.4 GHz), however there are no additional radio detections and limits at other radio frequencies are not limiting on the nature (core or non-core) of the emission. Therefore make extrapolations from the NVSS detection, using the approriate indices to obtain upper limits on both the core and non-core components.

S0301 IC1860. The BCG is associated with a radio source that is detected in both SUMSS (Mauch et al., 2003) and NVSS (Condon et al., 1998). However, the index between these detections is not sufficiently steep or shallow to unambiguously label the source as core dominated (or otherwise) and hence the only reasonable approach is to extrapolate for limits on both components using appropriate indices.

A281 2MASX J01570689-0553102. The BCG is associated with an NVSS source, although it has no other radio detections available. Survey limits at other radio frequencies do not elucidate whether this emission can be attributed definitely to either core or

non-core emission. Therefore extrapolations with appropriate indices are made from the NVSS flux to place upper limits on both components.

RXJ1501.1+0141 NGC5813. This source was studied by Nagar et al. (2005) as part of a survey of nearby LINERs and is also well sampled in the NRAO Image Archive. There is a flat spectrum component that persists to above 10 GHz that can be fitted to estimate a core component at 10 GHz. The source appears slightly resolved at L-band, showing that there should be a sizeable non-core contribution at lower frequencies. Extrapolate from L-band, accounting for the expected core contribution to obtain an estimate of the non-core component at 1 GHz.

REFLEX(NVSS) - NLEs

A3695 2MASX J20344470-3549019. BCG associated with a WAT radio source. The archival SED is well sampled and appears to be dominated by the extended emission, hence perform a fit to this to obtain a measure of the non-core component. Higher resolution VLA observations at X, K and Q-band are available in the NRAO Image Archive that allow the core to be isolated. Fitting to the core-only SED derived from these maps returns a relatively steep index ($\alpha \approx 0.7$). However this core is distinctly resolved and hence this can be used to confidently estimate the core component.

A3560 PKS1329-328. This system appears in the optical to perhaps be a merging BCG, with two clear peaks visible. There is a large WAT radio source centred on brighter of the optical peaks. The archival SED is well sampled and dominated by the extended emission and so fit to this to derive the non-core component. In the NRAO Image Archive there are higher resolution images available at X-band (hybrid VLA C/B-array) and C-band (hybrid VLA B/A-array) that allow measures of the core-only flux. These suggest that there is a sub-dominant, inverted spectrum core component. Extrapolate from the fit to these for an estimate of this core component at 10 GHz.

A3528S ESO 443- G 007. The BCG is associated with a large extended WAT radio source. The archival SED appears to be dominated by the extended emission and can therefore be fitted directly for an estimate of the non-core component. Several observa-

tions of this source appear in the NRAO Image Archive, although most do not appear to clearly isolate the core component. Obtain a best estimate of the core component by extracting a core-only region flux measurement at X-band (from a hybrid VLA B/C-array observation) and extrapolate from this for the expected core contribution at 10 GHz.

A3165 PKS0344-291. The BCG appears to be associated with an extended, steep spectrum radio source, the SED of which can be fitted to obtain a measure of the non-core component. The best estimate of the core component is obtained using an X-band VLA map from the NRAO Image Archive that allows the core to be isolated. Measure the core-only flux from this and then extrapolate with α_{flat}=0.2 for an estimate of the core component at 10 GHz.

A2717 ESO 349- G 022. The BCG is associated with a powerful WAT radio source. Supplementing the archival SED with fluxes measured from maps retrieved from the NRAO IMage Archive, the non-core component can be measured by fitting the integrated SED. The highest frequency observation available is at C-band and the core is not isolated. Therefore extrapolate from the peak flux at C-band for an upper limit on the core component.

A2399 2MASX J21573344-0747393. The BCG is associated with a powerful WAT. Retrieving images from the NRAO Image Archive allows the core to be isolated at several frequencies above C-band and so a core-only SED can be produced. Fit this for a measure of the core component and then fit the integrated flux SED at lower frequencies to determine the non-core component at 1 GHz. Note that the non-core has a relatively flat index $\alpha\approx$0.62) but is clearly morphologically differentiated and so the estimate should be robust.

A3490 PKS1142-341. This source has a reasonably steep SED and appears to be marginally resolved at C-band in the NRAO Image Archive. It therefore seems that the SED is dominated by the non-core, and so fit directly for an estimate of this component. The source is undetected by AT20g (Murphy et al., 2010) so showing it not to contain a strong core component to higher frequencies. Extrapolate from this non-detection for an upper limit on the core component.

S753 NGC5419. This is a peculiar source, potentially host to an amorphous or mini-halo radio source. Higher resolution imaging from the NRAO Image Archive with the VLA-A

array (at L-band) and the VLA-B array (at C-band) show the system to have a morphologically distinguished point source associated with the BCG. This is also distinguishable in the imaging from the SUMSS survey (Mauch et al., 2003). The archival images show that there is a low surface brightness, amorphous source of ≈7kpc extent centred on this point source. There is no larger scale extent seen in archival VLA-D images which suggests that this cluster does not host a true, powerful mini-halo on ≈few hundred kpc scales however the lower resolution data does have higher flux than is resolved in the higher resolution images, which may suggest the presence of very large scale extent. Alternatively it could be that the source is confused with other nearby galaxies. Fit the integrated SED for a measure of the non-core and then create a core-only SED from which to estimate the core component. Note that rather than a core to non-core system, an alternative interpretation of this system is that it may be a CSS dominated BCG sat in the centre of a cluster-centric amorphous halo.

A3528N ESO 443- G 004. This is the fainter of the two BCGs (see A3528S above), it is however also associated with a reasonably bright radio source. Excising fluxes that appear to have the two radio source confused, the SED for this source returns a steep index from which the non-core component can be measured. The source is resolved in an X-band image (with the hybrid VLA-C/B array) from the NRAO Image Archive although the core is not clearly isolated and so a robust measurement of this is unavailable. Instead, extrapolate from the peak flux at X-band to get an upper limit on the core component.

A1791 2MASX J13485423-2527242. The BCG is associated with a WAT radio source. The archival SED is dominated by the extended emission and hence can be fitted to obtain a measure of the non-core component. The core cannot be clearly isolated in any of the available imaging from the NRAO Image Archive. A VLA-C array observation at C-band provides the highest available resolution although the core is not isolated. Extrapolate from the peak flux at C-band to put an upper limit on the core component at 10 GHz.

RXJ2043.2-2144 2MASX J20431459-2144343. The BCG is associated with a compact steep spectrum radio source. Fit for a non-core measure and then extrapolate for a limit on the core component.

A3376 2MASX J06020973-3956597. The BCG is associated with a WAT radio source. Fit the extended emission dominated SED for a measure of the non-core component and

then extrapolate from the C-band peak (from NRAO Image Archive) for an upper limit on the core.

A2984 ESO 298- G 017. The BCG is associated with a CSS. Fit the SED for a measure of the non-core component and then extrapolate from the AT20g limit (Murphy et al., 2010) for an upper limit on the core component.

RXJ1332.9-2519 PMN J1332-2519. This is an extended source with clear lobes seen at both NVSS (Condon et al., 1998) and TGSS resolutions. Fit the SED for a measure of the non-core component and then extrapolate from the AT20g limit (Murphy et al., 2010) to put an upper limit on the core component.

RXJ0359.1-0320 PMNJ0359-0320. The BCG is associated with a lobe dominated FRI. Fit the SED for a measure of the non-core and then extrapolate from the AT20g limit (Murphy et al., 2010) for an upper limit on the core.

A3856 2MASX J22183938-3854018. The BCG is matched to a radio source, however this is only detected in NVSS and SUMSS. The source is unresolved at these, although the index is steep enough $\alpha \approx 1.36$) to classify this source as a non-core dominated CSS. Fit the for a measure of the non-core and then extrapolate from the AT20g limit (Murphy et al., 2010) for an upper limit on the core component.

RXJ0137.2-0912 MCG -02-05-020. The BCG is associated with an extended radio source that appears to be dominated by a core relic. This inner relic appears to have been associated with the BCG in most historical observations and hence the flux of this is included as part of our definition for the non-core. Fit the integrated SED for a measure of the non-core. Highest frequency flux available is at C-band (Griffith et al., 1995), however there is no image available. In the snapshot image from the FIRST catalogue (White et al., 1997) the core is clearly isolated. For an estimate of the core component extrapolate from the L-band core-only flux with generous uncertainty.

A2355 PMN J2135+0126. The BCG is associated with a steep spectrum radio source. Fit the archival SED for a non-core measurement. Laurent-Muehleisen et al. (1997) obtain a core only flux measurement at C-band using the VLA-A array. Extrapolate from this measurement to get an estimate fo the core component at 10 GHz.

A499 PMN J0437-2027. This is potentially a head-tail or lobed source, although note that it could be two coincidentally aligned and confused sources. Fit the archival steep SED

to get a non-core estimate. There is a slight spectral flattening at C-band although this is a single dish (Griffith et al., 1994) and non detection at AT20g suggests that there is no strong core component, hence the single dish observation may be partially confused. Extrapolate for an upper limit on the core component.

RBS0540 MCXC J0425.8-0833. The BCG is associated with a small double radio source and was studied by Belsole et al. (2005). Can reasonably claim the SED to be non-core dominated hence fit for a measure of this component. Extrapolate from the peak flux at C-band to get an upper limit on the core. This cluster is also known as RXJ0425.8-0833.

RXJ1301.6-0650 MCXC J1301.6-0650. The BCG is associated with a small, barely resolved double source detected in FIRST. Fit the archival SED for a measure of the non-core. Single dish observations at C-band (Griffith et al., 1995) do not resolve the core and hence the best limit on this component is obtained by extrapolating from the peak of the FIRST emission.

A3027 NVSS J023049-330619. This source is detected only in the NVSS (Condon et al., 1998), SUMSS (Mauch et al., 2003) and TEXAS (Douglas et al., 1996) surveys and would be expected to be below the detection limit of other surveys. Fitting to these three detections only returns an intermediate index of α=0.63. The source is unresolved and undetected in both Parkes (Griffith & Wright, 1993; Griffith et al., 1994, 1995) and AT20g (Murphy et al., 2010) however the detection limits do not restrict the source to being unambiguously core or non-core dominated. Interpolate for a limit on the non-core component and then extrapolate from the AT20g limit for an upper limit on the core component.

A2331 2MASX J20581214-0745346. The BCG is associated with a CSS radio source, with no detections above L-band. Fit the archival SED for a measure of the non-core. The SED appears to flatten out to lower frequencies (e.g VLSS, Cohen et al., 2007), which can be attribuated to being a a low frequency effect rather than evidence of a low peaking core as this source is undetected in both the AT20g (Murphy et al., 2010) and also PMN (equatorial region, Griffith et al., 1994) surveys. Extrapolate from these to obtain an upper limit on the core component. Note that if the SED was better sampled then perhaps this source would be best fit with a dropline model, hence the reported index here may be underestimating true spectral shape.

S617 ESO 565- G 030. This cluster could be argued to be a double BCG system with

the also radio loud ABELL S0617:[GMT93]. However, ESO 565- G 030 appears to be the dominant galaxy and is matched with a steep spectrum radio source. Fit the SED for a measurement of the non-core component and then extrapolate from the AT20g limit (Murphy et al., 2010) for an upper limit on the core.

A3764 6dF J2125455-344352. The BCG is matched to a radio source that appears in both NVSS (Condon et al., 1998) and SUMSS (Mauch et al., 2003) although there appear to be no other radio detections. Nonetheless, inerpolating between these two detections show the source to be steep enough ($\alpha \approx 1.09$) to claim that the system is not core dominated. Use this interpolation therefore to estimate the non-core component and then extrapolate from the non-detections with Parkes (e.g Griffith & Wright, 1993) for an upper limit on the core.

RXJ0340.1-1835 NGC1407. The BCG is associated with a radio source that displays a steep spectrum to C-band (e.g Disney & Wall, 1977). There are no detections at higher raido frequencies so fit the archival SED for a measure of the non-core and then extrapolate from C-band for an upper limit on the core component.

RXJ2034.9-2143 2MASX J20345447-2144019. The BCG is matched to an NVSS source (Condon et al., 1998). The only other cross-matched radio detection is with PMN J2034-2143 (Griffith et al., 1994). Simple interpolation between these two detections would give a shallow ($\alpha \approx 0.27$) index indicative of a core-dominated source, however the source does not appear in the AT20g catalogue (Murphy et al., 2010) as would be expected were this index to be persistent although the source could have a GPS-like spectrum. However, there is another reasonably bright NVSS source within the Parkes resolution limit and hence it is highly likely that these two sources are confused in the 5 GHz map. There is too much doubt therefore to unambiguously claim this to be a core dominated system but likewise not enough data to disprove this, hence only quite high upper limits can be claimed on each component with any degree of certainty.

A2389 2MASX J21541313-0359527. The BCG is matched to a steep spectrum radio source that is unresolved at NVSS resolution (Condon et al., 1998). Fit the SED for a measure of the non-core and then extrapolate from the C-band detection (highest frequency detected at, Griffith et al., 1995) for an upper limit on the core.

RXJ1254.7-1526 2MASX J12544491-1526228. The BCG is matched to a steep spec-

trum, head-tail radio source. The steep index of the archival SED persists down to low frequency (e.g. 74 MHz with VLSS, Cohen et al., 2007). The source is undetected in the PMN surveys (Griffith & Wright, 1993; Griffith et al., 1994, 1995) and AT20g (Murphy et al., 2010) so fit the SED for a measure of the non-core and then extrapolate for an upper limit on the core.

A907 2MASX J09582201-1103500. The BCG is optically matched to a steep spectrum radio source. The archival SED remains steep to low frequency and the source is undertected in AT20g (Murphy et al., 2010) and C-band surveys (e.g. Griffith & Wright, 1993) showing that the spectrum does not flatten to higher frequency. Fit the SED for a measure of the non-core and then extrapolate for an upper limit on the core.

RBS1712 2MASX J21020985-2432011. This is a moderate redshift ($z\approx0.2$) cluster whose BCG is matched to a flat spectrum radio source ($\alpha\approx0.34$), that appears to be core dominated. Fit the archival SED for an estimate of the core component. The best limit on the non-core contribution is obtained by extrapolating from the NVSS (Condon et al., 1998) detection.

RXJ1655.9-0113 2MASX J16555506-0112315. The BCG is radio-loud and matched to an unresolved NVSS source (Condon et al., 1998). There appear to be no archival observations of this source, however it does appear within the (flux corrected) primary beam of C-band (VLA-C array and VLA-B array) observations of another nearby source that are in the NRAO Image Archive. From the higher resolution VLA-B array image it is apparent that the source has a resolved miniature FRI morphology and hence its SED can be expected to be lobe dominated. Fit the archival SED for a measure of the non-core and then extrapolate from the resolved core component for an estimate of the core component.

RXJ1139.4-3327 6dF J1139235-332648. The BCG appears to be associated with an unresolved steep spectrum source. Note however that the centroid of the radio source is slightly off the optical position and hence could perhaps be a background source. Fit the SED for a measurement of the non-core component and then extrapolate from the NVSS detection (Condon et al., 1998) for the best upper limit on the core.

A2384B ESO 600- G 014. The BCG is associated with an NVSS radio source (Condon et al., 1998) although there are no other radio-observations attributed to it in NED. PKS 2149-20 is nearby ($\approx$16') and bright ($\approx$1.7Jy at 1.4 GHz in NVSS). This source is

well sampled in the VLA-archive, however ESO 600- G 014 lies just outside the C-band VLA-D primary beam and so unfortunately these observations cannot be used to constrain the BCG further. Upper limits from non-detections in the major surveys do not restricit the source to be unambiguously steep or shallow and so the conservative approach is to extrapolate using the relevant indices for upper limits on both the core and non-core components.

A3694 2MASX J20344138-3403569. The BCG is matched to a radio source that appears in both the NVSS (Condon et al., 1998) and SUMSS (Mauch et al., 2003) catalogues. There are no other radio detections but the interpolation between these points is steep enough to claim that the source is non-core dominated so take a measurement of this and then extrapolate for an upper limit on the core.

A295 UGC 01525. The BCG is matched to a radio source, although this is detected only at 1.4 GHz in NVSS (Condon et al., 1998) and FIRST (White et al., 1997). The source is unresolved in NVSS but appears to have miniature FRII-like morphology in FIRST. Extrapolate from the NVSS detection for an estimate of the non-core component and then extrapolate from a core-only flux obtained from the FIRST image for an estimate of the core component at 10 GHz..

A1391 LCRS B114712.7-120204. There appears to be a distinct NVSS source (Condon et al., 1998) aligned with the BCG. However, this could potentially be associated with the nearby bright source PMN J1149-1218, particularly if PMN J1149-1218 is a head-tail (or heavily antisymmetric FRII), which would require higher resolution data to determine. If the BCG is radio-loud in its own right then this is not matched to anything other NVSS so the best approach is to extrapolate from the ambiguous NVSS detection to obtains upper limits on both the core and non-core components, using appropriate indices.

A3934 2MASX J22533252-3343057. The BCG is associated with a steep spectrum radio source. Fit the SED for a measure of the non-core component and then extrapolate for an upper limit on the core.

A2401 2MASX J21582246-2006145. The BCG is matched to an unresolved NVSS source (Condon et al., 1998) however no further radio detections are available. The nature of this radio emission is therefore ambiguos so extrapolate from the NVSS flux for limits on both components.

A3570 ESO-LV 3250191. This system has two bright ellipticals, this galaxy appears to be dominant. The source is marginally resolved in NVSS (Condon et al., 1998). The archival SED has a steep spectrum although it is not sampled above L-band. In the NRAO Image Archive there is a map at L-band using the VLA-B array of a nearby source that has ESO-LV 3250191 within the field and shows it to be marginally resolved. This therefore all points towards the SED being non-core dominated. Fit the steep spectrum for a measure of the non-core component and then extrapolate from the resolved core peak at L-band for an estimate of the core component.

A1300 2MASX J11315413-1955391. This is a moderately high redshift cluster ($z \approx 0.3$) with multiple radio-loud constituents. The BCG is matched to NVSS (Condon et al., 1998) and VLSS (Cohen et al., 2007) but there are no other radio detections. INterpolating between these gives a steep index so use this to obtain a measurement of the non-core component (however note that the source is potentially partially confused in VLSS and so this index could be unrepresentatively steep). There are no high radio frequency or high resolution observations available, hence extrapolate from the NVSS detection for an upper limit on the core component.

A3814 2MASX J21490737-3042043. The BCG is matched to a radio source that appears only in the NVSS (Condon et al., 1998) and SUMSS (Mauch et al., 2003) catalogues. Interpolating between these show the source to be steep index and hence most likely dominated by its non-core emission. Obtain a measure for this component and then extrapolate for an upper limit on the core.

A4038 IC 5358. This cluster appears to contain two large ellipticals, of which this one appears to be dominant. Matched to a radio detection in NVSS (Condon et al., 1998) but not otherwise detected in the radio. The source is resolved, thus showing it to not be a core-only system. Extrapolate from the integrated flux for an estimate of the non-core component. The resolution of NVSS is insufficient to isolate the core, so extrapolate from the peak flux for an upper limit on the core component.

RXJ1459.0-0843 2MASX J14590518-0842367. Optical overlay of the NVSS region shows that the BCG is associated with a radio source (although note that this is not associated in NED). There are no other radio detections available and survey limits do not restrict the nature of the emission so can only extrapolate with representative indices to

get upper limit on both the core and non-core components.

S721 ESO 382- G 007. The BCG is associated with a steep spectrum radio source. Fit the SED to get a measure of the non-core component and then extrapolate to place an upper limit on the core.

RXJ1256.9-3119 ESO 443- G 014. The BCG is associated with a steep spectrum radio source. Fit the SED for a measurement of the non-core and then extrapolate from the NVSS detection (the highest frequency that the source is detected at, Condon et al., 1998) for an upper limit on teh core.

A2420 2MASX J22101878-1210141. Optically matched to an NVSS source (Condon et al., 1998) although no other radio detections are available an so the nature of the emission is inconclusive. Extrapolate with representative indices to put upper limits on both the core and non-core components.

RXJ1252.5-3116 2MASX J12523429-3116186. The BCG is associated with a very steep spectrum unresolved (NVSS resolution) radio source. Fit the archival SED for a measurement of the non-core component. There are no detections above L-band and the higher frequency survey limits are not restrictively deep. Extrapolate from the L-band flux (NVSS, Condon et al., 1998) to get an upper limit on the core component.

A3497 2MASX J12000606-3123162. The BCG is associated with a steep spectrum radio source Fit the SED to get a measure of the non-core and then extrapolate to put an upper limit on any active core component.

A3364 2MASX J05473773-3152237. The BCG appears to be associated with a steep spectrum radio source. Fit the archival SED for an estimate of the non-core component and then extrapolate for an upper limit on any core component. Note that the match for this source is tentative and may represent a projection related mis-match.

REFLEX(SUMSS) - LEs

A3526 NGC4696. The BCG is associated with the powerful, extended radio source PKS1246-410. The archival SED is steep spectrum and dominated by the extended emission, hence fit this to obtain a measure of the non-core component. The source was studied

by Taylor et al. (2006b) who used a combination of the VLA-A array and the VLBA to uncover its core properties, hence can fit a separate SED to obtain a measure of the core component only. This cluster is also commonly referred to as the Centaurus cluster.

RXJ1840.6-7709 ESO 045- G 011. The BCG is matched to a powerful, relatively flat spectrum radio source. The source is unresolved at 843 MHz in SUMSS (Mauch et al., 2003) and tagged as a point source in the 8.4 GHz ATCA imaging of the CRATES survey (Healey et al., 2007). There is however a large flux decrement between this and a lower resolution single dish observation (Wright & Otrupcek, 1990) although the source is unresolved at 20 GHz in AT20g (Murphy et al., 2010). The SED is relatively flat $\alpha \approx 0.58$) although the source does not appear to be only a core. Interpolate between the unresolved X-band flux and the AT20g detection for an estimate of the core component and then fit the integrated spectrum, accounting for the expected core contribution for a measure of the non-core.

A3363 2MASX J05451060-4756596/PKS 0543-479. Note that this galaxy lies at $z \approx 0.12$ (VLT redshift, Edge et al.in prep.) whereas NED has it at $z \approx 0.2768$. The BCG appears to be associated with a strong head-tail radio source. However, note that in an optical overlay of the SUMSS imaging of this region (Mauch et al., 2003) the centroid is not exactly aligned and this source may therefore be mis-matched. The index is ambiguous ($\alpha \approx 0.69$), however using a MOST observation Jones & McAdam (1992) claim the source to be marginally resolved at 408 MHz and hence the flux can be attributed to non-core emission. Fit the SED for a measure of the non-core. There is no isolated measure of the core available hence extrapolate for an upper limit on the core component.

A3396 2MASX J06284979-4143373. The BCG is matched to a steep spectrum radio source. Fit the SED for a measure of the non-core and then extrapolate to put an upper limit on the core.

RXJ2151.3-5521 PKS 2148-555. The BCG is associated with a flat spectrum radio-source (see e.g., Healey et al., 2007). The archival SED is somewhat confusing however an overlay of the SUMSS image shows that the reported SUMSS flux for this source is actually the flat-spectrum core of an FRII and that confusion with the lobes accounts for the confused SED. Jones & McAdam (1992) show it to be a double in MOST imaging at 408 MHz. Fit the integrated SED (ensuring inclusion of all source components) for

a measurement of the non-core component. Observed in AT20g at multiple frequencies (Murphy et al., 2010), hence can fit a separate core-only SED to get a measure of the active core component. This cluster is also known as A3816.

RXJ2124.3-7446 2MASX J21240939-7445538. The BCG is matched to a reasonably bright SUMSS source (≈75mJy, Mauch et al., 2003) although there are no other radio detections. Survey limits do not restrict the nature of the emission and hence this is ambiguous so extrapolate with representative indices for limits on both the core and non-core components.

A2871 SARS 016.37936-36.99021. The BCG is matched to a steep spectrum radio source that appears slightly extended in the SUMSS map (Mauch et al., 2003). Fit the for a measure of the non-core component and then extrapolate for an upper limit on the core.

RXJ1317.1-3821 2MASX J13171224-3821544. This is a moderate redshift cluster (z≈0.26) with a fairly weak BCG. Nonetheless, this source is matched to SUMSS (Mauch et al., 2003), NVSS (Condon et al., 1998) and an ATCA observation (Feain et al., 2009) and fitting to these gives a flat spectrum and hence implies that the source is core dominated. Fit the flat component for a core estimate and then extrapolate for an upper limit on the non-core. Note that morphologically, in SUMSS this source appears to look a bit like an FRII although considering the optical overlay the most likely explanation appears to be that this is chance alignment with two background sources.

S540 ESO 306- G 017. The BCG is matched to a SUMSS source (Mauch et al., 2003) although there are no other radio detections and hence the nature of the emission is ambiguous. Extrapolate using appropriate indices to put limits on both the core and non-core components.

S301 IC 1860. The BCG is associated with a steep spectrum radio source. Fit the archival SED for a measure of the non-core component and then extrapolate to put an upper limit on the core.

RXJ0303.7-7752 2XMM J030345.6-775243. The BCG appears to be associated with a SUMSS source (Mauch et al., 2003) although no other radio detections are available. There are a number of other radio sources nearby. Extrapolate using appropriate indices to put upper limits on both the core and non-core components.

REFLEX(SUMSS) - NLEs

S41 ESO 350- G 015. The BCG is not associated with the strong radio source PKS 0023-33 in NED, but overlay of the radio map onto the optical shows them to be associated. This is a powerful, extended steep spectrum source where the archival SED potentially slighly flattens to higher radio frequencies. Fit the SED for an estimate of the non-core component. The source is not detetced in AT20g (Murphy et al., 2010) showing that the spectrum does not flatten out, hence extrapolate from the non-detection to put an upper limit on the core.

A3330 FAIRALL 0790. The BCG is matched to a slightly one-sided radio source in SUMSS (Mauch et al., 2003). The spectral index of the archival SED is on the cusp of being considered steep, which coupled with the observed extent suggests that this source is most likely dominated by its non-core emission. Fit the SED for an estimate of this component and then extrapolate from the AT20g non-detection (Murphy et al., 2010) to put an upper limit on the core.

A3911 AM 2243-525. This cluster appears to contain a merging BCG-pair. There is a SUMSS source (Mauch et al., 2003) matched to this that appears slightly elongated. Note that the centroid of the radio source actually lies between the two optical centres. It could be that this is a double AGN with two radio-loud cores. The archival SED is steep spectrum, which can be fitted to obtain an estimate of the non-core component. Extrapolate for an upper limit on the core component.

S861 2MASX J20184779-5242334. The BCG is associated with an amorphous radio source in SUMSS (Mauch et al., 2003). The SED appears to be steep (associating it with a PMN detection, Griffith & Wright, 1993) which along with the resolved nature of this source shows it to be non-core dominated, hence fit for this then extrapolate from the C-band detection to put an upper limit on the core component.

A3360 2MASX J05401053-4323182. The BCG is associated with a CSS radio source. Fit the SED to obtain an estimate of the non-core component and then extrapolate from the AT20g non-detection to put an upper limit on the core component.

A3728 2MASX J21050350-8243367. This cluster appears to be a double BCG system,

this one of which is matched to a steep spectrum radio source. Fit the SED for an estimate of the non-core component and then extrapolate from the C-band detection (Wright et al., 1994) to place an upper limit on the core component. The partner BCG ([GSB2009] J210456.52-824351.6, z≈0.0974) is undetected in SUMSS (Mauch et al., 2003).

RXJ2143.9-5637 2MASX J21435923-5637206. The BCG is matched to a steep spectrum radio source. This source is classified as a point source at 843 MHz in the SUMSS catalogue (Mauch et al., 2003) but is extended at 408 MHz with the MOST Jones & McAdam (1992). Interpolating between these would then suggest that the SED must flatten towards the higher frequency detection at C-band (5 GHz, Wright et al., 1994). However, visual inspection of the SUMSS imaging overlaid onto the optical image shows the source to actually be extended and that the lobes are classified as distinct source in the SUMSS catalogue. Including these with the central component gives an integrated flux that is consistent with a single steep index source and consistent morphologies at different frequencies. Fit the SED for a measure of the non-core component and then extrapolate from the C-band flux to put an upper limit on the core. This source is also known as APMCC699.

S547 ESO 253- G 027. The BCG is matched to a SUMSS radio source (Mauch et al., 2003). Note that there is a small offset in the centroid between the unresolved radio source and the optical position. However, this is within one resolution element and there appear to be no other potential optical counterparts seen and hence we leave this as a match. The source is undetected elsewhere in the radio, however a non-detection with Parkes (PMN Southern region, Wright et al., 1994) restricts the spectral index to be steeper than $\alpha_{steep}>0.7$ and hence we classify the source as most likely non-core dominated. Extrapolate from the SUMSS detection for an estimate of the non-core component and then extrapolate from the non-detection to put an upper limit on the core.

A4023 2MASX J23401245-8511328. The BCG is matched to a one-sided extended radio source at 843 MHz in the SUMSS catalogue (Mauch et al., 2003). The extent coupled to the source not being detected in the PMN catalogue (Wright et al., 1994) show the source to be steep spectrum and most likely non-core dominated. Extrapolate from the SUMSS detection for an estimate of the non-core component and then extrapolate from the non-detection to place an upper limit on the core.

RXJ2018.4-4102 IC4991. The BCG is associated with an elongated radio source in SUMSS (Mauch et al., 2003). The source was observed by Slee et al. (1994) with the Parkes-Tidbinbilla-Interferometer (PTI). They found no parsec-scale core and gave an upper limit of $<$4mJy on the milli-arcsecond scale structure at 2.3 GHz, with a lower resolution integrated flux for the system of 20mJy at 5 GHz. Interpolate between this 5 GHz flux and the SUMSS detection for an estimate of the non-core component and then extrapolate from the PTI non-detection to place an upper limit on the core component at 10 GHz.

S927 FAIRALL 0095. The optical BCG is mathed to a radio-source in the SUMSS catalogue (Mauch et al., 2003). However, there are no other radio detections available and survey limits at other radio frequencies do not limit the index to be unambiguously core or non-core dominated. Extrapolate therefore with relevant indices to put limits on both the core and non-core components.

S592 2MASX J06384515-5358225. The BCG appears associated with a SUMSS radio source (Mauch et al., 2003). No other radio detections are available and survey limits do not clearly restrict the source to be sufficiently steep or flat spectrum to unambiguously attribute the emission with a core or non-core origin. Therefore, extrapolate from the SUMSS detection with appropriate indices to place a limit on both the core and the non-core components.

RXJ0658.5-5556 2MASX J06583806-5557256. The BCG is matched to the SUMSS radio source SUMSS J065837-555718 (Mauch et al., 2003) although no other radio detections are available to restrict the nature of the emission. Extrapolate with appropriate indices to put upper limits on both the core and non-core components. This source is also known as IES0657 or perhaps more popularly, the 'bullet cluster'.

RXJ0738.1-7506 2MASX J07380644-7506269. The BCG is matched to a potentially marginally resolved SUMSS source (Mauch et al., 2003). Note that the radio centroid is slightly off from the optical centroid but visual inspection of the overlaid images suggests that the sources are associated. There are however no other radio detections and the source is not unambiguously resolved. Extrapolate therefore with appropriate indices to put limits on both the core and non-core components.

RXJ2031.8-4037 SUMSS J203153-403728. This is a reasonably high redshift cluster

(z≈0.34) whose BCG is matched to a SUMSS source (Mauch et al., 2003). There are no other radio observations available that allow the nature of this emission (core or non-core) to be unambiguously defined so extrapolate with appropriate indices to put limits on both the core and non-core components.

A3718 APMBGC 187+014+002. This system appears to contain a central galaxy pair. The redshift of this component (z≈0.13) places it within the cluster. The southern counterpart galaxy has a higher redshift given to it in NED (z≈0.17) and so it is possible that the pair is only associated in projection. The named galaxy appears to be associated with a radio source in SUMSS (Mauch et al., 2003). There are no other radio detections and survey limits do not allow the nature of the emission (core or non-core) to be clearly defined hence extrapolate with appropriate indices to put upper limits on both the core and non-core components. Note that if the galaxies are physically associated then the companion, 2MASX J20555594-5455493, would appear to be dominant and is radio undetected.

S405 FAIRALL 1274. The BCG is matched to an unresolved SUMSS source (Mauch et al., 2003) but has no other radio detections available. Furthermore, survey limits do not allow the nature of this emission to be unambiguosly attributed to either the core or non-core and so extrapolate with appropriate indices to put upper limits on both the core and non-core components.

RXJ2224.4-5515 2MASX J22241856-5514513. The BCG is matched to an unresolved SUMSS source (Mauch et al., 2003). There are no other radio detections and survey limits to not restrict the index to be unambigously steep or flat. Extrapolate with appropriate indices to place upper limits on both the core and non-core components. This source is also known as APMCC772.

RXJ0217.2-5244 APMUKS(BJ) B021530.61-525927.7. This is a reasonably high redshift cluster (z≈0.34) whose BCG position appears tentatively matched to a SUMSS radio source (Mauch et al., 2003). The match is within the resolution of SUMSS but the centroid position is more than the catalogue's given positional accuracy from the optical position. The source could be extended just below the resolution limit but no higher resolution radio data are available to confirm or deny this. We leave this source as an associated match but conservatively extrapolate to place only limits on both the core and non-core components.

RXJ0322.2-5310 IC 1917. There is a faint radio source centred on the BCG as seen by

overlaying the SUMSS map onto an optical image of the region (Mauch et al., 2003). There are no other radio detections and so the nature of this emission cannot be unambiguously attributed to either a core or a non-core. Extrapolate therefore, with appropriate indices, to place upper limits on both the core and non-core components. The source is also known as APMCC391.

A3736 2MASX J21032863-4320360. The BCG is matched to an unresolved SUMSS radio source (Mauch et al., 2003). There are no other radio detections and so the nature or the emission (core or non-core) cannot be clearly identified. Extrapolate using appropriate indices to place upper limits on both the core and non-core components.

S849 2MASX J20090639-5422478. The BCG is matched to a SUMSS radio source (Mauch et al., 2003). No other radio detecions are available to unambiguosly associate this to either core or non-core emission so the best approach is to extrapolate with appropriate indices to put upper limit on both the core and non-core components.

RXJ2254.0-6315 2MASX J22540401-6314509. The BCG is matched to a SUMSS source (Mauch et al., 2003) but there are no other radio detections and available survey limits do not restrict the source to have an unambiguously steep or flat spectral index. The exact nature of the emission cannot therefore be classifed and so we extrapolate with the representative indices to place upper limits on both the core and non-core components. The source is also known as AM2250.

A3158 ESO 156- G 008 NED01. This galaxy is a large elliptical that is matched to a SUMSS source (Mauch et al., 2003). No other radio observation are available to restrict the nature of the emission and so extrapolate with representative indices to put upper limits on both the core and non-core components. Note that there is another large elliptical, ESO 156- G 008 NED02, whose redshift ($z \approx 0.0581$) places it within the cluster. This galaxy appears equally dominant although is radio undetected and so this cluster may contain twin BCGs, only of of which is currently radio-loud.

RXJ2023.4-5535 2MASX J20232088-5535495. The BCG is matched with the radio source SUMSS J202319-553545 (Mauch et al., 2003). No other detections are available and survey limits do not unambiguously restrict the spectral index. Therefore, extrapolate with appropriate indices to put upper limits on both the core and non-core components.

Appendix G

Main Sample+ - SED Decomposition Values

Table G.1: Decompositions for the sources in the Main Sample+. Parameters as for Table C.1.

Cluster	Non-core (1 GHz)	Core (10 GHz)	Steep Index	Flat Index	Flat normalisation	Redshift	Lines?
BCS							
Core and Non-core Values							
Hercules-A	62484 ± 4802	4.9 ± 1.1	1.01 ± 0.06	0.2 ± 0.2	7.8 ± 3.7	0.155	1
A2052	7124 ± 107	302.6 ± 79.3	1.09 ± 0.24	0.14 ± 0.03	420.4 ± 104.3	0.0355	1
A2199	4966 ± 14	20.3 ± 0.5	1.26 ± 0.12	-0.07 ± 0.04	17.3 ± 1.7	0.031	1
A1795	1295 ± 20	26.6 ± 8.5	0.94 ± 0.03	0.51 ± 0.08	86.1 ± 17.4	0.0632	1
A1367	6860 ± 17	111.0 ± 49.0	0.72 ± 0.01	0.35 ± 0.19	250.1 ± 111.4	0.0217	1
A2029	757.1 ± 6.7	2.7 ± 0.1	1.23 ± 0.04	0.2 ± 0.2	4.3 ± 2.5	0.0780	0
A1656	235.9 ± 27.3	7.7 ± 4.7	0.72 ± 0.05	0.46 ± 0.23	7.7 ± 4.7	0.0240	0
Non-core Values with Core Upper Limits							
RXJ0338.7+0958	62.5 ± 0.8	<3.3	1.48 ± 0.01	0.2	5.2	0.0338	1

Continued on Next Page...

Table G.1 – Continued

A2312	125.7 ± 3.4	<17.0	1.39 ± 0.08	0.2	26.9	0.0945	0
A1314	43.8 ± 8.7	<2.4	0.83 ± 0.12	0.2	3.8	0.0336	0
A2147	20.1 ± 6.2	<2.1	0.67 ± 0.07	0.2	3.3	0.0355	0
A2065	19.0 ± 1.4	<1.1	1.0 ± 0.2	0.2	1.7	0.0749	0
eBCS							
Core and Non-core Values							
A923	112.0 ± 5.3	0.5 ± 0.4	0.86 ± 0.02	0.00 ± 0.20	0.5 ± 0.3	0.1168	1
RXJ1844.1+4553	6843.7 ± 14.8	51.2 ± 3.6	0.73 ± 0.03	0.34 ± 0.03	111.6 ± 7.9	0.0917	0
A1446	667.1 ± 18.2	8.9 ± 5.4	1.14 ± 0.02	-0.36 ± 0.43	3.9 ± 2.4	0.1028	0
RXJ2250.0+1137	2335.5 ± 89.0	118.0 ± 56.0	0.53 ± 0.20	0.0 ± 0.2	118 ± 56	0.0262	0
A2149	99.4 ± 9.7	7.0 ± 0.9	0.83 ± 0.05	0.2 ± 0.2	11.0 ± 4.5	0.0655	0
A2152	86.4 ± 3.5	3.3 ± 0.5	1.39 ± 0.21	0.2 ± 0.2	5.2 ± 1.9	0.0441	0
RXJ0004.9+1142	46.1 ± 11.5	16.6 ± 3.4	1.08 ± 0.09	0.36 ± 0.14	37.7 ± 7.6	0.0761	1

Continued on Next Page…

Table G.1 – Continued

Non-core Values with Core Upper Limits							
A2396	729.6 ± 9.3	<41.8	1.08 ± 0.06	0.2	66.2	0.1924	1
A2036	482.0 ± 8.7	<11.0	1.01 ± 0.06	0.2	17.4	0.1159	1
A580	53.2 ± 3.3	<1.3	1.24 ± 0.31	0.2	2.1	0.1113	1
Z1883	36.8 ± 7.9	<3.3	1.52 ± 0.45	0.2	5.2	0.198	1
Z1370	61.5 ± 4.5	<0.3	2.24 ± 0.05	0.2	0.5	0.216	1
Z3959	25.4 ± 6.2	<3.8	1.33 ± 0.09	0.2	6.0	0.3521	1
A853	129.2 ± 9.4	<12.1	1.0 ± 0.2	0.2	25.4	0.1664	1
A278	498.4 ± 9.8	<7.6	0.85 ± 0.09	0.2	12.0	0.0891	0
A2625	146.6 ± 6.8	<40.7	0.85 ± 0.02	0.2	64.5	0.1005	0
A2445	113.6 ± 66.7	<36.3	0.71 ± 0.02	0.2	57.6	0.1700	0
RXJ0027.6+2616	88.0 ± 2.5	<15.5	0.71 ± 0.01	0.2	24.6	0.3668	0
RXJ1652.6+4011	73.6 ± 6.0	<2.9	0.63 ± 0.04	0.2	4.6	0.1475	0
A1291	56.5 ± 5.7	<2.5	1.12 ± 0.04	0.2	4.0	0.0500	0
RXJ1852.1+5711	91.3 ± 3.1	<0.7	1.01 ± 0.02	0.2	1.1	0.1068	0
A1986	58.1 ± 1.5	<15.5	0.97 ± 0.01	0.2	24.6	0.1108	0
A2315	22.8 ± 5.0	<11.1	0.97 ± 0.10	0.2	17.6	0.0931	0

Continued on Next Page...

Table G.1 – Continued

REFLEX - NVSS

Core and Non-core Values

Hydra A	59472.6 ± 55.6	242.8 ± 8.6	0.92 ± 0.01	0.35 ± 0.01	541.0 ± 19.2	0.0549	1
A2597	2648.0 ± 127.0	30.5 ± 5.0	1.12 ± 0.11	0.2 ± 0.2	48.3 ± 28.3	0.0830	1
RXJ0132.6-0804	136.0 ± 14.1	77.7 ± 3.6	1.0 ± 0.2	0.45 ± 0.03	217.8 ± 10.1	0.1489	1
A2415	239.4 ± 9.8	107.2 ± 18.6	1.15 ± 0.02	0.54 ± 0.09	373.8 ± 64.8	0.0573	1
RXJ1347.5-1144	24.4 ± 16.1	17.8 ± 3.0	1.08 ± 0.30	0.33 ± 0.08	38.3 ± 6.4	0.4500	1
RXJ1050.4-1250	46.2 ± 3.1	1.6 ± 0.6	1.0 ± 0.2	0.42 ± 0.19	2.5 ± 0.9	0.0154	1
RXJ1501.1+0141	18.9 ± 2.6	2.2 ± 1.5	1.0 ± 0.2	0.15 ± 0.37	3.2 ± 2.1	0.0066	1
A3695	2039.9 ± 14.8	39.0 ± 3.4	0.83 ± 0.04	0.71 ± 0.03	200.0 ± 17.4	0.0888	0
A3560	1620.7 ± 16.0	5.7 ± 1.3	0.85 ± 0.07	-0.48 ± 0.12	1.9 ± 0.4	0.0480	0
A3528S	1485.1 ± 15.2	2.3 ± 0.1	1.18 ± 0.04	0.2 ± 0.2	3.6 ± 1.8	0.0574	0
A3165	1089.5 ± 12.1	26.5 ± 0.9	0.84 ± 0.01	0.2 ± 0.2	42.0 ± 24.6	0.1423	1

Continued on Next Page…

Table G.1 – Continued

A2399	412.2 ± 15.8	7.6 ± 1.5	0.62 ± 0.02	0.20 ± 0.06	12.1 ± 2.5	0.0567	0
S753	444.4 ± 9.5	13.5 ± 1.2	0.60 ± 0.02	0.71 ± 0.14	68.8 ± 6.1	0.0138	0
RXJ0137.2-0912	300.1 ± 9.0	7.9 ± 3.2	1.78 ± 0.01	0.2 ± 0.2	12.5 ± 7.3	0.0413	0
A2355	260.7 ± 9.3	2.6 ± 0.3	0.80 ± 0.15	0.2 ± 0.2	4.1 ± 2.4	0.1244	0
RXJ1655.9-0113	99.9 ± 4.2	3.0 ± 0.5	1.38 ± 0.20	0.2 ± 0.2	4.8 ± 2.3	0.0408	0
A295	58.4 ± 3.9	2.5 ± 1.0	1.0 ± 0.2	0.2 ± 0.2	4.0 ± 1.9	0.0428	0
A3570	76.9 ± 5.6	2.2 ± 0.7	2.48 ± 0.36	0.2 ± 0.2	3.5 ± 1.7	0.0375	0
Core Values with Non-core Upper Limits							
A1644	<14.8	103.2 ± 9.1	1.0	0.06 ± 0.05	119.5 ± 10.5	0.0475	1
RXJ0445.1-1551	<10.9	65.0 ± 7.6	1.0	0.21 ± 0.08	104.6 ± 12.2	0.0360	1
RXJ1506.4+0136	<7.9	7.1 ± 1.9	1.0	0.06 ± 0.12	8.2 ± 2.2	0.0057	1
RBS1712	<95.8	33.4 ± 3.6	1.0	0.34 ± 0.09	73.6 ± 7.9	0.1899	0
Non-core Values with Core Upper Limits							
A3532	1439.2 ± 15.5	<59.7	0.89 ± 0.04	0.2	94.6	0.0542	1
RXJ1206.2-0848	268.5 ± 8.9	<46	1.23 ± 0.01	0.2	72.9	0.4413	1
RXJ0501.6+0110	162.4 ± 9.6	<15.5	0.69 ± 0.03	0.2	24.6	0.1245	1

Continued on Next Page...

Table G.1 – Continued

A85	74.4 ± 6.1	<2.5	1.05 ± 0.03	0.2	4.0	0.0557	1
A383	52.5 ± 6.7	<5.4	0.74 ± 0.10	0.2	6.5	0.1883	1
A2717	854.2 ± 20.9	<39.2	1.74 ± 0.06	0.2	62.1	0.0498	0
A3490	493.4 ± 9.8	<46	0.97 ± 0.15	0.2	72.9	0.0682	0
A3528N	490.5 ± 14.7	<9.2	0.80 ± 0.01	0.2	14.6	0.0541	0
A1791	401.9 ± 10.2	<8.8	1.22 ± 0.01	0.2	14.0	0.1263	0
RXJ2043.2-2144	448.8 ± 13.7	<46	1.03 ± 0.03	0.2	72.9	0.2041	1
A3376	381.2 ± 10.0	<24.8	1.10 ± 0.11	0.2	24.8	0.0456	0
A2984	289.0 ± 7.2	<46	0.72 ± 0.03	0.2	72.9	0.1050	0
RXJ1332.9-2519	277.1 ± 52.5	<46	0.72 ± 0.02	0.2	72.9	0.1206	0
RXJ0359.1-0320	270.9 ± 10.0	<46	0.92 ± 0.04	0.2	72.9	0.1195	0
A3856	295.9 ± 8.8	<46	1.36 ± 0.12	0.2	72.9	0.1423	0
A499	291.0 ± 8.7	<46	0.81 ± 0.14	0.2	72.9	0.1550	0
RBS0540	119.9 ± 8.0	<8.7	0.71 ± 0.03	0.2	13.8	0.0397	0
RXJ1307.6-0650	176.9 ± 8.2	<15.9	0.82 ± 0.02	0.2	25.1	0.0903	0
A2331	169.7 ± 9.5	<40	0.70 ± 0.03	0.2	63.4	0.0790	0
S617	148.8 ± 9.2	<46	0.72 ± 0.03	0.2	72.9	0.0336	0
A3764	120.4 ± 5.6	<45.9	1.09 ± 0.19	0.2	72.7	0.0739	0

Continued on Next Page...

Table G.1 – Continued

RXJ0340.1-1835	114.1 ± 7.3	<29.3	0.75 ± 0.07	0.2	46.4	0.0059	0
A2389	126.8 ± 7.2	<39.8	0.78 ± 0.06	0.2	63.1	0.1507	0
RXJ1254.7-1526	98.5 ± 2.1	<46	0.91 ± 0.01	0.2	72.9	0.1506	0
A907	133.9 ± 8.1	<46	0.88 ± 0.03	0.2	72.9	0.1620	1
RXJ1139.4-3327	93.1 ± 3.7	<38.9	1.23 ± 0.02	0.2	61.7	0.1095	0
A3694	57.5 ± 4.4	<27.5	0.96 ± 0.35	0.2	43.6	0.0927	0
A3934	49.5 ± 4.3	<23.3	1.19 ± 0.03	0.2	36.9	0.2240	0
A1300	56.6 ± 7.1	<21.3	1.53 ± 0.05	0.2	33.8	0.3077	0
A3814	51.1 ± 4.3	<21.3	1.41 ± 0.39	0.2	33.8	0.1205	0
A4038	38.5 ± 3.0	<18.6	1.0 ± 0.2	0.2	29.5	0.0288	0
S721	35.0 ± 3.0	<18.4	0.74 ± 0.34	0.2	29.2	0.0511	0
RXJ1256.9-3119	35.0 ± 3.0	<15.6	1.08 ± 0.35	0.2	24.7	0.0565	0
RXJ1252.5-3116	29.1 ± 2.3	<12.7	1.51 ± 0.03	0.2	20.1	0.0542	0
A3497	25.8 ± 3.7	<10.7	1.65 ± 0.06	0.2	17.0	0.0683	0
A3364	26.2 ± 2.6	<10.3	1.47 ± 0.42	0.2	16.3	0.1483	0
Upper Limits on both Core and Non-core							
A1663	<52.1	<15.5	1.0	0.2	24.6	0.0847	1

Continued on Next Page...

Table G.1 – Continued

A3698	<45.2	<15.5	1.0	0.2	24.6	0.0195	1
A2402	<45.5	<21.4	1.0	0.2	33.8	0.0806	1
A2566	<38.9	<17.5	1.0	0.2	27.7	0.0825	1
RXJ2147.0-1019	<29.1	<13.1	1.0	0.2	20.7	0.0793	1
S0301	<27.4	<12.3	1.0	0.2	19.5	0.0229	1
A281	<24.4	<11.0	1.0	0.2	17.4	0.1276	1
A3027	<129.0	<46	1.0	0.2	72.9	0.0760	0
RXJ2034.9-2143	<115.4	<46	1.0	0.2	72.9	0.1531	0
A2384B	<78.5	<36.7	1.0	0.2	58.2	0.0956	0
A1391	<48.5	<23.2	1.0	0.2	36.8	0.1555	0
A2401	<47.6	<22.9	1.0	0.2	36.4	0.0578	0
RXJ1459.0-0843	<35.7	<18.4	1.0	0.2	29.2	0.1057	0
A2420	<27.5	<13.3	1.0	0.2	21.1	0.0830	0

REFLEX - SUMSS

Continued on Next Page…

Table G.1 – Continued

Core and Non-core Values							
A3526	5171.1 ± 15.3	66.9 ± 16.1	0.83 ± 0.01	0.50 ± 0.10	212.7 ± 51.0	0.0099	1
RXJ1840.6-7709	1093.5 ± 11.2	213.9 ± 48.7	0.58 ± 0.01	-0.06 ± 0.09	186.3 ± 34.9	0.0182	1
RXJ2151.3-5521	1511.9 ± 20.5	101.7 ± 7.9	0.73 ± 0.11	0.06 ± 0.04	117.1 ± 9.1	0.0388	1
Core Values with Non-core Upper Limits							
RXJ1317.1-3821	<18.5	11.0 ± 1.7	1.0	0.28 ± 0.53	20.9 ± 3.2	0.2567	1
Non-core Values with Core Upper Limits							
A3363	770.6 ± 11.3	<46	0.69 ± 0.01	0.2	72.9	0.1265	1
A3396	467.3 ± 6.5	<46	1.60 ± 0.02	0.2	72.9	0.1784	1
A2871	17.4 ± 2.5	<6.4	1.80 ± 0.70	0.2	10.2	0.1218	1
S301	20.2 ± 3.0	<9.4	0.89 ± 0.56	0.2	14.9	0.0229	1
S41	1811.4 ± 16.3	<46	0.90 ± 0.04	0.2	72.9	0.0498	0
A3330	880.0 ± 12.1	<46	0.69 ± 0.01	0.2	72.9	0.0918	0
A3911	337.5 ± 9.4	<46	1.08 ± 0.04	0.2	72.9	0.0965	0
S861	273.3 ± 14.2	<46	0.69 ± 0.05	0.2	72.9	0.0508	0

Continued on Next Page...

Table G.1 – Continued

A3360	195.4 ± 10.6	<46	0.76 ± 0.06	0.2	72.9	0.0853	0
A3728	127.8 ± 6.8	<22.5	0.99 ± 0.08	0.2	35.7	0.0977	0
RXJ2143.9-5637	246.8 ± 11.4	<33.7	1.18 ± 0.06	0.2	53.4	0.0819	0
S547	120.9 ± 4.3	<46	1.0 ± 0.2	0.2	72	0.0515	0
A4023	120.6 ± 4.1	<46	1.0 ± 0.2	0.2	72.9	0.1941	0
RXJ2018.4-4102	93.3 ± 5.8	<3.0	0.96 ± 0.10	0.2	4.8	0.0188	0
Upper Limits on both Core and Non-core							
RXJ2124.3-7446	<63.4	<45.9	1.0	0.2	72.7	0.0583	1
S540	<16.9	<12.3	1.0	0.2	19.5	0.0358	1
RXJ0303.7-7752	<16.8	<12.1	1.0	0.2	19.2	0.2769	1
S927	<56.1	<40.5	1.0	0.2	64.2	0.0584	0
S592	<45.7	<33.0	1.0	0.2	52.4	0.2236	0
RXJ0658.5-5536	<37.4	<28.0	1.0	0.2	44.4	0.2969	0
RXJ0738.1-7506	<37.1	<27.7	1.0	0.2	43.9	0.1110	0
RXJ2031.8-4037	<34.3	<25.7	1.0	0.2	40.7	0.3396	0
A3718	<26.8	<20.1	1.0	0.2	31.9	0.1332	0
S405	<23.2	<17.4	1.0	0.2	27.6	0.0616	0

Continued on Next Page...

Table G.1 – Continued

RXJ2224.4-5515	<20.8	<15.5	1.0	0.2	24.6	0.0790	0
RXJ0217.2-5244	<19.1	<14.3	1.0	0.2	22.7	0.3410	0
RXJ0322.2-5310	<18.9	<14.1	1.0	0.2	22.3	0.0775	0
A3736	<17.2	<12.9	1.0	0.2	20.4	0.0487	0
S849	<16.5	<12.3	1.0	0.2	19.5	0.0531	0
RXJ2254.0-6315	<15.6	<11.7	1.0	0.2	18.5	0.2114	0
A3158	<14.1	<10.5	1.0	0.2	16.6	0.0577	0
RXJ2023.4-5535	<13.3	<9.9	1.0	0.2	15.7	0.2381	0

Appendix H

Additional Breakdowns for Supplementary OIII Sample

Table H.1: Extra decompositions for the 28 sources which fit the initial selection criteria but for various reasons were not in the Main Sample but do have observations for [OIII]. NGC1275 included twice here to illustrate the huge variation of its core component. The sources from the Main Sample+ for which [OIII] flux measurements were available are: A2495 (*[OIII]* $<0.1 \times 10^{-15}$ *erg* s^{-1} cm^{-2}), A2052 (*5.9*±*0.3*), A2199 (*2.4*±*0.3*), Hercules-A (*5.0*±*0.4*), A1795 (*2.0*±*0.5*), RXJ0132.6-0804 (*4.2*±*0.2*), A2415 (*1.3*±*0.3*), RXJ2043.2-2144 (*0.4*±*0.2*), RXJ1317.1-3821 (*0.25*±*0.1*), A2597 (*3.8*±*0.3*), RXJ0338.7+0958 (*4.4*±*1.6*), A2566 (*0.4*±*0.2*), A3934 (*0.3*±*0.3*), A3698 (*0.42*±*0.2*), RXJ1206.5+2810 (*<0.5*), MACS1532.9+3021 (*1.4*±*0.1*), Z8197 (*0.5*±*0.1*), A1835 (*1.5*±*0.1*), A795 (*0.7*±*0.2*), A1991 (*0.4*±*0.3*), Z2701 (*0.1*±*0.1*), A115 (*0.2*±*0.2*), Z3916 (*0.2*±*0.1*), Z3179 (*0.8*±*0.3*), RXJ0331.1-2100 (*0.45*±*0.1*), A3112 (*6.7*±*0.5*), AS555 (*4.75*±*0.1*), A1668 (*1.7*±*0.2*), A2072 (*0.2*±*0.1*), A2580 (*0.2*±*0.1*), A3378 (*0.45*±*0.2*), RXJ2014.9-2430 (*4.7*±*0.2*), A2734 (*0.34*±*0.2*), RXJ1947.2-7623 (*0.35*±*0.2*), A3992 (*0.05*±*0.05*), AS805 (*0.15*±*0.1*), A3638 (*0.5*±*0.2*), AS384 (*0.4*±*0.2*), Z7160 (*<0.1*), A1930 (*<0.3*), RXJ2129.6+0005 (*<0.2*), Z1121 (*<0.5*), A1084 (*<0.2*), Z808 (*<0.2*), RXJ1720.1+2638 (*0.2*±*0.1*), Z8276 (*1.6*±*0.2*), A2204 (*3.8*±*0.2*), A478 (*0.4*±*0.3*), RXJ1320.1+3308 (*1.2*±*0.3*), A1664 (*1.5*±*0.2*), A2009 (*0.3*±*0.2*), A2390 (*1.0*±*0.2*), A2634 (*1.9*±*0.9*), RXJ0107.4+3227 (*2.1*±*0.5*), A262 (*2.2*±*0.4*), Z8193 (*1.4*±*0.3*), RXJ1750.2+3505 (*0.7*±*0.2*), RXJ0352.9+1941 (*1.4*±*0.2*), RXJ1715.3+5725 (*1.4*±*0.3*), RXJ1733.0+4345 (*0.6*±*0.2*), A291 (*0.3*±*0.1*), RXJ0751.3+5012 (*1.6*±*0.6*), A646 (*0.3*±*0.2*), A1204 (*0.1*±*0.1*), RXJ1442.2+2218 (*0.7*±*0.4*), A1885 (*0.4*±*0.2*), Z235 (*0.4*±*0.2*), A2665 (*0.1*±*0.1*), A1361 (*0.9*±*0.2*), RXJ0439.0+0520 (*1.3*±*0.1*), A4059 (*3.4*±*0.2*), A3017 (*1.95*±*0.1*), A496 (*1.65*±*0.1*), RXJ1504.1-0248 (*7.0*±*0.4*), RXJ1558.4-1410 (*5.35*±*0.4*), A1348 (*2.15*±*0.1*), A11 (*2.5*±*0.1*), A3581 (*1.1*±*0.2*), RXJ0543.4-4430 (*0.3*±*0.2*), RXJ1524.2-3154 (*1.5*±*0.2*), A3880 (*2.0*±*0.3*), RXJ2213.1-2753 (*1.15*±*0.1*), A2667 (*0.25*±*0.1*), A3639 (*1.6*±*0.2*), RXJ1304.3-3031 (*0.425*±*0.2*), RXJ1315.4-1623 (*0.25*±*0.1*), AS851 (*2.2*±*0.2*), A2746 (*0.15*±*0.1*), AS701 (*0.05*±*0.03*), RXJ1539.5-8335 (*0.6*±*0.2*), RXJ1931.6-3354 (*1.0*±*0.2*) and A3605 (*0.15*±*0.1*).

Cluster	Non-core (1 GHz)	Core (10 GHz)	OIII ($\times 10^{-15}$ erg s^{-1} cm^{-2})

Continued on Next Page...

Table H.1 – Continued

M87	263000 ± 50000	951.1 ± 47.5	21.0 ± 3.5
Cygnus-A	2500000 ± 500000	856.3 ± 35.3	100 ± 10
NGC1275	4000 ± 400	16000 ± 1600	200 ± 20
NGC1275	4000 ± 400	6000 ± 600	200 ± 20
3C295	29957 ± 548	4.4 ± 0.1	1.05 ± 0.05
AS463	6870.2 ± 864.5	57.4 ± 1.9	1.3 ± 0.2
RXJ0745.0+3312	289.9 ± 8.0	<39.0	1.65 ± 0.1
RXJ1000.5+4409	6.4 ± 1.6	<2.7	<0.1
A2270	<31.6	140.2 ± 44.2	1.06 ± 0.03
A2292	<94.1	34.9 ± 4.1	0.2 ± 0.2
RXJ1350.3+0940	<10.0	264.6 ± 44.9	4.5 ± 0.3
RXJ1938.3-4748	<8.2	<6.1	0.06 ± 0.04
A3866	<9.9	<3.6	0.05 ± 0.03
AS1020	<5.1	<3.8	0.04 ± 0.03
A3574W	<13.2	<5.9	0.08 ± 0.06
A368	<7.6	<3.6	0.07 ± 0.03

Appendix I

Variability Sub-sample - Data Tables for High Radio Frequency Observations

Table I.1: GISMO (150 GHz) fluxes of the observed clusters. Where a position is given for a GISMO limit then it is the targeted position, otherwise the given positions are the GISMO peak position.

Cluster	Obs. Date	RA	DEC	Tau	Exposure (min)	CRUSH Option	Flux (mJy)	FWHM (“)	Peak (mJy)	Map RMS
Epoch 1 : April 2012										
Z235	20/04/12	00:43:52.30	24:24:24.5	0.32	10	-faint	4.7 ± 1.2	18.0	4.4	0.9
RXJ0132-08	20/04/12	01:32:41.16	-08:04:07.6	0.17	7	-faint	28.8 ± 4.7	17.7	30.9	1.1
MACS0242-21	21/04/12	02:42:36.11	-21:32:27.3	0.20	2	-faint	35.6 ± 6.0	18.1	37.5	1.8
A496	21/04/12	04:33:37.82	-13:15:46.5	0.23	10	-faint	6.1 ± 1.3	16.4	5.9	0.9
RXJ0439+05	18/04/12	04:39:02.32	05:20:37.0	0.35	5	-faint	56.0 ± 9.2	16.4	56.5	2.1
PKS0745-191	18/04/12	07:47:31.34	-19:17:42.7	0.19	25	-faint	4.9 ± 1.1	21.9	4.7	0.8
A646	17/04/12	08:22:08.86	47:05:54.1	0.49	20	-faint	11.5 ± 2.1	13.4	10.9	1.0
4C+55.16	17/04/12	08:34:55.21	55:34:20.6	0.10	2	-faint	81.7 ± 13.2	15.6	79.4	1.7
Hydra-A	17/04/12	09:18:05.84	-12:05:41.1	0.14	4	-faint	266.7 ± 42.7[1]	24.8	179.9	2.3
A1348	18/04/12	11:41:24.26	-12:16:37.7	0.15	2	-faint	<6.3	-	-	2.1
RXJ1347-11	21/04/12	13:47:31.84	-11:45:10.9	0.20	20	-deep	<3.3	-	-	1.1

[1]Resolved source, integrated flux

Table I.1 – Continued

RXJ1350+09	11/04/12	13:50:22.01	09:40:16.9	0.10	10	-faint	16.0 ± 2.8	12.7	14.9	1.1
A3581	21/04/12	14:07:30.19	-27:01:08.6	0.18	2	-faint	71.0 ± 11.6	16.4	72.4	2.1
AS780	18/04/12	14:59:29.98	-18:10:47.8	0.10	5	-faint	17.0 ± 3.2	16.1	16.0	1.6
A2052	11/04/12	15:16:44.50	07:01:16.8	0.10	30	-faint	41.7 ± 6.7	17.3	42.5	0.7
A2055	22/04/12	15:18:46.13	06:13:49.3	0.26	5	-faint	13.2 ± 2.5	17.2	12.9	1.3
RXJ1558-14	18/04/12	15:58:22.19	-14:10:02.7	0.10	5	-faint	39.2 ± 6.4	14.4	38.4	1.5
Z8193	18/04/12	17:17:19.06	42:26:59.2	0.13	2	-faint	12.8 ± 3.1	10.5	13.8	2.7
A2270	18/04/12	17:27:23.71	55:10:52.3	0.11	2	-faint	70.8 ± 4.1	14.9	70.0	2.4
Z8276	23/04/12	17:44:14.88	32:59:30.8	0.29	5	-faint	35.1 ± 5.8	17.4	36.8	1.3
E1821+644	18/04/12	18:21:57.49	64:20:35.6	0.13	10	-faint	5.8 ± 2.8	13.3	5.4	1.4
RXJ1832+68	18/04/12	18:32:35.80	68:48:06.3	0.12	10	-faint	10.0 ± 2.3	11.5	9.3	1.7
MACS1931-26	21/04/12	19:31:49.74	-26:34:33.2	0.12	20	-faint	7.2 ± 2.1	18.9	7.6	0.9
A2390	22/04/12	21:53:36.74	17:41:40.2	0.09	10	-faint	8.1 ± 1.6	13.3	7.7	0.9
A2415	18/04/12	22:05:38.62	-05:35:35.1	0.12	5	-faint	31.2 ± 5.3	19.1	33.0	1.9
A2597	18/04/12	23:25:19.93	-12:07:26.8	0.11	5	-faint	15.0 ± 2.8	16.3	15.2	1.4
A2627	20/04/12	23:36:42.29	23:55:31.4	0.40	5	-faint	16.8 ± 3.0	17.9	16.8	1.3
RXJ2341+00	18/04/12	23:41:07.10	00:18:30.9	0.10	5	-faint	41.8 ± 6.9	16.1	42.2	1.5

Table I.1 – Continued

Epoch 2 : November 2012

RXJ0352+19	31/10/12	03:52:58.97	19:40:59.6	0.13	10	-deep	<3.6	-	-	1.2
RXJ0439+05	31/10/12	04:39:02.11	05:20:42.9	0.15	5	-faint	52.0 ± 8.5	16.6	52.5	1.6
PKS0745-191	31/10/12	07:47:31.30	-19:17:45.9	0.13	5	-faint	5.8 ± 1.8	17.8	5.3	1.5
A646	31/10/12	08:22:10.05	47:05:54.9	0.10	6	-faint	11.4 ± 2.1	18.4	12.0	1.0
4C+55.16	31/10/12	08:34:55.26	55:34:22.9	0.13	5	-faint	77.8 ± 12.5	18.0	80.1	1.4
Hydra-A	31/10/12	09:18:05.83	-12:05:46.5	0.11	5	-faint	273.8 ± 43.8[3]	24.5	167.8	1.8
A1084	31/10/12	10:44:33.11	-07:04:11.1	0.11	10	-faint	4.5 ± 1.2	19.0	4.1	1.0
A1348	31/10/12	11:41:24.37	-12:16:40.0	0.11	5	-faint	6.9 ± 1.7	10.7	6.5	1.3
A1774	31/10/12	13:41:05.19	39:59:47.1	0.15	10	-faint	6.9 ± 1.5	19.7	6.9	1.0
RXJ1347-11	31/10/12	13:47:31.84	-11:45:10.9	0.12	10	-deep	<3.0	-	-	1.0
A1795	31/10/12	13:48:52.25	26:35:32.2	0.19	10	-faint	5.1 ± 1.4	17.7	5.4	1.1
RXJ1350+09	31/10/12	13:50:22.04	09:40:07.9	0.19	10	-faint	16.0 ± 2.7	17.0	15.7	1.0
A3581	31/10/12	14:07:30.00	-27:01:07.8	0.12	5	-faint	62.1 ± 10.1	19.0	63.2	2.0
A1885	31/10/12	14:13:43.86	43:39:40.0	0.10	10	-deep	4.0 ± 1.0	12.4	4.2	0.8
AS780	31/10/12	14:59:29.14	-18:10:51.3	0.11	10	-faint	15.4 ± 2.7	17.9	15.3	1.2

Table I.1 – Continued

A2052	31/10/12	15:16:44.64	07:01:16.3	0.11	5	-faint	38.0 ± 6.3	16.3	38.4	1.7
A2055	02/11/12	15:18:46.19	06:13:56.5	0.50	10	-faint	10.4 ± 2.5	18.9	10.2	1.8
RXJ1558-14	31/10/12	15:58:22.22	-14:10:03.1	0.11	5	-faint	27.8 ± 4.8	15.1	27.6	1.9
NGC6338	31/10/12	17:15:23.25	57:24:41.5	0.12	10	-faint	7.3 ± 1.5	11.0	6.8	1.0
Z8193	31/10/12	17:17:19.11	42:26:59.2	0.11	10	-faint	15.6 ± 2.8	15.9	15.0	1.2
A2270	31/10/12	17:27:23.52	55:10:52.5	0.11	5	-faint	56.2 ± 9.1	18.0	58.3	1.3
Z8276	02/11/12	17:44:14.82	32:59:27.4	0.53	10	-faint	12.5 ± 2.7	16.1	13.2	1.8
E1821+644	31/10/12	18:21:57.00	64:20:32.9	0.11	10	-faint	7.9 ± 1.7	11.3	7.8	1.2
RXJ1832+68	31/10/12	18:32:35.08	68:48:02.2	0.12	7	-faint	8.9 ± 1.7	17.2	9.0	1.0
Epoch 3 : April 2013										
RXJ0132-08	11/04/13	01:32:41.05	-08:04:07.8	0.83	5	-faint	27.6 ± 13.7	17.4	24.0	13.0
M0242-21	11/04/13	02:42:35.99	-21:32:24.9	0.70	10	default	17.9 ± 6.6	15.4	22.9	6.0
A496	10/04/13	04:33:37.75	-13:15:40.7	0.57	20	-faint	4.4 ± 1.1	13.1	4.3	0.8
RXJ0439+05	10/04/13	04:39:02.31	05:20:42.7	0.69	5	-faint	47.6 ± 7.8	17.4	48.6	1.6
A646	10/04/13	08:22:09.50	47:05:53.4	0.59	10	-faint	12.2 ± 2.3	10.7	11.4	1.3
4C+55.16	10/04/13	08:34:54.79	55:34:19.8	0.63	5	-faint	61.7 ± 10.0	16.9	62.7	1.8

Table I.1 – Continued

Hydra-A	10/04/13	09:18:05.79	-12:05:39.6	0.61	5	-extended	201.9 ± 32.9[3]	25.0	153.5	6.2
RXJ1504-02	11/04/13	15:04:07.43	-02:48:15.8	0.59	10	-faint	5.5 ± 1.4	11.2	5.1	1.1
A2052	11/04/13	15:16:44.48	07:01:18.9	0.58	5	-faint	35.0 ± 5.8	17.0	36.6	1.6
RXJ1558-14	11/04/13	15:58:22.01	-14:09:58.2	0.63	5	-faint	25.1 ± 4.3	14.9	23.8	1.6
A2270	11/04/13	17:27:23.58	55:10:52.8	0.64	5	-faint	50.4 ± 8.2	14.5	51.2	1.7
Z8276	11/04/13	17:44:14.47	32:59:29.4	0.68	5	default	<44.7	-	-	14.9
A2390	11/04/13	21:53:36.96	17:41:40.4	0.65	10	-faint	8.6 ± 2.0	14.1	8.6	1.4
A2415	11/04/13	22:05:38.64	-05:35:31.7	0.65	5	-faint	26.7 ± 4.7	16.3	25.8	1.9
A2627	11/04/13	23:36:41.84	23:55:28.2	0.66	10	-faint	16.9 ± 3.0	14.9	15.9	1.3
RXJ2341+00	15/04/13	23:41:07.01	00:18:33.0	0.39	5	-faint	33.0 ± 2.9	15.2	32.5	1.8

Table I.2: AMI (16 GHz) fluxes of the observed BCGs.

Cluster	Obs. Date	Flux	RMS	Obs. Date	Flux	RMS	Obs. Date	Flux	RMS
Z235	11/04/12	17.7 ± 0.9	0.2	04/06/12	16.7 ± 0.9	0.3	-	-	-
RXJ0132-08	17/04/12	139.5 ± 8.3	4.5	02/06/12	126.1 ± 6.9	2.7	-	-	-
RXJ0439+05	12/04/12	324.8 ± 16.3	1.6	30/05/12	307.5 ± 15.5	2.1	29/09/12	299.9 ± 15.1	2.0
A646	10/04/12	45.6 ± 2.3	0.5	30/05/12	45.7 ± 2.7	1.4	27/09/12	47.3 ± 2.5	0.7
4C+55.16	14/04/12	1317.7 ± 66.0	3.5	30/05/12	1372.3 ± 70.6	16.8	-	-	-
RXJ1350+09	24/04/12	133.7 ± 6.7	0.9	14/06/12	107.4 ± 5.6	1.5	-	-	-
A2052	24/04/12	231.8 ± 11.8	2.2	14/06/12	220.8 ± 11.2	1.9	-	-	-
A2055	24/04/12	66.7 ± 3.5	1.2	14/06/12	68.6 ± 3.6	1.2	-	-	-
Z8193	24/04/12	79.8 ± 4.1	1.1	26/06/12	79.3 ± 4.1	1.2	-	-	-
A2270	24/04/12	185.0 ± 9.4	1.6	26/06/12	253.8 ± 12.8	1.4	26/09/12	226.9 ± 11.6	2.6
Z8276	14/04/12	88.6 ± 4.5	0.7	31/05/12	95.9 ± 4.9	0.8	26/09/12	87.6 ± 4.6	1.3
E1821+644	25/04/12	9.0 ± 0.5	0.2	30/06/12	10.8 ± 0.8	0.2	-	-	-
RXJ1832+68	19/05/11	45.6 ± 2.3	0.4	25/04/12	42.2 ± 2.1	0.1	05/07/12	42.3 ± 2.1	0.3
A2390	14/04/12	68.5 ± 12.4	0.8	31/05/12	66.4 ± 3.4	0.9	-	-	-
A2415	11/04/12	77.4 ± 4.2	1.7	02/06/12	77.2 ± 4.5	2.3	-	-	-
A2627	14/04/12	83.1 ± 4.2	0.7	31/05/12	73.3 ± 4.0	1.5	-	-	-
RXJ2341+00	11/04/12	147.0 ± 7.4	1.2	31/05/12	140.9 ± 7.2	1.5	28/09/12	209.2 ± 11.8	5.4

Table I.3: CARMA (90 GHz) fluxes of the observed BCGs.

Cluster	Obs. Date	RA	DEC	Flux	RMS
Z235	11/06/12	00:43:52.21	24:24:21.5	9.9 ± 1.8	4.5
RXJ0132-08	21/05/12	01:32:41.11	-08:04:05.7	98.8 ± 11.9	6.7
MACS0429-02	15/06/12	04:29:36.00	-02:53:07.0	<14.1	4.7
A496	15/06/12	04:33:37.89	-13:15:42.3	11.4 ± 3.6	3.4
RXJ1350+09	21/05/12	13:50:22.12	09:40:10.7	22.8 ± 2.8	1.7
A3581	21/05/12	14:07:29.83	-27:01:04.2	82.5 ± 9.1	2.8
AS780	21/05/12	14:59:28.78	-18:10:44.9	29.5 ± 4.4	2.3
A2052	21/05/12	15:16:44.58	07:01:18.1	126.7 ± 14.3	9.1
A2055	21/05/12	15:18:46.45	06:13:57.9	53.6 ± 9.0	21.6
RXJ1504-02	21/05/12	15:04:07.50	-02:48:16.9	8.3 ± 1.6	1.4
RXJ1558-14	21/05/12	15:58:21.91	-14:09:58.9	44.8 ± 4.9	6.3
Z8193	22/05/12	17:17:19.21	42:26:57.8	22.4 ± 2.9	1.8
A2270	22/05/12	17:27:23.49	55:10:53.9	164.7 ± 17.2	14.4
Z8276	22/05/12	17:44:14.47	32:59:27.4	35.4 ± 6.0	4.9
E1821+644	24/05/12	18:21:56.24	64:20:58.0	7.2 ± 1.8	1.7
RXJ1832+68	22/05/12	18:32:35.52	68:48:07.2	19.6 ± 4.0	3.5
MACS1931-26	11/06/12	19:31:49.64	-26:34:32.4	9.6 ± 2.9	2.7
A2390	04/06/12	21:53:36.81	17:41:44.8	22.3 ± 3.2	2.3
A2415	04/06/12	22:05:38.53	-05:35:33.7	25.7 ± 3.4	2.3
A2597	21/05/12	23:25:19.82	-12:07:28.6	19.7 ± 5.8	2.0
A2627	04/06/12	23:36:42.82	23:55:23.8	19.8 ± 4.5	4.0
RXJ2341+00	21/05/12	23:41:06.94	00:18:33.3	72.8 ± 8.0	3.2

Table I.4: SCUBA-2 (353 GHz) fluxes of the observed BCGs. Note: these data were not reduced by the author, all credit lies with Dr. James Geach and the data are included here only for completeness.

Cluster	Observation Date	Flux (mJy)	RMS
RXJ0132-08	23/10/12	-	13.1
MACS0242-21	01/10/12	34.0	7.6
RXJ0439+05	01/10/12	18.7	5.2
A646	27/02/12	25.9	6.6
4C+55.16	27/02/12	29.0	6.5
Hydra-A	08/10/12	76.3	8.8
A1348	27/12/12	-	7.9
RXJ1347-11	29/12/12	-	5.5
A1795	27/12/12	-	7.4
RXJ1350+09	23/02/12	-	5.7
A3581	28/01/13	59.2	9.1
AS780	15/04/12	-	5.0
RXJ1504-02	12/01/13	13.7	4.0
A2052	28/01/13	-	7.8
RXJ1558-14	15/04/12	40.3	4.7
Z8193	14/05/12	-	8.5
A2270	30/09/12	34.9	4.7
Z8276	30/09/12	27.7	5.0
RXJ1832+68	05/09/12	-	5.8
MACS1931-26	16/09/12	16.8	4.8
A2390	24/04/13	-	4.9
A2415	01/10/12	18.2	6.7
A2597	24/10/12	-	7.2
A2627	24/10/12	20.1	7.3
RXJ2341+00	31/08/12	33.2	3.9

Appendix J

High Frequency Variability Sample - Comments on Individual Sources

Individual source SEDs were populated using the main radio catalogues (e.g. Australia Telescope 20 GHz Survey (AT20G), Murphy et al. 2010; NVSS and Faint Images of the Radio Sky at Twenty-cm (FIRST) at 1.4 GHz, Condon et al. 1998; White et al. 1997; SUMSS at 843 MHz, Mauch et al. 2003; Texas Survey of Radio Sources (TEXAS) at 365 MHz, Douglas et al. 1996; Westerbork Northern Sky Survey (WENSS) and Westerbork In the Southern Hemisphere (WISH) at 325 MHz, Rengelink et al. 1997; De Breuck et al. 2002; VLA Low-Frequency Sky Survey (VLSS) at 74 MHz, Cohen et al. 2007), the NASA/IPAC Extragalactic Database (NED) and the High Energy Astrophysics Science Archive Research Center (HEASARC) database, the National Radio Astronomy Archive (NRAO), literature searches, the data presented within this thesis.

Due to the lack of self-similarity between these spectra each source was fit on an individual basis. Where possible, active components were isolated and fit using the GPS model of (Orienti & Dallacasa, 2014, :)

$$Log(S) = A_0 + Log(\nu)(A_1 + A_2 Log(\nu)) \tag{10.0.1}$$

Steep spectrum components and active flat spectrum components where no peak was

apparent were both fit using a simple power-law of the form:

$$S = A_0 \nu^{-\alpha} \tag{10.0.2}$$

Where both an active and inactive component were found to be present, the core contribution is removed from the total emission prior to fitting the more extended emission. In a couple of cases clear spectral curvature attributable to synchrotron ageing is present in the steeper spectrum components and is modelled as described in the notes below. Additionally, flattening of a steep spectrum component to low frequencies (below 100 MHz) is seen in a minority of sources. Where morphologically it is clear that this is extended emission, and hence the flattening, is most likely due to free-free absorption then these data are excised from the fits as described below.

4C+55.16

2MFGC 06756, z=0.2411. This is a powerful radio source that is clearly extended on milliarcsecond scales as observed using VLBI (see Chapter 5, Helmboldt et al. 2007). The SED has a flat index in the GHz range that appears to be caused by the superposition of a broad peaked GPS-like component with a steep spectrum power-law component to lower frequency (below about 100 MHz). The SED is fit using a GPS-like model with parameters 3.90$\pm$0.03, -0.04$\pm$0.02 and -0.43$\pm$0.01 and a steep power-law to lower frequency with α=1.1$\pm$0.1 and A=500.0$\pm$10.0.

A1084

2MASX J10443287-0704074, z=0.1326. The SED is sparsely sampled, although the non-detection in VLSS (Cohen et al., 2007) coupled to its flat returned index shows the source to be core-dominated. The SED is fit with a power-law of α=0.36$\pm$0.04 and A=36.7$\pm$2.9.

A1348

LCRS B113851.7-115959, z= 0.1195. The source is best fit using a GPS-like model, with parameters 1.96$\pm$0.20, 0.62$\pm$0.41 and -0.53$\pm$0.20 and then a steeper spectrum component that becomes apparent below 1 GHz that is fit using a power-law with α=1.05$\pm$0.07 and A=80.2$\pm$1.5.

A1774

2MASX J13410515+3959456, z=0.1715. The SED of this source is consistent with a single power-law fit with parameters of α=0.61$\pm$0.03 and A=104.9$\pm$5.0, that persists to high frequency. Note that the FIRST (White et al., 1997) datum-point was removed from this fit as it appears to have resolved out some emission. The source appears one-sided in FIRST but the core is not isolated and the lack of higher-resolution data therefore means that a separate core component cannot be fit. The intermediate spectral index combined with the resolved morphology suggests that an active core is likely to be present in this system, which may be distinguishable with higher resolution observations.

A1795

CGCG 162-010, z=0.0632. Extended source with several observations of high enough resolution to create a separate SED for the isolated core only (see Laurent-Muehleisen et al., 1997; Lin et al., 2009; Liuzzo et al., 2009). This core spectrum is flat to high frequency, and fit using a power-law with α=0.65$\pm$0.06 and A=120.2$\pm$14.2. The SED of the more extended emission appears to exhibit spectral curvature to high frequency, hence to account for this we allow an exponential rollover to the steep power-law, of the form:

$$S = A_0 \nu^{-\alpha}(1 - A_1 e^{-\frac{\nu_0}{\nu}}) \tag{10.0.3}$$

(also see Chapter 3). The best fit returns parameters 1262.8, 0.86, 1.07 and 7.51 for the four unknowns in this model respectively.

A1885

2MASX J14134379+4339450, z=0.090. The SED is core dominated with a hint of variability seen from historical C-band observations (Laurent-Muehleisen et al., 1997; Gregory & Condon, 1991). Additionally, the WENSS (Rengelink et al., 1997) detection alongside the VLSS (Cohen et al., 2007) non-detection shows that the spectrum must peak in the GHz range. The SED can be fit with a GPS model, returning parameters of 1.66$\pm$0.03, 0.24$\pm$0.04 and -0.33$\pm$0.03.

A2052

UGC 09799/3C 317, z=0.0355. A seperate core only SED can be created for the resolved isolated core. This can be fit with a GPS model (returning parameters; 2.54$\pm$0.02, 0.10$\pm$0.02 and -0.24$\pm$0.01). Accounting for this core contribution, fit a power-law (with

α=1.20$\pm$0.08 and A=6404.5$\pm$1142.8) to the lower frequency emission. Note that there are a number of very low frequency (less than 50 MHz) data-points that are flatter than this steep spectrum would imply. These are possibly affected by free-free absorption and hence were excised from the power-law fit.

A2055

2MASX J15184574+0613554, z=0.1019. High resolution data reveals an underlying core component with a GPS-like spectrum. Note that the CARMA datum is tagged as potentially unreliable and indeed appears inconsistent and has therefore been excluded from the fit. A GPS fit to the core-only SED returns parameters of 1.28$\pm$0.04, 1.13$\pm$0.02 and -0.57$\pm$0.01. The integrated SED is increasingly dominated by a power-law component at frequencies less than 1 GHz. Fit this separately, accounting for the expected core contribution, to recover a power-law fit with α=0.70$\pm$0.04 and A=519.2$\pm$122.7.

A2270

2MASX J17272346+5510538, z=0.2473. Source appears highly variable. There is a limit only in the VLSS-redux catalogue (Lane et al., 2014) but an overlay of the map shows there to be a 3σ map detection at the optical position of the BCG. Along with other low frequency detections from 7C (Hales et al., 2007) and WENSS (Rengelink et al., 1997), this hints at there being a low-powered low frequency power-law component within this source. The data are widely spaced in observation date, making separate fits by epoch for the GPS component unfeasible. Fitting a GPS to fit to all the available data at higher frequencies than L-band, recovers an average GPS with parameters 2.11$\pm$0.06, 0.56$\pm$0.06 and -0.31$\pm$0.04. Account for the contribution of this to the lower frequency data and find a resultant power-law component with α=0.94$\pm$0.07 and A=28.0$\pm$0.7

A2390

ABELL 2390:[YEA96] 101084, z=0.2328. The spectrum appears to have a split power-law like shape below 10 GHz although the higher frequency observations show that the active component curves. Hence the SED is best fit using a combination of a GPS component (that returns parameters; 2.28$\pm$0.03, 0.26$\pm$0.04 and -0.42$\pm$0.05) and then a power-law component with α=1.34$\pm$0.25 and A=121.5$\pm$60.6. A SCUBA detection at 330 GHz (Smail et al., 2002) suggests that there may be additional intermittent activity at these higher frequencies or alternatively there may be a dust component coming in (although

non-detection at 660 GHz suggests against this).

A2415

2MASX J22053865-0535330, z=0.0573. The SED has a flat index from around 1 GHz up to high frequency although a subtle drop-off means that this is best fit with a broad-peaked GPS model (returned parameters: 2.09$\pm$0.08, 0.26$\pm$0.02 and -0.29$\pm$0.01) in addition to a steep power-law component at lower frequencies with α=1.31$\pm$0.02 and A=193.2$\pm$9.4.

A2597

PKS 2322-12, z=0.0830. Source appears very flat to higher frequencies. Archival VLA observations at C, X and U-bands from the NRAO Image Archive allow isolated core measurements which in conjunction with higher frequency data suggest a broad GPS-like core that is well fit with parameters 1.92$\pm$0.05, 0.27$\pm$0.09 and -0.30$\pm$0.04, although there may be further flattening to yet higher frequencies as suggested by SCUBA observations (Zemcov et al., 2007; Knudsen et al., 2008). Lower frequency data are fit with a power-law of α=1.18$\pm$0.06 and A=2336.4$\pm$13.4, where the data below 100 MHz have been excluded as here the spectrum flattens, possibly due to free-free affected. Note that a simple extrapolation of this power-law in conjunction with the GPS core gives a wholly inaccurate integrated spectrum and hence the older, extended component must roll-off at some frequency. This has been simulated here by subtracting the GPS from the simple power-law to give the presented curved spectrum.

A2627

This cluster has two bright galaxies in close proximity, both of which are radio-sources. The more dominant source - A2627(a) / B2 2334+23 ‘the BCG’ - is at position 23:36:42.12 23:55:29.0 and z=0.126. The other galaxy - A2627(b) / 2MASX J23364245+2354442 is at position 23:36:42.47 23:54:44.6 and has a redshift given in NED as z=0.122. VLA C-band data (Chapter 3) separates the sources and overlaying other maps onto this we see that at NVSS (1.4 GHz, Condon et al., 1998) and lower frequencies the sources are confused. They are similarly confused in our AMI maps. The BCG can be isolated in the CARMA map and a VLA-A array image from the NRAO Image Archive. These show it to be flat spectum. Along with the GISMO data, fit a flat spectrum power-law to this (α=0.37$\pm$0.06 and A=109.0$\pm$22.9). Morphologically, A2627(a) is core dominated although it does show some wispy emission that is likely to contribute at lower frequen-

cies. A2627(b) is fainter (by roughly a factor of 4 at C-band) but appears to be steep spectrum and is likely to become increasingly dominant at lower frequency. Fit the integrated emission (accounting for the flat component) with a power-law of α=0.65$\pm$0.06 and A=499.8$\pm$6.4 noting that this is highly confused. We currently do not have suffiient coverage to fully deblend the sources.

A3581

IC 4374, z=0.0218. Flat spectrum core dominated system with hints of variation in repeat observations around C- and X-bands. Unresolved at VLA-A in a map from the NRAO Image Archive but the source is resolved on milli-arcsecond scales with the VLBA (Chapter 5). This small-scale resolved emission is linked to ongoing activity and the integrated recovered with the VLBA is consistent with lower resolution fluxes showing that source is core-only. Fit a power-law to the integrated SED (returning a fit of α=0.49$\pm$0.04 and A=758.2$\pm$6.9) and then highlight the VLBA peaks on the SED.

A496

MCG -02-12-039, z=0.0328. This source has a GPS-like core with a steeper power-law component to low frequency. The core is fit with the GPS-like model with parameters 1.45$\pm$0.02, 0.60$\pm$0.02 and -0.43$\pm$0.03 and then accounting for this component, the remaining extended emission is fit with a power-law of α=1.71$\pm$0.03 and A=99.8$\pm$6.4.

A646

2MASX J08220955+4705529, z=0.1268. The SED of this source can be fit using a GPS model for the core component, which returns parameters 1.89$\pm$0.02, 0.14$\pm$0.01 and -0.25$\pm$0.08 and a power-law component of α=1.54$\pm$0.09 and A=13.5$\pm$0.3 to account for the lower frequency, extended emission. Note that the combination of these two components at 1.4 GHz over-estimates the NVSS flux (Condon et al., 1998) which may be attributable either to variation of the core component or perhaps indicating that this source should in reality have a more sharply peaked profile.

AS780

2MASX J14592875-1810453, z=0.2344. This source has previously identified as a flat spectrum source (e.g. Healey et al., 2007). This GHz range flat spectrum falls off above about 20 GHz. The source is undetected in VLSS (Cohen et al., 2007) and WISH (De Breuck et al., 2002), which suggests that the spectrum must turnover around 1 GHz.

The SED is fit with a GPS model, that returns parameters 2.16±0.02, 0.34±0.02 and -0.35±0.01. Note that the source is mildly confused in the WISH map. The flux used here is deblended BCG emission however there could still be wrongfully attributed flux contributing to this 352 MHz measurement. Equally, this 353 MHz point lying above the curve could be indicative of a steeper spectrum component (which would push the GPS peak to higher frequency). Future low frequency observations will determine this.

E1821+644

HB89 1821+643, z=0.2970. This source is one of the few radiatively efficient AGN known to reside within a cool core cluster (see e.g. Russell et al., 2010, and references therein). Nevertheless, the radio-properties appear to be consistent with its more inefficent brethren. Multiple high resolution VLA observations from the NRAO Image Archive allow the core to be isolated at multiple frequencies which are consistent with the spectral flattening seen above about 10 GHz. The source shows significant variation. Fit the core-only measurements with a GPS-like model, returning parameters of 0.83±0.10, 0.40±0.06 and -0.19±0.03. This suggests a broad, flat profiled core. Independently fit a steep power-law to the low frequency data, returning a fit with α=1.06±0.13 and A=94.6±3.6.

Hydra-A

This source is associated with the bright radio source 3C 218, z=0.0549. This source is very well studied (e.g. McNamara et al., 2000; Hamer et al., 2014, and references therein) . VLBA observations at multiple frequencies (e.g. Taylor, 1996; Araya et al., 2010) allow the SED of the core only to be independently fit with a GPS model (returning parameters: 2.01±0.05, 0.95±0.06 and -0.59±0.06). The integrated SED is dominated by flux from the extended emission and remains persistent to frequencies higher than 100 GHz. Accounting for the minimal core contribution, fit the SED using a power-law with α=1.00±0.02 and A=47214.3±43.0.

MACS0242-21

PKS 0240-217, z=0.314. This source appears to be a CSS or low-peaking GPS, that can be fit using a GPS model with parameters of 3.14±0.02, -0.14±0.02 and -0.30±0.02. VLBA observations of the source at S- and X-band (Beasley et al., 2002) show that it is ‘wispy’ on parsec scales, with the integrated flux consistent with the unresolved emission

at VLA resolutions. That the source has a low spectral peak, alongside it being very structured on parsec scales, is consistent with this source being in a late-stage of core activity.

MACS1931-26

PMN J1931-2635, z=0.3520. There are two radio-sources in close proximity within the cluster core; the BCG at 19:31:49.67 -26:34:33.4 and a Wide-Angled Tail (WAT) source, PMN 1931-2635, at 19:31:50.0 -26:35:16.4. These sources are confused in many radio maps of the region. The BCG core is isolated in ATCA-6km observations at 5.5 and 9.0 GHz along with CARMA and GISMO at higher frequencies. The SED of only these points is well fit with a GPS model, returning parameters 0.95$\pm$0.04, 0.42$\pm$0.03 and -0.21$\pm$0.01. The sources are confused in lower resolution observations. The sources cannot therefore be fully distinguished, however by fitting to the flux peaks coincident with the optical positions it appears as if PMN 1931-2635 has a steeper spectrum (as would be expected for a lobe-dominated WAT). Further confounding the picture, high resolution VLA-A observations at L-band by Ehlert et al. (2011) show that the BCG is surrounded by an amorphous halo (see also Mittal et al., 2009) that is likely to be very steep spectrum. This structure is most likely confused emission from previous activity cycles of the BCG (see Chapter 3). The integrated emission of this amorphous halo component does not account for all of the flux in the confused observations. However, such high resolution observations at other frequencies to fully detangle this amorphous halo emission are not available currently. Shown on the SED are the core only observations along with highlighted confused, amorphous halo and WAT data points.

RXJ0132-08

PKS 0130-083, z=0.1489. This source appears to be either a low-peaking GPS or a CSS. The source does not appear above the 5σ cut-off of the VLSS catalogue (Cohen et al., 2007) but overlaying the VLSS map, the source is present at the optical position as a 3σ detection. The central engine is resolved in VLBI maps (Bourda et al., 2010, 2011; Petrov, 2011, []). Fit a GPS model to the integrated emission (that returns parameters; 2.55$\pm$0.04, -0.24$\pm$0.03 and -0.11$\pm$0.03) and show the VLBI peaks on the SED (although note that these are not included in the fit).

RXJ0352+19

2MASX J03525901+1940595, z=0.109. The SED is relatively poorly sampled, consist-

ing of only four detections and limits from the pointed GISMO observation (at 150 GHz) and the VLSS (Cohen et al., 2007). A single power-law fit returns α=0.41$\pm$0.18 and A=20.4$\pm$5.8, which is consistent with the limits and suggests a flat spectrum source. However, there could be a small GPS-like component with a tail but available data are not sufficient to confirm nor deny this, hence the power-law is perhaps the most robust fit possible with current data.

RXJ0439+05

2MASX J04390223+0520443, z=0.208. The SED can be well fit with a strong GPS component, that returns parameters 1.42$\pm$0.03, 1.67$\pm$0.02 and -0.72$\pm$0.01 and then a steep spectrum tail to lower frequency (less than 1 GHz) with α=1.10$\pm$0.04 and A=60.2$\pm$5.5.

RXJ0747-19

PKS 0745-191, z=0.1028. The SED potentially flattens below around 200 MHz but other than that presents as a steady power-law out to higher than 150 GHz, with α=1.26$\pm$0.07 and A=3064.7$\pm$23.4.

RXJ1347-11

GALEX J134730.7-114509, z=0.450. The BCG is surrounded by a confirmed 500kpc radio mini-halo (see Gitti et al., 2007). Using high resolution VLA observations from the NRAO Image Archive, an SED of only the BCG is created. This suggests an active AGN, whose SED is well fit with the GPS model with parameters of 1.35$\pm$0.05, 0.30$\pm$0.01 and -0.35$\pm$0.01. The mini-halo emission has a steep spectrum with α=1.20$\pm$0.04 and A=47.2$\pm$4.1. The similarity of the SED of this source to other observed spectra in systems without observed mini-halos, but with smaller amorphous haloes lends evidence to the belief that the seed populations for true mini-haloes are built from repeated AGN activity in the BCG (see Chapter 3).

RXJ1350+09

2MASX J13502209+0940109, z=0.1325. This source appears to be highly variable, and has previously been identified as a BL-LAC (e.g. Massaro et al., 2009; Richards et al., 2011). A non-detection in the VLSS (Cohen et al., 2007) shows that this source has no steep component at low frequencies and hence the SED appears to be GPS-like. Fit the SED with a GPS model, which returns a sharp peaked spectrum with parameters 2.42$\pm$0.04, 0.70$\pm$0.03 and -0.65$\pm$0.03.

RXJ1504-02

LCRS B150131.5-023636, z=0.2171. This cluster contains a confirmed radio mini-halo (Giacintucci et al., 2011b), 140kpc in extent. This mini-halo manifests itself as a steep spectrum tail in the SED to low frequencies (below about 1 GHz). There appears to be an active core within the central BCG that gives rise to a GPS-like component in the integrated SED, that can be fit using the GPS model with parameters 1.67$\pm$0.01, -0.09$\pm$0.01 and -0.16$\pm$0.04. The mini-halo emission can be isolated from that of the AGN at L-band (White et al., 1997) and agrees well with lower frequency data (see SED), giving a power-law fit to this lower frequency component with α=1.19$\pm$0.05 and A=31.4$\pm$3.9.

RXJ1558-14

PKS 1555-140, z=0.0970. This is an actively evolving system with good historical coverage. See section **??** for a more detailed description of this system. Here we perform an average GPS model fit of the core over the previous 40 years, recovering parameters of 2.69$\pm$0.04, 0.31$\pm$0.10 and -0.45$\pm$0.06 and then fit a power-law for the steep spectrum tail which has α=1.30$\pm$0.20 and A=71.6$\pm$4.0.

RXJ1715+57

NGC6338, z=0.0282. Considering the archival C-band measurements (e.g. Gregory & Condon, 1991) suggests that this source may show some long-term variability in here. Without the GISMO observation the SED would perhaps be interpreted as a GPS, however the 150 GHz detection shows that the spectrum remains flat up to high frequency. The GISMO flux could be interpreted as evidence of 'flickering' at high frequencies or variability. Either way, the SED is most reliably fit using a power-law with α=0.41$\pm$0.04 and A=53.1$\pm$3.1. This shows the source to be flat spectrum and is consistent with the non-detection in VLSS (Cohen et al., 2007).

RXJ1832+68

2MASX J18323551+6848059, z=0.205. The SED is dominated by steep spectrum emission to about 10 GHz that is fit using a power-law with α=0.92$\pm$0.03 and A=194.8$\pm$7.7. Above this frequency the spectrum appears to 'bump' outwards. VLBA observations (Chapter 5) at C-band show that there is an active core component in here (see also Laurent-Muehleisen et al., 1997). By considering measurements of the core flux only, this active component can be well fit with a relatively high-peaking GPS component with

returned parameters of 0.78±0.36, 1.31±0.53 and -0.56±0.20. When combined with the power-law this interpretation appears to well explain the integrated spectral shape.

RXJ2341+00

PKS 2338+000, z=0.2767. This is an unresolved radio source (at few-arcsecond resolution) whose SED is steeper at higher frequency yet is flattening at less than a few GHz. The 365 MHz flux from the TEXAS survey (Douglas et al., 1996) shows that the SED does turnover. Fit the SED with a low peaking GPS, with returned parameters of 2.62±0.01, -0.16±0.06 and -0.15±0.04. This source is a non-detection at the 5σ detection limit of the VLSS catalogue (Cohen et al., 2007), and the limit is consistent with the inferred turnover. Looking at the VLSS map overlaid onto an optical image of the region, we see that there is a faint ($<3\sigma$) detection at the correct position. This point was not included in the fit but is included on the SED to highlight that it is consistent with being a genuine detection.

Z235

2MASX J00435213+2424213, z=0.083. The SED of this source has a flat spectral index, that can be fit with a single power-law of α=0.45±0.06 and A=61.7±7.3. The returned index is consistent with the non-detection in VLSS (Cohen et al., 2007).

Z8193

B3 1715+425, z=0.1754. This source appears to contain a variable core component that is confirmed by VLBI measurements (see Chapter 5, Bourda et al. 2010, 2011). The SED is fit by a combination of a GPS model to account for the spectral flattening above about 1 GHz and a steep power-law tail to lower frequencies. Note that the source is below the detection threshold of the VLSS catalogue (Cohen et al., 2007) but appears as a $\approx3\sigma$ detection at the correct position in the map overlay. The flux is therefore retrived using the AIPS task IMFIT from a VLSS cut-out. The returned parameters for the GPS component are 1.82±0.01, 0.26±0.01 and -0.26±0.01. Accounting for the core contribution, a power law with α=0.82±0.04 and A=89.2±5.7 is fitted to the low frequency tail.

Z8276

2MASX J17441450+3259292, z=0.075. There is a distinct split in the spectral index of the SED at approximately 1 GHz. There also appears to be large amplitude variability at higher frequencies. Fit the steeper component using a power-law with α=1.26±0.03 and

A=80.0±6.0 and then fit the GPS model to the core only measurements, which returns GPS-model parameters of 1.57±0.50, 0.52±0.76 and -0.30±0.26.

Appendix K

High Frequency Sample - SEDs

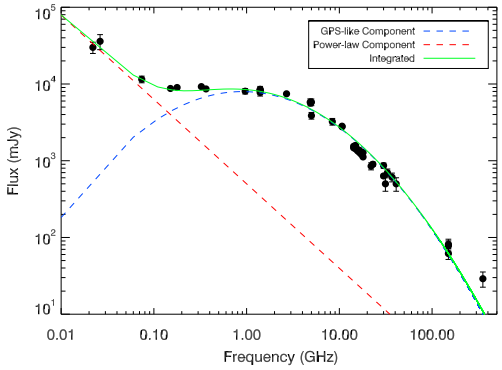

4C+55.16

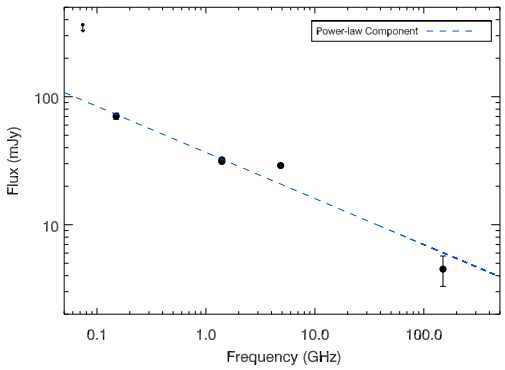

A1084

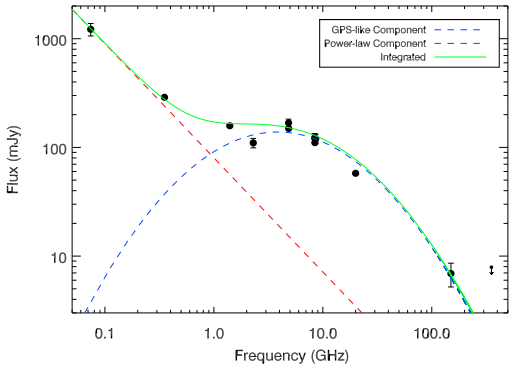

A1348

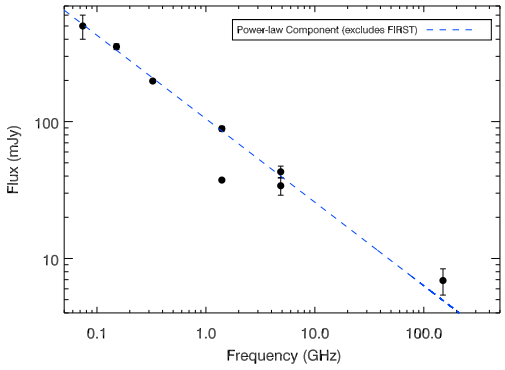

A1774

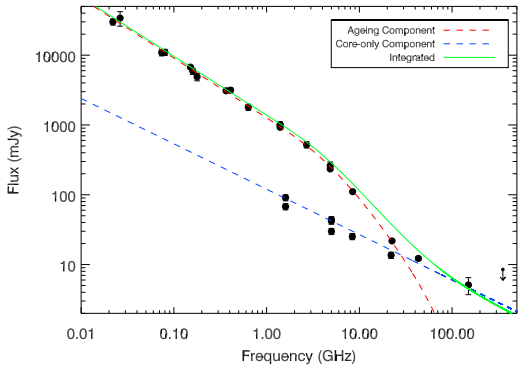

A1795

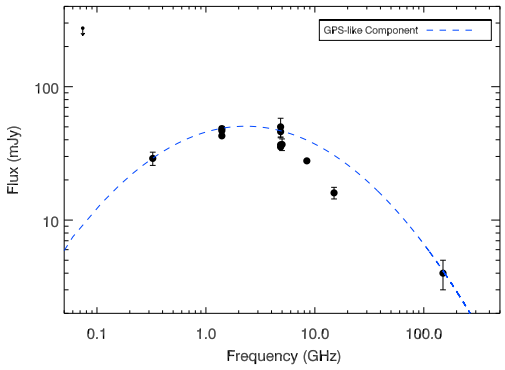

A1885

Figure K.1: SEDs for the High Frequency Sample. See preceding section for more information on the spectral fits.

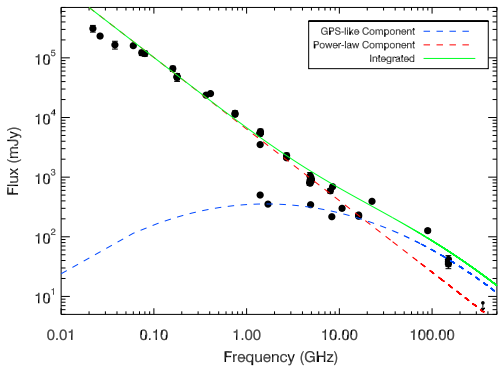

A2052

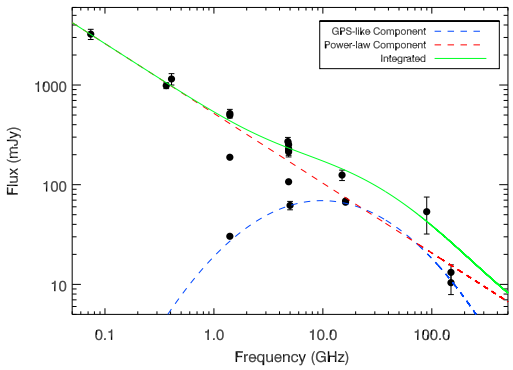

A2055

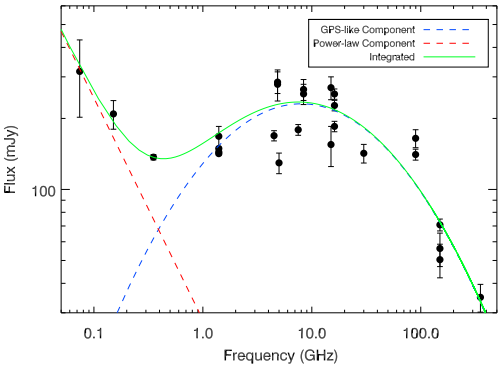

A2270

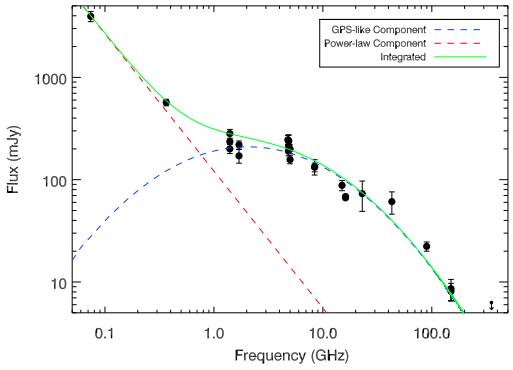

A2390

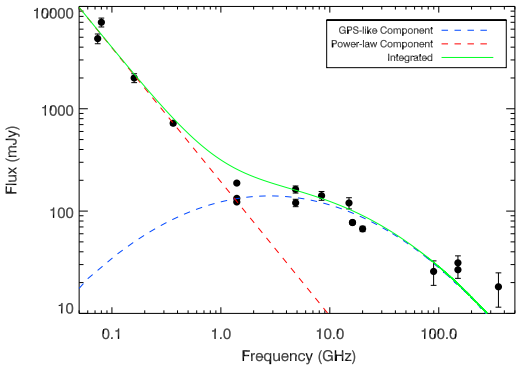

A2415

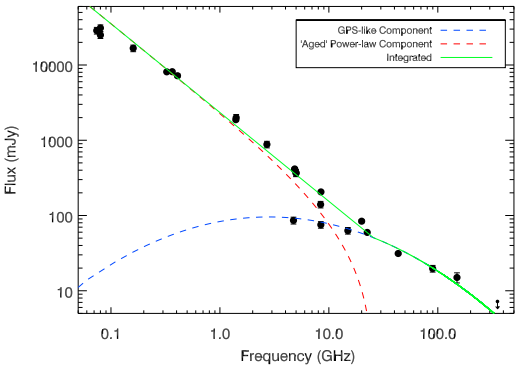

A2597

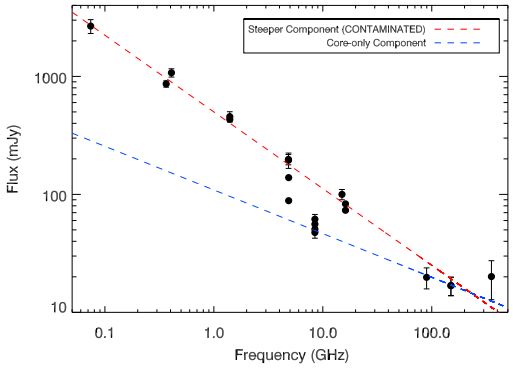

A2627

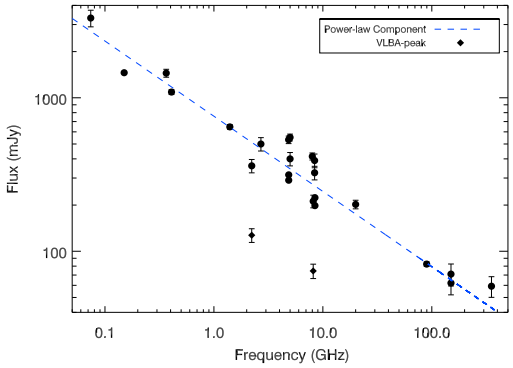

A3581

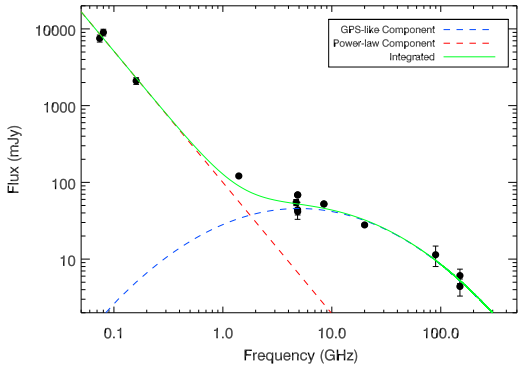

A496

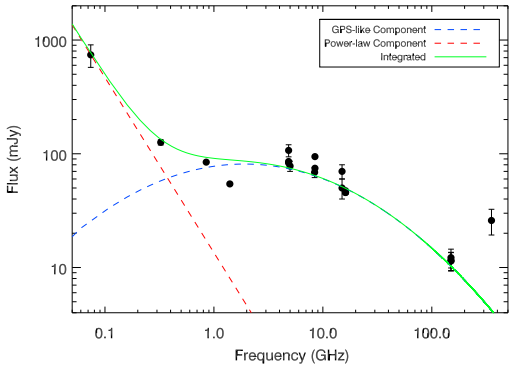

A646

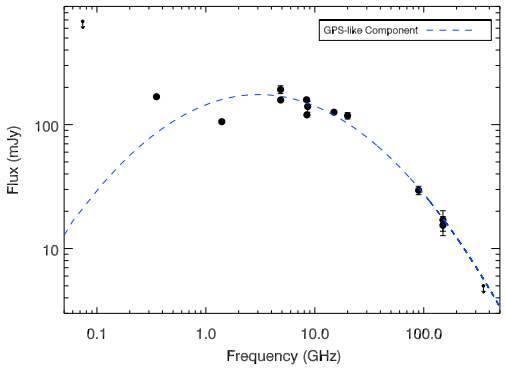

AS780

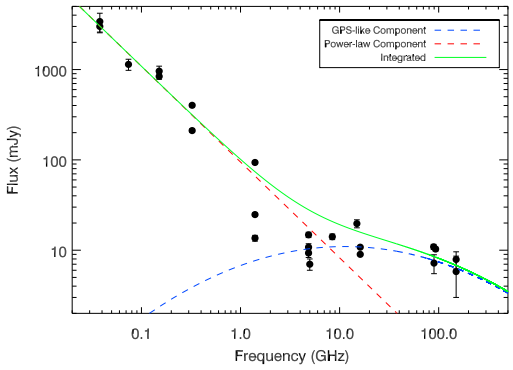

E1821+644

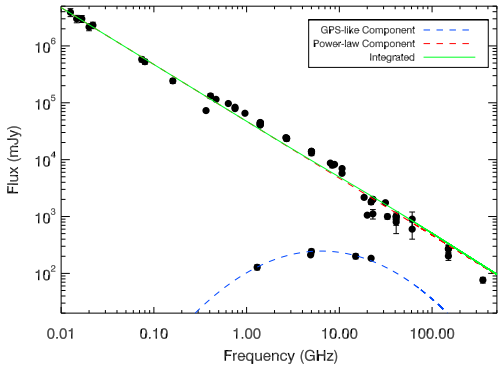

Hydra-a

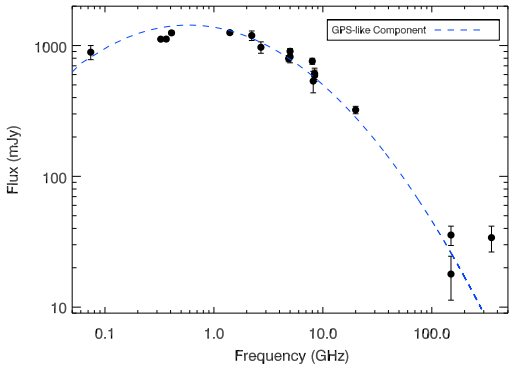

MACS0242-21

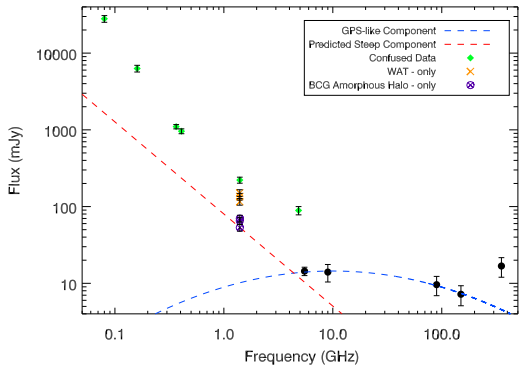

MACS1931-26

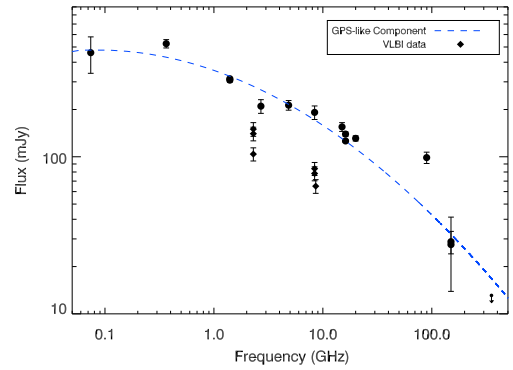

RXJ0132.6-0804

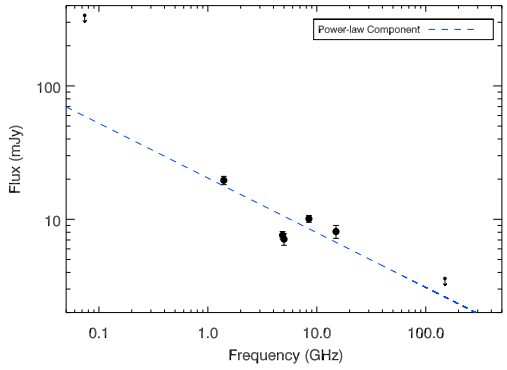

RXJ0352.9+1941

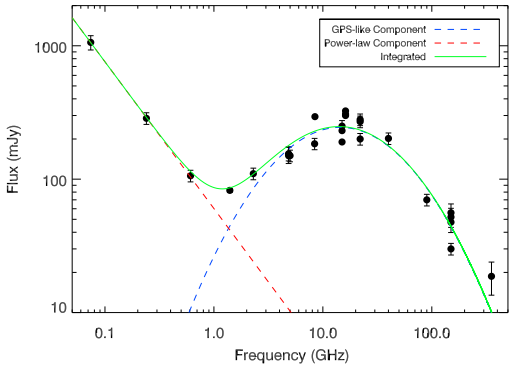

RXJ0439.0+0520

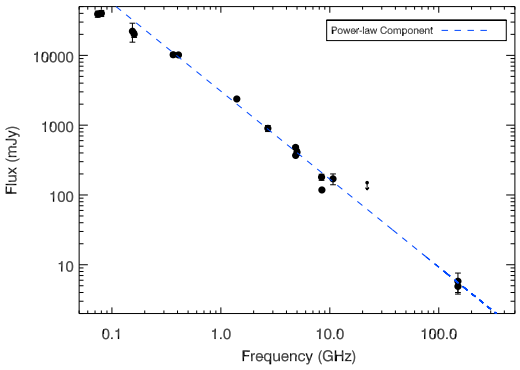

RXJ0747.5-1917

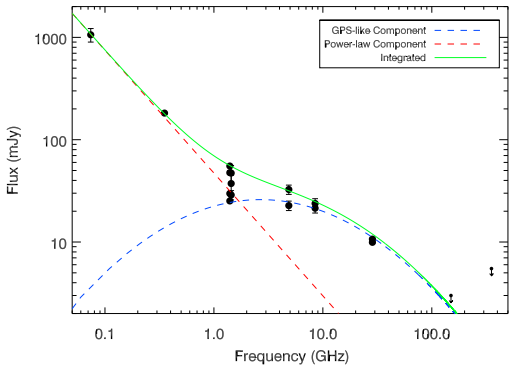

RXJ1347.5-1145

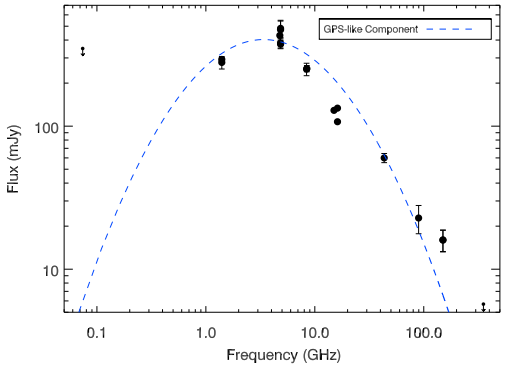

RXJ1350.3+0940

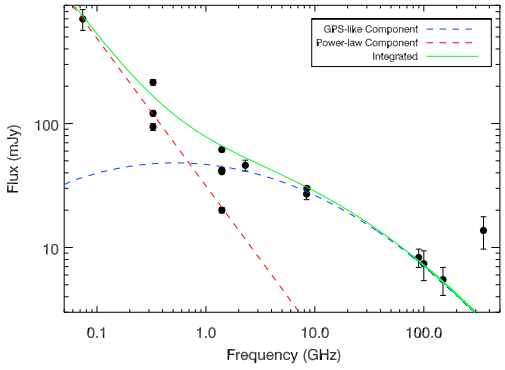

RXJ1504.1-0248

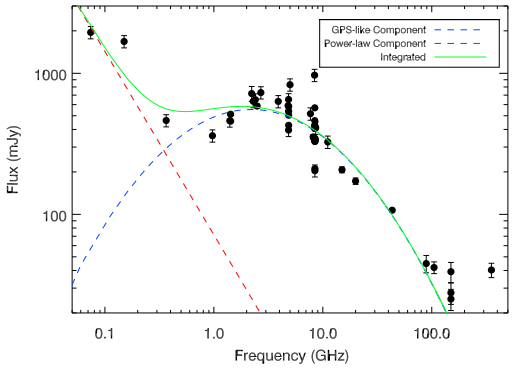

RXJ1558.4-1410

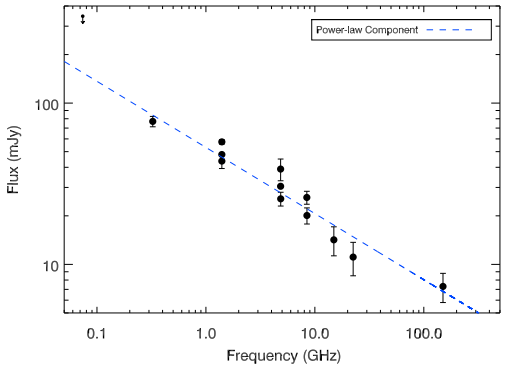

RXJ1715.3+5725 (NGC6338)

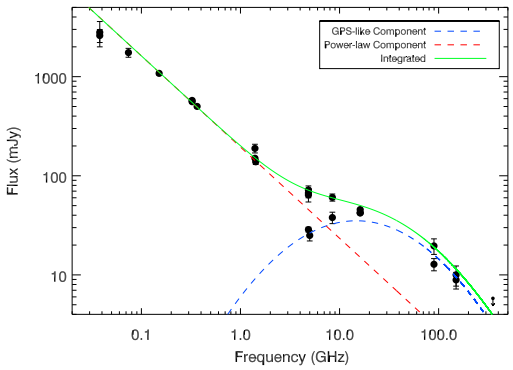

RXJ1832.5+6848

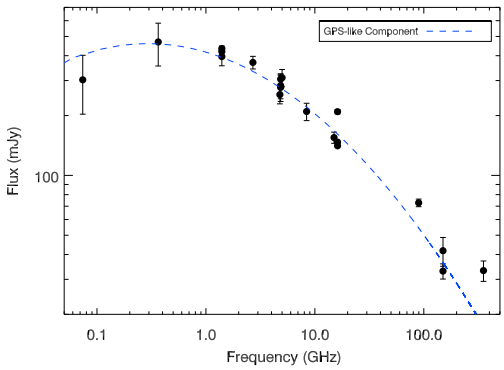

RXJ2341.1+0018

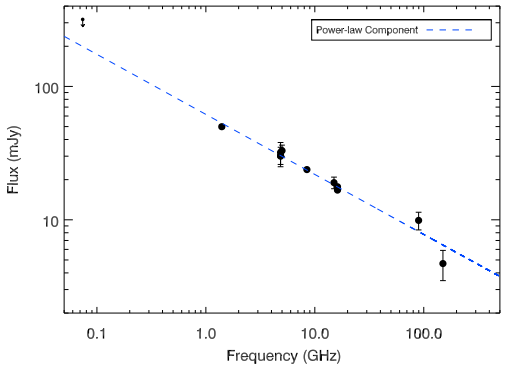

Z235

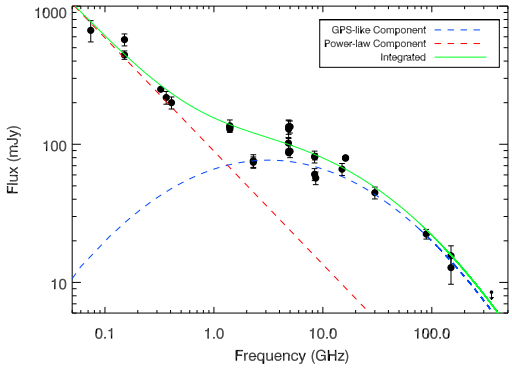

Z8193

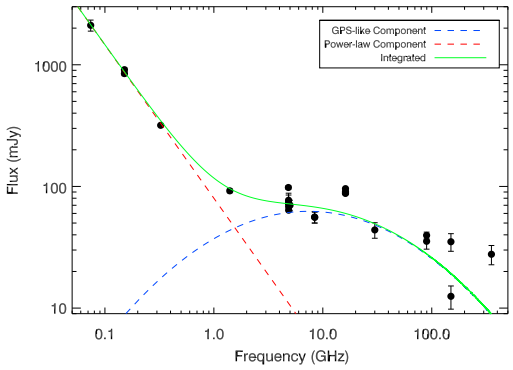

Z8276

Appendix L

VLBA - Fluxes

Table L.1: Parameters for sources observed during VLBA program BE056. Columns shown are: a) cluster containing BCG, b) Redshift, c) Corresponding angular scale, d) RA(J2000), e) DEC(J2000), f) Fringing scheme employed; note SF = self-fringed for strong sources and not self-fringed (NSF) for weaker sources, g) Synthesised beam size for chosen imaging (See Appendix M for further details), h) Peak flux, i) Integrated flux, and j) map RMS. [1] No VLBA-source detected, position taken as optical position of identified BCG from NED. [2] Naturally weighted.

		Scale	Position(J2000)			Beam	Peak	Integrated	RMS
Cluster	Redshift	pc/mas	RA	DEC	Fr.	(mas)	mJy/bm	(mJy)	(mJy)
Run 1: 23rd/24th December 2009									
A11	0.151	2.629	00:12:33.874	-16:28:07.553	NSF	5.22×2.76^{2}	6.80	24.03	0.30
Z235	0.083	1.561	00:43:52.170	24:24:21.456	NSF	3.12×1.27	11.83	24.60	0.29
RXJ0132-08	0.149	2.593	01:32:41.130	-08:04:04.800	SF	3.21×1.24	86.55	141.18	0.31
RXJ0331-21	0.189	3.156	03:31:06.04	-21:00:32.9[1]	NSF	5.29×4.65^{2}	<0.48	<0.48	0.16
A496	0.033	0.655	04:33:37.841	-13:15:42.989	NSF	5.06×2.71^{2}	25.28	43.19	0.39
RXJ0439+05	0.208	3.402	04:39:02.262	05:20:43.674	SF	3.50×1.43	105.93	155.16	1.56
A646	0.127	2.268	08:22:09.548	47:05:52.870	SF	3.71×1.14	61.04	64.98	0.33
Z8276	0.075	1.424	17:44:14.480	32:59:29.400	SF	3.71×1.26	72.78	76.82	0.43
Z8197	0.114	2.069	17:18:11.88	56:39:56.0[1]	NSF	4.02×1.16	<0.54	<0.54	0.18

Continued on Next Page...

Table L.1 – Continued

A2390	0.233	3.708	21:53:36.827	17:41:43.726	SF	3.29 × 1.21	96.06	99.34	1.32
A2415	0.057	1.110	22:05:38.630	-05:35:32.500	SF	3.44 × 1.30	95.49	121.98	1.21
Run 2: 5th February 2010									
A646	0.127	2.268	08:22:09.548	47:05:52.870	SF	3.63 × 1.28	58.13	66.69	0.17
A795	0.136	2.400	09:24:05.3	14:10:22[1]	NSF	3.33 × 1.36	<0.30	<0.30	0.10
Z3179	0.143	2.515	10:25:58.00	12:41:08.0[1]	NSF	3.30 × 1.30	<0.42	<0.42	0.14
A1348	0.120	1.069	11:41:24.197	-12:16:38.639	SF	4.97 × 2.74[2]	80.08	102.06	0.39
A1668	0.064	1.231	13:03:46.60	19:16:17.0[1]	NSF	3.23 × 1.25	<0.48	<0.48	0.16
RXJ1350+09	0.133	2.354	13:50:22.136	09:40:10.656	SF	3.41 × 1.34	205.82	300.31	0.66
RXJ1504-02	0.217	3.516	15:04:07.519	-02:48:16.624	NSF	11.84 × 1.38	18.58	32.43	0.35
RXJ1558-14	0.097	1.795	15:58:21.948	-14:09:59.052	SF	5.47 × 3.96[2]	235.8	343.35	1.24
Z8193	0.175	2.972	17:17:19.210	42:26:59.848	NSF	3.81 × 1.24	30.40	68.20	0.26
Z8276	0.075	1.424	17:44:14.480	32:59:29.400	SF	3.55 × 1.26	84.52	89.97	0.22
RXJ2014-24	0.158	2.724	20:14:51.740	-24:30:22.572	NSF	5.76 × 4.11[2]	4.93	>8.78	0.39
A2390	0.233	3.708	21:53:36.827	17:41:43.726	SF	3.24 × 1.26	104.31	117.15	0.40

Continued on Next Page...

Table L.1 – Continued

Run 3: 31st May - 1st June 2010									
A795	0.136	2.400	09:24:05.3	14:10:22[1]	NSF	3.12 × 1.21	<0.33	<0.33	0.11
A646	0.127	2.268	08:22:09.548	47:05:52.870	SF	3.86 × 1.12	57.15	67.52	0.26
Z3179	0.143	2.515	10:25:58.00	12:41:08.0[1]	NSF	3.55 × 1.17	<0.42	<0.42	0.14
A1348	0.120	1.069	11:41:24.197	-12:16:38.639	SF	5.11 × 3.80[2]	75.31	104.12	0.28
A1668	0.064	1.231	13:03:46.60	19:16:17.0[1]	NSF	3.19 × 1.18	<0.42	<0.42	0.14
RXJ1350+09	0.133	2.354	13:50:22.136	09:40:10.656	SF	3.60 × 1.21	190.65	295.47	0.98
S780	0.234	3.727	14:59:28.763	-18:10:45.187	SF	4.75 × 2.94	107.68	140.42	0.29
RXJ1558-14	0.097	1.795	15:58:21.948	-14:09:59.051	SF	4.81 × 2.91[2]	231.90	387.30	1.36
Z8193	0.175	2.972	17:17:19.210	42:26:59.845	SF	3.58 × 1.12	24.94	57.98	0.51
Z8276	0.075	1.424	17:44:14.480	32:59:29.400	SF	3.55 × 1.22	84.32	92.98	0.26
RXJ2014-24	0.158	2.724	20:14:51.739	-24:30:22.587	NSF	5.22 × 3.32[2]	7.33	>10.62	0.40
A2390	0.233	3.708	21:53:36.827	17:41:43.726	SF	3.21 × 1.18	110.15	122.58	0.36
Z8197	0.114	2.069	17:18:11.88	56:39:56.0[1]	NSF	4.22 × 1.14	<0.45	<0.45	0.15

Table L.2: Parameters for sources observed during VLBA program BE063. Columns shown are: a) cluster containing BCG, b) Observation date (dd/mm/yy), c) Redshift, d) Corresponding angular scale, e)RA(J2000), f) DEC(J2000), g) Fringing scheme employed; note SF = self-fringed for strong sources and not self-fringed (NSF) for weaker sources, h) Synthesised beam size for imaging with robust=0 weighting unless stated (see Appendix M for further details), i) Peak flux, j) Integrated flux, and k) map RMS. [1] No VLBA-source detected, position taken as optical position of identified BCG from NED. [2] Naturally weighted.

				Position(J2000)			Beam	Peak	Integrated	RMS
Cluster	Date	Redshift	pc/mas	RA	DEC	Fr.	mas	mJy/bm	mJy	mJy
RXJ0000+08	09/03/13	0.040	0.791	00:00:07.031	08:16:45.051	SF	3.80 × 1.69	9.44	10.08	0.47
MACS0159-08	10/03/13	0.405	5.414	01:59:49.380	-08:49:58.505	SF	5.67 × 1.41	61.17	64.00	0.21
MACS0242-21	10/03/13	0.314	4.596	02:42:35.910	-21:32:25.939	SF	6.61 × 1.31	208.98	245.08	2.78
A383	10/03/13	0.188	3.146	02:48:03.395	-03:31:44.856	NSF	4.57 × 1.43	3.81	3.90	0.08
RXJ0341+15	10/03/13	0.029	0.581	03:41:17.533	15:23:47.568	NSF	9.29 × 2.25	3.61	4.06	0.10
RXJ0341+15	07/03/13	0.029	0.581	03:41:17.533	15:23:47.568	NSF	3.44 × 1.64	3.42	4.12	0.12
RXJ0352+19	07/03/13	0.109	1.990	03:52:59.007	19:40:59.588	NSF	3.38 × 1.51	3.27	4.40	0.07
A478	07/03/13	0.086	1.612	04:13:25.278	10:27:54.776	NSF	3.59 × 1.54	1.72	3.11	0.08
MACS0429-02	07/03/13	0.399	5.365	04:29:36.020	-02:53:06.761	NSF	4.34 × 1.53	13.48	17.40	0.55
RXJ0747-19	11/03/13	0.103	1.890	07:47:31.326	-19:17:39.982	NSF	6.36 × 3.81	3.99	6.47	0.34

Continued on Next Page...

Table L.2 – Continued

RXJ0751+50	05/03/13	0.024	0.476	07:51:21.018	50:14:09.900	NSF	3.43 × 1.52	3.58	3.58	0.06
Z1665	11/03/13	0.031	0.622	08:23:21.665	04:22:20.785	NSF	3.86 × 1.80	3.81	5.00	0.13
4C+55.16	05/03/13	0.241	3.806	08:34:54.904	55:34:21.071	SF	3.47 × 1.23	463.3	2654.2	6.5
Z2701	05/03/13	0.215	3.490	09:52:49.2	51:53:05[1]	NSF	3.56 × 1.44	<0.12	<0.12	0.04
Z2844	05/03/13	0.050	0.981	10:02:36.542	32:42:24.267	NSF	3.30 × 1.46	2.69	3.00	0.14
A1084	11/03/13	0.133	2.357	10:44:32.874	-07:04:07.445	NSF	4.35 × 1.45	7.63	13.06	0.19
A1664	16/03/13	0.128	2.281	13:03:42.565	-24:14:42.218	NSF	6.61 × 1.13	2.71	7.60	0.34
NGC5044	16/03/13	0.009	0.191	13:15:23.961	-16:23:07.551	NSF	1.41 × 1.41	3.12	15.38	0.22
NGC5098	29/03/13	0.038	0.748	13:20:14.730	33:08:36.278	NSF	3.35 × 1.35	3.83	4.15	0.01
MACS1347-11	16/03/13	0.450	5.759	13:47:30.625	-11:45:09.510	NSF	11.24 × 1.89	20.40	24.17	0.18
A3581	16/03/13	0.022	0.441	14:07:29.762	-27:01:04.293	SF	6.95 × 1.13	96.41	154.92	0.77
A1885	29/03/13	0.090	1.679	14:13:43.719	43:39:45.005	NSF	3.72 × 1.29	14.52	27.08	0.47
RXJ1442+22	17/06/13	0.097	1.795	14:42:19.369	22:18:11.811	NSF	3.48 × 1.17	1.73	1.88	0.08
MACS1447+08	17/06/13	0.323	4.684	14:47:26.022	08:28:25.168	NSF	5.33 × 1.12	11.63	14.77	0.15
A2052	17/06/13	0.035	0.686	15:16:44.513	07:01:18.100	SF	3.63 × 1.39	205.6	327.3	0.2
A2055	17/06/13	0.102	1.875	15:18:45.837	06:13:56.210	SF	5.24 × 1.20	32.39	34.82	0.17
MACS1532+30	29/03/13	0.362	5.044	15:32:53.778	30:20:59.416	NSF	3.41 × 1.29	2.21	3.02	0.14

Continued on Next Page...

Table L.2 – Continued

A2146	22/05/13	0.234	3.726	15:56:13.930	66:20:53.637	NSF	4.66 × 1.89	0.68	0.78	0.06
NGC6338	22/05/13	0.028	0.566	17:15:22.961	57:24:40.210	SF	4.05 × 1.26	15.51	22.79	0.09
RXJ1720+26	06/07/13	0.161	2.773	17:20:10.038	26:37:32.100	NSF	3.18 × 1.17	0.67	0.68	0.06
A2270	22/05/13	0.247	3.878	17:27:23.469	55:10:53.536	SF	4.07 × 1.35	124.3	136.9	0.64
IC1262	06/07/13	0.033	0.660	17:33:02.017	43:45:34.816	NSF	3.76 × 1.18	2.11	2.43	0.09
RXJ1750+35	06/07/13	0.171	2.915	17:50:16.867	35:04:58.550	NSF	3.52 × 1.15	5.88	16.83	0.12
RXJ1832+68	22/05/13	0.205	3.364	18:32:35.530	68:48:07.100	SF	4.70 × 1.13	11.94	28.66	0.21
MACS1931-26	09/03/13	0.352	4.958	19:31:49.642	-26:34:32.990	NSF	8.04 × 1.34[2]	7.45	20.15	1.08
RXJ2129+00	09/03/13	0.235	3.729	21:29:39.960	00:05:21.184	NSF	3.75 × 1.59	2.48	2.58	0.14
A2627	09/03/13	0.127	2.271	23:36:42.096	23:55:29.192	NSF	3.40 × 1.36	7.67	25.95	0.14
RXJ2341+00	09/03/13	0.277	4.209	23:41:06.910	00:18:33.341	SF	4.59 × 1.49	52.07	88.56	0.73
A2667	09/03/13	0.235	3.729	23:51:39.423	-26:05:02.945	NSF	7.69 × 1.29	1.25	1.38	0.26

Table L.3: Combined sample. Columns are 1) Cluster, 2) Observing campaign, 3) Classified morphology, 4) Percentage of unresolved arcsecond scale C-band flux recovered by VLBA, 5) Line emitting or non-line emitting cluster. * Confused morphology. [1] Estimated from L-band assuming flat spectral index. [2] Potentially multiple components, see Appendix M. [3] Estimated from L-band assuming flat spectral index.

Cluster	Campaign	Morphology	% Recovered	LE/NLE
RXJ0000+08	BE063	Unresolved	21	LE
MACS0159-08	BE063	Unresolved	110	LE
MACS0242-21	BE063	One-sided	27	LE
A383	BE063	Unresolved	24	LE
RXJ0352+19	BE063	Unresolved	57	LE
A478	BE063	One-sided	50[1]	LE
MACS0429-02	BE063	One-sided	>24[2]	LE
RXJ0747-19	BE063	One-sided	3	LE
RXJ0751+50	BE063	Unresolved	60	LE
Z1665	BE063	One-sided	43	LE
4C+55.16	BE063	Two-sided	>47[2]	LE
Z2701	BE063	Non-detection	<3	LE
A1084	BE063	One-sided	45	LE
A1664	BE063	One-sided	51	LE
NGC5044	BE063	One-sided*	>117[2]	LE
NGC5098	BE063	Unresolved	39	LE
MACS1347-11	BE063	Unresolved	>80	LE
A3581	BE063	One-sided	49	LE
A1885	BE063	Two-sided	74	LE
RXJ1442+22	BE063	One-sided	17	LE
MACS1447+08	BE063	Unresolved	34[1]	LE

Continued on Next Page...

Table L.3 – Continued

A2052	BE063	Two-sided	128	LE
A2055	BE063	Unresolved	33	LE
MACS1532+30	BE063	One-sided	34	LE
A2146	BE063	Unresolved	8	LE
NGC6338	BE063	One-sided	75	LE
RXJ1720+26	BE063	Unresolved	25	LE
A2270	BE063	Unresolved	60	LE
IC1262	BE063	One-sided	44	LE
RXJ1750+35	BE063	One-sided	53	LE
RXJ1832+68	BE063	Two-sided	115	LE
MACS1931-26	BE063	One-sided*	$>23^2$	LE
RXJ2129+00	BE063	Unresolved	29	LE
A2627	BE063	One-sided*	29	LE
RXJ2341+00	BE063	One-sided	30	LE
A2667	BE063	Unresolved	15	LE
A11	BE056	One-sided	76	LE
Z235	BE056	Two-sided	80	LE
RXJ0132-08	BE056	One-sided	66	LE
RXJ0331-21	BE056	Non-detection	<1	LE
A496	BE056	One-sided	78	LE
RXJ0439+05	BE056	One-sided	104	LE
A646	BE056	Unresolved	82	LE
Z8276	BE056	Unresolved	129	LE
Z8197	BE056	Non-detection	<5	LE
RXJ2014-24	BE056	Confused	>25	LE
A2390	BE056	Two-sided	$>61^2$	LE
A2415	BE056	Unresolved*	75	LE
A795	BE056	Non-detection	<1	LE

Continued on Next Page...

Table L.3 – Continued

Z3179	BE056	Non-detection	<2	LE
A1348	BE056	Unresolved	70	LE
A1668	BE056	Non-detetion	<1	LE
RXJ1350+09	BE056	One-sided	83	LE
RXJ1504-02	BE056	Unresolved*	83[3]	LE
RXJ1558-14	BE056	Two-sided	95	LE
Z8193	BE056	Two-sided	80	LE
S780	BE056	Unresolved	93	LE
RXJ0341+15	BE063	One-sided	33	NLE
Z2844	BE063	Unresolved	33	NLE

Appendix M

VLBA - Comments on Individual Sources

Here we provide brief descriptions of the imaging parameters and recovered structure on milli-arcsecond scales for all BCGs in our VLBA sample. Where a source is observed at multiple epochs with the VLBA, these are discussed and compared under the same header.

M.0.1 BE056

A646

BCG identified as 2MASX J08220955+4705529. Source is flat spectrum and unresolved on arcsecond scales, expected to contain strong core component. Observed at C-band with VLA-C in 1997 and 1999 (AE125 and AE110, see Chapter 3) to be 85.5 and 84.4mJy respectively. Predicted to contain $\approx$90.0$\pm$7.5mJy core component at 10 GHz. Observed during all three epochs, recovered fluxes self-consistent with no variability over these few-month timescales. Similarly, images using robust=0 (beam sizes vary slightly between runs, see Table L.1) are all consistent with the source being unresolved on parsec scales. Concatenated image of all three observations (using AIPS task DBCON to combine the uv-data), imaged using robust=0 to give a beam 3.38$\times$1.12 milli-arcseconds also shows no extent, recovering $\approx$82% of the 1999 arcsecond flux. The source is line emitting and does not appear in the VLBA calibrators list.

A795

BCG identified as 2MASX J09240529+1410217. This is a compact steep spectrum radio-source, observed to be contain 24.8mJy in an unresolved VLA-C observation in 1997 (AE110, see Chapter 3). However, there is no evidence of spectral flattening towards high frequencies, which coupled to the lack of observed variability suggests this source has no significant ongoing central activity and the predicted core component was limited to $<$7.2mJy at 10 GHz. The BCG was observed twice in project BE056, during runs 2 and 3. We do not recover the source in either run. A map produced using the concatenated uv-data of both runs, weighted using robust=0 to give a beam 3.27 $\times$ 1.29 milli-arcseconds similarly recovers no source. Using a 3σ limit above the local noise as our detection threshold we set that $<$0.9% of the arcsecond scale flux is on milliarcsecond scales and therefore expect siginficant flux on intermediate scales. The source is line emitting and does not appear in the VLBA calibrators list.

Z3179

BCG identified as 2MASX J10255796+1241086. Similar to A795, this is a compact steep spectrum source, observed twice with VLA-C and found to be 24.6mJy in 1994 and a consistent within error 24.8mJy in 1999 (AE099 and AE125 respectively, see Chapter 3). The integrated SED steepens above a few GHz and there are no high frequency detections, suggesting an ageing electron population with no replenishing central activity ongoing. Core component predicted to be $<$8.2mJy at 10 GHz. Observed twice with the VLBA, during BE056 runs 2 and 3. We do not recover the source in either run. A concatenated map of the two runs using robust=0 with beam 3.33 $\times$ 1.26 milli-arcseconds similarly recovers no source. Using a 3σ limit above the noise as our detection threshold we set that $<$1.5% of the arcsecond scale flux recovered in 1999 is on parsec scales and therefore expect siginficant flux on intermediate scales. The source is line emitting and is not in the VLBA calibrators list.

A1348

BCG identified as LCRS B113851.7-115959. The source has a GPS-like spectrum with

additional steep component seen at low frequencies (see Chapter 4). An observed with the ATCA-6km recovered an unresolved core of ≈149.2mJy in 2008 and the source is predicted to contain a core component contribution of ≈106.3±26.8mJy at 10 GHz (see Chapter 3). Source is a VLBA calibrator, available maps at 2.3 and 8.3 GHz from 2005 (Kovalev et al., 2007). There is possibly slight extension to the SW although this and potential extent to the NE in the 8.3 GHz map are consistent with noise. There is additionally nothing in the visibility plot to suggest there should be extent. FITBM fails (no failure message is reported by AIPS although experimenting with other weighting schemes shows that the recovered beam shape collapses to a delta function at robust=0) when using robust=0 weighting for both runs, and so the beam collapses to 1.41×1.41 milli-arcseconds for both (equivalent to pure uniform sampled maps). However, the recovered fluxes remain consistent with previous VLBA observations (Kovalev et al., 2007) and self-consistent within 1σ. The source appears unresolved in both runs, with the potential weak jet to the South-East most likely attributed to the poor beam. Natural weighting (robust=5, see Table L.1) allows successful beam reconstruction although the result is the same, no extent is seen. A concatenated map produced from the DBCON combined uv-data, weighted using using robust=0.5 (as a compromise between the 'fat' beam for natural weighting and the failed beam for anything more uniform) with a beam 7.61 × 1.39 milli-arcsec confirms the source to be unresolved and contains ≈70% of the ATCA-6km flux. The source is line-emitting.

A1668

BCG identified as IC 4130. The radio source is a CSS and observed to be unresolved and 21.0mJy with the VLA-C array in 1999 (AE125, see Chapter 3) although it was resolved into two lobes with the VLA-A at X-band in 1997 (AE117). There is no evidence for high frequency flattening or variability, and a limit on the core component at 10 GHz was placed at <2.8mJy. Observed twice with the VLBA, during BE056 runs 2 and 3. We do not recover the source in either run. Similarly, the concatenated map of the two runs weighted with robust=0 to give a synthesised beam 3.31 × 1.21 milli-arcseconds recovers no source. Using a 3σ limit above the local noise as our detection threshold we set that <1.4% of the arcsecond scale flux recovered in 1999 is on parsec scales and therefore

expect siginficant flux on intermediate scales. The source is line emitting and not in the VLBA calibrators list.

R1350+09

BCG identified as 2MASX J13502209+0940109. This source appears to contain a highly active core component and has a GPS-like SED (see Chapter 4). There is no apparent low-frequency tail and the source is undetected in VLSS (Cohen et al., 2007). The source is a VLBA calibrator, 1995 observations at both 2.3 and 8.3 GHz (Beasley et al., 2002) show it to appear unresolved in maps, however the visibility plot at 8.3 GHz suggests there should be some extent. Only appear to be old, single-dish observations at C-band, the most recent being 374$\pm$22mJy in the PMN survey, 1995 (Wright et al., 1994). The source is recovered, with self-consistent flux in both run 2 and run 3, with a small one-sided jet to the West seen in both images with a brightness around 2% of the peak level. An image of the concatenated uv-data weighted using robust=0 to give a beam 3.38$\times$1.31 arcseconds reconfirms this western extent. The total recovered flux is $\approx$83% of the PMN measurement. Source is line emitting.

R1504-02

BCG identified as LCRS B150131.5-023636. Flat spectrum source, previously observed to be unresolved at VLBI scales (Bourda et al., 2010). Not observed with VLA-C at C-band although VLA-A X-band observation found it to be unresolved and contain 30.0mJy in 1997 (AE117, see Chapter 3). Predicted to be highly core dominated and contain a core component of $\approx$28.0$\pm$14.0mJy. Only observed with the VLBA during BE056 run 2. Robust=0 weighting gives a highly elliptical beam of 11.84$\times$1.38 milli-arcseconds. There is potentially some extent Eastwards although the interpretation of this is limited by the highly elongated beam shape. The recovered flux contains $\approx$83% of the expected arcsecond scale flux at C-band, assuming a flat index from the 8.4 GHz observation, thus confirming this source to be core dominated. Remapping with robust=0.5 weighting improves the beam shape to 4.95$\times$2.97mas and recovers consistent flux, again with possible extent to the East but which is not strong enough to confirm. The souce is line emitting and is not in the VLBA calibrators list.

R1558-14

BCG identified as PKS 1555-140. GPS-like source with additional low-frequency steep spectrum component. Expected to be highly core dominated in the GHz range, observed to be unresolved 427.7mJy with ATCA-6km in 2008 (C1958, see Chapter 3). Source is in the VLBA calibrators list, with images available at 2.3 GHz in 1998 and 8.3 GHz in 1997 (Beasley et al., 2002). Two-sided symmetric structure is seen at both of the frequencies. In the 2.3 GHz map, see strong jet/knot ≈7.5mas to the South-East with weaker (factor ≈15) counter-knot a similar distance to the North-West. Knots also observed at 8.3 GHz although now of similar strength and with SE knot only ≈5mas away from core (which is relatively much weaker) with the NW knot ≈4mas from core. This target was observed twice with the VLBA, in BE056 runs 2 and 3. FITBM fails for run 2 with robust=0 weighting, collapsing to a 1.41×1.41mas uniform beam and gives a poor 22.73×1.12mas beam for run 3 (although it should be noted that both recover consistent flux and structure, if this variation of the beam shape is accounted for). Natural weighting (robust=5) allows a beam to be more properly formed, at expense of some sharpness (5.47×3.96mas for run 2, 4.81×2.91mas for run 3). Both images recover similar structure to the archival observations. However, now see that the NW knot is ≈factor 7 times brighter than the SE knot. NW knot ≈7.5mas from core whereas SE knot is ≈8mas away. An image produced using the concatenated uv-data (using robust=5, with a beam 4.79×2.79mas) serves only to confirm the structure seen in the maps produced in the individual runs and confirms the core dominance of this source, with ≈95% of the ATCA-6km flux recovered on parsec scales. The source is line emitting.

Z8193

BCG identified as B3 1715+425. The SED is steep spectrum at low frequencies, although shows clear spectral flattening at ≈ GHz range that extends out to higher frequencies suggesting presence of strong active component, hence expect to recover strong emission on parsec scales (see Chapter 4). Observed to be unresolved with the VLA-C array in both 1997 and 1999, showing 86.7mJy and 88.7mJy respectively (AE110 and AE125, see Chapter 3). The source is in the VLBA calibrators list but no images are available - it is

one of the additional sources from the geodesic catalogues (Bourda et al., 2010; Petrov, 2011). Additionally observed at 2.3 GHz and 8.3 GHz by Bourda et al. (2011) and found to contain high percentage of the VLA core flux. The source was observed with the VLBA in both BE056 run 2 and run 3. Using robust=0 weighting with beams 3.81×1.24mas and 3.58×1.12mas respectively, in both cases recovers a two-sided structure in roughly NWW-SEE orientation, potentially with low-level variability. The concatenated image of these two data sets (using robust=0, beam 3.63×1.19mas) confirms the extended structure, which is ≈2mas in extent in either direction from core with a total recovered flux that is ≈81% of that found with the 1999 VLA observation.

Z8276

BCG identified as 2MASX J17441450+3259292. Source has a split spectrum, steep at low frequencies but with flattening to higher frequencies suggesting presence of active component (see Chapter 4). Observed to be unresolved with the VLA-C array in both 1997 and 1999, displaying 72.7mJy and 71.7mJy respectively (AE110 and AE125, see Chapter 3). Predicted to contain a core component of ≈59.2±11.8mJy. This source was observed in all three BE056 runs and appears unresolved at all epochs (using robust=0, slightly varying beams see Table L.1). However the source increases in brightness by ≈17% between runs 1 and 2, before plateauing. Note that this is consistent with the high frequency monitoring showing that this source to currently be in a highly active state. The concatenated image using data from all runs (robust=0, beam 3.15×1.28mas) confirms the source to be unresolved. The recovered flux is ≈129% of the 1999 VLA-C measurement suggesting strong core dominance and variability. The source is line emitting and not in the VLBA calibrators list.

R2014-24

BCG identified as 2MASX J20145171-2430229. This object is a bright, steep spectrum radio source. Observed to be an unresolved 49.8mJy source at C-band with the ATCA-6km in 2008 (C1958, see 3) although no strong core component was apparent given previous observations and a limit on the core contribution at 10 GHz was set at <19.3mJy. This source was observed with the VLBA in all three BE056 runs. Numerous imaging

techniques were attempted and the calibration was extensively checked and seems fine. However, consistent results between the runs could not be recovered for this source, perhaps as a combination of its southern position and extensive structure on milli-arcsecond scales. Natural weighting is required to successfully form a beam. The maps for each of the three runs are poor, with multiple disjointed components perhaps suggesting that errors persist in the phase calibration. The source is recovered with comparable flux in both runs 2 and 3, however the positions are not consistent and the source is not recovered at all in run 1. The fluxes are perhaps most reasonably interpreted as lower limits, since this source appears to have significant amounts of structure that is being unsatisfactorily recovered. Furthermore, images using DBCON concatenated uv-data suggest a multiple component source. Again, this cannot reliably be recovered and it appears as if the multiple components could be due to the individual runs combining badly. This source is line emitting and not in VLBA calibrators list.

A2390

BCG identified as ABELL 2390:[YEA96] 101084/B2151+174?. The source appears to be core dominated at few GHz frequencies and was observed to contain 213.6mJy unresolved flux with the VLA-C array at C-band in 1999 (AE125) and is predicted to contain a $\approx$122.1$\pm$47.5mJy core component at 10 GHz (see Chapter 3). This target was observed and recovered (images weighted with robust=0, see Table L.1 for beams) in all three BE056 runs. The source is in the VLBA calibrator list as a supplementary and so images are not available. However, this source was also observed by Augusto et al. (2006) at 5 GHz with the VLBA where they found a $\approx$15mas extension to the South and mulitiple other nearby components. Runs 2 and 3 both recover this southern extent although this extended structure is not seen in Run 1. Recovered jet is $\approx$8mas, which is consistent with inner contours of Augusto et al. (2006). An image of the concatenated uv-data of runs 2 and 3 confirms the extent and that $\approx$61% of the 1999 VLA-C flux is recovered on parsec scales. There also appears to be an additional weak component, $\approx$20mas North-East of the core which is consistent in position with, yet fainter than a component detected by Augusto et al. (2006) in 1996, which classifies this source as being two-sided. Adding run 1 to the concatenation does not improve the map, and indeed the errors in this run

actual worsen the result. The source is a line emitter.

S780

BCG identified as 2MASX J14592875-1810453. The source observed has a flat spectrum SED down to 325 MHz (WISH, De Breuck et al., 2002) and exhibits fairly high levels of variability (see Chapter 4) . Observed to be unresolved and have 158.1mJy of flux at C-band with the ATCA-6km in 2008 (C1958). Expected to be highly core dominated, predicted to contain $\approx$136.7$\pm$15.1mJy core component at 10 GHz (see Chapter 3). This source is listed as a VLBA X-band calibrator (Petrov et al., 2005), where there is minimal, if any deviation from the beam shape seen at 8.6 GHz in 2005, suggesting it is unresolved. This source was only observed with the VLBA during BE056 run 3, when it was recovered to be unresolved when using natural weighting with a beam 4.75$\times$2.84 milli-arcseconds (beam failure for robust=0) and contain $\approx$92.7% of the ATCA flux. This is a line emitting source.

Z8197

BCG identified as 2MASX J17181198+5639563. Compact steep spectrum source, observed to be unresolved and 8.9mJy at C-band in 1997 with the VLA-C array (AE110, see Chapter 3) but shows no spectral flattening or variability to suggest active component. Not predicted to contain a strong nuclear source, the core component was predicted to contribute $<$3.7mJy at 10 GHz. This source was observed with the VLBA during project BE056 in runs 1 and 3. It was not detected in either, when imaged using robust=0 weighting with 4.02$\times$1.16mas and 4.22$\times$1.14mas beams respectively. A concatenated map of the two runs using robust=0 with beam 4.06$\times$1.15 milli-arcseconds also recovers no source. Using a 3σ limit above the local noise as our detection threshold we set that $<$5% of the arcsecond scale flux is on parsec scales and therefore expect siginficant flux on intermediate scales. The source is line emitting and not in the VLBA calibrators list.

A2415

BCG identified as 2MASX J22053865-0535330. The SED is steep at low frequencies but see flattening or potential inversion to higher frequencies. Detected with GISMO,

suggestion of variability shows powerful core component in this source (see Chapter 4). No interferometric observations at C-band are available although this source does appear in the PMN catalogue (Griffith et al., 1995) as an unresolved source with 163±13mJy. Source is listed as a VLBA calibrator yet no images are available, similarly no images in the Radio Fundamental Catalogue (RFC) VLBI calibrators catalogue. Observed with the VLBA only during BE056 run 1. The source is unresolved. Using robust=0 weighting with a beam 3.44×1.30 milli-arcsec requires a relatively deep clean to remove sidelobes suggesting some calibration errors may remain in this run. The peak-to-integrated flux ratio when using natural weighting (beam 4.85×2.77mas) agrees with that seen at X-band (≈83%) in the RFC catalogue[1], which was also mapped using natural weighting. The recovered flux contains ≈74.8% of the single-dish flux on parsec scales hence confirming this object to be highly core dominated at 5 GHz. The source is line emitting.

Z235

BCG identified as 2MASX J00435213+2424213. The source is a flat spectrum radio source and was observed to be unresolved with the VLA-C array in 1999 (AE125, see Chapter 3), containing 30.3mJy and predicted to have a dominant core component of 23.2±17.1mJy at 10 GHz. This source was observed with the VLBA in project BE056 only during run 1. Imaging with robust=0 weighting which gives a beam 3.12×1.27 milli-arcseconds shows this source to have a weak two-sided jet structure oriented NE to SW. The integrated emission recovers ≈80% of the arcsecond scale flux seen in 1999. The source is line emitting and is not in the VLBA calibrators list.

A11

BCG identified as 2MASX J00123392-1628086. This source has a steep spectrum at low frequencies which flattens to higher (>1 GHz) frequencies. There is a hint of variability at C-band and a strong 20 GHz (AT20g Murphy et al., 2010) detection suggesting the presence of a powerful sub-dominant core component. An unresolved C-band flux of 33.4mJy was seen with the ATCA-6km in 2008 (C1958, see Chapter 3). This source

[1] http://astrogeo.org/vlbi/solutions/rfc_2014c/

was observed with the VLBA during BE056 run 1. The source is recovered and shown to be extended on milli-arcsecond scales. Robust=0 weighting leads to a FITBM failure. Natural weighting (robust=5, with beam 5.22×2.76 milli-arcsecs) recovers a one-sided source that is extended to the South-West, whose integrated flux recovers ≈75.8% of the arcsecond core. Note that using a a uniform weighting gives a beam 1.41×1.41mas. The resulting imaging suggests that the one-sided structure may breakdown further however significant imaging errors arise when attempting this so best classfication of the source is one-sided on the scale given by a naturally weighted beam. The source is line emitting and is not in the VLBA calibrators list.

R0132-08

BCG identified as PKS 0130-083. This source appears to be core dominated and its SED is well fit with a low peaking GPS-like model (see Chapter 4). Single dish PMN observations (Griffith et al., 1995) recover an unresolved source at 213±15mJy. The source is in the VLBA calibrators list although no images are present (Bourda et al., 2010, 2011; Petrov, 2011). It also appears in the Bordeaux VLBI Image Database (BVID) where an X-band image shows it to be unresolved whereas a ≈10mas one-sided extension is seen to the South-West at S-band. Observed with the VLBA during BE056 run 1. Imaging with robust=0 to give a beam 3.21×1.24 milli-arcseconds recovers a two component source in similar orientation to the archival S-band image although the South-Western component is only ≈8mas from the apparent nuclear core. The integrated flux recovers ≈66% of the PMN measurement. The source is line emitting.

R0331-21

BCG identified as 2MASX J03310587-2100326. This is a fairly bright radio source, however the spectrum steepens to high frequency which is more indicative of an ageing population than the presence of an active core. Observed to be 32.9mJy at C-band in 2008 with the ATCA-6km (C1958, see Chapter 3) but predicted to contain no active core component above <3.4mJy at 10 GHz. This source was observed with the VLBA in BE056 run 1. FITBM fails and collapses to a uniform weighted beam for a robust=0 weighted map. Use of natural weighting (robust=5) gives a beam 5.29×4.65 milli-arcsecs. Neither

weighting scheme detects a source. Using a 3σ limit above the local noise as our detection threshold we set that $<$0.9% of the arcsecond scale flux is on parsec scales and therefore expect significant flux on intermediate scales. The source is line emitting and not in the VLBA calibrators list.

A496

BCG identified as MCG -02-12-039. Source has an ultra-steep ($\alpha \approx 1.8$) index below $\approx$1 GHz whereas above this it flattens and appears to be variable and highly core dominated (see Chapter 4). Observed to be 68.6mJy and unresolved with the ATCA-6km at C-band in 2008 (C1958, see Chapter 3) and predicted to contain a dominant core component of $\approx$40.1$\pm$3.7mJy at 10 GHz. Observed with the VLBA during BE056 run 1. Again, FITBM fails when using robust=0 weighting. Using natural weighting (robust=5, beam 50.6$\times$2.71mas), the source is recovered and found to have a one-sided jet structure extending $\approx$5mas to the South-East. The total recovered flux represents $\approx$77.8% of the ATCA arcsecond-scale core, confirming the high core dominance. This source is line emitting and is not in VLBA calibrators list.

R0439+05

BCG identified as 2MASX J04390223+0520443. This source is highly core dominated and has a GPS-like spectrum in the few GHz-range and above with a low frequency steep-spectrum tail below 1 GHz (see Chapter 4). Observed to be 149.6mJy and unresolved with the VLA-C array in 1999 (AE125, see Chapter 3) and predicted to contain a $\approx$226.3$\pm$74.3mJy dominant core component at 10 GHz. The source is a VLBA calibrator at both 2.3 and 8.6 GHz (Bourda et al., 2010, 2011; Petrov, 2011). It appeared unresolved at 2.3 GHz in 2004 although had a short ($\approx$4mas) westwards extension seen at 8.6 GHz, also in 2004. Observed with the VLBA during BE056 run 1. Robust=0 imaging with a corresponding 3.50$\times$1.43 milli-arcsecond beam recovers extended emission in the same direction as the archival X-band image, 2 milli-arcsecs in extent. The integrated flux recovers $\approx$104% of the 1999 arcsecond core flux showing extreme core dominance and also suggesting variability in this source. The source is line emitting source.

M.0.2 BE063

RXJ0000.1+0816

BCG identified as UGC12890. This source appear to be core dominated and was predicted to contain a ≈28.3±11.3mJy core component at 10 GHz. The source was observed to be 46.6mJy and unresolved at C-band with the VLA-C array in 1999 (AE125, see Chapter 3). The source is recovered in the VLBA imaging. Imaging using robust=0 weighting with a synthesised beam of 3.80×1.69 milliarcsecs gives an unresolved source whose flux is ≈21% of the arcsecond flux. The source is line emitting cluster, not in VLBA calibrators list.

MACS0159-08

BCG identified as SDSS J015949.34-084958.7. This source has an inverted spectrum between 1.4 – 20 GHz, and is expected to be very core dominated with a predicted core component of ≈78.3±15.4mJy at 10 GHz (see Chapter 3). No interferometric arcsecond scale fluxes are available at C-band although the source was seen to be 59.2mJy at X-band with the VLA-A array in 1999 (AE117) and is in the PMN catalogue as a single dish observation of 58mJy at C-band (Griffith et al., 1995). 110% of this single-dish C-band flux is recovered in an unresolved component with the VLBA, when mapped using robust=0 weighting to give a beam of 5.67×1.41 milliarcsecs, suggesting that this core is variable. This source is line emitting and not in the VLBA calibrators list.

MACS0242-21

BCG identified as PKS 0240-217. This source is expected to be core dominated and its SED is well-fit with a low-peaking GPS-like model (see Chapter 4). The source was obseved with the ATCA-6km array at 5 GHz in 2011 (C1958, see Chapter 3) and found to be 904±45mJy. The VLBA observation is imaged with robust=0 weighting to give a beam of 6.61×1.31 milli-arcsecs. There is a distinct component to the south-east, which is also recovered at both 2.3 GHz and 8 GHz in maps from the VLBA calibrator list (Beasley et al., 2002). The integrated VLBA flux recovers ≈27% of the arcsecond scale flux seen

with the ATCA. The source is line emitting.

A383

BCG identified as 2MASX J02480342-0331447. This source was claimed to be 16.3$\pm$1.6mJy at 4.85 GHz with the Effelsberg telescope in 2009 but not recovered at 10.45 GHz ($<$6.5mJy) in simultaneous observations (Angelakis et al., 2009). The source is detected to be 4.4mJy with BIMA at 28.5mJy (Coble et al., 2007). The source is not in the Main Sample (see Chapter 3) so some confusion remains. The source is detected with the VLBA in project BE063 and found to be unresolved, with $\geq$23.9% of the Effelsberg C-band flux recovered, when imaged with robust=0 weighting and a beam 4.57$\times$1.43 milliarcsecs. The source is line-emitting and not in the VLBA calibrators list.

RXJ0341+15

BCG identified as III Zw054. This object has a flat spectrum SED and was found to be $\approx$11-13mJy at C-band when observed with the VLA-C array in 1996, 1997 and 1999 (AE107, AE110 and AE125 respectively, see Chapter 3). This is the only source to be observed twice with the VLBA in project BE063. The recovered fluxes for each of these two runs are consistent with no change in the 3 days between observations, when imaged using robust=0 weighting to give synthesised beams of 3.44$\times$1.64 milli-arcsec and 9.29$\times$2.25 milli-arcsec for 7th March and 10th March 2013 observations respectively. The individual maps for each of the runs are fairly messy although there is a hint of extent. Combining the uv-data with DBCON and then imaging with a beam 3.32$\times$1.71 milli-arcsecs returns a source with a consistent peak flux but a slightly higher total flux ($\approx$4.9mJy) as there now appears to be steady extent to South-East. Note that this is lower than the predicted core component of $\approx$9.47$\pm$1.58mJy at 10 GHz. The source is non-line emitting and is not in VLBA calibrators list.

RXJ0352+19

BCG identified as 2MASX J03525901+1940595. This source has a flat SED, was observed to be 7.68mJy at C-band in 1994 with the VLA-C array (AE099, see Chapter 3) and predicted to have a core component of $\approx$11.4$\pm$5.7mJy at 10 GHz. The object is

detected with the VLBA and is unresolved when imaged using robust=0 weighting that gives a beam of 3.38×1.51 milli-arcsecs. The recovered flux is ≈57% of that seen on arcsecond scales with the VLA. This is line emitting and is not in the VLBA calibrator list.

A478

BCG identified as 2MASX J04132526+1027551. This has a flat spectrum component to its SED and is expected to contain an active core within steeper spectrum lower frequency emission. There appear to be no previous C-band observations of this BCG although it was seen to be 5.8mJy at L-band in 1997 with the VLA-A (AE117, see Chapter 3). When imaged with robust=0 weighting and a beam of 3.59×1.54 milli-arcsecs, the source appears to have a one-sided jet to the South-West. The integrated flux on milli-arcsecond scales is ≈50% of that seen on arcsecond scales, assuming a core dominated flat spectrum SED. This is line emitting and not in the VLBA calibrators list.

MACS0429-02

BCG identified as PMN J0429-0253/2MASX J04293604-0253073. There is very little radio coverage of this source. It does not appear within the Main Sample (see Chapter 3) although it was observed to be 71±11mJy at 5 GHz in the PMN catalog (Griffith et al., 1995) and undetected at 90 GHz with CARMA (see Chapter 4). The source is detected with the VLBA in project BE063, and when imaged using robust=0 weighting to give a beam 4.34×1.53 appears to have a jet to the North-East. The integrated flux is ≈24.5% of that in the archival low-resolution C-band observation. There is potentially also another component in here a few milli-arcsecs to the East but the mapping capability is limited (snapshot uv-coverage) so cannot robustly claim this component. The source is not in the VLBA calibrators list.

RXJ0747-19

BCG identified as PKS 0745-191. This is a large extended source at lower frequencies and is dominated by the diffuse radio component in low-resolution maps. Observed at C-band in 2008 with the ATCA-6km and found to have a peak of 247.1mJy from a total

flux of 368.1mJy (C1958, see Chapter 3). Lack of high resolution observations means that previously only a limit of $<$75.0mJy could be placed on the core component at 10 GHz although apparent variability at C- and X-bands hinted at the presence of a active core. A weak nuclear component is recovered in the BE063 VLBA imaging. Imaging with uniform (robust=-5) weighting gives no sensible map whereas both robust=0 and natural weighting (robust=5) suggest a jet to the North-East. Robust=0 gives a beam 6.36$\times$3.81 milli-arcseconds. The integrated milliarcsecond flux constitutes only $\approx$2.6% of that seen at lower resolution with the ATCA. The source is line emitting and not in the VLBA calibrators list.

RXJ0751+50

BCG identified UGC 04052. Observed to be 5.98mJy at C-band in 1997 with the VLA-C array (AE110, see Chapter 3), this source appears to be core dominated and has a flat spectrum SED. It is predicted to contain a core component of $\approx$4.80$\pm$1.08mJy at 10 GHz. The source is detected in VLBA BE063 imaging, using robust=0 weighting with beam of 3.43$\times$1.52 milli-arcseconds and on milli-arcsecond scales is unresolved and recovers $\approx$60% of the lower-resolution flux. This source is line emitting and not in the VLBA calibrator list.

Z1665

BCG identified as IC505. This source does not have overly extensive radio-coverage, although it was observed as 8.29mJy at C-band in 1997 with the VLA-C array (AE110, see Chapter 3) and has an apparently flat spectrum. It was predicted to contain a core component of $\approx$5.97$\pm$2.88mJy at 10 GHz. The source is detected on milli-arcsecond scales with the VLBA. Imaging using robust=0 weighting gives a beam of 3.86$\times$1.80 milli-arcsecs and shows a weak, one-sided jet to the North-West. The integrated flux contains $\approx$43% of that seen in the unresolved VLA-C array map. This source is line emitting and is not a VLBA calibrator.

4C+55.16

BCG identified as 2MFGC 06756. This is a large, well-observed and extended source on

arcsecond scales. A VLA-derived core flux measurement from 1997 (Laurent-Muehleisen et al., 1997) put the arcsecond core at 5600mJy. The source is detected with the VLBA and appears to be highly structured on milli-arcsecond scales. Imaging with robust=0 weighting gives a beam of 3.47×1.23 milli-arcseconds and shows a two-sided structure with the opposing jets in a SW/NE orientation, the integrated flux of which constitutes $\approx$47% of the core attributed flux in the lower resolution VLA imaging. There appears to be a lot of structure in this source which with limited uv-coverage does not seem to be fully recovered so this recovered fraction is maybe best interpreted as a lower limit. This source is a VLBA-calibrator and has multi-frequency VLBI coverage (e.g Beasley et al., 2002; Horiuchi et al., 2004; Kovalev et al., 2005; Helmboldt et al., 2007). Much extended emission is seen at 2.3 GHz, not all of which appears to be present (in particular a large, extended lobe to NE) in the current data although it should be noted that there is very little extended emission at 8.6 GHz. This suggests we are seeing the intermediate extent of steeper spectrum extended emission (on few parsec scales) that falls below the detection limits to higher frequency, although the limited uv-coverage should also be considered when interpreting the maps.

Z2701

BCG identified as 2MASX J09524915+5153053. This is a steep spectrum radio source at low frequency, that was observed twice with the VLA-C array, being measured at 4.20mJy in 1994 and 3.85mJy in 1999 (AE099 and AE125 respectively, see Chapter 3). However, as a result of its spectral properties this source was predicted to not contain an active core component and a limit of $<$3.14mJy was predicted at 10 GHz. No source is detected with the VLBA using either robust=0 or fully natural weighting. A map with robust=0 returns a beam size of 3.56×1.44 milli-arcseconds. Using a 3σ limit above the local noise as our detection threshold we set that $<$3% of the arcsecond scale flux can be on parsec scales. This is a line emitter and is not a VLBA calibrator.

Z2844

BCG identified as NGC 3099. This source has a flat radio spectrum at low frequency. It was observed twice with the VLA-C array and found to contain 9.1mJy at C-band in

1997 and 8.9mJy at C-band in 1999 (AE110 and AE125 respectively, see Chapter 3), It was predicted to contain a core component of $\approx$7.4$\pm$4.0mJy at 10 GHz. The source appears unresolved in VLBA mapping, using a robust=0 weighting and a beam 3.30$\times$1.46 milli-arcseconds. $\approx$33% of the VLA-C flux is recovered on VLBA scales. This is a non-line emitter and is not in the VLBA calibrators list.

A1084

BCG identified as 2MASX J10443287-0704074. The source has a flat radio spectrum and is unresolved at arcsecond scale resolution in the GHz-range, suggestive of a dominant core. It was predicted to contain a core component $\approx$27.3$\pm$4.5mJy at 10 GHz and was observed to be 29.0mJy at C-band with the VLA-C array in 1994 (AE099, see Chapter 3). In the VLBA mapping using robust=0 weighting with a beam 4.35$\times$1.45 milli-arcsecs the source appears to be extended to the North-East, with a semi-distinct hot-spot that may be best interpreted as a one-sided jet. The integrated milli-arcsecond scale flux recovers $\approx$45% of the unresolved arcsecond scale flux This object is line emitting and is not in the VLBA calibrators list.

A1664

BCG identified as 2MASX J13034252-2414428. Unresolved at arcsecond scales and exhibits spectral flattening towards higher frequencies indicative of containing an active core. Predicted to contain a $\approx$10.1$\pm$1.4mJy core component at 10 GHz and observed at C-band to contain 14.4mJy with the VLA-C array in 1994 and 14.9mJy with the ATCA-6km in 2011 (AE099 and C1958 respectively, see Chapter 3). Imaging with robust=0 weighting gives a beam 6.61$\times$1.13 milli-arcsecs. The source is extended, with a second component visible to the north of the nucleus (note that this is more obvious when using a naturally weighted map). The integrated VLBA flux recovers $\approx$51% of the more recent lower resolution measurement with ATCA. This is a line-emitter and is not in the VLBA calibrators list.

NGC5044 / RXJ1315-16

BCG identified as NGC 5044. Unresolved GPS-like source. Observed with the ATCA-

6km in 2008 and measured to contain 21.1mJy at C-band (C1958, see Chapter 3), this source has a predicted core component of $\approx$10.4$\pm$6.7mJy at 10 GHz. The object is clearly extended on VLBA-scales. Imaging with robust=0 weighting causes FITBM to fail and the mapping collapses to a uniformly weighted deconvolution with a beam 1.41$\times$1.41 milli-arcseconds. Even with this unsatisfactory beam, two main components are detected with a combined flux recovering $\approx$73% of the 2008 flux, with potential further components to North-West. Using natural weighting (robust=5) with the corresponding larger beam of 6.13$\times$3.40mas, merges the main components but does add weight to the likely presence of additional emission to the North-West, although at the expense of quite large sidelobes which appear to make the flux less reliable. Using the uniformly weighted map but measuring the flux within the extended emission region defined using the naturally weighted image, $\approx$117% of the 2008 ATCA flux is recoved with the VLBA. This is highly suggestive of strong variability in the core of this source, expecially when we consider that further, extended few-parsec scale emission may be being lost to uv-coverage. Clearly a very active core dominating the total radio output of this source at 5 GHz. This is a line emitter and is not a VLBA calibrator.

NGC5098 / RXJ1320+33

BCG identified as NGC5098. This object has a relatively shallow radio spectral index yet is clearly resolved and dominated by diffuse emission at arcsecond resolutions with an unresolved central component, that remains to higher frequency, indicative of ongoing activity within the centre. Predicted to contain a core component of $\approx$7.0$\pm$2.4mJy at 10 GHz and observed in 1999 with the VLA-C array to have an unresolved central component of 10.8mJy (AE125, see Chapter 3). Imaging with robust=0 weighting with a corresponding beam size of 3.35$\times$1.35 milli-arcsecs gives an unresolved source (although there is potentially very faint extent to the south-west). The integrated VLBA flux recovers $\approx$38.5% of the 1999 VLA-C central unresolved component's flux. This source is line emitting and not a VLBA calibrator.

MACS1347-11

BCG identified as NVSS J134730-114508. This source has a reasonably steep spectral

index although there is some flattening to a 28.5 GHz OVRO flux of 9.93±0.23mJy measured in 2007 (Coble et al., 2007) that suggests there may be an underlying but nevertheless active core. There are no direct C-band measurements although L-band observations suggest a core component (≈29.8mJy) is present. Gitti et al. (2007) show the presence of a mini-halo in this cluster. VLBA imaging, with robust=0 weighting gives a fairly elliptical beam of 11.24×1.89 milli-arcsecs. The central source is recovered and appears to be unresolved and contain >80% of the extrapolated arcsecond scale flux. This is a line emitter and is not in the VLBA calibrators list.

A3581

BCG identified as IC 4374. This object has a flat spectrum SED down to low frequencies (e.g. 74 MHz with VLSS, Cohen et al., 2007). It was observed to be 314.7mJy at C-band and unresolved on arcsecond scales with the ATCA-6km in 2008 (C1958, see Chapter 3). This source was predicted to contain a core-component of 92.7±13.2mJy at 10 GHz. The source is in the VLBA calibrators list. At 2.3 GHz, extended emission is seen as a one-sided jet to the West extending ≈15mas. This is further resolved into a core and two apparent knots in the jet to the West, that extend ≈15mas at 8.3 GHz. The source is recovered at C-band in our BE063 VLBA data. Imaging using robust=0 weighting gives an elliptical beam 6.95×1.13 milli-arcsecs. The inner of the two knots seen at 8.3 GHz is recovered (≈6mas from core) although the further component is not apparent. A naturally weighted map (robust=5) gives a larger beam of 7.52×4.90mas, which covers the inner knot and no further extent Westwards is seen. Uniform weighting (robust=-5) gives a sharp 1.41×1.41mas beam and recovers the same two components as the robust=0 weighted map, although the image is noisier. Using the robust=0 map, the recovered flux from the two unambiguous components accounts for ≈49% of the unresolved ATCA flux, suggesting that some flux may be lost or that there is significant emission on intermediate scales. Note also that the peak of the knot recovered at C-band is slightly lower than the archived X-band peak, whereas this trend is reversed for the core This suggests that the knot may have a strongly self-absorbed peak. This is a line emitter.

A1885

BCG identified as 2MASX J14134379+4339450. This source is flat spectrum, with a 325 MHz WISH (De Breuck et al., 2002) observation suggesting it could be classified as GPS-like. Measured unresolved C-band flux of 35.3mJy in 1994 and 36.7mJy in 1999, both with VLA-C array (AE099 and AE125 respectively, see Chapter 3). Predicted to contain a core component of $\approx$41.4$\pm$22.1mJy at 10 GHz. Imaged using robust=0 weighting with a corresponding beam 3.72$\times$1.29 milli-arcsec, on parsec scales this object has a jet to the SE and a weak opposing counter-jet showing it to be two-sided. The integrated flux on VLBA-scales is $\approx$73.7% of the 1999 VLA measurement, confirming the source to be highly core dominated. This source is line emitting and is not in the VLBA calibrators list.

RXJ1442+22

BCG identified as UGC9480. This object is unresolved at arcsecond resolution and seen to be 11.0mJy at C-band with the VLA-C array in 1999 (AE125, see Chapter 3). Classified as flat spectrum and so likely core-dominated, with a predicted core component of $\approx$8.35$\pm$1.10mJy at 10 GHz. Imaging our VLBA BE063 data with robust=0 weighting and a beam 3.48$\times$1.17 milli-arcseconds recovers a faint central object with a weak one-sided jet to the South-west. The integrated emission on milli-arcsecond scales accounts for only $\approx$17% of the VLA-C array unresolved flux, suggesting that this object is likely to contain significant flux on intermediate scales. Source is not in the VLBA calibrators list and is line-emitting.

MACS1447+08

Not in main sample. BCG identified as 2MASX J14472597+0828253. The only archival radio measurement of this source available in NED is 43.6$\pm$1.4mJy at 1.4 GHz as seen in NVSS (Condon et al., 1998). A parsec-scale source is detected in our VLBA data. This is imaged using robust=0 weighting with a beam 5.33$\times$1.12 milli-arcsecs and is unresolved. Cannot put a meaningful value on the recovered flux fraction. This BCG is line emitting and is not in the VLBA calibrators list.

A2052

BCG identified as 3C317/UGC 09799. The SED of this source is dominated by steep

spectrum, extended amorphous halo emission on large scales, although spectral flattening and archival VLBI observations (Venturi et al., 2004) show there is an active parsec scale core (see also Chapter 4). Venturi et al. (2004) observed this source with the VLBA at 1.7, 4.9 and 8.3 GHz, finding a consistent two-sided jet structure in a roughly NNE-SSW orientation, which they suggest shows that this is a young, possibly restarted core. Our snapshot C-band map, imaged with robust=0 weighting and beam size 3.63×1.39 milli-arcsec recovers similar structure with comparable extent (≈14mas) and consistent flux (within 1-sigma) to their C-band image. This recovered flux is actually ≈128% of the unresolved central component in a 1997 VLA-A array core measurement (Laurent-Muehleisen et al., 1997) although is only ≈35% of the integrated arcsecond scale flux at C-band. The BCG is line emitting and is not in the VLBA calibrators list.

A2055

BCG identified as 2MASX J15184574+0613554. This is a resolved head-tail source with a flat component in its SED suggesting the presence of an active component (see also Chapter 4). Predicted to contain a core contribution of ≈92.4±38.7mJy at 10 GHz and observed to have a 'head' of 107.0mJy from a 213.4mJy integrated flux using the VLA-C array in 1999 at C-band (AE125, see Chapter 3). An unresolved nuclear component is detected in our VLBA observation which when mapped using robust=0 weighting with a 5.24×1.20 milli-arcsecond beam contains ≈32.5% of the 'head' flux as seen with the VLA-C. The BCG is line emitting and is not in the VLBA calibrator list.

MACS1532+30

BCG identified as SDSS J153253.78+302059.3. A compact steep spectrum source. The presence of an active component could not robustly be determined from low-resolution observations and a limit was placed on any such component of <4.0mJy at 10 GHz. The source was observed with the VLA-C in 1997 (AE110, see Chapter 3) and found to contain 8.8mJy of unresolved flux at C-band. Imaging our BE063 VLBA data with robust=0 imaging gives a beam size 3.41×1.29 milli-arcseconds. A faint parsec-scale source with a weak one-sided jet to the East is detected, whose total integrated emission recovering ≈34% of the VLA-C array value. This is line emitting and not in the VLBA calibrator list.

A2146

BCG identified as 2MASX J15561395+66205303. Flat spectrum source that appears to be core dominated. It has a predicted core component of $\approx$6.0$\pm$0.7mJy at 10 GHz and was observed to be unresolved and 9.7mJy at C-band with the ATCA-6km in 2008 (C1958, see Chapter 3). A nuclear component is detected with the VLBA, which appears unresolved when imaged using robust=0 weighting with a beam 4.66$\times$1.89 milli-arcseconds. The recovered flux is less than expected, accounting for $\approx$8% of the ATCA measure. This suggests that there may be significant emission on intermediate scales. The BCG is line emitting and not in the VLBA calibrators list.

NGC6338 / RXJ1715+57

BCG identified as NGC 6338. Source is flat spectrum and expected to be core dominated (see Chapter 4). Observed to be 30.5mJy at C-band with the VLA-C array in 1997 (AE110, see Chapter 3) and predicted to contain a $\approx$29.9$\pm$6.7mJy core component at 10 GHz. Imaging the VLBA data with robust=0 weighting with a beam 4.05$\times$1.26 milli-arcseconds shows the nuclear source to have a one-sided jet to the South-East. The integrated milli-arcsecond flux accounts for $\approx$74.7% of the 1997 VLA measurement. This is a line emitting BCG and is not in the VLBA calibrators list.

RXJ1720+26

BCG identified as 2MASX J17201001+2637317. Spectrally expected to contain an active core component in amongst reasonably bright diffuse emission that dominates at low frequencies. Observed with the VLA-C array in 1999 and found to be extended radio source with an unresolved central component of 2.7mJy (AE125, see Chapter 3). Predicted to have a core component of $\approx$3.4$\pm$1.8mJy at 10 GHz. A faint, unresolved nuclear source is detected with the VLBA, when imaged using robust=0 weighting with a beam 3.18$\times$1.17 milli-arcseconds. The recovered flux constitutes $\approx$25% of that in the the unresolved central component on arcsecond scales seen with the VLA-C array. This source is line emitting and does not appear in the VLBA calibrators list.

A2270

BCG identified as 2MASX J17272346+5510538. This source is highly active and expected to be highly core dominated (see Chapter 4). On VLBA scales, a strong and unresolved source is detected when imaged using robust=0 weighting with a beam 4.07×1.35 milli-arcseconds. This is consistent with similarly unresolved detections at 2.3 and 8.3 GHz in the VLBA calibrators list (see Bourda et al., 2010, 2011; Petrov, 2011). The recovered flux is consistent with a previous VLBA observation (Helmboldt et al., 2007) and accounts for ≈60% of the unresolved arcsecond scale flux. This BCG is a line emitter.

IC1262 / RXJ1733+43

BCG identified as IC1262. At low frequencies (<1 GHz) this source is be dominated by diffuse emission on few arcsecond scales. It appears to have a flat spectrum component to its SED that is predicted to contain a ≈4.1±1.1mJy core contribution at 10 GHz. It was observed to have an unresolved arcsecond scale central component of 5.5mJy at C-band with the VLA-C array in 1997 (AE110, see Chapter 3). Imaging the VLBA data using robust=0 weighting with a beam 3.76×1.18 milli-arcseconds shows the central regions to contain a weak one-sided jet to the South-West. The total recovered parsec scale flux equivalent to ≈44% of the 1997 arcsecond scale flux. This BCG is a line emitter and is not in the VLBA calibrator list.

RXJ1750+35

BCG identified as 2MASX J17501683+3504587. This object has a flat spectrum and appears to be core dominated. Observed to be 31.9mJy and unresolved at C-band with the VLA-C array in 1996 (AE107, see Chapter 3). It was predicted to contain a core component of ≈26.3±4.1mJy at 10 GHz. The source is detected with the VLBA and contains a one-sided jet to the West. The integrated emission on milli-arcsecond scales recovering ≈52.8% of the measured flux in the 1996 VLA observation, when imaged using robust=0 weighting with a beam 3.52×1.15 milli-arcseconds. The BCG is a line emitter and is not in the VLBA calibrator list.

RXJ1832+68

BCG identified as 2MASX J18323551+6848059. High frequency variability suggests presence of an active core below the low-frequency dominant steep spectrum emission (see Chapter 4). There was an arcsecond scale core measurement of 25mJy taken with the VLA-A array by Laurent-Muehleisen et al. (1997). The source is detected with the VLBA. When imaged using robust=0 weighting and a beam 4.70×1.13 milli-arcseconds it appears extended to both the SWW and NEE, with the SWW appearing to have a distinct 'hot-spot' whereas the NEE extent appears to be a steady jet. The integrated flux in our VLBA map recovers $\approx$115% of the 1997 arcsecond scale core measurement, suggesting that this source is variable over $\approx$decade timescales. The BCG is line emitting and is not in the VLBA calibrators list.

MACS1931-26

BCG identified as PMN J1931-2635. This BCG is surrounded by (at least) two other radio sources that appear confused in at some lower resolution maps of the cluster and leads to a difficult to interpret SED (see Chapter 4). The source is however predicted to contain parsec-scale core activity. The only previous C-band measurement appears to be detection of 89 ± 11mJy in the PMN catalogue (Griffith et al., 1994). This source appears to have significant structure on milli-arcsecond scales and hence calibration and mapping are more awkward. Self-fringing provides unsatisfactory results. The source is consistently detected when the data is not self-fringed but the final map suffers from artefacts that suggest significant phase errors remain. Source appears to have multiple components that are not being adequately recovered. When imaged using robust=0 weighting with a beam 8.04×1.34 milli-arcseconds, most artefacts can removed by interactive CLEANing but the recovered components are dependent on the CLEANing priors, which are naturally likely to be uncertain and hence these components are not considered robust. Natural weighting (robust=5) improves the beam slightly to 8.00×4.19mas and allows more reliable clean boxing. Some detail is lost with this weighting but consistent central components are recovered, albeit still with many apparent mapping artefacts. A similar result is achived using a sharp beam (1.41×1.41mas) formed using purely uniform weighting. Use the naturally weighted image and take a flux measurement from only the components that are consistent across the differently weighted maps. These suggest a core with a one

sided jet to the North-East and a second component to the South-East. It is likely that there is still missing flux so best to take this as a lower-limit of $>$22.6% of the PMN flux being recovered. This BCG is line emitting and is not in the VLBA calibrators list.

RXJ2129+00

BCG identified as 2MASX J21293995+0005207. This source was observed to be 9.1mJy and unresolved on arcsecond scales with the VLA-C array in 1996 (AE107, see Chapter 3). Predicted to contain an active core component with sub-arcsecond scale diffuse emission, with a core contribution at 10 GHz of $\approx$3.7$\pm$1.0mJy. An unresolved milli-arcsecond scale source is detected with the VLBA using a robust=0 weighted map with a beam 3.75$\times$1.59 milli-arcseconds. This recovers $\approx$ 28.5% of the 1996 arcsecond scale flux. The BCG is a line emitter and is not in the VLBA calibrators list.

A2627

BCG identified as B2 2334+23, although the nearby 2MASX J23364245+2354442 is also radio-loud and appears to be confused in some lower resolution observations particularly at low-frequency. A parsec-scale core is predicted to contribute $\approx$54.8$\pm$9.2mJy at 10 GHz, although significant flux is expected on intermediate scales. Observed in 1996 with the VLA-C array and found to be slighly resolved with the central unresolved component being 88.4mJy (AE107, see Chapter 3). The source is detected with the VLBA and is imaged using robust=0 weighting with a beam 3.40$\times$1.36 milli-arcsecs. The source is extended East-West with an additional jet-like component to the North-East. The total recovered flux on milli-arcsecond scales is $\approx$29.4% of the unresolved central component observed with the VLA-C array in 1996. The BCG is a line emitter and not in the VLBA calibrators list.

RXJ2341+00

BCG identified as PKS 2338+000. This source has a low frequency ($\approx$0.1 GHz) peaking GPS-like SED (see Chapter 4). Multiple single-dish C-band observations all recover around 300mJy (e.g Wright & Otrupcek, 1990; Becker et al., 1991; Griffith et al., 1995). The source is a VLBA calibrator (Petrov et al., 2005) with available images from 1995.

At 2.3 GHz it has a one-sided jet structure extending ≈30mas to the North-West whereas at 8.3 GHz this structure is mainly resolved out, with the only extent being a knot ≈12mas to the North-west of the core. The source is detected in the BE063 data. When imaged with robust=0 weighting and beam 4.59×1.49 milli-arcseconds, the source appears to be largely unresolved with only a potential one-sided jet to the North-West. There is a suggestion of a second component at a similar position to the earlier observations, however this falls on the first side-lobe position and hence to clean it is potentially also cleaning a lobe leading to uncertain flux. Minimising sidelobe levels using uniform weighting (robust=-5, beam somewhat curiously 4.40×1.37mas) does now minimise the counter-lobe much more than the unfortunately positioned one so do believe there is probably a real component in there. Image with clean boxes in relevant positions using robust=0. Recover a two component source, which when combined account for ≈30% of the single-dish C-band flux. This BCG is a line emitter.

A2667

BCG identified as 2MASX J23513947-2605032. This source has a flat spectrum SED and was found to be unresolved on arcsecond scales at C-band with flux of 9.0mJy in 2008 when observed with the ATCA-6km (C1958, see Chapter 3). This object is predicted to contain a ≈7.6±2.1mJy core component at 10 GHz. The source is unresolved on parsec scales with the VLBA when imaged using robust=0 weighting with a beam 7.69×1.29 milli-arcseconds. The recovered flux accounts for ≈15.3% of that recovered on arcsecond scales with the ATCA. The BCG is a line emitter and is not in the VLBA calibrators list.

Bibliography

Abdo, A. A., Ackermann, M., Ajello, M., et al. 2009, ApJ, 699, 31

Abramowicz, M. A., Chen, X., Kato, S., Lasota, J.-P., & Regev, O. 1995, ApJ, 438, L37

Abramowicz, M. A., Czerny, B., Lasota, J. P., & Szuszkiewicz, E. 1988, ApJ, 332, 646

Abramowicz, M. A., & Fragile, P. C. 2013, Living Reviews in Relativity, 16, 1

Aharonian, F., Akhperjanian, A. G., Barres de Almeida, U., et al. 2008, Physical Review Letters, 101, 261104

Ahn, C. P., Alexandroff, R., Allende Prieto, C., et al. 2014, ApJS, 211, 17

Akritas, M. G., & Bershady, M. A. 1996, ApJ, 470, 706

Alexander, D. M., & Hickox, R. C. 2012, New A Rev., 56, 93

Allen, S. W., Dunn, R. J. H., Fabian, A. C., Taylor, G. B., & Reynolds, C. S. 2006, MNRAS, 372, 21

Allen, S. W., & Fabian, A. C. 1998, MNRAS, 297, L63

Aller, H. D., Aller, M. F., Latimer, G. E., & Hodge, P. E. 1985, ApJS, 59, 513

Aller, M. F., Aller, H. D., Hughes, P. A., & Plotkin, R. M. 2002, in Proceedings of the 6th EVN Symposium, ed. E. Ros, R. W. Porcas, A. P. Lobanov, & J. A. Zensus, 131

Aller, M. F., Hughes, P. A., Aller, H. D., Latimer, G. E., & Hovatta, T. 2014, ApJ, 791, 53

AMI Consortium, Franzen, T. M. O., Davies, M. L., et al. 2011, MNRAS, 415, 2699

Angelakis, E., Kraus, A., Readhead, A. C. S., et al. 2009, A&A, 501, 801

Antonucci, R. 1993, ARA&A, 31, 473

Arav, N. 1996, ApJ, 465, 617

Araya, E. D., Rodríguez, C., Pihlström, Y., et al. 2010, AJ, 139, 17

Arnaud, M., Rothenflug, R., Boulade, O., Vigroux, L., & Vangioni-Flam, E. 1992, A&A, 254, 49

Augusto, P., Edge, A. C., & Chandler, C. J. 2006, MNRAS, 367, 366

Azadi, M., Aird, J., Coil, A., et al. 2014, ArXiv e-prints

Baade, W., & Minkowski, R. 1954, ApJ, 119, 206

Baars, J. W. M., Genzel, R., Pauliny-Toth, I. I. K., & Witzel, A. 1977, A&A, 61, 99

Barvainis, R., Lehár, J., Birkinshaw, M., Falcke, H., & Blundell, K. M. 2005, ApJ, 618, 108

Beasley, A. J., Gordon, D., Peck, A. B., et al. 2002, ApJS, 141, 13

Becker, R. H., White, R. L., & Edwards, A. L. 1991, ApJS, 75, 1

Becker, R. H., White, R. L., & Helfand, D. J. 1995, ApJ, 450, 559

Beckmann, V., & Shrader, C. 2012a, in Proceedings of "An INTEGRAL view of the high-energy sky (the first 10 years)" - 9th INTEGRAL Workshop and celebration of the 10th anniversary of the launch (INTEGRAL 2012). 15-19 October 2012. Bibliotheque Nationale de France, Paris, France.

Beckmann, V., & Shrader, C. R. 2012b, Active Galactic Nuclei

Beers, T. C., & Tonry, J. L. 1986, ApJ, 300, 557

Bell, A. R. 1978a, MNRAS, 182, 147

—. 1978b, MNRAS, 182, 443

Bell, E. F., Wolf, C., Meisenheimer, K., et al. 2004, ApJ, 608, 752

Belsole, E., Birkinshaw, M., & Worrall, D. M. 2005, MNRAS, 358, 120

Bennett, A. S. 1962, MmRAS, 68, 163

Benson, A. J., Bower, R. G., Frenk, C. S., et al. 2003, ApJ, 599, 38

Benson, J. M. 1995, in Astronomical Society of the Pacific Conference Series, Vol. 82, Very Long Baseline Interferometry and the VLBA, ed. J. A. Zensus, P. J. Diamond, & P. J. Napier, 117

Best, P. N., & Heckman, T. M. 2012, MNRAS, 421, 1569

Best, P. N., Kaiser, C. R., Heckman, T. M., & Kauffmann, G. 2006, MNRAS, 368, L67

Best, P. N., Kauffmann, G., Heckman, T. M., et al. 2005, MNRAS, 362, 25

Best, P. N., von der Linden, A., Kauffmann, G., Heckman, T. M., & Kaiser, C. R. 2007, MNRAS, 379, 894

Biretta, J. A., Bartel, N., & Deng, J. 1991, in Astronomical Society of the Pacific Conference Series, Vol. 19, IAU Colloq. 131: Radio Interferometry. Theory, Techniques, and Applications, ed. T. J. Cornwell & R. A. Perley, 334–337

Bîrzan, L., McNamara, B. R., Nulsen, P. E. J., Carilli, C. L., & Wise, M. W. 2008, ApJ, 686, 859

Bîrzan, L., Rafferty, D. A., McNamara, B. R., Wise, M. W., & Nulsen, P. E. J. 2004, ApJ, 607, 800

Blandford, R. D., & Payne, D. G. 1982, MNRAS, 199, 883

Blandford, R. D., & Rees, M. J. 1978, in BL Lac Objects, ed. A. M. Wolfe, 328–341

Blandford, R. D., & Znajek, R. L. 1977, MNRAS, 179, 433

Blanton, E. L., Sarazin, C. L., McNamara, B. R., & Wise, M. W. 2001, ApJ, 558, L15

Blanton, M. R., Eisenstein, D., Hogg, D. W., & Zehavi, I. 2006, ApJ, 645, 977

Boehringer, H., Voges, W., Fabian, A. C., Edge, A. C., & Neumann, D. M. 1993, MNRAS, 264, L25

Böhringer, H., Voges, W., Huchra, J. P., et al. 2000, ApJS, 129, 435

Böhringer, H., Schuecker, P., Guzzo, L., et al. 2004, A&A, 425, 367

Bolton, J. G., & Stanley, G. J. 1948, Nature, 161, 312

Bolton, J. G., Stanley, G. J., & Slee, O. B. 1949, Nature, 164, 101

Bonafede, A., Intema, H. T., Brüggen, M., et al. 2014, ArXiv e-prints

Bondi, H. 1952, MNRAS, 112, 195

Booth, R. S., de Blok, W. J. G., Jonas, J. L., & Fanaroff, B. 2009, ArXiv e-prints

Bourda, G., Charlot, P., Porcas, R. W., & Garrington, S. T. 2010, A&A, 520, A113

Bourda, G., Collioud, A., Charlot, P., Porcas, R., & Garrington, S. 2011, A&A, 526, A102

Bower, R. G., Benson, A. J., Malbon, R., et al. 2006, MNRAS, 370, 645

Boylan-Kolchin, M., Springel, V., White, S. D. M., Jenkins, A., & Lemson, G. 2009, MNRAS, 398, 1150

Broten, N. W., Legg, T. H., Locke, J. L., et al. 1967, Science, 156, 1592

Brough, S., Collins, C. A., Burke, D. J., Mann, R. G., & Lynam, P. D. 2002, MNRAS, 329, L53

Buote, D. A. 2001, ApJ, 553, L15

Burke, D. J., Collins, C. A., & Mann, R. G. 2000, ApJ, 532, L105

Burns, J. O. 1990, AJ, 99, 14

Burns, J. O., Sulkanen, M. E., Gisler, G. R., & Perley, R. A. 1992, ApJ, 388, L49

Burns, J. O., White, R. A., & Hough, D. H. 1981, AJ, 86, 1

Buta, R. J. 2011, ArXiv e-prints

Butcher, H., & Oemler, Jr., A. 1978, ApJ, 219, 18

Canning, R. E. A., Sun, M., Sanders, J. S., et al. 2013, MNRAS, 435, 1108

Cappellari, M., Emsellem, E., Krajnović, D., et al. 2011, MNRAS, 413, 813

Carlstrom, J. E., Ade, P. A. R., Aird, K. A., et al. 2011, PASP, 123, 568

Cassano, R., Ettori, S., Giacintucci, S., et al. 2010, ApJ, 721, L82

Cattaneo, A., Faber, S. M., Binney, J., et al. 2009, Nature, 460, 213

Cavagnolo, K. W., Donahue, M., Voit, G. M., & Sun, M. 2008, ApJ, 683, L107

Cavagnolo, K. W., McNamara, B. R., Nulsen, P. E. J., et al. 2010, ApJ, 720, 1066

Chapin, E. L., Berry, D. S., Gibb, A. G., et al. 2013, MNRAS, 430, 2545

Chen, Y.-M., Tremonti, C. A., Heckman, T. M., et al. 2010, AJ, 140, 445

Christiansen, W. N., & Hindman, J. V. 1952, Australian Journal of Scientific Research A Physical Sciences, 5, 437

Christiansen, W. N., & Warburton, J. A. 1955, Australian Journal of Physics, 8, 474

Churazov, E., Brüggen, M., Kaiser, C. R., Böhringer, H., & Forman, W. 2001, ApJ, 554, 261

Churazov, E., Ruszkowski, M., & Schekochihin, A. 2013, MNRAS, 436, 526

Cleary, K. A., Taylor, A. C., Waldram, E., et al. 2005, MNRAS, 360, 340

Coble, K., Bonamente, M., Carlstrom, J. E., et al. 2007, AJ, 134, 897

Cohen, A. S., & Clarke, T. E. 2011, AJ, 141, 149

Cohen, A. S., Lane, W. M., Cotton, W. D., et al. 2007, AJ, 134, 1245

Comerford, J. M., Schluns, K., Greene, J. E., & Cool, R. J. 2013, ApJ, 777, 64

Condon, J. J., Broderick, J. J., Seielstad, G. A., Douglas, K., & Gregory, P. C. 1994, AJ, 107, 1829

Condon, J. J., Cotton, W. D., Greisen, E. W., et al. 1998, AJ, 115, 1693

Conselice, C. J. 2014, ArXiv e-prints

Conselice, C. J., Gallagher, III, J. S., & Wyse, R. F. G. 2001, AJ, 122, 2281

Conway, J. E., & Blanco, P. R. 1995, ApJ, 449, L131

Cooper, A. P., Gao, L., Guo, Q., et al. 2014, ArXiv e-prints

Cowie, L. L., & Binney, J. 1977, ApJ, 215, 723

Cowie, L. L., Hu, E. M., Jenkins, E. B., & York, D. G. 1983, ApJ, 272, 29

Coziol, R., Andernach, H., Caretta, C. A., Alamo-Martínez, K. A., & Tago, E. 2009, AJ, 137, 4795

Crane, P., van der Hulst, J., & Haschick, A. 1982, in IAU Symposium, Vol. 97, Extragalactic Radio Sources, ed. D. S. Heeschen & C. M. Wade, 307

Crawford, C. S., Allen, S. W., Ebeling, H., Edge, A. C., & Fabian, A. C. 1999, MNRAS, 306, 857

Crenshaw, D. M., Kraemer, S. B., & George, I. M. 2003, ARA&A, 41, 117

Croton, D. J., Springel, V., White, S. D. M., et al. 2006, MNRAS, 365, 11

Curran, S. J., Allison, J. R., Glowacki, M., Whiting, M. T., & Sadler, E. M. 2013a, MNRAS, 431, 3408

Curran, S. J., & Whiting, M. T. 2010, ApJ, 712, 303

Curran, S. J., Whiting, M. T., Murphy, M. T., et al. 2006, MNRAS, 371, 431

Curran, S. J., Whiting, M. T., Sadler, E. M., & Bignell, C. 2013b, MNRAS, 428, 2053

Curran, S. J., Whiting, M. T., Wiklind, T., et al. 2008, MNRAS, 391, 765

Curtis, H. D. 1917, PASP, 29, 206

Dallacasa, D., Stanghellini, C., Centonza, M., & Fanti, R. 2000, A&A, 363, 887

David, L. P., Nulsen, P. E. J., McNamara, B. R., et al. 2001, ApJ, 557, 546

De Breuck, C., Tang, Y., de Bruyn, A. G., Röttgering, H., & van Breugel, W. 2002, A&A, 394, 59

De Grandi, S., & Molendi, S. 2001, ApJ, 551, 153

De Lucia, G., & Blaizot, J. 2007, MNRAS, 375, 2

de Vries, N., Snellen, I. A. G., Schilizzi, R. T., Mack, K.-H., & Kaiser, C. R. 2009, A&A, 498, 641

de Vries, W. H., Hodge, J. A., Becker, R. H., White, R. L., & Helfand, D. J. 2007, AJ, 134, 457

De Young, D. S., Roberts, M. S., & Saslaw, W. C. 1973, ApJ, 185, 809

Deller, A. T., Tingay, S. J., Bailes, M., & West, C. 2007, PASP, 119, 318

Dewdney, P. E., Hall, P. J., Schilizzi, R. T., & Lazio, T. J. L. W. 2009, IEEE Proceedings, 97, 1482

Dexter, J., McKinney, J. C., Markoff, S., & Tchekhovskoy, A. 2014, MNRAS, 440, 2185

Dicke, R. H., Peebles, P. J. E., Roll, P. G., & Wilkinson, D. T. 1965, ApJ, 142, 414

Dicken, D., Tadhunter, C., Morganti, R., et al. 2008, ApJ, 678, 712

Disney, M. J., & Wall, J. V. 1977, MNRAS, 179, 235

Djorgovski, S., & Davis, M. 1987, ApJ, 313, 59

Donahue, M., de Messières, G. E., O'Connell, R. W., et al. 2011, ApJ, 732, 40

Donahue, M., Horner, D. J., Cavagnolo, K. W., & Voit, G. M. 2006, ApJ, 643, 730

Done, C., Gierliński, M., & Kubota, A. 2007, A&A Rev., 15, 1

Dong, R., Rasmussen, J., & Mulchaey, J. S. 2010, ApJ, 712, 883

Douglas, J. N., Bash, F. N., Bozyan, F. A., Torrence, G. W., & Wolfe, C. 1996, AJ, 111, 1945

Dressler, A. 1980, ApJ, 236, 351

—. 1984, ApJ, 281, 512

Dressler, A., Lynden-Bell, D., Burstein, D., et al. 1987, ApJ, 313, 42

Dubinski, J. 1998, ApJ, 502, 141

Duffy, P., & Blundell, K. M. 2012, MNRAS, 421, 108

Dullemond, C. P., & van Bemmel, I. M. 2005, A&A, 436, 47

Dunn, R. J. H., & Fabian, A. C. 2008, MNRAS, 385, 757

Dutson, K. L., Edge, A. C., Hinton, J. A., et al. 2014, MNRAS, 442, 2048

Dwarakanath, K. S., Owen, F. N., & van Gorkom, J. H. 1995, ApJ, 442, L1

Dwarakanath, K. S., van Gorkom, J. H., & Owen, F. N. 1994, ApJ, 432, 469

Ebeling, H., Edge, A. C., Allen, S. W., et al. 2000, MNRAS, 318, 333

Ebeling, H., Edge, A. C., Bohringer, H., et al. 1998, MNRAS, 301, 881

Ebeling, H., Edge, A. C., & Henry, J. P. 2001, ApJ, 553, 668

Ebeling, H., Edge, A. C., Mantz, A., et al. 2010, MNRAS, 407, 83

Edge, A. C. 1991, MNRAS, 250, 103

—. 2001, MNRAS, 328, 762

Edge, A. C., Ivison, R. J., Smail, I., Blain, A. W., & Kneib, J.-P. 1999, MNRAS, 306, 599

Edge, A. C., Stewart, G. C., Fabian, A. C., & Arnaud, K. A. 1990, MNRAS, 245, 559

Edge, A. C., Wilman, R. J., Johnstone, R. M., et al. 2002, MNRAS, 337, 49

Edge, A. C., Oonk, J. B. R., Mittal, R., et al. 2010a, A&A, 518, L46

—. 2010b, A&A, 518, L47

Edge, D. O., & Mulkay, M. J. 1976, Astronomy transformed. The emergence of radio astronomy in Britain

Edge, D. O., Shakeshaft, J. R., McAdam, W. B., Baldwin, J. E., & Archer, S. 1959, MmRAS, 68, 37

Egami, E., Rieke, G. H., Fadda, D., & Hines, D. C. 2006, ApJ, 652, L21

Egami, E., Rex, M., Rawle, T. D., et al. 2010, A&A, 518, L12

Ehlert, S., Allen, S. W., von der Linden, A., et al. 2011, MNRAS, 411, 1641

Ekers, R. D. 2012, in From Antikythera to the Square Kilometre Array: Lessons from the Ancients

Ekers, R. D., & Simkin, S. M. 1983, ApJ, 265, 85

Emonts, B. H. C., Morganti, R., Struve, C., et al. 2010, MNRAS, 406, 987

Emsellem, E., Cappellari, M., Krajnović, D., et al. 2011, MNRAS, 414, 888

Ensslin, T. A., Biermann, P. L., Klein, U., & Kohle, S. 1998, A&A, 332, 395

Everett, J. E. 2005, ApJ, 631, 689

Ewen, H. I., & Purcell, E. M. 1951, Nature, 168, 356

Fabbiano, G., Wang, J., Elvis, M., & Risaliti, G. 2011, Nature, 477, 431

Fabello, S., Catinella, B., Giovanelli, R., et al. 2011, MNRAS, 411, 993

Faber, S. M., & Jackson, R. E. 1976, ApJ, 204, 668

Fabian, A. C. 1994, ARA&A, 32, 277

—. 2012, ARA&A, 50, 455

Fabian, A. C., Reynolds, C. S., Taylor, G. B., & Dunn, R. J. H. 2005, MNRAS, 363, 891

Fabian, A. C., Sanders, J. S., Ettori, S., et al. 2000, MNRAS, 318, L65

Falcke, H. 1996, ApJ, 464, L67

Falomo, R., Pian, E., & Treves, A. 2014, ArXiv e-prints

Fanaroff, B. L., & Riley, J. M. 1974, MNRAS, 167, 31P

Fanti, C., Fanti, R., de Ruiter, H. R., & Parma, P. 1986, A&AS, 65, 145

Fath, E. A. 1909, Lick Observatory Bulletin, 5, 71

Faucher-Giguère, C.-A., & Quataert, E. 2012, MNRAS, 425, 605

Feain, I. J., Ekers, R. D., Murphy, T., et al. 2009, ApJ, 707, 114

Fender, R. P. 2001, MNRAS, 322, 31

Feretti, L. 2000, ArXiv Astrophysics e-prints

Feretti, L., Giovannini, G., Govoni, F., & Murgia, M. 2012, A&A Rev., 20, 54

Ferland, G. J., Fabian, A. C., Hatch, N. A., et al. 2009, MNRAS, 392, 1475

Ferrarese, L., & Merritt, D. 2000, ApJ, 539, L9

Ferrari, C., Govoni, F., Schindler, S., Bykov, A. M., & Rephaeli, Y. 2008, Space Sci. Rev., 134, 93

Fey, A. L., & Charlot, P. 2000, ApJS, 128, 17

Fixsen, D. J. 2009, ApJ, 707, 916

Fomalont, E. B., Frey, S., Paragi, Z., et al. 2000, ApJS, 131, 95

Fomalont, E. B., Petrov, L., MacMillan, D. S., Gordon, D., & Ma, C. 2003, AJ, 126, 2562

Förster Schreiber, N. M., Genzel, R., Newman, S. F., et al. 2014, ApJ, 787, 38

Foschini, L. 2011, Research in Astronomy and Astrophysics, 11, 1266

Franzen, T. M. O., Sadler, E. M., Chhetri, R., et al. 2014, MNRAS, 439, 1212

Gebhardt, K., Bender, R., Bower, G., et al. 2000, ApJ, 539, L13

Gentile, G., Rodríguez, C., Taylor, G. B., et al. 2007, ApJ, 659, 225

Gereb, K., Morganti, R., & Oosterloo, T. 2014, ArXiv e-prints

Giacintucci, S., Markevitch, M., Brunetti, G., Cassano, R., & Venturi, T. 2011a, A&A, 525, L10

Giacintucci, S., Markevitch, M., Brunetti, G., et al. 2014, ArXiv e-prints

Giacintucci, S., Venturi, T., Murgia, M., et al. 2007, A&A, 476, 99

Giacintucci, S., O'Sullivan, E., Vrtilek, J., et al. 2011b, ApJ, 732, 95

Gioia, I. M., Henry, J. P., Mullis, C. R., et al. 2003, ApJS, 149, 29

Giovannini, G., Cotton, W. D., Feretti, L., Lara, L., & Venturi, T. 2001, ApJ, 552, 508

Gitti, M., Brighenti, F., & McNamara, B. R. 2012, Advances in Astronomy, 2012, 6

Gitti, M., Brunetti, G., & Setti, G. 2002, A&A, 386, 456

Gitti, M., Feretti, L., & Schindler, S. 2006, A&A, 448, 853

Gitti, M., Ferrari, C., Domainko, W., Feretti, L., & Schindler, S. 2007, A&A, 470, L25

Gitti, M., Giroletti, M., Giovannini, G., Feretti, L., & Liuzzo, E. 2013, A&A, 557, L14

Gonzalez, A. H., Zabludoff, A. I., Zaritsky, D., & Dalcanton, J. J. 2000, ApJ, 536, 561

González-Martín, O., Masegosa, J., Márquez, I., & Guainazzi, M. 2009, ApJ, 704, 1570

Gooch, R. 1996, in Astronomical Society of the Pacific Conference Series, Vol. 101, Astronomical Data Analysis Software and Systems V, ed. G. H. Jacoby & J. Barnes, 80

Gopal-Krishna, Sirothia, S. K., Mhaskey, M., et al. 2014, ArXiv e-prints

Graham, A. W. 2007, MNRAS, 379, 711

Greene, J. E., Zakamska, N. L., Ho, L. C., & Barth, A. J. 2011, ApJ, 732, 9

Gregory, P. C., & Condon, J. J. 1991, ApJS, 75, 1011

Greisen, E. W. 2003, Information Handling in Astronomy - Historical Vistas, 285, 109

Griffith, M. R., & Wright, A. E. 1993, AJ, 105, 1666

Griffith, M. R., Wright, A. E., Burke, B. F., & Ekers, R. D. 1994, ApJS, 90, 179

—. 1995, ApJS, 97, 347

Gunn, J. E., & Gott, III, J. R. 1972, ApJ, 176, 1

Guo, Y., McIntosh, D. H., Mo, H. J., et al. 2009, MNRAS, 398, 1129

Hales, S. E. G., Riley, J. M., Waldram, E. M., Warner, P. J., & Baldwin, J. E. 2007, MNRAS, 382, 1639

Hamer, S. L., Edge, A. C., Swinbank, A. M., et al. 2012, MNRAS, 421, 3409

—. 2014, MNRAS, 437, 862

Hancock, P. J., Sadler, E. M., Mahony, E. K., & Ricci, R. 2010, MNRAS, 408, 1187

Hardcastle, M. J., Evans, D. A., & Croston, J. H. 2007, MNRAS, 376, 1849

Hardcastle, M. J., & Sakelliou, I. 2004, MNRAS, 349, 560

Harrison, C. M., Alexander, D. M., Swinbank, A. M., et al. 2012, MNRAS, 426, 1073

Harwood, J. J., Hardcastle, M. J., Croston, J. H., & Goodger, J. L. 2013, MNRAS, 435, 3353

Hashimoto, Y., Henry, J. P., & Boehringer, H. 2014, MNRAS, 440, 588

Hasselfield, M., Hilton, M., Marriage, T. A., et al. 2013, J. Cosmology Astropart. Phys., 7, 8

Hazard, C., Mackey, M. B., & Shimmins, A. J. 1963, Nature, 197, 1037

Heald, G., & LOFAR Collaboration. 2013, in American Astronomical Society Meeting Abstracts, Vol. 221, American Astronomical Society Meeting Abstracts 221, 215.07

Heald, G., & LOFAR Collaboration. 2014, in American Astronomical Society Meeting Abstracts, Vol. 223, American Astronomical Society Meeting Abstracts 223, 236.07

Healey, S. E., Romani, R. W., Taylor, G. B., et al. 2007, ApJS, 171, 61

Heckman, T., & Best, P. 2014, ArXiv e-prints

Heckman, T. M. 1980, A&A, 87, 152

Heckman, T. M., Armus, L., & Miley, G. K. 1990, ApJS, 74, 833

Heckman, T. M., Baum, S. A., van Breugel, W. J. M., & McCarthy, P. 1989, ApJ, 338, 48

Heeschen, D. S., & Wade, C. M. 1964, AJ, 69, 277

Helmboldt, J. F., Taylor, G. B., Tremblay, S., et al. 2007, ApJ, 658, 203

Herschel, J. F. W. 1864, Royal Society of London Philosophical Transactions Series I, 154, 1

Herschel, W. 1786, Royal Society of London Philosophical Transactions Series I, 76, 457

—. 1800, Royal Society of London Philosophical Transactions Series I, 90, 255

Hewett, P. C., & Foltz, C. B. 2003, AJ, 125, 1784

Hewish, A., Bell, S. J., Pilkington, J. D. H., Scott, P. F., & Collins, R. A. 1968, Nature, 217, 709

Hey, J. S. 1946, Nature, 157, 47

Hickox, R. C., Jones, C., Forman, W. R., et al. 2009, ApJ, 696, 891

Hirabayashi, H., Hirosawa, H., Kobayashi, H., et al. 2000, PASJ, 52, 955

Hlavacek-Larrondo, J., & Fabian, A. C. 2011, MNRAS, 413, 313

Hlavacek-Larrondo, J., Fabian, A. C., Edge, A. C., et al. 2013, MNRAS, 431, 1638

—. 2012a, MNRAS, 421, 1360

Hlavacek-Larrondo, J., Fabian, A. C., Edge, A. C., & Hogan, M. T. 2012b, MNRAS, 424, 224

Ho, L. C. 2008, ARA&A, 46, 475

Högbom, J. A. 1974, A&AS, 15, 417

Holland, W. S., Bintley, D., Chapin, E. L., et al. 2013, MNRAS, 430, 2513

Horiuchi, S., Fomalont, E. B., Taylor, W. K., et al. 2004, ApJ, 616, 110

Hovatta, T., Tornikoski, M., Lainela, M., et al. 2007, A&A, 469, 899

Hubble, E. 1929, Proceedings of the National Academy of Science, 15, 168

Hubble, E. P. 1925, Popular Astronomy, 33, 252

—. 1926, ApJ, 64, 321

Hudson, D. S., Mittal, R., Reiprich, T. H., et al. 2010, A&A, 513, A37

Ichimaru, S. 1977, ApJ, 214, 840

Iwasawa, K., Allen, S. W., Fabian, A. C., Edge, A. C., & Ettori, S. 1999, MNRAS, 306, 467

Jaffe, W. 1990, A&A, 240, 254

Jaffe, W. J., de Bruyn, A. G., & Sijbreng, D. 1988, in NATO ASIC Proc. 229: Cooling Flows in Clusters and Galaxies, ed. A. C. Fabian, 145–147

Jaffe, W. J., & Perola, G. C. 1973, A&A, 26, 423

Jansky, K. G. 1933a, Popular Astronomy, 41, 548

—. 1933b, Nature, 132, 66

Jansky, K. G. 2005, in Astronomical Society of the Pacific Conference Series, Vol. 345, From Clark Lake to the Long Wavelength Array: Bill Erickson's Radio Science, ed. N. Kassim, M. Perez, W. Junor, & P. Henning, 3–15

Janssen, R. M. J., Röttgering, H. J. A., Best, P. N., & Brinchmann, J. 2012, A&A, 541, A62

Jenness, T., Berry, D., Chapin, E., et al. 2011, in Astronomical Society of the Pacific Conference Series, Vol. 442, Astronomical Data Analysis Software and Systems XX, ed. I. N. Evans, A. Accomazzi, D. J. Mink, & A. H. Rots, 281

Jetha, N. N., Hardcastle, M. J., & Sakelliou, I. 2006, MNRAS, 368, 609

Jiang, L., Fan, X., Ivezić, Ž., et al. 2007, ApJ, 656, 680

Johnston, S., Taylor, R., Bailes, M., et al. 2008, Experimental Astronomy, 22, 151

Jones, P. A., & McAdam, W. B. 1992, ApJS, 80, 137

Kardashev, N. S. 1962, Soviet Ast., 6, 317

—. 1997, Experimental Astronomy, 7, 329

Kaspi, S., Maoz, D., Netzer, H., et al. 2005, ApJ, 629, 61

Kauffmann, G., & Heckman, T. M. 2009, MNRAS, 397, 135

Kellermann, K. I., Pauliny-Toth, I. I. K., & Williams, P. J. S. 1969, ApJ, 157, 1

Kempner, J. C., Blanton, E. L., Clarke, T. E., et al. 2004, in The Riddle of Cooling Flows in Galaxies and Clusters of galaxies, ed. T. Reiprich, J. Kempner, & N. Soker, 335

Kempner, J. C., & Sarazin, C. L. 2001, ApJ, 548, 639

Kharb, P., Gabuzda, D. C., O'Dea, C. P., Shastri, P., & Baum, S. A. 2009, ApJ, 694, 1485

King, A. 2003, ApJ, 596, L27

Kirkpatrick, C. C., Gitti, M., Cavagnolo, K. W., et al. 2009, ApJ, 707, L69

Kirkpatrick, C. C., McNamara, B. R., & Cavagnolo, K. W. 2011, ApJ, 731, L23

Knox, L., Holder, G. P., & Church, S. E. 2004, ApJ, 612, 96

Knudsen, K. K., van der Werf, P. P., & Kneib, J.-P. 2008, MNRAS, 384, 1611

Komatsu, E., Smith, K. M., Dunkley, J., et al. 2011, ApJS, 192, 18

Komossa, S., Burwitz, V., Hasinger, G., et al. 2003, ApJ, 582, L15

Konigl, A., & Kartje, J. F. 1994, ApJ, 434, 446

Körding, E. G., Jester, S., & Fender, R. 2006, MNRAS, 372, 1366

Kormendy, J. 1993, in The Nearest Active Galaxies, ed. J. Beckman, L. Colina, & H. Netzer, 197–218

Kormendy, J., & Ho, L. C. 2013, ARA&A, 51, 511

Kormendy, J., & Richstone, D. 1995, ARA&A, 33, 581

Koss, M., Mushotzky, R., Treister, E., et al. 2011, ApJ, 735, L42

Kovács, A. 2008, in Society of Photo-Optical Instrumentation Engineers (SPIE) Conference Series, Vol. 7020, Society of Photo-Optical Instrumentation Engineers (SPIE) Conference Series

Kovalev, Y. Y., Petrov, L., Fomalont, E. B., & Gordon, D. 2007, AJ, 133, 1236

Kovalev, Y. Y., Kellermann, K. I., Lister, M. L., et al. 2005, AJ, 130, 2473

Kravtsov, A. V., & Borgani, S. 2012, ARA&A, 50, 353

Krichbaum, T. P., Witzel, A., Graham, D. A., et al. 1992, A&A, 260, 33

Labiano, A. 2009, Astronomische Nachrichten, 330, 241

Laing, R. A., & Bridle, A. H. 2014, MNRAS, 437, 3405

Lane, W. M., Cotton, W. D., van Velzen, S., et al. 2014, MNRAS, 440, 327

Laporte, C. F. P., White, S. D. M., Naab, T., & Gao, L. 2013, MNRAS, 435, 901

Lara, L., Feretti, L., Giovannini, G., et al. 1999, ApJ, 513, 197

Lara, L., Giovannini, G., Cotton, W. D., Feretti, L., & Venturi, T. 2004, A&A, 415, 905

Large, M. I., Mills, B. Y., Little, A. G., Crawford, D. F., & Sutton, J. M. 1981, MNRAS, 194, 693

Larson, R. B., Tinsley, B. M., & Caldwell, C. N. 1980, ApJ, 237, 692

Laurent-Muehleisen, S. A., Kollgaard, R. I., Ryan, P. J., et al. 1997, A&AS, 122, 235

Lehnert, M. D., & Heckman, T. M. 1996, ApJ, 462, 651

Li, Y., & Bryan, G. L. 2014, ApJ, 789, 54

Lim, J., Leon, S., Combes, F., & Dinh-V-Trung. 2000, ApJ, 545, L93

Lin, Y.-T., & Mohr, J. J. 2004, ApJ, 617, 879

—. 2007, ApJS, 170, 71

Lin, Y.-T., Partridge, B., Pober, J. C., et al. 2009, ApJ, 694, 992

Lintott, C. J., Schawinski, K., Slosar, A., et al. 2008, MNRAS, 389, 1179

Liu, F. S., Mao, S., & Meng, X. M. 2012, MNRAS, 423, 422

Liu, G., Zakamska, N. L., Greene, J. E., Nesvadba, N. P. H., & Liu, X. 2013, MNRAS, 436, 2576

Liuzzo, E., Giovannini, G., Giroletti, M., & Taylor, G. B. 2010, A&A, 516, A1

Liuzzo, E., Taylor, G. B., Giovannini, G., & Giroletti, M. 2009, A&A, 501, 933

Livio, M., Pringle, J. E., & King, A. R. 2003, ApJ, 593, 184

Loewenstein, M., & Mushotzky, R. F. 1996, ApJ, 466, 695

Longair, M. S. 2011, High Energy Astrophysics

Lonsdale, C. J., Cappallo, R. J., Morales, M. F., et al. 2009, IEEE Proceedings, 97, 1497

Loubser, S. I., Sánchez-Blázquez, P., Sansom, A. E., & Soechting, I. K. 2009, MNRAS, 398, 133

Ly, C., Walker, R. C., & Wrobel, J. M. 2004, AJ, 127, 119

Ma, C.-J., McNamara, B. R., & Nulsen, P. E. J. 2013, ApJ, 763, 63

Machalski, J., Chyży, K. T., Stawarz, Ł., & Kozieł, D. 2007, A&A, 462, 43

Madau, P., & Dickinson, M. 2014, ArXiv e-prints

Madau, P., Ferguson, H. C., Dickinson, M. E., et al. 1996, MNRAS, 283, 1388

Madau, P., Pozzetti, L., & Dickinson, M. 1998, ApJ, 498, 106

Magorrian, J., Tremaine, S., Richstone, D., et al. 1998, AJ, 115, 2285

Mahadevan, R. 1997, ApJ, 477, 585

Maiolino, R., & Rieke, G. H. 1995, ApJ, 454, 95

Marchese, E., Della Ceca, R., Caccianiga, A., et al. 2012, A&A, 539, A48

Marconi, A., & Hunt, L. K. 2003, ApJ, 589, L21

Marriage, T. A., Baptiste Juin, J., Lin, Y.-T., et al. 2011a, ApJ, 731, 100

Marriage, T. A., Acquaviva, V., Ade, P. A. R., et al. 2011b, ApJ, 737, 61

Marscher, A. P. 2006, in American Institute of Physics Conference Series, Vol. 856, Relativistic Jets: The Common Physics of AGN, Microquasars, and Gamma-Ray Bursts, ed. P. A. Hughes & J. N. Bregman, 1–22

Marscher, A. P., Jorstad, S. G., Gómez, J.-L., et al. 2002, Nature, 417, 625

Martin, D. C., Wyder, T. K., Schiminovich, D., et al. 2007, ApJS, 173, 342

Marziani, P., Sulentic, J. W., Dultzin-Hacyan, D., Calvani, M., & Moles, M. 1996, ApJS, 104, 37

Mason, B. S., Weintraub, L., Sievers, J., et al. 2009, ApJ, 704, 1433

Massardi, M., Ekers, R. D., Murphy, T., et al. 2011, MNRAS, 412, 318

Massaro, E., Giommi, P., Leto, C., et al. 2009, A&A, 495, 691

Mathews, W. G., & Guo, F. 2012, ApJ, 755, 13

Mauch, T., Murphy, T., Buttery, H. J., et al. 2003, MNRAS, 342, 1117

McCarthy, I. G., Schaye, J., Bower, R. G., et al. 2011, MNRAS, 412, 1965

McConnell, N. J., Ma, C.-P., Graham, J. R., et al. 2011, ApJ, 728, 100

McConnell, N. J., Ma, C.-P., Murphy, J. D., et al. 2012, ApJ, 756, 179

McCready, L. L., Pawsey, J. L., & Payne-Scott, R. 1947, Royal Society of London Proceedings Series A, 190, 357

McDonald, M., Roediger, J. C., Veilleux, S., & Ehlert, S. 2014, ArXiv e-prints

McDonald, M., Bayliss, M., Benson, B. A., et al. 2012, Nature, 488, 349

McDonald, M., Benson, B. A., Vikhlinin, A., et al. 2013, ApJ, 774, 23

McHardy, I. M. 1978, MNRAS, 185, 927

McNamara, B. R., & Jaffe, W. 1994, A&A, 281, 673

McNamara, B. R., Kazemzadeh, F., Rafferty, D. A., et al. 2009, ApJ, 698, 594

McNamara, B. R., & Nulsen, P. E. J. 2007, ARA&A, 45, 117

—. 2012, New Journal of Physics, 14, 055023

McNamara, B. R., & O'Connell, R. W. 1989, AJ, 98, 2018

McNamara, B. R., O'Connell, R. W., & Bregman, J. N. 1990, ApJ, 360, 20

McNamara, B. R., Rohanizadegan, M., & Nulsen, P. E. J. 2011, ApJ, 727, 39

McNamara, B. R., Wise, M., Nulsen, P. E. J., et al. 2000, ApJ, 534, L135

McNamara, B. R., Russell, H. R., Nulsen, P. E. J., et al. 2014, ApJ, 785, 44

Meier, D. L. 2003, New A Rev., 47, 667

Meier, D. L., Koide, S., & Uchida, Y. 2001, Science, 291, 84

Merloni, A., & Heinz, S. 2013, Evolution of Active Galactic Nuclei, ed. T. D. Oswalt & W. C. Keel, 503

Merloni, A., Heinz, S., & di Matteo, T. 2003, MNRAS, 345, 1057

Merloni, A., Rudnick, G., & Di Matteo, T. 2004, MNRAS, 354, L37

Merritt, D. 1985, ApJ, 289, 18

Messier, C. 1781, Catalogue des Nébuleuses & des amas d'Étoiles (Catalog of Nebulae and Star Clusters), Tech. rep.

Miley, G. 1980, ARA&A, 18, 165

Million, E. T., & Allen, S. W. 2009, MNRAS, 399, 1307

Mirabel, I. F., & Rodríguez, L. F. 1994, Nature, 371, 46

Mirabel, I. F., Rodriguez, L. F., Cordier, B., Paul, J., & Lebrun, F. 1992, Nature, 358, 215

Mittal, R., Hicks, A., Reiprich, T. H., & Jaritz, V. 2011, A&A, 532, A133

Mittal, R., Hudson, D. S., Reiprich, T. H., & Clarke, T. 2009, A&A, 501, 835

Mocanu, L. M., Crawford, T. M., Vieira, J. D., et al. 2013, ApJ, 779, 61

Moore, B., Katz, N., Lake, G., Dressler, A., & Oemler, A. 1996, Nature, 379, 613

Morabito, L. A., & Meyer, D. 2012, ArXiv e-prints

Morganti, R., Oosterloo, T. A., Tadhunter, C. N., et al. 2001, MNRAS, 323, 331

Morganti, R., de Zeeuw, P. T., Oosterloo, T. A., et al. 2006, MNRAS, 371, 157

Morris, D., Palmer, H. P., & Thompson, A. R. 1957, The Observatory, 77, 103

Mullaney, J. R., Daddi, E., Béthermin, M., et al. 2012, ApJ, 753, L30

Muller, C. A., & Oort, J. H. 1951, Nature, 168, 357

Müller, D. 2001, Advances in Space Research, 27, 659

Murphy, T., Sadler, E. M., Ekers, R. D., et al. 2010, MNRAS, 402, 2403

Naab, T., Johansson, P. H., & Ostriker, J. P. 2009, ApJ, 699, L178

Nagai, H., Suzuki, K., Asada, K., et al. 2010, PASJ, 62, L11

Nagar, N. M., Falcke, H., & Wilson, A. S. 2005, A&A, 435, 521

Narayan, R., Mahadevan, R., Grindlay, J. E., Popham, R. G., & Gammie, C. 1998, ApJ, 492, 554

Narayan, R., & McClintock, J. E. 2008, New A Rev., 51, 733

Narayan, R., & Yi, I. 1994, ApJ, 428, L13

—. 1995, ApJ, 452, 710

Nemmen, R. S., Storchi-Bergmann, T., & Eracleous, M. 2014, MNRAS, 438, 2804

Nenkova, M., Ivezić, Ž., & Elitzur, M. 2002, ApJ, 570, L9

Nenkova, M., Sirocky, M. M., Ivezić, Ž., & Elitzur, M. 2008a, ApJ, 685, 147

Nenkova, M., Sirocky, M. M., Nikutta, R., Ivezić, Ž., & Elitzur, M. 2008b, ApJ, 685, 160

Nesvadba, N. P. H., Lehnert, M. D., De Breuck, C., Gilbert, A. M., & van Breugel, W. 2008, A&A, 491, 407

Nulsen, P. E. J., Jones, C., Forman, W. R., et al. 2007, in Heating versus Cooling in Galaxies and Clusters of Galaxies, ed. H. Böhringer, G. W. Pratt, A. Finoguenov, & P. Schuecker, 210

Nulsen, P. E. J., & McNamara, B. R. 2013, Astronomische Nachrichten, 334, 386

O'Dea, C. P. 1998, PASP, 110, 493

O'Dea, C. P., Baum, S. A., & Gallimore, J. F. 1994a, ApJ, 436, 669

O'Dea, C. P., Baum, S. A., Maloney, P. R., Tacconi, L. J., & Sparks, W. B. 1994b, ApJ, 422, 467

O'Dea, C. P., Baum, S. A., Privon, G., et al. 2008, ApJ, 681, 1035

Oegerle, W. R., & Hill, J. M. 2001, AJ, 122, 2858

Oegerle, W. R., & Hoessel, J. G. 1991, ApJ, 375, 15

Oemler, Jr., A. 1976, ApJ, 209, 693

Oosterloo, T., Morganti, R., Crocker, A., et al. 2010, MNRAS, 409, 500

Opik, E. 1922, ApJ, 55, 406

Orienti, M., & Dallacasa, D. 2014, MNRAS, 438, 463

Oser, L., Ostriker, J. P., Naab, T., Johansson, P. H., & Burkert, A. 2010, ApJ, 725, 2312

Ostriker, J. P., & Hausman, M. A. 1977, ApJ, 217, L125

Ostriker, J. P., & Tremaine, S. D. 1975, ApJ, 202, L113

O'Sullivan, E., Vrtilek, J. M., Harris, D. E., & Ponman, T. J. 2007, ApJ, 658, 299

Owen, F. N., Eilek, J. A., & Kassim, N. E. 2000, ApJ, 543, 611

Owen, F. N., & Ledlow, M. J. 1994, in Astronomical Society of the Pacific Conference Series, Vol. 54, The Physics of Active Galaxies, ed. G. V. Bicknell, M. A. Dopita, & P. J. Quinn, 319

Pacholczyk, A. G. 1970, Radio astrophysics. Nonthermal processes in galactic and extragalactic sources

Paczyński, B., & Wiita, P. J. 1980, A&A, 88, 23

Panagoulia, E. K., Fabian, A. C., & Sanders, J. S. 2014, MNRAS, 438, 2341

Parma, P., Murgia, M., de Ruiter, H. R., et al. 2007, A&A, 470, 875

Pauliny-Toth, I. I. K., & Kellermann, K. I. 1966, ApJ, 146, 634

Pawsey, J. L. 1946, Nature, 158, 633

—. 1955, ApJ, 121, 1

Penzias, A. A., & Wilson, R. W. 1965, ApJ, 142, 419

Peres, C. B., Fabian, A. C., Edge, A. C., et al. 1998, MNRAS, 298, 416

Perlman, E. S., Schachter, J. F., & Stocke, J. T. 1999, in Bulletin of the American Astronomical Society, Vol. 31, American Astronomical Society Meeting Abstracts, 1396

Peterson, J. R., Kahn, S. M., Paerels, F. B. S., et al. 2003, ApJ, 590, 207

Petrov, L. 2011, AJ, 142, 105

Petrov, L., Kovalev, Y. Y., Fomalont, E., & Gordon, D. 2005, AJ, 129, 1163

Pfrommer, C., & Enßlin, T. A. 2003, A&A, 407, L73

Pimbblet, K. A., Smail, I., Edge, A. C., et al. 2006, MNRAS, 366, 645

Pizzolato, F., & Soker, N. 2005, ApJ, 632, 821

—. 2010, MNRAS, 408, 961

Planck Collaboration, Ade, P. A. R., Aghanim, N., et al. 2011a, A&A, 536, A8

—. 2011b, A&A, 536, A13

—. 2013a, ArXiv e-prints

—. 2013b, ArXiv e-prints

—. 2013c, A&A, 550, A133

Portinari, L., Moretti, A., Chiosi, C., & Sommer-Larsen, J. 2004, ApJ, 604, 579

Pratt, G. W., Arnaud, M., Piffaretti, R., et al. 2010, A&A, 511, A85

Proga, D., & Begelman, M. C. 2003, ApJ, 592, 767

Quilis, V., Moore, B., & Bower, R. 2000, Science, 288, 1617

Rafferty, D. A., McNamara, B. R., & Nulsen, P. E. J. 2008, ApJ, 687, 899

Raimundo, S. I., & Fabian, A. C. 2009, MNRAS, 396, 1217

Randall, S. W., Forman, W. R., Giacintucci, S., et al. 2011, ApJ, 726, 86

Rawle, T. D., Edge, A. C., Egami, E., et al. 2012, ApJ, 747, 29

Rawlings, S., Saunders, R., Eales, S. A., & Mackay, C. D. 1989, MNRAS, 240, 701

Reber, G. 1940, ApJ, 91, 621

—. 1944, ApJ, 100, 279

Rector, T. A., Stocke, J. T., & Perlman, E. S. 1999, ApJ, 516, 145

Rees, M. J. 1984, ARA&A, 22, 471

Rees, M. J., Begelman, M. C., Blandford, R. D., & Phinney, E. S. 1982, Nature, 295, 17

Reeves, J. N., O'Brien, P. T., & Ward, M. J. 2003, ApJ, 593, L65

Reichardt, C. L., Stalder, B., Bleem, L. E., et al. 2013, ApJ, 763, 127

Reiprich, T. H., & Böhringer, H. 2002, ApJ, 567, 716

Remillard, R. A., & McClintock, J. E. 2006, ARA&A, 44, 49

Rengelink, R. B., Tang, Y., de Bruyn, A. G., et al. 1997, A&AS, 124, 259

Richards, J. L., Max-Moerbeck, W., Pavlidou, V., et al. 2011, ApJS, 194, 29

Rodriguez, C., Taylor, G. B., Zavala, R. T., et al. 2006, ApJ, 646, 49

Rodríguez, L. F., Carrasco-González, C., Montes, G., & Tapia, M. 2014, AJ, 148, 20

Roettgering, H. J. A., Lacy, M., Miley, G. K., Chambers, K. C., & Saunders, R. 1994, A&AS, 108, 79

Rosario, D. J., Santini, P., Lutz, D., et al. 2012, A&A, 545, A45

Rosse, T. E. O. 1850, Royal Society of London Philosophical Transactions Series I, 140, 499

Rossi, P., Mignone, A., Bodo, G., Massaglia, S., & Ferrari, A. 2008, A&A, 488, 795

Rottgering, H. J. A., Wieringa, M. H., Hunstead, R. W., & Ekers, R. D. 1997, MNRAS, 290, 577

Rupke, D. S., Veilleux, S., & Sanders, D. B. 2005, ApJ, 632, 751

Russell, H. R., Fabian, A. C., Sanders, J. S., et al. 2010, MNRAS, 402, 1561

Russell, H. R., McNamara, B. R., Edge, A. C., et al. 2013, MNRAS, 432, 530

—. 2014, ApJ, 784, 78

Ruszkowski, M., & Springel, V. 2009, ApJ, 696, 1094

Ryle, M. 1952, Royal Society of London Proceedings Series A, 211, 351

Ryle, M., & Hewish, A. 1960, MNRAS, 120, 220

Ryle, M., & Neville, A. C. 1962, MNRAS, 125, 39

Ryle, M., Smith, F. G., & Elsmore, B. 1950, MNRAS, 110, 508

Ryle, M., & Vonberg, D. D. 1946, Nature, 158, 339

Sadler, E. M., Ekers, R. D., Mahony, E. K., Mauch, T., & Murphy, T. 2014, MNRAS, 438, 796

Sadler, E. M., Ricci, R., Ekers, R. D., et al. 2008, MNRAS, 385, 1656

—. 2006, MNRAS, 371, 898

Salomé, P., & Combes, F. 2003, A&A, 412, 657

Salpeter, E. E. 1964, ApJ, 140, 796

Samuele, R., McNamara, B. R., Vikhlinin, A., & Mullis, C. R. 2011, ApJ, 731, 31

Sanders, D. B., Phinney, E. S., Neugebauer, G., Soifer, B. T., & Matthews, K. 1989, ApJ, 347, 29

Sanders, J. S., & Fabian, A. C. 2011, MNRAS, 412, L35

Sanderson, A. J. R., Edge, A. C., & Smith, G. P. 2009a, MNRAS, 398, 1698

Sanderson, A. J. R., O'Sullivan, E., & Ponman, T. J. 2009b, MNRAS, 395, 764

Santos, J. S., Tozzi, P., Rosati, P., & Böhringer, H. 2010, A&A, 521, A64

Sarazin, C. L. 1986, Reviews of Modern Physics, 58, 1

Sault, R. J., Teuben, P. J., & Wright, M. C. H. 1995, in Astronomical Society of the Pacific Conference Series, Vol. 77, Astronomical Data Analysis Software and Systems IV, ed. R. A. Shaw, H. E. Payne, & J. J. E. Hayes, 433

Sayers, J., Mroczkowski, T., Czakon, N. G., et al. 2013, ApJ, 764, 152

Schawinski, K., Urry, C. M., Virani, S., et al. 2010, ApJ, 711, 284

Schmidt, M. 1963, Nature, 197, 1040

Schmitt, H. R., & Kinney, A. L. 1996, ApJ, 463, 498

Schombert, J. M. 1986, ApJS, 60, 603

—. 1987, ApJS, 64, 643

Seigar, M. S., Graham, A. W., & Jerjen, H. 2007, MNRAS, 378, 1575

Serra, P., Oosterloo, T., Morganti, R., et al. 2012, MNRAS, 422, 1835

Seyfert, C. K. 1943, ApJ, 97, 28

Shabala, S., & Alexander, P. 2007, Ap&SS, 311, 311

Shakura, N. I., & Sunyaev, R. A. 1973, A&A, 24, 337

Shields, G. A. 1999, PASP, 111, 661

Silk, J. 1976, ApJ, 208, 646

Silk, J., & Rees, M. J. 1998, A&A, 331, L1

Simkin, S. M. 1979, ApJ, 234, 56

Skrutskie, M. F., Cutri, R. M., Stiening, R., et al. 2006, AJ, 131, 1163

Slee, O. B. 1995, Australian Journal of Physics, 48, 143

Slee, O. B., Roy, A. L., Murgia, M., Andernach, H., & Ehle, M. 2001, AJ, 122, 1172

Slee, O. B., Sadler, E. M., Reynolds, J. E., & Ekers, R. D. 1994, MNRAS, 269, 928

Slipher, V. M. 1913, Lowell Observatory Bulletin, 2, 56

—. 1915, Popular Astronomy, 23, 21

—. 1917, Lowell Observatory Bulletin, 3, 59

Smail, I., Ivison, R. J., Blain, A. W., & Kneib, J.-P. 2002, MNRAS, 331, 495

Soker, N. 2006, New A, 12, 38

Southworth, G. C. 1945, Franklin Institute, 239, 285

Springel, V., White, S. D. M., Jenkins, A., et al. 2005, Nature, 435, 629

Staguhn, J., Allen, C., Benford, D., et al. 2008, Journal of Low Temperature Physics, 151, 709

Stanghellini, C., Dallacasa, D., & Orienti, M. 2009, Astronomische Nachrichten, 330, 223

Steidel, C. C., Erb, D. K., Shapley, A. E., et al. 2010, ApJ, 717, 289

Stein, W. A., Odell, S. L., & Strittmatter, P. A. 1976, ARA&A, 14, 173

Stockton, A., & MacKenty, J. W. 1987, ApJ, 316, 584

Stott, J. P., Edge, A. C., Smith, G. P., Swinbank, A. M., & Ebeling, H. 2008, MNRAS, 384, 1502

Stott, J. P., Hickox, R. C., Edge, A. C., et al. 2012, MNRAS, 422, 2213

Struve, C., & Conway, J. E. 2010, A&A, 513, A10

Sullivan, III, W. T. 1982, Classics in radio astronomy

Sullivan, III, W. T. 1991, in Astronomical Society of the Pacific Conference Series, Vol. 19, IAU Colloq. 131: Radio Interferometry. Theory, Techniques, and Applications, ed. T. J. Cornwell & R. A. Perley, 132

Sun, M., Voit, G. M., Donahue, M., et al. 2009, ApJ, 693, 1142

Sunyaev, R. A., & Zeldovich, Y. B. 1972, Comments on Astrophysics and Space Physics, 4, 173

Suzuki, K., Nagai, H., Kino, M., et al. 2012, ApJ, 746, 140

Szomoru, A., Biggs, A., Garrett, M., et al. 2004, in European VLBI Network on New Developments in VLBI Science and Technology, ed. R. Bachiller, F. Colomer, J.-F. Desmurs, & P. de Vicente, 257–260

Tadhunter, C. N., Morganti, R., di Serego-Alighieri, S., Fosbury, R. A. E., & Danziger, I. J. 1993, MNRAS, 263, 999

Tadhunter, C. N., Morganti, R., Robinson, A., et al. 1998, MNRAS, 298, 1035

Tarter, J. 2001, ARA&A, 39, 511

Taylor, G. B. 1996, ApJ, 470, 394

Taylor, G. B., Carilli, C. L., & Perley, R. A., eds. 1999a, Astronomical Society of the Pacific Conference Series, Vol. 180, Synthesis Imaging in Radio Astronomy II

Taylor, G. B., Gugliucci, N. E., Fabian, A. C., et al. 2006a, MNRAS, 368, 1500

Taylor, G. B., O'Dea, C. P., Peck, A. B., & Koekemoer, A. M. 1999b, ApJ, 512, L27

Taylor, G. B., Sanders, J. S., Fabian, A. C., & Allen, S. W. 2006b, MNRAS, 365, 705

Tingay, S. J., Goeke, R., Bowman, J. D., et al. 2013, PASA, 30, 7

Toba, Y., Oyabu, S., Matsuhara, H., et al. 2014, ApJ, 788, 45

Torniainen, I., Tornikoski, M., Lähteenmäki, A., et al. 2007, A&A, 469, 451

Torniainen, I., Tornikoski, M., Teräsranta, H., Aller, M. F., & Aller, H. D. 2005, A&A, 435, 839

Tornikoski, M., Torniainen, I., Lähteenmäki, A., et al. 2009, Astronomische Nachrichten, 330, 128

Tremaine, S. 1990, The origin of central cluster galaxies., ed. R. Wielen, 394–405

Ulvestad, J. S., & Ho, L. C. 2001, ApJ, 562, L133

Urry, C. M., & Padovani, P. 1995, PASP, 107, 803

Valentijn, E. A., & Bijleveld, W. 1983, A&A, 125, 223

van den Bergh, S. 1998, Galaxy Morphology and Classification

van Gorkom, J. H., Knapp, G. R., Ekers, R. D., et al. 1989, AJ, 97, 708

van Haarlem, M. P., Wise, M. W., Gunst, A. W., et al. 2013, A&A, 556, A2

van Weeren, R. J., Röttgering, H. J. A., & Brüggen, M. 2011, A&A, 527, A114

Vanderlinde, K., Crawford, T. M., de Haan, T., et al. 2010, ApJ, 722, 1180

Veilleux, S., Cecil, G., & Bland-Hawthorn, J. 2005, ARA&A, 43, 769

Venturi, T., Castaldini, C., Cotton, W. D., et al. 1995, ApJ, 454, 735

Venturi, T., Dallacasa, D., & Stefanachi, F. 2004, A&A, 422, 515

Vermeulen, R. C., Readhead, A. C. S., & Backer, D. C. 1994, ApJ, 430, L41

Véron-Cetty, M. P., & Véron, P. 2000, A&A Rev., 10, 81

Véron-Cetty, M.-P., Woltjer, L., Staveley-Smith, L., & Ekers, R. D. 2000, A&A, 362, 426

Vikhlinin, A. 2006, ApJ, 640, 710

Voigt, L. M., & Fabian, A. C. 2004, MNRAS, 347, 1130

Voit, G. M., & Donahue, M. 2014, ArXiv e-prints

von der Linden, A., Best, P. N., Kauffmann, G., & White, S. D. M. 2007, MNRAS, 379, 867

Waldram, E. M., Yates, J. A., Riley, J. M., & Warner, P. J. 1996, MNRAS, 282, 779

Walker, R. C., Romney, J. D., & Benson, J. M. 1994, ApJ, 430, L45

Walker, S. A., Fabian, A. C., & Sanders, J. S. 2014, MNRAS, 441, L31

Wall, J. V., & Peacock, J. A. 1985, MNRAS, 216, 173

Wampler, E. J., Burbidge, E. M., Baldwin, J. A., & Robinson, L. B. 1975, ApJ, 198, L49

Werner, N., Oonk, J. B. R., Sun, M., et al. 2014, MNRAS, 439, 2291

Whiley, I. M., Aragón-Salamanca, A., De Lucia, G., et al. 2008, MNRAS, 387, 1253

White, R. L., Becker, R. H., Helfand, D. J., & Gregg, M. D. 1997, ApJ, 475, 479

White, S. D. M. 1976, MNRAS, 174, 19

Whittle, M., & Wilson, A. S. 2004, AJ, 127, 606

Williamson, R., Benson, B. A., High, F. W., et al. 2011, ApJ, 738, 139

Willott, C. J., Rawlings, S., Blundell, K. M., & Lacy, M. 1999, MNRAS, 309, 1017

Wilman, R. J., Edge, A. C., & Johnstone, R. M. 2005, MNRAS, 359, 755

Wilman, R. J., Edge, A. C., & Swinbank, A. M. 2006, MNRAS, 371, 93

Wilson, W. E., Ferris, R. H., Axtens, P., et al. 2011, MNRAS, 416, 832

Wolfe, A. M., & Burbidge, G. R. 1975, ApJ, 200, 548

Wolszczan, A., & Frail, D. A. 1992, Nature, 355, 145

Woody, D. P., Beasley, A. J., Bolatto, A. D., et al. 2004, in Society of Photo-Optical Instrumentation Engineers (SPIE) Conference Series, Vol. 5498, Z-Spec: a broadband millimeter-wave grating spectrometer: design, construction, and first cryogenic measurements, ed. C. M. Bradford, P. A. R. Ade, J. E. Aguirre, J. J. Bock, M. Dragovan, L. Duband, L. Earle, J. Glenn, H. Matsuhara, B. J. Naylor, H. T. Nguyen, M. Yun, & J. Zmuidzinas, 30–41

Wright, A., & Otrupcek, R. 1990, in PKS Catalog (1990), 0

Wright, A. E., Griffith, M. R., Burke, B. F., & Ekers, R. D. 1994, ApJS, 91, 111

Wu, Q., Yuan, F., & Cao, X. 2007, ApJ, 669, 96

York, D. G., Adelman, J., Anderson, Jr., J. E., et al. 2000, AJ, 120, 1579

Yuan, F., & Narayan, R. 2014, ArXiv e-prints

Zdziarski, A. A., Johnson, W. N., Done, C., Smith, D., & McNaron-Brown, K. 1995, ApJ, 438, L63

Zdziarski, A. A., Johnson, W. N., & Magdziarz, P. 1996, MNRAS, 283, 193

Zemcov, M., Borys, C., Halpern, M., Mauskopf, P., & Scott, D. 2007, MNRAS, 376, 1073

Zhao, J.-H., Burns, J. O., & Owen, F. N. 1989, AJ, 98, 64

Zubovas, K., & King, A. R. 2014, MNRAS, 439, 400

ZuHone, J. A., Markevitch, M., Brunetti, G., & Giacintucci, S. 2013, ApJ, 762, 78

Zwart, J. T. L., Barker, R. W., Biddulph, P., et al. 2008, MNRAS, 391, 1545